Developments in Ceramic Materials Research

Dena Rosslere
Editor

NOVA

DEVELOPMENTS IN CERAMIC MATERIALS RESEARCH

DEVELOPMENTS IN CERAMIC MATERIALS RESEARCH

DENA ROSSLERE
EDITOR

Nova Science Publishers, Inc.
New York

Library of Congress Cataloging-in-Publication Data

Developments in ceramic materials research / Dena Rosslere (editor).
p, cm
Include index.
ISBN 13: 978-1-60692-738-0

1. Ceramic materials. I. Rosslere, Dena.
TA455.C43D48 2007
620.1'4--dc22

2007021184

Published by Nova Science Publishers, Inc. ✣ New York

CONTENTS

PREFACE

Ceramics are refractory, inorganic, and nonmetallic materials. They can be divided into two classes: traditional and advanced. Traditional ceramics include clay products, silicate glass and cement; while advanced ceramics consist of carbides (SiC), pure oxides (Al2O3), nitrides (Si3N4), non-silicate glasses and many others. Ceramics offer many advantages compared to other materials. They are harder and stiffer than steel; more heat and corrosion resistant than metals or polymers; less dense than most metals and their alloys; and their raw materials are both plentiful and inexpensive. Ceramic materials display a wide range of properties which facilitate their use in many different product areas. This new book presents leading-edge research in this field from around the world.

Chapter 1 - On-going research into the Postclassic (ca. A.D. 950-1500) Maya of northern Yucatán, Belize and Guatemala reveals that it was a time of dynamic sociopolitical alliances and dominance relations, changing religious cults, long-distance exchange, and migrations of sociopolitical groups from northern Yucatán to central Petén and vice versa. New approaches to understanding the Postclassic Maya have centered on the exchanges of obsidian, salt, symbol sets, and pottery styles. While these studies have advanced our understanding of the sociopolitical complexity and far-reaching trade of some items, the most ubiquitous artifact at most Postclassic Maya sites—pottery—has not been examined to its fullest potential. With few exceptions, pottery is not being analyzed using both mineralogical and chemical techniques. As a result, Maya archaeologists are overlooking data that could identify places of manufacture, manufacturing recipes for different pottery wares, groups, and types, and ultimately exchange patterns.

In order to identify patterns of Postclassic sociopolitical group-specific pottery manufacture, exchange patterns of those groups, and compositional similarities, slipped pottery from the central Petén lakes region of Guatemala was examined using three kinds of analyses that produced stylistic (type-variety classification), technological (petrographic analysis), and chemical compositional data (laser ablation inductively coupled plasma spectroscopy and instrumental neutron activation analysis) of the ceramic pastes and slips. The three different kinds of analyses are complementary in nature as each provides a different categories of data so as to create a more robust and comprehensive dataset. This holistic and interdisciplinary approach is the first in the Maya area to comprehensively combine stylistic and technological characteristics of pottery (technological styles) and will ultimately address issues data about changing social relations during the Postclassic period and how, during

times of stress, people used pottery to help identify themselves as part of a cohesive sociopolitical group.

Chapter 2 - Rotary ultrasonic machining (RUM) is one of the nontraditional machining processes for ceramics. This chapter overviews the recent advances in RUM of ceramics since 2001. It first reports the progress on quality improvement of RUM machined parts – reduction and elimination of edge chipping in RUM of ceramics. After discussing the effects of RUM process parameters (spindle speed, feedrate, ultrasonic vibration power, and grit size) on the edge chipping thickness, practical ways to reduce the edge chipping are presented.

It then presents recent studies on the effects of coolant type, pressure, and delivery mode (continuous versus intermittent) on cutting force and surface roughness when RUM of ceramics.

Finally, it reports the exploratory efforts to apply RUM to machine silicon carbide and ceramic matrix composites (CMC). It discusses the effects of RUM process parameters (spindle speed, feedrate, ultrasonic vibration power, and grit size etc.) on cutting force, surface roughness, tool wear, and chipping size.

Chapter 3 - Laser oxide ceramics ($Y_3Al_5O_{12}$, Y_2O_3, etc. doped with Nd^{3+}, Yb^{3+}, etc.) is the most serious innovation of last years in the field of laser materials.

However, the chapter summarizes new efforts of General Physics Institute of Russian Academy of Sciences, Moscow and State Optical Institute, S.-Petersburg for the research and development of optical ceramics of two other classes of chemical compounds: fluorides and oxysulfides.

The technique of preparation and results of study of a structure of ceramic samples as well as its mechanical, thermal, optical and fluorescence properties is reported.

The analysis of development tendencies in modern photonics shows that recent progress in the area relates substantially with the devices based on the fluoride optical ceramics due to:

- wide spectral transparency window from 0.16 to 11 microns and low phonon spectra preventing from strong fluorescence quenching by the multiphonon relaxation of radiative transitions of impurity ions;
- long lifetimes of metastable levels;
- ease of high level doping of the ceramic host by rare-earth ions (up to 10^{21} cm^{-3});
- excellent mechanical properties, e.g. the CaF_2 optical ceramics, both natural and artificial, has anomalously high fracture toughness, which is three - six fold higher than that for single fluoride crystals;
- high moisture resistance compared to other classes of optical materials with a wide spectral transmission window;
- high thermal conductivity;
- low level of optical losses in ceramic samples, about 10^{-2} - 10^{-3} cm^{-1} in one micron spectral range.

The material properties of natural CaF_2 optical nanoceramics (Suran Deposit, South Ural) as a model object is discussed first. Then the technology development of preparation of synthetic optical fluoride ceramics of different chemical composition is introduced starting from a nanotechnology of preparation of initial raw materials. After that the material properties and advantages of artificial fluoride optical ceramics versus the fluoride single

crystals is discussed. At last, optical and fluorescence properties of rare - earth doped optical fluoride ceramics is presented.

Finally, the synthesis technology and material and spectroscopic properties of translucent oxysulfide optical ceramics of different composition doped with Nd^{3+}, which can be perspective for one micron lasing with high quantum efficiency is considered.

Chapter 4 - The solid state chemistry of polyphosphates in which the transition metal exhibits a trivalent oxidation state is traditionally considered unusual. The great ability of the phosphate frameworks to stabilize this oxidation state is produced for the relatively high charge in $(PO_4)^{3-}$ tetrahedra that favors the formation of anionic frameworks with high degree of mechanical, chemical, and thermal stability. The literature about this kind of compounds shows the existence of several polymorphic forms of these phases which crystal structure has been solved. Unfortunately, even if good crystals for X-ray structure determination were obtained, pure phases had not been prepared. This fact has precluded carrying out any study on the physical properties of these materials. A method based on the control of M/P ratio in the reaction medium has allowed us the synthesis of pure phases. On this basis, the $M(PO_3)_3$ metaphosphates (M^{III}= Ti, V, Cr, Mo and Fe) have been synthesized starting from a mixture of the metallic oxides and $(NH_4)_2HPO_4$, with different M:P ratios by using the ceramic method.

These phases exhibit a crystal structure constructed from (MO_6) octahedra linked through infinite $(PO_3)_\infty$ chains of (PO_4) tetrahedra to give rise to compact three-dimensional crystal structures. The IR spectra of these phases show the characteristic bands of the methaphosphates with ring or chain structure. The absorption electronic spectroscopy recordered by the diffuse reflectance method shows the presence of the spin allowed transitions, being calculated the values of the splitting parameter of the crystalline field (Dq), as well as, these ones of the Racah parameters (B and C). The ESR spectra of these compounds exhibit isotropic signals, centered at values of the *g*-giromagnetic tensor that depends of the nature of the metal and of its S-number of spin. The magnetic study indicates the existence of antiferromagnetic interactions in the majority of the compounds, being detected for several metaphosphates a weak ferromagnetic spin canting phenomenon at low temperatures. In the case of the Ti(III) a ferromagnetic behavior has been observed. The values of the J-exchanger parameter have been calculated using the Rushbrooke and Wood equations for 3D-antiferromagnetic lattices with different values of the spin. In some case, the D-zero field splitting parameter has been calculated from the simultaneously combination of the ESR and susceptibility measurements. The neutron powder diffraction study of the $M(PO_3)_3$ (M^{III}= Cr, Mo and Fe) metaphosphates shows antiferromagnetic structures.

Chapter 5 - During the Romanesque and Gothic time, certain churches and mosques were fitted with ceramic pots embedded in the walls or in the ceiling vaults. The purpose of this action was probably related to acoustic problems, since ceramic pots were the only available way to control and adjust the acoustic response of large rooms. Their effectiveness though is still unknown. Research in old orthodox churches in Greece was performed to investigate the kind of ceramic pots used, the way of embedding on the wall and finally their effect based on most of the acoustic indexes used today for the determination of the acoustic quality in a room. The results were compared with other research performed in Churches and Mosques in other countries.

An analysis of the impulse response of closed spaces with and without ceramic pots, which actually are Helmholtz resonators, showed that their effect on the acoustic quality of a

room is rather poor. Their effectiveness is restricted mainly to the low frequency region. A selective amplification of sound in the near field of resonators was observed as well as a small attenuation in the reverberant part of the field in the resonant frequency and near a higher overtone. A remarkable increase of Clarity and Definition at resonant frequency was also observed. A computer simulation program, based on energy coupling method between the pots and the room, showed that the number of pots per unit volume is the most important parameter that affects the sound quality.

Chapter 6 - Modelling and analysis of a unique geometrically representative Unit Cell has been shown here as the key to predicting the macro thermal transport behaviour of composites, which otherwise requires the employment of a vast experimental infrastructure. Sophisticated materials, such as woven Ceramic Matrix Composites (CMCs), have very complex and expensive manufacturing routes, used by just a few research organizations. This broadens the scope of a modelling strategy to be adopted for the characterization of all possible material designs with various possible constituent volume fractions by using a commercial FE code such as ABAQUS. The variation of material constituents can be incorporated in the Unit Cell model geometry with subtle manipulation of key parameters dictated by quantitative SEM morphological data. Two CMC material systems have been modeled in the present study. The first material has been analysed with a focus on the homogenization of microscopic constituent material properties into the macroscopic thermal transport character. The actual set of property data used for the Unit Cell of this material is obtained from the cumulative property degradation results extracted from the analyses of three sub-models based on the material's unique porosity data. After validating the modeling methodology through a comparison with the experimental data, a geometrically more challenging CMC is modelled with a detailed incorporation of its morphological complexity in order to predict its macroscopic thermal transport behavior. Finally, it is shown how these models can be more efficiently analysed in a multi-processing parallel environment.

Chapter 7 - Synthesis, characterization, device fabrication, modeling and underwater evaluation of porous piezoceramics used in the form of 3-3 piezocomposites are discussed in detail. Piezocomposites have drawn considerable attention in recent years due to their potential application in medical ultrasonic and underwater transducers. Piezocomposites with 3-3 connectivity are produced from porous piezoceramics by filling the pores with suitable polymer materials. In this two-phase material, the PZT and the polymer are self-connected in three dimensions. Synthesis of porous PZT structure by two techniques, namely, BURnout Plastic Spheres (BURPS) and foam reticulation techniques used to obtain wide range of porosity are described. Samples with ceramic volume fraction ranging from 10% to 100% are synthesised and are characterized in terms of their microstructure, piezoelectric charge (d_{33}, d_{31}) and voltage (g_{33},g_{31}) coefficients, the hydrostatic coefficients (d_H and g_H) and hydrostatic Figure-of-Merit. Variations in dielectric, mechanical and piezoelectric properties as a function of ceramic volume fraction/ porosity are discussed. The experimental results are compared with that of a simple analytical model. Finite element modeling (FEM) studies are carried out on hydrophones constructed from porous and dense PZT discs. An axisymmetric model is proposed for dense PZT hydrophone and is validated by an analytical model. A 3-dimensional model is proposed for porous PZT hydrophones. The FEM results agree well with that of the experiments. Details of the hydrophones fabricated with PZT-air and PZT-polymer composites with different configurations are presented. The acoustic performance of the transducers is evaluated underwater. The receiving sensitivity, the electrical impedance

spectra and the directional response of the hydrophones are measured in the frequency range (10-100) kHz. These studies show that the 3-3 piezocomposite transducers have better properties than the transducers made out of dense PZT. The improved properties are the higher hydrostatic coefficients, higher receiving sensitivity and flat response over a wide frequency range. This suggests that the 3-3 piezocomposites made up of porous piezoceramics are very useful for wide-band hydrophone applications. A detailed picture of these studies and the salient features of these materials will be discussed.

Chapter 8 - Scientific advances concerning many ceramic materials have enabled technological breakthroughs globally. The superior combinations of thermal, insulating, electrical and mechanical properties have become the basis of huge applications in the packaging of microelectronics and power semiconductors. Miniaturization and integration of metal via into ceramic substrate make it feasible to construct multilayer circuit inter connections. This advantage provides the possibility to mount electronics component and circuitry directly onto both side of ceramic substrate. This packaging advance makes ceramic very attractive to field emission display application. Field emission display is able to combine the high quality images and large viewing angles of cathode ray tube, while delivering it in the flatness attributed to liquid crystal display, and utilizing just a fraction of the electrical power required by plasma display panel. Field emission display is predicted to be one of the most promising flat panel displays that will take off in the future. Currently relying on the semiconductor thin film micro-fabrication technology, field emission displays are fabricated mostly on soda-lime glass substrate. Although this is compatible to the liquid crystal display technology, the row and column electrodes of a field emission display have to be allocated to the sides of glass substrate. Furthermore, the existing technology still has difficulties to deliver large area micro field emitters with acceptable uniformity. If the key components of micro field emitter matrix pixels can be produced entirely on the front side of ceramic substrate, and are electrically connected to the backside drive and control circuit through the micro via, this allows construction of micro field emitters right up to the edge of ceramic substrate. In addition, a large size display can be constructed by tiling ceramic substrates precisely. In this chapter, the micro-fabrication of field emitters on ceramic substrate is presented. Electron emission characteristics of these micro field emitters were studied, and results from the microstructures are analysed.

Chapter 9 - A sol-gel reaction starting from Si and Zr alkoxides, in water-ethanol mixtures, was employed to obtain praseodymium, vanadium and iron doped zirconium silicate powders (zircon). The reactions were performed by modulating both: a) the amount of metal salt in the starting mixture (Me/Zr molar ratio in the range 0.05-0.1) and b) the temperature of firing (600-1200°C). In the case of V-doped pigments, samples were synthesized also in the presence of a constant amount (0.26 salt/Zr molar ratio) of mineralizers (LiF, LiCl, NaF, NaCl, KF, KCl).

The samples were characterised by X-ray diffraction, SEM micrographs, specific surface area determinations and UV-Vis diffuse reflectance spectroscopy. XPS analyses were performed on V-doped zircon pigments by studying in particular the Zr 3d, Si 2p and V 2p regions. The colour of the pigments was characterized on the grounds of the CIE (Commission Internationale de l'Eclairage) standard procedure (CIE L*a*b* measurements). Results from the structural, morphological and optical characterisations are examined and cross-compared to produce a consistent picture of the key factors leading to the formation, growth and optical properties of the reaction products.

In: Developments in Ceramic Materials Research
Editor: Dena Rosslere, pp. 1-34
ISBN 978-1-60021-770-8

Chapter 1

POSTCLASSIC MAYA CERAMIC ADVANCES: CONJOINING STYLISTIC, TECHNOLOGICAL, AND CHEMICAL COMPOSITIONAL DATA

Leslie G. Cecil*
Stephen F. Austin State University
Department of Sociology, Anthropology, and Gerontology,
Nacogdoches, TX 75962

ABSTRACT

On-going research into the Postclassic (ca. A.D. 950-1500) Maya of northern Yucatán, Belize and Guatemala reveals that it was a time of dynamic sociopolitical alliances and dominance relations, changing religious cults, long-distance exchange, and migrations of sociopolitical groups from northern Yucatán to central Petén and vice versa. New approaches to understanding the Postclassic Maya have centered on the exchanges of obsidian, salt, symbol sets, and pottery styles. While these studies have advanced our understanding of the sociopolitical complexity and far-reaching trade of some items, the most ubiquitous artifact at most Postclassic Maya sites—pottery—has not been examined to its fullest potential. With few exceptions, pottery is not being analyzed using both mineralogical and chemical techniques. As a result, Maya archaeologists are overlooking data that could identify places of manufacture, manufacturing recipes for different pottery wares, groups, and types, and ultimately exchange patterns.

In order to identify patterns of Postclassic sociopolitical group-specific pottery manufacture, exchange patterns of those groups, and compositional similarities, slipped pottery from the central Petén lakes region of Guatemala was examined using three kinds of analyses that produced stylistic (type-variety classification), technological (petrographic analysis), and chemical compositional data (laser ablation inductively coupled plasma spectroscopy and instrumental neutron activation analysis) of the ceramic pastes and slips. The three different kinds of analyses are complementary in nature as each provides a different categories of data so as to create a more robust and

* Phone: (936) 468-3980; Fax: (936) 468-2162; Email: cecillg@sfasu.edu

comprehensive dataset. This holistic and interdisciplinary approach is the first in the Maya area to comprehensively combine stylistic and technological characteristics of pottery (technological styles) and will ultimately address issues data about changing social relations during the Postclassic period and how, during times of stress, people used pottery to help identify themselves as part of a cohesive sociopolitical group.

INTRODUCTION

Analysis of pottery manufacture in many regions of the world has focused on stylistic, mineralogical, *or* chemical analyses to provide information concerning identity, boundary maintenance/establishment, and exchange patterns. While many of these studies have proven fruitful, they have been limited in scope due in most part to the limitation of the methodology used. However, when data from stylistic, mineralogical, and chemical analyses of pottery are examined together with ethnohistorical, architectural, and burial data, it is possible to infer patterns of manufacture that relate to identity and exchange.

In this chapter, I argue that this combination of analyses, and not any single methodology used alone, provides the data sets that allow me to suggest which sociopolitical groups in central Petén, Guatemala may have manufactured what kinds of pottery with different stylistic and technological characteristics. This is possible because the different kinds of pottery result from choices made by Postclassic Petén Maya potters within a social structure that embodies their identity. The existence of these stylistically- and technologically-based pottery groups that are embedded in structure and agency allow the archaeologist to study materials such as clay and mineral inclusions and patterns of pottery manufacture as practice. As such, the patterns of manufacture are not merely " 'added on' in order to signal group identity," but are choices made by the potter "by which a sense of group identity is formed and transformed as being coeval with and identical to the process by which a sense of technique is formed and transformed" (Dietler and Herbich 1998:247). As such, potters, as well as other members of a society, may continually construct and reconstruct their identity by creating and recreating their social structures through daily activities such as pottery manufacture (Giddens 1984:17).

As a daily activity, pottery manufacture becomes a social activity when the choices made during the manufacturing process are examined as a social phenomenon. The patterns of manufacture (choices) are made in a specific manner, under the umbrella of the culture's social structure and reproduced. As such, patterns of manufacture may be reproduced without the potter being fully cognizant of the set of "rules" or operational sequences established through the mediation of structure and agency (Lechtman 1977; Lemonnier 1992). For example, a clay source may be continually used without question because one social group does not have access to clays in another territory or because it is customary to use that source. "These dispositions of choice and perceptions in the domain are interwoven with similarly formed patterns of choice and perceptions in the domain of social relations and cultural categories in ways that evoke and reinforce each other such that they come to be perceived as 'natural'" (Dietler and Herbich 1998:246). Therefore, clusters of pottery traits (stylistic, mineralogical, and chemical), as well as architectural designs and burial practices, are compatible with the social structures and they reflect the social identity and history of the culture.

According to ethnohistorical documents, Petén Postclassic (ca. AD 1000-1525) sociopolitical groups, primarily the Itza and Kowoj, contested political boundaries and changed alliances (Jones 1998). If boundaries were established because of this unrest, access to resources may have influenced the choices that Maya potters made during manufacturing because some social groups may not have had access to specific resources within another sociopolitical group's territory. Choices based on resources include, but are not limited to, clays and pigments.

The example of pottery manufacture and trade that follows demonstrates that neither descriptive nor archaeometric analyses alone would be able to answer how Petén Postclassic potters defined themselves through their material culture. I conjoin classification with mineralogical and chemical analyses to define groups of pottery characteristics of the two main warring Petén Postclassic sociopolitical groups at the time of the Spanish conquest.

THE KOWOJ AND ITZA OF NORTH-CENTRAL YUCATÁN, MÉXICO AND CENTRAL PETÉN, GUATEMALA

In the mid-sixteenth century, Bishop Diego de Landa identified 16 provinces in northern Yucatán (Tozzer 1941:17-18) some headed by different leaders (*cuchcabalob* or *kuchcabaloob'*). Each group is described as being a distinct social and/or political group (Roys 1957). During the Late Postclassic period, these provinces/territories were under the rule of the League of Mayapán headed by the Xiw, the Kokoms, and the Canuls, although the Kokoms and Xiws dominated rule and are the best documented in the ethnohistoric record (Ringle and Bey 2001; Roys 1972). Cultures at sites on the east coast of the Yucatán Peninsula and Belize had friendly ties with Mayapán (Kepecs and Masson 2003:43).

According to the *Chilam Balam of Mani*, in a Katun 2 Ajau (A.D. 751?), the Xiw (also Tutul-Xiw) arrived in the Pu'uc region from the west (the land of Tulapan) after stopping in Petén 500 years earlier; there they founded and governed Uxmal (Craine and Reindorp 1970:138-139; Restall 1998:141). Kowalski (1987:56-58) suggests that they came from Tabasco. They joined with the Kokom/Itza as part of a *multepal* ("joint rule") that ruled Mayapán. The Xiw presence within the walled city of Mayapán may relate to construction of basic ceremonial groups near the cenote Ch'en Mul (Proskuriakoff 1962; Pugh 2001a, 2001b) as well as to the red-decorated pottery with a light-colored clay paste. Edmonson (1982:*x*, 24, 45-46) states that the Xiw controlled the western half of Yucatán, had a different ritual calendar from the Kokom/Itza, and were represented by the *yaxum* or blue bird (*Cotinga amabilis*). After a series of internal revolts with the Kokom and the later Spanish presence, the Xiw moved the seat of the *may* (256 years) and the center of their rule to Maní by A.D. 1539 (Edmonson 1986:41).

The *Chilam Balam of Tizimin* states that the Kokoms claim to have come from Chich'en Itza after two *k'atuns* (one *k'atun* is 20 years) of exile (Edmonson 1986; Roys 1962). This Itza lineage founded Mayapán and seated the *may* in a Katun 8 Ajau (ca. A.D. 1080-1104 or A.D. 1185-1204) (Milbrath and Peraza Lope 2003:Table 1; Roys 1962:43). At this time, the earliest structures in the Mayapán ceremonial core that resemble those from Chich'en Itza (the Itza homeland) were constructed: the Castillo-like center temple, serpent-column facades, colonnaded halls, and small sacrificial altars (Proskouriakoff 1962:133).

Ringle et al. (1998) believe that the feathered serpent imagery at Mayapán is associated with the Kokom presence, the Quezalcoatl-Kukulcan cult, and Itza religious identity. The Itza lineage of the Kokom ruled Mayapán for approximately 100 years, and in A.D. 1362/82 a revolt brought a different Kokom lineage (the rival Itza) into power at Mayapán (Roys 1962:44-46; Tozzer 1941:26). However, problems soon arose for the Kokom as the Xiw revolted against them. Ralph Roys (1962:47) notes that the Kokom lineage ruler at Mayapán and other followers "fled by sea down the east coast, and went inland to Lake Petén" and settled at Tayasal, which may indicate an earlier migration of the Itza to Petén. Munro Edmonson (1986:58) also states that a migration occurred after the destruction of Mayapán and "they went to the heart of the forest—Chak'an Putun, Tan Xuluc Mul by name." Chak'an Putun is believed to be located in the territory of Chak'an Itza—the northwestern quarter of Petén Itza territory (Jones 1998; Schele and Mathews 1998:204). As a result of the expulsions and revolts, Kokom rulership at Mayapán ended, Mayapán was destroyed, and nobles carried codices to, and built temples in, their homelands—the 16 independent states (Roys 1962:47; Tozzer 1941:38, 98). In the end, the Kokom remained in eastern Yucatán and the Xiw in western Yucatán. Kokom patronyms, such as Balam, Chan, and Tun, were most numerous in the sixteenth century provinces of Sotuta and Mani (Roys 1957:Table 1).

Another lineage at Mayapán was the Kowoj (also Couoh). According to the *Chilam Balam of Chumayel* (Roys 1933:69), these Kowoj were the guardians of the east gate and may have been related to the Xiw. Their association with the Xiw is strengthened by the highest frequency of Kowoj lineage names outside of the Petén lakes region occurring at Maní, the Xiw capital after the fall of Mayapán (Roys 1957:9, 66). Kowoj, Kab', Kamal, and Kawich patronyms were recorded in the towns of Tekit, Pencuyut, and Peto in the sixteenth and seventeenth centuries in northern Yucatán (Roys 1957:Table 5; also Jones 1998:Table 1.1). In addition to lineage names, Landa (Tozzer 1941:56) and Roys (1957:168) state that the Kowoj lineage powerfully ruled the province of Champoton in the sixteenth century, and that they recreated architecture similar to that present at Mayapán at towns in that region (e.g., Isla Cilvituk) (Alexander 1998, 2005a, 2005b). In addition to the presence of Kowoj lineage names in northern Yucatán, lineage names have also been documented in eastern Yucatán (Cozumel), Belize (Tipuj), and central Petén (Zacpetén and Topoxté Island) (Jones 1998).

In central Petén, ethnohistorical research has indicated that the Itza and Kowoj (as well as other sociopolitical groups) occupied territory in the region in the sixteenth and seventeenth centuries (Jones 1998:18). Spanish documents and Postclassic to Colonial period (thirteenth through eighteenth centuries) native histories of these groups (especially the Xiw and the Itza) record their presence, various alliances in Petén, as well as repeated movements to and from northern Yucatán. The documents suggest that Petén was divided into administrative provinces headed by and named after a dominant lineage, each controlling several subprovinces throughout the area.

The Itza controlled the southern and western basin of Lake Petén Itzá, an area stretching from Lake Quexil west to Lake Sacpuy, with their capital, Nojpeten (or Taiza), on modern Flores Island (Figure 1) (Boot 2005; Jones 1998; Jones et al. 1981). The Itza may have been an alliance of multiple sociopolitical groups (Jones 1998). Their Late Postclassic ruler, Kan Ek', claimed ancestry from Chich'en Itza in the northern Yucatán peninsula, and he stated that the Itza migrated from Chich'en Itza when it fell at approximately A.D. 1200 (Edmonson 1986; Jones 1998; Roys 1933). In A.D. 1695, AjChan, Kan Ek's nephew, also claimed that his deceased mother was from Chich'en Itza, and "members of the Itza nobility were still

living there in the seventeenth century and successfully avoiding Spanish recognition" (Jones 1998:11).

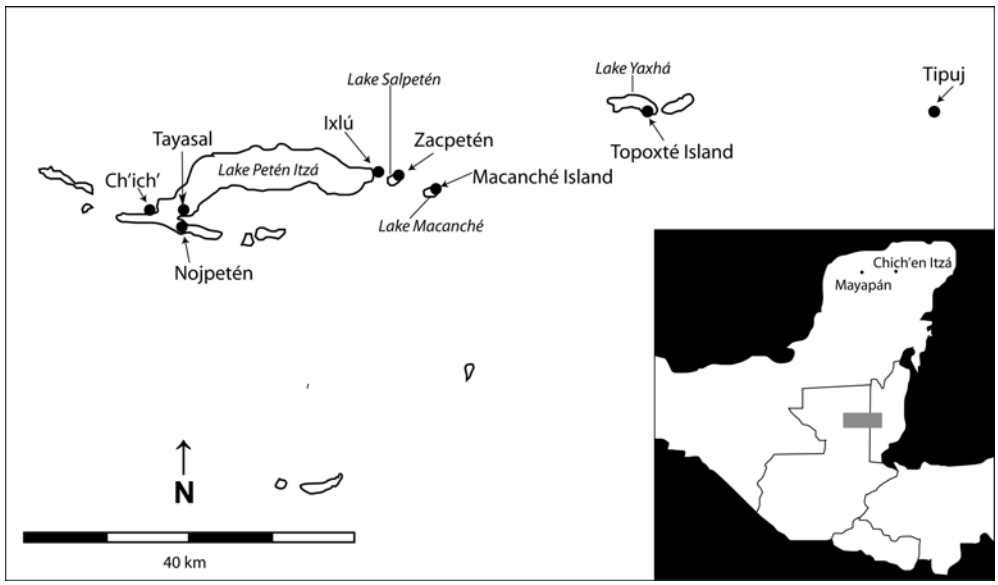

Figure 1. Map of the Postclassic archaeological sites from central Petén and western Belize discussed in the text.

Additionally, A.D. 1584 and A.D. 1688 lists of married residents record Can (Kan) as the most prominent name in Hocaba and Sotuta and Ek' commonly occurs in the Cehpech and Cochuah provinces (Roys 1957:Table 1). Although this indicates a later migration of Itza to central Petén, many scholars (Boot 1997, 2005; Rice et al. 1996; Schele and Grube 1995; Schele et al. 1998; Schele and Mathews 1998) state that epigraphic and archaeological materials suggest that Itza origins might have been in central Petén in the Classic period, and portions of the Itza may have begun migrations to and from northern Yucatán as early as A.D. 900. Regardless of their migration history, the Itza were present at Lake Petén Itzá when Cortés traveled through Petén on his way to Honduras in A.D. 1525 (Cortés 1976:219-285).

Itza architecture is characterized by formal open halls, raised shrines, and architectural sculpture that include raptorial birds, coyotes, serpents, and small phalli and turtles (Pugh 1996:206-211; D. Rice 1986, Rice et al.1996). Associated with the temple structures on an east-west axis are caches of east-facing human skulls placed in rows or caches of two human crania (Duncan 2005). Similar associations of architecture and crania are found at Chich'en Itza (Duncan 2005; D. Rice 1986; Rice et al. 1996).

The Kowoj controlled the northeastern area of Lake Petén Itzá and the east-central Petén lakes (Lake Salpetén, and possibly Lake Yaxhá and Lake Macanché) (Jones 1998). They claimed to have migrated from Mayapán around A.D. 1530; however, they too may have had a series of earlier migrations to and from Mayapán, of which one occurred after the fall of that site (ca. A.D. 1450) and the last may have been ca. A.D. 1530 (Cecil 2001, 2004; Rice et al. 1996). Petén Kowoj kinship patronyms were linked to those of prestigious individuals at Mayapán (Jones 1998:Table 1.1; Roys 1957:Table 1) and the *Chilam Balam of Chumayel* stated that the guardian of the east gate of Mayapán was a Kowoj (Roys 1933:79).

The main architectural pattern shared by the Petén and Yucatecan Kowoj is the temple assemblage (Pugh 2001a). First defined by Proskouriakoff (1962) at Mayapán, this complex is present at Topoxté Island and Zacpetén and variants also occur at Ixlú and Muralla de León in central Petén (Pugh 2001b:253), Tipuj in western Belize (Cecil and Pugh 2004), and Isla Cilvituk in Campeche, México (Alexander 1998). In addition to temple assemblages, ossuaries and individual skull deposits are common among the Kowoj (Duncan 2005).

Given this ethnohistorical and archaeological context, it is important to make use of the Postclassic slipped pottery of the central Petén lakes area to delineate differences among sociopolitical identities, especially between sites/territories of the Kowoj and Itza. One way to accomplish this task is through the analysis of the stylistic and technological characteristics of the pottery. These pottery characteristics will demonstrate that: 1) technological and stylistic choices have a social context; 2) style and technology are social reproductions of Postclassic society; 3) some stylistic and technological choices were more compatible than others within Postclassic Maya society; and 4) these compatible choices reinforced the existing technology and social ideology. By identifying distinct patterns of choices made during pottery manufacture through a variety of stylistic, technological, and chemical methods, it will be possible to refine our understanding of the sociopolitical relations and exchange networks of the Kowoj and Itza of central Petén.

METHODOLOGY

In order to identify stylistic and technological patterns manifest in pottery manufacture and exchange patterns that reflect the Postclassic sociopolitical group identities discussed above, three kinds of analyses were conducted to gather stylistic (type-variety classification), technological (petrographic analysis), and chemical compositional data (INAA and LA-ICP-MS) of the three ceramic wares discussed below. These three different levels of analyses are complementary in nature as each provides a different kind of data so as to create a more robust and comprehensive dataset. Because I seek to identify manufacturing and exchange patterns in the central Petén lakes region, one kind of analysis cannot take precedence over another (Blomster et al. 2005; Flannery et al. 2005; Neff et al. 2006; Neff et al. 2006; Sharer et al. 2006; Stoltman et al. 2005). Past experience has demonstrated that a combination of these three kinds of analyses is a productive methodology for understanding the stylistic, technological, and chemical parameters of pottery manufacture and exchange and its associations with different sociopolitical groups (Cecil 2001, 2004; Cecil and Neff 2006).

Stylistic Analysis—Type-Variety Classification

The first level of study consisted of a typological analysis using the type-variety system (Smith et al. 1960). This hierarchical system uses a series of categories—ware, group, type, and variety, in descending inclusiveness—to organize levels of variability in archaeological pottery. Postclassic slipped sherds from Ch'ich', Ixlú, Zacpetén, and Tipuj were classified as to ware, group, type, and, where possible, variety. For purposes of studying technological and stylistic attributes, it is particularly useful to consider pottery at the ware and group levels

because these levels of classification convey information about geographical location, time period, decoration, and function (Rice 1982:50). Three paste-based (as opposed to slip-based) wares had been identified in previous studies of these materials: Snail-Inclusion, Vitzil Orange-Red, and Clemencia Cream (Chase 1983; Rice 1979). These distinctive wares were used in producing the five slipped Postclassic ceramic groups that were used in the analysis of technological styles: Paxcamán, Fulano, and Trapeche in Snail-Inclusion Paste ware, Augustine in Vitzil Orange-Red Paste ware, and Topoxté in Clemencia Cream Paste ware (Table 1).[1] As part of the classification procedure, information was recorded concerning slip color, thickness, and degree of fireclouding, decorative programs, and combination of motifs.

While the type-variety system is the primary method for pottery classification in Mesoamerica, there are many assumptions and problems with this kind of classification. First, pottery types do not necessarily correspond to different cultural affiliations, potter's knowledge, potter's capacity, or accidents of production (Shepard 1956:317). Second, many archaeologists magnify slight differences and unnecessarily define new pottery types (Ball 1982; Forsyth 1989; Rice 1976). This is a result of archaeologists not adhering to the original classification rules. Finally, a strict use of the type-variety system often leads to misclassification of sherds that come from the same vessel. Because of differences in firing over the surface or a vessel, uneven erosion patterns due to deposition or placement of decoration or slip on a vessel, sherds from the same vessel may appear as two distinct types (Demarest 1986). While there are limitations to this descriptive methodology, it is the commonly-used schema by which Mesoamerican archaeologists discuss ceramics and as long as the researcher understands these limitations, type-variety analysis of a ceramic sample can be fruitful.

Mineralogical Analysis—Petrographic Analysis

In order to further investigate the possibility of different manufacturing recipes that may contribute to technological and stylistic groupings that reflect Postclassic Maya sociopolitical identity, I examined 278 sherds from the different pottery wares that were excavated from Ch'ich', Ixlú, Zacpetén, and Tipuj. I non-randomly chose samples from the larger 551 data set to ensure that paste variability visible to the unaided eye was represented. Petrographic analysis allowed me to identify minerals that were present in the clay pastes of different vessels. Petrography allows analysis of many clay materials and inclusions at one time. One

[1] A stratified random sample of 551 sherds was selected to represent the diversity present in the total sample to be used in the subsequent analyses. After conducting the typological analysis, I determined the variability present (pottery pastes, decorative, and excavated structures represented) and selected a smaller proportional allocation with the goal of selecting 50 decorated sherds from each ceramic group and archaeological site. In cases where 50 decorated sherds were not available, I selected monochrome slipped sherds by stratified random sampling. First, I placed all decorated sherds from one site on a table grouped according to the identification number of the structure from which they were recovered. Second, I ascertained the number of pottery types and varieties represented at each structure. The number of sherds per type and variety and structure determined the number to be randomly selected and the number selected varied depending on the structure, so that buildings with more decorated types were sampled more often. Third, each lot number was recorded on a piece of paper and the numbers were placed in a container according to the structure, type, and variety. The predetermined number of sherds to be selected for each structure determined how many lot numbers were drawn for inclusion in the sample.

can study “the clay itself, natural inclusions in the clay, purposefully added inclusions, and glazes or slips on the clay surface” (Childs 1989:24).

Petrographic analysis has been adapted from geological techniques of analysis for the study of soils and rocks and is useful for archaeological ceramics because, to a large extent, geological sources differ enough across regions to allow for comparison of different clays (Blatt 1992). These methods are applicable to pottery analysis because pottery can be regarded as a metamorphosed sedimentary rock due to the composition of a sherd consisting of clastic grains imbedded in a clay matrix which has been transformed to “rock” through the process of firing (Bishop et al. 1982; Rice 1987b:376). Understanding these basic principles of geology, plus other principles of optical mineralogy, allow the description of pottery pastes and clays.

Additionally, petrographic analysis can be used to establish technological characteristics within the Postclassic ceramic complex because petrographic analysis aids in the classification of sherds into specific groups (Childs 1989:24). This aspect of petrography is most helpful when a sherd or vessel cannot be assigned to a typology based on surface decoration, vessel form, or rim diagnostics (Shepard 1956:165). I anticipated that the above situation would arise because many of the sherds are highly eroded and because the variability within pastes may be great enough that I could not easily identify the ceramic group. As a result, paste characteristics (clay matrix and inclusions) were examined to establish possible differences between types.

Once a sherd or vessel was assigned to a ceramic group, I could develop additional behavioral information from a classification based on petrography because petrography can answer process-oriented questions from a diachronic or synchronic perspective (Carr 1990; Childs 1989). It is possible to create a time series that models shifts in technological characteristics such as paste and temper characteristics (Braun 1982, 1985; Carr 1990).

All of the samples (described above) were cut with a wet saw for the preparation of thin section slides. The cut sherds were sent to Spectrum Petrographics where they were embedded in an epoxy block. The most fragile sherds were vacuum impregnated and then embedded in an epoxy block. The block was cut in such a manner that a thin section measuring .03 mm thick resulted. The resulting thin section allowed me to identify minerals in the clay paste with the use of a polarizing microscope.

Mineral size, shape, roundness, and frequency provide qualitative and quantitative data by which to infer manufacturing recipes. Mineral size, shape, and roundness (qualitative data) are established through a comparison of various graphs and tables (Shackley 1975:44-51). The most common geological method of determining the quantity of minerals in a thin section (quantitative data) is point counting. Point counting determines the number of different minerals along a predetermined area (for example, 10 mm) of the length and width of the section (Chayes 1956). Various studies have employed different methods for counting the frequency of inclusions (e.g., Middleton et al. 1985; Peacock 1973). However, because I was not interested in the absolute number of minerals in the thin section, but rather in what minerals exist and their relative frequency, I used a non-volumetric area frequency counting method (Cecil 2001; Dickenson and Shutler 1979). Area counting pertains to counting all of the minerals in the standard image.

Table 1. Postclassic Slipped Pottery, Ware, Groups, and Types

Ware	Ceramic Groups	Ware Description
Clemencia Cream Paste	Topoxté	Clemencia Cream Paste ware ceramics are characterized by a white to cream-colored marly paste with a red slip. Vessel forms include dishes, bowls, and jars (Bullard 1970; Rice 1979:15-21). Pastel Polychrome has a cream-colored marly paste with black painted decoration on unslipped areas of red-slipped Topoxté group vessels (Rice 1979:21-28). Canté Polychrome has red-and-black painted decoration on unslipped areas of red-slipped vessels. Chompoxté Red-on-cream vessels have red painted decorations on unslipped interiors of red slipped vessels (Rice 1979:28-42).
Snail-Inclusion Paste	Paxcamán	Paxcamán ceramics are characterized by red to red-orange slips with a brown to gray snail-inclusion paste (Adams and Trik 1961:125-137). Ceramic forms include simple hemispherical bowls, collared bowls, narrow neck jars, and neckless jars (tecomates). Ixpop Polychrome has a band of decoration of black lines on the usually unslipped background paste color of the vessel (Adams and Trik 1961:125-127). Sacá Polychrome is another Paxcamán type that is distinguished by red-and-black-on-cream decoration with red slipping on undecorated portions of the vessel (Cowgill 1963:237-243). Macanché Red-on-paste is characterized by red painted decoration on paste and undecorated areas are slipped red. Paxcamán ceramics can also be incised and are classified as Picú Incised: Picú Variety (pre-fire incising) and Picú Incised: Thub Variety (post-fire incising) (Chase 1983).
Snail-Inclusion Paste	Fulano	Fulano ceramics are similar to Paxcamán and Trapeche ceramics, but the slip is black with a low luster (Cecil 2001: 169-180). This ceramic group includes tripod dishes, narrow neck jars, and collared bowls. Some vessels are slipped black with red-on-paste decoration on the unslipped portions of tripod dishes (Sotano Red-on-paste) (Cecil 2001:173-177). Fulano ceramics can also be incised (Mengano Incised) with pre-fire (Bobo Variety) or post-fire (Mengano) varieties (Cecil 2001:177-180).
Snail-Inclusion Paste	Trapeche	Trapeche ceramics have a paste similar to Paxcamán ceramics, but the slip varies from pink to tan-orange. Forms in the Trapeche ceramic group include hemispherical bowls, collard bowls, narrow-neck jars, and ncekless jars (Chase 1979:104-105, 110-112). Within the Trapeche ceramic group, the Mul Polychrome type is decorated with a design band of reddish-brown to black paint on an unslipped or cream-slipped surface (Chase 1979:110-112). Picté Red-on-paste types are characterized by a band of red painted decoration on pink to tan-orange slipped vessels (Rice 1987a:149). The incised variety of the Trapeche ceramic group is Xuluc Incised and has two varieties: Tzalam Variety (pre-fire incised) and Ain Variety (post-fire incised) (Chase 1979:106-110).
Vitzil Orange-Red	Augustine	The Augustine ceramic group is characterized by reddish-brown to orange coarse paste with a glossy orange-red slip (Sharer and Chase 1976). The most common forms are jars and tripod dishes with effigy feet. Zaczuuz Tan vessels have characteristic tan areas on the exterior of the vessels that are slipped orange. Pek Polychrome is characterized by black decoration on unslipped portions of jars and dishes. Graciela Polychrome occurs on tripod dishes and is characterized by red-and-black painted decoration (Cecil 2001:209-211). This ware also has an incised type (Hobonmo Incised) with two varieties: Hobonmo (pre-fire) and Ramsey (post-fire).

Middleton et al. (1985) compared area counting to standard geological point counting and determined that the number of minerals counted was equal and the only difference was that area counting resulted in a smaller mean mineral diameter. Because mean diameter of minerals was not critical to this study, I implemented area counting where I counted two standard image areas to ensure that each area was representative of the sherds as a whole and to detect changes in the clay matrix (for more specific methodology see Cecil 2001). Ultimately the frequency data were converted to percentages based on the actual counts and the percentages examined by ternary diagrams to aid in the identification of Postclassic slipped pottery technological styles.

Although petrographic analysis is important to this research design, there are some limitations. Thin-sectioning may not produce the full mineralogical composition of a pottery sample due to sampling error and because the method of producing thin-section slides involves grinding and polishing of the sample (Orton et al. 1993). In addition to problems with sample preparation, petrographic analysis alone cannot determine the type of clay mineral in the sherd because of the refractive characteristics of clay minerals. Because of these limitations, petrography will be combined with neutron activation analysis (hereafter, INAA) to obtain a more comprehensive data set of clays and tempers.

Chemical Analyses—Instrumental Neutron Activation Analysis and Laser-Ablation Inductively Coupled Mass Spectroscopy

Although petrography can identify the different minerals and culturally added temper to the clay, petrography cannot determine differences in clay sources and pigments used for painted decoration and it cannot detect trace and rare earth elements that are often used to distinguish between chemical composition groups. INAA was used to identify the variability in chemical signatures that may indicate differences in clay resources and/or recipes as well as possible trade routes of the Postclassic Maya. In addition to understanding different manufacturing traditions with regard to ceramic paste, variations in the pigments used for decoration also can be analyzed. The best analytical technique for analyzing pottery paints *in situ* is laser ablation inductively coupled plasma spectroscopy (hereafter LA-ICP-MS). Thus, by combining the strengths of petrography and INAA and LA-ICP-MS, I can obtain results that infer sociopolitical group specific activities (i.e. pottery manufacture) because variability informs archaeologists about choices in technology and resources that are essential to understanding the sociopolitical milieu during the Postclassic period.

Instrumental Neutron Activation Analysis (INAA)

Two hundred and fourteen sherds representing the three Postclassic slipped pottery wares that were excavated from the archaeological sites of Ch'ich', Ixlú, Zacpetén, and Tipuj and 14 clay samples were analyzed by INAA. Pottery and clay samples were prepared for INAA using procedures standard at MURR (Glascock 2007). Fragments of about $1cm^2$ were removed from each sherd and abraded using a silicon carbide burr to remove glaze, slip, paint, and adhering soil, thereby reducing the risk of measuring contamination. The samples were washed in deionized water and allowed to dry in the laboratory. Once dry, the individual sherds were ground to powder in an agate mortar to homogenize the samples.

Clay samples weighing approximately 400 mg were dried overnight in a drying oven and

then fired to 700ºC in an electric kiln. After the clays cooled, they are processed in the same manner as ceramic samples.

Portions of approximately 150 mg of powder were weighed into clean high-density polyethylene vials used for short irradiations at MURR. At the same time, 200 mg of each sample were weighed into clean high-purity quartz vials used for long irradiations. Along with the unknown samples, standards made from National Institute of Standards and Technology (NIST) certified standard reference materials of SRM-1633a (coal fly ash) and SRM-688 (basalt rock) were similarly prepared, as were quality control samples (e.g., standards treated as unknowns) of SRM-278 (obsidian rock) and Ohio Red Clay (a standard developed for in-house applications).

Neutron activation analysis of ceramics at MURR, which consists of two irradiations and a total of three gamma counts, constitutes a superset of the procedures used at most other NAA laboratories (Glascock 1992; Neff 1992, 2000). The 720-second count yields gamma spectra containing peaks for nine short-lived elements aluminum (Al), barium (Ba), calcium (Ca), dysprosium (Dy), potassium (K), manganese (Mn), sodium (Na), titanium (Ti), and vanadium (V). The long irradiation is analogous to the single irradiation utilized at most other laboratories. After the long irradiation, samples decay for seven days, and then are counted for 1,800 seconds (the "middle count") on a high-resolution germanium detector coupled to an automatic sample changer. The middle count yields determinations of seven medium half-life elements, namely arsenic (As), lanthanum (La), lutetium (Lu), neodymium (Nd), samarium (Sm), uranium (U), and ytterbium (Yb). After an additional three- or four-week decay, a final count of 8,500 seconds is carried out on each sample. The latter measurement yields the following 17 long half-life elements: cerium (Ce), cobalt (Co), chromium (Cr), cesium (Cs), europium (Eu), iron (Fe), hafnium (Hf), nickel (Ni), rubidium (Rb), antimony (Sb), scandium (Sc), strontium (Sr), tantalum (Ta), terbium (Tb), thorium (Th), zinc (Zn), and zirconium (Zr) (Glascock 1992).

Laser Ablation Inductively Coupled Mass Spectroscopy (LA-ICP-MS)

Of the 210 sherds submitted for INAA, 100[1] exterior slips recovered from excavations at Ch'ich', Ixlú, Zacpetén, and Tipuj were analyzed by LA-ICP-MS at California State University-Long Beach (Cecil and Neff 2006). In addition to analyzing exterior slips, black (n=17) and red (n=17) painted decorations were also tested on those sherds with decoration. LA-ICP-MS was chosen because of its success with analyzing slips and paints (Neff 2002; Speakman 2005; Vaughn et al. 2005; among others). In addition to previous success with the technique, it is very difficult to extricate the Postclassic slip and paint pigments from the sherd paste without also including part of the sherd paste in the analysis. Therefore, analyzing slips and paints *in situ* is ideal. Because the laser ablates only the first five microns (Neff 2002), it is unlikely to penetrate beyond the level of the slip and/or painted decoration to include chemical analysis of the underlying pottery sherd paste composition.

The laboratory at California State University-Long Beach operates a Perkin-Elmer ELAN 6100 DRC quadrupole ICP-MS and a New Wave UP-213 laser ablation system. The laser was run with a raster spacing of 150 microns, a spot size of 100 microns, and a laser scan speed of 70 microns/second. Laser power was set at 60% and the repetition rate was 20Hz.

[1] Exterior slips on three samples were too thin (paste was also ablated) and not included in the study. As a result, only 97 exterior slip samples are included in this study.

The laser ablated the same raster twice. NIST SRM612 and SRM610 glasses, Little Glass Buttes obsidian, and Ohio Red clay were used as the standard reference materials. Forty-six elements were detected, but for the data presented below only 16 of the 46 were used due to small sample sizes of the red and black paints. The 16 elements were chosen after examination of numerous bivariate plots of elemental concentrations of the complete data showed that sub-grouping tendencies were clearest on the 16 selected for retention. It should also be noted that a principal components analysis (hereafter PCA) was conducted with the 46 elements on only the exterior slips and the basic structure is the same as indicated by the principal components analysis with only 16 elements. Therefore, limiting the number of elements in the study does not affect the overall results.

The interpretation of compositional data obtained from the analysis of archaeological materials is discussed in detail elsewhere (e.g., Baxter 1994; Bieber et al. 1976; Bishop and Neff 1989; Glascock 1992; Harbottle 1976; Neff 2000) and will only be summarized here. The main goal of data analysis is to identify distinct homogeneous groups within the analytical database. Based on the provenance postulate of Weigand et al. (1977), different chemical groups may be assumed to represent geographically restricted sources. The locations of pottery sources can also be inferred by comparing unknown specimens (i.e., ceramic artifacts) to knowns (i.e., clay samples) or by indirect methods such as the "criterion of abundance" (Bishop et al. 1982) or by arguments based on geological and sedimentological characteristics (e.g., Steponaitis et al. 1996). The ubiquity of ceramic raw materials usually makes it impossible to sample all potential "sources" intensively enough to create groups of knowns to which unknowns can be compared.

Compositional groups can be viewed as "centers of mass" in the compositional hyperspace described by the measured elemental data. The variables (measured elements) in archaeological and geological data sets are often correlated and frequently large in number. This makes handling and interpreting patterns within the data difficult. Therefore, it is often useful to transform the original variables into a smaller set of uncorrelated variables in order to make data interpretation easier. Of the above-mentioned pattern recognition techniques, PCA is a technique that transforms the data from the original correlated variables into uncorrelated variables most easily.

Principal component analysis creates a new set of reference axes arranged in decreasing order of subsumed variance. The individual principal components are linear combinations of the original variables. The data can be displayed on combinations of the new axes, just as they can be displayed on the original elemental concentration axes. Generally, compositional differences between specimens can be expected to be larger for specimens in different groups than for specimens in the same group, and this implies that groups should be detectable as distinct areas of high point density on plots of the first few components.

Whether a group can be discriminated easily from other groups can be evaluated visually in two dimensions or statistically in multiple dimensions. A metric known as the Mahalanobis distance (or generalized distance) makes it possible to describe the separation between groups or between individual samples and groups on multiple dimensions. The Mahalanobis distance of a specimen from a group centroid (Bieber et al. 1976, Bishop and Neff 1989) is defined by:

$$D^2_{y,X} = [y - \overline{X}]^t \, I_x [y - \overline{X}]$$

where *y* is the 1 x m array of logged elemental concentrations for the specimen of interest, *X* is the n x m data matrix of logged concentrations for the group to which the point is being compared with $\overline{X}$ being it 1 x m centroid, and I_x is the inverse of the m x m variance-covariance matrix of group *X*. Because Mahalanobis distance takes into account variances and covariances in the multivariate group it is analogous to expressing distance from a univariate mean in standard deviation units. Like standard deviation units, Mahalanobis distances can be converted into probabilities of group membership for individual specimens. For relatively small sample sizes, it is appropriate to base probabilities on Hotelling's T^2, which is the multivariate extension of the univariate Student's t.

Ultimately, the goal of chemical analyses is to distinguish compositionally homogenous groups within the database of analytical samples that may reflect geographically restricted zones. Thus, INAA and LA-ICP-MS data will be combined with the typological, stylistic, and petrographic data previously attained to create technologically- and stylistically-based groups that can be used to infer various manufacturing recipes and trade/exchange networks during the Postclassic period.

RESULTS

Stylistic Analyses

As a result of the stylistic analysis of pottery, I was able to determine that various associations of slip colors, combinations of different pigments used for painted decoration, and visible paste variability would provide useful information concerning manufacturing recipes and sociopolitical-specific pottery. Postclassic slipped pottery has four different painting modes (monochromatically slipped, red-on-paste, black-on-paste, and red-and-black) and two incising modes (pre- and post-firing incising). All of the ware categories have types that are monochromatically slipped, that have black-on-paste decoration, and have both modes of incising. The difference occurs with the red-on-paste and red-and-black decoration. The red-on-paste decorative program does not occur on pottery from the Vitzil Orange-Red ware and the red-and-black painted designs occur rarely on pottery from the Vitzil Orange-Red ware and not on the Trapeche or Fulano types (Snail-Inclusion Paste ware). While many of the decorative programs occur on most of the ceramic wares, the sites from which they were excavated provides more evidence as to choices made by Postclassic Maya potters. Red-on-paste and red-and-black decorative programs occur more frequently at the archaeological sites of Zacpetén and Tipuj (eastern sites) and extremely rarely at the archaeological sites of Ch'ich' and Ixlú (western sites).

In addition to differences in general decorative programs, the motifs used to decorate the pottery provide an interesting glimpse into possible Maya choice selections. *Ajau* glyphs, s-curved mat motifs, and curvilinear abstract images without a banded decorative panel (Figure 2) occur more commonly on pottery that is decorated only in red paint (and only on Clemencia Cream Paste and Snail-Inclusion Paste wares). On the other hand, reptilian motifs and hook motifs (Figure 3) occur more frequently as black painted designs on Vitzil Orange-Red and Snail-Inclusion Paste ware pottery.

There are two general qualities of the slips that are visible to the unaided eye: 1) some "pink," red, and black slips are the result of a double-slipping and 2) slips have either a glossy or a matte finish. Postclassic "pink" slips along with some red and black slips are the result of double-slipping technology that was common during the Late Classic period (Cecil 2001; Cecil and Neff 2006; Reents-Budet et al.1994).

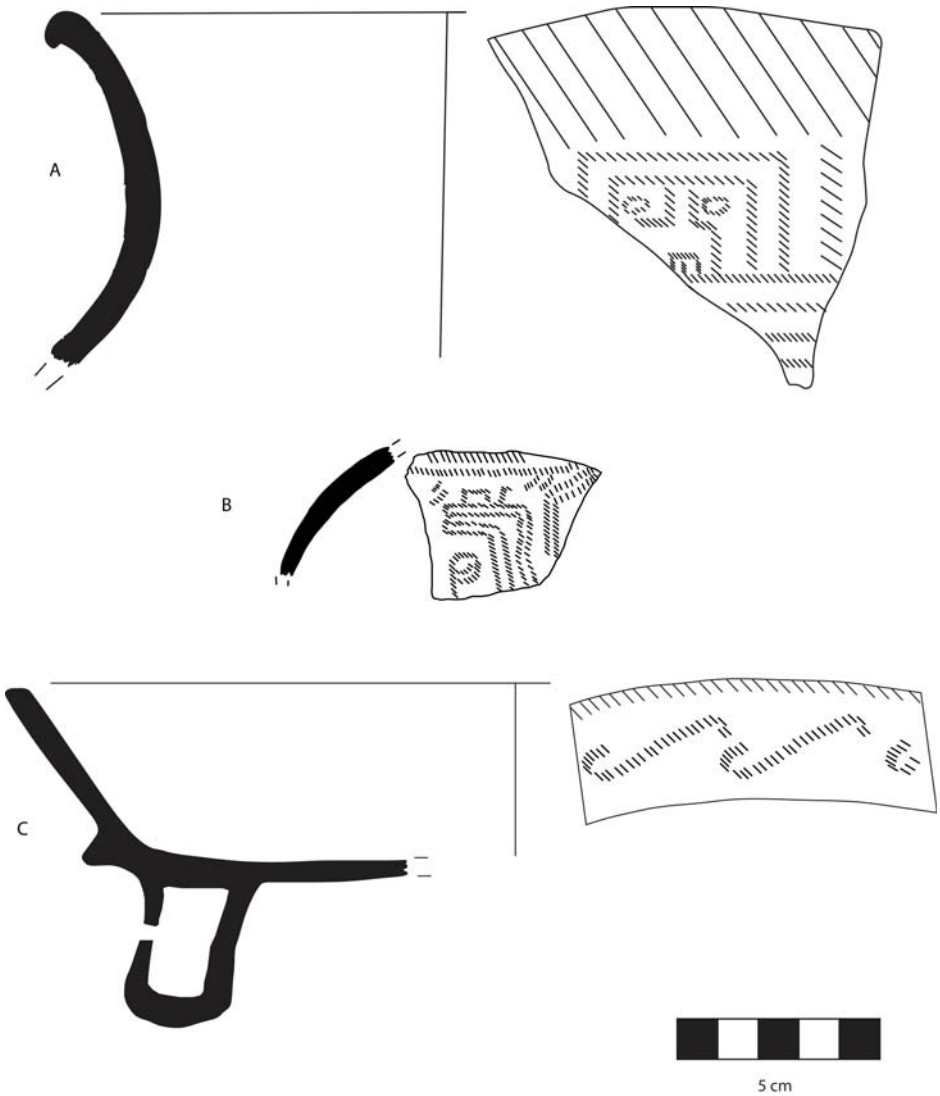

Figure 2. Petén Postclassic pottery decorated with A) *ajau* glyphs (Chompoxté Red-on-paste: Akalché Variety), B) unbanded, curvilinear motif (Chompoxté Red-on-paste: Chompoxté Variety), and C) s-curve mat motif (Macanché Red-on-paste: Macanché Variety. All sherds were excavated from Zacpetén.

The double slipping is a result of Maya potters first applying a red, brownish-red, or black slip to the vessel and then applying a creamy translucent overslip. This slipping process resulted in a "waxy" feel to the exterior of the vessels and a thick slip that eroded differentially (the two layers of slip are visible because the overslip erodes in some places and

not in others). While double slipping occurs on some of the earlier Postclassic pottery, most later Postclassic red slips are thin and have not been burnished resulting in a matte finish. This matte finish erodes easily. While the majority of Postclassic slips are thin, excavations at Ch'ich', Zacpetén, and Tipuj yielded small quantities of Postclassic pottery with highly burnished, glossy red slips (they are not double slipped). These slips are thicker and not eroded.

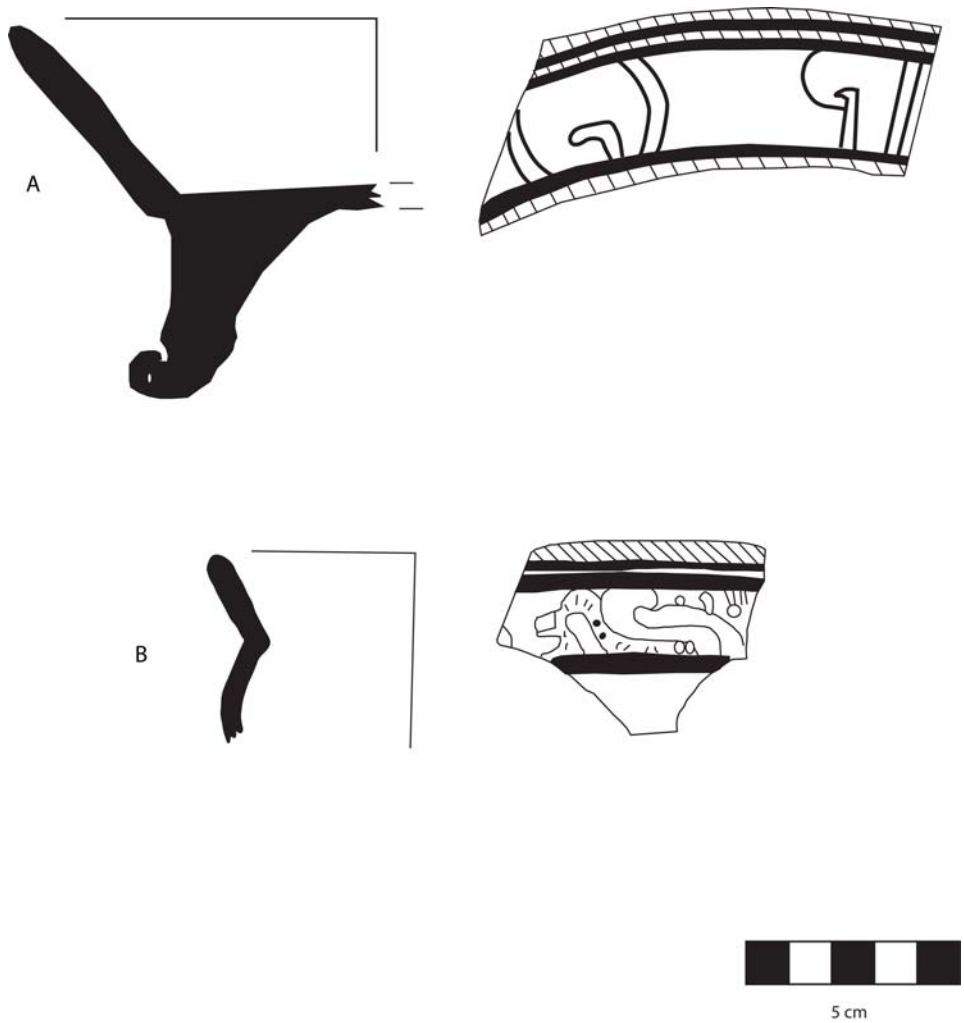

Figure 3. Petén Postclassic pottery decorated with A) hook motifs and B) reptilian motifs. Both sherds represent the Ixpop Polychrome type and were excavated from Zacpetén.

Mineralogical Analyses

Within each of the three ceramic wares, variations in the type and quantity of mineral and organic inclusions provides information to suggest that Postclassic Maya potters were making different "recipes" with similar colored clays. Clemencia Cream Paste ware sherds have three

distinct recipes (Figure 4). One recipe (Figure 4A) involves volcanic ash inclusions as well as a small percentage of plagioclase and feldspar minerals that are approximately .15-.025 mm in size (Cecil 2001:357-358).

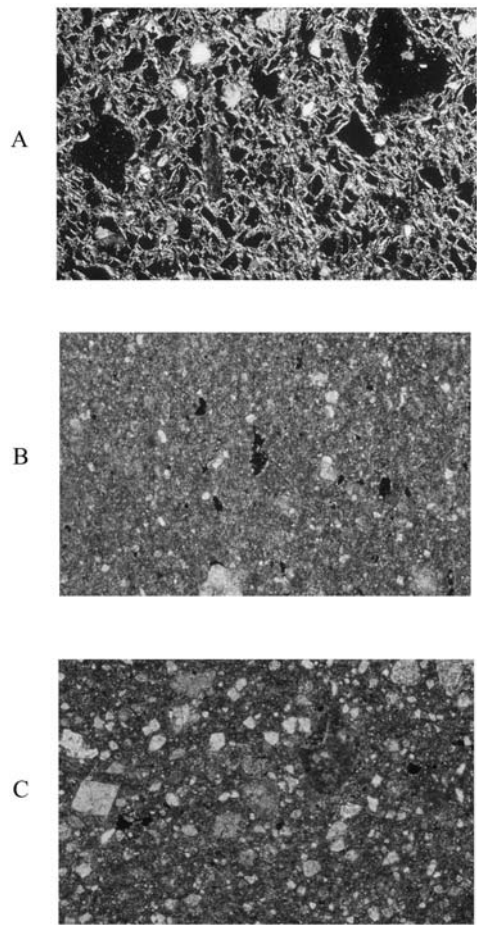

Figure 4. Thin section photographs of Clemencia Cream Paste ware pottery: A) volcanic ash tempered (Topoxté Red type excavated from Ixlú), B) small cryptocrystalline calcite inclusions (Chompoxté Red-on-paste: Akalché Variety excavated from Zacpetén), and C) calcite (euhedral, polycrystalline, and cryptocrystalline), hematite, biotite, shell, chert, and chalcedony inclusions (Chompoxté Red-on-paste: Akalché Variety excavated from Zacpetén). All photographs were taken at 40X with cross polarized light.

The second clay paste (Figure 4B) consists of cream-colored marly clay with calcite (euhedral, polycrystalline, and cryptocrystalline), hematite, and biotite minerals, and organics. The third Clemencia Cream Paste ware recipe (Figure 4C) includes the same cream-colored clay but with calcite (euhedral, polycrystalline, and cryptocrystalline), hematite, biotite, shell, chert, and chalcedony mineral inclusions.

The Vitzil Orange-Red ware pottery also has three different combinations of mineral and organic inclusions that were detected through petrographic analysis (Figure 5). The first combination is volcanic ash and small (.15-.025 mm) feldspar minerals (Figure 5A)(Cecil 2001:361-363). The second recipe consists of the distinctive reddish-orange clay and quartz,

chert, chalcedony, hematite, biotite, and calcite (euhedral, polycrystalline, and cryptocrystalline) mineral inclusions (Figure 5B). The majority of Vitzil Orange-Red ware sherds were made with this combination of clay and minerals. High quantities of cryptocrystalline calcite and lesser amounts of quartz together with the reddish-orange clay comprise the third mineralogically-different group (Figure 5C).

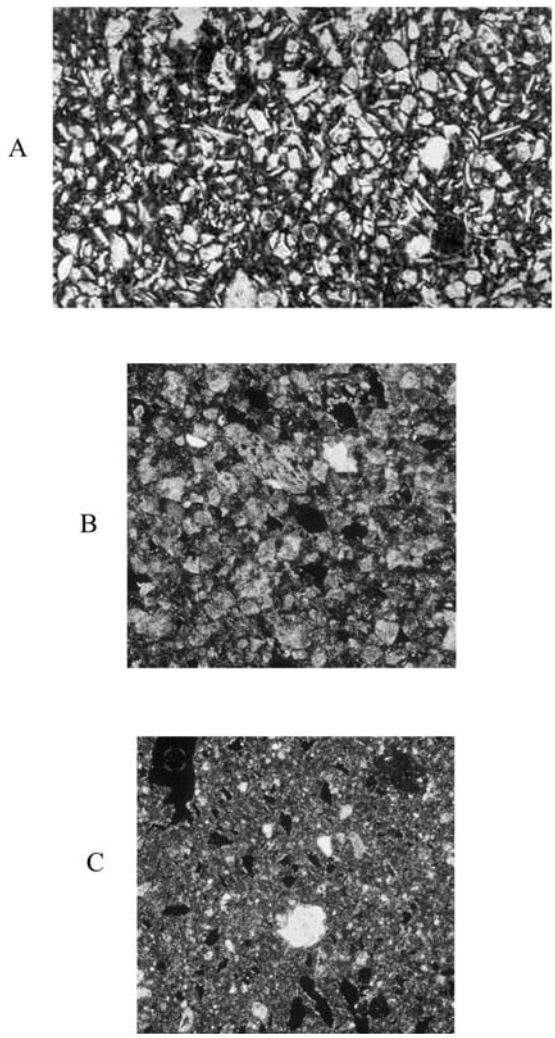

Figure 5. Thin section photographs of Vitzil Orange Red ware pottery: A) volcanic ash tempered (Augustine Red excavated from Zacpetén), B) quartz, chert, chalcedony, hematite, biotite, and calcite (euhedral, polycrystalline, and cryptocrystalline) inclusions (Graciela Polychrome type excavated from Zacpetén), and C) cryptocrystalline calcite and lesser amounts of quartz inclusions (Augustine Red type excavated from Zacpetén). Figure A was photographed at 40X with plane polarized light and B and C were photographed at 40X with cross polarized light.

Unlike the Clemencia Cream Paste and Vitzil Orange-Red wares, the Snail-Inclusion Paste ware sherds only form two different recipe groups (Figure 6). The first group (Figure 6A) is characterized by the inclusion of quartz, chert, chalcedony, hematite, biotite, calcite (euhedral, polycrystalline, and cryptocrystalline), lacustrine shell, and organic material. The

second group (Figure 6B) is quite different than the first because it contains abundant quantities of small (.25-.05 mm) sized cryptocrystalline calcite and minor quantities of quartz, hematite, and shell (Cecil 2001:366-367).

Based on the mineralogical data presented above, petrographic analysis of the 278 Postclassic slipped sherds detected four basic manufacturing recipes. The first group consists of sherds of the Clemencia Cream Paste and Vitzil Orange-Red wares and has an abundance of volcanic ash and minor quantities of feldspar.

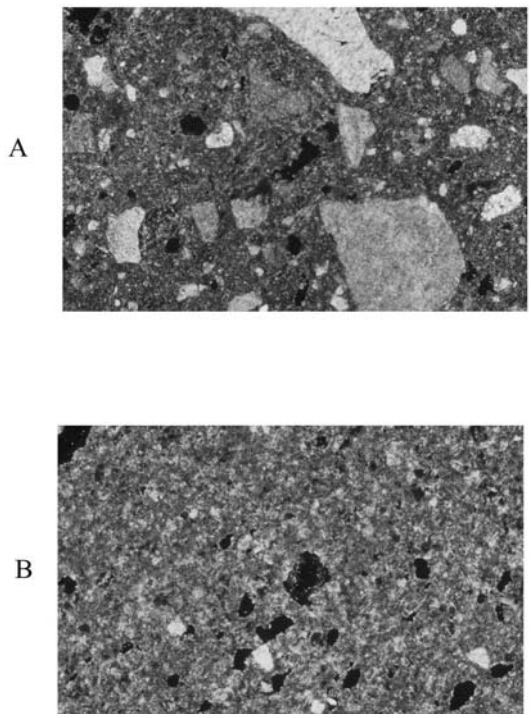

Figure 6. Thin section photographs of Snail-Inclusion Paste ware pottery: A) quartz, chert, chalcedony, hematite, biotite, calcite (euhedral, polycrystalline, and cryptocrystalline), and lacustrine shell inclusions (Macanché Red-on-paste: Macanché Variety excavated from Zacpetén), B) cryptocrystalline calcite and minor quantities of quartz, hematite, and shell inclusions (Trapeche Pink type excavated from Ixlú). All photographs were taken at 40X with crossed polarized light.

The second group is characterized by large quantities of cryptocrystalline calcite (small in size) inclusions and is represented by the Snail-Inclusion Paste and Vitzil Orange-Red wares. Inclusions of quartz, chert, chalcedony, hematite, and calcite in the sherd pastes of all of the ceramic wares comprise the third mineralogically-distinct group. Finally, the fourth manufacturing recipe consists of the inclusion of calcite, biotite, and hematite minerals in the cream-colored marly clays of the Clemencia Cream Paste ware.

The differences that delineate these four mineralogically-based groups demonstrate that Postclassic Petén potters were making choices during the manufacturing process with regard to clays and minerals used as tempering material. These choices may have been influenced by the resources that were readily available because if the Itza and Kowoj Maya were in conflict with each other, it is probable that potters from the different communities may have been restricted to resources within their culturally-defined territories.

Chemical Analyses

The interpretation of the compositional data of the ceramic pastes (INAA data) produced a general separation of the three Postclassic wares as well as divisions within each ware (Figure 7). The first nine eigenvalues account for 96% of the variability present in the sample (Table 2).

For the most part, it supports the results obtained through petrographic analysis. The Clemenica Cream Paste ware demonstrates a division of three groups: a group higher in sodium and rubidium (volcanic ash tempered), a group (n=6) higher in calcium and lower in rubidium, cesium, and potassium, and a group (the majority of the sample) that has minor quantities of the rare earth and lanthanide series elements, but higher frequencies of calcium and potassium.

Table 2. Principal Components Analysis of Central Petén Slipped Pottery (R-Q Factor Analysis based on Variance-Covariance Matrix)

Element	Factor 1	Factor 2	Factor 3	Factor 4	Factor 5	Factor 6	Factor 7	Factor 8	Factor 9
As	0.2022	0.2069	-0.0580	0.0049	-0.1277	0.2738	0.3085	0.1691	0.5356
La	0.1861	0.0591	-0.0498	0.1431	0.0601	-0.2385	-0.1538	-0.0128	0.1324
Lu	0.1968	0.0726	-0.0424	0.0138	-0.0577	-0.0110	0.0337	-0.0032	-0.0716
Nd	0.1891	0.0696	-0.0723	0.1516	0.0453	-0.2286	-0.1055	0.0308	0.1196
Sm	0.1887	0.0710	-0.0704	0.1389	0.0339	-0.1847	-0.0793	-0.0236	0.1040
U	0.1515	0.0555	0.1161	-0.0530	-0.1361	0.2075	0.1178	0.0728	-0.2527
Yb	0.2090	0.0879	-0.0690	0.0651	-0.0252	-0.1054	0.0050	-0.0077	0.0246
Ce	0.2690	-0.0580	0.0477	0.3558	0.0064	-0.1206	-0.0490	-0.2512	-0.4188
Co	0.0708	0.0655	-0.1897	0.0777	0.4536	0.1867	0.1231	0.0133	-0.0562
Cr	0.0578	0.0303	-0.2410	-0.1240	0.1013	0.0245	-0.2052	-0.1204	-0.0753
Cs	0.2482	-0.3168	0.0187	-0.3292	0.1616	-0.3596	0.3188	-0.0749	-0.0132
Eu	0.1734	0.1047	-0.0824	0.1581	0.0831	-0.1793	-0.0884	-0.0393	0.1351
Fe	0.1129	0.1446	-0.1382	-0.1339	0.0811	0.1355	0.0036	0.0554	-0.0089
Hf	0.1860	0.0857	-0.0849	-0.0418	-0.1331	0.1419	-0.0257	-0.0289	-0.0811
Rb	0.2396	-0.2709	0.1631	-0.4140	0.1903	-0.1709	0.2683	0.0132	-0.0193
Sb	0.1477	0.0642	-0.0779	-0.1211	0.0401	0.1302	0.0469	0.0710	-0.334
Sc	0.1329	0.1270	-0.0739	-0.1330	0.0218	0.0562	-0.0133	0.0518	-0.1309
Sr	-0.0307	0.5183	0.5892	0.0286	0.2039	-0.2094	0.0314	0.3751	-0.2264
Ta	0.1962	0.0793	-0.0509	-0.1333	-0.1093	0.0001	-0.0308	0.0400	-0.1300
Tb	0.1955	0.0694	-0.0853	0.1423	0.0472	-0.2055	-0.0738	0.0051	0.1458
Th	0.2392	0.0624	-0.0017	-0.0524	-0.1733	0.0649	0.0506	0.0079	-0.2482
Zn	0.1079	0.0263	-0.0927	-0.0511	0.0154	0.0448	-01429	0.0757	-0.0350
Zr	0.1816	0.0937	-0.0604	-0.0237	-0.1483	0.1618	-0.0338	-0.1184	-0.0831
Al	0.1501	0.0814	0.0055	-0.0388	-0.0656	0.1062	0.0323	0.0315	-0.1423
Ba	0.1069	0.1946	0.4629	-0.1253	0.2113	0.2077	-0.1267	-0.7063	0.2679
Ca	-0.2453	0.2029	-0.1629	-0.1401	0.2396	-0.2454	-0.0140	0.0942	0.0943
Dy	0.1947	0.0841	-0.0977	0.0784	-0.0064	-0.1828	-0.0568	0.0034	0.1226
K	0.1348	-0.3150	0.1069	-0.1625	0.2857	0.2074	-0.6712	0.2756	0.0039
Mn	0.0846	0.1508	-0.0428	0.4260	0.5275	0.3180	0.3033	0.0922	-0.0634
Na	0.2734	-0.2773	0.3584	0.1484	-0.2023	0.0831	-0.0458	0.3182	0.2955
Ti	0.1302	0.2029	-0.1210	-0.1707	0.0002	0.0886	-0.0790	0.0475	-0.0275
V	0.0508	0.2454	-0.1417	-0.2801	0.1662	0.0538	-0.0418	0.0942	0.0765

The Vitzil-Orange Red wares also divide into three chemical composition groups. The first group has high frequencies of sodium and rubidium (tempered with volcanic ash). The remaining two groups separate because of the different quantities of rare earth and lanthanide series elements. Those sherds with higher quantities of rare earth and lanthanide elements also have higher concentrations of calcium. This would infer that there are more different kinds of minerals in one of the ceramic pastes than in the other group.

The Snail-Inclusion Paste ware also can be divided into three chemical compositional groups (petrography could only distinguish two different groups).

The main difference between the three groups is the difference in concentrations of cerium, cesium, strontium, calcium, and many of the first row transition metal elements (Figures 7, 8). Group 1 (Figure 8) is composed only of decorated (black, red, and red-and-black designs and both kinds of incising) sherds primarily from the archaeological sites of Zacpetén, Ixlú, and Tipuj. Group 2 contains Snail- Inclusion Paste ware sherds primarily from the archaeological site of Ch'ich' (with equal, but fewer, quantities from Ixlú, Zacpetén, and Tipuj). The majority of these sherds are undecorated; however, the ones that are decorated are decorated only with black painted decoration or are incised. The final group, Group 3, is again composed primarily of sherds from Zacpetén (with minor amounts from Ixlú and Ch'ich') and with few exceptions, those sherds are decorated with either red or red-and-black painted decoration.

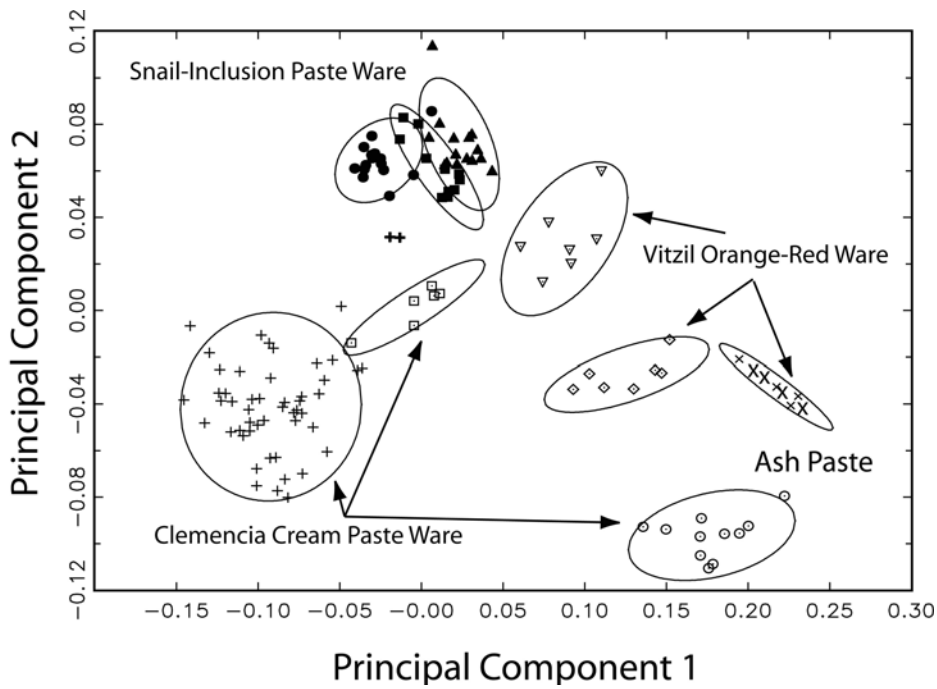

Figure 7. Ceramic samples from central Petén, Guatemala projected onto the first two principal component axes. Samples were analyzed by INAA. Ellipses represent 90% confidence intervals for group membership.

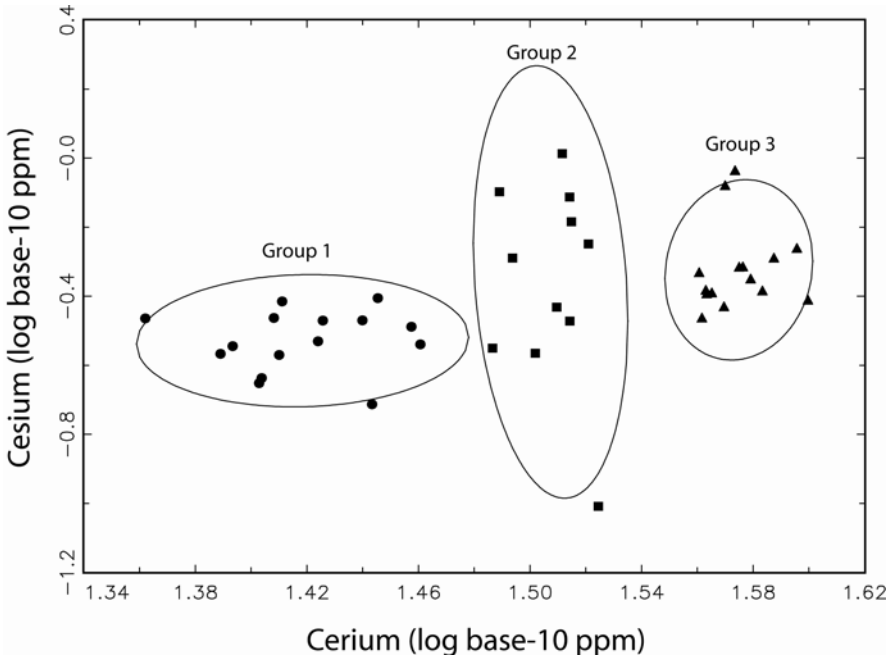

Figure 8. Plot of cerium and cesium base-10 logged concentrations showing the separation of the three Snail-Inclusion Paste ware chemical compositional groups. Samples were analyzed by INAA. Ellipses represent 90% confidence intervals for group membership.

In addition to reaffirming the differences within each ware that were obtained from mineralogical analyses, INAA is the best method by which to compare clays to pottery in an attempt to locate resource areas. In this study several clays (white, orange, yellow, and gray in color) were obtained from around Lake Yaxhá and Lake Petén Itzá[2] in an attempt to infer local resources used in pottery manufacture. The clays from around Lake Yaxhá plot within two Clemencia Cream Paste ware macro-groups (ash paste and non-ash paste) (Figure 9). Four clays demonstrate statistical membership[3] within the non-ash paste ceramic group suggesting that these clays could have been used to manufacture Clemencia Cream Paste ware pottery (Table 3).

Clay sample LGC111 consistently plots within the ash group, but because the sherd sample size for that group is small, statistical membership cannot be determined with any certainty. In addition to the Clemencia Cream Paste wares, two clay samples (one orange and one yellow) were collected from private property near the archaeological site of Ch'ich'. They were projected against the three chemical compositional groups of the Vitzil Orange-Red ware pottery.

[2] All but one of the white clays were sampled by Prudence M. Rice during the Historical Ecology Project. Sample LGC111 was a non-naturally occurring deposit excavated from Structure 719 at Zacpetén. The red clays were collected in 2006 by the author from private land between the archaeological sites of Ch'ich' and Trinidad de Nosotros. The gray clay samples were collected in 1998 by the boat launch area at the archaeological site of Zacpetén.

[3] The threshold for statistical membership of clay samples within ceramic sherd compositional groups is much lower than that for creating ceramic sherd compositional groups (typically above 5.000) because the addition of tempering material to raw clays does changes the chemical composition so much so that there is rarely a match at the 5.000 level. Therefore, it is common practice at MURR to suggest that clays may represent sources for pottery manufacture if there is a probability above 0.300.

Table 3. Mahalanobis Distance Calculation for the Clay Samples Projected against the Non-Ash Paste Group

Clay Samples	Probability of Membership in Non-ash Paste group
LGC110	0.047
LGC111	0.000
LGC112	0.002
LGC113	2.867
LGC114	0.025
LGC115	0.453
LGC116	0.313
LGC117	0.764
LGC119	0.000

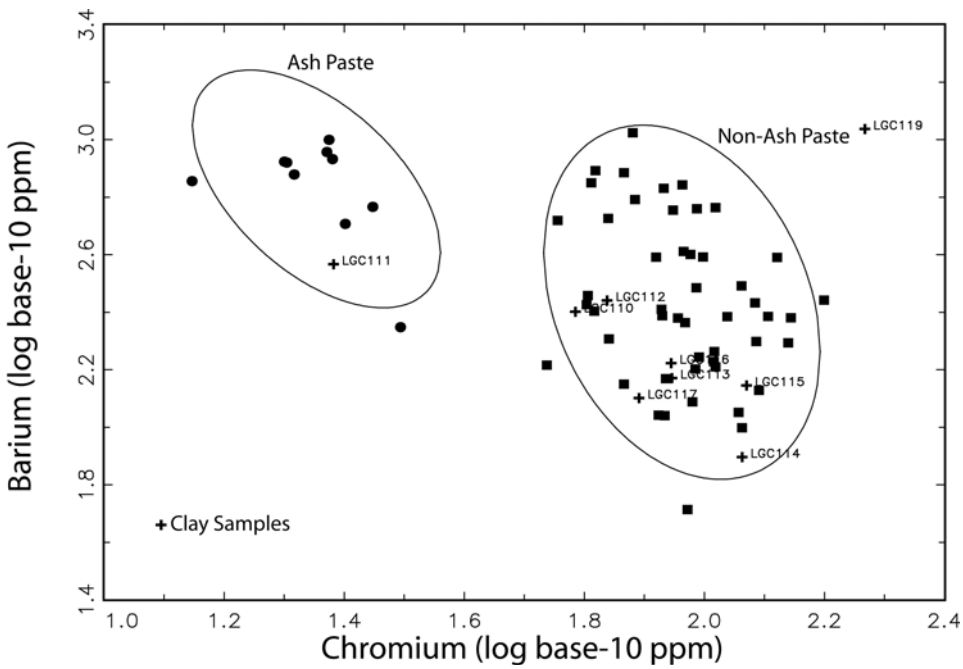

Figure 9. Plot of chromium and barium base-10 logged concentrations demonstrating the possible membership of the white clay samples (identified by sample number) in the two basic Clemencia Cream Paste ware compositional groups (ash tempered and non-ash tempered). Samples were analyzed by INAA. Ellipses represent 90% confidence intervals for group membership.

The clay samples consistently plot within the ellipse (90% confidence interval) that represents pottery from Ch'ich' (Figure 10). Unfortunately, the small sample size of the pottery does not allow for statistical testing; however, because the clay samples always plot within this sherd group, I am confident that they represent the clays used for some sherds manufactured at Ch'ich'. None of the collected gray clay samples correspond to the Snail-Inclusion Paste ware sherds.

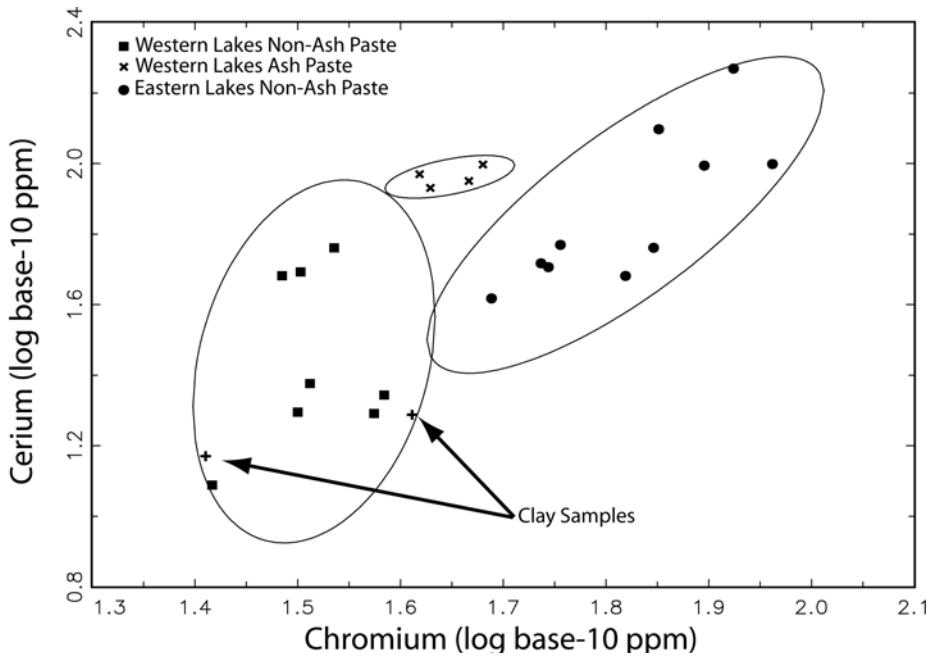

Figure 10. Plot of chromium and cerium base-10 logged concentrations demonstrating the possible membership of the orange-red clay samples (identified as +) within the non-ash paste Vitzil Orange-Red ware compositional group. Samples were analyzed by INAA. Ellipses represent 90% confidence intervals for group membership.

In addition to ceramic paste analyses, understanding the differences in exterior slips and the various pigments used for the painted decoration of the Postclassic slipped pottery is important to this study and could only be achieved through chemical analysis. Petrographic analysis did include an examination of the slips; however, no obvious differences in the kinds of slips being used for different types of pottery were detectable. Clemencia Cream Paste ware exterior slips divide into three different chemical compositional groups. One of the exterior slip groups corresponds to the Clemencia Cream Paste ware volcanic ash tempered group. The other two slip groups correspond to pottery excavated from Zacpetén and Tipuj (Cecil and Neff 2006:1487) and the slips excavated from Tipuj are thinner and of a poorer quality (fireclouding and matte finish) than those excavated from structures at Zacpetén.

Exterior slips of the Vitzil Orange-Red ceramic group form two main groups with some outlierers (Figure 11). The two slip groups correspond to archaeological sites from the western lakes region (Ch'ich' and Ixlú) and those from the eastern lakes region (Red Slip Group B—Zacpetén and Tipuj). The outliers represent decorated sherds from the eastern lakes. The slips from the western lakes region are thicker, have a glossy finish, and the sherds are generally not decorated. These slips correspond to the paste group discussed above from Ch'ich' further suggesting that there was a manufacturing zone for Vitzil Orange-Red pottery at or near the archaeological site of Ch'ich'.

Snail-Inclusion Paste ware exterior slips as a whole (pink, red, and black) do not form any statistically significant compositional groups; however, the Trapeche "pink" exterior slips separate into two chemical compositional groups that are statistically significant (Figure 12) (Cecil and Neff 2006:1487-1488). Group 1 is composed primarily of pink double-slipped pottery from Zacpetén and Group 2 contains the same kind of slipped pottery primarily from

Ixlú and Ch'ich'. This division may suggest two zones of Trapeche Pink manufacture or slip recipes: one at Zacpetén and another at Ch'ich' or Ixlú.

When the Fulano (black slipped) and the Paxcamán (red slipped) exterior slips are plotted with the Trapeche pink slip compositional groups, many of samples plot within the Group 1 and Group 2 ellipses, but their membership is not statistically significant. I suggest that the earlier Trapeche ceramic group technology evolved into the slips and pastes of the Paxcamán ceramic group (a red slip without the creamy overslip). Additionally, the Fulano black slips are very similar to the Paxcamán slips, but because they were fired in a reducing environment, the slips are black (Cecil 2001:169). Therefore, it is not unusual that the later ceramic group slips (Paxcamán and Fulano) plot within the earlier Trapeche ceramic group slips.

The remaining samples that do not form a statistically significant chemical composition group and represent all of the exterior slips from Tipuj (black and red, no Trapeche ceramic group sherds were excavated at Tipuj) as well as a number of samples excavated from Zacpetén and Chi'ch'. Upon a visual examination of these slips, they are thicker and glossy which may suggest that potters at Tipuj (or Zacpetén or Ch'ich') are creating higher quality slips than potters at other archaeological sites in central Petén.

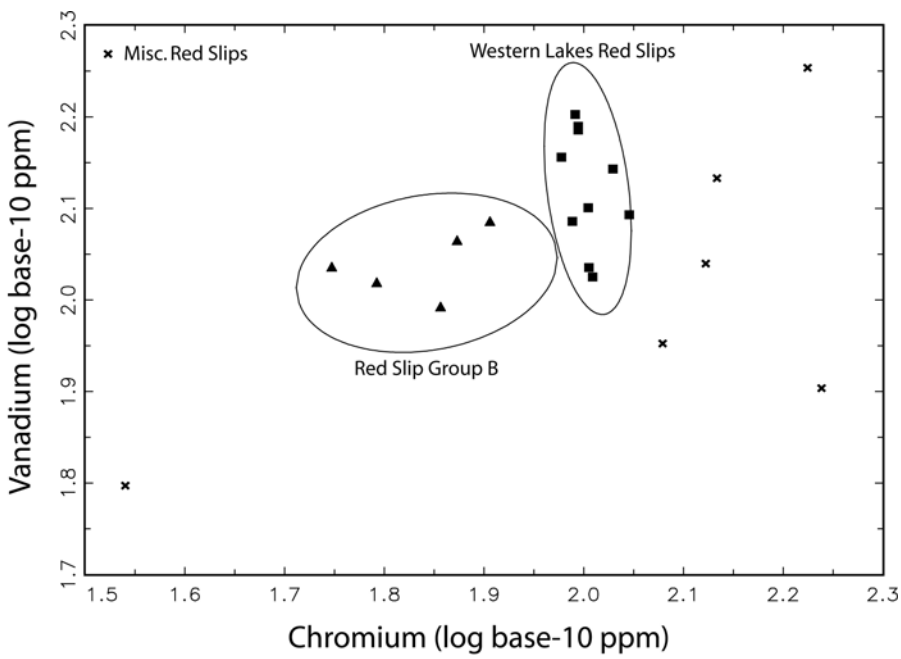

Figure 11. Plot of chromium and vanadium base-10 logged concentrations of Vitzil Orange-Red exterior slips showing the difference between western archaeological sites (Ch'ich' and Ixlú) and other red slips. Samples were analyzed by LA-ICP-MS. Ellipses represent 90% confidence intervals for group membership.

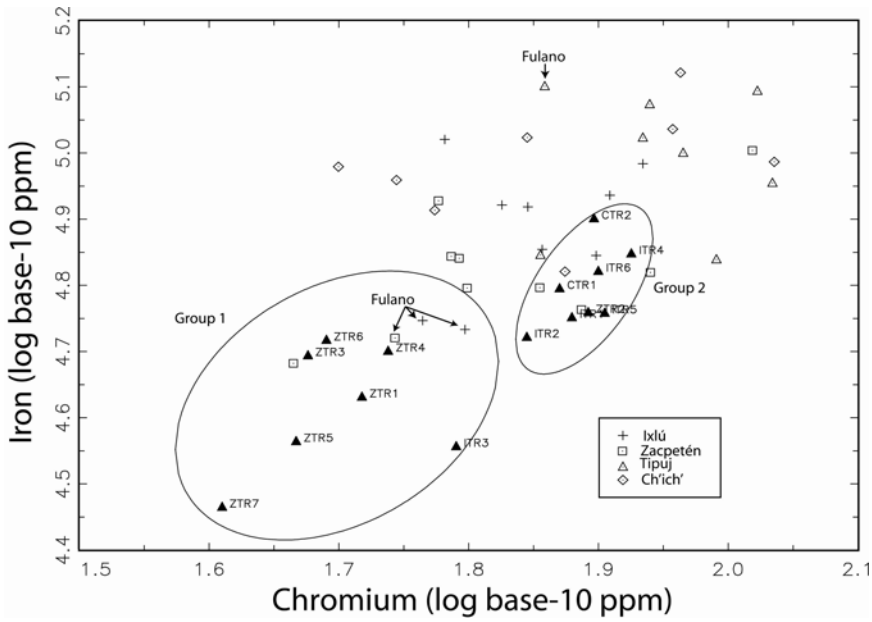

Figure 12. Plot of chromium and iron base-10 logged concentrations showing the separation of Snail-Inclusion Paste ware samples. Labeled samples represent the Trapeche ceramic group and unlabeled samples represent the Paxcamán and Fulano ceramic groups. Ellipses represent 90% confidence level for membership in the two Trapeche Pink compositional groups (Cecil and Neff 2006:Figure 8).

The paint used for the painted decoration on many of the vessels during the Postclassic period is a different value and chroma than that of the slips. This may suggest that Maya potters are using different pigments for the painted decoration and the slips. Through the LA-ICP-MS analysis of the red and black painted decoration, I was able to suggest that this is indeed the case. The red paint used for painting red-on-paste decorations is chemically different from that used for red-and-black painted decoration and the exterior slips. Additionally, the black paints used for black-on-paste decoration and red-and-black decoration are chemically distinct (Cecil and Neff 2006:1488-1489). This suggests that the Maya potters chose different pigments depending on the decorative programs being created.

CONCLUSION

While the different kinds of analyses presented above provide various categories of information about Postclassic slipped pottery, it is not until all three categories are examined together with the ethnohistorical record and other archaeological excavation data that the power of analyzing pottery with a combination of analytical techniques comes to light. By conjoining these data some interesting technological and stylistic combinations occur reflecting the choices made by Postclassic potters. These choices in turn reflect the potter's (and presumably the society in which they live) different sociopolitical identities.

During the late Terminal Classic to Early Postclassic (ca. AD 900-1250) period in central Petén, new types of architecture and pottery indicate that new sociopolitical groups may have entered into the area. Civic-ceremonial architecture (Pugh 2001a) and C- and L-shaped range

structures (D. Rice 1986) replaced the large Late Classic temples and elite structures. Codex style pottery with ornate depictions from the *Popul Vuh* (the Maya creation story) and rows of Maya hieroglyphs were replaced with less ornate pottery manufactured with cream- and orange-red-colored ceramic pastes. While there is a difference in the quality of artifacts at archaeological sites in central Petén during this time period, several archaeologists (Boot 1997, 2005; Rice et al. 1996; Schele and Grube 1995; Schele et al. 1998; Schele and Mathews 1998) have stated that the Itza may have migrated to the Petén lakes region from northern Yucatán before or during the Terminal Classic/Early Postclassic period. While the Itza may have been a newer presence in the Petén lakes region, other sociopolitical groups (the Yalain and Mopan) may be present in the area reflecting the Late Classic inhabitants that remained after the collapse (Jones 1998).

Pottery dating to the Early Postclassic period (ash paste Clemencia Cream Paste and Vitzil Orange-Red wares) is thin-walled, volcanic-ash tempered paste pottery. It was being manufactured and traded throughout the central Petén lakes area as is apparent by its existence at Ch'ich, Ixlú, Zacpetén, and Tipuj. The chemically distinct red slips of the volcanic-ash tempered Postclassic slipped pottery wares are fairly thick and appear glossy. The volcanic-ash tempered Clemencia Cream Paste ware pottery was manufactured at or around Topoxté Island and traded to Maya at Ixlú and Tipuj (Cecil 2001; P. Rice 1986). The location of production of the organish-red paste pottery that is volcanic-ash tempered is not known; however, Maya at Ch'ich' manufactured one version of this non-volcanic-ash tempered paste ware.

In addition to these two wares, the Snail-Inclusion Paste ware with "pink" (Trapeche ceramic group) and black (Fulano ceramic group) slips are being produced in the Petén lakes region during the Early Postclassic period. This ceramic paste is characteristic of lacustrine clays and could have been procured from any of the lake beds in the region. The pink slips result from a double slip of a red slip covered by a semi-translucent cream colored slip. The black slip is thick and glossy. These slips are similar to those of Late Classic Petén Gloss wares. When examining this pottery, the pink slipped pottery pastes separated into two distinct paste groups. While both groups have samples from Zacpetén, samples from Ch'ich' and Ixlú are distinct. All but one sample (from Tipuj) of the black slipped pottery occurs in the Zacpetén slip group. There appear to be two recipes for the pink slips—one representing manufacture of pottery excavated at Zacpetén and one representing manufacture of pottery excavated from Ch'ich' and Ixlú. Interestingly, none of the pink slipped pottery has been excavated from Tipuj and the one black slipped sample from Tipuj is chemically distinct from the others.

The pottery with the thick, glossy double slips and those with compact volcanic-ash tempered pastes suggests that social groups remained in the area and attempted to mimic traits of Late Classic period Petén Gloss Wares (the pottery of their ancestors). In addition to this pottery, it is likely that the Itza, Yalain, and/or Mopan manufactured and traded the "new" orange paste pottery throughout the central Petén lakes region because it is found throughout the region. As a result of the distribution pattern of these wares, slips, and pigments, sociopolitical boundaries may not have been established/enforced and the corridor from the Petén lakes to Tipuj was not under any one sociopolitical group's control.

At approximately A.D. 1250, sociopolitical groups from northern Yucatán migrated to central Petén. In general, the Kowoj arrived and occupied territory in the east and the Itza controlled territory in the west. At this time, the Kowoj occupied Topoxté Island, and most

likely Zacpetén (Pugh 2001a), and produced cream paste pottery with at least three different paste recipes. The pottery with higher calcite is decorated with red-on-paste decoration and pottery with higher biotite and chert inclusions is decorated with red-and-black or black-only decoration. All of this cream-colored paste pottery used in this analysis was excavated from the archaeological sites of Zacpetén and Tipuj. While there does not seem to be a pattern as to which site had more pottery from the different paste groups, the quality of the pottery excavated from the sites is interesting. In general, the pottery excavated from Zacpetén is of a higher quality—fewer fireclouds, higher fired, and better execution of design. Additionally, two different slips are being used for the three different paste groups. The slips on pottery excavated from Tipuj are thinner and have a higher frequency of fireclouds as opposed to those excavated from Zacpetén which are thicker and not fireclouded. As a result of patterns present in the cream paste pottery, I was able to define the "hallmark" signatures of how the Kowoj displayed their sociopolitical identity through their pottery: red-on-paste and red-and-black motifs on cream-colored pottery (Clemencia Cream Paste ware).

Unlike the cream-colored pottery produced at Topoxté Island, the gray paste pottery was most likely manufactured from any number of lake clays in the region. Three paste chemical groups occur that demonstrate differences in decorative mode and cultural affiliation. Group 1 represents pottery high in cryptocrystalline calcite and quartz from Zacpetén and is decorated with red-and-black decoration as well as black decorated pottery from Ixlú and Tipuj. Their slips cluster in one group suggesting one place of manufacture. Pastes of Group 2 have lower frequencies of cryptocrystalline calcite and higher amounts of iron and primarily consist of undecorated sherds from Ch'ich' and incised sherds from Ixlú, Tipuj, and Ch'ich'. This group demonstrates the largest variability in slips suggesting a variety of slip recipes and possible locations of production. Finally, Group 3 sherd pastes have abundant small-sized cryptocrystalline calcite and smaller quantities of quartz and iron and contains pottery from Zacpetén that is decorated with red-and-black or red only motifs as well as smaller quantities of undecorated pottery from Ixlú and Ch'ich'. All of these slips group together. Potters at Zacpetén may have produced two different clay recipes used for the different decorative programs. Tipuj may have manufactured the incised pottery (all with the *ilhuitl* motif) and traded it to Ixlú as is suggested by the differences in pastes and slips. Additionally, two paste and slip recipes also exist that correspond to the association of the communities of Ch'ich' and Ixlú.

While much of the Snail-Inclusion Paste pottery could have come from any of the lake shores in the central Petén lakes region, some of the pottery can be attributed to the Kowoj. Some of the Kowoj traditions/customs that began at Topoxté Island continued at Zacpetén throughout the Postclassic period. The Kowoj at Zacpetén recreated and/or imported gray paste pottery with the red decoration, rather than cream-colored paste, to reinforce their sociopolitical identity (Cecil 2007). The Snail-Inclusion Paste ware with red-on-paste decoration (Macanché Red-on-paste) is found almost exclusively at Zacpetén. This manifestation represents a very Late Postclassic and Contact period type and as such may reflect the practice of expressing Kowoj ethnicity with red-on-paste decoration as they moved westward and used different clays (Jones 2007). The same pattern repeats with the red-and-black decorated pottery (Cecil 2001, 2007; Cecil and Neff 2006).

A chemical analysis of the red and black pigments used to decorate the slipped Postclassic pottery further suggests that the Kowoj used different resources for pottery manufacture. The red pigments used to decorate red-on-paste pottery (Chompoxté Red-on-

paste and Macanché Red-on-paste) are chemically different from those red pigments used in conjunction with black decoration (Sacá Polychrome and Canté Polychrome) (Cecil and Neff 2006:1490). Additionally, the black pigments used to decorate Kowoj-specific pottery (Sacá Polychrome, Pastel Polychrome, and Canté Polychrome) are also compositionally different than those of Itza-specific black decorations (Ixpop Polychrome). It also appears that different black pigments were used depending on the motifs being painted (mats, circles, and birds versus hooks and reptiles).

By comparing these data to those from the Early Postclassic period, we can begin to see the effect of different sociopolitical groups establishing and maintaining boundaries during the Postclassic period. First, during the later Postclassic period, Topoxté Island Kowoj manufactured pottery with at least two different pastes and two different slips. They traded this pottery to other communities in the Kowoj territory and there may be preferences as to which community received the better quality pottery. This preference may suggest closer affilitations between Kowoj at Topoxté Island and Zacpetén rather that between Kowoj at Topoxté Island and Tipuj. Less than 10 sherds of this pottery have been excavated from archaeological sites within the Itza territory. Second, it appears that Postclassic potters were using different gray clays for different decorative programs. Pottery decorated in red and red-and-black is associated with the Kowoj and occurs predominately at Zacpetén with lesser amounts at Tipuj. The pastes and slips cluster together suggesting a manufacturing zone at or around Zacpetén and trade between Zacpetén and Tipuj. One the other hand, Snail-Inclusion Paste ware pottery with the incised *ilhuitl* glyph and thick glossy slips characteristic of Tipuj manufacture appears to be produced at Tipuj and traded to the west. This may reflect the ethnohistorical account of the Itza temporarily loosing control of Tipuj and then regaining it after A.D. 1618 (Jones 1998).

To the west, two paste groups represent pottery excavated from the archaeological sites of Ch'ich' and Ixlú. This pottery is undecorated and represents the largest diversity in slips. Thus, it appears that the Itza utilized a larger resource base when manufacturing their pottery and/or more extensive trade is occurring that we have not yet been able to detect.

Nevertheless, these data demonstrate that various chemical composition groups were established that reflect the differences in paste, slip, manufacturing, and trade characteristics that are associated with pottery from the archaeological sites of Ch'ich', Ixlú, Zacpetén, and Tipuj in the central Petén lakes region. When these data are examined in light of the ethnohistorical and archaeological record, changes in manufacturing characteristics and trading patterns throughout the Postclassic period can be recognized. During the Early Postclassic period, pottery from all of the sites seems to suggest that potters in the central Petén lakes region were making similar pottery or that trade was not restricted. In addition to similar manufacturing traditions and unrestricted trade, some potters were attempting to continue the Late Classic pottery technique of creating hard, compact pastes that were then painted with polychrome decoration and gloss slips. The Late Postclassic period is characterized by migrations of sociopolitical groups from the north as well as the manufacture of sociopolitical specific decorative programs and paste groups.

While these data advance our understanding of pottery manufacture and trade of the Itza and Kowoj, more research needs to be conducted to obtain a clearer view of Maya life at the time of Spanish contact. More extensive excavations at archaeological sites in the Itza territory as well as analyzing possible clay and pigment raw material sources will

undoubtedly better define Itza-specific pottery as well as further defining local trade that involved Ch'ich', Ixlú, Zacpetén, and Tipuj.

ACKNOWLEDGMENT

I would like to thank Michael D. Glascock (MURR) and Hector Neff (California State University-Long Beach) for their assistance with my training and understanding of INAA and LA-ICP-MS techniques, respectively. The INAA research and operating support for the MURR Archaeometry Laboratory was provided by a grant from the National Science Foundation (BCS- 0504015). This research was also supported in part by a grant from the US Department of Energy Office of Nuclear Energy, Science and Technology Award No. DE-FG07-03ID14531 to the Midwest Nuclear Science and Engineering Consortium under the Innovations in Nuclear Infrastructure and Education program. The LA-ICP-MS research was funded by the National Science Foundation (BCS-0228187). The archaeological research was supported by funding from Proyecto Maya Colonial of Southern Illinois University Carbondale, from the National Science Foundation (Dissertation Improvement Grant SBR-9816325), and from Sigma Xi Grants-In-Aid of Research. I would also like to thank the Instituto de Antropología e Historia (IDEAH) of Guatemala for allowing the export of the pottery sample to the United States for study. All errors and omission are my own.

REFERENCES

Adams, R. E. W., and Trik, A. S. (1961). Temple I (Str. 5-1): Post-Constructional Activities: Vol. 7. *Tikal Reports University Monograph No. 20*. Philadelphia, PA: University of Pennsylvania.

Alexander, R.T. (1998). Postclassic Settlement Pattern at Isla Cilvituk, Campeche, México. *Paper presented at the 63rd Annual Meeting of the Society for American Archaeology*, Seattle, WA.

Alexander, R.T. (2005a). Isla Cilvituk and the Difficulties of Colonization in Southwestern Campeche. In S. Kepecs and R. Alexander (Eds.), *The Postclassic to Spanish-Era Transition in Mesoamerica: Archaeological Perspectives* (pp. 161-183). Albuquerque: University of New Mexico Press.

Alexander, R.T. (2005b). La Comunidad Postclásica en la Isla Cilvituk, Campeche: ¿Comprende una Frontera Interna? In T.O. Harada and A. L. Izquierdo (Eds.), *Nuevas perspectivas sobre la geografía política de los mayas* (pp. 210-228). México D.F.: Centro de Estudios Mayas, UNAM.

Ball, J. W. (1982). Appendix I: The Tancah Ceramic Situation: Cultural and Historical Insights from an Alternative Material Class. In A. Miller (Ed.), *On the Edge of the Sea: Mural Painting at Tancah-Tulum*, Quintana Roo, Mexico (pp. 105-111). Washington D.C.: Dumbarton Oaks.

Baxter, M. J. (1994). *Exploratory Multivariate Analysis in Archaeology*. Edinburgh: Edinburgh University Press.

Bieber, A. M. Jr., Brooks, D.W., Harbottle, G., and Sayre, E. V. (1976). Application of Multivariate Techniques to Analytical Data on Aegean Ceramics. *Archaeometry*, 18, 59–74.

Bishop, R. L., and Neff, H. (1989). Compositional Data Analysis in Archaeology. In R. O. Allen (Ed.), *Archaeological Chemistry* IV (pp. 576–586). Washington D.C.: American Chemical Society.

Bishop, R. L., Rands, R. L., and Holley, G. R. (1982). Ceramic Compositional Analysis in Archaeological Perspective. In M.B. Schiffer (Ed.), *Advances in Archaeological Method and Theory*: Vol. 5 (pp. 275-330). New York: Academic Press.

Blatt, H. (1992). Sedimentary Petrology. New York: Freeman Press.

Bloomster, J. P., Neff, H., and Glascock, M. D. (2005). Olmec Pottery Production and Export in Ancient Mexico Determined Through Elemental Analysis. *Science*, 307, 1068-1072.

Boot, E. (1997). Kan Ek', Last Ruler of the Itsá. *Yumtzilob*, 9, 5-22.

Boot, E. (2005). Continuity and Change in Text and Image at Chichén Itzá, Yucatán, Mexico. *A Study of the Inscriptions, Iconography, and Architecture at a Late Classic to Early Postclassic Maya Site*. Leiden, Netherlands: CNWS.

Braun, D. P. (1982). Radiographic Analysis of Temper in Ceramic Vessels: Goals and Initial Methods. *Journal of Field Archaeology*, 9, 183-192.

Braun, D. P. (1985). Ceramic Decorative Diversity and Illinois Woodland Regional Integration. In B. A. Nelson (Ed.), *Decoding Prehistoric Ceramics* (pp. 128-153). Carbondale, IL: Southern Illinois University Press.

Bullard, W. R. (1970). Topoxté: A Postclassic Maya Site in Petén, Guatemala. In W. Bullard (Ed.) *Monographs and Papers in Maya Archaeology* (No. 61) (pp. 245-308). Cambridge, MA: Harvard University.

Carr, C. (1990). Advances in Ceramic Radiography and Analysis: Applications and Potentials. *Journal of Archaeological Science*, 17, 13-34.

Cecil, L. G. (2001). *Technological Styles of Late Postclassic Slipped Pottery from the Central Petén Lakes Region*, El Petén, Guatemala. Ph.D. dissertation. Carbondale, IL: Southern Illinois University Carbondale.

Cecil L.G. (2004). Inductively Coupled Plasma Spectroscopy and Postclassic Petén Slipped Pottery: An Examination of Wares and Social Identity. *Archaeometry*, 46, 385-404.

Cecil, L.G. (2007, in press). Technological Styles of the Kowoj. In D. S. Rice, and P. M. Rice (Eds.), *The Kowoj: Identity, Migration, and Politics in Late Postclassic Petén*, Guatemala. Boulder, CO: University Press of Colorado.

Cecil, L. G., and Neff, H. (2006). Postclassic Maya Slips and Paints and Their Relationship to Socio-Political Groups in El Petén, Guatemala. *Journal of Archaeological Sciences*, 33, 1482-1491.

Cecil, L. G., and Pugh, T. W. (2004). Kowoj Symbolism and Technology at Late Postclassic Tipuj. *Paper presented at the 69th Annual Meeting of the Society for American Archaeology*, Montreal, Canada.

Chase, A. F. (1979). Regional Development in the Tayasal-Paxcamán Zone, El Petén, Guatemala: A Preliminary Statement. *Cerámica de Cultura Maya*, 11, 86-119.

Chase, A. F. (1983). *A Contextual Consideration of the Tayasal-Paxcamán Zone*, El Petén, Guatemala. Ph.D. dissertation. Philadelphia, PA: University of Pennsylvania.

Chayes, F. (1956). *Petrographic Modal Analysis*. New York: John Wiley.

Childs, S. T. (1989). Petrographic Analysis of Archaeological Ceramics. *Material Research Science*, 25, 24-29.

Cortés, H. (1976). *Cartas de Relación* (9th edition). México: Editorial Porrua.

Cowgill, G. L. (1963). *Postclassic Period Culture in the Vicinity of Flores*, Petén, Guatemala. Ph.D. dissertation. Cambridge: Harvard University.

Craine, E. R., and Reindorp, R. C. (1970). *The Chronicles of Michoacan*. Norman, OK: University of Oklahoma Press.

Demarest, A. A. (1986). *The Archaeology of Santa Leticia and the Rise of Maya Civilization*. (Middle American Research Institute Publication 52). New Orleans, LA: MARI, Tulane University.

Dickenson, W. R., and Shutler, R. Jr. (1979). *Petrography of Sand Tempers in Pacific Island Potsherds*. Geological Society of America Bulletin Part II, 90, 1644-1701.

Dietler, M., and Herbich, I. (1998). Habitus, Techniques, Style: An Integrated Approach to the Social Understanding of Material Culture and Boundaries. In M. T. Stark (Ed.), *The Archaeology of Social Boundaries* (pp. 232-263). Washington D.C.: Smithsonian Institution Press.

Duncan, W. N. (2005). *The Bioarchaeology of Ritual Violence in Postclassic El Petén, Guatemala* (AD 950-1524). Ph.D. dissertation. Carbondale, IL: Southern Illinois University Carbondale.

Edmonson, M. S. (1982). *The Ancient Future of the Itza: The Book of Chilam Balam of Tizimin*. Austin, TX: University of Texas Press.

Edmonson, M. S. (1986). *Heaven Born Merida and Its Destiny: The Book of Chilam Balam of Chumayel.* Austin, TX: University of Texas Press.

Flannery, K. V., Balkansky, A. K., Feinman, G. M., Grove, D. C., Marcus, J., Redmond, E. M., Reynolds, R. G., Sharer, R. J., Spencer, C. S., and Yaeger, J. (2005). Implications of New Petrographic Analysis for the Olmec "Mother Culture" Model. *PNAS*, 102,11219-11223.

Forsyth, D. W. (1989). The Ceramics of El Mirador, Petén, Guatemala, *El Mirador Series*, Part 4. Provo, UT: Brigham Young University.

Giddens, A. (1984). *The Constitution of Society: Outline of the Theory of Structuration.* Berkeley, CA: University of California Press.

Glascock, M. D. (1992). Characterization of Archaeological Ceramics at MURR by Neutron Activation Analysis and Multivariate Statistics. In H. Neff (Ed.), *Chemical Characterization of Ceramic Pastes in Archaeology* (pp. 11-26). Madison, WI: Prehistory Press.

Glascock, M. D. (2007). The Archaeometry Laboratory at the University of Missouri Research Reactor [hyper-text document] http://archaeometry.missouri.edu.

Harbottle, G. (1976). Activation Analysis in Archaeology. *Radiochemistr*y, 3, 33–72.

Jones, G. D. (1998). *The Conquest of the Last Maya Kingdom*. Stanford, CA: Stanford University Press.

Jones, G. D. (2007, in press). The Kowojs in Ethnohistorical Perspective. In D. S. Rice, and P. M. Rice (Eds.), *The Kowoj: Identity, Migration, and Politics in Late Postclassic Petén,* Guatemala. Boulder, CO: University Press of Colorado.

Jones, G. D., Rice, D. S., and and Rice, P. M. (1981). The Location of Tayasal: A Reconsideration in Light of Petén Maya Ethnohistory and Archaeology. *American Antiquity*, 46, 530-547.

Kepecs, S. M., and Masson, M. A. (2003). Political Organization in Yucatán and Belize. In M. E. Smith, and F. F. Berdan (Eds.), *The Postclassic Mesoamerican World* (pp. 40-44). Salt Lake City, UT: University of Utah Press.

Kowalski, J. K. (1987). *The House of the Governor: A Maya Palace at Uxmal*, Yucatan, Mexico. Norman, OK: University of Oklahoma Press.

Lechtman, H. (1977). Style in Technology—Some Early Thoughts. In H. Lechtman, and R. S. Merrill (Eds.), *Material Culture: Styles, Organization, and Dynamics of Technology* (pp. 3-20). St. Paul, MN: West Publishing Company.

Lemonnier, P. (1992). *Elements for an Anthropology of Technology* (No. 88). Ann Arbor: MI: Museum of Anthropology, University of Michigan.

Middleton, A. P., Freestone, I. C., and Leese, M. N. (1985). Textural Analysis of Ceramic Thin Sections: Evaluations of Grain Sampling Procedures. *Archaeometry*, 27, 64-74.

Milbrath, S., and Peraza Lope, C. (2003). Revisiting Mayapán. *Ancient Mesoamerica*, 14, 1-46.

Neff, H. (1992). Introduction. In H. Neff (Ed.), *Chemical Characterization of Ceramic Pastes in Archaeology* (pp. 1–10). Madison, WI: Prehistory Press.

Neff, H. (2000). Neutron Activation Analysis for Provenance Determination in Archaeology. In E. Ciliberto, and G. Spoto (Eds.), *Modern Analytical Methods in Art and Archaeology* (pp. 81–134). New York: John Wiley and Sons, Inc.

Neff, H. (2002). Quantitative Techniques for Analyzing Ceramic Compositional Data. In D. M. Glowacki, and H. Neff (Eds.), *Ceramic Source Determination in the Greater Southwest* (No. 44). Los Angeles, CA: Cotsen Institute of Archaeology.

Neff, H., Blomster, J. P., Glascock, M. D., Bishop, R. L., Blackman, M. J., Coe, M. D., Cowgill, G. L., Cyphers, A., Diehl, R.A., Houston, S., Joyce, A. A., Lipo, C. P., and Winters, M. (2006). Smokescreens in the Provenance Investigation of Early Formative Mesoamerican Ceramics. *Latin American Antiquity*, 17, 104-118.

Neff, H., Blomster, J. P., Glascock, M. D., Bishop, R. L., Blackman, M. J., Coe, M. D., Cowgill, G. L., Cyphers, A., Diehl, R. A., Houston, S., Joyce, A. A., Lipo, C. P., Stark, B. L., and Winters, M. (2006). Methodological Issues in the Provenance Investigation of Early Formative Mesoamerican Ceramics. *Latin American Antiquity*, 17, 54-76.

Orton, C., Tyers, P., and Vince, A. (1993). *Pottery in Archaeology*. Cambridge, England: Cambridge University Press.

Peacock, D. P. S. (1973). The Black-Burnished Pottery Industry in Dorset. *Research Reports Council for British Archaeology*, 10, 63-65.

Proskouriakoff, T. (1962). Civic and Religions Structures of Mayapán. In H. E. D. Pollock, R. L. Roys, T. Proskouriakoff, and A. L. Smith (Eds.), *Mayapán, Yucatán, México* (No. 619) (pp. 87-164). Washington D.C.: Carnegie Institution of Washington.

Pugh, T. W. (1996). La Zona del lago Salpetén-Zacpetén. In D. S. Rice, P. M. Rice, R. Sánchez-Polo, and G. D. Jones (Eds.), *Proyecto Maya-Colonial: Geografía Política del Siglo XVII en el Centro del Petén, Guatemala* (pp. 206-221). Informe Preliminar al Instituto de Antropología e Historia de Guatemala sobre Investigaciones del Campo en los Años 1994 y 1995.

Pugh, T. W. (2001a). *Architecture, Ritual, and Social Identity at Late Postclassic Zacpetén, Petén, Guatemala: Identification of the Kowoj*. Ph.D. dissertation. Carbondale, IL: Southern Illinois University Carbondale.

Pugh, T.W. (2001b). Flood Reptiles, Serpent Temples, and the Quadripartite Universe: The Imago Mundi of Late Postclassic Mayapán. *Ancient Mesoamerica*, 12, 247-258.

Reents-Budet, D., Ball, J. W., Bishop, R. L., Fields, V. M., and MacLeod, B. (1994). *Painting the Maya Universe: Royal Ceramics of the Classic Period.* Durham, NC: Duke University Press.

Restall, M. (1998). *Maya Conquistador*. Boston, MA: Beacon.

Rice, D. S. (1986). The Petén Postclassic: A Settlement Perspective. In J. A. Sabloff, and E. W. Andrews V (Eds.), *Late Lowland Maya Civilization: Classic to Postclassic* (pp. 301-344). Albuquerque, NM: University of New Mexico Press.

Rice, Don S., Rice, P. M., Sánchez Polo, R., and and Jones, G.D. (1996). Proyecto Maya-Colonial: Geografía Política del Siglo XVII en el Centro del Petén, Guatemala. Informe Preliminar al Instituto de Antropología e Historia de Guatemala sobre Investigaciones del Campo en los Años 1994 y 1995.

Rice, P. M. (1976). Rethinking the Ware Concept: Inconsistencies Between Logic and Practice in Type-Variety of Mesoamerica. *American Antiquity*, 41, 538-543.

Rice, P. M. (1979). Ceramic and Nonceramic Artifacts of Lakes Yaxha-Sacnab, El Petén, Guatemala, Part I. The Ceramics. *Cerámica de Cultura Maya*, 11, 1-85.

Rice, P. M. (1982). Pottery Production, Pottery Classification, and the Role of Physiochemical Analyses. In J. S. Olin and A. D. Franklin (Eds.), *Archaeological Ceramics* (pp. 47-56). Washington D.C.: Smithsonian Institution Press.

Rice, P. M. (1986). The Petén Postclassic: Perspective from the Central Petén Lakes. In J.A. Sabloff, and E. W. Andrews V (Eds.), *Late Lowland Maya Civilization: Classic to Postclassic* (pp. 251-299). Albuquerque, NM: University of New Mexico Press.

Rice, P. M. (1987a). *Macanché Island, El Petén, Guatemala: Excavation, Pottery, and Artifacts*. Gainesville, FL: University of Florida Press.

Rice, P. M. (1987b). *Pottery Analysis*. Chicago, IL: University of Chicago Press.

Ringle, W. M., and Bey, G. J. III, (2001). Post-Classic and Terminal Classic Courts of the Northern Maya Lowlands. In T. Inomata, and S. D. Houston (Eds.), *Royal Courts of the Ancient Maya, Vol 2: Data and Case Studies* (pp. 266-307). Boulder, CO: Westview Press.

Ringle, W. M., Gallareta Regrón, T., and Bey, G. J. III (1998). The Return of Quetzalcoatl: Evidence for the Spread of a World Religion during the Epiclassic Period. *Ancient Mesoamerica*, 9, 183-232.

Roys, R. (1933). *The Book of Chilam Balam of Chumayel* (No. 438).Washington D.C.: Carnegie Institution of Washington.

Roys, R. (1957). *The Political Geography of the Yucatán of México* (No. 613). Washington, D.C.: Carnegie Institution of Washington.

Roys, R. (1962). Literary Sources for the History of Mayapán. In H. E. D. Pollock, R. L. Roys, T. Proskouriakoff, and A. L. Smith (Eds.), *Mayapán, Yucatán, México* (No, 619) (pp. 25-86). Washington D.C.: Carnegie Institution of Washington.

Roys, R. (1972). *The Indian Background of Colonial Yucatan*. Norman, OK: University of Oklahoma Press.

Schele, L., and Grube, N. (1995). *The Proceedings of the Maya Hieroglyph Workshop: Late Classic and Terminal Classic Warfare, March 11-12, 1995*. Transcribed and edited by Phil Wanyerka, Austin, Texas.

Schele, L., Grube, N., and Boot E., (1998). Some Suggestions on the K'atun Prophecies in the Books of Chiam Balam in Light of Classic-period History. *In Memorias del Tercer Congreso Internacional de Mayistas* (pp. 399-446). México: Universidad Autonoma de México, Centro de Estudios Maya.

Schele, L., and Mathews, P. (1998). *The Code of King*s. New York: Scribner.

Shackley, M. L. (1975). *Archaeological Sediments: A Survey of Analytical Methods*. New York: John Wiley.

Sharer, R. J., Balkansky, A. K., Burton, J. H., Feinman, G. M., Flannery, K. V., Grove, D. C., Marcus, J., Moyle, R. J., Price, T. D., Redmond, E. M., Reynolds, R. G., Rice, P. M., Spencer, C. S., Stoltman, J. B ., and Yaeger, J. (2006). On the Logic of Archaeological Inference: Early Formative Pottery and the Evolution of Mesoamerican Studies. *Latin American Antiquity*, 17, 90-103.

Sharer, R. J., and Chase, A. F. (1976). New Town Ceramic Complex. In J.C. Gifford (Ed.), *Prehistoric Pottery Analysis and the Ceramics of Barton Ramie in the Belize Valley* (No. 18) (pp. 288-311). Cambridge, MA: Harvard University.

Shepard, A.O. (1956). *Ceramics for the Archaeologist*. Washington D.C.: Carnegie Institution of Washington.

Smith, R. E., Willey, G. E., and Gifford, J. C. (1960). The Type-Variety Concept as a Basis for the Analysis of Maya Pottery. *American Antiquity*, 25, 30-340.

Speakman, R. J. (2005). *Laser Ablation-ICP-MS in Archaeological Research*. Albuquerque, NM: University of New Mexico Press.

Steponaitis, V., Blackman, M. J., and Neff, H. (1996). Large-Scale Compositional Patterns in the Chemical Composition of Mississippian Pottery. *American Antiquity*, 61, 555–572.

Stoltman, J. B., Marcus, J., Flannery, K. V., Burton, J. H., and Moyle, R. G. (2005). Petrographic Evidence Shows That Pottery Exchange Between The Olmec and Their Neighbors Was Two-Way. *PNAS*, 10, 11213-11218.

Tozzer, A. (1941). *Landa's Relacion de las Cosas de Yucatán* (Vol 18). Cambridge, MA: Peabody Museum, Harvard.

Vaughn, K. J., Conlee, C. A., Neff, H, and Schreiber, K. J. (2005). A Compositional Analysis of Nasca Pigments: Implications for Craft Production on the Pre-Hispanic South Coast of Peru. In R. J. Speakman (Ed.), *Laser Ablation-ICP-MS in Archaeological Research* (pp. 139-153). Albuquerque, NM: University of New Mexico Press.

Weigand, P. C., Harbottle, G., and Sayre, E.V. (1977). Turquoise Sources and Source Analysis: Mesoamerica and the Southwestern U.S.A. In T. K. Earle, and J. E. Ericson (Eds.), *Exchange Systems in Prehistory* (pp. 15–34). New York: Academic Press.

In: Developments in Ceramic Materials Research
Editor: Dena Rosslere, pp. 35-52
ISBN 978-1-60021-770-8

Chapter 2

RECENT ADVANCES IN ROTARY ULTRASONIC MACHINING OF CERAMICS

***Z. C. Li*[*], *Z. J. Pei*[*] *and C. Treadwell*[**]**

[*]Department of Industrial and Manufacturing Systems Engineering,
Kansas State University, Manhattan, KS 66506
[**]Sonic-Mill Company
7500 Bluewater Road N.W. Albuquerque, NM 87121

ABSTRACT

Rotary ultrasonic machining (RUM) is one of the nontraditional machining processes for ceramics. This chapter overviews the recent advances in RUM of ceramics since 2001. It first reports the progress on quality improvement of RUM machined parts – reduction and elimination of edge chipping in RUM of ceramics. After discussing the effects of RUM process parameters (spindle speed, feedrate, ultrasonic vibration power, and grit size) on the edge chipping thickness, practical ways to reduce the edge chipping are presented.

It then presents recent studies on the effects of coolant type, pressure, and delivery mode (continuous versus intermittent) on cutting force and surface roughness when RUM of ceramics.

Finally, it reports the exploratory efforts to apply RUM to machine silicon carbide and ceramic matrix composites (CMC). It discusses the effects of RUM process parameters (spindle speed, feedrate, ultrasonic vibration power, and grit size etc.) on cutting force, surface roughness, tool wear, and chipping size.

1. INTRODUCTION

Thanks to their superior properties in hardness, strength, and resistance to wear and corrosion, advanced ceramics are attractive for many industrial applications [Inasaki and Nakayama, 1986; Zhang and Howest, 1994; Malkin and Hwang, 1996; Zeng et al., 2005]. However, their high machining cost is a major barrier for the widespread utilizations of

advanced ceramics [Zhang and Howest, 1994; Malkin and Hwang, 1996; Zeng et al., 2005]. Therefore, it is desirable to develop more cost-effective machining processes for advanced ceramics.

Rotary ultrasonic machining (RUM) is one of the cost-effective processes for machining advanced ceramics. It combines the material removal mechanisms of diamond grinding and ultrasonic machining [Legge, 1964; Legge, 1966]. Figure 1 illustrates the RUM process. A rotating diamond core drill is ultrasonically vibrated and fed to the workpiece.

Table 1 summarizes the types of advanced ceramics machined by RUM up to 2001. Much efforts have been exerted to study the RUM process experimentally and theoretically. Reported studies on RUM up to 2001 are summarized in Table 2. More comprehensive reviews on these reported studies are in the literature [Pei et al., 1995[a]; Li et al., 2004].

This chapter reports the recent advances in RUM of advanced ceramics since 2001. It first reports the progress on quality improvement of RUM machined parts – reduction and elimination of edge chipping in RUM of ceramics. Then, recent studies on the effects of coolant type, pressure, and delivery mode (continuous versus intermittent) on cutting force and surface roughness when RUM of ceramics are presented. Finally, it reports the exploratory efforts to apply RUM to machine silicon carbide and ceramic matrix composites (CMC).

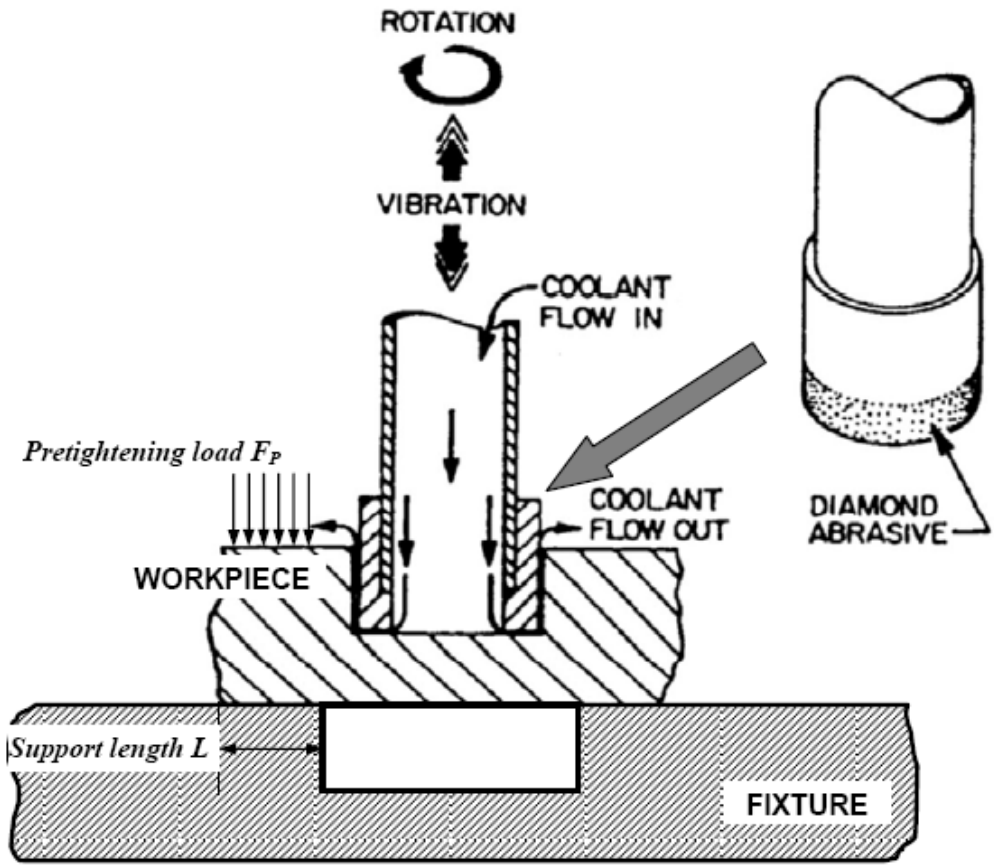

Figure 1. Illustration of RUM.

Table 1. Ceramic materials machined by RUM till 2001

Ceramic material	References
Alumina	Anantha Ramu et al., 1989, Zhang et al., 1995
Canasite	Khanna et al., 1995
Glass	Lunzer, 1973; Anonymous, 1966; Anonymous, 1973
Silicon nitride	Cleave, 1970; Dam et al., 1995
Zirconia	Anantha Ramu et al., 1989; Prabhakar, 1993; Pei, 1995; Pei et al., 1995[b]; Pei et al., 1995[c] ; Pei and Ferreira, 1998

Table 2. Reported studies on RUM till 2001

Study	Reference
Material removal mechanism (brittle/ductile removal modes)	Prabhakar et al., 1993; Spur and Holl, 1997; Zhang et al., 1995
Material removal models based upon different material removal modes	Pei, 1995; Pei et al., 1995[a]; Pei et al., 1998
Effects of process parameters (rotating speed; feedrate; ultrasonic vibration amplitude and frequency; diamond type, size and concentration; bond type for the cutting tool, etc.) on the performances (material removal rate, cutting force, surface roughness, etc.)	Petrukaha et al., 1970; Markov and Ustinov, 1972; Markov and Ustinov, 1977; Prabhakar, 1992; Spur et al., 1997; Kubota et al., 1997
Extension to face milling	Pei and Ferreira, 1999
Extension to disk grinding	Khanna et al., 1995
Extension to complex contour machining	Uhlmann et al., 1999 ; Ya et al., 2001

2. EDGE CHIPPING

2.1. Edge Chipping Phenomenon in RUM

Figure 2 illustrates the edge chipping phenomenon in the RUM process. RUM is a core drilling process and produces two pieces as shown in Figure 2(a). One piece is the machined part with the desired hole, the other is a rod (or slug) removed from the workpiece. Figure 2(b) shows the side view and top view of the machined rod. In RUM, when the cutting tool nearly drills through the workpiece, the rod breaks off from the workpiece, causing the edge chipping around the hole exit edge.

The edge chipping in a machined ceramic component not only compromises geometric accuracy, but also causes possible failure of the component during service [Ng et al., 1996; Yoshifumi et al., 1995]. Generally, edge chipping is not acceptable on finished products, and has to be machined off by other processes after the RUM operation. The larger the edge chipping, the higher the total machining cost.

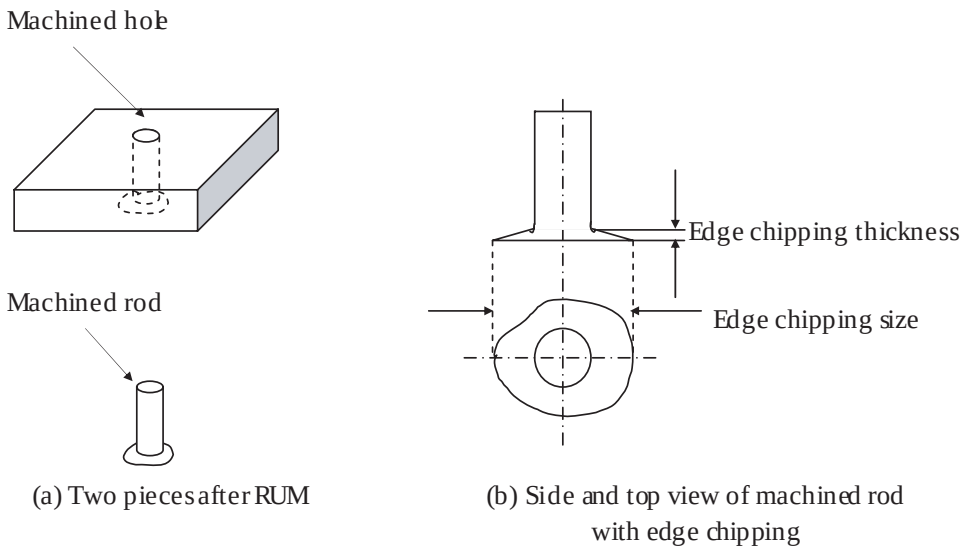

Figure 2. Illustration of edge chipping phenomenon in RUM (after [Jiao et al., 2005]).

2.2. Effects of Process Parameters on Edge Chipping

The spindle speed is the rotational speed of the core drill. It has a significant effect on edge chipping thickness when RUM of alumina [Jiao et al., 2005]. The edge chipping thickness decreases as spindle speed increases, as shown in Figure 3(a).

The feedrate is the rate at which the core drill drills into the workpiece. It affects the edge chipping thickness significantly [Jiao et al., 2005]. The edge chipping thickness decreases as feedrate decreases, as shown in Figure 3(b).

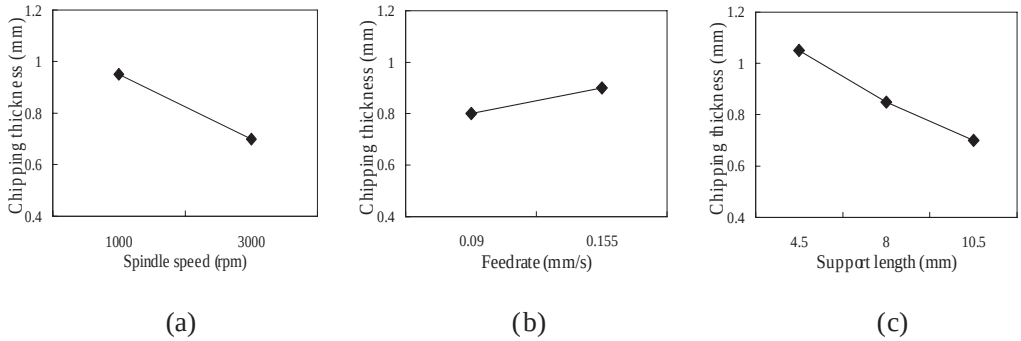

Figure 3. Effects of process parameters on edge chipping thickness (After [Jiao et al., 2005; Li et al., 2006]).

The support length is the radial length of the contact area between the workpiece and the fixture, as shown in Figure 1. It also has a significant effect on the edge chipping thickness [Li et al., 2006]. The edge chipping thickness decreases as the support length increases, as shown in Figure 3(c).

It is reported that grit size, ultrasonic vibration power, and pretightening load do not affect the edge chipping thickness significantly [Jiao et al., 2005, Li et al., 2006].

The interaction between spindle speed and feedrate has a significant effect on edge chipping thickness when RUM of alumina [Jiao et al., 2005]. As shown in Figure 4(a), at the high level of feedrate (0.155 mm/s), a change in spindle speed causes a larger change in edge chipping thickness than at the low level of feedrate (0.09 mm/s).

The interaction between feedrate and grit size also has a significant effect on edge chipping thickness. As shown in Figure 4(b), at the low level of grit size (mesh 140/170), a change in feedrate causes a larger change in edge chipping thickness than at the level of grit size (mesh 270/350).

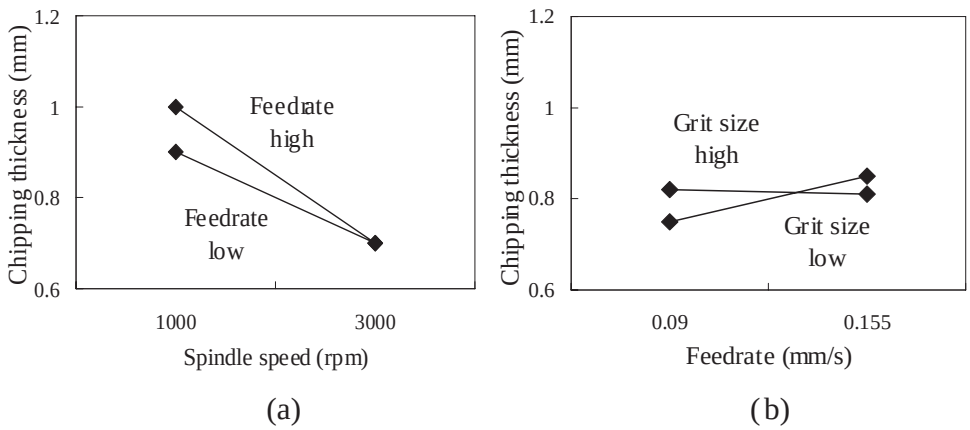

Figure 4. Two-factor interaction effects on edge chipping thickness (after [Jiao et al., 2005]).

2.3. Practical Ways to Reduce Edge Chipping

The cutting force is related to RUM process parameters (including spindle speed, feedrate, and ultrasonic vibration power, etc.). It also has a correlation with the edge chipping thickness. It is reported that larger edge chipping is almost always accompanied by a higher cutting force as shown in Figure 5 [Jiao et al., 2005]. Therefore, any ways to reduce the cutting force will also reduce the edge chipping. Since higher spindle speed and lower feedrate result in smaller cutting force [Jiao et al., 2005], higher spindle speed and lower feedrate should be used in order to reduce edge chipping thickness.

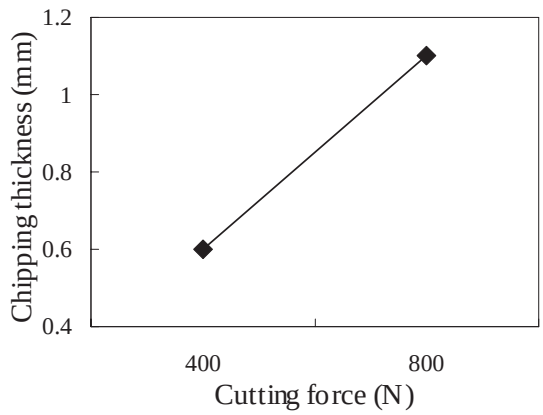

Figure 5. Relationship between the cutting force and edge chipping thickness (after [Jiao et al., 2005).

Based upon finite element analysis and experimental verifications, it has been found that the maximum values of the maximum normal stress and von Mises stress (in the edge chipping initiation area) decrease significantly as the support length increases [Li et al., 2005]. The smaller the maximum values, the deeper the tool can drill into the workpiece without edge chipping. Therefore, another practical way to reduce edge chipping thickness is to increase the support length when RUM of alumina [Li et al., 2005].

3. COOLANT

Coolant is an important factor in RUM. It is pumped through the core of the drill, washing away the swarf, preventing jamming of the drill, and keeping the drill cool [Pei et al., 1995[a]]. Without coolant, the debris will stick on the tool and workpiece surface, causing the feed speed to slow down, and the tool may be burnt or even completely ruined by high temperatures in the cutting zone [Hu et al., 2003].

3.1. Effects of Coolant Type

Coolant type (Coolant type A: Water-based coolant; Coolant type B: Synthetic coolant; and Coolant type C: Tap water) has significant effects on the cutting force [Hu et al., 2003].

The cutting force with the water-based coolant is much lower than those with the synthetic coolant and tap water. The difference of surface roughness between these three coolant types is not statistically significant.

3.2. Effects of Coolant Pressure

Coolant pressure (in continuous coolant delivery mode) has a significant effect on hole surface roughness as shown in Figure 6. As the coolant pressure increases, the hole surface roughness decreases. The hole surface roughness is improved because the higher coolant output pressure would wash away more micro swarfs, which had a negative effect on the machined surface roughness [Hu et al., 2003].

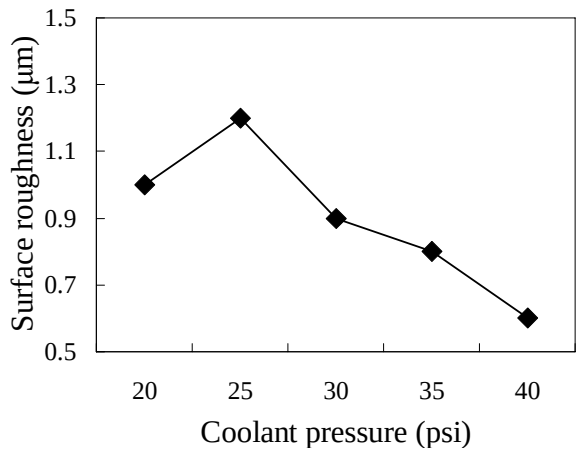

Figure 6. Effect of coolant pressure (in the continuous coolant delivery mode) on surface roughness (after [Hu et al., 2003]).

3.3. Effects of Coolant Delivery Mode

In RUM, the coolant can be delivered to the cutting zone in at least two modes: continuous and intermittent. The continuous mode, which delivers the coolant at a constant pressure, as shown in Figure 7(a), can be realized with the regular centrifugal pump. In the intermittent mode, the coolant pressure will alter between on and off status, as shown in Figure 7(b).

The intermittent coolant delivery mode has been set up approximately using an air-operated double diaphragm pump (AODDP) [Li et al., 2005]. Figure 8 shows the actual coolant delivery mode when using AODDP. The coolant pressure in this mode is adjusted by changing the air pressure.

At a similar coolant pressure level, compared to the continuous mode, the surface roughness on the machined hole surface can be much improved using the intermittent mode, as shown in Figure 9. When using the intermittent coolant delivery mode, the surface

roughness decreases as the air pressure increases, as shown in Figure 10. The coolant delivery mode does not have significant effects on the cutting force [Li et al., 2005].

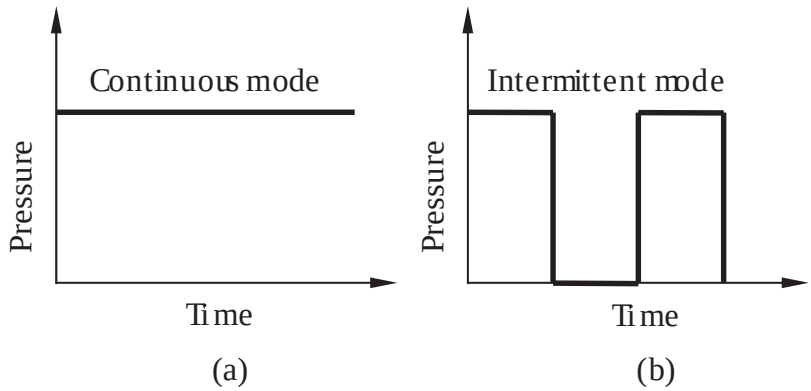

Figure 7. Two coolant delivery modes (after [Li et al., 2005]).

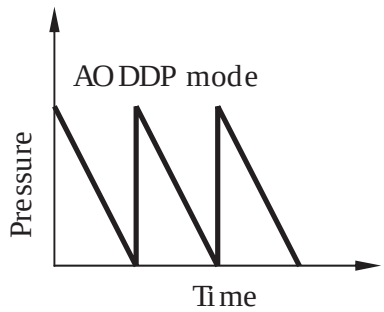

Figure 8. Coolant delivery mode when using AODDP (after [Li et al., 2005]).

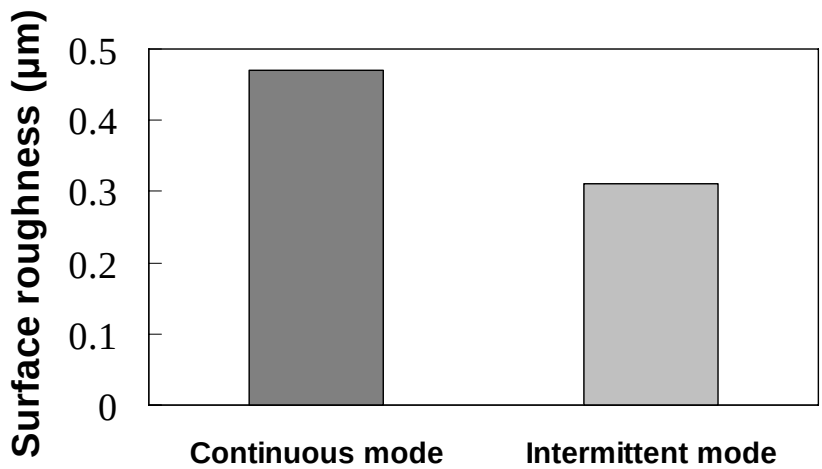

Figure 9. Comparison of surface roughness between different coolant delivery modes (after [Li et al., 2005]).

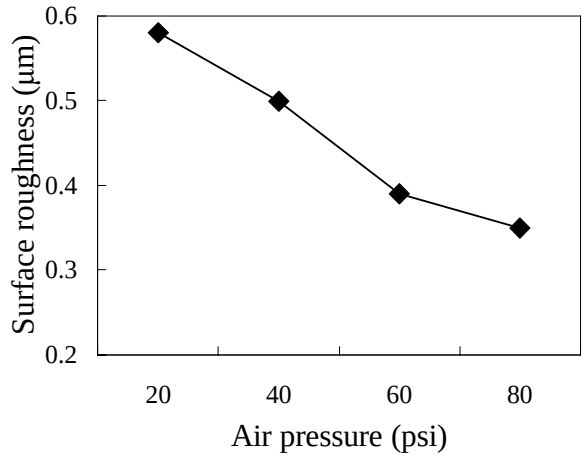

Figure 10. Effect of air pressure (in the intermittent coolant delivery mode) on surface roughness (after [Li et al., 2005]).

4. RUM OF SILICON CARBIDE

Silicon carbide has superior properties such as high strength at elevated temperatures, resistance to chemical degradation, wear resistance, low density, high stiffness, low coefficient of thermal expansion, and superior creep resistance. The combination of these properties makes them attractive in many engineering applications but difficult to machine into desired geometry and surface quality [Datta et al., 2004; Yin et al., 2004].

Up to 2001, no attempt has been reported to machine silicon carbide by RUM.

4.1. Effects of Process Parameters on Cutting Force

The spindle speed has a significant effect on the cutting force when RUM of silicon carbide. The cutting force increases as the spindle speed decreases, as shown in Figure 11(a).

The feedrate also has a significant effect on the cutting force. The cutting force increases as the feedrate increases, as shown in Figure 11(b).

The ultrasonic vibration power and grit size do not affect the cutting force significantly.

Figure 12 shows the interactions effects of process parameters on cutting force in RUM of silicon carbide. The interaction effect between spindle speed and feedrate is significant. As shown in Figure 12(a), at the high level of feedrate, the change of spindle speed causes a larger change in cutting force than at the low level of feedrate.

The interaction effect between ultrasonic vibration power and feedrate is significant. As shown in Figure 12(b), at the high level of feedrate, the cutting force increases with the change of vibration power from low level to high level, whereas, at the low level of feedrate, the cutting force decreases with the change of vibration power from low level to high level.

The interaction effect between ultrasonic vibration power and grit size are significant. As shown in Figure 12(c), at low level of grit size, the cutting force increases with change of

vibration power from low level to high level, whereas, at high level of grit size, the cutting force remains about the same with change of vibration power from low level to high level.

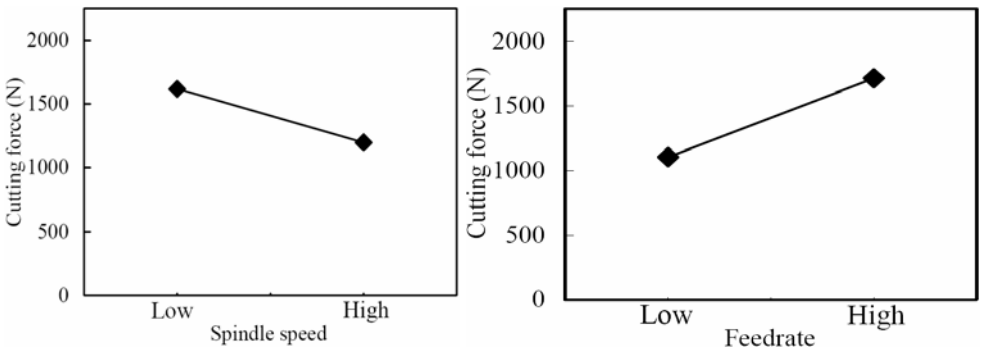

Figure 11. Effects on cutting force in RUM of SiC (after [Churi et al., 2007]).

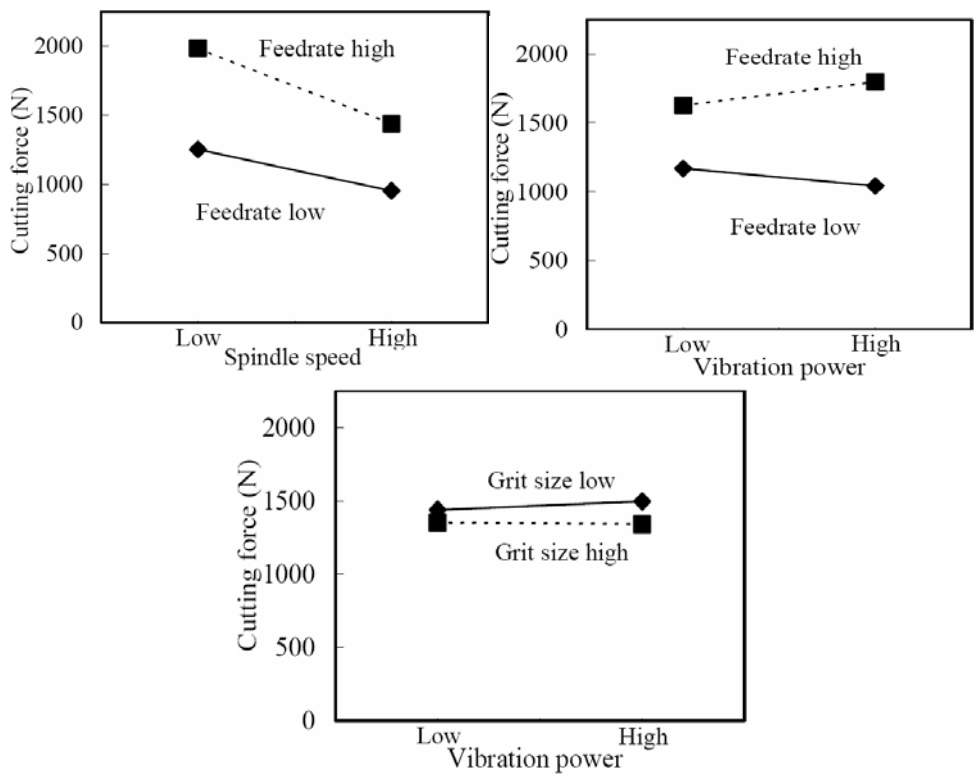

Figure 12. Two-factor interaction effects on cutting force in RUM of SiC (after [Churi et al., 2007]).

The results about main effects of process parameters on the cutting force when RUM of silicon carbide agree well with those when RUM of alumina. For interaction effects, RUM of silicon carbide shows more complicated interactions between process parameters than RUM of alumina.

4.2. Effects of Process Parameters on Surface Roughness

All the process parameters have significant effects on surface roughness. Surface roughness (R_a) decreases as spindle speed increases, as shown in Figure 13(a). R_a decreases as vibration power increases, as shown in Figure 13(b). R_a increases as feedrate increases, as shown in Figure 13(c). R_a decreases as grit size decreases, as shown in Figure 13(d).

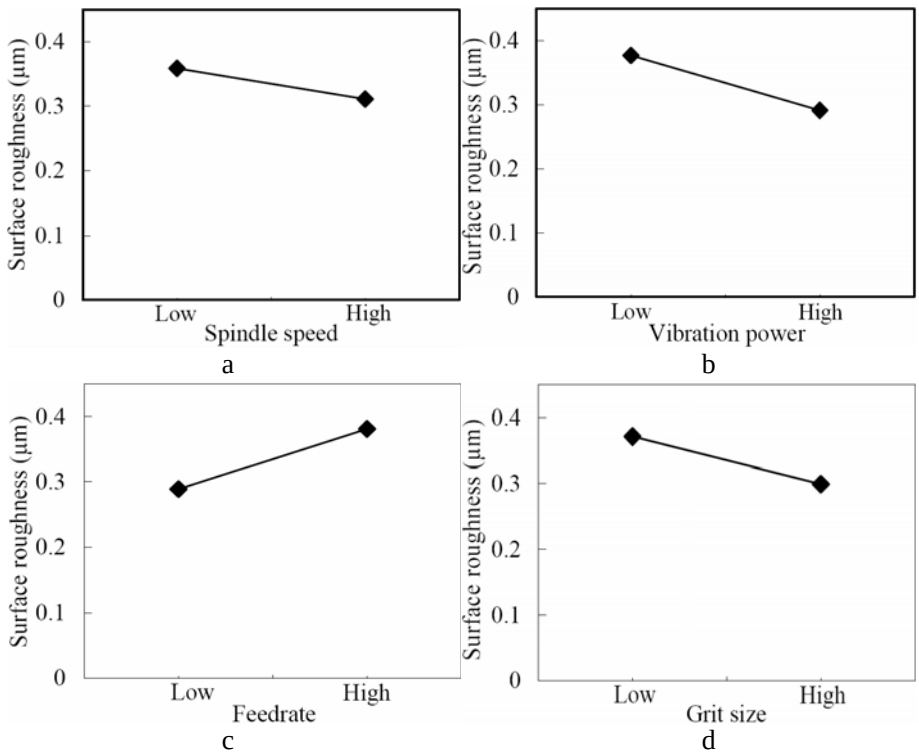

Figure 13. Effects on surface roughness in RUM of SiC (after [Churi et al., 2007]).

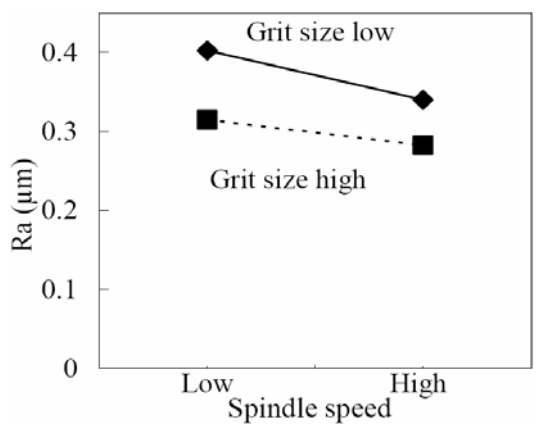

Figure 14. Two-factor interaction effects on surface roughness in RUM of SiC (after [Churi et al., 2007]).

Figure 14 shows the interactions effects of process parameters on surface roughness in RUM of Silicon carbide. The interaction effect between spindle speed and grit size is significant. At the low level of grit size, the change of spindle speed causes a larger change in surface roughness than at the high level of grit size.

4.3. Effects of Process Parameters on Edge Chipping Size

The edge chipping size decreases as spindle speed increases, as shown in Figure 15(a). The edge chipping size increases as vibration power increases, as shown in Figure 15(b). The edge chipping size increases as feedrate increases, as shown in Figure 15(c). The edge chipping size decreases as grit size increases, as shown in Figure 15(d).

Figure 16 shows the interactions effects of process parameters on edge chipping size in RUM of Silicon carbide. The interaction effect between spindle speed and vibration power is significant. It can be seen that at the high level of vibration power, the change of spindle speed causes a smaller change in chipping size than at the low level of vibration power.

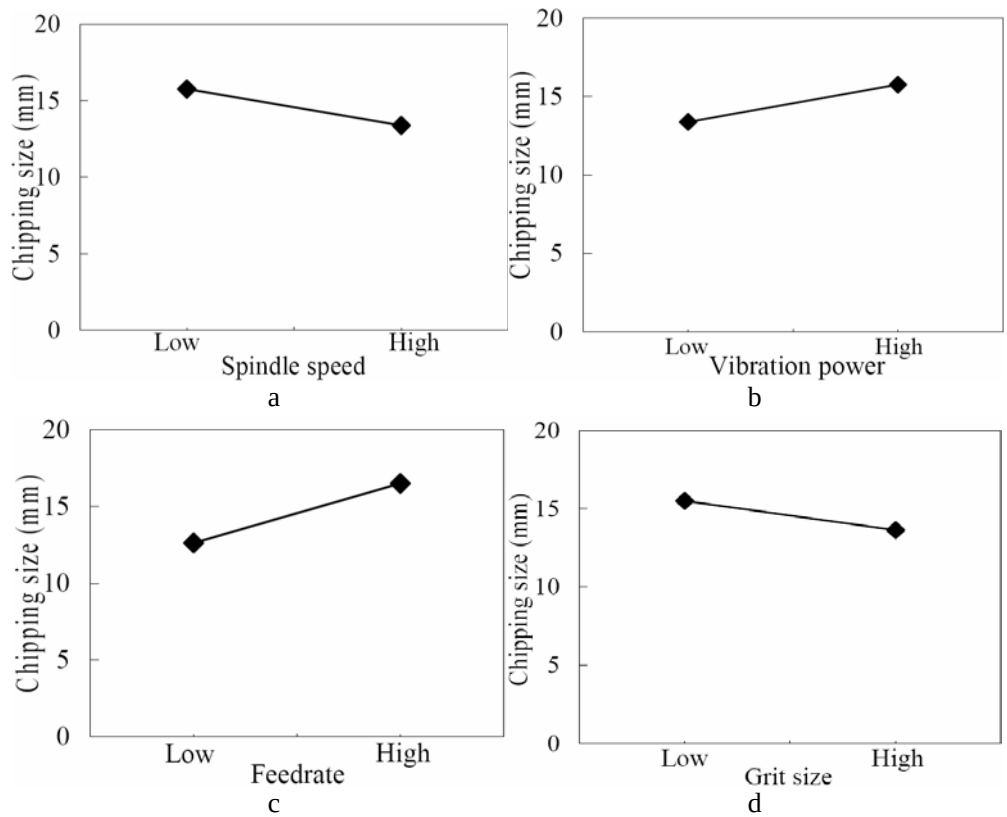

Figure 15. Effects on edge chipping size in RUM of SiC (after [Churi et al., 2007]).

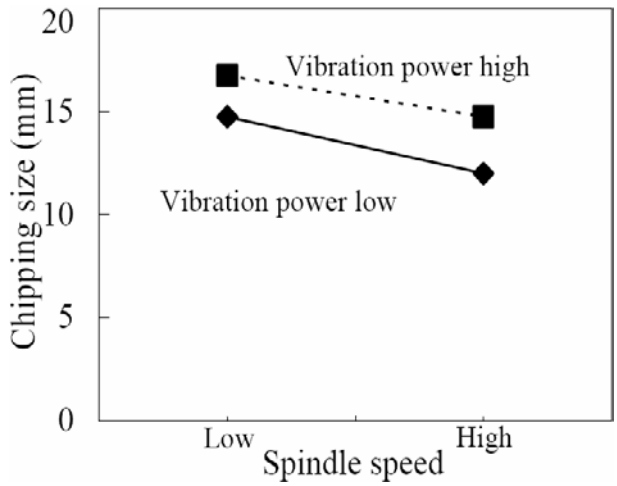

Figure 16. Two-factor interaction effects on edge chipping size in RUM of SiC (after [Churi et al., 2007]).

4.4. Tool wear

In RUM of silicon carbide, compared to the tool end face, the wear of diamond grains on the tool lateral face was obviously small. It indicates that it is unnecessary to have so many diamond grains on the lateral face of a RUM tool [Zeng et al., 2005]. Therefore, the length of the lateral face can be shorter, thus reducing the manufacturing cost of the RUM tool. However, wear of the diamond grains at the tool edge intersected by the lateral face and the end face was quite severe.

The tool end face has a server tool wear. Most of the diamond grains on the tool end face are pulled out after a few RUM tests. It shows that the wear of tool end face is so severe that most of diamond grains are dislodged. It is clearly shown that the diamond grain dislodgment is due to bond fracture in RUM of Silicon carbide. Some diamond grains were pulled out of the metal bond prematurely, before completing their effective working lives. Weakening of the interfaces between diamond grains and metal bond may be due to mechanical impact and high temperature.

Grain fracture which is commonly seen in metal grinding and conventional grinding of ceramic materials has not been observed when RUM of Silicon carbide. It seems that diamond grains are more susceptible to bond fracture from the bond prior to grain fracture. The tool wear in RUM of silicon carbide seems to have two different stages. In the first stage, attritious wear dominates. In the second stage, bond fracture dominates. The tool fails to function any longer when the bond fracture becomes too severe.

Another interesting phenomenon is associated with the color of diamond grains. It has been observed that the surface color of these diamond grains is different, implying that the temperature on these grain surfaces during RUM was high. The reason could be that during the RUM process, the diamond grains become extremely dull, thereby causing large friction and high temperature at the interface of the diamond grains and the workpiece.

5. RUM OF CERAMIC MATRIX COMPOSITES

Ceramic matrix composites (CMC) combine reinforcing ceramic phases with a ceramic matrix to create materials with superior properties (like high-temperature stability, high thermal-shock resistance, and lightweight), providing unique engineering solutions [Richerson, 1997]. The combination of these characteristics makes CMC an attractive alternative to traditional materials such as high alloy steels and refractory metals [Richerson, 1997; Okamura, 1995; Freitag and Richerson, 1998]. Benefits of using CMC include increased energy efficiency, increased productivity, and regulatory compliance. CMC have been used in some areas for years, such as cutting tools and wear parts [Anonymous, 2000]. Other emerging applications being field-tested or in the development stage include gas turbine seals, hot gas filters and high-pressure heat exchangers [Anonymous, 2000]. Currently, a major obstacle to broad applications of CMC is that the CMC materials, especially those with continuous reinforcements, generally require more costly manufacturing processes [Freitag and Richerson, 1998].

5.1. Effects of Process Parameters on Cutting Force

The cutting force shows a significant undulation when machining CMC using RUM. This is due to the fiber lamellar structure and some hard inclusions in the CMC materials. These two characteristics of CMC make it difficult to estimate main and interaction effects for the maximum cutting forces. Therefore, the average cutting forces instead of the maximum cutting forces are used for analysis in RUM of CMC materials.

The average cutting force increases with the increase of feedrate as shown in Figure 17. This trend is consistent with that when RUM of alumina [Jiao et al., 2005] and when RUM of Silicon carbide [Churi et al., 2007].

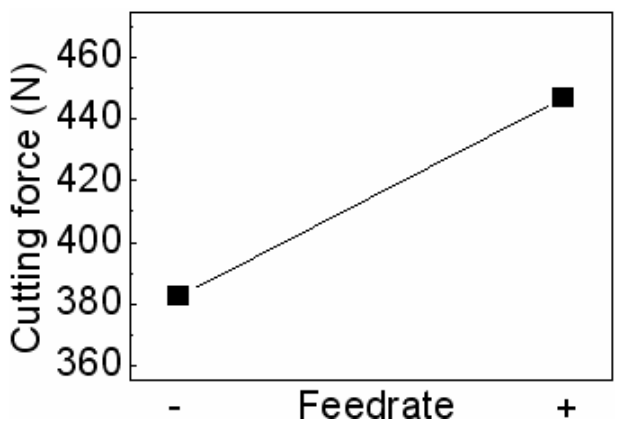

Figure 17. Effect on cutting force in RUM of CMC (after [Li et al., 2006]).

5.2. Effects of Process Parameters on Edge Chipping

The spindle speed has a significant effect on edge chipping thickness. From Figure 18(a), it can be seen that the chipping thickness decreases with an increase of spindle speed. That is to say, higher spindle speed will be effective to reduce the chipping thickness. The feedrate also has a significant effect on edge chipping thickness. The edge chipping thickness increases as feedrate increases as shown in Figure 18(b). The effects of spindle speed and feedrate are consistent with those when RUM of alumina [Jiao et al., 2005]. For the edge chipping thickness, there exists an obvious interaction effect between spindle speed and feedrate. The effect of spindle speed is much stronger at the higher level of the feedrate as shown in Figure 18(c).

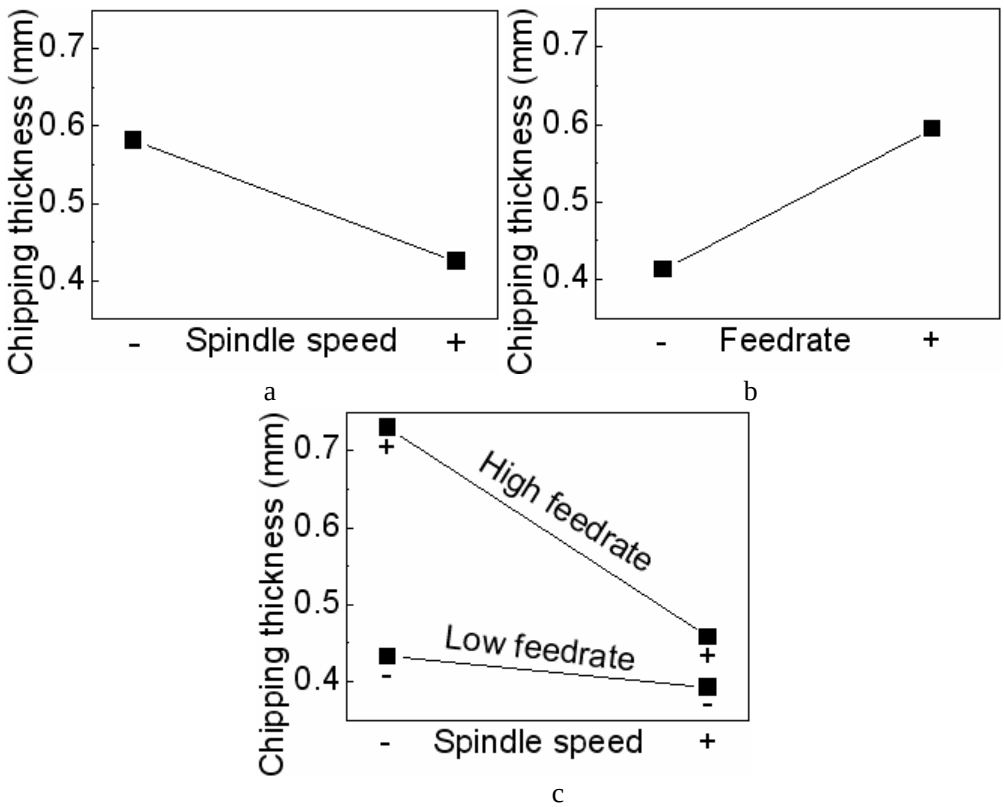

Figure 18. Main and interaction effects on edge chipping thickness in RUM of CMC (after [Li et al., 2006]).

Figure 19 shows the main and interaction effects on chipping size. The spindle speed has a significant effect on chipping size. From Figure 19(a), it can be observed that the chipping size decreases with an increase of spindle speed. This trend is consistent with that when RUM of Silicon carbide [Churi et al., 2007]. It indicates that higher spindle speed will be effective to prevent larger chippings. The two-factor interactions between spindle speed and feedrate has a significant effect on chipping size. The effect of spindle speed is stronger at the higher level of the feedrate as shown in Figure 19(b), which is consistent with that when RUM of Silicon carbide [Churi et la., 2007].

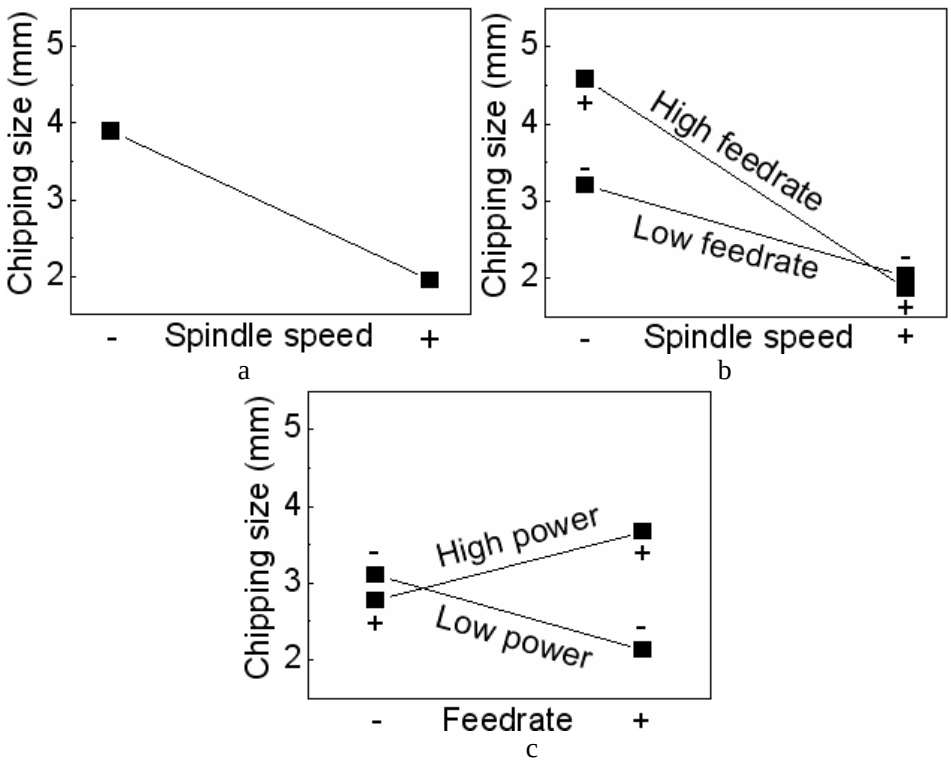

Figure 19. Main and interaction effects on edge chipping size in RUM of CMC (after [Li et al., 2006]).

The interaction between feedrate and ultrasonic power is also significant. With the increase of feedrate, the chipping size will increase at the higher level of ultrasonic power while decrease at the lower level of ultrasonic power as shown in Figure 19(c).

REFERENCES

Anantha Ramu, B.L., Krishnamurthy, R., and Gokularathnam, C.V., Machining performance of toughened zirconia ceramic and cold compact alumina ceramic in ultrasonic drilling, *Journal of Mechanical Working Technology* 20 (1989) 365-375.

Anonymous, An improved ultrasonic machine tool for glass and ceramics, *Industry Diamond Review* 26 (3) (1966) 274-278.

Anonymous, *Drilling deep holes in glass, Ultrasonic* (May) (1973) 103-106.

Anonymous, *Market survey report of ceramic matrix composites*, Business Communications Company, Inc., 2000.

Cleave, D. V., Ultrasonics Gets Bigger Jobs in Machining and Welding, *Iron Age* 218 (11) (1970) 69-72.

Dam, H., Quist, P., and Schreiber, M.P., Productivity, surface quality and tolerances in ultrasonic machining of ceramics, *Journal of Materials Processing Technology* 51 (1-4) (1995) 358-368.

Datta, M., Bandyopadhyay, A., Chaudhari, B., Preparation of nano α-silicon carbide crystalline particles by attrition grinding, *International Ceramic Review* 53 (4) (2004) 242-244.

Freitag, D.W., Richerson, D.W., Ceramic matrix composites in opportunities for advanced ceramics to meet the needs of the industries of the future, *Advanced Ceramic Association and Oak Ridge National Laboratory*, Oak Ridge, Tennessee, USA, 1998.

Hu, P., Zhang, J.M., Pei, Z.J., Experimental investigation on coolant effect in rotary ultrasonic machining, in: *Proceedings of the NSF workshop on research needs in Thermal aspects of material removal processes*. Stillwater. OK, USA, June 10-12, 2003, pp. 340-345.

Inasaki, I. and Nakayama, K., High Efficiency Grinding of Advanced Ceramics, *Annals of the CIRP* 35 (1) (1986) 211-214.

Khanna, N., Pei, Z.J., P. and Ferreira, M., Experimental investigation of rotary ultrasonic grinding of ceramic disks, *Transactions of the North American Manufacturing Research Institution of SME 23* (1995) 67-72.

Kubota, M., Tamura, Y., and Shimamura, N., Ultrasonic machining with a diamond impregnated tool, *Bulletin of Japanese Society of Precision Engineering 11* (3) (1977) 127-132.

Legge, P., Ultrasonic drilling of ceramics, Industrial Diamond Review 24 (278) (1964) 20-24.

Legge, P., Machining without abrasive slurry, *Ultrasonics* (July) (1966) 157-162.

Li, Z.C., Treadwell, C., and Pei, Z.J., Drilling small holes in hard–to–machine materials by rotary ultrasonic machining, in: *CD–ROM Proceedings of WESTEC Conference–New Frontiers in Manufacturing Technology*, Los Angeles, CA, March 22–25, 2004, also SME Technical Paper TP04PUB137, Society of Manufacturing Engineers, Dearborn, MI.

Li, Z.C., Jiao, Y., Deines, T.W., Pei, Z.J., and Treadwell, C., Development of an innovative coolant system for rotary ultrasonic machining, *International Journal of Manufacturing Technology and Management* 7 (2-4) (2005) 318-328.

Li, Z.C., Cai, Liang-wu, Pei, Z.J., Treadwell, C., Finite element simulation of rotary ultrasonic machining for advanced ceramics, in: *CD-ROM Proceedings of ASME International Mechanical Engineering Congress and Exposition*, Anaheim, CA, USA, Nov 13-19, 2004.

Li, Z.C., Cai, Liang-wu, Pei, Z.J., and Treadwell, C., Edge-chipping reduction in rotary ultrasonic machining of ceramics: finite element analysis and experimental verification, *International Journal of Machine Tools and Manufacture* 46 (12-13) (2006) 1469-1477.

Lunzer, J.P., Diamond Drilling in Glass, *Proceedings of the 18th Symposium on the Art of Glassblowing also Machine Design 3* (1977) 21-25.

Malkin, S., and Hwang, T.W., Grinding mechanisms for ceramics, *Annals of CIRP 45* (2) (1996) 569-580.

Markov, A.I., Ultrasonic drilling and boring of hard non-metallic materials with diamond tools, *Machines and Tooling* 48 (9) (1977) 45-47.

Ng, S., Le, D., Tucker, S., Zhang, G., Control of machining induced edge chipping on glass ceramics, in: *Proceedings of the 1996 ASME International Mechanical Engineering Congress and Exposition, Manufacturing Engineering Division, MED(4)*, Atlanta, GA, USA, Nov 17-22, 1996, pp. 229-236.

Pei, Z.J., Prabhakar, D., Ferreira, P.M., Haselkorn, M., Ultrasonic drilling and milling of ceramics, *Ceramic Transactions* 49 (1995) 185-190.

Pei, Z.J., Khanna, N., and Ferreira, P.M., Rotary ultrasonic machining of structural ceramics-a review, *Ceramic Engineering and Science Proceedings* 16 (1) (1995[a]) 259-278.

Pei, Z.J., *Rotary Ultrasonic machining of Ceramics*, PhD thesis, University of Illinois at Urbana-Champaign, 1995.

Pei, Z.J., and Ferreira, P.M., Modeling of ductile-mode material removal in rotary ultrasonic machining, *International Journal of Machine Tools and Manufacture* 38 (10-11) (1998) 1399-1418.

Pei, Z. J., and Ferreira, P.M., An experimental investigation of rotary ultrasonic face milling, *International Journal of Machine Tools and Manufacture* 39 (8) (1999) 1327-1344.

Petrukha P.G., Ultrasonic diamond drilling of deep hole in brittle materials, *Russian Engineering Journal* 50 (10) (1970) 70-74.

Prabhakar, P.D., *Machining advanced ceramic materials using rotary ultrasonic machining process*, M.S. Thesis, University of Illinois at Urbana-Champaign, 1992.

Prabhakar, P.D., Ferreira, P.M., and Haselkorn, M., An experimental investigation of material removal rate in rotary ultrasonic machining, *Transactions of the North American Manufacturing Research Institution of SME* 20 (1992) 211-218.

Prabhakar, D., Pei, Z.J., and Ferreira, P.M., Mechanistic approach to the prediction of material removal rates in rotary ultrasonic machining, *ASME Journal of Engineering for Industry* 64 (2) (1993) 771-784.

Richerson, D.W., Ceramic matrix composites, *Composite Engineering Handbook*, Marcel Dekker Inc., New York, 1997.

Spur, G., Uhlmann, E., Holl, S.E., Daus, N.A., Influences on surface and subsurface during ultrasonic assisted grinding of advanced ceramics, in: *Proceedings of the 14th Annual Meeting, the American Society for Precision Engineering, Monterey*, CA, USA, Oct 31-Nov 5, 1997, pp.481-484.

Spur, G., Holl, S.E., Material removal mechanisms during ultrasonic assisted grinding, *Production Engineering* 4 (2) (1997) 9-14.

Uhlmann, E., Spur, G., Holl, S.E., Machining of complex contours by ultrasonic assisted grinding, *Technical Paper of Society of Manufacturing Engineers MR99-284* (1999) 1-13.

Ya, G., Qin, H.W., Yang, S.C., Xu, Y.W., Analysis of the rotary ultrasonic machining mechanism, *Journal of Materials Processing Technology* 129 (1-3) (2002) 182-185.

Yin, L., Vancoille, E., Lee, L., Huang, H., K. Ramesh, Liu, X., High quality grinding of polycrystalline silicon carbide spherical surfaces, *Wear* 256 (1-2) (2004) 197-207.

Yoshifumi, O., Tetsuo, M., Minoru, S., Chipping in high precision slot grinding of Mn-Zn ferrite, *Annals of the CIRP 44* (1) (1995) 273-277.

Zhang, B., and Howest, T.D., Material removal mechanisms in grinding ceramics, *Annals of CIPR 43* (1) (1994) 305-308.

Zhang, Q.H., Wu, C.L., Sun, J.L., and Jia, Z.X., The mechanism of material removal in ultrasonic drilling of engineering ceramics, Proceedings of the Institution of Mechanical Engineers, Part B, *Journal of Engineering manufacture 214* (9) (1995) 805-810.

In: Developments in Ceramic Materials Research
Editor: Dena Rosslere, pp. 53-95
ISBN 978-1-60021-770-8

Chapter 3

OPTICAL FLUORIDE AND OXYSULFIDE CERAMICS: PREPARATION AND CHARACTERIZATION

T. T. Basiev[1], V. A. Demidenko[2], K. V. Dykel'skii[2], P. P. Fedorov[1], E. I. Gorokhova[2], I. A. Mironov[2], Yu. V. Orlovskii[1], V. V. Osiko[1], and A. N. Smirnov[2]

[1]Laser Materials and Technology Research Center, General Physics Institute RAS,
38 Vavilov Street, Bld. D, Moscow, 119991, Russia
[2]Federal State Unitary Organization "Research and
Technological Institute of Optical Materials"
All-Russia Scientific Center "S.I. Vavilov State Optical Institute",
36-1, Babushkin Street, S.-Petersburg, 193171, Russia

ABSTRACT

Laser oxide ceramics ($Y_3Al_5O_{12}$, Y_2O_3, etc. doped with Nd^{3+}, Yb^{3+}, etc.) is the most serious innovation of last years in the field of laser materials.

However, the chapter summarizes new efforts of General Physics Institute of Russian Academy of Sciences, Moscow and State Optical Institute, S.-Petersburg for the research and development of optical ceramics of two other classes of chemical compounds: fluorides and oxysulfides.

The technique of preparation and results of study of a structure of ceramic samples as well as its mechanical, thermal, optical and fluorescence properties is reported.

The analysis of development tendencies in modern photonics shows that recent progress in the area relates substantially with the devices based on the fluoride optical ceramics due to:

- wide spectral transparency window from 0.16 to 11 microns and low phonon spectra preventing from strong fluorescence quenching by the multiphonon relaxation of radiative transitions of impurity ions;
- long lifetimes of metastable levels;
- ease of high level doping of the ceramic host by rare-earth ions (up to 10^{21} cm^{-3});

- excellent mechanical properties, e.g. the CaF_2 optical ceramics, both natural and artificial, has anomalously high fracture toughness, which is three - six fold higher than that for single fluoride crystals;
- high moisture resistance compared to other classes of optical materials with a wide spectral transmission window;
- high thermal conductivity;
- low level of optical losses in ceramic samples, about 10^{-2} - 10^{-3} cm^{-1} in one micron spectral range.

The material properties of natural CaF_2 optical nanoceramics (Suran Deposit, South Ural) as a model object is discussed first. Then the technology development of preparation of synthetic optical fluoride ceramics of different chemical composition is introduced starting from a nanotechnology of preparation of initial raw materials. After that the material properties and advantages of artificial fluoride optical ceramics versus the fluoride single crystals is discussed. At last, optical and fluorescence properties of rare - earth doped optical fluoride ceramics is presented.

Finally, the synthesis technology and material and spectroscopic properties of translucent oxysulfide optical ceramics of different composition doped with Nd^{3+}, which can be perspective for one micron lasing with high quantum efficiency is considered.

INTRODUCTION

One of the most serious innovation progress of late years in the field of laser materials is a development of oxide laser ceramics of yttrium aluminum garnet and yttrium oxide which compares well with single crystals in laser properties [1, 2]. Since "Konoshima Chemical" technological break - through was achieved as a result of using self – assembly of nanoparticles [3], such a product is known as nanoceramics.

Ceramics transparent in visible spectral range has been well known for several decades (see, for example, [4 – 7]). One of the criterions of ceramics transparency is supposed that a text can be read throw a 1 mm thick sample lying on the paper. It corresponds to more than 40 % transparency.

Stimulus for the development of optical transparent ceramics was a progress in sodium rim light with transparent inner tubes as well as a need in materials transparent in IR spectral range. Transparent ceramics is obtained for a great quantity of materials (abbreviation and/or trade mark are given in brackets): Al_2O_3 (Lukalox), Y_2O_3 and Y_2O_3:10% ThO_2 (Ittralox), $MgAl_2O_4$ spinel, ZrO_2:Y_2O_3 stabilized zirconia, MgF_2 (Irtran – 1, Irtran – 51, KO – 1, AV – 1), CaF_2 (Irtran – 3, KO – 3), ZnS (Irtran – 2, KO – 2), ZnSe (Irtran – 4, KO – 4), lead titanate – zirconate, sodium – potassium niobate and others.

Ceramics production with nominal 100% density makes possible due to systematic study of kinetics and mechanisms of sintering processes and after development of the applicable theory [8 – 11]. It includes resolution of such issues as role of surface diffusion, mechanisms of shrinkage and disappear of pores and the role of the grain boundaries and dislocations in the latter process, a control of the grains build - up due to the blockade of the surfaces by special dopants, control of a mass transfer by non stoichiometry, precursor powders activation, etc. Establishing of the influence of the temperature, pressure, controlled-atmosphere, thermal prehistory of the precursors and their defect structure, and impurities on

the sintering process leads to the development of two fundamental methods of the preparation of optical polycrystalline materials.

First, is a classic ceramic preparation which consists in sintering of the previously formed green compact at the temperature slightly below melting temperature of the material. Sintering process realizes in vacuum or controlled atmosphere. Application of nanopowders allows to decrease a temperature of a process for several hundred degrees.

Second way is to obtain optical ceramics from different materials by a hot pressing (HP) assisted sintering method. This method consists of application of sintering process with both the temperature (0.5 – 0.8 from $T_{mel.}$) and the pressure (up to 300 Mpa) that allows decrease both the sintering temperature and the recrystallization rate. Bulk diffusion, plastic deformation and twinning take place in this situation, i.e. mass transfer mechanisms, which set conditions for obtaining the dense, microcrystalline and mechanically rigid and transparent ceramics.

In last years glass ceramics is used as an optical material. In this ceramics nanosized crystalline grains form purposefully in glass matrix. Glass ceramics can keep optical transparency with content of crystalline phase up to 90 % [12, 13].

Preparation of laser optical ceramics is a special process, which is more complicated in practice. For laser generation the loss factor at specific wavelength must not exceed $10^{-3} – 10^{-2}$ cm^{-1}. Laser ceramics as a material has some advantages over the crystals [4, 5] such as possibility of preparation of large samples with an enhanced content and uniform distribution of activator, improved mechanical characteristics as well as a synthesis of laser materials when the process of single crystal growth is difficult (decomposition under heating, incongruent melting, phase transitions).

In present time laser ceramics development is successfully realized for the row of oxide materials [1, 2, 14 - 18]. As for the optical ceramics for the photonics based on the other classes of materials the level of their development decelerates, though a first ceramic fluoride laser ($CaF_2:Dy^{3+}$) was developed in the beginning of laser era (in the middle of 1960s) by Kodak (USA) [19, 20].

In the chapter preparation of fluoride and oxysulfide optical ceramics by hot pressing assisted sintering method and its properties will be considered.

FLUORIDE OPTICAL CERAMICS PREPARATION AND INITIAL CHARACTERIZATION

Specific physicochemical properties of the fluorides such as water vapor interaction during a heating process places a specific requirements upon the technology of ceramics preparation and upon the equipment. Production of colorless transparent fluoride ceramics from fluorides precursors meets with some difficulties. Fluoride ceramics with nominally 100% density prepared by hot pressing assisted sintering method every so often has a black color [21]. Even good samples have typical defect such as grey or yellowish disseminations, which decreases the transparency. Annealing in fluorinating atmosphere leads to higher transparency of the samples [22]. Preparation of optical ceramics with complex chemical composition results in a problem with optical homogeneity [23, 24].

At the same time analysis of the modern trends in photonics shows that within the next few years the devices on the basis of fluoride materials will play an important role. Physical basics of this thesis are:

- transparency in wide spectral range from 0.16 to 11 μm;
- reduced rates of multiphonon relaxation in impurity ions due to low phonon spectra;
- long lifetimes of metastable levels;
- easy activation of fluoride composition by large concentrations of rare – earth ions (up to 10^{21} см$^{-3}$);
- high thermal conductivity of fluorides;
- unlike another classes of materials which has wide window transparency such as chlorides and halcogenides, fluorides have better mechanical properties and higher water – resistance.

Due to the advantages of the fluorides listed above the latter are used in form of single crystals for production of active and passive elements of laser systems, for medicine, ecology, information science and in particular as unique elements of tunable lasers.

Main drawback of the most fluoride crystals is crystal cleavage, which hinders their use in practice. The more clear and more perfect the crystal the lower radiation stability and mechanical resistance and resistivity to the thermal tension. Another drawback is a difficulty of synthesis of numerous complex fluorides in the form of optically homogeneous crystals [25]. The necessity of preparation of optical fluoride based elements as the devices of modern photonics with high radiation resistance and high optical homogeneity will lead to the development of the technology of optical nanoceramics. As shown in Ref. [13] during the last 5 years the formation of new field of science named physicochemistry and technology of the nanofluorides was launched. This direction has practical application (catalysts, effective phosphors, etc). Synthesis of the fluoride nanoceramics is in compliance with this direction. The development of the technology of laser fluoride ceramics is in progress right now [26 – 29].

For example, the translucent colorless optical fluorite (CaF_2) from the Suran deposit (Russia) is quite an interesting object (Figure 1a). It has a cryptocrystalline structure and is actually a natural analog of the optical ceramics. This fluorite characterized by a high homogeneity and purity and associates with the sellaite mineral (MgF_2). The age of the deposit is about 1 billion years. Typical factor of the Suran cryptocrystalline optical fluorite (SCOF) is its unusually high "shock resistance" which manifests itself in the process of fragmentation of this material. Microstructure of the chip of the samples of natural fluoride ceramics measured by atomic force microscopy (AFM) method [30] is presented in Figure 2. Transmission spectrum of the SCOF in the IR range is identical to the same spectrum of single crystal. X – ray diffraction (XRD) (diffractometer DRON – 2, CuKα radiation) shows complete disorder in orientation of grains. AFM and cathode luminescence studies shows that SCOF samples consists of the differently oriented grains with size from several to dozens of microns and that unlike for the CaF_2 single crystals the grains have a layered – type structure (Figure 2a). Chemical etching of the SCOF sample shows small grains with the size of 50 – 200 microns within the dimensions of layers (Figure 2b). This result correlates with the data

on the structure of oxide laser ceramics and shows that optically transparent ceramics is formed at nanosized level.

a

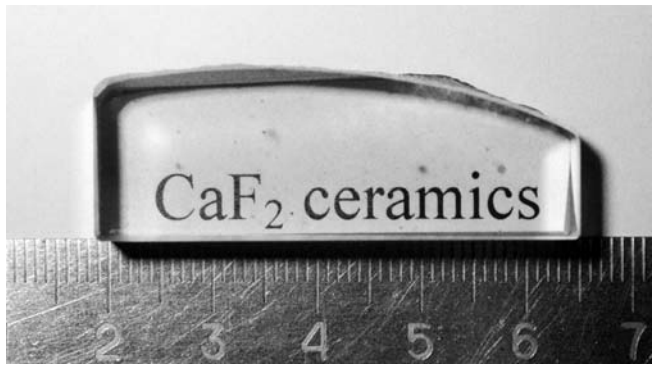

b

Figure 1. (a) - Overview of the polished samples of the fluorite (CaF_2) with 10 mm thickness. On the left is a artificial single crystal, on the right is the cryptocrystalline fluorite from Suran deposit, (b) – the CaF_2 artificial ceramics.

Experiments on hot pressing of fluoride optical ceramics are performed in K – 4772 high temperature vacuum furnace with the graphite resistance heating element and MV – 4 MP heatproof molybdenum alloy mould using a PSU – 50 hydraulic press capable of pressure at the head of 50 t. The pressing parameters are as follows: temperature up to 1300 $^{\circ}$C, pressure up to 250 MPa.

This process allows to obtain ceramics with 100% density, but optical transparency is varied in wide ranges. Results of the hot pressing of different precursors are presented in Figure 3 and electron microphotographs of some powders used are in Figure 4. These experiments confirm that the optical transparency of the ceramics depends on the quality of precursors [7]. Unlike the glass melting and single crystals growth a hot pressing method of preparation of optical ceramics does not include the purification of the initial materials. Organic impurities and embedded foreign particles raise absorption and scattering of the light in the sample. Even apparently highly purified raw material leads to the non – transparent ceramics. An increase of evacuation value every so often leads to an improvement of the optical transparency.

As a result of careful selection of the precursors the CaF_2 ceramics with high homogeneity and small optical losses is prepared. (Figure 1b). The electronic scanning

microscopy shows the fine layered – type structure of the grains (Figure 5) which is similar to the fine structure of the CaF_2 natural optical ceramics (Figure 2).

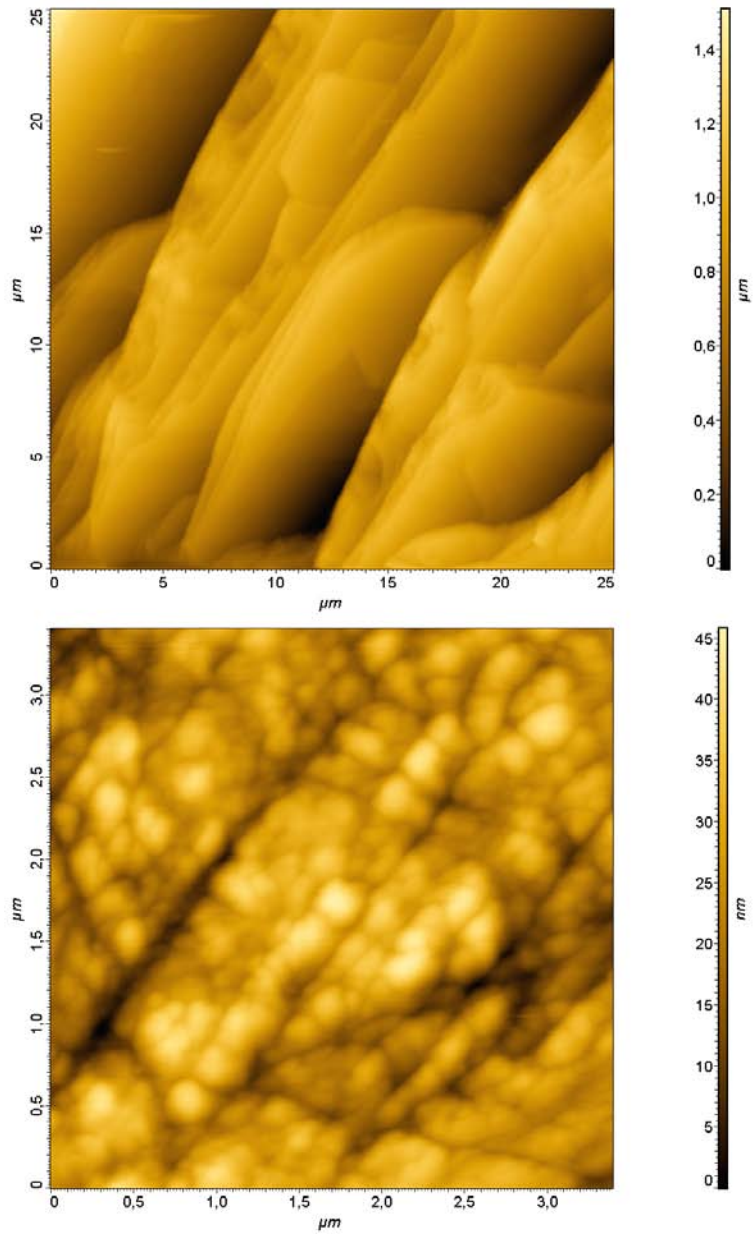

Figure 2. Images of the chip of the cryptocrystalline fluorite sample got by atomic force microscopy (AFM) (a) and fine structure of the grains at the chemical dropped surface of the chip (b). Shoot is in the contact mode got at the atomic force microscope Solver P47 (NT – MDT, Moscow).

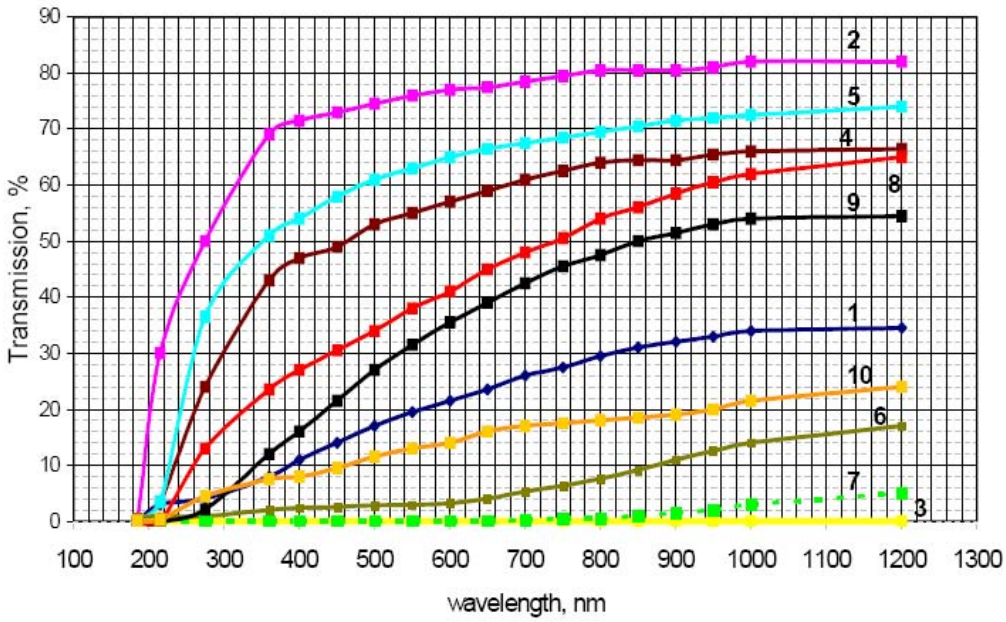

Figure 3. Transmission spectra of the CaF_2 ceramic samples prepared from different precursors. Thickness of the samples is 2 mm.

1. B(1)7 - 05 – p.2. «Krasnyi khimik»
2. B(1)9 - 05 – p.1. «Krasnyi khimik»
3. B(2)31 - 05 – «IREA»
4. B(2)30 - 05 – «Stella», Japan
5. B(2)33 - 05 – «Stella», Japan
6. B(2)42 - 05 – VNIIKHT, M1
7. B(2)32 - 05 – VNIIKHT, M4
8. B(2)36 - 05 – Angarsk electrolysis chemical factory
9. B(2)41 - 05 – VNIIKHT, M2
10. B(2)1 - 06 – VNIIKHT, M3

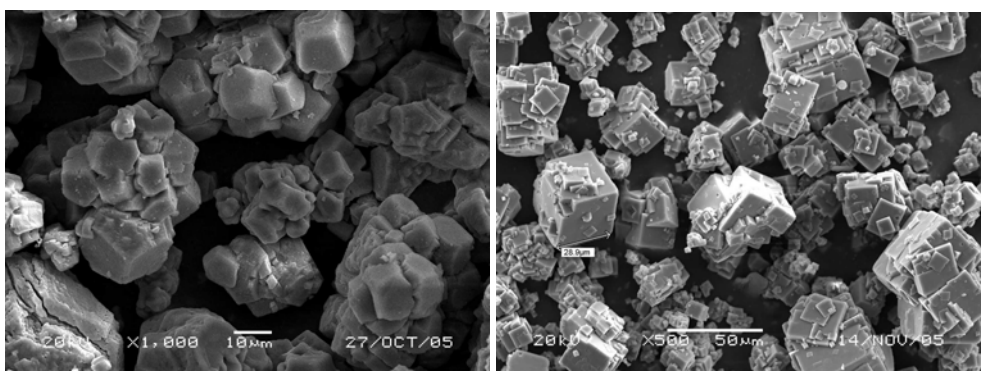

a b

Figure 4. (Continued)

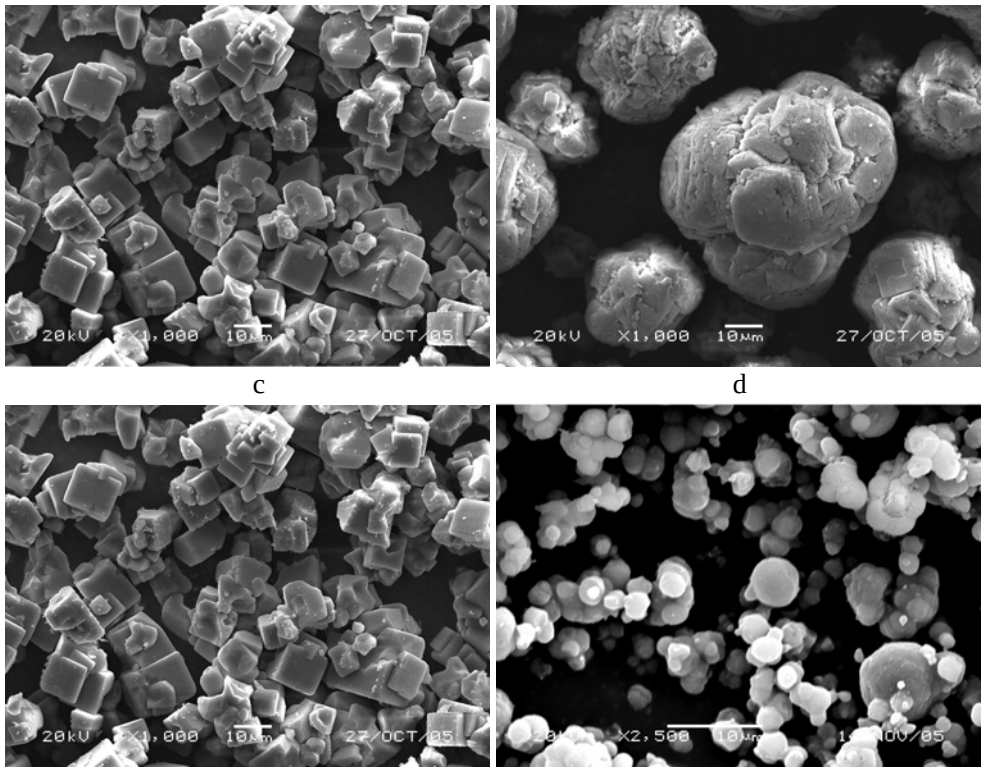

Figure 4. Characteristic microphotographs of the CaF2 powders of different precursors.

a) « Krasnyi khimik »;
b) «IREA»;
c) «Stella», Japan;
d) Angarsk electrolysis chemical factory;
e) CaF_2 VNIIKHT;
f) CaF_2: Er, VNIIKHT, M1.

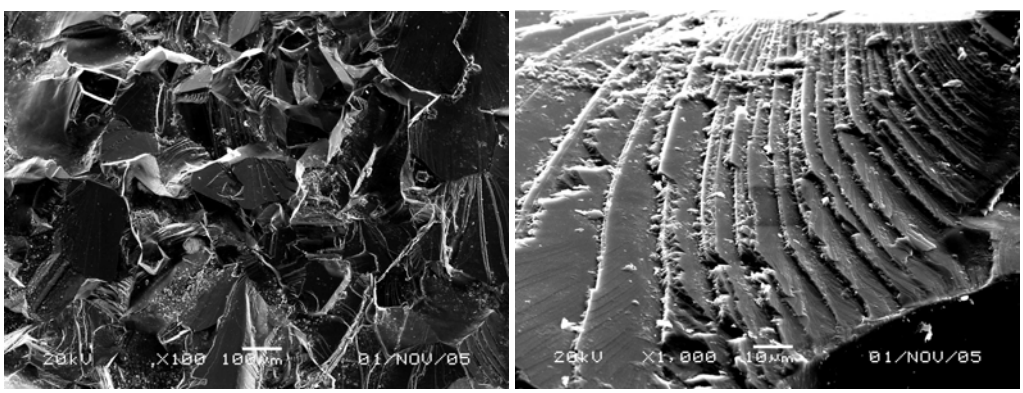

Figure 5. Characteristic microphotographs of the chip of the CaF_2 artificial optical ceramics – (a) and fine structure of the grains – (b).

When employing the fluoride ceramics as an active laser media the doping of the matrix is supposed primarily with the rare – earth activator ions. The first experiments show that a mixture of powders is unacceptable for preparation of solid solution as an optical ceramics. Distribution of cations in the $Ca_{0,9}Er_{0,1}F_{2,1}$ ceramic sample prepared by hot pressing method of a mixture of powders is presented in Figure 6. It is seen that conditions of the experiment are not suitable for the diffusion homogenization of the components. The erbium concentration in points 1 and 2 in Figure 6 differs 30 times. The variations of the components of solid solution lead to the variation of the refraction index. This leads to the optical inhomogeneity of the ceramic sample and makes it unsuitable for the use in photonics.

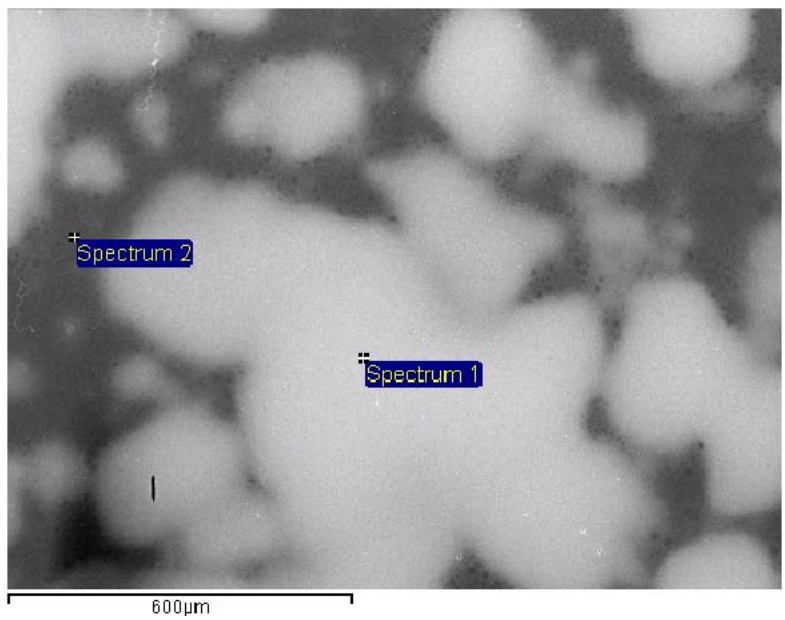

Figure 6. Microphotographs of the $Ca_{1-x}Er_xF_{2+x}$ (x=0,1) ceramics prepared from the CaF_2 : ErF_3 mixture in the rays of Er. Shoot made at “Camebax”.

For the preparation of the precursors for optical fluoride ceramics the co-precipitation method of fluorides of the alkaline – earth and rare - earth elements from the water solution is provided [31]. With the reverse dropping of the solution of the mixture of nitrates into the hydrofluoric acid it is managed by trial and error to select the conditions for co-precipitation, washing, and drying. This leads to the preparation of the raw materials with uniform chemical composition (see Figure 7).

The ceramics samples of the $Ca_{1-x}R_xF_{2-x}$ solid solutions prepared are presented in Figures 8 and 9. The microhardness H and fracture toughness K_{1C} of the ceramic samples and comparison with single crystals is provided by micro-indentation method [30]. The ceramic samples are cut by the diamond saw, and then they are ground and mechanically polished. The mechanical tests of single crystals are performed at cleaved [111] facets. The strain is induced at room temperature by the diamond Vickers pyramid. Indentation is preformed using a microhardness meter PMT-3. For the scratch-hardness tests, we use a Martens sclerometer. The indentation load (P = 0.5 -1 H) is chosen so, as to reliably observe not only the impressions themselves but also radial cracks outgoing from them.

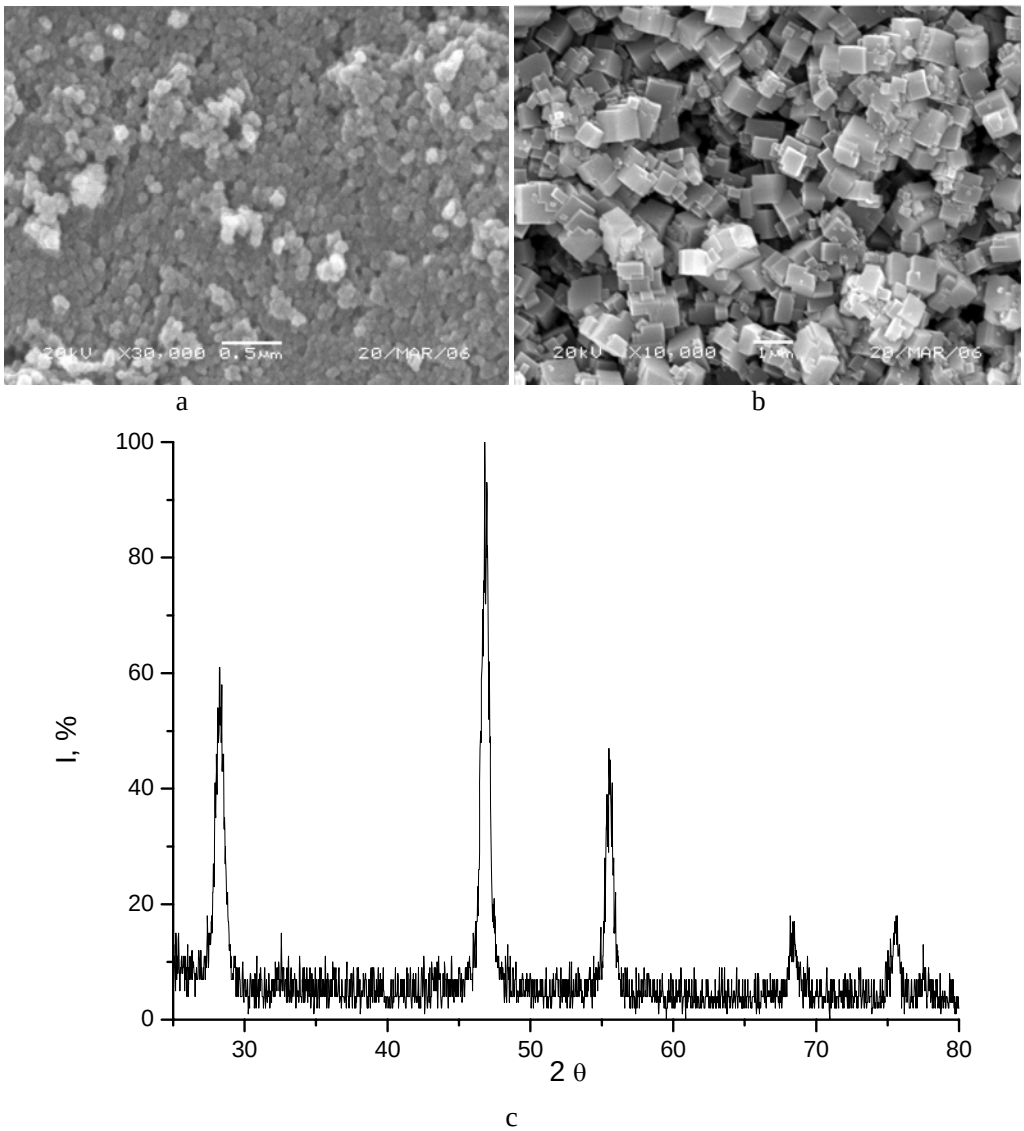

Figure 7. Characteristic microphotographs of the $Ca_{0,9}Er_{0,1}F_{2,1}$ particles prepared by sedimentation from the water solution with reverse dropping into the hydrofluoric acid with further washing in the ethanol – (a), after the drying at 150 °C – (b) and their XRD, CuK_α radiation – (c).

Taking into account that the homogeneity of ceramic samples is sufficiently high, we put 50 impressions on them (as well as on the single crystals). In the single crystals, the arrangement of diagonals in an impression corresponds to the {110} direction characterized by the highest hardness. The microhardness H was calculated by the conventional formula $H = KP/d^2$, where P is the indentation load, d is the length of the diagonal for the indenter impression, K is the factor depending on the shape of the indenter (for the Vickers pyramid, $K = 1.854$). The fracture toughness K_{1C} as a function of the indentation load is determined from the measurements of the linear size of radial cracks (C) arising near the place where the indentation load is applied.

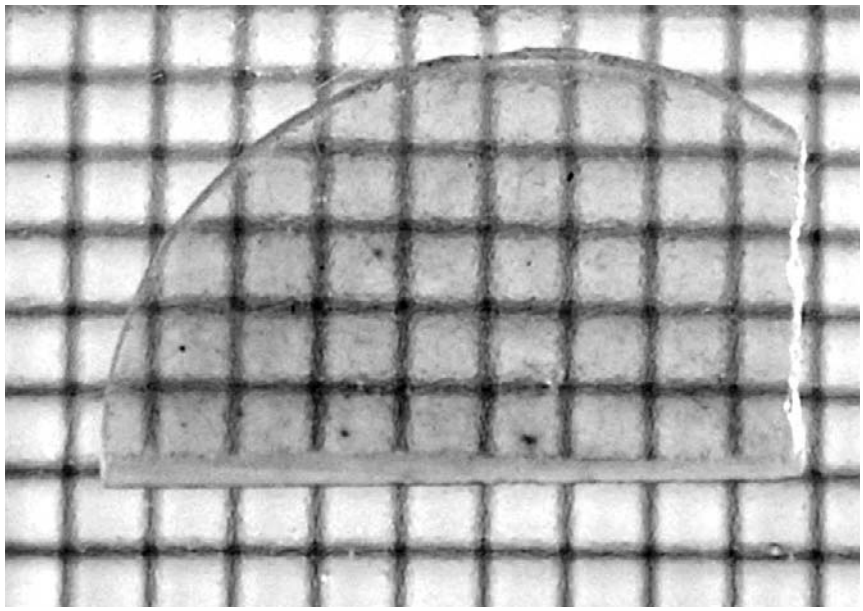

Figure 8. The $CaF_2:Er^{3+}$ ceramic sample with 3 mm thickness and at 1" distance from the "substrate".

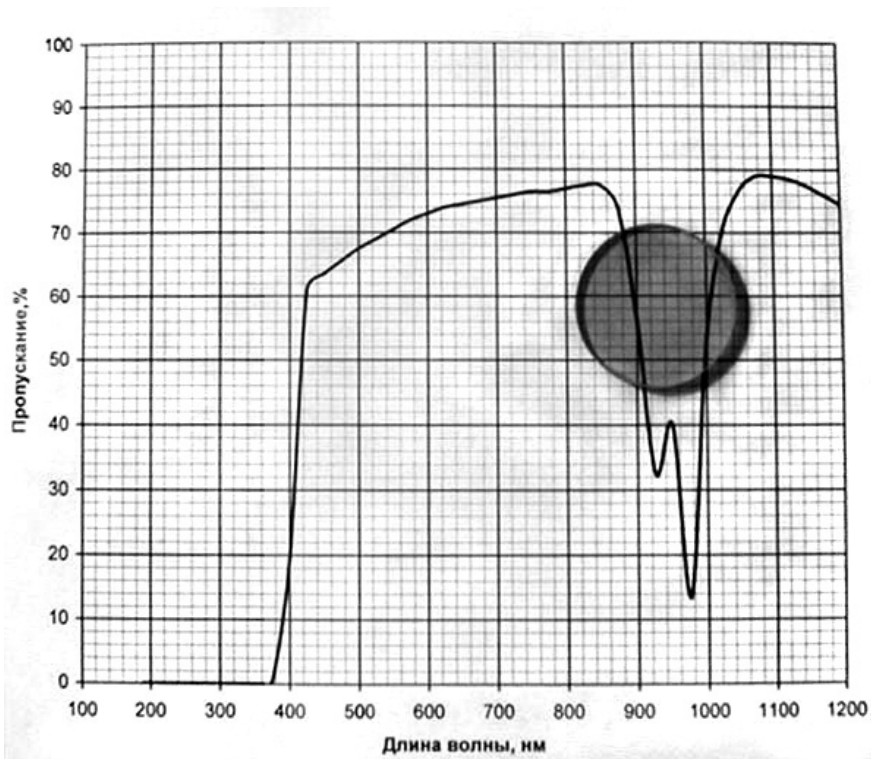

Figure 9. Transmission spectrum and overview of the B(2)16 - 06 ceramic sample of the $Ca_{0,95}Yb_{0,05}F_{2,05}$ composition, 3.5 mm sample thickness.

It is estimated based on the approved formula taking into account the elastic and hardness characteristics of the material under study [32]. For the Vickers indenter, we have $K_{1C} = 0.016(E/H)^{1/2} P/C^{3/2}$, where E is Young's modulus. For fluorite, $E = 8.73\ 10^{11}$ dyne/cm^2 [32]. The experiments demonstrate that the microhardness of ceramic samples is only slightly higher (by 10 - 12%) than that of CaF_2 single crystals, but their crack resistance increases significantly: the fracture toughness K_{1C} is higher by a factor of approximately 3 - 6 (see Table 1).

Table 1. The values of microhardness H and fracture toughness K1C

Samples		microhardness *H*, GPa		fracture toughness K_{1C}, MPa·m$^{-0,5}$	
Composition	Designation	at P=0,5 H	at P =1 H	at P = 0,5 H	at P = 1 H
CaF_2	Single crystal	-	200± 7	-	1,5 ± 0.15
CaF_2	Natural ceramics	-	225 ± 5	-	6,3 ± 0.6
CaF_2	Artificial ceramics	-	260±10	-	4,7±0.3
$Ca_{0.98}Er_{0.02}F_{2.02}$	Artificial ceramics sample B(2)4-06	305	250	9,9	9,4

The scratch-hardness tests of the ceramic samples (scratches are made from the centre of a circle along the radius with a step of 15 [degree]) does not reveal any hardness anisotropy, whereas for CaF_2 single crystals the <110> directions are characterized by the highest hardness.

The thermal conductivity k is an important technological parameter. It is due to the high thermal conductivity of calcium fluoride single crystals this material is attractive for the development of powerful laser systems. One of the purposes of this work is to compare the thermal conductivity of a fluorite single crystal and samples of natural and artificial optically transparent CaF_2 ceramic. The thermal conductivity is determined experimentally by the absolute stationary method of longitudinal thermal flux [28]. The objects of research are three samples of CaF_2 with almost the same geometry dimensions 5 x 5 x 40 mm^3. One of the samples is cut from a single-crystal boule grown by the method of vertical directed crystallization. Another sample is cut from a piece of natural optical ceramic from the Suran deposit. The third sample is cut from ceramic prepared by the hot pressing method. The distance between the temperature sensors is 20 mm. The temperature range of 50 - 300 K is provided by evacuation of nitrogen vapor from the chamber. The results of measurements are presented in Figure 10. The values of thermal conductivity for all samples coincide within experimental error of 5%. At T = 300 K the thermal conductivity is $k = 10.3 \pm 0.1$ W/m K; and it strongly increases with decreasing temperature to $k = 245 \pm 7$ W/m K at T = 50 K.

Analysis of transmission spectra of CaF_2 single crystals and ceramic samples in wide spectral range is provided (Figure 11). In the IR spectral range the transmission of the single crystal and ceramics is identical (Figure 11a), but in UV the difference is significant (Figure 11b).

The optical losses in the ceramics are determined quantitatively by calorimetric method of absorption coefficients measurement in highly transparent solids described elsewhere [33]. In doing so rectangular parallelepiped samples 8.8 x 14 x 45 mm^3 are cut and polished. The loss factors are found to be $2.05\ 10^{-2}$ cm^{-1} and $6.3\ 10^{-3}$ cm^{-1} for the ceramics and the CaF_2 single crystal, respectively.

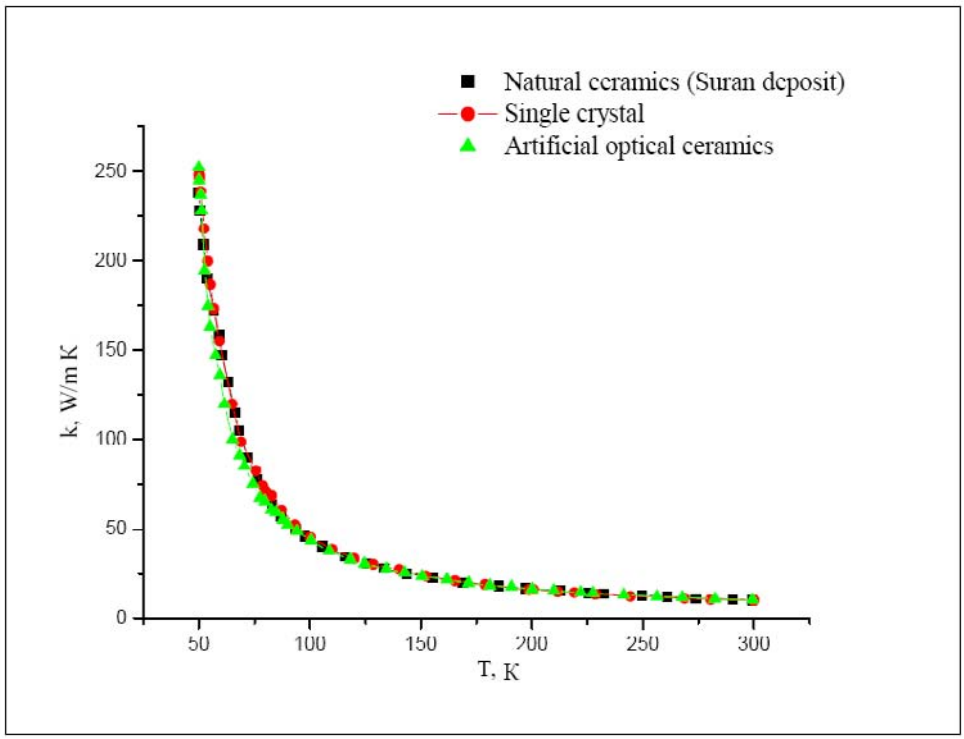

Figure 10. Temperature dependence of the thermal conductivity of the CaF_2 single crystal and optical ceramics.

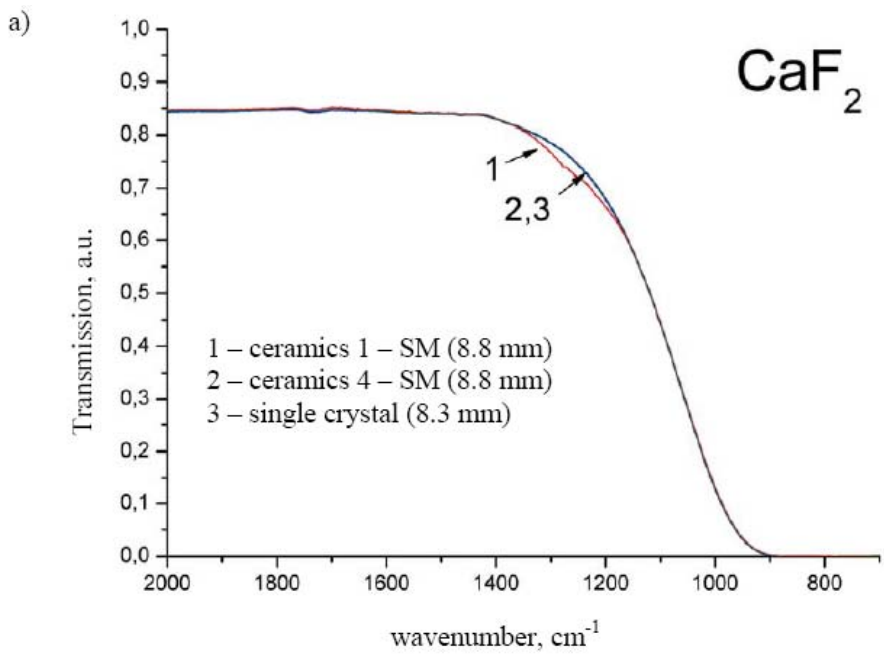

Figure 11. (Continued)

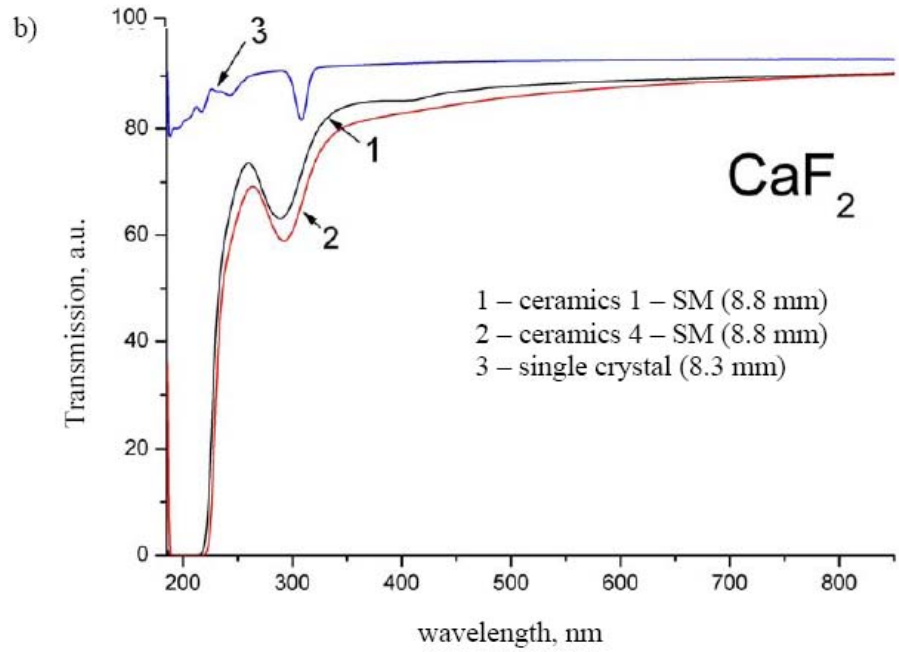

Figure 11. Transmission spectra of the CaF_2 single crystal (#3) and CaF_2 artificial optical ceramics (# 1, 2) in the UV and IR ranges. Shoot at λ – 900 (Perkin – Elmer) spectrophotometer and Brucker IFS – 113v Fourier spectrometer.

Besides, a comparison of the optical properties of single crystals and optically transparent ceramics made for the same samples by thermo-stimulated depolarization method of laser radiation [29] is provided. As a result the absorption coefficients $\alpha < 4.5\ 10^{-4}$ cm^{-1} for the single crystal and $\alpha < 1.33\ 10^{-3}$ cm^{-1} for the ceramics are estimated.

Absorption and Fluorescence Properties of the CaF_2 Optical Ceramics Doped With Er^{3+}

Cheap and eye – safe lasers with 1.5 μm wavelength are attractive as an optical range - finder, for environment monitoring, telecommunication, etc. due to good atmosphere transparency and transparency of fused silica optical fibers and availability of sensitive detectors at this wavelength. As a result preparation of transparent fluoride ceramics doped with Er^{3+} is of practical interest. Besides, this material can be used for laser generation in the 3 μm mid - IR spectral range.

The CaF_2:Er^{3+} ceramic samples with 1 and 5 mol.% of ErF_3 are prepared by hot - pressing assisted sintering method. The CaF_2:5% ErF_3 ($Ca_{0,95}Er_{0,05}F_{2,05}$) ceramic sample (B(2)39-05) is prepared by pressing of two powders (CaF_2 and ErF_3). The CaF_2:1% ErF_3 (B(2)2-06) and CaF_2:5% ErF_3 (B(1)3-06) ceramic samples are prepared from chemically homogeneous precursors.

The absorption of the ceramic samples must be studied for its use as a laser medium. The absorption spectra at the $^4I_{15/2} \rightarrow {}^4I_{13/2}$, $^4I_{15/2} \rightarrow {}^4I_{11/2}$, $^4I_{15/2} \rightarrow {}^4I_{9/2}$ and $^4I_{15/2} \rightarrow {}^2G(1)_{9/2}$

transitions are measured in three ceramic samples at T=300 K using Shimadzu UV – 3101 PC UV – VIS – NIR spectrometer (Figure 12).

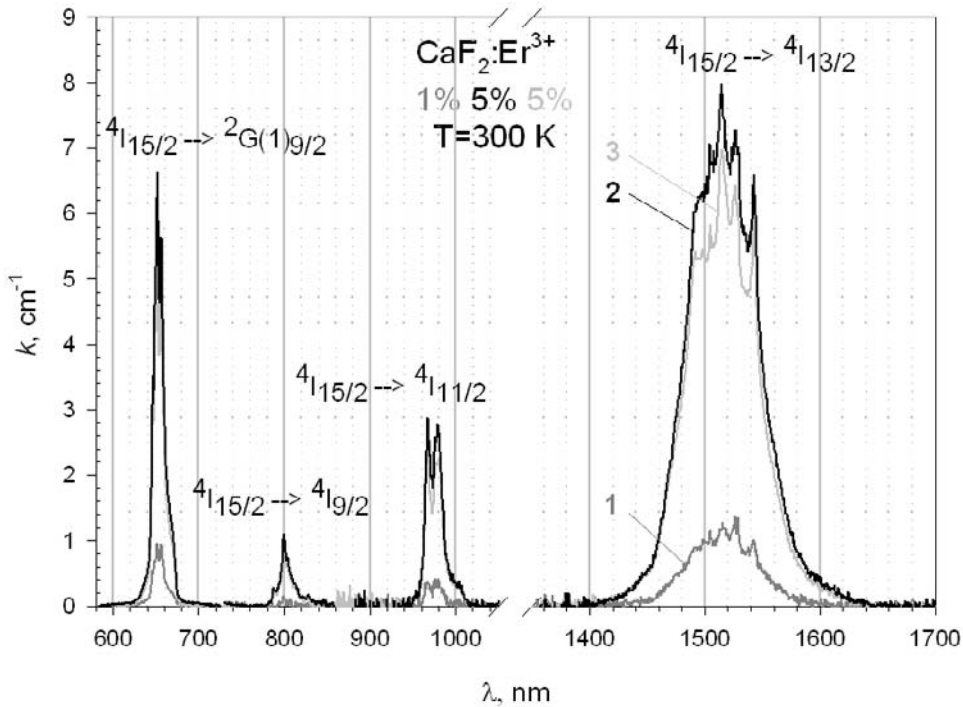

Figure 12. Absorption spectra of the CaF_2: Er^{3+} ceramic samples with different concentrations of the Er^{3+} ion measured at room temperature: CaF_2: Er^{3+} (1%) – dark grey curve (B(2)2-06 sample) - 1, CaF_2: Er^{3+} (5%) – black curve (B(2)39-05 sample) - 2, CaF_2: Er^{3+} (5%) – grey curve (B(1)3-06 sample) - 3.

As seen from the measured spectra the transitions in the samples with 5% concentration of the Er^{3+} ions is ~ five – fold more intensive in comparison with the sample with 1% concentration. But for the same mean concentration of Er^{3+} (5%) in two samples the absorption spectra are different. Thus, for the measured transitions in the B(2)39-05 ceramic sample the absorption is larger than that in the B(1)3-06 one. It seems, the absorption spectrum for the B(2)39-05 ceramic sample is measured in the range where mean concentration of the Er^{3+} ions is higher than in precursors (Figure 6). The ratio of the areas for the $^4I_{15/2} \rightarrow {}^4I_{13/2}$ transition for the B(1)3-06 and B(2)2-06 ceramic samples with the 5% and 1% concentration of the Er^{3+} ions is 5.76 that is more or less in an agreement with the concentration of ErF_3 in raw materials. Thus, preliminary chemical homogenization of raw materials is required to obtain fluoride ceramics with uniform distribution of activator impurities.

Fluorescence spectra at the $^4I_{11/2} \rightarrow {}^4I_{15/2}$ transition are measured under 810 nm CW laser excitation in the CaF_2:Er^{3+} (5 mol. %) ceramic sample and the powdered ceramic sample of the same composition at T=300 K (Figure 13). Comparison of the fluorescence spectra in the ceramics and in the CaF_2:Er^{3+} (5 %) crystal shows small spectral shift to the shorter wavelengths in the former and some modification in spectral shape in the CaF_2: Er^{3+} (5 mol. %) ceramic sample, but the difference is not significant.

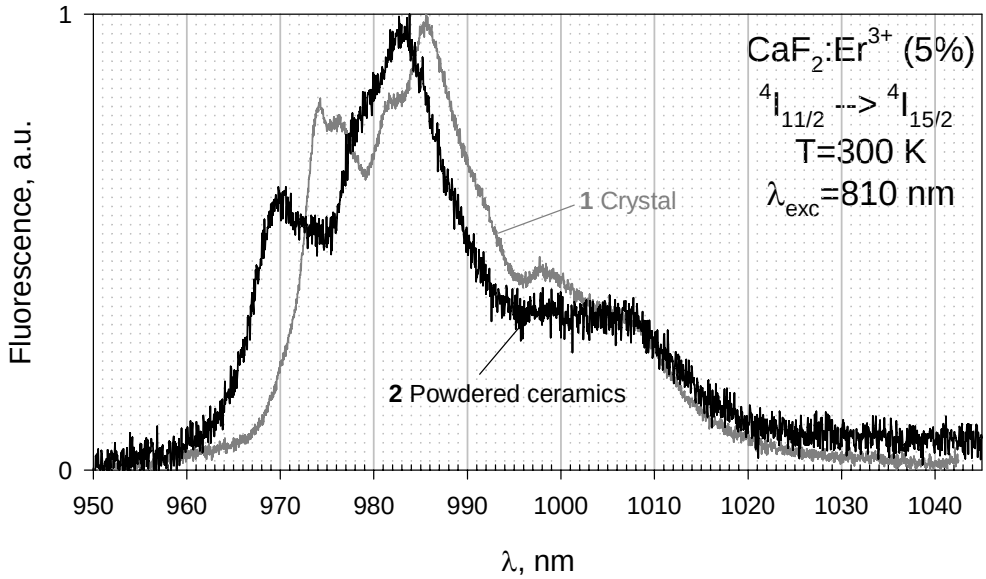

Figure 13. Normalized fluorescence spectra at the $^4I_{11/2} \rightarrow {}^4I_{15/2}$ transition measured in the $CaF_2 : Er^{3+}$ crystal – 1 and in the powdered ceramics of same composition – 2 under CW laser excitation at 810 nm wavelength at room temperature.

Normalized to the unity at each fluorescence maximum the spectra of three ceramic samples (Figure 14) practically do not differ from each other that denotes to the independence of the fluorescence spectra form – factor on the concentration. Absence of narrow spectral lines of the transitions between crystal – field (Stark) levels of the different manifolds ($^4I_{11/2}$ and $^4I_{15/2}$) in comparison with ErF_3 powder fluorescence spectrum (Figure 15) points to inhomogeneous splitting, i.e. to the multi - site structure of the samples.

Fluorescence kinetics decay of the $^4I_{11/2}$ manifold is measured in the $CaF_2:Er^{3+}$ (5 %) and $CaF_2:Er^{3+}$ (10 %) crystals under 980 nm pulsed LiF: $F_2 \rightarrow F_2^+$ laser excitation and 987 nm fluorescence detection and in the $CaF_2:Er^{3+}$ (5 mol. %) ceramic samples, and in the ErF_3 precursors for the ceramics at 974 nm laser excitation and 987.5 nm fluorescence detection (Figure 16). It is necessary to note that the $^4I_{11/2}$ level is the initial laser level for lasing in the spectral range of 3 μm, therefore, its fluorescence quenching because of ion – ion interaction have to be minimized. Strong acceleration of fluorescence decay (Figure 16, curves 2 and 6) is observed for different ErF_3 precursors in comparison with the ceramic samples (Figure 16, curves 1 and 5) and especially with the crystals (Figure 16, curves 3 and 4). There is no difference in kinetics decay found between ceramic sample and the powdered ceramics that confirms the absence of fluorescence trapping for the large concentration of the Er^{3+} ions. Acceleration of fluorescence kinetics decay can be explained by the fluorescence quenching by uncontrolled impurities as a result of direct energy transfer and/or migration over the donors (Er^{3+} ions). Analysis of the disordered stage of energy transfer kinetics for the CaF_2: Er^{3+} (5 mol. %) ceramics (B(2)39-05 sample) and the ErF_3 precursor (Eqs. (4) and (5)) gives quadrupole – quadrupole interaction (multipolarity of interaction s = 10) between the energy donors (excited erbium ions) and the acceptors (uncontrolled impurities).

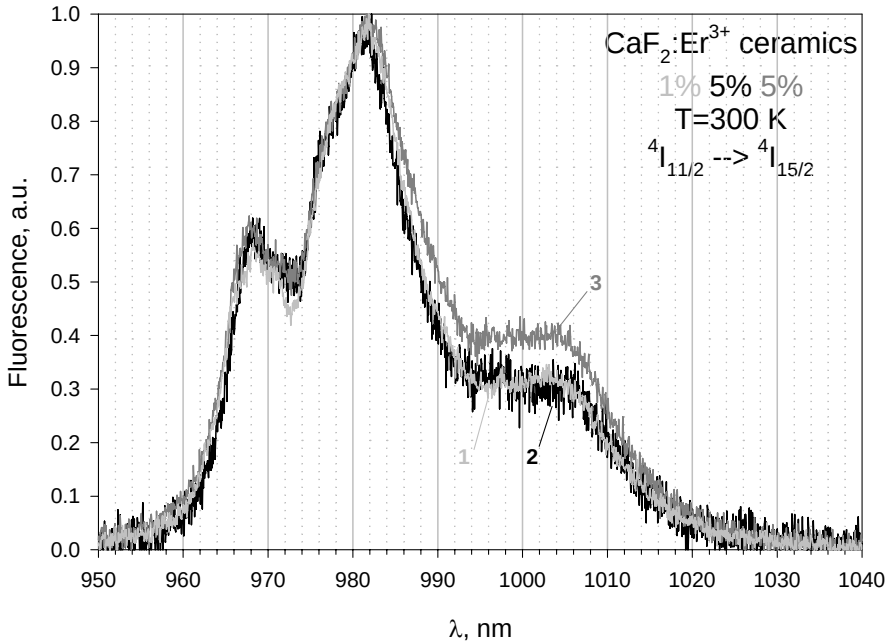

Figure 14. Normalized fluorescence spectra of the CaF_2: Er^{3+} ceramic samples measured at the $^4I_{11/2} \rightarrow {}^4I_{15/2}$ transition with different concentration of the Er^{3+} ion at room temperature: CaF_2: Er^{3+} (1%) – grey curve (B(2)2-06 sample) - 1, CaF_2: Er^{3+} (5%) – black curve (B(2)39-05 sample) - 2, CaF_2: Er^{3+} (5%) – dark grey curve (B(1)3-06 sample) - 3.

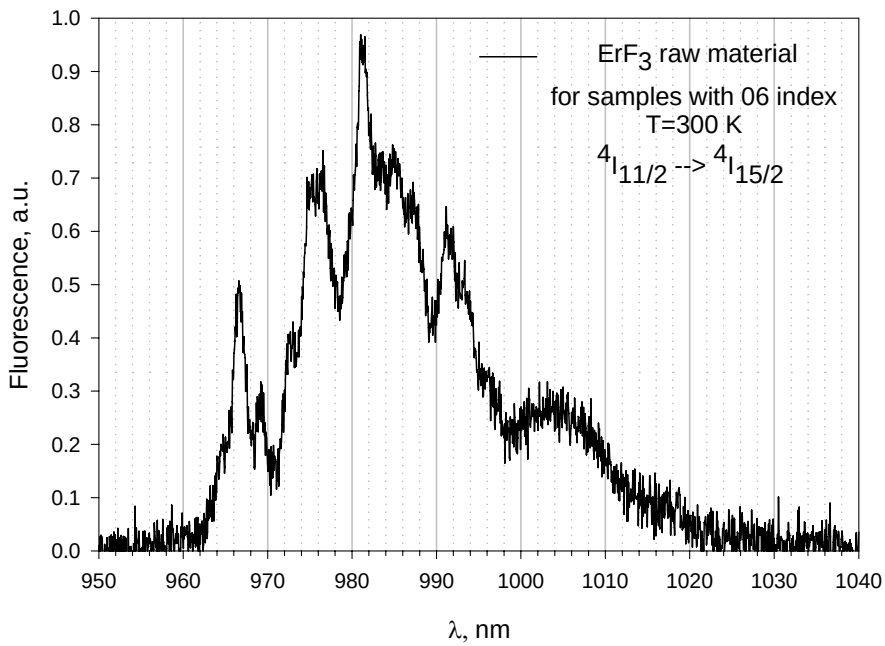

Figure 15. Normalized fluorescence spectra of the ErF_3 precursor used for sample preparation with 06 index measured at room temperature.

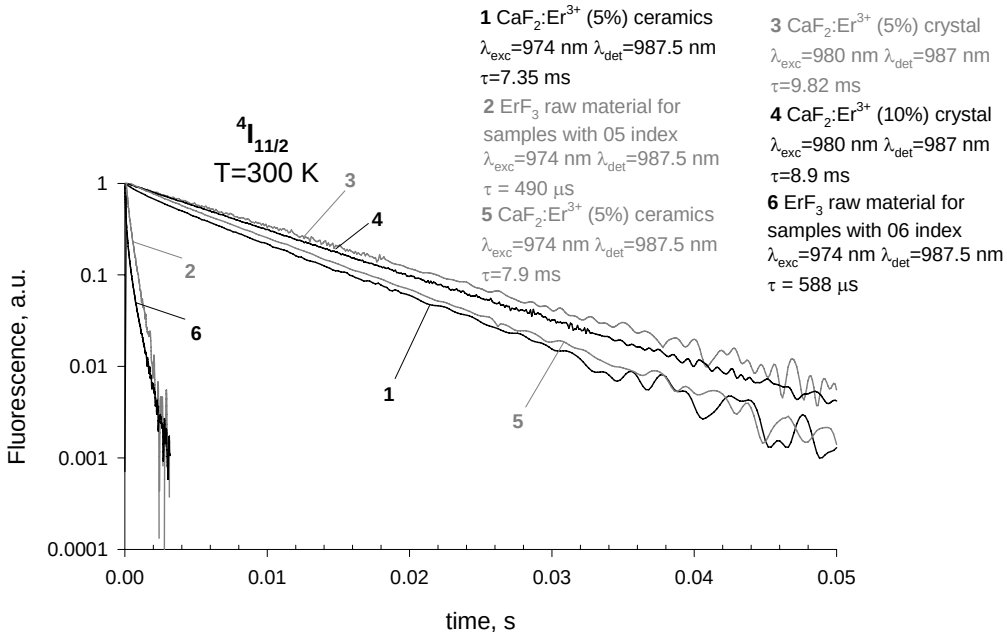

Figure 16. Fluorescence kinetics decay of the $^4I_{11/2}$ level measured under pulsed laser excitation in the CaF_2: Er^{3+} (5%) ceramics (B(2)39-05 sample) (curve 1), in its ErF_3 precursor (curve 2), in the CaF_2:Er^{3+} (5%) (curve 3) and the CaF_2:Er^{3+} (10%) (curve 4) crystals, in the CaF_2:Er^{3+} (5%) (B(1)3-06 sample) (curve 5) and in its ErF_3 precursor (curve 6) at room temperature.

Also, the disordered stage of energy transfer kinetics for the new CaF_2: Er^{3+} (5 mol. %) (B(1)3-06) ceramic sample and its ErF_3 precursor is analyzed. Analysis of the disordered stage of energy transfer kinetics for ceramics gives the sum of two mechanisms of interaction between the energy donors (erbium ions) and the acceptors (uncontrolled impurities), i.e. quadrupole – quadrupole (s = 10) and dipole- quadrupole (s = 8). However, for the ErF_3 precursors the only quadrupole – quadrupole interaction is observed. This result shows that in the new CaF_2: Er^{3+} (5 mol. %) ceramic sample (B(1)3-06) the average distance between the Er^{3+} ions and uncontrolled impurities ions is larger, which is, to say that the latter concentration is lower.

Fluorescence spectrum at the $^4I_{13/2} \rightarrow {}^4I_{15/2}$ transition in the CaF_2:Er^{3+} (5 mol. %) (B(2)39-05) ceramic sample is measured under 810 nm CW laser excitation at room temperature (Figure 17a). Fluorescence kinetics decay of the $^4I_{13/2}$ manifold in this sample was measured by pulsed LiF: $F_2 \rightarrow F_2^+$ color centers laser excitation at 974 nm wavelength and 1.53 μm detection at T=300 K (Figure 17b). A build - up of the fluorescence is observed with the duration of 6 ms. Fluorescence kinetics decay at the long time scale is exponential with the decay time τ_{final} = 15.7 ms. The powdered ceramic sample exhibits exponential decay with τ = 6.7 ms which is ~3 times shorter than for the ceramic sample and indicates the fluorescence trapping for the latter one because of high absorption cross – section at the $^4I_{15/2} \rightarrow {}^4I_{13/2}$ transition.

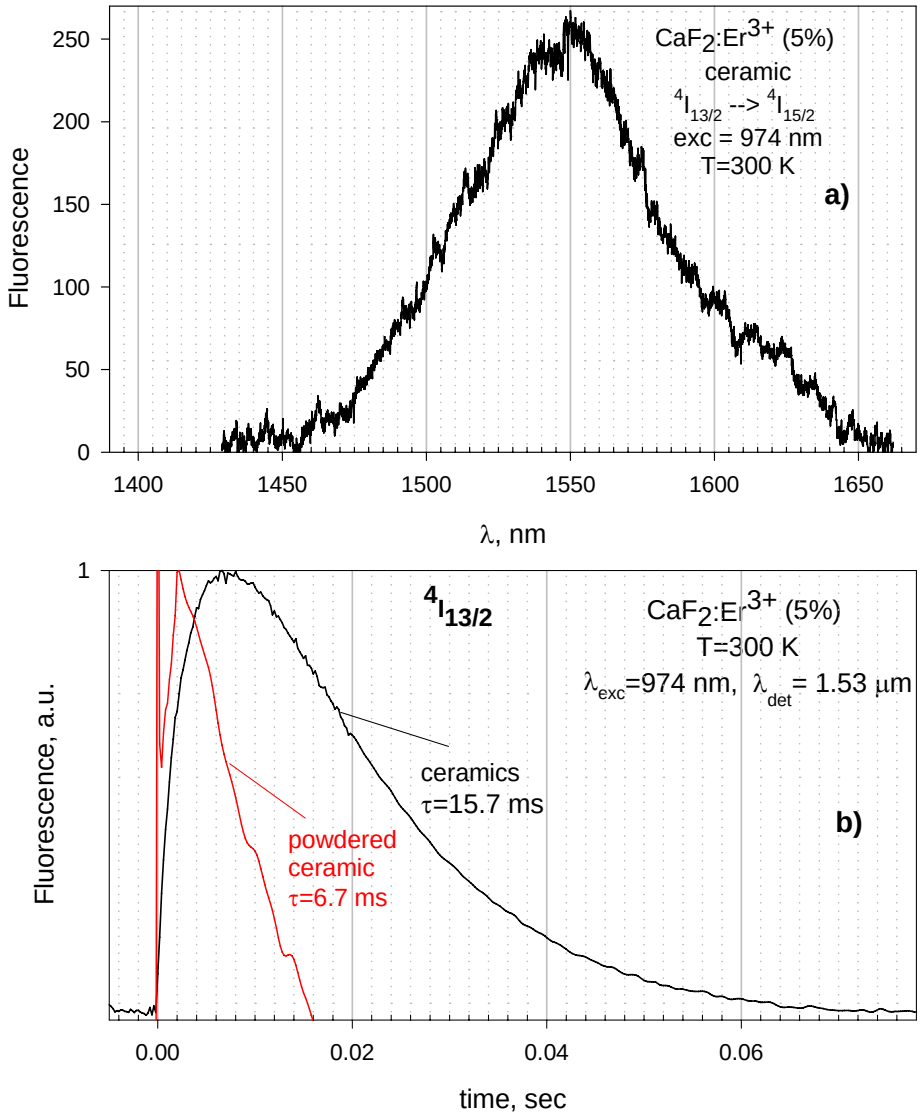

Figure 17. Fluorescence spectrum measured under CW laser excitation with 810 nm wavelength at the $^4I_{13/2} \rightarrow {}^4I_{15/2}$ transition in the $CaF_2:Er^{3+}$ (5%) ceramic sample (B(2)-39-05) at room temperature – a, and fluorescence kinetics decay of the $^4I_{13/2}$ level measured under pulsed laser excitation with 1.53 μm wavelength detection at room temperature – b in the $CaF_2:Er^{3+}$ (5%) (B(2)-39-05 sample) ceramics – 1 and powdered ceramic sample – 2.

OXYSULFIDE OPTICAL CERAMICS

Powder phosphors based on La, Gd, and Y oxysulfides hold unique position among other phosphors due to highly- efficient conversion of different types of radiation including UV, cathode beam and X – rays. These materials have a high density (La_2O_2S – 5.77 g/cm^3, Gd_2O_2S - 7.33 g/cm^3, Y_2O_2S - 4.089 g/cm^3) that provides high x-ray adsorption coefficients

in a wide energy range and high conversion efficiency. Homovalent substitution in cation sublattice of a matrix for any rare – earth (RE) ions from lanthanide row allows to vary spectral and fluorescence kinetic properties and develop oxysulfide materials for different applications.

Rare earth oxysulfides crystallize in trigonal system, space group $P3\text{-}m1$, Z = 1 [34]. Its crystal structure corresponds to the A-R_2O_3 structural type of cerium subgroup rare earth oxides, with substitution of oxygen by sulfur in the crystallographic position. Cation coordination number is seven, with four atoms of oxygen and three atoms of sulfur. Three oxygen and three sulfur atoms form regular Archimedean antiprism, the oxygen bottom of antiprism is capped by forth oxygen atom.

Hexagonal structure of oxysulfides anticipates anisotropy of optical properties of RE ions. In the La, Gd, Y oxysulfide row a minimal value of $\Delta n = n_e - n_o$ is observed in La_2O_2S. Moreover, for λ = 0.56 μm Δn is zero in La_2O_2S [35]. A La, Gd, Y oxysulfides have high melting points – 2000 – 2100C [34]. Together with high reactivity, that is a reason of a lack of high advances in oxysulfide single crystals growth. There are only few papers, which communicate about rather small not of a top quality the La_2O_2S and Y_2O_2S single crystals doped with Nd^{3+} or Er^{3+} [35 - 38]. In this connection methods of synthesis of luminescent optical oxysulfide ceramics are of interest to material science as alternative. One of them that is gaining acceptance in recent years is a hot- pressing of micro- and, especially, nanopowder precursor. As a result, the Gd_2O_2S: Pr, Ce ceramic scintillators are synthesized and profitably employed in X-ray tomography by Hitachi (Japan) [39] and Siemens (Germany) [40].

In Russia, the work towards creating the rare-earth oxysulfide based luminescent optical ceramics is carried out at FGUP NITIOM VNC "S.I. Vavilov GOI". The Y_2O_2S and La_2O_2S based transparent ceramics doped with a variety of impurities has been obtained [41 - 43]. In 1999 – 2003 the Gd_2O_2S:Pr,Ce and Gd_2O_2S:Tb,Ce optical ceramics is developed that offeres scintillation characteristics being on a par with the world best samples, but unlike the latter features quite high transparency in the visible and IR in spite of anisotropy [44 - 47] (Figure 18).

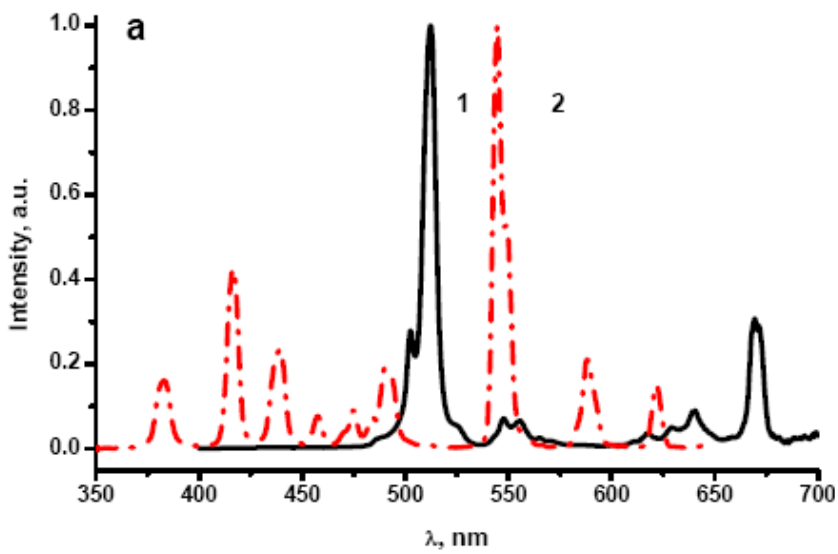

Figure 18 (Continued).

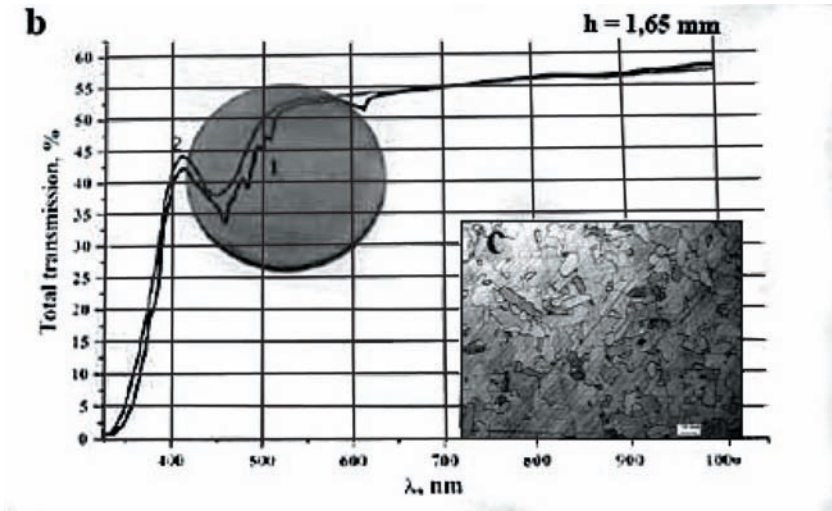

Figure 18. Fluorescence spectra (a), total transmission spectrum (b), and microstructure (c) of the Gd_2O_2S-Pr,Ce (1) and Gd_2O_2S -Tb,Ce (2) ceramic samples.

The research carried out allows to assign that the Gd_2O_2S - Pr, Ce and Gd_2O_2S:Tb, Ce ceramics obtained features high transparency for its own emission for 1.65 mm thick sample. Its x-ray luminescence intensity commensurate with that of their powder counterparts and reveals fast luminescence damping after 500 ms - I/I_0 = 0.001-0.002% and 0.004% for Gd_2O_2S - Pr, Ce and Gd_2O_2S:Tb, Ce, respectively. This part of the chapter summarizes the results of study of the Gd_2O_2S: Nd^{3+} and La_2O_2S: Nd^{3+} ceramics. The technique for preparation of oxysulfide ceramics is similar to that for fluoride ceramics. The raw materials used are the Gd_2O_2S: Nd^{3+} and La_2O_2S: Nd^{3+} powders of 3 - 5 μm particle size. The powders featured a uniform grain composition with the predominantly isometric shape of grain (Figure 19). In order to obtain a high density and transparency of the ceramics, the hot pressing process is provided in presence of fusible LiF additive.

The introduction of LiF speeds up the densification process significantly and raises the degree of densification of powder oxysulfides. Employing liquid phase mechanisms in the densification process due to the fusible compound promotes the slip at grain borders, intensifies the mass transfer due to diffusion and recrystallization processes. This all allows to obtain the ceramics of x-ray structural density and high transparency. The Nd^{3+} concentration in Gd_2O_2S is 0.1 and 0.5 wt. %, and in La_2O_2S - 1.0 wt. %. The samples after hot pressing appear as 35 mm disks in diameter and up to 2 mm thick. The density of ceramics corresponds to more than 0.99 of x-ray structural ceramics.

The lattice parameters in ceramic samples are measured on a diffractometer with copper anode and nickel filter, and are determined with a reference to a system of crystallographic planes (312) and (205) at large reflection angles (112^0 - 120^0). The measured parameters for the Gd_2O_2S: Nd^{3+} samples (0.1-0.5 wt. %) are a = 3.854 ± 0.001 Å, c= 6.670 ± 0.002 Å, for the La_2O_2S: Nd ceramics (1.0 wt. %) – a = 4.051 ± 0.001 Å, c = 6.942 ± 0.002 Å.

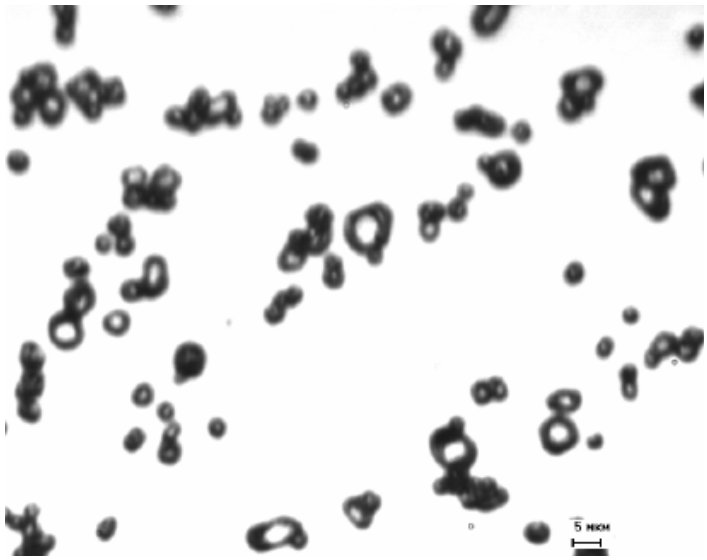

Figure 19. Characteristic microphotograph of precursor for the Gd_2O_2S: Nd^{3+} and La_2O_2S: Nd^{3+} ceramics.

The microstructure of the ceramics is studied using optical and electron microscopes. Characteristic microphotographs of the ceramic samples are presented in Figure 20. For the Gd_2O_2S based samples the most typical is the elongated grains shape (Figure 20a, b), as for the La_2O_2S ceramics it is isometric (Figure 20c). For the Gd_2O_2S based ceramics, a clear-cut correlation between the grain shape and the Nd^{3+} impurity concentration is observed. Whereas for 0.1 wt.% concentration of Nd^{3+} the microstructure of ceramics consists of the mixed shape grains (Figure 20a), a five-fold increase of the impurity concentration makes the long bar shape the dominant (Figure 20b).

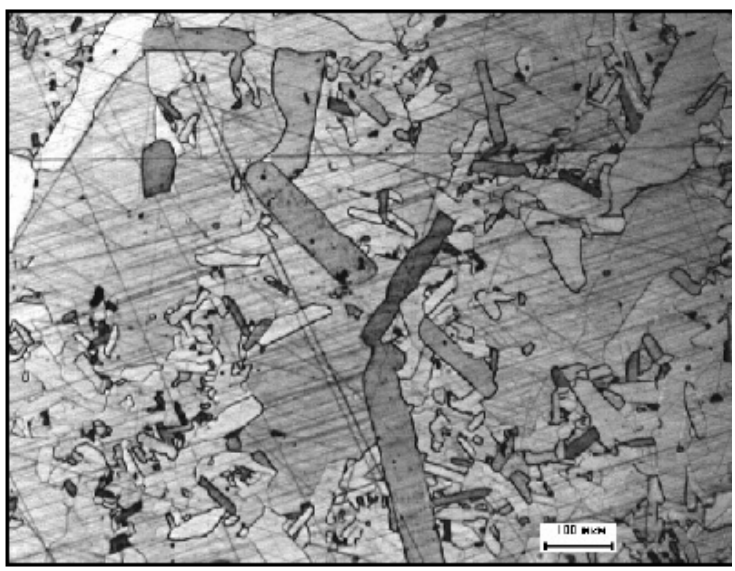

a

Figure 20 (Continued).

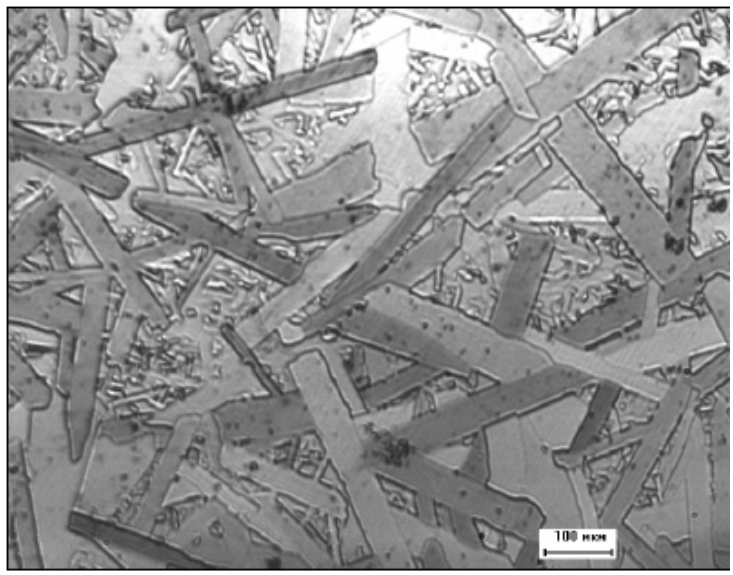

b

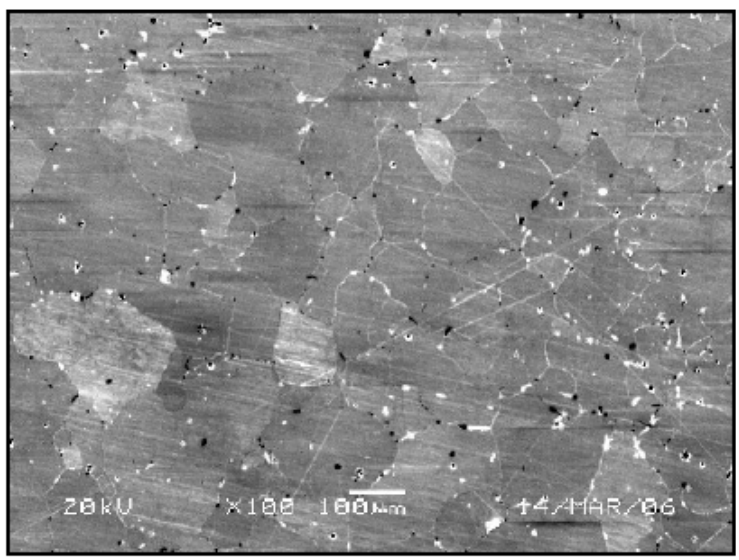

c

Figure 20. Characteristic microphotographs of ceramic samples: a - Gd_2O_2S:Nd (0,1wt.%), b - Gd_2O_2S:Nd (0,5wt.%), c - La_2O_2S:Nd (1wt.%).

The texture over the (001) plane in Gd_2O_2S: Nd^{3+} samples is estimated by x-ray diffraction and reveals the influence of the impurity concentration: the texture in (001) plane get halved upon raising the Nd^{3+} concentration from 0.1 to 0.5 wt. %, that corresponds to reduction of quantity of grains oriented along this plane.

Further a spectroscopic characteristics of oxysulfide translucent optical ceramics which can be perspective for 1-μm lasing with high quantum efficiency [48, 49] is given.

OPTICAL PROPERTIES OF OXYSULFIDE CERAMICS [49]

Let us first consider the optical properties of $Gd_2O_2S:Nd^{3+}$ (0.1 wt%) oxysulfide optical ceramics. Transmission spectra of the samples are measured by a single-channel spectrometer using incandescent halogen lamp. A double grating high spectral resolution DFS-12 spectrometer with 600 grooves/mm grating is used for spectral measurement. The transmitted signal is detected by PMT-79 and is recorded using an ADC and a PC. Transmission spectrum for the sample with thickness d = 0.175 cm at the $^4I_{9/2} \rightarrow {}^4F_{3/2}$ transition is measured at 77 K and absorption spectrum is calculated (Figure 21a).

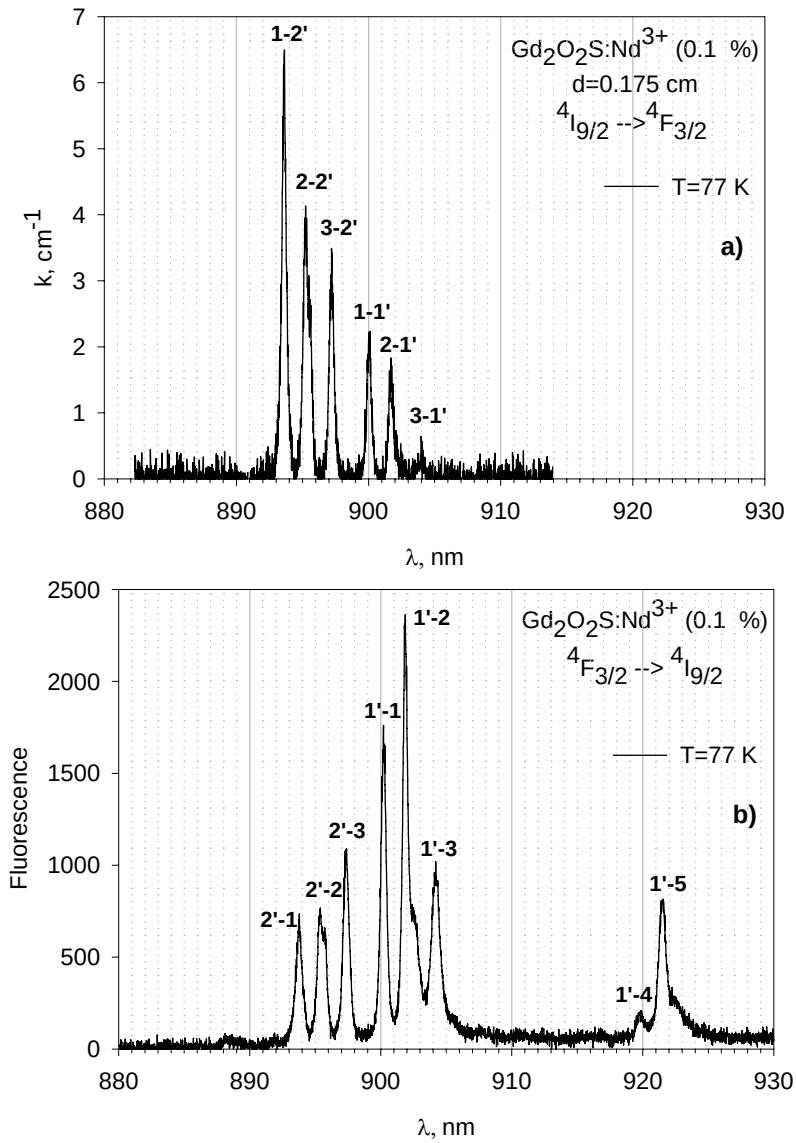

Figure 21. Absorption spectrum of the $Gd_2O_2S:Nd^{3+}$ (0.1 wt%) oxysulfide optical ceramics measured at the $^4I_{9/2} \rightarrow {}^4F_{3/2}$ transition of the Nd^{3+} ion—a; and fluorescence spectrum at the $^4F_{3/2}$–$^4I_{9/2}$ transition under 812 nm CW laser excitation—b. Both spectra are at 77 K.

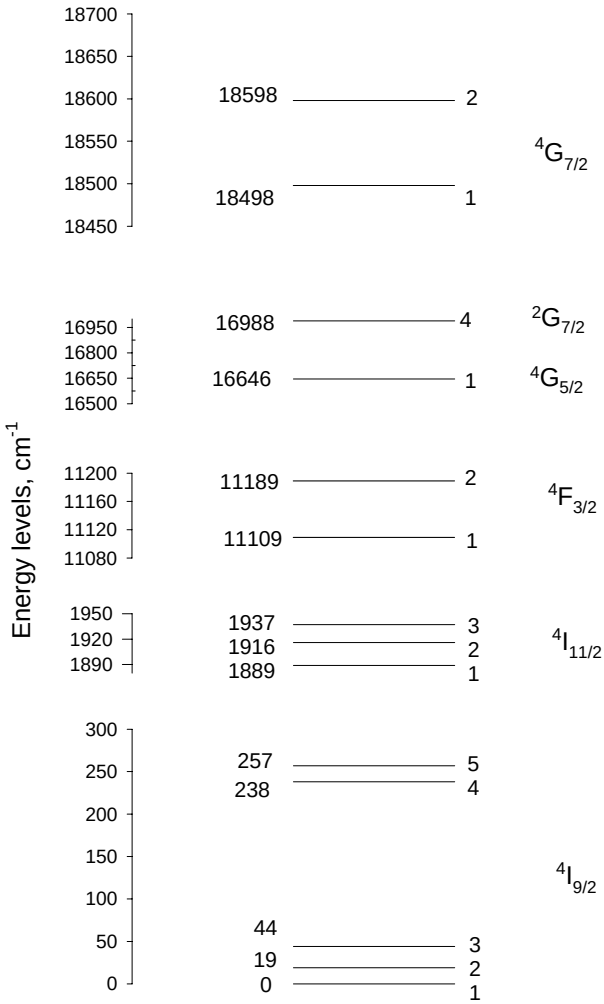

Figure 22. Identified crystal-field (Stark) levels diagram of the $^4I_{9/2}$, $^4I_{11/2}$, $^4F_{3/2}$, $^4G_{5/2,}$ $^2G_{7/2}$ and $^4G_{7/2}$ manifolds of the Nd^{3+} ion in the $Gd_2O_2S:Nd^{3+}$ (0.1 wt%) oxysulfide optical ceramics.

The notations near the spectral lines denote the transitions between the crystal-field (CF) levels of corresponding manifolds. The primed numbers denote the CF levels of the excited manifold and those without prime — the CF levels of the ground manifold. Counting is from bottom to top. Corresponding fluorescence spectrum at the $^4F_{3/2}\rightarrow{}^4I_{9/2}$ transition (Figure 21b) allows to determine the CF (Stark) splitting of the $^4I_{9/2}$ and $^4F_{3/2}$ manifolds (Figure 22).

Absorption spectra of the $^4I_{9/2}\rightarrow{}^4G_{7/2}$ and $^4I_{9/2}\rightarrow{}^2G_{7/2}$; $^4G_{5/2}$ transitions at 77 and 300 K (Figure 23) allow to separate the $^2G_{7/2}$ and $^4G_{5/2}$ manifolds. A spin-forbidden $^4I_{9/2}\rightarrow{}^2G_{7/2}$ transition has lower intensity than the spin-allowed $^4I_{9/2}\rightarrow{}^4G_{5/2}$ transition and takes up higher position on the energy scale. Thus the minimal energy gap ΔE_{min}=1517 cm^{-1} is in between the lowest CF level of the $^4G_{7/2}$ manifold and the upper CF level of the $^2G_{7/2}$ manifold. The absorption spectral lines measured in the $Gd_2O_2S:Nd^{3+}$ (0.1%) optical ceramics are well pronounced as opposed to those in the $La_2O_2S:Nd^{3+}$ (1%) optical ceramics (not presented). The later may be concerned with the inhomogeneous broadening of the CF transition spectral lines at larger concentration of Nd^{3+} in the La_2O_2S ceramics.

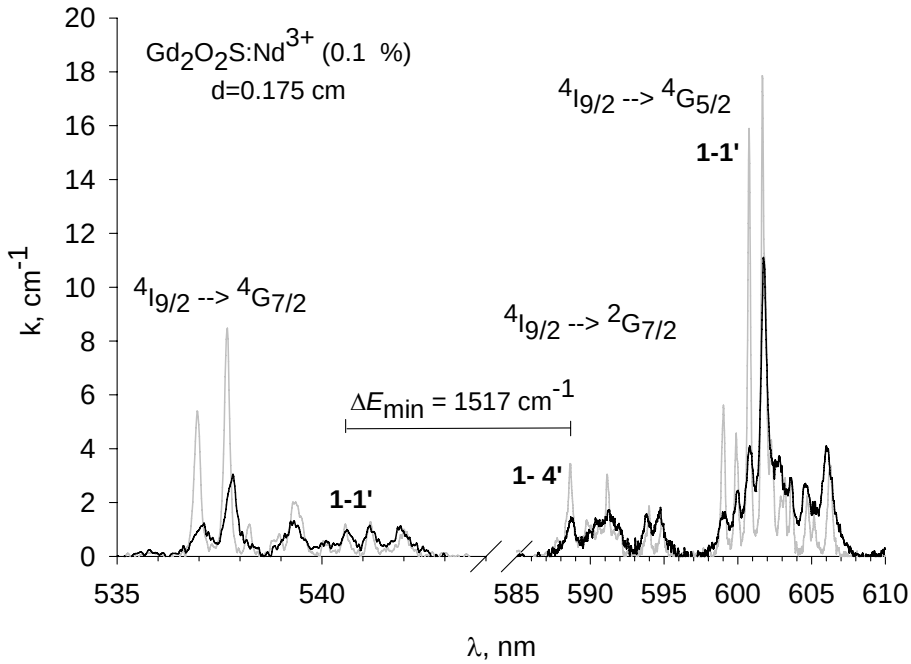

Figure 23. Absorption spectra of the $Gd_2O_2S:Nd^{3+}$ (0.1 wt%) oxysulfide optical ceramics at the $^4I_{9/2}\rightarrow{}^4G_{7/2}$, $^4I_{9/2}\rightarrow{}^2G_{7/2}$, and $^4I_{9/2}\rightarrow{}^4G_{5/2}$ transitions at 77 K (gray curve) and 300 K (black curve).

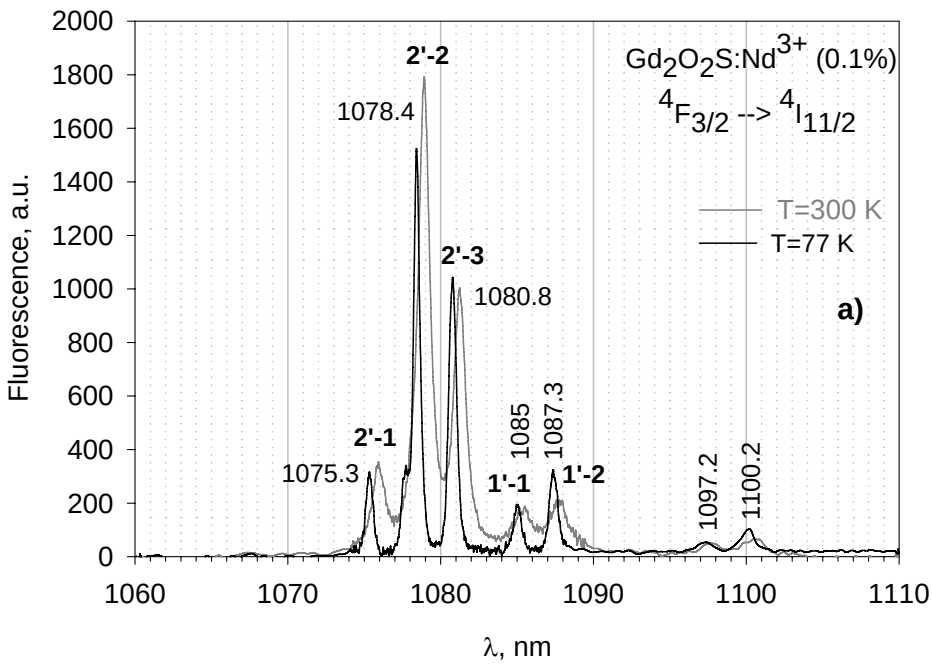

a

Figure 24 (Continued).

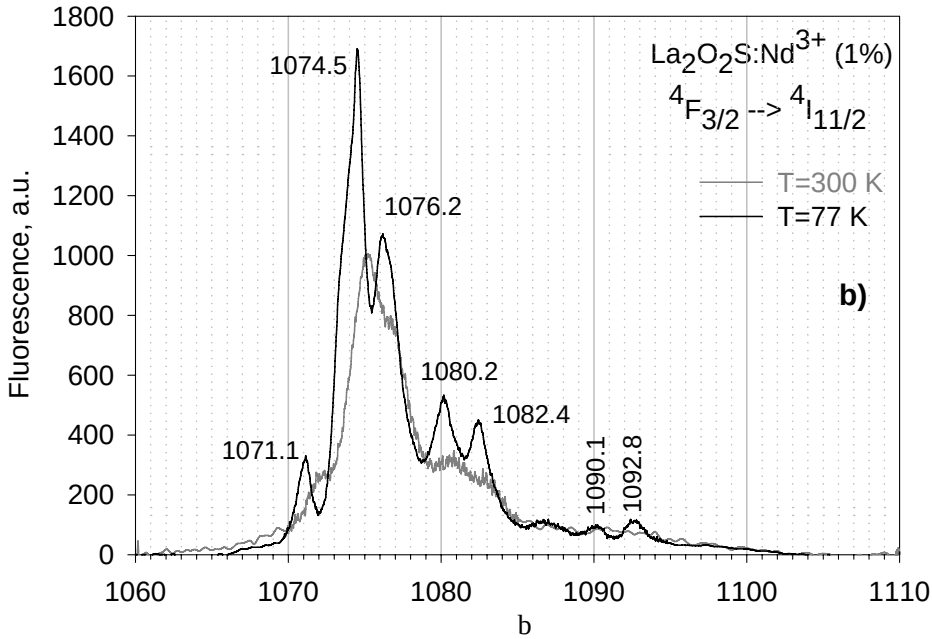

Figure 24. Fluorescence spectra of the $^4F_{3/2}\rightarrow{}^4I_{11/2}$ transition in $Gd_2O_2S:Nd^{3+}$ (0.1 wt%)—a and $La_2O_2S:Nd^{3+}$ (1 wt%)—b under 812 nm laser excitation at 77 and 300 K.

The fluorescence spectrum at the $^4F_{3/2}\rightarrow{}^4I_{11/2}$ transition is measured with high spectral resolution in $Gd_2O_2S:Nd^{3+}$ (0.1 wt%) (Figure 24a) and $La_2O_2S:Nd^{3+}$ (1 wt%) (Figure 24b) at 77 and 300 K using CW diode laser excitation. The positions of the three lowest CF levels of the $^4I_{11/2}$ manifold are found in the $Gd_2O_2S:Nd^{3+}$ ceramics (Figure 22). The fluorescence spectral lines measured at the $^4F_{3/2}\rightarrow{}^4I_{11/2}$ CF level transitions in the $Gd_2O_2S:Nd^{3+}$ (0.1 wt%) optical ceramics at 77 and 300 K are much more narrow (Figure 24a) comparing to those in the $La_2O_2S:Nd^{3+}$ (1 wt%) optical ceramics (Figure 24b), because of the same reasons as in the case of absorption spectra.

MULTIPHONON RELAXATION IN OXYSULFIDE CERAMICS [49]

The $^4I_{11/2}$ state can be potentially a bottleneck during 1-μm lasing and gives rise to transient absorption at laser wavelength. So, the faster the rate of multiphonon relaxation (MR), faster the depletion of the $^4I_{11/2}$ level and the smaller the losses [50].

It is a well-known fact that the energy gaps of the $^4G_{7/2}\rightarrow{}^4G_{5/2}$; $^2G_{7/2}$ and the $^4I_{11/2}\rightarrow{}^4I_{9/2}$ transitions of Nd^{3+} are nearly the same in oxide ($\hbar\omega_{max}$ = 800 cm^{-1}) and fluoride ($\hbar\omega_{max}$ = 400 cm^{-1}) crystals and their relaxation rates are mostly determined by MR. The cut-off frequencies about 440 and 400 cm^{-1}, respectively, are found from Raman spectra of the Gd_2O_2S and La_2O_2S optical ceramics doped by Nd^{3+} (Figure 25). Highly sensitive Raman spectrometer with photon counting is used for measurements. The value $\hbar\omega_{max}$ for the La_2O_2S optical ceramics is in a good agreement with that measured in the La_2O_2S crystal [51]. Therefore, one can estimate the rate of the $^4I_{11/2}\rightarrow{}^4I_{9/2}$ transition from the rate of the $^4G_{7/2}\rightarrow{}^4G_{5/2}$; $^2G_{7/2}$

transition. Table 1 presents approximate values of energy gaps ΔE_{min}, $\hbar\omega_{max}$ and a minimal number of phonons p_{min} for the samples in study.

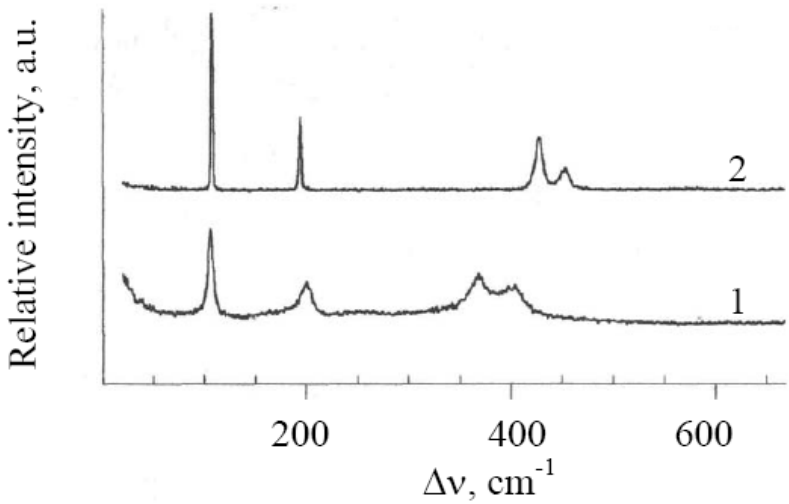

Figure 25. Raman spectra of the $La_2O_2S:Nd^{3+}$—1 and $Gd_2O_2S:Nd^{3+}$—2 optical ceramics at 300 K.

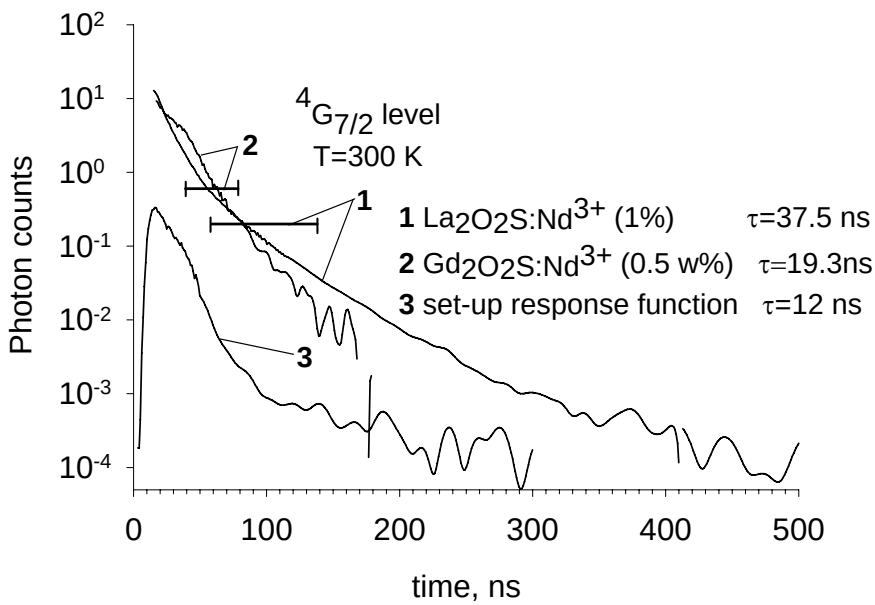

Figure 26. Fluorescence kinetics of the $^4G_{7/2}$ manifold in La_2O_2S: Nd^{3+} (1 wt%)—1, $Gd_2O_2S:Nd^{3+}$ (0.5 wt%)—2 at room temperature under 511 nm excitation detected at the $^4G_{7/2}\rightarrow{}^4I_{13/2}$ transition and the setup response function−3, and the positions of time gates for the fluorescence spectra measurements at the same transition.

The fluorescence decay curves of the high-lying strongly quenched $^4G_{7/2}$ level in the $Gd_2O_2S:Nd^{3+}$ (0.5 wt%) and $La_2O_2S:Nd^{3+}$ (1 wt%) optical ceramics are measured at the visible $^4G_{7/2}\rightarrow{}^4I_{13/2}$ transition at room (Figure 26) and liquid nitrogen temperatures (Figure

27) under pulsed copper vapor laser excitation at 511 nm (t_p = 10 ns; f = 10 kHz) and a time-correlated single-photon counting detection technique. The time- resolved fluorescence spectrum at the $^4G_{7/2} \rightarrow {}^4I_{13/2}$ transition is measured at room temperature for the $La_2O_2S:Nd^{3+}$ (1 wt%) optical ceramics with gate width t_{gate}=79 ns and gate delay t_d=59 ns (curve 1 at Figure 28) and for the $Gd_2O_2S:Nd^{3+}$ (0.5 wt%) optical ceramics these values are set to t_{gate} = 40 ns and t_d= 39 ns (curve 2 at Figure 28) using the same technique and a special program of our own for multichannel amplitude analyzer (MCA, EGandG Ortec) operation. The gate delays are set to minimize the influence of a small fraction of the powerful pump radiation passing through the monochromator and KS-11 glass filter. The decay times are measured at the long time scale of fluorescence kinetics decay. The measured decay times (Table 2) are determined by MR of the $^4G_{7/2} \rightarrow {}^4G_{5/2}$; $^2G_{7/2}$ transition, because a contribution of radiative decay is negligible [52]. The MR rate of the $^4I_{11/2} \rightarrow {}^4I_{9/2}$ transition is of the order of magnitude of the measured rate of the $^4G_{7/2} \rightarrow {}^4G_{5/2}$; $^2G_{7/2}$ transition. So, the depletion of the low laser level is not slower than several hundred nanoseconds.

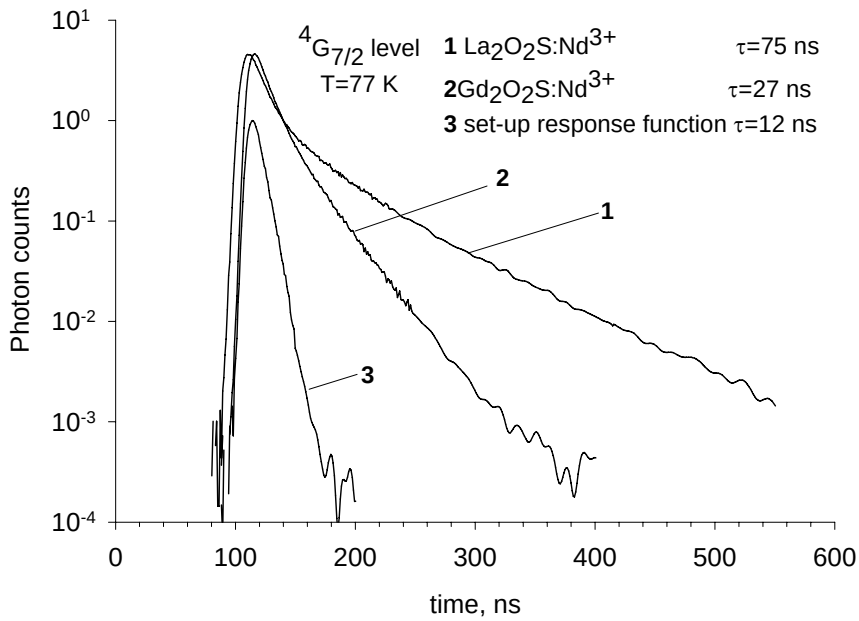

Figure 27. Fluorescence kinetics of the $^4G_{7/2}$ manifold in $La_2O_2S:Nd^{3+}$ (1 wt%)—1, $Gd_2O_2S:Nd^{3+}$ (0.5 wt%)−2 at 77 K under 511 nm excitation detected at the $^4G_{7/2} \rightarrow {}^4I_{13/2}$ transition and the set- up response function—3.

Table 2. The measured and multiphonon relaxation decay times for the $^4G_{7/2}$ level of Nd^{3+} in optical ceramics with low-phonon spectra at 77 K and room temperature and parameters having influence on multiphonon transition rate

Optical samples	ΔE_{min} (cm^{-1})	$\hbar\omega_{max}$	p_{min}	$\tau_{meas} = \tau_{MR}$ at 77 K (ns)	$\tau_{meas} = \tau_{MR}$ at 300 K (ns)
$La_2O_2S:Nd^{3+}$	1517	400	4	75	38
$Gd_2O_2S:Nd^{3+}$	1500	440	4	27	19

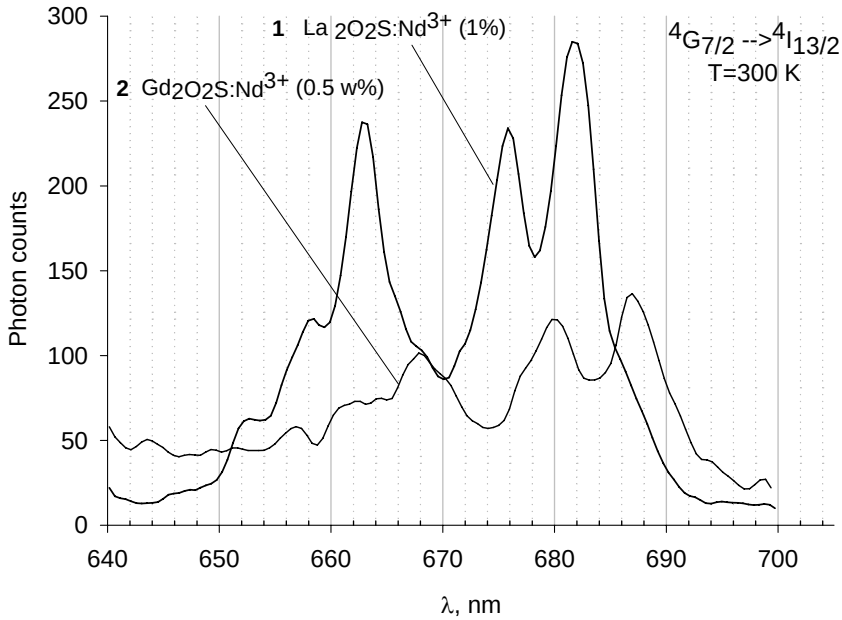

Figure 28. Time-resolved fluorescence spectra of the $^4G_{7/2} \rightarrow {}^4I_{13/2}$ transition of Nd^{3+} of $La_2O_2S:Nd^{3+}$ (1 wt%) with 79 ns time gate t_{gate} and 59 ns gate delay t_d — 1; and $Gd_2O_2S:Nd^{3+}$ (0.5 wt%) — t_{gate} = 40 ns, t_d = 39 ns — 2 under 511 nm laser excitation at room temperature.

ENERGY TRANSFER IN OXYSULFIDE OPTICAL CERAMICS [49]

The nonradiative energy transfer of electronic excitation energy in solid state laser materials is one of the fundamental problems of solid state physics and quantum electronics, and is of considerable applied interest. For example, the concentration quenching of fluorescence emitted in transitions from the upper working laser level produces a reduction in the quantum yield, a lifting of the laser threshold and an increase of dissipation heat.

In continual approximation and when $W(R_{min})\ t \gg 1$ ($W(R_{min})$ is the energy transfer rate for the minimal distance between donor and acceptor) the nonexponential decay of donor states is well described by the following expression [53] and [54]:

$$I(t) = I_0 \exp\left[-t/\tau - \gamma t^{3/s} - \overline{W}t\right], \tag{1}$$

where $1/\tau$ is the probability of intracenter decay, which is the sum of radiative decay ($1/\tau_R$) and multiphonon relaxation ($1/\tau_{MR}$), $\gamma t^{3/s}$ describes the Forster kinetics of nonradiative energy transfer from donor to the acceptor (quencher) in the absence of energy migration over the donors, and $\overline{W}$ is the nonradiative decay constant due to the migration of energy over the donors to the acceptors.

For crystalline lattice even in the diluted case we have some order in the donor and acceptor positions and a minimal distance between donor and acceptor $R_{DA}=R_{min}$ is nonzero.

In the first approximation, the experimental data on nontradiative energy transfer kinetics due to the multipole interaction between ions, for which electronic excitation prior to emission or quenching keeps its position unchanged [55], [56] and [57], can be analyzed in terms of the theory of direct energy transfer (DET) when the process of energy migration over the donors to the acceptors can be neglected. The quantity $\overline{W}$ in Eq. (1) is then equal to zero, and the nonradiative transfer kinetics is reasonably described by a two-stage process. During the initial stage, i.e., the so called ordered stage, decay proceeds with the maximal possible rate for a given activator and is described by the simple exponential law [58]:

$$I_{tr}(t) = I(t)/\exp(-t/\tau) = I_0 \exp(-W_0 t), \tag{2}$$

where the quenching rate is given by

$$W_0 = c_A C_{DA} \sum_n R_n^{-s}, \tag{3}$$

and the sum is evaluated over all the sites of the acceptor sublattice, taking into account its occupation $c_A=n_A/n_{max}$. For Nd^{3+} doped laser crystals the unexcited Nd^{3+} ions whose concentration is much greater than the concentration of excited ions, can act as acceptors, i.e., $n_A=n(Nd^{3+})$, and s=6 for the dipole–dipole interaction, s=8 for the dipole–quadrupole interaction, s=10 for the quadrupole–quadrupole interaction, and so on.

From a certain instant t_1 onward, the ordered stage goes over to the so-called Forster or disordered stage, which means that acceptor ensemble is stochastic or disordered due to accidental occupation of acceptor sublattice positions.

For the analysis of the disordered stage of the kinetics decay the following equations for the static nonradiative energy transfer can be used [56] and [58]:

$$I_{tr}(t) = \exp(-\gamma t^{3/s}), \tag{4}$$

where

$$\gamma = 4/3\pi\Gamma(1 - 3/s)C_{DA}^{3/s} n_A, \tag{5}$$

and $\Gamma(x)$ is the gamma function. These expressions were derived by integration, assuming a continuous medium and neglecting the particle sizes or the crystal lattice constant.

The intra center decay time τ can be found from the fluorescence kinetics measured in a diluted sample. Fluorescence of the optical samples for the transitions from the $^4F_{3/2}$ manifold are excited by tunable LiF: $F_2 \rightarrow F_2^+$ color center laser pumped by YAG:Nd laser (t_p=10 ns, f=12 Hz). High throughput MDR-2 monochromator and a PMT-83 are used for fluorescence selection and detection. A Tektronix TDS 3032B digital oscilloscope is employed for fluorescence kinetics measurements. The fluorescence kinetics of the $^4F_{3/2}$ manifold in the $Gd_2O_2S:Nd^{3+}$ (0.1 wt%) optical crystal ceramics measured under laser excitation at 893.5 nm for 1.08 μm fluorescence detection at 300 K exhibits exponential decay (τ=107 μs) in the measured temperature range 77–300 K (Figure 29a).

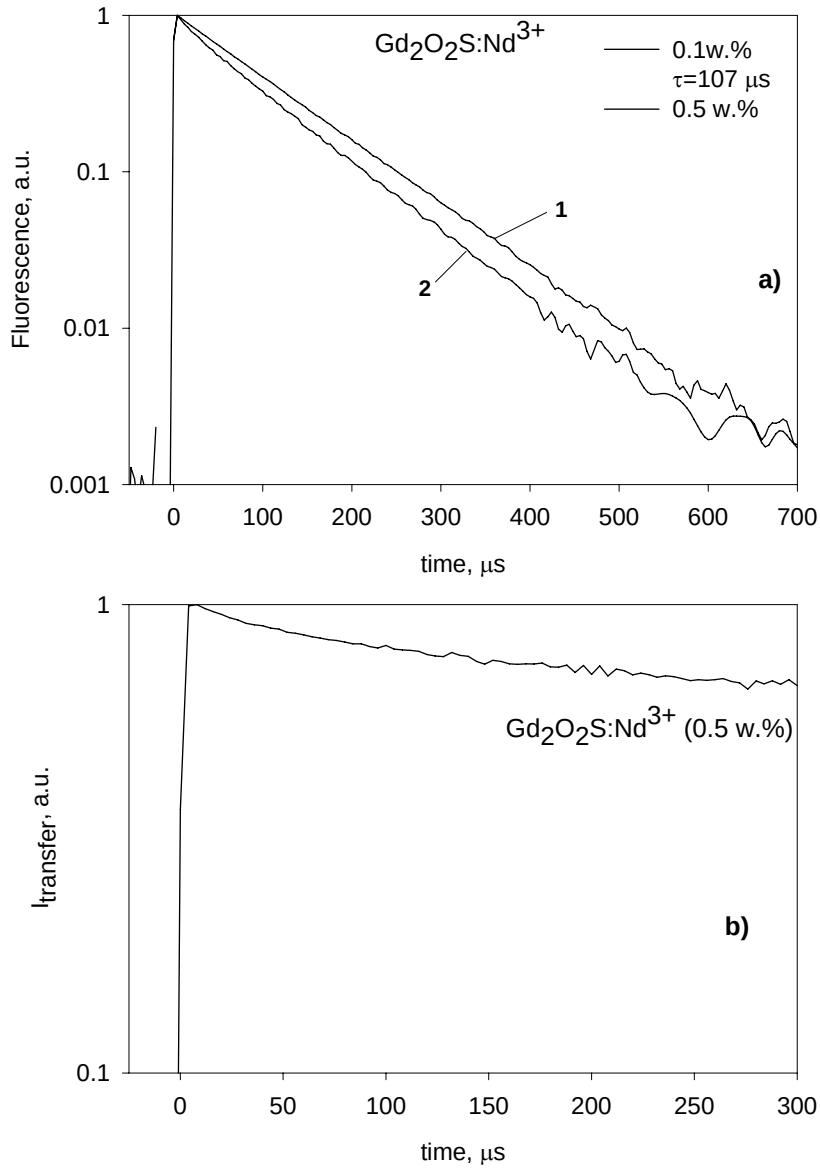

Figure 29. Fluorescence kinetics decay of the $^4F_{3/2}$ manifold of the Nd^{3+} ion in the $Gd_2O_2S:Nd^{3+}$ (0.1 wt%) (curve 1—a) and $Gd_2O_2S:Nd^{3+}$ (0.5 wt%) (curve 2—a) crystal ceramic samples measured under 893.5 nm laser excitation at 1.08 μm fluorescence detection; and the energy transfer kinetics from the same manifold of the Nd^{3+} ion in the $Gd_2O_2S:Nd^{3+}$ (0.5 wt%) ceramic sample—b.

It should be pointed out that the $^4F_{3/2}$ manifold decay times found are much shorter than those for commonly used laser crystals such as YAG:Nd^{3+} (τ=230 μs) [59] and YLF:Nd^{3+} (τ=520 μs) [60] and is comparable with the lifetime measured in the $PbCl_2:Nd^{3+}$ (τ=119 μs) [61]. The main reason for this is the high refractive index n=2.2 for the oxysulfide optical ceramics [35]. This leads to an increased radiative rate A due to higher photon density of the states and high polarizability of the surrounding medium in $Gd_2O_2S:Nd^{3+}$. For $PbCl_2:Nd^{3+}$ the refractive index n is also high (n=2.2) in comparison with YLF: Nd^{3+} (n=1.62) and YAG:Nd^{3+} (n =1.82).

At higher concentration of Nd^{3+} (0.5 wt%) the fluorescence kinetics shows nonexponential decay independent on the temperature. This can be a result of concentration quenching or presence of different types of optical centers (Figure 29a). To check these ideas time-resolved fluorescence spectra are measured using standard gated Boxcar averager (PAR 162/164) with variable time gate t_{gate} and gate delay t_d. Time-resolved fluorescent spectra measured at 77 K under 893.5 nm pulsed laser excitation at different time gates and gate delays do not show any significant changes for this sample (Figure 30). This indicates the absence of different types of optical centers in the $Gd_2O_2S:Nd^{3+}$ optical ceramics for the concentrations of Nd^{3+} up to 0.5 wt% and confirms that nonexponential fluorescence decay deals with concentration quenching. The energy transfer kinetics for the $Gd_2O_2S:Nd^{3+}$ (0.5 wt%) (Figure 29b) was obtained by subtracting the intracenter decay using the lifetime measured for the Gd_2O_2S: Nd^{3+} (0.1 wt%) ceramic sample with minimal concentration of Nd^{3+} (τ_{meas}=107.0 μs) (curve 1 in Figure 29a). The energy transfer kinetics in the $Gd_2O_2S:Nd^{3+}$ (0.5 wt%) ceramic sample can be analyzed in terms of the model of Eqs. (4), (5).

By plotting the energy transfer kinetics $-\lg(-\ln I(t))$ as a function of $\lg(t)$ for $Gd_2O_2S:Nd^{3+}$ (0.5 wt%) (Figure 31a), we can determine from the slope of this graph the exponent of the time parameter tg $\phi=3/s$ [see Eq. (4)], and to determine the s parameter. We found that tgϕ eventually tends to $\frac{1}{2}$, which corresponds to s=6 and the dipole–dipole quenching interaction between the excited and unexcited Nd^{3+} ions.

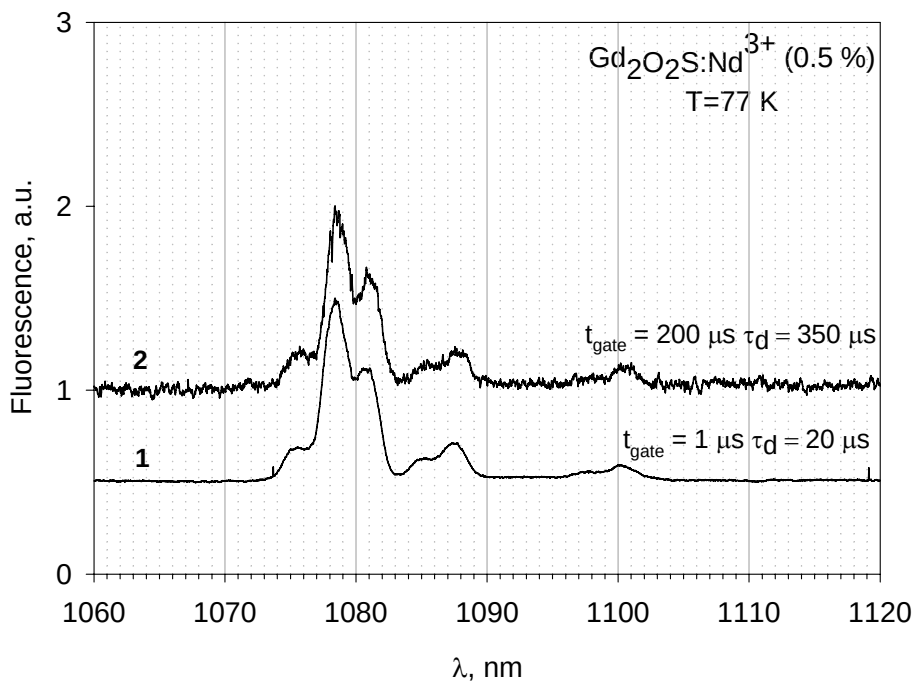

Figure 30. Time- resolved fluorescence spectra measured at the $^4F_{3/2} \rightarrow {}^4I_{11/2}$ transition of Nd^{3+} in the $Gd_2O_2S:Nd^{3+}$ (0.5 wt%) optical ceramics at 77 K under 893.5 nm pulsed laser excitation with 300 μm slits width, gate width t_{gate}=1 μs, and gate delay t_d=20 μs—1; and t_{gate}=200 μs and t_d=350 μs—2.

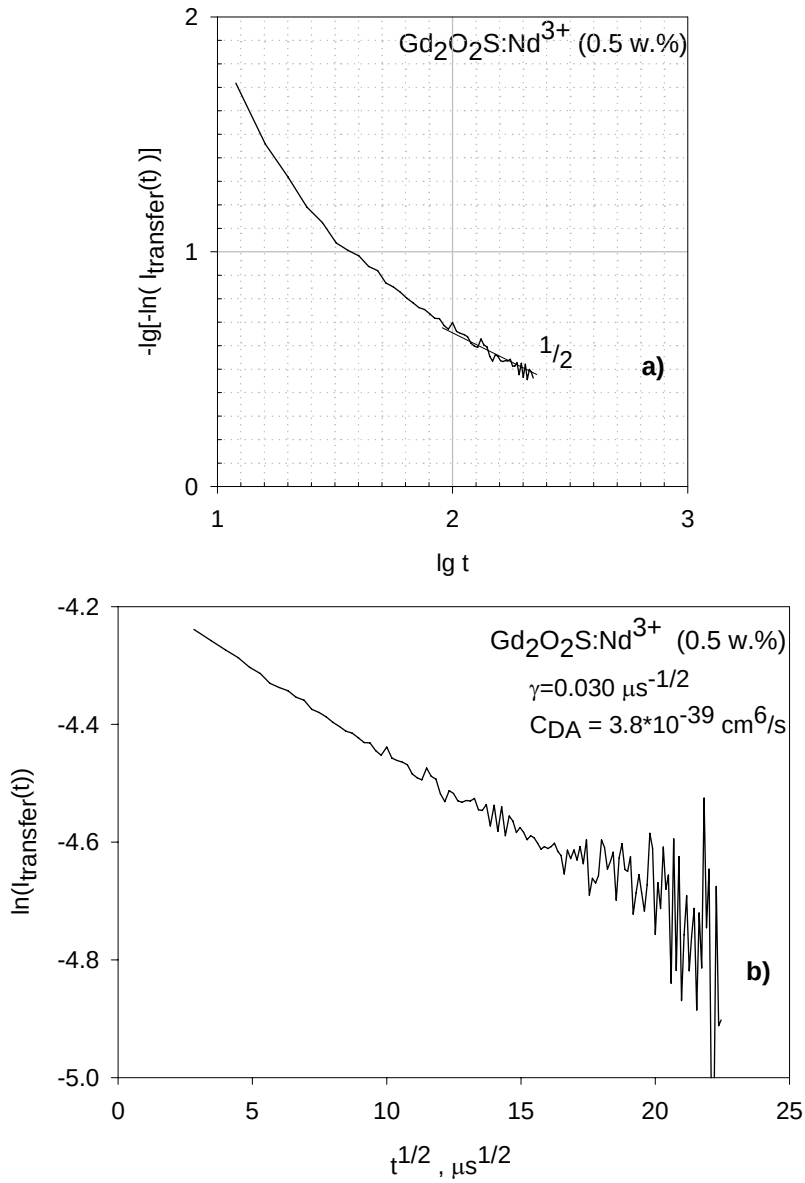

Figure 31. Nonradiative energy transfer kinetics from the $^4F_{3/2}$ manifold of the Nd^{3+} ion in the $Gd_2O_2S:Nd^{3+}$ (0.5 wt%) ceramic samples at 300 K: $-\lg[-\ln I(t)]$ as a function of lg t—a and ln $I(t)$ as a function of $t^{1/2}$—b.

The reason of it is a correlation between the dominant multipolar mechanism of energy transfer and the square of the reduced matrix elements $U^{(k)}$ of electronic transitions participating in the energy transfer [62]. All three matrix elements $U^{(2)}$, $U^{(4)}$ and $U^{(6}$ can be responsible for dipole transition in both the donor and the acceptor but for quadrupole transition only one matrix element $U^{(2)}$ matters. Only nonzero matrix element $U^{(2)}$ gives contribution to quadrupole part of energy transfer. If one analyzes the matrix elements of the transitions participated in the cross-relaxational energy transfer from the $^4F_{3/2}$ metastable level of the Nd^{3+} ion, namely, ($^4F_{3/2}\rightarrow{}^4I_{13/2}$; $^4I_{9/2}\rightarrow{}^4I_{15/2}$) and ($^4F_{3/2}\rightarrow{}^4I_{15/2}$; $^4I_{9/2}\rightarrow{}^4I_{15/2}$) he finds that

the matrix element $U^{(2)}$ for all the transitions is equal or close to zero and most contribution to the line strengths of the electronic transitions comes from $U^{(6)}$ and to a lesser extent from $U^{(4)}$.

Hence, only dipole–dipole mechanism of cross-relaxational energy transfer is allowed. The same situation occurs for the case of energy migration over the $^4F_{3/2}$ manifold of the Nd^{3+} ion where $U^{(2)}$ for the $^4F_{3/2} \rightarrow {}^4I_{9/2}$ transition is also equal to zero. The dipole–dipole nature of the above-mentioned processes were confirmed elsewhere [63]. If we use now the dependence 1n $I_{tr}(t)$ as a function of $t^{1/2}$ (Figure 31b), this graph is linearized, which proves Forster-like decay law and its slope can be used to determine the γ macroparameter (γ=0.03 $\mu s^{-1/2}$) for 0.5 wt% of the Nd^{3+} ion (N_A=1.31×10^{20} cm^{-3}) and s=6. The value of the quenching microparameter C_{DA} for the $^4F_{3/2}$ level determined from the slope of the decay curve at the disordered stage can be calculated using Eq. (5) and is equal to 3.8×10^{-39} cm^6/s. Similar analysis of fluorescence decay curves are provided for the $La_2O_2S:Nd^{3+}$ (1 wt%) (N_A=2.03×10^{20} cm^{-3}) ceramic sample. The measured fluorescence kinetics exhibits nonexponential decay at T=300 K (Figure 32a). Exponential decay at the far stage of the decay curve gives τ_{fin}=50.3 μs ($1/\tau_{meas.}$=19881 s^{-1}) and points out the presence of energy migration over the donors to acceptors, because the radiative decay time for the $La_2O_2S:Nd^{3+}$ crystal measured in Ref. [48] at zero-concentration limit is equal to τ_R=95 μs. The kinetics decay at the Forster (disordered stage) can be found by multiplying the measured curve by exp(+t/τ_{fin}) (Figure 32b), where τ_{fin} is the measured lifetime at the far stage of kinetics decay and accounts for both intracenter decay and energy migration. The same slope $(tg = \frac{1}{2})$ in terms of the coordinates [lg(−ln $I(t)$)] and [lgt] was observed (Figure 33a) and, hence, the dipole–dipole interaction was found for La_2O_2S: Nd^{3+} as well. The γ parameter was obtained from the slope of the graph presented in Figure 33b and is equal to γ=0.07 $\mu s^{-1/2}$. The obtained value of C_{DA}=2.2×10^{-39} cm^6/s in La_2O_2S: Nd^{3+} was found to be 1.8 times smaller than in $Gd_2O_2S:Nd^{3+}$.

The C_{DA} microparameter in oxysulfide ceramics was found to be rather high and to exceed by two orders of magnitude the quenching microparameter for the $^4F_{3/2}$ metastable level of the Nd^{3+} ion in the LaF_3 crystal ($\boldsymbol{C}_{DA}$=1.4×10^{-41} cm^6/s at 300 K) [63]. The reason according to Refs. [62] and [64] may be the much higher absorption and emission cross-sections of electronic transitions in oxysulfide ceramics comparing to LaF_3. The latter exhibits itself, for example, in several times higher radiative rates in the ceramics.

The boundary time between the so called ordered stage of the decay and the disordered one can be calculated from the formula [65]

$$t_{bound1} = R_{min}^{s} / C_{DA}. \quad (6)$$

In the $Gd_2O_2S:Nd^{3+}$ crystal it was found to be 744 ns for R_{min} (Nd–Nd)=3.76 Å taken from the data for Nd_2O_2S crystal [66]. The value of t_{bound1} is rather small in $Gd_2O_2S:Nd^{3+}$ because of large value of $\boldsymbol{C}_{DA}$ and small R_{min}. The latter is smaller than, for example, in $LaF_3:Nd^{3+}$ (R_{min}=4.151 Å) [63], and even smaller than in $SrF_2:Nd^{3+}$ (R_{min}=4.09 Å) [67], in $CaF_2:Nd^{3+}$ (R_{min}=3.85 Å) [67], and $CdF_2:Nd^{3+}$ (R_{min}=3.82 Å) [67]. For La_2O_2S: Nd^{3+} at T=300 K the boundary time was calculated to be t_{bound1}=1.3 μs which is approximately two times longer than in $Gd_2O_2S:Nd^{3+}$ due to 1.8 times lower value of the $\boldsymbol{C}_{DA}$ microparameter.

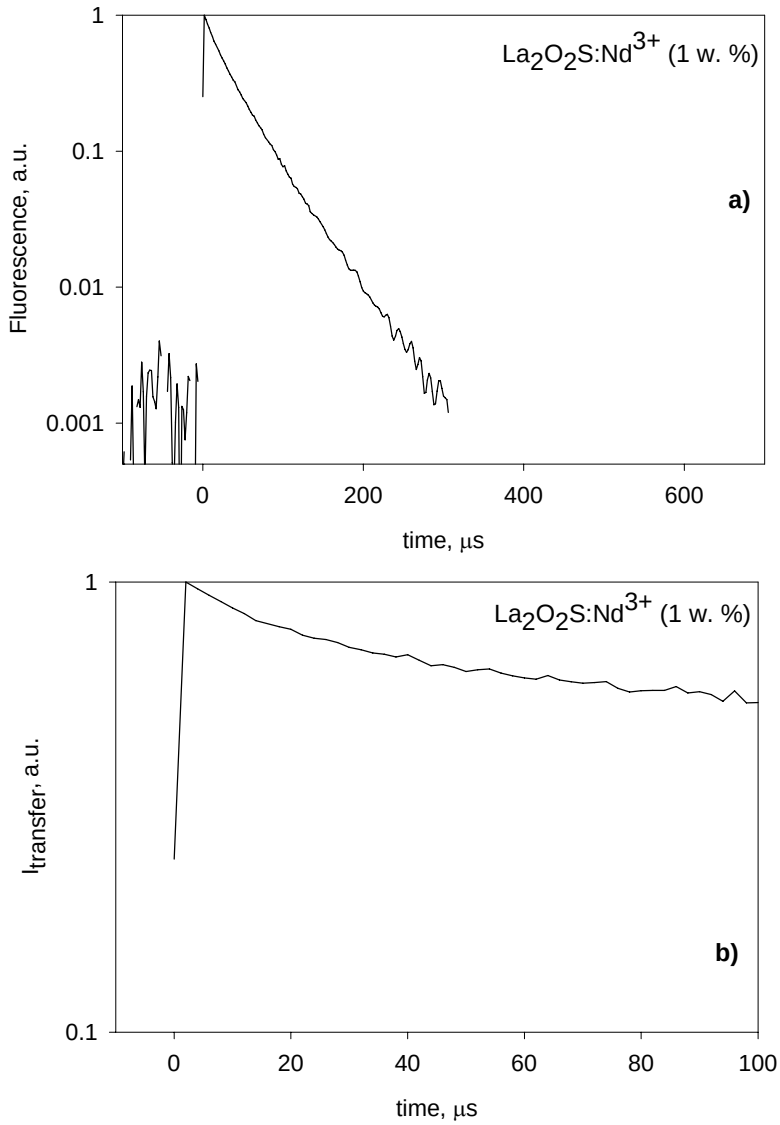

Figure 32. Fluorescence kinetics decay of the $^4F_{3/2}$ manifold of the Nd^{3+} ion in the $La_2O_2S:Nd^{3+}$ (1 wt%) ceramic sample measured under 904 nm laser excitation at 1.08 μm fluorescence detection at 300 K—a and the Forster stage of energy transfer kinetics—b.

An average rate $\bar{W}$ of energy migration can be calculated from experimental data with the following equation:

$$\bar{W} = \frac{1}{\tau_{\text{fin}}} - \frac{1}{\tau_{\text{R}}}. \tag{7}$$

Using the following equation for hopping model of energy migration:

$$\bar{W} = \pi(2/3\pi)^{5/2} C_{\text{DA}}^{1/2} C_{\text{DD}}^{1/2} n_{\text{A}} n_{\text{D}}, \tag{8}$$

the microparameter of donor–donor interaction C_{DD} is found to be 6.2×10^{-38} cm^6/s for $La_2O_2S:Nd^{3+}$ at 300 K which is about one order of magnitude higher than that in the Nd-doped glasses. The boundary time t_{bound2} between the disordered Förster stage and the migration-controlled stationary stage can be determined using the following equation:

$$\bar{W} = \gamma_F / \sqrt{t_{bound2}}. \quad (9)$$

The value of t_{bound2} was found to be 54.6 μs for $La_2O_2S:Nd^{3+}$ (1%) at T=300 K. The value of C_{DD} is found to be about 30 times larger than C_{DA} which confirms a hopping model of energy migration.

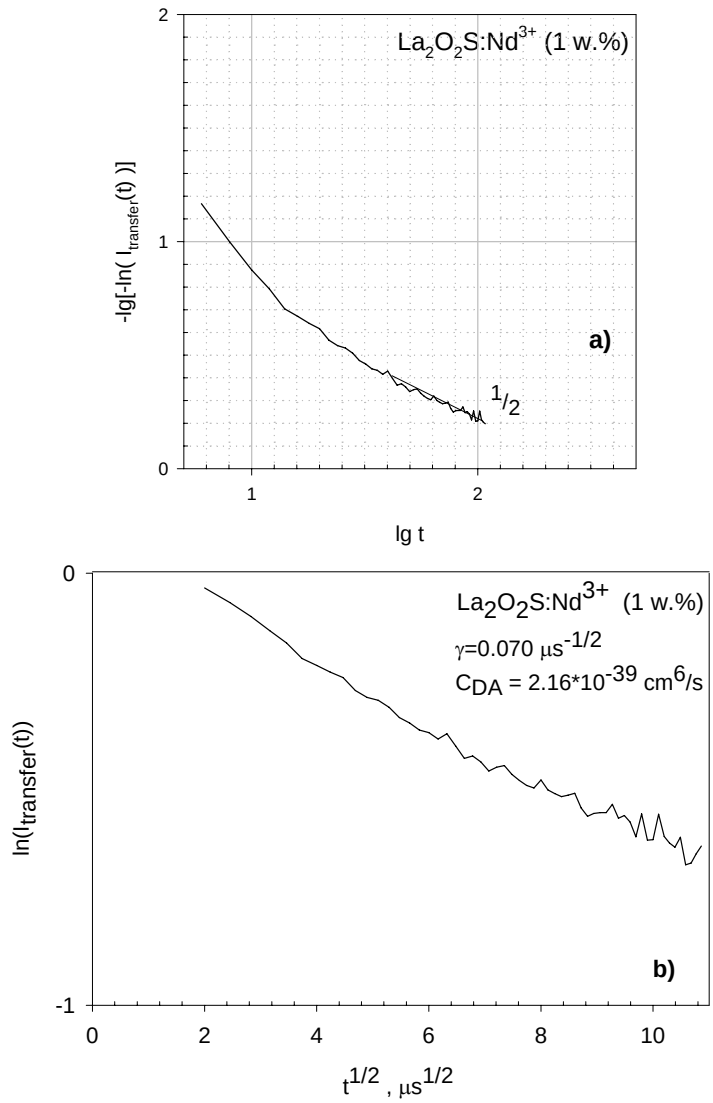

Figure 33. Nonradiative energy transfer kinetics from the $^4F_{3/2}$ manifold of the Nd^{3+} ion in the $La_2O_2S:Nd^{3+}$ (1 wt%) ceramic samples at 300 K: $-\lg[-\ln I(t)]$ as a function of lg t—a; and ln $I(t)$ as a function of $t^{1/2}$—b.

CONCLUSION

Thus, the possibility of preparation of transparent fluoride ceramics with low optical losses at the level of 10^{-2} - 10^{-3} cm^{-1} is demonstrated. Such a loss factor achieved indicates that the prepared materials are appropriate to use for the development of the photonics elements. The measurements are carried out for the ceramics at 1 μm wavelength. At this wavelength the transparency of the ceramics is much worse than that for the single crystal (optical absorption of the single crystal is lower than 10^{-4} cm^{-1}). The difference increases in passing from IR to UV range. The CaF_2 single crystal has more far absorption edge in the UV range than the optical ceramics. However, in passing from near to mid IR range the difference between the single crystal and the optical ceramics goes down and practically disappears. Elucidation of the nature of such behavior requires additional studies. Evidently, this is not concerned with the cation contamination. The results show that right now fluoride optical ceramics is a material for the near and mid IR ranges (1 – 8 μm).

Like an oxide laser ceramics the fluoride optical ceramics reveals improved mechanical properties comparing to single crystals. The fluoride ceramics keeps very important property of single crystals – high thermal conductivity that makes it attractive for high power laser systems.

The spectroscopic properties of fluoride ceramics are not differ strongly from the single crystals of similar composition.

It is demonstrated for Gd and La oxysulfide optical ceramics that in spite of anisotropy of raw materials preparation of optically transparent material by hot pressing assisted method is possible.

High emission rate A about 10^4 s^{-1} is measured for the $^4F_{3/2}$ laser level in $Gd_2O_2S:Nd^{3+}$ due to the large refractive index (n=2.2) of this oxysulfide. That is together with narrow fluorescence spectral lines provides high emission cross- section at 1.08 μm wavelength, which is one of the most IR shifted among neodymium doped laser media. Rather short depletion time of the order of hundred nanoseconds for the $^4I_{11/2}$ low laser level is estimated as well.

For the $^4F_{3/2}$ laser level in the $Gd_2O_2S:Nd^{3+}$ and $La_2O_2S:Nd^{3+}$ ceramic samples the detailed fluorescence kinetics decay measurements and analysis are provided. Analysis of the kinetics decay and concentration behavior for the $Gd_2O_2S:Nd^{3+}$ (0.1; 0.5 wt%) ceramic samples in the temperature range from T = 77 to 300 K leads to the conclusion that the transfer of energy from the $^4F_{3/2}$ excited state of the Nd^{3+} ion occurs directly to the acceptors (unexcited Nd^{3+} ions) in accordance with the dipole–dipole mechanism (s=6). A high value of the quenching microparameter C_{DA}, i.e. 3.8×10^{-39} cm^6/s, because of large emission and absorption cross-sections of electronic transitions is found. In the $La_2O_2S:Nd^{3+}$ (1 w%) ceramic sample at T=300 K together with direct energy transfer (DET) with $C_{DA}=2.2\times10^{-39}$ cm^6/s a stationary migration-controlled stage is observed starting from t_{bound2}=54.6 μs with microefficiency of donor–donor Nd–Nd interaction $C_{DD}=6.2\times10^{-38}$ cm^6/s calculated in hopping model of energy migration. It can be concluded that moderate and small concentrations of Nd^{3+} ions should be used for synthesis of effective oxysulfide transparent optical ceramics for 1 μm lasing.

ACKNOWLEDGMENTS

This work was partially support by Russian Government, Contract #02.435.11.2011 from July 15, 2005 -2006 and CRDF #RUP2-1517-MO-06.

Authors are very grateful for their help to M.Sh. Akchurin, O.K. Alimov, G.V. Anan'eva, L.S. Bolyasnikova, I.V. Khristich, O.A. Khristich, M.V. Kocherova, S.V. Kuznetsov, S.V. Lavrishchev, E.O. Orlovskaya, O.P. Ovsyannikova, O.V. Palashov, P.A. Popov, V.G. Plotnichenko, V.G. Rygikov, A.A. Sobol, V.V. Voronov, E.V. Yarotzkaya.

REFERENCES

[1] Lu, J.; Prabhu, M.; Song, J.; Li, C.; Xu, J.; Ueda, K.; Kaminskii, A.; Yagi, H.; Yanagitani, T. Optical properties and highly efficient laser oscillation of Nd:YAG ceramics. *J. of Appl. Phys*. B. 2000, 71, 469-474.

[2] Kaminskii, A.; Akchuryn, M.; Alshits, V.I., et. al. New results on investigation of physical properties of monocrystalline laser ceramic on the base of $Y_3Al_5O_{12}$. *Crystallography Reports*. 2003, 48, 515-519.

[3] Yanagitani, T.; Yagi, H.; Ishikawa, T. *Japanese Patent* 10-101333, 1998.

[4] Volynets, F.K. Methods of preparation, structure, and physico-chemical properties of optical ceramics. *Opt.-mekh. prom-st. 1973*, N 9, 48-60 (in Russian).

[5] Vydrik, G.A.; Solov'eva, T.V.; Kharitonov, F.V. Prozrachnaya keramika (Transparent ceramics). Moscow, *Energiya*, 1980, 96. (in Russian)

[6] Tonkaya tekhnicheskaya keramika (Fine technical ceramics). Ed. Yanagita, H. Moscow, *Metallurgiya*, 1986 (Russian translation from Japanease)

[7] Ryzhikov, E.N. Itogi i perspektivy razvitiya polikristallicheskikh opticheskikh materialov (Results and prospects of development of polycrystalline optical materials). *Trudy GOI*, Leningrad. 1985, P.21. (in Russian)

[8] Geguzin, Ya.E. Fizika spekaniya (Physics of sintering). Moscow*: Nauka*. 1967, 360 (in Russian).

[9] Geguzin, Ya.E. Pochemu i kak ischezaet pustota (Why and how void dissapears). Moscow: *Nauka*. 1976, 360 (in Russian).

[10] Tret'yakov Yu.D.; Lepis Kh. Khimiya i tekhnologiya tverdofaznykh materialov (Chemistry and technology of solid state materials). Moscow: *MGU.* 1985 (in Russian).

[11] German, R.M. *Sintering theory and practice*. John Wiley and Sons, INC., New York. 1996, 550.

[12] Mortier, M.; Monteville, A.; Patriarche, G.; Maze, G.; Auzel, F. New progresses in transparent rare-earth doped glass-ceramics. *Opt. Mat*. 2001, 16, 255-267.

[13] Kouznetzov, S.V.; Osiko, V.V.; Tkatchenko, E.A.; Fedorov, P.P. Inorganic nanofluorides and related nanocomposites, *Russian Chemical Rev*. (Uspekhi Khimii). 2006, 75, 1065-1082.

[14] Greskovich, C.; Chernoch, J.P. Polycrystalline ceramic lasers. *J. of Appl. Phys*. 1973, 44, 4599-4606.

[15] Greskovich, C.; Chernoch, J.P. Improved polycrystalline ceramic lasers. *J. of Appl. Phys*. 1974, 45, 4495-4502.

[16] Ikesue, A. Fabrication and optical properties of high-performance polycrystalline Nd:YAG ceramic lasers. *Opt. Mat*. 2002, 19, 183-187.

[17] Kaminskii, A.A.; Akchurin, M.Sh.; Gainutdinov, R.V.; Takaichi, K.; Shirakawa, A.; Yagi, H.; Yanagitani, T.; Ueda, K. Microhardness and Fracture Toughness of Y_2O_3- and $Y_3Al_5O_{12}$-Based Nanocrystalline Laser Ceramics. *Crystallography Reports*. 2005, 50, 869.

[18] Shirakawa, A.; Takaichi, K.; Yagi, H.; Bisson, J.-F.; Lu, J.; Musha, M.; Ueda, K.; Yanagitani, T.; Petrov, T.S.; Kaminskii, A.A. Diode-pumped mode-locked Yb^{3+}:Y_2O_3 ceramic laser. *Optics Express*. 2003, 11, 2911-2916.

[19] Hatch, S.E.; Parson, W.F.; Weagley, R.J. Hot-pressed polycrystalline CaF_2:Dy^{2+} laser. J. of Appl. Phys. Letters. 1964, 5, 153-154.

[20] Carnall, E.; Hatch, S.E.; Parson, W.F.; Weagley, R.J. *Hot pressed polycrystalline laser material*. US Patent 3,453,215. 1969.

[21] Trnovcova, V.; Hanic, F.; Smirnov, A.N.; Fedorov, P.P.; Sobolev, B.P. Superionic Fluoride Ceramic. Int. Conf. Ingineering Ceramics'92. Smolenice Castle, Czechslovakia. Oct. 19022, 1992, *Proceedings. Inst. Inorg. Chem*. Bratislava, 183-191.

[22] Sobolev, B.P.; Krivandina, E.A.; Smirnov, A.N.; Shakhova T.I.; Lyamina, O.I. *Russian Patent №153838*, 23 Oct., 1987.

[23] Chernyavskaya, E.G.; Ananieva, G.V.; Merkulaeva, T.I.; Shakhova, T.I.; Pavlova, L.N. Struktura dvukhkomponentnykh opticheskikh keramik na osnove ftoridov bariya, ittriya, gadoliniya (The structure of double component ceramics based on barium, yttrium, and gadolinium fluorides). *Neorg. Mater*. 1990, 26, 658-659 (in Russian).

[24] Ivanova, O.A.; Shakhova, T.I.; Smirnov, A.N.; Alaev, V.Ya. Strukturnaya odnorodnost' polikristallicheskikh tverdykh rastvorov (Structural homogeneity of polycrystalline solid solutions). *Optich. Zhurn*. 1993, 1, 15-18 (in Russian).

[25] Fedorov, P.P.; Osiko, V.V. Crystal growth of fluorides. In *Bulk Crystal Growth of Electronic, Optical and Optoelectronic Materials*. Ed. Capper, P. John Wiley and Sons, Ltd., 2005.

[26] Hitoshi Ishizawa. *Proceedings of the 13th International Workshop on Sol-Gel Sciences Technology*. Los Angeles. CA, 2005, 289.

[27] Grass, R.N.; Stark, W.J. Flame synthesis of calcium-, barium fluoride nanoparticles and sodium chloride. *Chem. Commun*. 2005, 1767-1769.

[28] Popov, P.A.; Dykel'skii, K.V.; Mironov, I.A.; Smirnov, A.N.; Smolyanskii, P.L.; Fedorov, P.P.; Osiko, V.V.; Basiev, T.T. Thermal conductivity of optical CaF_2 ceramics. *Doklady Physics*. 2007, 52, 7-9.

[29] Palashov, O.V.; Khazanov, E.A.; Mukhin, I.B.; Mironov, I.A.; Smirnov, A.N.; Dykel'skii, K.V.; Fedorov, P.P.; Osiko, V.V.; Basiev, T.T. Comparison of the optical parameters of a CaF_2 single crystal and optical ceramics. *Quantum Electronics*. 2007, 37, 27-28.

[30] Akchurin, M.Sh.; Gainutdinov, R.V.; Smolyanskii, P.L.; Fedorov, P.P. Anomalously high fracture toughness of polycrystalline optical fluorite from the Suran deposit (South Urals). *Doklady Physics*. 2006, 51, 10-12.

[31] Kouznetzov, S.V.; Yarotzkaya, I.V.; Fedorov, P.P.; Voronov, V.V.; Lavrishchev, S.V.; Basiev, T.T.; Osiko, V.V. Preparation of nanopowders of solid solutions $M_{1-x}R_xF_{2+x}$ (M=Ca, Sr, Ba; R=Ct, Nd, Er, Yb). *Russian J. Inorg. Chem*. 2007, 52, in press.

[32] Lan B.R., Evans A.G., Marshall D.B. Indentation damage in ceramics: the median radial crack system. *J. Amer. Ceram. Soc*. 1980, 63, 574-581.

[33] Plotnichenko V.G.; Sysoev V.K.; Firsov I.G. Analyz kalorimetricheskikh izmerenii koefficientov pogloshcheniya vysokoprozrachnyh tverdotel'nyh materialov (Analysis of calorimetric measurements of absorption coefficient of high transparent solid state materials) *Zh. Tekhnich. Fiziki*. 1981, 51, 1903-1908 (in Russian).

[34] Sulfides, Oxide Sulfides, Alkali Thiometallates. In *Gmelin's Handbook of Inorganic Chemistry*. Rare earth elements, System Number 39, C7. Sc, Y, La-Lu: Sulfides, Oxide Silfides, Alkali Thiometallates. Springer, Berlin–Heidelberg–New York–Tokyo, 1983. Founded by Leopold Gmelin, 8th Edition; 8th Edition begun under the auspices of the Deutsche Chemische Gesellschaft by R.J. Meyer Continued by E.H.E. Pietsch and A. Kotowski, and by Margot Becke-Goehring.

[35] Sobon, L.E.; Wickersheim, K.A.; Buchanan, R.A.; Alves, R.V. Growth and properties of lanthanum oxysulfide crystals. *J. of Appl. Phys.* 1971, 42, 3049 – 3052.

[36] Baughman, R.J. Growth of lanthanum oxysulfide. *Mater. Res. Bull.* 1973, 8, 1421.

[37] Fadly, M.; Ostorero, J.; Makram, H.; Michell, J.C.; Auzel, F. Single crystal growth from the fluxed melt of new neodymium doped materials for mini-laser. *XIII Rare Earth Res.* conf. London: Plenum Press. 1978, 15, 275.

[38] Amanyan, S.N.; Antonov, V.A.; Arsen'ev, P.A.; Bagdasarov, Kh.S.; Kholodny, D.S. Physico-chemical properties of lanthanum and yttrium oxosulphides activated by erbium and neodymium ions. Izv. Akad. Nauk SSSR ser. chem. *Inorganic Materials*, 1985, 21, 1726-1730.

[39] Ito, Y.; Yamada, H.; Yoshida, M.; Fujii, H.; Toda, G.; Takeuchi, H.; Tsukuda, Y. Hot isostatic pressed Gd_2O_2S:Pr, Ce, F translucent scintillator ceramics for X-ray computed tomography detectors, Japan. *J. Appl. Phys*. 1988, 27, L1371-1373.

[40] Rossner, W.; Ostertag, M.; Jermann, F. Properties and applications of gadolinium oxysulfide based ceramic scintillators. *Pros. Electrochem. Soc*. 1999, 98, 187-194.

[41] Artukh, E.P.; Ananieva, G.V.; Gorokhova, E.I.; Khristich, O.A.; Merkulaeva, T.I.; et al. Crystal lattice parameters and thermal linear expansion coefficients of doped rare-earth oxsulfides based ceramics. *J. Opt. Technol*. 1992, #9, 25-27.

[42] Gorokhova, E.I; Ananieva, G.V; Demidenko, V.A; Khristich, O.A; Merkulaeva, T.I; Savostianov, V.A. Doped rare-earth oxysulfides luminescent ceramics. *Int. Conf. on Inorganic Scintillators and Their Applications*, Moscow, Book of Abstracts, 1999, 517.

[43] Ananieva, G.V; Gorokhova, E.I; Khristich, O.A; Merkulaeva, T.I; et al., Luminescent optical ceramics based on terbium-doped yttrium oxysulfide. *J. Opt. Technol*., 1999, 66, 27-32.

[44] Gorokhova, E.I; Demidenko, V.A; Khristich, O.A; Mikhrin, S.B; and Rodnyi P.A. Luminescence properties of ceramics based on terbium-doped gadolinium oxysulfide, *J. Opt. Technol*., 2003, 70, 603-608.

[45] Gorokhova, E.I; Demidenko, V.A; Eron'ko, S.B; Khristich, O.A; Mikhrin, S.B; and Rodnyi, P.A. Spectrokinetic characteristics of the emission of Gd_2O_2S:Tb,Ce ceramics. *J. Opt. Technol*., 2005, 72, 53-57.

[46] Gorokhova, E.I; Demidenko, V.A; Mikhrin, S.B; Rodnyi, P.A; and C.W.E. van Eijk. Luminescence and scintillation properties of Gd_2O_2S:Tb,Ce. *IEEE Trans. Nuclear Science*, 2005, 52, 3129-3132.

[47] Gorokhova, E.I; Demidenko, V.A; Eron'ko, S.B; Khristich, O.A; Mikhrin, S.B; and Rodnyi P.A. Spectrokinetic characteristics of Gd_2O_2S:Pr,Ce. *J. Opt. Technol*., 2006, 73, 130-137.

[48] Alves, R.V; Buchanan, R.A; Wickershelm, K.A and E.A.C. Yates, Neodimium-activated lanthanum oxysulfide: a new high-gain laser material, *J. Appl. Phys*. 1971, V.42, p.3043 -3048.

[49] Orlovskii, Yu.V.; Basiev, T.T.; Pukhov, K.K.; Polyachenkova, M.V.; Fedorov, P.P.; Alimov, O.K.; Gorokhova, E.I.; Demidenko, V.A.; Khristich, O.A. Oxysulfide optical ceramics doped by Nd^{3+} for one micron lasing. *J. of Lumin*. 2007, 125, 201-215.

[50] Payne, S.A.; Bibeau, C. Picosecond nonradiative processes in neodymium-doped crystals and glasses: mechanism of the energy gap law. *J. of Lumin*. 1998, 79, 143-159.

[51] Antonov, V.A.; Arsen'ev, P.A.; Melnik, N.N.; Popova M.N.; Kholodny, D.S. Spektry kombinatzionnogo rasseyaniya sveta i ikh otragheniya v kristallakh La_2O_2S i Y_2O_2S (Raman spectra and reflection of the light in the La_2O_2S and Y_2O_2S crystals). *Optika i spektroskopiya*. 1987, 63, 302-306 (in Russian).

[52] Basiev, T.T.; Dergachev, A.Y.; Kirpichenkova, E.O.; Orlovskii Yu.V.; Osiko, V.V. Direct measurement of the rate of nonradiative relaxation and luminescence spectra from the $^4G_{7/2}$, $^4G_{5/2}$ + $^2G_{7/2}$, and $^4F_{9/2}$ levels of Nd^{3+} ions in LaF_3, SrF_2, and $YAlO_3$ laser crystals. *Sov. J. Quantum Electron.* 1987, 17, 1289-1291.

[53] Basiev, T.T. Selective kinetic spectroscopy of quenching and migration of optical excitation in disordered solids. *J. Phys. C7*. 1985, 46, 159-163.

[54] Alimov, O.K.; Basiev, T.T.; Ashurov, M.K.; Kirpichenkova, E.O.; Murav'ev, V.B. In *Selective laser spectroscopy of activated crystals and glasses*; Osiko V.V.; Editor, Proceedings of GPI—9 Chapter II; Nova Science Publishers: New York, NY, 1990.

[55] Forster, T. Experimentelle und theoretische Untersuchung des zwischenmolekularen Ubergangs von Electronenanregungsenergie. Z. Naturforschg. 1949, A4, 321-327.

[56] Sveshnikov, B.Y.; Shirokov, V.I. O zavisimosti izmeneniya srednei dlitelnosti i vykhoda lyuminestzentzii v protzesse tusheniya ot zakona vzaimodeistviya molecul (About the dependence of the changes of average duration and luminescence quantum yield for the process of quenching on the law of the molecule interaction).Optika i spectroskopiya. 1962, 12, 576-581 (in Russian).; Ynokuti, M.; Hirayama, F. Influence of energy transfer by the exchange mechanism on donor luminescence. *J. Chem. Phys*. 1965, 46, 1978-1989.

[57] Golubov, S.I.; Konobeev, D.V. About the procedure of resonance energy transfer of electronic excitation. *Sov. Phys. Solid State*. 1971, 13, 2679-2683.

[58] Basiev, T.T.; Orlovskii, Yu.V. Nonradiative energy transfer from high-lying highly-quenched multiplets of Nd^{3+} in the LaF_3 laser crystal. *Sov. Phys. JETP* 1989, 69, 1109-1118.

[59] Koechner, W. In *Solid-State Laser Engineering; fifth revised and updated edition*; Springer: Berlin, 73.

[60] Harmer, A.L.; Lintz, A.; Gabbe, D.R. Fluorescence of Nd^{3+} in lithium yttrium fluoride. *J. Phys. Chem. Solids*. 1969, 30, 1483-1491.

[61] Orlovskii, Yu.V.; Basiev, T.T.; Pukhov, K.K.; Alimov, O.K.; Doroshenko, M.E.; Polyachenkova, M.V.; Dmitruk, L.N.; Osiko, V.V.; Badikov, D.V.; Badikov, V.V.; Mirov, S.B. Mid- IR transitions of trivalent neodymium in low phonon laser crystals. *Opt. Mater*. 2007, 29, 1115 – 1128.

[62] Basiev, T.T.; Orlovskii, Yu.V.; Privis, Y.S. High -order multipole interaction in nanosecond Nd-Nd energy transfer. *J. of Lumin*. 1996, 69, 187-202.

[63] Voronko, Yu.K.; Mamedov, T.G.; Osiko, V.V., et. al. Investigation of the nature of nonradiative energy relaxation in condensed media with a high activator concentration. *Sov. Phys. JETP*. 1976, 71, 478-496.

[64] Dexter, D.L. A theory of sensitized luminescence in Solids. *J. Chem. Phys*. 1953, 21, 836-850.

[65] Sakun, V.P. Kinetics of the energy transfer in crystals. *Sov. Phys. Solid State*. 1972, 14, 1906-1917.

[66] Lissner, F.; Schleid, T. Crystal structure refinement of di-neodimium (III) di-Oxide mono-Sulfide, Nd_2O_2S. *Z. Kristallogr*. 205 (1993), 117-118.

[67] Basiev, T.T.; Orlovskii, Yu.V.; Papashvili, A.G.; Doroshenko, M.E.; Pelle, F.; Heber, J. Dynamic splitting of high- lying excited state of cluster centers in the Nd^{3+} doped crystals with fluorite structure. *J. of Lumin.* 2001, 94-95, 123-126.

In: Developments in Ceramic Materials Research
Editor: Dena Rosslere, pp. 97-140
ISBN 978-1-60021-770-8

Chapter 4

SYNTHESIS, SPECTROSCOPIC AND MAGNETIC STUDIES OF THE $M(PO_3)_3$ (M^{III}= TRANSITION METAL IONS) METAPHOSPHATES

José M. Rojo, José L. Mesa and Teófilo Rojo*

Dpto. de Química Inorgánica, F. Ciencia y Tecnología,
Universidad del País Vasco/EHU,
Apdo. 644, E-48080 Bilbao, Spain

ABSTRACT

The solid state chemistry of polyphosphates in which the transition metal exhibits a trivalent oxidation state is traditionally considered unusual. The great ability of the phosphate frameworks to stabilize this oxidation state is produced for the relatively high charge in $(PO_4)^{3-}$ tetrahedra that favors the formation of anionic frameworks with high degree of mechanical, chemical, and thermal stability. The literature about this kind of compounds shows the existence of several polymorphic forms of these phases which crystal structure has been solved. Unfortunately, even if good crystals for X-ray structure determination were obtained, pure phases had not been prepared. This fact has precluded carrying out any study on the physical properties of these materials. A method based on the control of M/P ratio in the reaction medium has allowed us the synthesis of pure phases. On this basis, the $M(PO_3)_3$ metaphosphates (M^{III}= Ti, V, Cr, Mo and Fe) have been synthesized starting from a mixture of the metallic oxides and $(NH_4)_2HPO_4$, with different M:P ratios by using the ceramic method.

These phases exhibit a crystal structure constructed from (MO_6) octahedra linked through infinite $(PO_3)_\infty$ chains of (PO_4) tetrahedra to give rise to compact three-dimensional crystal structures. The IR spectra of these phases show the characteristic bands of the methaphosphates with ring or chain structure. The absorption electronic spectroscopy recordered by the diffuse reflectance method shows the presence of the spin allowed transitions, being calculated the values of the splitting parameter of the crystalline field (Dq), as well as, these ones of the Racah parameters (B and C). The ESR spectra of these compounds exhibit isotropic signals, centered at values of the *g*-

* Corresponding author: e-mail: teo.rojo@.ehu.es; Phone: +34-946012458; Fax: +34-946013500 (T. Rojo)

giromagnetic tensor that depends of the nature of the metal and of its S-number of spin. The magnetic study indicates the existence of antiferromagnetic interactions in the majority of the compounds, being detected for several metaphosphates a weak ferromagnetic spin canting phenomenon at low temperatures. In the case of the Ti(III) a ferromagnetic behavior has been observed. The values of the J-exchanger parameter have been calculated using the Rushbrooke and Wood equations for 3D-antiferromagnetic lattices with different values of the spin. In some case, the D-zero field splitting parameter has been calculated from the simultaneously combination of the ESR and susceptibility measurements. The neutron powder diffraction study of the $M(PO_3)_3$ (M^{III}= Cr, Mo and Fe) metaphosphates shows antiferromagnetic structures.

1. INTRODUCTION

The study of phosphates of transition elements with low oxidation states has received great interest in recent years. These compounds exhibit interesting properties such as magnetic, heterogeneous catalysis, ionic exchange, etc., with potential applications [1,2]. In this way, the $M(PO_3)_3$ materials are interesting owing to the activity of Cr-containing aluminophosphates (CrAPO-5 materials) which are well known for their catalytic performance [3, 4].

The $M(PO_3)_3$ (M= Al, Sc, Ti, V, Mo, Rh, Ru,…) metaphosphates are the most condensed phosphate systems in which the metal ions present unusual oxidation states [5-10]. We are centering this work on the M^{III}= Ti, V, Cr, Mo and Fe, metallic cations, which exhibit some of them an unusual +III reduced oxidation state in their metaphosphate compounds. In the molybdenum and vanadium metaphosphates only one crystalline phase, the monoclinic C-type [$M(PO_3)_3$] structure, has been isolated and the structures have recently been reported [9,10]. However, six different polymorph phases denoted A, B, C, D, E and F have been described in chromium and iron metaphosphates [11,12] but, to our knowledge, the crystal structures of only two phases (B and C) are known [13-15]. One of them adopts the C-type [$Cr(PO_3)_3$] structure and is characterized by one-dimensional infinite metaphosphate $(PO_3)_\infty$ chains and isolated (CrO_6) octahedra. The superstructure found in single crystals X-ray investigations for this $Cr(PO_3)_3$ structure type, in which the monoclinic *y* axis is tripled, could be the responsible of the three crystallographic different (CrO_6) octahedral units of almost ideal geometry [13]. The reason for this subcell effect is not immediately apparent in this complex structure and could be necessary to perform an analysis of the symmetry in order to elucidate any translational pseudosymmetry that may occur *via* concerted polyhedral rotation [7]. The crystal structure for the other chromium phase, B-type [$Cr(PO_3)_3$], namely the hexametaphosphate $Cr_2(P_6O_{18})$, is formed by (CrO_6) octahedra linked through (PO_4) tetrahedra belonging to $(P_6O_{18})^{6-}$ cycles.

Taking into account the structural features of these compounds and the nature of the metallic cations, their magnetic properties are expected to be very interesting. In this way, the magnetic study of these compounds reveals different types of magnetic exchange interactions, which range from antiferromagnetic to ferromagnetic for the chromium, molybdenum or iron phases and the titanium compound, respectively. In the vanadium metaphosphate, the magnetic behavior is determined by both the antiferromagnetic interactions and the zero-field splitting parameter characteristic of this cation. To understand the magnetic structures in the

ordered phases of some of these compounds, neutron diffraction measurements have been carried out.

2. SYNTHESIS

The $M(PO_3)_3$ metaphoshates were synthesized using the ceramic method. The starting reagents were the salt or oxide of the metallic cation in its oxidation state of +3. The phosphorous element was incorporated to the composition of the corresponding metaphosphate in the form of $(NH_4)_2H(PO_4)$, with a M:P ratio, depending on the kind of metaphosphate prepared.

The synthesis of the $M(PO_3)_3$ metaphosphates with M^{III}= V, Cr, Mo and Fe, was carried out using the ratio M:P of 1:10. This mixture reaction was heated, under air, in an alumnina crucible at 800 °C, after of a previously heating in the, approximately, 300-400 °C range, in order to decompose the $(NH_4)_2H(PO_4)$ reagent. Exceptionally, the $Cr_2(P_6O_{18})$ phase was obtained using the same conditions but with a Cr:P ratio of 1:5. All the resulting phases exhibit green color [16-18].

Attempts to prepare the $Ti(PO_3)_3$ compound by reduction of TiO_2 oxide with an excess of the $(NH_4)_2H(PO_4)$ were unsucceful. This fact can be attributed to the instability of the Ti(III) cation in air. So, the experimental synthetic method was modified, using as starting reagents metallic titanium and an excess of $(NH_4)_2H(PO_4)$. A flux of nitrogen was maintained during the reaction time in order to avoid the oxidation to Ti(IV). The resulting product shows blue color [19].

3. PHYSICOCHEMICAL CHARACTERIZATION TECHNIQUES

IR spectra (KBr pellets) were obtained with a Nicolet FT-IR 740 spectrophotometer. Diffuse reflectance spectra were registered at room temperature on a Cary 5000 spectrophotometer, in the range 8000–50000 cm^{-1}. Mössbauer spectroscopy measurements were performed in the transmission geometry using a ^{57}Co-Rh source in the constant acceleration method. Mössbauer spectra at different temperatures were recordered using a bath cryostat. The velocity was calibrated using α Fe foil. The spectra were fitted using the NORMOS program. The isomer shifts are quoted relative to α-Fe at 300 K. A Bruker ESP 300 spectrometer, operating at X and Q-bands, was used to record the ESR polycrystalline spectra between 4.2 and 300 K. The temperature was stabilized by an Oxford Instrument (ITC 4) regulator. The magnetic field was measured with a Bruker BNM 200 gaussmeter and the frequency inside the cavity was determined using a Hewlet-Packard 5352B microwave frequency counter. Magnetic measurements were performed on polycristalline samples between 1.8 and 300 K, using a Quantum Design SQUID magnetometer (MPMS-7) with a magnetic field of 0.1 T, at which the magnetization *vs.* magnetic field is linear even at 1.8 K. About 5 g of the $M(PO_3)_3$ (M^{III}= Cr, Mo and Fe) were employed in the neutron diffraction experiments, contained in a cylindrical vanadium container and held in a liquid helium cryostat. The high resolution of D2B was used to obtain extensive and accurate structural data for both phases at room temperature over the angular range $0 \leq 2\theta \leq 160°$. For the iron

metaphosphate wavelengths of 2.41 Å (D2B) at 2 K were used in order to obtain a better resolution of the magnetic data at lower angles. D1B has a 400 element linear multidetector covering an angular range of 80 °. High flux and medium resolution of D1B at 2.52 Å were used to study the thermal evolution of $Fe(PO_3)_3$ in the temperature range 1.5 – 20 K to resolve the magnetic contributions of the neutron patterns. The magnetic and nuclear structures were refined simultaneously, taking as starting parameter of each pattern those resulting from the refinement of the preceding one. A pseudo-Voigth function was chosen to generate the line shape of the diffraction peaks.

4. RESULTS AND DISSCUSION

4.1. Nuclear Crystal Structure Description

The $M(PO_3)_3$ (M= Ti, V, Cr, Mo and Fe) metaphosphates are the most condensed phosphate systems where the metal ions present the unusual +3 oxidation state [5-10]. For these compounds, the crystal structure may be described as formed by isolated (MO_6) octahedra linked through $(PO_3)_\infty$ chains of (PO_4) tetrahedra (see Figure 1a). Each (MO_6) group is bridged to six neighbouring (MO_6) octaedra by phosphate groups and each octahedron shares it six apices with different (PO_4) tetrahedra. These tetrahedra lie in adjacent layers and lead to a three-dimensional network, in which the metallic cations occupy three different crystallographic positions for every metallic center.

The crystal structure for the other chromium phase, namely the hexametaphosphate, is formed by (CrO_6) octahedra linked through (PO_4) tetrahedra belonging to $(P_6O_{18})^{6-}$ cycles (see Figure 1b). The (CrO_6) coordination polyhedra are not vertex- or edge-shared, and are isolated by (PO_4) tetrahedra. Each (CrO_6) octahedron interacts with four $(P_6O_{18})^{6-}$ cycles, three phosphorous atoms lie in the plane defined by the Cr(III) ions and the other three are place below and above of the metallic cations in a perpendicular plane, leading to a three-dimensional network [14].

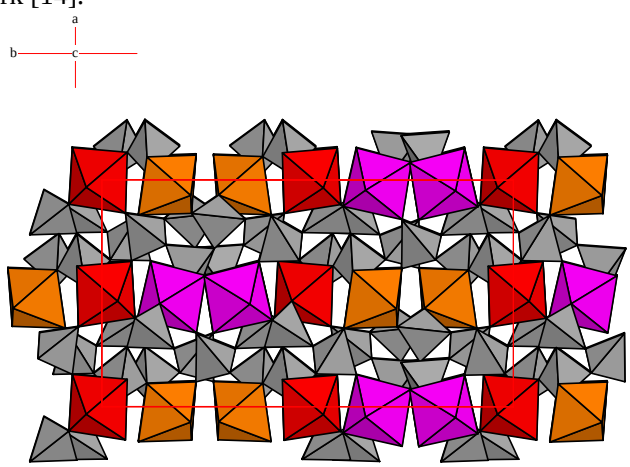

Figure 1 (Continued).

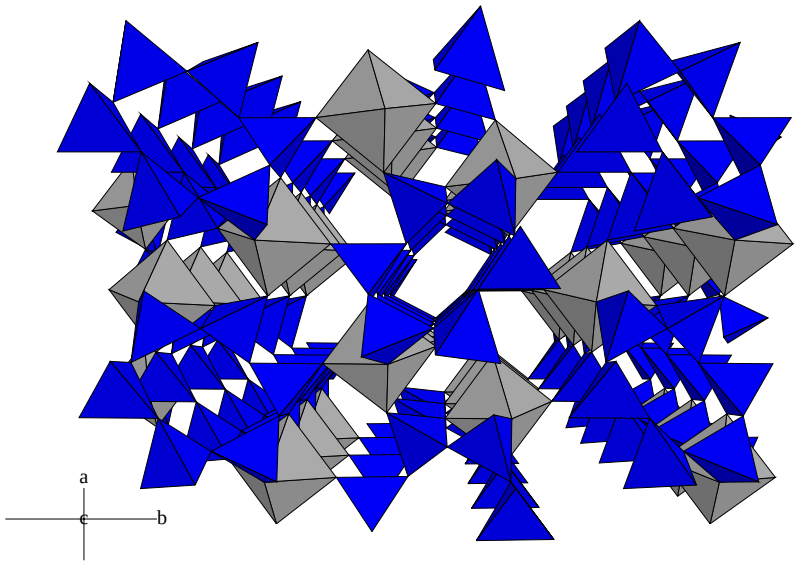

Figure 1. Crystal structure of (a) $M(PO_3)_3$ (M= Ti, V, Cr, Mo and Fe) and (b) $Cr_2(P_6O_{18})$.

4.2. IR Spectroscopy

Different kinds of phosphates with a definite structural type (orto, pyro, chaing o ring structure) can be identified by IR spectroscopy [20,21]. Metaphosphate phases are classified in two large families of chain o ring structures. For these condensed phosphates an approximation may be needed due to the existence of two types of P-O bonds: for an "external" oxygen, the $P\text{-}O_{ext}$ distance is shorter (and the stretching frequency accordingly higher) than for an "internal" (or bridging) oxygen whitin the P-O-P chaing o ring. Moreover, in short chain polyphosphates a further splitting takes place owing the existence of PO_2 and PO_3 groups in the oxoanions. The common features that exhibit all of metaphosphates are the existence in the PO_2 groups of $P\text{-}O_{ext}$ distances shorter than those observed in the PO_3 and PO_4 groups of diphosphate and phosphate compounds, respectively [21,22].

In Table 1 the most important bands of the metaphosphates studied in this work are given, together with their empirical assignments. In all cases can be observed the most characterized feature of a metaphosphate (whatever its chain or ring structure) the existence of one or several and strong IR bands at frequencies higher than 1200 cm^{-1}.

4.3. UV-VIS Spectroscopy

The most important bands obtained for the $M(PO_3)_3$ (M^{III}= Ti, V, Cr, Mo and Fe) metaphosphates from the absorption electronic spectra, collected by the diffuse reflectance method, are listed in Table 2.

Table 1. Selected IR bands (cm^{-1}) and empirical assignments for the $M(PO_3)_3$ (M^{III}= Ti, V, Cr, Mo and Fe) metaphosphates between 400 and 1500 cm^{-1}

Assignment	*Ti*	*V*	*Cr*	*Mo*	*Fe*
$\nu_{as}(P\text{-}O_{ext})\|PO_2\|$	1385 vs	1240 vs	1240 vs	1250 vs	1230 vs
	1115 s	1150 s	1160 s		
			1130 s	1125 s	1120 s
$\nu_s(P\text{-}O_{ext})\|PO_2\|$	1090 s	1095 s	1095 vs	1085 s	1075 s
	1040 s		1050 s		
		1200 s	1020 s	1025 s	1020 s
				1010 s	
$\nu_{as}(P\text{-}O_{int})\|P\text{-}O\text{-}P\|$	960 s	975 s	975 s	955 s	970 s
	770 m	770 m	775 m	775 m	
	750 m	765m	760 w		750 m
$\nu_s(P\text{-}O_{int})\|P\text{-}O\text{-}P\|$	715 m	715 m		745 m	
			725 m		
				705 m	705 m
	690 w	685 m	685 w	675 m	675 m
$\nu_{as}(M\text{-}O)$				610 w	615 w
			570 m		580 w
	560 m	560 m	560 m		
$\delta_{as}(O\text{-}P\text{-}O)$				545 m	545 m
			520 m		
		510 m		500 s	505 m
			490 m		
	470 m	480 m		470 m	470 m

vs, very strong; s, strong; m, medium; w, weak.

Table 2. Diffuse reflectance data of $M(PO_3)_3$ (M^{III}= Cr 1, Mo 3 and $Cr_2(P_6O_{18})$ 2

		Cr **1**		Mo **3**		Cr **2**	
		E (cm^{-1})	E/B	E (cm^{-1})	E/B	E (cm^{-1})	E /B
$^4A_{2g}$	$^4T_{2g}(F)$	16000	22.1	23000	50.3	15800	25.5
$^4A_{2g}$	$^4T_{1g}(F)$	22500	34.6	28100	61.5	22000	35.5
$^4A_{2g}$	^2E_g	14700	20.3	10200	22.3	14600	23.5
$^4A_{2g}$	$^2T_{1g}$	15400	21.3	10600	23.2	15300	24.5
$^4A_{2g}$	$^2T_{2g}$	21300	29.4	16000	35.0	21800	35.0
Dq (cm^{-1})		1600		2300		1580	
B (cm^{-1})		650		457		620	
C (cm^{-1})		3390		2180		3412	
% reduction		71		75		68	

The diffuse reflectance spectrum of $Ti(PO_3)_3$ exhibits a strong band centered at 17300 cm^{-1} which corresponds to the spin allowed transition $^2E_g \rightarrow {}^2T_{2g}$ in an octahedral symmetry and can be associated with the ligand-field splitting parameter 10 Dq. A shoulder can be observed at 14800 cm^{-1} which is attributed to the Jahn-Teller splitting of the excited ^2E_g state.

The diffuse reflectance spectrum of $V(PO_3)_3$ shows two absorptions centered at 24400 and 33600, which are assigned to the spin allowed transitions $^3T_{1g}(F) \rightarrow {}^3T_{2g}(F)$ and $^3T_{1g}(P)$, respectively. Moreover, there is a weak signal about 10200 cm^{-1} which corresponds to the spin forbidden transition $^3T_{1g}(F) \rightarrow {}^1E_g, {}^1T_{2g}$. Using a simple crystal field approximate model for an octahedral d^2 system the Dq and Rach (B and C) parameters were calculated as Dq= 1610 cm^{-1}, B= 665 cm^{-1} and C= 1863 cm^{-1}.The values obtained are in good agreement with those given in the literate for this kind of compounds [23-25].

For chromium compounds, $Cr(PO_3)_3$ (1) and $Cr_2(P_6O_{18})$ (2), two strong absorptions were observed at 16000, 22500 and 15800, 22000 cm^{-1} for (1) and (2), respectively. The bands corresponding to the $Mo(PO_3)_3$ (3) were observed at 23000 and 28100 cm^{-1}. These results are in good agreement with those observed for the Cr(III) and Mo(III) in octahedral geometry [23,26-29]. Using a simple crystal field approximate model, the ligand-field splitting parameter 10 Dq and the Racah parameter B may be calculated from the energies of the two lowest spin allowed transitions. For (1) we are find Dq= 1600 cm^{-1} and B= 690 cm^{-1} and for (3) Dq= 2300 cm^{-1} and B= 475 cm^{-1}. The values obtained for compound (2) are 1580 and 620 cm^{-1} for the Dq and B parameters, respectively. The B values for (1)-(3) are approximately 70% of those corresponding to the free ions (918 and 610 cm^{-1} for the chromium and molybdenum, respectively). This fact implies a significant degree of covalence in the M-O-M (M= Cr and Mo) bonds.

The weak absorptions observed at 14700, 15400 and 14600, 15300 for (1) and (2), respectively and 10200 and 10600 for phase (3) may be assigned to the spin forbidden transitions $^4A_{2g} \rightarrow {}^2E_g\ {}^2T_{1g}$ considering the ratios Dq/B of 2.46 and 2.55 and 5.03 for the chromium and molybdenum compounds. The signals of lower energy can be attributed to the transition $^4A_{2g} \rightarrow {}^2E_g$ given in the diagram levels of Figure 2. The values of the C parameters obtained from the forbidden transition are 3390, 3412 and 2180 cm^{-1}, respectively. Finally, the weak absorptions observed at 21300, 21800 and 16000 cm^{-1} for compounds (1), (2) and (3), respectively, may be assigned to the spin forbidden transition $^4A_{2g} \rightarrow {}^2T_{2g}$. In the case of the molybdenum metaphosphate this band appears at lower frequency than that observed for the spin-allowed transition $^4A_{2g} \rightarrow {}^2T_{2g}(F)$ as expected following the energy levels of these compounds (Figure 2).

The diffuse reflectance data show that both allowed and forbidden transitions have higher E/B ratios in the molybdenum metaphosphate than in the chromium phases. This fact is due to the different positions of these metallic ions in the transition series (Table 2). Besides, the value of the Racah parameter B is higher in the chromium compounds than in the molybdenum phase, but the percentage of reduction of the B parameter ($\cong$ 70%) is indicative of a similar degree of covalence in the M-O (M= Cr, Mo) bonds, in these compounds.

In the diffuse reflectance spectrum of $Fe(PO_3)_3$ very weak characteristic bands belonging to Fe^{3+} are present. These bands correspond to the forbidden transitions of a d^5 high spin configuration cation from the ground level $^6A_{1g}(^6S)$ to the excited $^4T_{1g}(^4G)$, $^4T_{2g}(^4G)$, $^4A_{1g}(^4G)$, $^4E_g(^4G)$ and $^4T_{2g}(^4D)$ levels. The low intensity of the bands makes difficult the assignation of their maxima and, so, to calculate both the Dq and Racah (B and C) parameters.

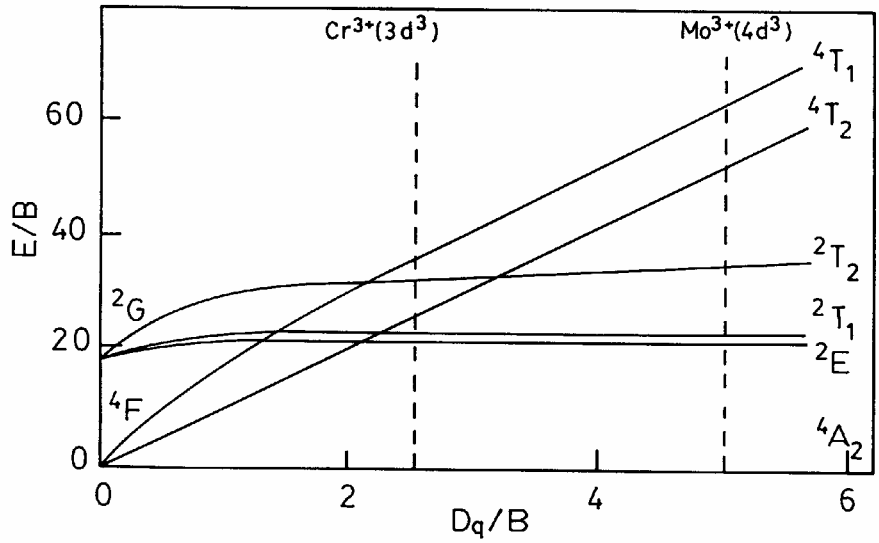

Figure 2. Energy-level diagram for the d^3 configuration in an octahedral field.

4.4. Mössbauer Spectroscopy

The Mössbauer spectra of $Fe(PO_3)_3$ metaphosphate were collected at temperatures of 300, 77 and 4.2 K (Figure 3).

At room temperature the spectrum shows one doublet paramagnetic quadrupolar that is characteristic of high spin, d^5, Fe(III) in octahedral geometry [30]. The spectrum was fitted using the NORMOS program [31] employing three doublets. One of them for every iron(III) crystallographic independent, with equal isomer shift and quadrupolar splitting. The values of the isomer shift and quadrupolar splitting are in good agreement with those found in others iron(III) phophates, $NaFe(P_2O_7)$ and $Na_3Fe_2(PO_4)_3$ [32,33]. The spectrum collected at 77 K also shows a doublet quadrupolar that was also fitted with three doublets characteristic of the three iron(III) crystallographic independents. In comparison with the spectrum at room temperature this later exhibits larger values of the isomer shift and line-width a medium high. Finally, the spectrum at 4 K shows a sextet characteristic of the existence of an ordering of this phase at low temperature. The value of the isomer shift is 0.57 mm/s, being in the range of these ones observed for iron(III) compounds [34].The spectrum at 4 K was fitted with three magnetic sextuplets, being the line-width of 0.50 mm/s. This result is in good agreement with the structural data. The values at 4 K of the electronic perturbation are negatives. This result indicates the existence in the neighbouring of the Fe(III) nuclei of electric charge with slightly asymmetrical distribution. The magnetic interaction in this phase takes place through Fe(III) cations, which generate in the ordered state, 4K, approximately, hyperfine fields of <H>= 48.6, 50.90 and 52.3 T, under every iron(III) nuclei, respectively.

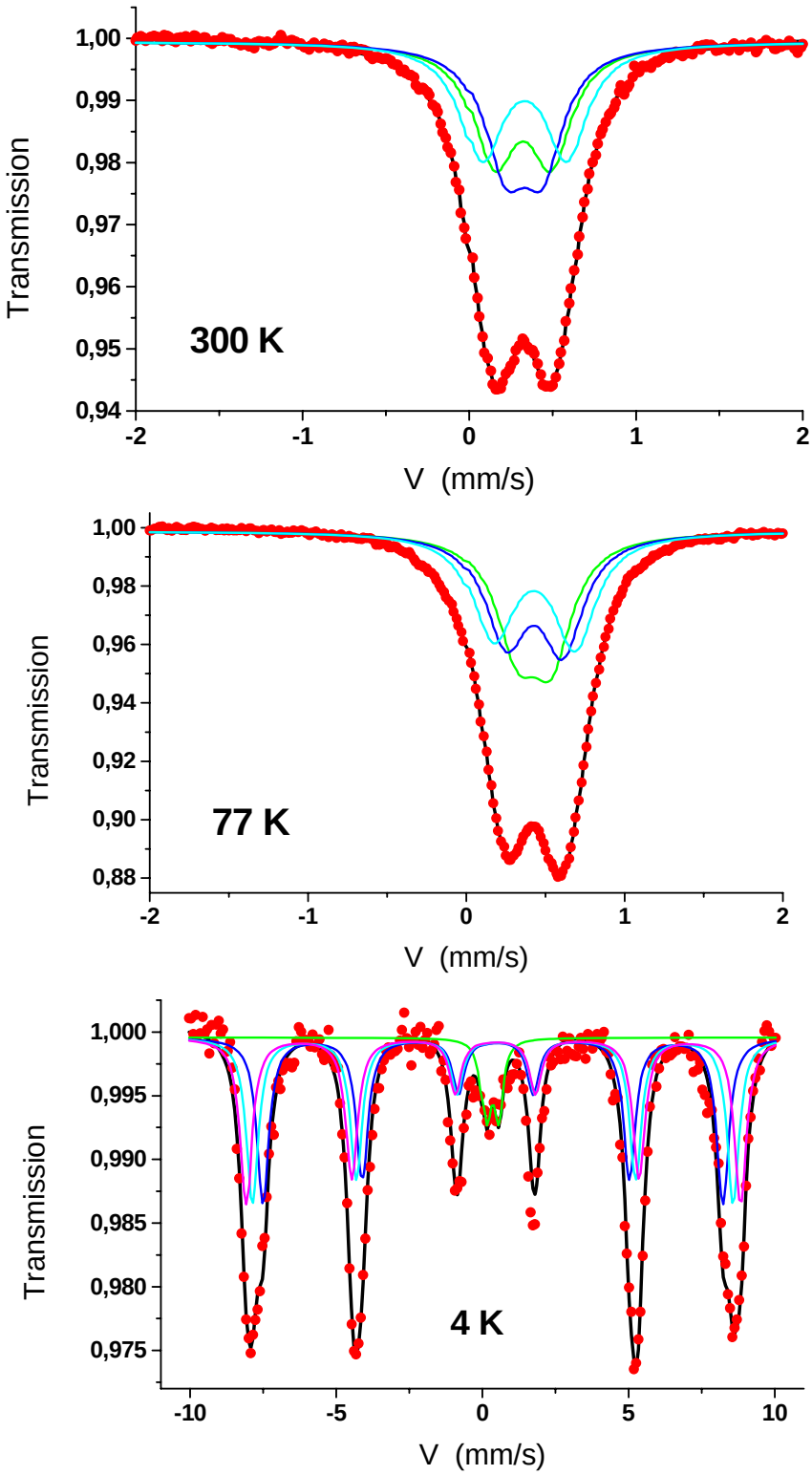

Figure 3. Mössbauer spectra of $Fe(PO_3)_3$ at 300, 77 and 4.2 K.

5. ESR BEHAVIOR

5.1. ESR of $Ti(PO_3)_3$

ESR spectra at 9.4 GHz were obtained in powder samples of $Ti(PO_3)_3$ and in samples of $Sc(PO_3)_3$ doped with 0.1% Ti^{3+} at temperatures between 4.2 and 100 K (see Figure 4). The Ti^{3+} shows a nearly Lorentizian resonance centered at g= 1.77 of about 500 Gauss at 4.2 K [see Figure 4a]. This resonance broadens with increasing temperature above 50 K. It losses intensity and disappears at 100 K. The Ti^{+3} doped sample [see Figure 4b] have a linewidth of about 400 Gauss at 4.2 K, which reduces with increasing temperature. The lineshape reflects the powder character of the sample and changes with temperature. The g-factor values corresponding to the peaks of the signal at 4 K are g=1.67 and 1.88 [see Figure 4b], the signal rapidly losses intensity above 50 K.

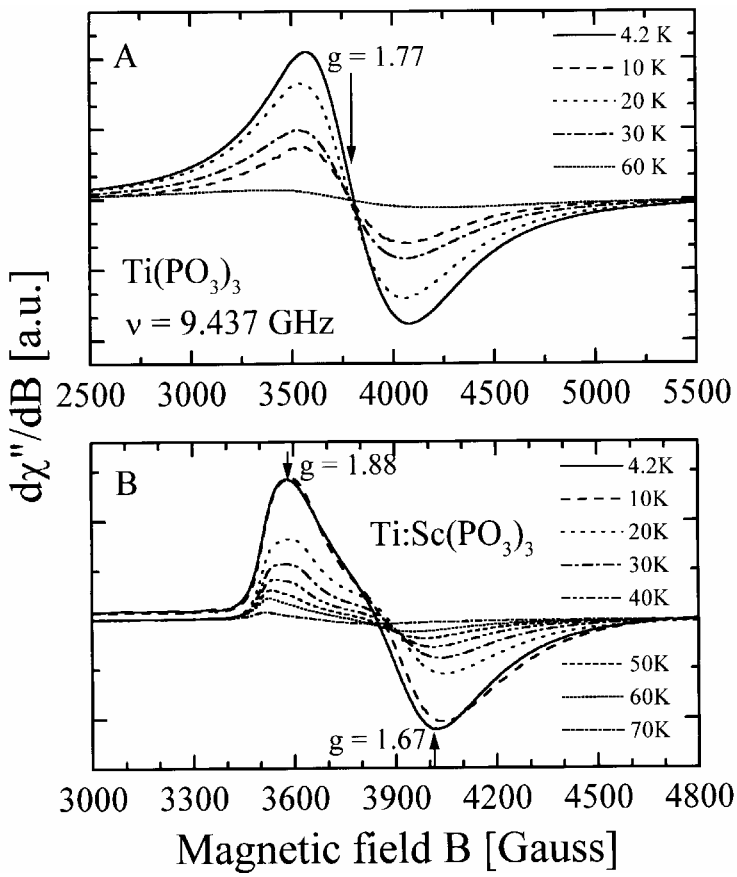

Figure 4. ESR spectra of (A) Ti(PO3)3 and (B) Sc(PO3)3, doped with 0.1% Ti3+ at several temperatures.

A detailed analysis of the ESR results is hampered by the presence of three Ti(III) sites and by the powder character of the samples. However, some conclusions may be obtained from the data. Since the structure of the Sc and Ti metaphosphates are very similar, most differences between results for the pure Ti(III) and the Ti(III) doped samples should be

attributed to the exchange interactions between the Ti(III) ions in the pure compound. The resonance shown in Figure 4(a) is the result of the collapse due to the exchange of those expected for the three different Ti(III) ions.

The ESR result in the Sc(III) compound doped with Ti(III) may be qualitatively understood considering the theory described by Abragam and Blaney [35]. The D ground state orbital of Ti(III) is broken by the cubic field of the octahedron of oxygen ligands in a ground state triplet (Γ_5) and an excited state doublet (Γ_3), the splitting being Δ= 10 Dq $\cong$ 17300 cm^{-1}, according to our spectroscopic data. A distortion of the octahedron having trigonal symmetry breaks the orbital degeneracy of the (Γ_5) triplet into a singlet and a doublet with an energy splitting δ. The spin orbit interactions λLS (λ= 145 cm^{-1} for the TI(III) ion) mixes these states and gives rise to g-values depending on the crystalline field splitting Δ and δ and on λ. The range of observed g-values indicates that the singlet orbital state is lowest in energy. Neglecting mixture of the group stated spin doublet with excited states at $\Delta \cong$ 17300 cm^{-1} due to the spin-orbital interactions, the g-factor were obtained from Ref. [35].

The presence of three Ti(III) sites introduces a large uncertainty in the g-factors calculated from the data. However, using the free ion spin-orbit parameter λ for Ti(III), the observed g-values indicate $\delta \cong$ 1000 cm^{-1} for the average trigonal splitting. In the Ti(III) doped sample, the resonance narrow and move to lower fields with increasing temperature [Figure (4b)]. This fact results as a consequence of a dynamic Jahn-Teller averaging of the signal that occurs above 50 K. The same process would be responsible for the last relaxation mechanism which vanishes at T> 100 K. These results are similar to those observed in single crystal samples of Chrysoberyl [36] and $LaMgAl_{11}O_{19}$ [37] two material investigated for their potential applications for tunable lasers, in which the Ti(III) ions occupy similar octahedral sites with oxygen ligands.

5.2. ESR of $V(PO_3)_3$

The X-band ESR spectrum of $V(PO_3)_3$ recordered at 4.2 K shows only a weak signal belonging to the V(III) ions at a magnetic field of about 1580 Gauss. This observed "half-field" signal corresponds to the forbidden $\Delta M_s = \pm 2$ transition [16]. The zero field splitting parameter D was estimated as between 2 and 8 cm^{-1}, which is in the range usually found for V(III) compounds [16,38].

5.3. ESR of $M(PO_3)_3$ (M= Mo and Cr) and $Cr_2(P_6O_{18})$

The ESR spectra of these compounds at 4.2 K are given in Figure 5. For the $Mo(PO_3)_3$ phase no signal was observed at temperatures higher than 120 K. Therefore, we can attributed the signal observed at low temperatures to Mo(III) ions present in the compound and enable us to exclude the existence of Mo(V) impurities [39,40]. The spectrum can only been explained by considering the presence of more than one different environment for molibdenum (Figure 5). Assuming that the *g* tensor is isotropic, as usually occurs for Mo(III) compounds. An average g value of 1.89 can be deduced. The intensity of the signal was so weak that the spectrum at Q-band cannot be recordered. In the case of the chromium phase,

the ESR spectra show isotropic signals with g= 1.97 (see Figure 5). The linewidth for the $Cr_2(P_6O_{18})$ compound is larger than that observed for the $Cr(PO_3)_3$ phase. This result is indicative of the important role of the magnetic exchange interactions in the latter phase.

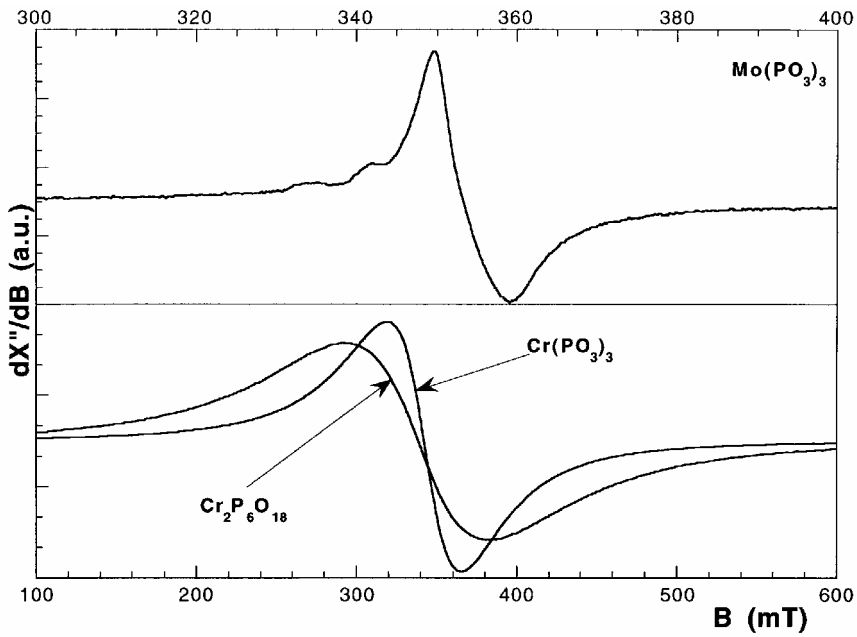

Figure 5. ESR spectra of $Mo(PO_3)_3$, $Cr(PO_3)_3$ and $Cr_2(P_6O_{18})$ recorded at 4.2 K.

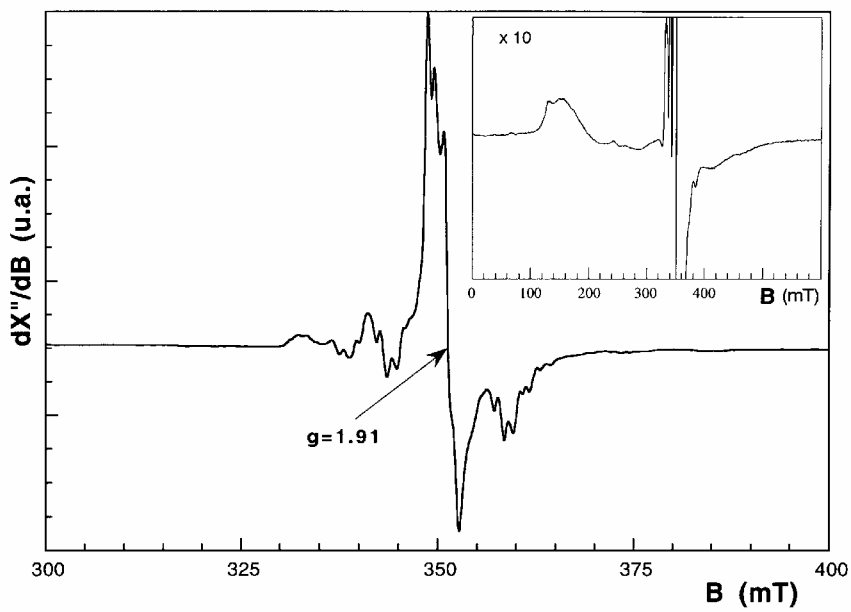

Figure 6. ESR spectra of $Al(PO_3)_3$:0.1%Mo at 4.2 K. Inset shows the signal corresponding to geff. ≅ 4.

In order to obtain more information about the local symmetry of the M(III) centers, ESR spectra were measured on molybdenum- and chromium-doped phases of the homologous aluminium metaphosphates between 4.2 and 300 K. In the case of the Mo(III) compounds the best resolution was obtained for $Al(PO_3)_3$:0.1%Mo (Figure 6). The central *g* value is 1.91. Effects of the zero-field splitting of the S= 3/2 ground sate are observed but it is not possible to obtain quantitative information of the structure in the spectrum. However the signals observed between 320 and 380 mT are indicative of at least two different Mo(III) sites with D values <0.1 cm^{-1}. A new signal, centered at *ca.* 180 mT, appears at temperatures lower than 30 K (see inset of Figure 6). This signal with $g_{eff.} \cong 4$ could be attributed to another metallic center for which $|D| >> h\nu$ [40].

All the attempts to prepare the aluminium hexametaphosphate phase doped with chromium were unsuccessful. The obtained compounds were the metaphosphate phases. In the case of the chromium metaphosphate the ESR resolution was obtained for $Al(PO_3)_3$:2%Cr (Figure 7). Lower concentrations of chromium give rise to new signals from a no identified phase. In spite of the analogies between Cr(III) and Mo(III) ions, the spectrum for the chromium phase is different from that obtained for $Al(PO_3)_3$:0.1%Mo. The X- and Q-band spectra (Figure 7) show that the observed splittings are nearly frequency independent and this can be attributed to the zero-field splitting of the Cr(III) ion. In the X-band spectrum, the most characteristic signals are observed *ca.* 350, 175 mT and near zero-field. We have not carried out any simulation of ESR spectra of these multiple chromium(III) phases.

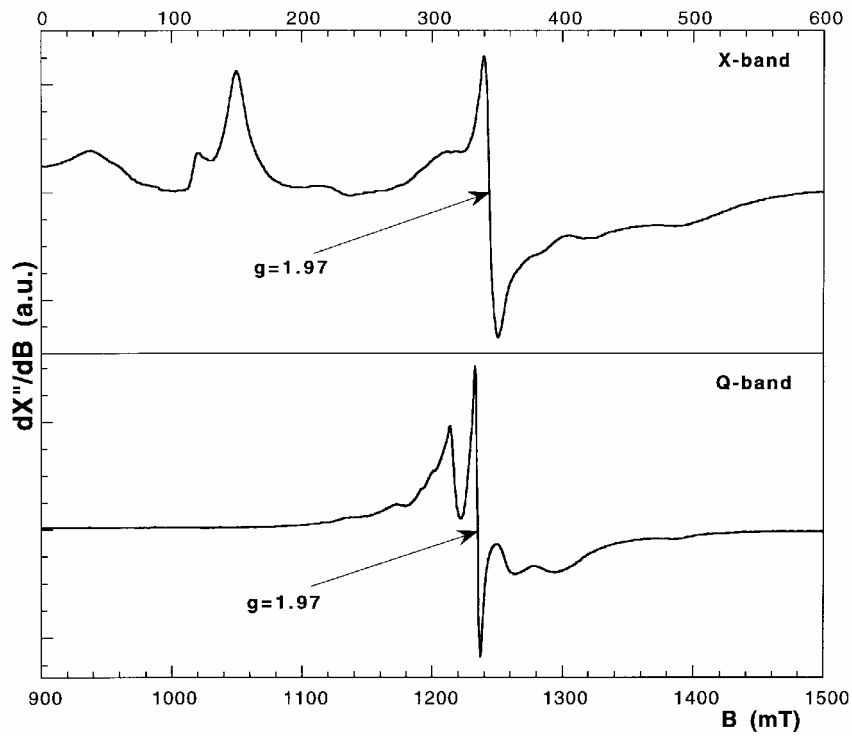

Figure 7. X- and Q-band ESR spectra of $Al(PO_3)_3$:2%Cr, registered at 4.2 and 100 K.

However, considering the simulations report by other authors [3,41,42] the observed ESR spectra may suggest the presence of three different sites for the chromium ions in the $Cr(PO_3)_3$ phase. One of them with $|D| > h\nu$ and the other two with $|D| < h\nu$. These results are in good agreement with the crystallographic data that show the existence of an octahedron with a larger distortion than that observed for the other two.

5.4. ESR of $Fe(PO_3)_3$

The powder X-band ESR spectra of $Fe(PO_3)_3$ at different selected temperatures are shown in Figure 8a.

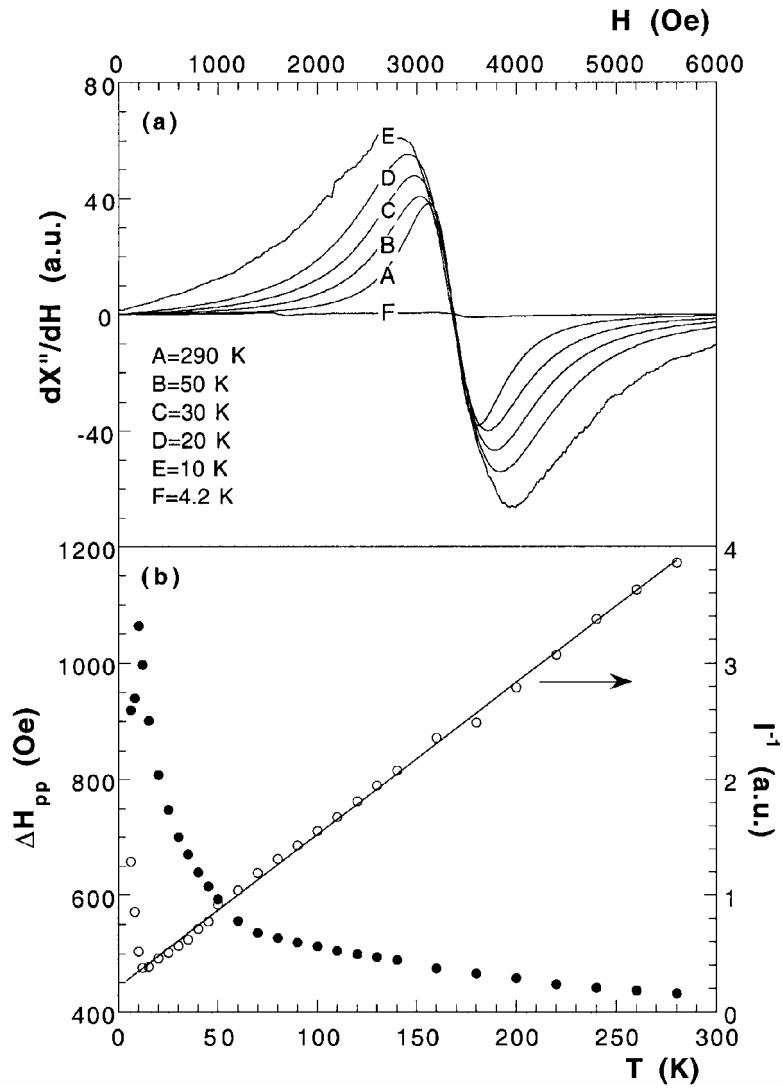

Figure 8. (a) Powder X-band ESR spectra at different temperatures and (b) temperature dependence of 1/I of the signal and the linewidth curves for the $Fe(PO_3)_3$ compound.

In all cases isotropic signals centered around g= 2 were observed. These signals are characteristic of Fe(III) cations in octahedral environment without large tetragonal distortion. The room temperature spectrum (g= 1.99) fits exactly the characteristic of a Lorentzian curve being the same result obtained for all spectra registered down 10 K. Below 10 K the fits are not considerably good. The temperature dependence of the intensity and linewidth of the signal calculated by simulation of the experimental spectra to Lorentzian curves is displayed in Figure 8a. The g values remain apparently unchanged in all the temperature range studied. The intensity of the signal increases with decreasing temperature, reaches a maximum at about 12 K and after that rapidly decreases [see Figure 8b]. In fact, at 4.2 K no relevant signal could be observed. As can be deduced from the straight line that fits the 1/I *vs.* T curve at high temperatures the magnetic susceptibility of the compound follows a Curie-Weiss law and no short order effects are detectable above 30 K.

As long as the high temperature conditions ($kT >> H_z$, H_{ex}, H_{dip},…) is expected to be satisfied than the line width observed has low temperature dependence. Only a small increase is observed between room temperature and 50 K probably due to the dipolar homogeneous broadening. Furthermore, when temperature is decreased the linewidth increases rapidly reaching a maximum at 8 K. This behavior is characteristic of systems with a three-dimensional order and, in this case, it must be of antiferromagnetic nature considering the thermal evolution of the intensity of the signal [43,44]. The apparent temperature independence of the resonance field is also in good agreement with a three-dimensional behavior with quasi-isotropic interactions. In any case, the presence of three different Fe(III) sites and the relatively large linewidth (430-1050 Gauss) imply that the conclusions observed from the powder spectra must be considered with caution. In fact, the observed isotropic signal is the result of the collapse by exchange of those expected for the three different Fe(III).

6. MAGNETIC PROPERTIES

6.1. Magnetic Properties of $Ti(PO_3)_3$

Variable-temperature magnetic susceptibility measurements, performed on a powder sample of $Ti(PO_3)_3$ from 1.8 to 100 K are shown in Figure 9. The χ_m^{-1} *vs.* T line follows a Curie-Weiss law in practically all the temperature range studied. The Curie constant value is C_m= 0.17 cm^3Kmol^{-1}, which is notably lower than that expected from the *g*-values obtained from the ESR spectra. The calculated value of the Curie-Weiss constant is θ= +0.31 K. The $\chi_m T$ product at room temperature is 1.17 μ_B and remains unchanged until 20 K. At lower temperatures than 20 K a slight increase of the $\chi_m T$ product can be observed. This result suggests the existence of ferromagnetic interactions in the $Ti(PO_3)_3$ compound.

6.2. Magnetic Properties of $V(PO_3)_3$

The thermal evolution of the molar magnetic susceptibility for the $V(PO_3)_3$ compound is shown in Figure 10. The susceptibility follows a Curie-Weiss law between 1.8 and 300 K

with C_m= 0.86 cm^3Kmol^{-1} and θ= -7.2 K. The negative temperature intercept together with the observed decrease in the effective magnetic moment with decreasing temperature (Figure 10) suggests the presence of antiferromagnetic interactions in this compound.

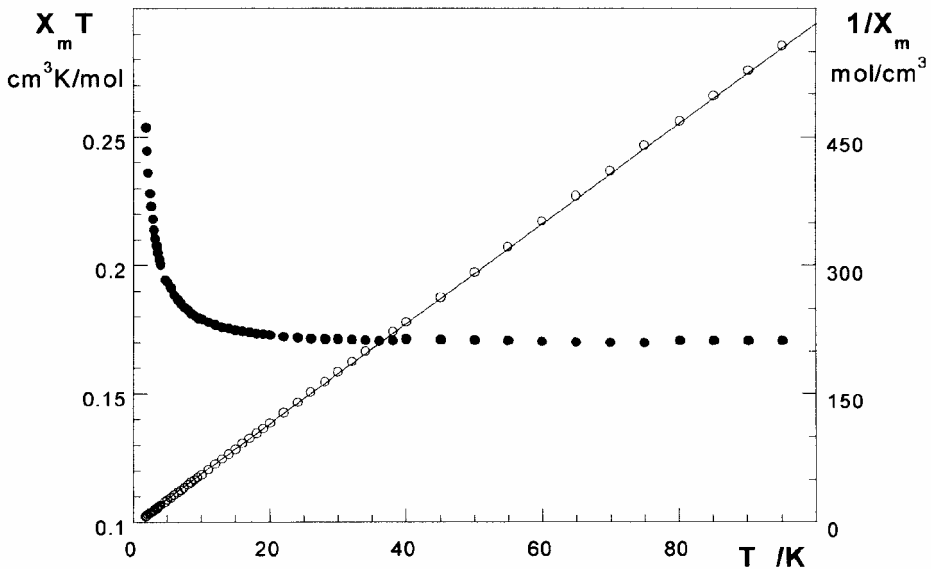

Figure 9. Thermal evolution of the χ_m^{-1} and χ_mT product of $Ti(PO_3)_3$.

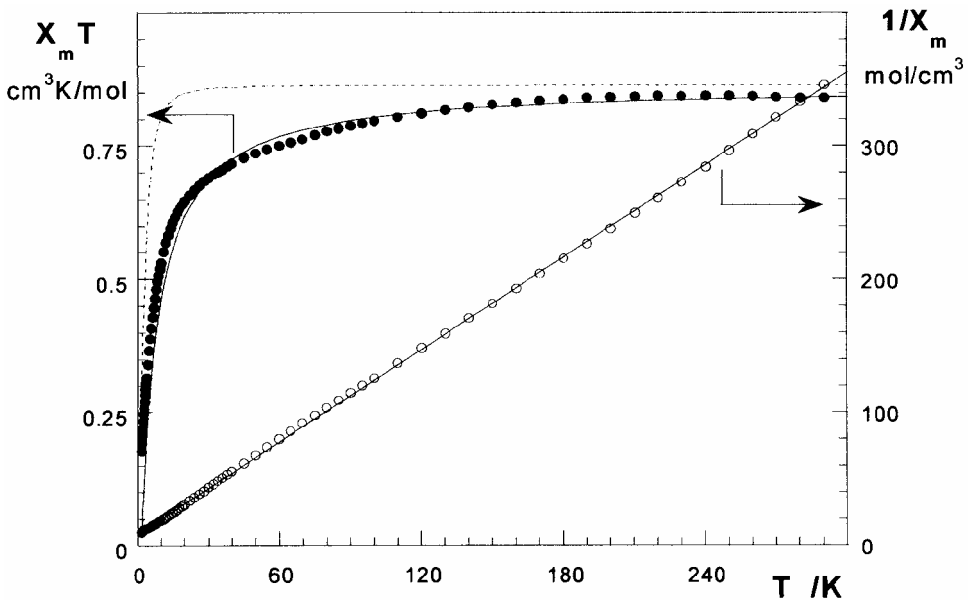

Figure 10. Thermal evolution of the χ_m^{-1} and χ_mT product of $V(PO_3)_3$. Dotted and continuous lines represent the best fit considering only the effect of the zero-field splitting and the J exchange parameters, respectively.

However, it is necessary take into occount that similar behavior could be also originate by a contribution such as a positive zero-field splitting, which was observed from the ESR data. Both contributions are qualitatively similar and to consider them simultaneously presents great difficulties. For this reason, we have tried to fit the experimental data under each of these hypothesis separately. Using the Van Vleck equation an analytical expression for the magnetic susceptibility as a function of the temperature and the D parameter was calculated [45]. However, considering the *D* value obtained from the Weiss temperature (θ= 2/3D), the calculated curve deviates drastically from the experimental ones (dotted line in Figure 10). Satisfactory fits can be obtained only by using *D* values higher than 40 K. However, these results are completely unrealistic considering the ESR measurements.

An expression for the magnetic susceptibility was derived from high temperature expansion series for an antiferromagnetic Heisenberg simple cubic lattice calculated by Rushbrooke and Wood [46]. The best fit corresponds to the continuous line in Figure 10 and was obtained with a J/k value of -0.92 K. The calculated curve agrees rather well with the experimental one at high temperatures, but deviates appreciably at low temperatures where the effect of the zero-field splitting is more important. So, we can conclude that both the antiferromagnetic interactions and the zero-field splitting determine the magnetic behavior observed for $V(PO_3)_3$.

6.3. Magnetic Properties of $M(PO_3)_3$ (M= Mo and Cr) and $Cr_2(P_6O_{18})$

The thermal evolution of the molar magnetic susceptibility for $Mo(PO_3)_3$ is shown in Figure 11. A sharp maximum is observed at 4.5 K, indicating the existence of an antiferromagnetic ordering in this compound. The high temperature data (T> 50 K) are well described by a Curie-Weiss law [$\chi=C_m/(T-\theta)$] with C_m= 1.71 cm^3Kmol^{-1} and θ= -6.8 K. The negative temperature intercept together with the decrease of the effective magnetic moment observed when the temperature is lowered (3.64μ_B at 300 K and 1.78μ_B at 2 K) are in good agreement with the predominance of antiferromagnetic interactions in this compound (Figure 11).

Considering the structural features of the molybdenum metaphosphate only superexchange interactions *via* (PO_4) tetrahedra can be expected. Due to the complexity of three-dimensional arrangement and the consequent presence of different exchange pathways it is not possible to find a simple magnetic model, representing exactly the characteristics of the magnetic ordering in this compound. However, taking into account the weakness of the exchange couplings and the packing of the (MoO_6) octahedra, a simple cubic network can be utilized in order to obtain an approximate value of the exchange parameter. Considering the usual isotropic magnetic behavior of Mo(III) ions a Heisenberg Hamiltonian was the starting point, $H = 2J \Sigma S_iS_j$, with i<j. The uses of the high-temperature series expansion developed by Rushbrooke and Wood [46] allowed us to obtain the best fit of the experimental data for g= 1.90 and J/k = -0.38 K, and it is represented by the solid line in Figure 11. In spite of the differences between the real system and the employed model, the calculated curve follows quite well the experimental data. Moreover, taking into account that the knowledge of only six terms of the infinite series are valid for the equation used when T decreases to near T_N it

can be concluded that the molybdenum metaphosphate is well described as a three-dimensional Heisenberg antiferromagnet with a J/k value ca. 0.4 K.

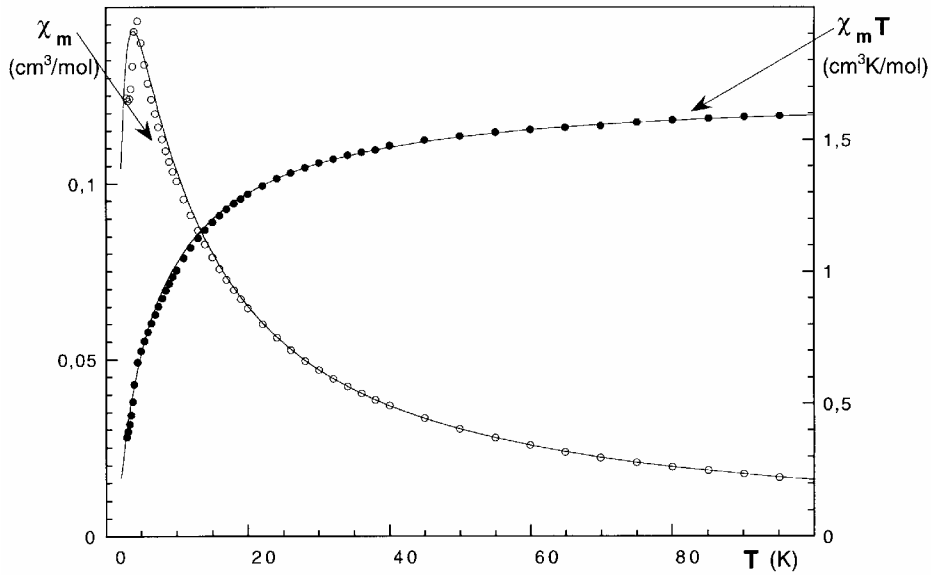

Figure 11. Thermal variation of χ_m and $\chi_m T$ product for $Mo(PO_3)_3$.

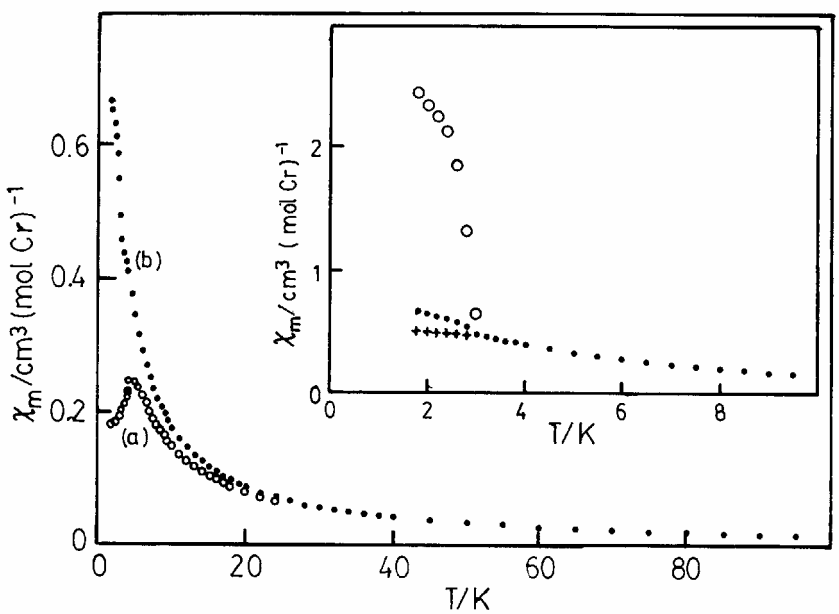

Figure 12. Thermal variation of χm for $Cr(PO_3)_3$ [(a), open circle] and $Cr_2(P_6O_{18})$ [(b), black circle]. Inset shows the thermal evolution of χ_m for the $Cr_2(P_6O_{18})$ compound at different magnetic fields (open circle, 10 mT; blac circle, 100 mT; +, 1T].

The magnetic behavior of $Cr(PO_3)_3$ is very similar to that exhibited by the homologous molybdenum compound. The susceptibility *vs.* temperature curve shows a maximum at 4.5 K

(Figure 12a), obeying the Curie-Weiss law with C_m= 1.83 cm^3Kmol^{-1} and θ= -2.7. Considering the analogies between both compounds, from the structural and electronic point of view, this result is not surprising. The most important difference is observed for the Curie constant, which exhibits higher values for the chromium than for the molybdenum compound. This fact results from the effect of the spin-orbit coupling which is less important for an element of the first transition series such as chromium. Consequently, a lower deviation from the free-electron *g* value and a higher C_m value are observed in this case. A simple treatment as was described above for the molybdenum metaphosphate allows us to conclude that the $Cr(PO_3)_3$ phase orders as a three-dimensional Heisenberg antiferromagnet with a J/k value of ca. 0.3 K.

The magnetic behavior of the $Cr_2(P_6O_{18})$ hexametaphosphate is substantially different from that observed for the chromium metaphosphate. The χ_m *vs*. T curve does not exhibit any appreciable anomaly at applied magnetic fields > 1T (Figure 12b). The high-temperature data follow a Curie-Weiss law with C_m= 1.83 cm^3Kmol^{-1} and θ= -0.2 K. The value of the Curie constant is practically the same as that observed for $Cr(PO_3)_3$. This result is in good agreement with the similar environment observed for the Cr(III) ions and the negligible influence of the magnetic interactions above 50 K for both compounds. The magnetic effective moment measured under an applied magnetic field of 0.1 T decreases from 3.82 μ_B at room temperature to 3.09 μ_B at 1.8 K, showing the existence of antiferromagnetic interactions in the compound. χ_m as a function of temperature at lower applied magnetic fields rise below *ca.* 3 K indicating a magnetic transition (inset in Figure 12). A very sharp peak in $-d(\chi T)/dT$ *vs.* T provides a more accurate ordering temperature of T_N= 2.2 K. Magnetization as a function of applied field at below and above T_N is shown in Figure 13. The linear increase of the magnetization above 0.1 T and the absence of saturation behavior up to 7 T imply and antiferromagnetic-like ordering.

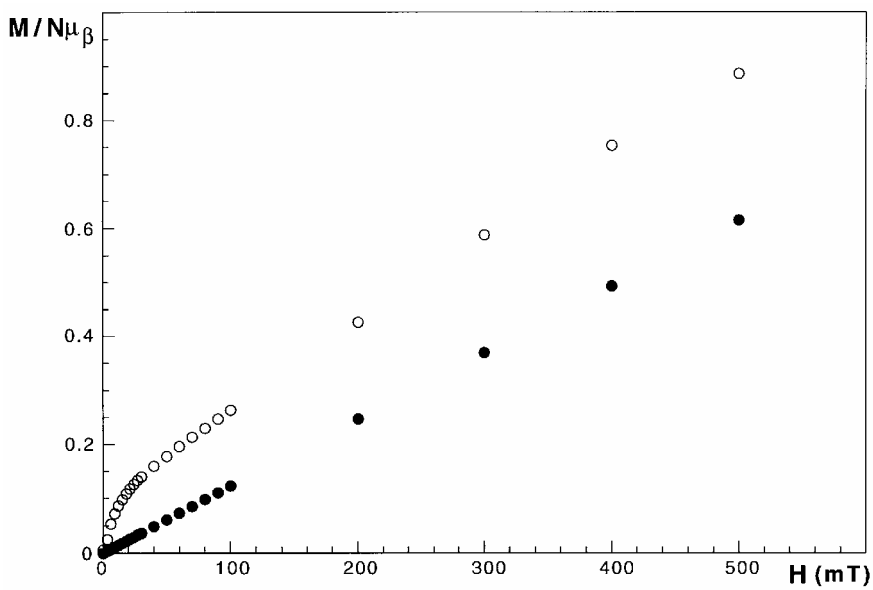

Figure 13. Magnetization vs. applied magnetic field, beloww (open circle) and above (black circle) TN for the $Cr_2(P_6O_{18})$ compound.

However, the magnetization data at low applied fields, as shown in Figure 13, indicate a small amount of a ferromagnetic component in the ordered state that appears to be responsible for the steep increase in χ_m at the ordering temperature. This magnetic behavior is consistent with the existence of a weak ferromagnetism intrinsic to the sample. To understand the magnetic structure in the ordered state, neutron diffraction studies above and below T_N would be necessary.

6.4. Magnetic Properties of $Fe(PO_3)_3$

The temperature and field dependence of the magnetic susceptibility and the magnetization have been investigated. At first glance, the thermal behavior of the magnetic susceptibility seems to be that expected for a three-dimensional system with an antiferromagnetic ordering at 8 K.When the magnetic measurements were carried out under a magnetic field of 1 T one can observe a maximum in the χ_m *vs.* T curve centered at about 8 K (Figure 14) and a continuous decrease in the magnetic effective moment with decreasing temperature from room temperature to 4.2 K. However, more detailed experiments have shown that the magnetic susceptibility is strongly dependent on the magnetic field at temperatures less than 10 K (Figure 14). Moreover, the magnetic history of the sample also has an important influence on the observed results. These facts suggest the presence of some ferromagnetic contribution in this compound.

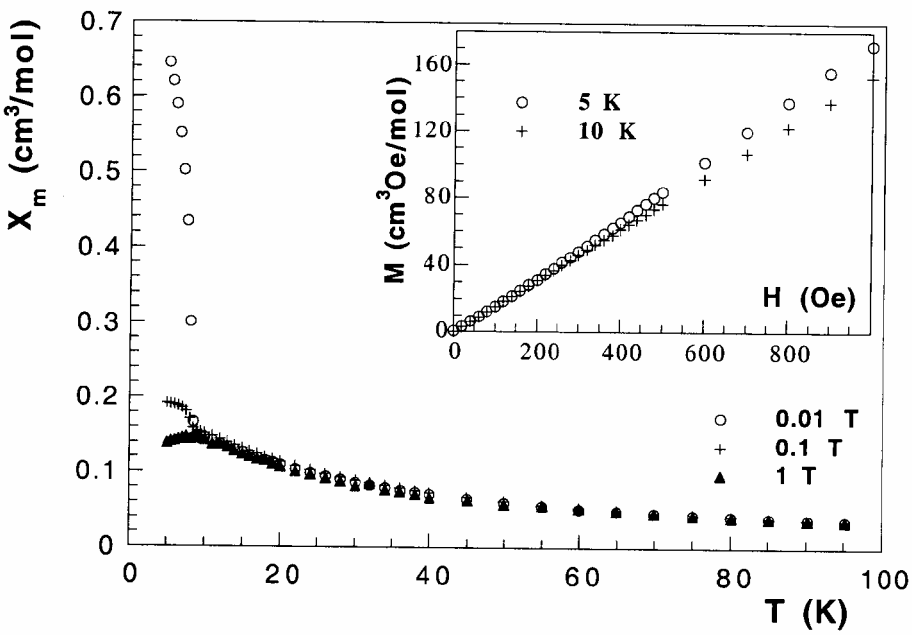

Figure 14. Thermal dependence of χ_m at different magnetic fields for $Fe(PO_3)_3$. Inset shows the magnetization vs. field curves, below and above of the Néel temperature.

The magnetization *vs.* field curves registered above (10 K) and below (5 K) the ordering temperature is apparently not too much different but two important points must be notice. In both cases the magnetization curves are nearly lineal up to 7 T, but at lower temperatures a small change on the slope is observed at about 0.04 T (inset in Figure 14). Moreover, a weak magnetization (about 50 cm^3Oe/mol) is retained at zero field. Taking into account these results, we performed magnetization measurements *vs.* temperature at a field of 100 Oe. The curves obtained are displayed in Figure 15. The field-cooled magnetization (FC) shows a rapid increase in *M* below T_N= 8 K. The zero-field-cooled magnetization (ZFC) measures upon cooling to 4.2 in zero field and heating the sample under 1000 Oe is less than that of the FC below T_N (it remains practically constant) and completely similar above the critical temperature. Finally, when the sample is cooled within the field and upon further heating in zero field, one can observed (inset in Figure 15) that the remnant magnetization decrease with increasing temperature and vanishes above 8 K. All these features are characteristic of a magnetically ordered state below 8 K [47], with the presence of weak ferromagnetism intrinsic to the sample.

As mentioned before the data above 10 K are no affected by the magnitude of the external field. Thus, measurements at higher fields (0.1 T) were carried out to study the whole behavior of the magnetic susceptibility without any appreciable sensitivity losses in the measurements. From a plot of the reciprocal molar magnetic susceptibility *vs.* temperature classical Curie-Weiss behavior can be deduced above 20 K (see Figure 16), being C_m= 4.40 cm^3K/mol and θ= -13.3 K. From the calculated Curie constant a *g* value of 2.00 can be derived, in good agreement with that calculated from the ESR spectra and with the topology of the Fe(III) octahedra in the title compound.

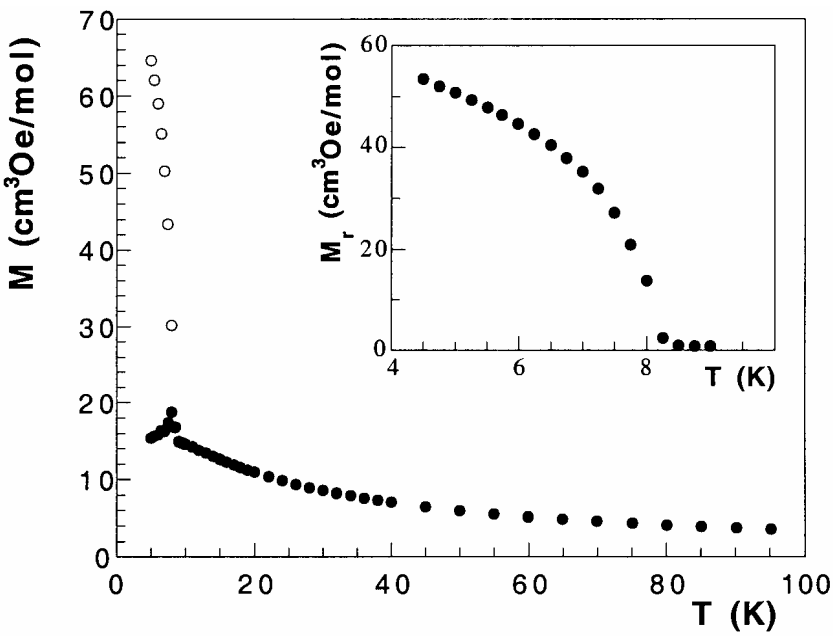

Figure 15. Thermal dependence of the magnetization at ZFC (black circles) and FC (open circles) for the $Fe(PO_3)_3$ compound. Inset shows the zero-field magnetization curve vs. T for the $Fe(PO_3)_3$ compound cooled under a magnetic field of 100 Oe.

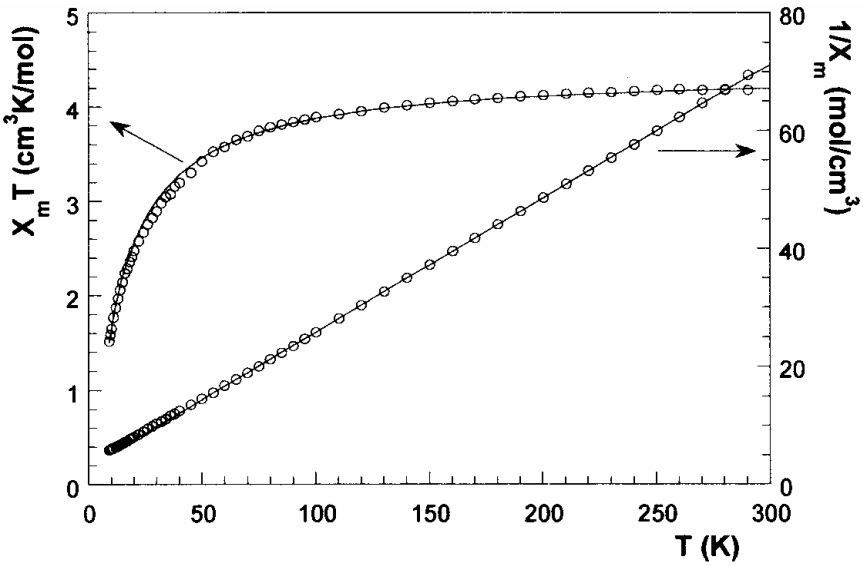

Figure 16. Thermal dependence of the $\chi_m T$ product and $1/\chi m$ for $Fe(PO_3)_3$.

The negative Weiss temperature and the observed decrease in the $\chi_m T$ product with decreasing temperature (Figure 16) are indicative of the existence of antiferromagnetic exchanges as major interactions in this compound.

Considering the structural features of the $Fe(PO_3)_3$ compound superexchange interactions *via* (PO_4) tetrahedra can only be expected. Despite the complexity of the three-dimensional arrangement a simple cubic network can be considered to be an acceptable description of the stacking of the iron(III) ions and can be utilized to obtain an approximate value of the exchange parameter. Considering the usual isotropic magnetic behavior of the Fe(III) cations, a Heisenberg Hamiltonian can be proposed as a theoretical approach to the magnetic behavior. The best fit of the experimental data was obtained for g= 2.00 and J/k= -0.36 K, and it is represented by the solid line in Figure 16. Despite the differences between the real system and the employed model, the calculated curve follows the experimental data rather well. Moreover, for such a system a sharp maximum in the thermal evolution of the magnetic susceptibility is expected at 8.5 K, in good agreement with the experimental data. Therefore, it can be concluded that the magnetic behavior of the iron(III) metaphosphate is well described as a three-dimensional Heisenberg antiferromagnetic with a J/k value about 0.4 K.

6.5. Specific Heat Measurements of the $M(PO_3)_3$ (M= Cr, Fe, Mo) Metaphosphates

The specific-heat measurements of the $M(PO_3)_3$ (M= Cr, Fe and Mo) metaphosphates between 1.8 and 35 K are shown in Figures 17 and 18 [48,49].

The heat capacity data exhibit three-dimensional magnetic ordering peaks at 4.2, 4 and 7.8 K for Cr, Fe and Mo phases, respectively. The temperatures at which these λ-type peaks appear are similar to those obtained from the magnetic susceptibility measurements (T = 4.5, 4.5 and 8.0 K for Cr, Fe and Mo metaphosphates, respectively).

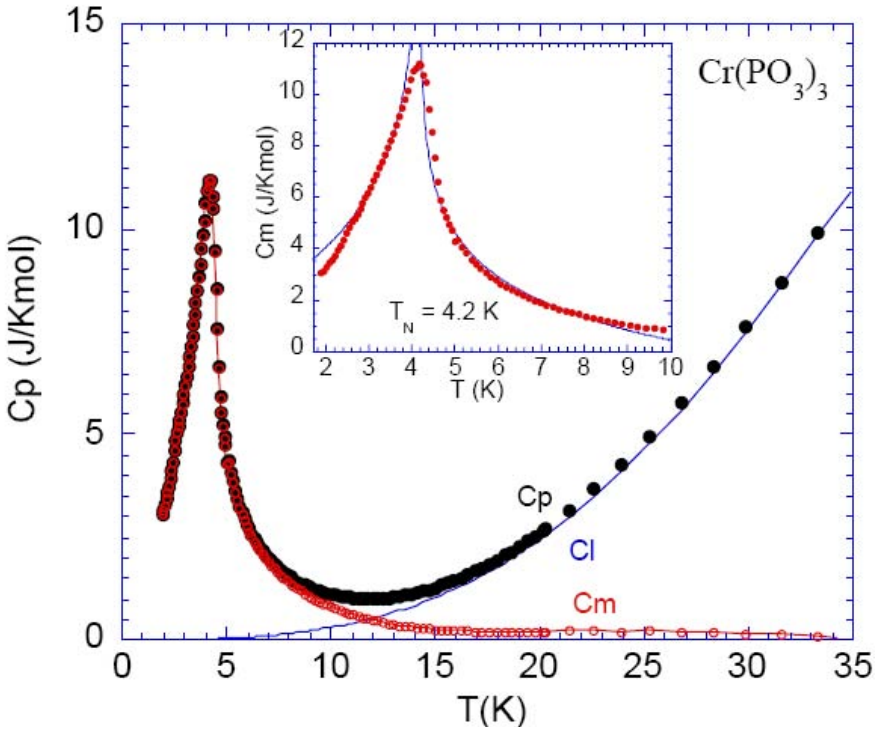

Figure 17. Specific heat (Cp) of $Cr(PO_3)_3$. Cl and Cm are the estimated lattice and magnetic contributions, respectively. Inset shows the heat capacity of $Cr(PO_3)_3$ in the neighbourhood of the ordering temperature. The solid lines correspond to the $T < T_N$ and $T > T_N$ equations.

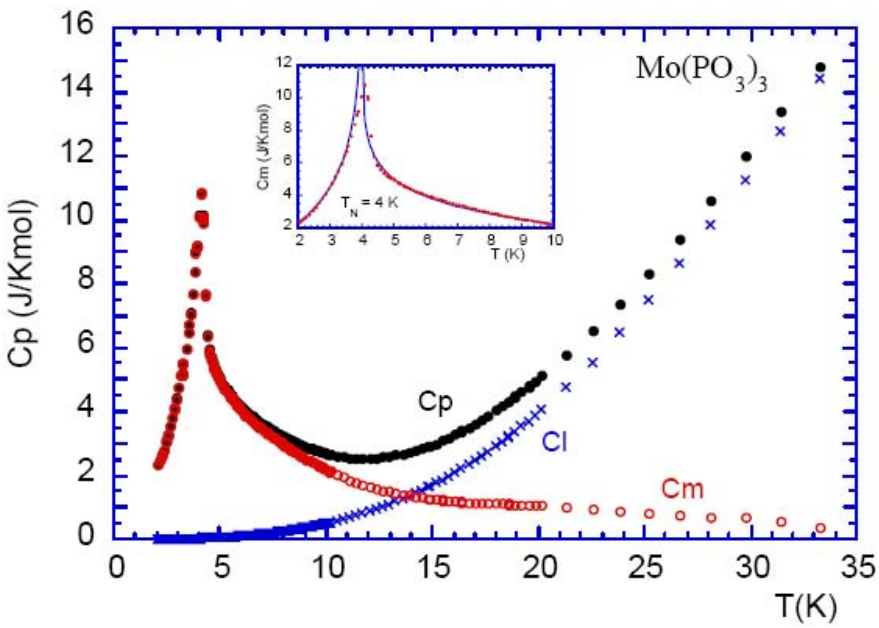

Figure 18. (Continued)

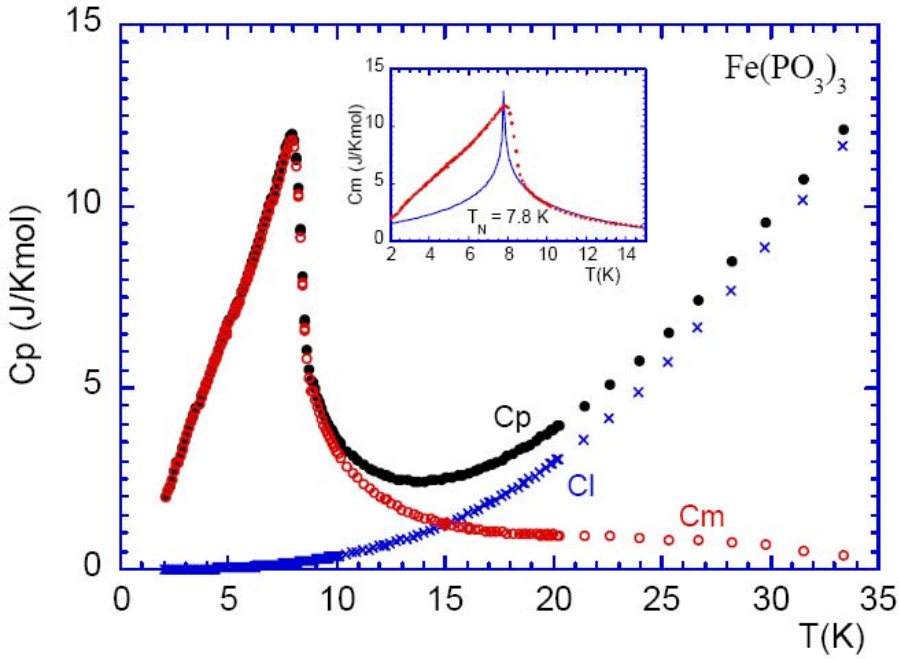

Figure 18. Specific heats (Cp) of (a) $Mo(PO_3)_3$ and (b) $Fe(PO_3)_3$. Cl and Cm are the estimated lattice and magnetic contributions, respectively. The nsets show the heat capacity of $Mo(PO_3)_3$ and $Fe(PO_3)_3$ in the neighbourhood of the ordering temperature. The solid lines correspond to the $T < T_N$ and $T > T_N$ equations.

The specific-heat data of these three metaphosphates have been fitted in the 10-25 K temperature range with the law $C_p = AT^3 + BT^{-2}$, which assumes a Debye model (AT^3) for the phonons and a BT^{-2} term for two-dimensional magnetic correlations (see Table 3).

The increase of C_p above 15 K is mainly due to the lattice vibrations which are given by the A values being similar in the three metaphosphates studied (see Table 3). The contribution of short-range 2D magnetic interactions, expected to give rise to a Schottky-type anomaly above T_N, associated with the B constant is practically neglected being significantly lower in the chromium than in the molybdenum and iron phases.

The specific-heat data for all the three metaphosphates, at temperatures higher than 10 K, have been fitted to the relationship $C_p = AT^3 + BT^{-2}$, where the first term is ascribed to the lattice contributions whereas the second one deals with the 2D magnetic correlations (Schottky tail). A linear plot of CT^2 *vs.* T^5 allowed the evaluation of the A= 3.05x10-4 $JK^{-4}mol$ and B= 73.5 $KJmol^{-1}$ constants for chromium; A= $5.22x10^{-4}$ $JK^{-4}mol$ and B= 273 $KJmol^{-1}$ for the molybdenum and A= $4.33x10^{-4}$ $JK^{-4}mol$ and B= 278 $JKmol^{-1}$ for the iron metaphosphate. The A values are related to the Debye temperatures (θ_D), given in Table 3, in the framework of the Debye model for all the metaphosphates studied. We used the inferred value of A to substract the lattice contribution from the measured specific heat in order to obtain the experimental magnetic specific heats (see insets Figures 17 and 18). The absence of appreciable anomalies in the magnetic heat-capacity obtained above T_N suggests that short-range orders would be small without any significant in the magnetic behavior of both compounds. These results are in good agreement with those obtained from the susceptibility measurements where decrease in the $\chi_m T$ *vs.* T curves, from 3.64 μ_B at room temperature to

1.78 μ_B at 2K for the Mo phase and from 5.58 μ_B to 2.52 μ_B for the Fe compound, is observed. The estimated Debye (θ_D) temperature for the chromium phase is 436 K which is higher than those of $M(PO_3)_3$ (M= Mo, Fe) phases due to the smaller atomic weight. These results are in good agreement with those obtained from susceptibility measurements of $Cr(PO_3)_3$ where a weak decrease in the $\chi_m T$ *vs.* T curve was observed (3.83 μ_B at 300 K and 1.55 μ_B at 2 K).

Table 3. Summary of specific-heat data of the $M(PO_3)_3$ (M^{III}= Cr, Mo and Fe) metaphosphates

$M(PO_3)_3$		*Cr (S= 3/2)*	*Mo (S=3/2)*	*Fe (S= 5/2)*
T_{max} (K)		4.2	4.1	7.8
Inflexion point (K)		4.4	4.2	8.3
$C_{m\,max}$ ($JK^{-1}mol^{-1}$)		11.2	10.8	11.8
$C_p = AT^3 + BT^{-2}$	Range of fit (K)	10-25	10-25	11.5-21.5
	A ($JK^{-4}mol^{-1}$)	3.05×10^{-4}	5.22×10^{-4}	4.33×10^{-4}
	B ($JKmol^{-1}$)	73.5	273	278
	Debye temperature, θ_D (K)	436	356	388
$Cm = \alpha - \beta Ln\lvert T - T_N\rvert$	$T \geq T_N$			
	Range of fit (K)	4.5-10	4.5-14	9-16
	α ($JK^{-1}mol^{-1}$)	4.16	5.01	4.77
	β ($JK^{-1}mol^{-1}$)	2.12	1.54	1.84
	$T \leq T_N$			
	Range of fit (K)	2.5-4	2-4	2-7
	α ($JK^{-1}mol^{-1}$)	6.83	4.5	[a]
	β ($JK^{-1}mol^{-1}$)	3.53	3.21	[a]
$S_m = \int (C_m/T)dT$				
	S_{max} (R)	1.39	1.39	1.79
	S at 35 K (R)	1.15	1.17	1.43
	S (35K)/S_{max} (%)	83	84	80
	S at T_N (R)	0.78	0.54	1.06
	S(T_N)/S(35 K)(%)	68	47	74

[a] The experimental data can not be fitted to a logarithmic expression for $T < T_N$.

As can be see in Table 3, the fit near the ordering temperature (T_N= 4.2 K) for $Cr(PO_3)_3$ follows the equation $C_m = \alpha - \beta Ln|T - T_N|$, equation [1], given by Kopinga et al [50] (see inset in Figure 17) allowed us to obtain α= 4.16JK^{-1} and β= 2.12 $JK^{-1}mol^{-1}$. Considering the similar λ-type maximum observed in the heat capacity measurements, especially for $Mo(PO_3)_3$, a fit near the ordering temperatures following the same equation [1], above indicated, was also carried out. The magnetic specific-heat data for Mo metaphosphate plotted versus $Ln|T - T_N|$ for T_N= 4 K show linear behavior below and above the ordering temperature. The values near the transition point, T_N, satisfy the equation $C_m = 4.37 - 2.81Ln|T - T_N|$ and $C_m = 5.01 - 1.54Ln|T - T_N|$ for $T < T_N$ and $T > T_N$, respectively. These equations are described by the solid lines given in the inset of Figure 18(a). In the case of $Fe(PO_3)_3$ only the region above the ordering temperature T_N= 7.8 K, can be fitted following the logarithmic expression $C_m = 4.77 - 1.84\ Ln|T - T_N|$ (see inset in Figure 18(b)). For $T < T_N$, the experimental data show a shoulder and therefore can no be fitted with a logarithmic expression. A temperature dependence of the specific-heat below the ordering temperature

has been also observed in some gadolinium and europium based compounds (S= 7/2), being attributed to the filling-up of the 2S + 1 quantum energy levels [51,52]. Preliminary studies using Mean Field Theory indicate that a shoulder superimposed onto the λ-type anomaly appears for systems with $S \geq 5/2$ as in the case of $Fe(PO_3)_3$.

The thermal evolution of the magnetic entropy, S_m, for $Cr(PO_3)_3$ is shown in Figure 19, in comparison with that of $Mo(PO_3)_3$. The total magnetic entropy for the chromium compound was found to be 1.15 R, which agrees with the 83% of the theoretical value (1.39 R) for a S= 3/2 system. The small difference of the experimental entropy with respect to the theoretical value could originate from the procedure to calculate the lattice contribution which is approximate. Specific heat measurements of $Cr_2(P_6O_{18})$ were not carried out due to its low magnetic ordering temperature (at the limit of our experimental temperature range). However, these ordering temperatures are accessible to neutron diffraction measurements which would allow us to determine the magnetic structure of both metaphosphates and to better understand the magnetic behavior of these compounds.

The total magnetic entropy, $S_m = \int (C_m/T)dT$, was found to be 1.17R and 1.43R for the Mo and Fe metaphosphates, respectively (Figure 20). These results agree with 84% of the theoretical value (1.39 R) for an S= 3/2 system and 80% for an S= 5/2 (1.79R) (see Figure 20). An amount of 0.54R (47%) of the experimental entropy of $Mo(PO_3)_3$ was gained below the ordering temperature, T_N= 4 K, whereas in the case of $Fe(PO_3)_3$ the magnetic entropy reaches 74% (1.06R) of the experimental entropy at the transition point. The value obtained for the Mo phase is similar to that observed in other three-dimensional phosphate systems where the entropy normally obtained near the Néel temperature reaches values of 1/3 of the theoretical value [50]. The high value obtained for $Fe(PO_3)_3$ must be attributed to the existence of magnetic anomalies as was previously described.

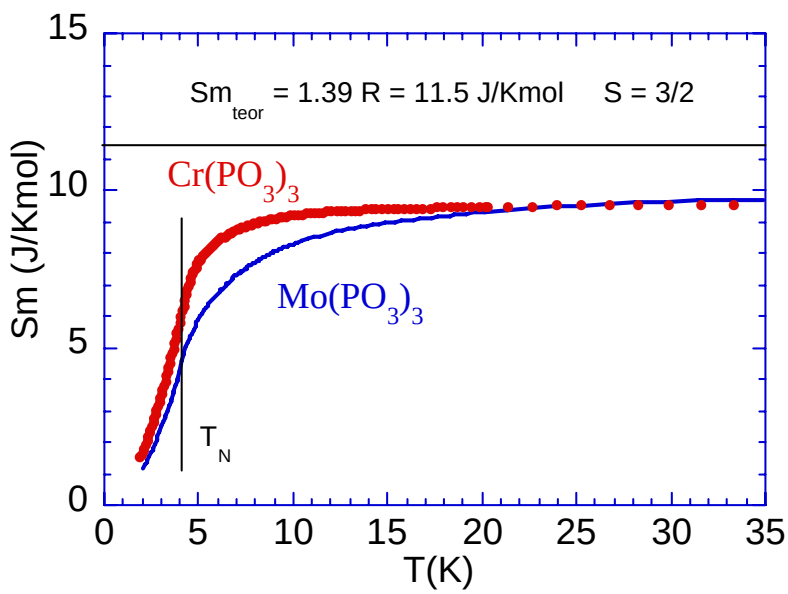

Figure 19. Magnetic entropy of $Cr(PO_3)_3$ as a function of temperature together with that of $Mo(PO_3)_3$ for comparison. The horizontal solid line represents the theoretical Sm. The vertical solid line indicates the ordering temperature.

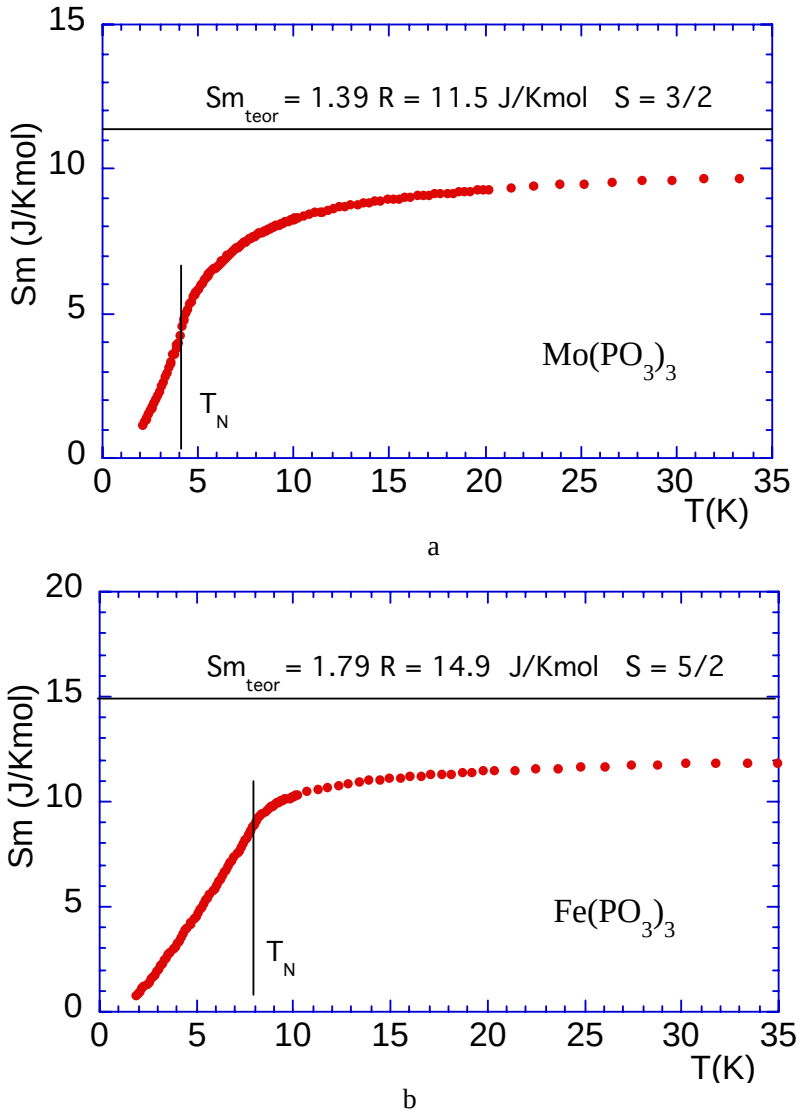

Figure 20. Magnetic entropy of (a) $Mo(PO_3)_3$ and (b) $Fe(PO_3)_3$ as a function of temperature. The horizontal solid line represents the ΔS maximum. The vertical solid line indicates the ordering temperature.

The most important difference between both S= 3/2 systems, Cr and Mo, is observed at the ordering temperature where the experimental entropy gained in $Cr(PO_3)_3$ is significantly higher than that obtained in $Mo(PO_3)_3$. This is probably due to the different size of the metallic cations (see Table 3). The $S(T_N)/S_{max}$ ratio exhibits similar values for the Cr (S= 3/2) and Fe (S= 5/2) metaphosphates, being higher than that of the Mo (S= 3/2) phase, indicating than in those compounds the relatively value of the entropy in the ordering temperature seems to be more dependent on the cation size than on the magnetic spin.

7. LOW-TEMPERATURE NEUTRON DIFFRACTION

7.1. B and C type $Cr(PO_3)_3$ Metaphosphates

The neutron diffraction petterns at 1.8 K for B and C chromium metaphosphates were collected in the D2B powder diffractometer. The patterns clearly exhibit extra magnetic peaks indicating that both compounds are magnetically ordered at 1.8 K. The thermal evolution for $Cr(PO_3)_3$ was followed in the D1B instrument form 1.8 to 10 K. The results confirm the presence of a three-dimensional order. The D1B diffraction pattern at 1.8 K shows a better resolution of the magnetic reflections. The magnetic reflections exhibit low intensities due to the low ordering magnetic temperatures observed in these compounds. All magnetic peaks were indexed with a propagation vector k = (0,0,0) referenced to the RT unit cells, indicating that both the magnetic and nuclear unit cells are similar. The possible magnetic structures compatible with *Cc* and $P2_1/a$ crystal symmetries for $Cr(PO_3)_3$ and $Cr_2(P_6O_{18})$, respectively, have been deduced with the help of Bertaut's macroscopic theory [53], which allows one to determine the symmetry constraints between each magnetic moment of the Cr(III) ions belonging to the same general crystallographic position. The ordering of the magnetic moments compatible with the symmetry operations was determined and the agreement between the observed and calculated diffraction patterns for each possible magnetic structure was evaluated.

7.1.1. C-Type $Cr(PO_3)_3$

The magnetic reflections observed for $Cr(PO_3)_3$ can be indexed on the basis of the crystal unit cell and obey the rules *(hkl)* wit h+k = 2n (i.e., C-centered mode remains) and (*h0l*) with *l* = 2n+1 (i.e., forbidden by the *c* glide plane). It is worth mentioning than some of the nuclear reflections could have magnetic contributions to their intensities. The magnetic atoms occupy three general 4a different crystallographic sites. The positions in the cell of the different atoms belonging to the Cr(1), Cr(2) and Cr(3) sublattices are numbered 1a, 1b, 1c, 1d; 2a, 2b, 2c 2d and 3a, 3b, 3c, 3d, respectively.

Using the method developed by Bertaut and taking into account the restraints imposed by symmetry elements of the space group Cc along the three directions *x*, *y* and *z*, the different possible orientations of the magnetic moments were evaluated. The refinement of the components of the magnetic moments gives M_y = 0, indicating than they lie in the (010) plane. The best fit of the D1B experimental patterns for $Cr(PO_3)_3$ at 1.8 K is plotted in Figure 21. The components of the refined magnetic moments of Cr(1), Cr(2) and Cr(3) are, respectively, M_x = 1.7(2) μB and M_z = 1.1(1) μ_B per chromium ion with a resultant magnetic moment of 2.58(9) μ_B per Cr(III) ion. The nuclear and magnetic discrepancy factors are R_p = 3.22, R_{wp} = 4.58, χ^2 = 18.3, R_{Bragg} = 4.35 and R_{mag} = 23.3. The magnetic structure of $Cr(PO_3)_3$ is shown in Figure 22. The results are similar to those observed for the $Mo(PO_3)_3$ phase, which was resolved in the *Ia* unit cell, and some chromium phosphates in which the magnetic moments are near 2.4 μ_B [54,55].

The magnetic structure of the C-type $Cr(PO_3)_3$ metaphosphate is consistent with the presence of (CrO_6) octahedra where the magnetic moments are antiferromagnetically ordered in the *x* direction whereas those along the *y* and *z* directions show parallel alignment (see Figure 22).

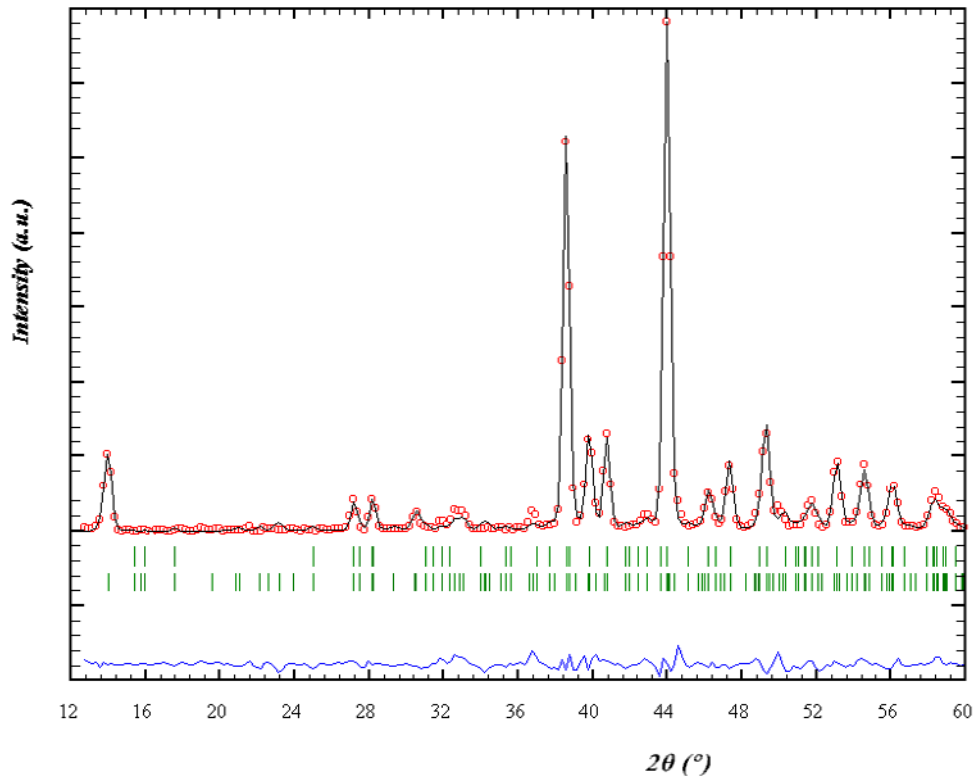

Figure 21. Refinement of the $Cr(PO_3)_3$ (D1B) neutron diffraction profiles at 1.8 K (the intensity is in arbitrary units). The positions of the Bragg reflections for the crystallographic (first row) and magnetic (second row) structures are presented, The fifference curve is plotted at the botton of the figure.

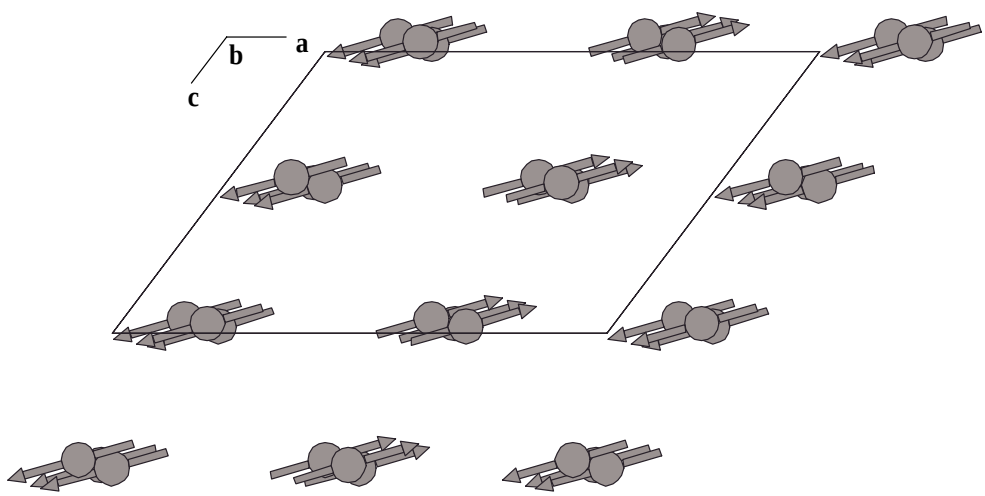

Figure 22. Projection of the magnetic structure of $Cr(PO_3)_3$ onto c. The direction of the electronic spins and the fundamental unit cell are shown.

Therefore, a three-dimensional (3D) antiferromagnetic coupling is formed by ferromagnetic layers in the (100) plane disposed antiparallel between them. This overall antiferromagnetic arrangement is ordered with superexchange interactions between moments of one chromium atom with its six nearest neighbors *via* (PO_4) tetrahedra. The magnetic ordering is similar to that obtained for $Mo(PO_3)_3$. However, the magnetic moments in the Cr metaphosphate are ferromagnetically ordered along the *z* direction in the (010) plane with an angle of 13° over the *x* axis (see Figure 22) whereas in the Mo phase the magnetic moments are along the *x* axis. This different ordering is probably the origin of the small differences observed in the magnetic behavior, where a good fit to a Heisenberg simple cubic antiferromagnetic system (S= 3/2) in the $Cr(PO_3)_3$ phase was not possible. The magnetic structure of $Fe(PO_3)_3$ is qualitatively different with ferromagnetic arrangements along the *x* and *y* directions and antiferromagnetic couplings along the *z* axis.

The thermal evolution of the D1B neutron diffraction patterns from 1.8 to 8.5 K for $Cr(PO_3)_3$ is shown in Figure 23(a). The extra magnetic peaks, which are caused by the antiferromagnetic long-range magnetic ordering in the sample, appear below 5 K. The lower 3D magnetic ordering temperature with respect to the $Fe(PO_3)_3$ metaphosphate ($T_N \cong$ 9 K) could be attributed to the higher spin number in Fe(III) (S= 5/2) than in Cr(III) (S= 3/2). The intensity of the magnetic reflections increases without reaching a maximum at 1.8 K probably due to the low temperature at which the three-dimensional antiferromagnetic ordering appears. The thermal variation of the refined magnetic moments is shown in Figure 23(b).

The M_x refined magnetic components are always higher than those of the M_z components and both curves seem to indicate the presence of a first contribution of the M_x moment near the ordering temperature.

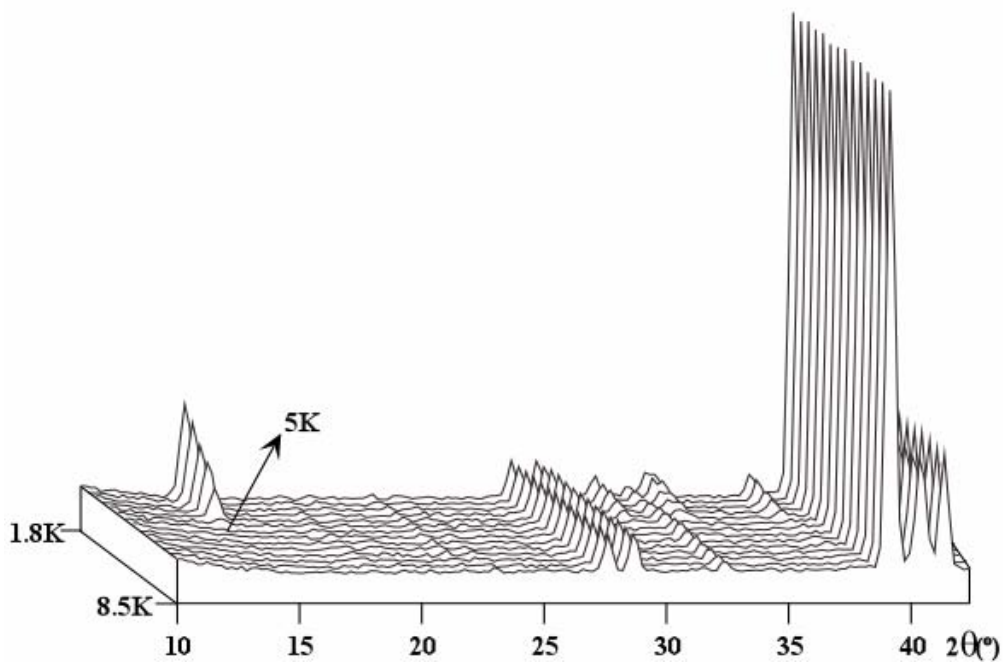

a

Figure 23 (Continued).

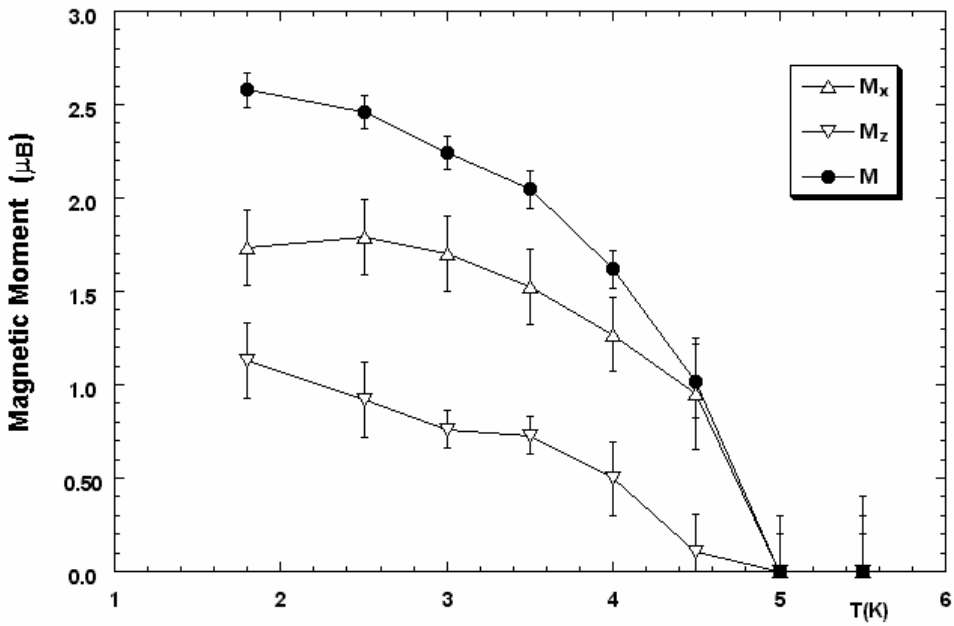

Figure 23. Thermal evolution of (a) the neutron diffraction patterns of $Cr(PO_3)_3$ and (b) the ordered magnetic moments [M, Mx and Mz] in $Cr(PO_3)_3$.

The thermal dependence of the ordered magnetic moments is different from that observed in the $Fe(PO_3)_3$ phase where the overall magnetic moment M, over the whole range of temperatures studied, is always lower than the M_x refined magnetic component although in both phases the *x* direction is the main direction to propagate the exchange interactions *via* (PO_4) tetraedra.

In this way, the presence of three different sites for the metallic ions in the structure is not relevant enough to give rise to local reorientations of the ordered moments and a weak ferromagnetic component is not observed in $M(PO_3)_3$ (M= Cr, Mo). In the $Fe(PO_3)_3$ phase, the competition of the magnetic interactions due to the higher spin number in Fe(III) (S= 5/2) than in Cr(III) (S= 3/2) and its magnetically isotropic behavior, together with the possible frustration between ions in the (100) layers, and the electronic configuration (d^5), are probably responsible for the presence of a weak ferromagnetic component as observed from magnetization measurements.

7.1.2. B-Type $Cr(PO_3)_3$

The magnetic peaks for $Cr_2(P_6O_{18})$ observed at 1.8 K in the D2B neutron diffraction data were indexing using the nuclear cell. In the crystal structure, the magnetic atoms occupy one crystallographic site in a 4e general position of $P2_1/a$ space group, numbered, 1a, 1b, 1c and 1d. The best agreement between the observed and calculated diffraction patterns (see Figure 24) is obtained when the magnetic moments lie in the (100) plane (M_x = 0). The refined magnetic components are M_y = 1.6(2) μ_B and M_z = 1.63(7) μ_B, with a resultant magnetic moment of 2.3(1) μ_B per Cr(III) ion. In the final refinement, the nuclear and magnetic discrepancy factors of $Cr_2(P_6O_{18})$ are R_p = 6.37, R_{wp} = 9.05, χ^2 = 3.92, R_{Bragg} = 10.7 and R_{mag} = 12.5. The value of 2.3(1) μ_B at 1.8 K is lower than that of the experimental Cr(III) ion (3.09

μ_B at 1,8 K) obtained from the magnetic data. This can be attributed to the low ordering temperature (T_N= 2.2 K) observed in this compound.

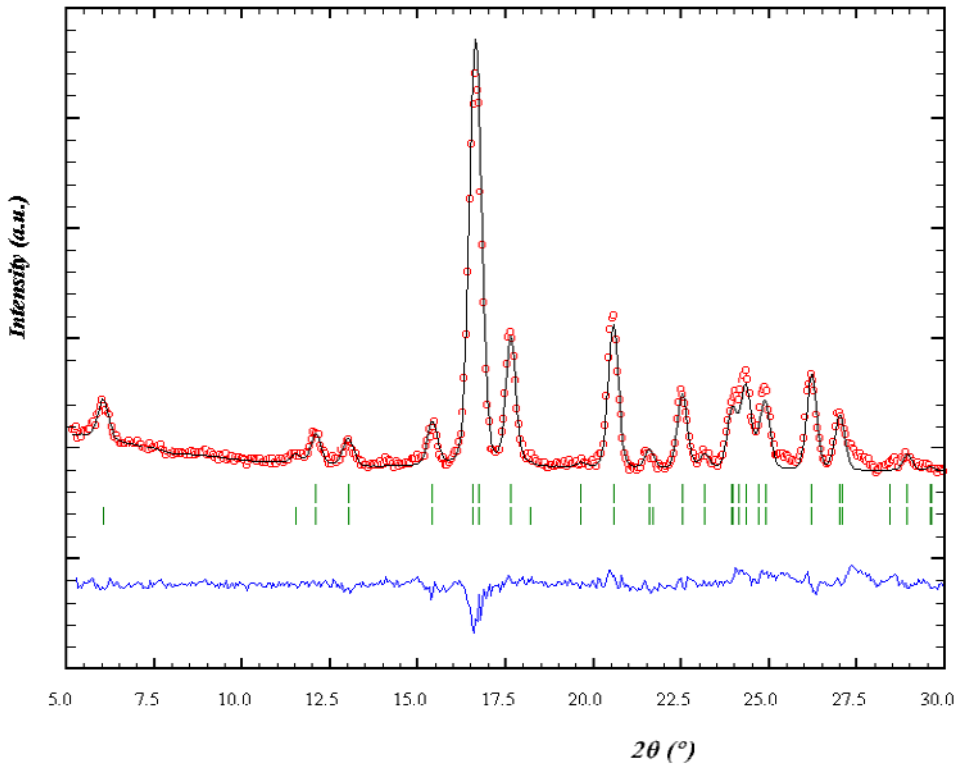

Figure 24. Refinement of the $Cr_2(P_6O_{18})$ neutron diffraction profiles at 1.8 K (the intensity is in arbitrary units. The position of Bragg reflections for the crystallographic (first row) and magnetic (second row) structures are presented. The difference curve is plotted at the botton of the figure.

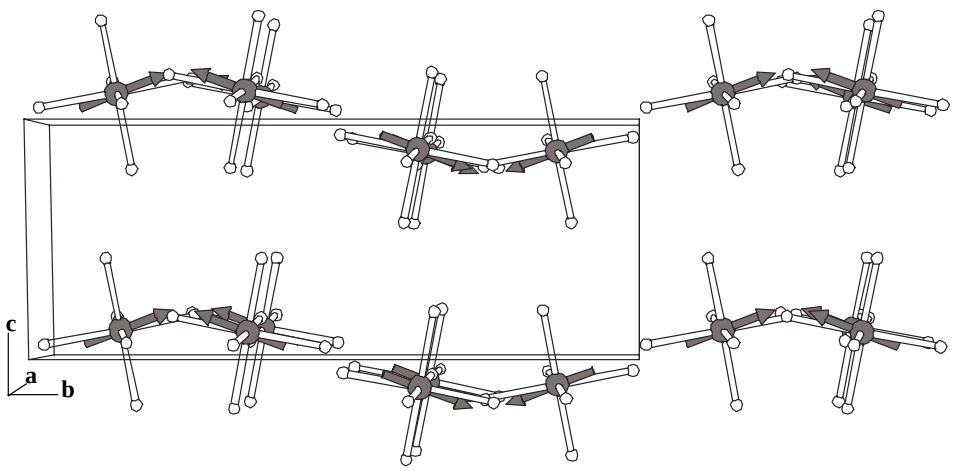

Figure 25. Projection of the magnetic structure of $Cr_2(P_6O_{18})$ onto the a axis. The directions of the electronic spins and the fundamental unit cells are shown.

The magnetic structure of the $Cr_2(P_6O_{18})$ phase is shown in Figure 25 where only the (CrO_6) octahedron and magnetic moments are represented for clarity. The model implies antiferromagnetic arrangements between the magnetic moments stabilising and overall three-dimensional (3D) antiferromagnetic order. The refined moments are aligned in the (100) plane pointing 45.3° from the *z* axis (seee Figure 25). This value induces the weak ferromagnetism detected in the magnetic measurements at low applied fields.

7.2. $M(PO_3)_3$ (M= Mo, Fe) Metaphosphates

The neutron diffraction patterns at 2 K for $M(PO_3)_3$ (M= Mo, Fe) were collected in the D2B powder diffractometer and are represented in Figure 26. The patterns exhibit extra magnetic peaks indicating than both compounds are magnetically ordered at 2 K. The magnetic reflections for the molybdenum metaphosphate exhibit small intensities due to the low ordering magnetic temperature observed in this compound. The thermal evolution of the neutron diffraction patterns for $Fe(PO_3)_3$ was followed in the D1B instrument from 1.5 to 20 K.

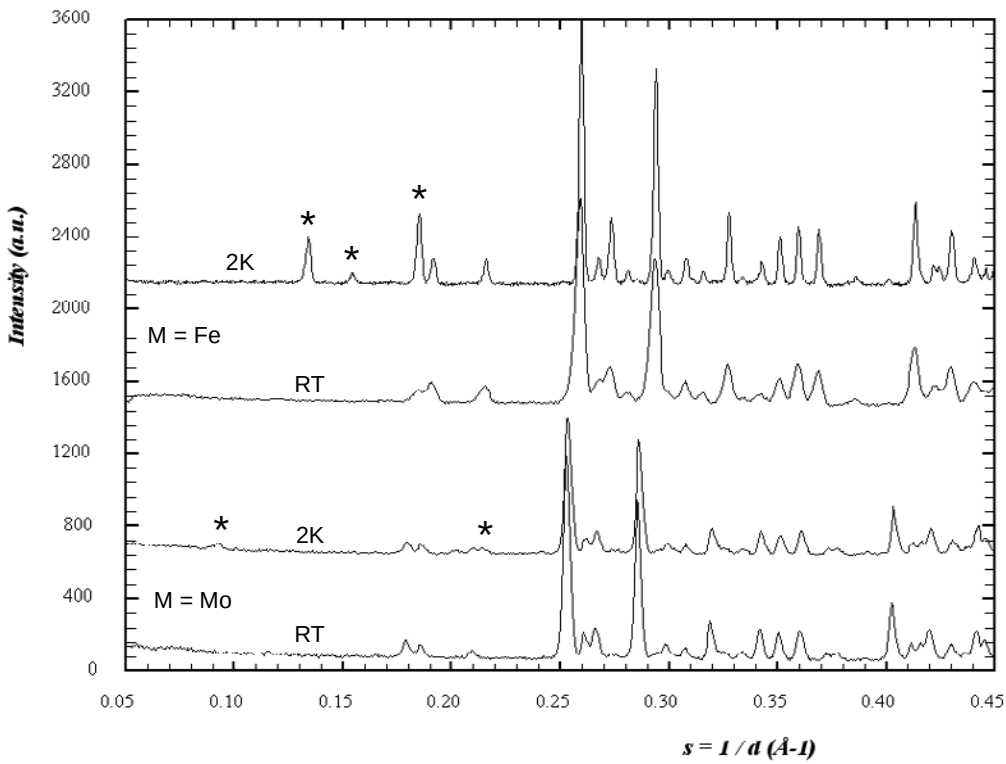

Figure 26. Comparison of D2B neutron diagrams of (a) $Mo(PO_3)_3$ (λ= 1.594 Å) and (b) $Fe(PO_3)_3$ (λ = 2.41 Å), at room temperature and 2 K. The diagrams are shown as a function of the inverse of the d spacing due to the different wavelengths used in the measurements. Magnetic ontribution an also marked.

The results confirm the presence of a three-dimensional magnetic ordering in both phases. Nevertheless, the different positions of the magnetic peaks for both compounds reveal than the magnetic structures are different. All magnetic peaks were indexed with a propagation vector k = (0,0,0) referenced to the room temperature unit cells, indicating that both the magnetic and nuclear lattices are similar.

The possible magnetic structures compatible with the *Ia* (Mo phase) and *Cc* (Fe phase) equivalent space groups have been evaluated with the help of Bertaut's macroscopic theory [53] that allows one determine the constraints imposed by the symmetry of the crystal structure between the orientation of each magnetic moment belonging to the same general crystallographic position. Taking into account the restraints, the different possible orientation of the magnetic moments along the three directions *x*, *y* and *z* were calculated. The agreement between the observed and calculated diffraction patterns for each possible magnetic structure has been tested. The best agreement for both compound was obtained with the component M_y = 0, indicating that the magnetic moments lie in the (010) plane.

The fits of the D2B patterns at 2 K for $M(PO_3)_3$ (M= Mo, Fe) are plotted in Figure 27. For the $Mo(PO_3)_3$ phase the refined magnetic components are M_x = 1.30(9) μ_B and M_z = 1.37(6) μ_B per ion (referenced to the *Ia* unit cell), with a resultant magnetic moment of M = 1.76(6) μ_B per Mo(III) ion, close to that obtained from magnetic measurements (1.78 μ_B at 2 K). The nuclear and magnetic discrepancy factors in the final Rietveld refinements of $Mo(PO_3)_3$ are R_p= 5.69, R_{wp}= 7.17, χ^2= 2.74, R_{Bragg}= 4.57 and R_{mag}= 16.3. For the $Fe(PO_3)_3$ compound, the components of the refined magnetic moments are M_x = 5.26(8) μB and M_z = 2.2(1) μ_B with a resultant magnetic moment per Fe(III) ion of 4.30(6) μ_B. The discrepancy factors of the refinement are R_p = 8.21, R_{wp} = 9.95, χ^2= 5.56, R_{Bragg}= 14.2 and R_{mag}= 16.2. The results for $Fe(PO_3)_3$ are similar to those obtained by Elbouaanani et al. [15] (M= 4.42(3) μ_B). After considering the effects of the covalence in the Fe-O bonds, the ordered moment for a six-coordinated Fe(III) cation should be expected to lie between 3.9 and 4.5 μ_B [56] which is in good agreement with those obtained for other Fe-O-P systems [52,57].

The resulting magnetic structures of $M(PO_3)_3$ (M= Mo, Fe) are shown in Figure 28 where the unit cell is represented in the standard *Cc* space group for comparison (solid lines). In both magnetic structures the moments are overall antiferromagnetically ordered with the spins ferromagnetically disposed along the *y* direction. The main difference between the magnetic structures of both compounds is the orientation of the spins in the *x*, *z* axes. In molybdenum phase, the magnetic moments are ferromagnetically coupled along the *y* and *z* directions whereas those corresponding to the *x* direction are antiparallel aligned [see Figure 28(a)]. However, for $Fe(PO_3)_3$ the magnetic model shows a ferromagmetic arrangement along *y* and *x* directions, with an antiferromagnetic coupling in the *z* axis [see Figure 28(b)]. The components are compensed leading to a three-dimensional (3D) antiferromagnetic ordering than can be described as formed by ferromagnetic layers [in the (100) and (001) planes for the molybdenum and iron metaphosphates, respectively] disposed antiparallel between them. These arrangements imply dominant antiferromagnetic superexchange interactions between moments from one metal atom with its neighbors *via* (PO_4) tetrahedra. However, the models can not be accurate in any details because they do not explain the field dependence of the magnetic susceptibility below 10 K, observed in the iron phase.

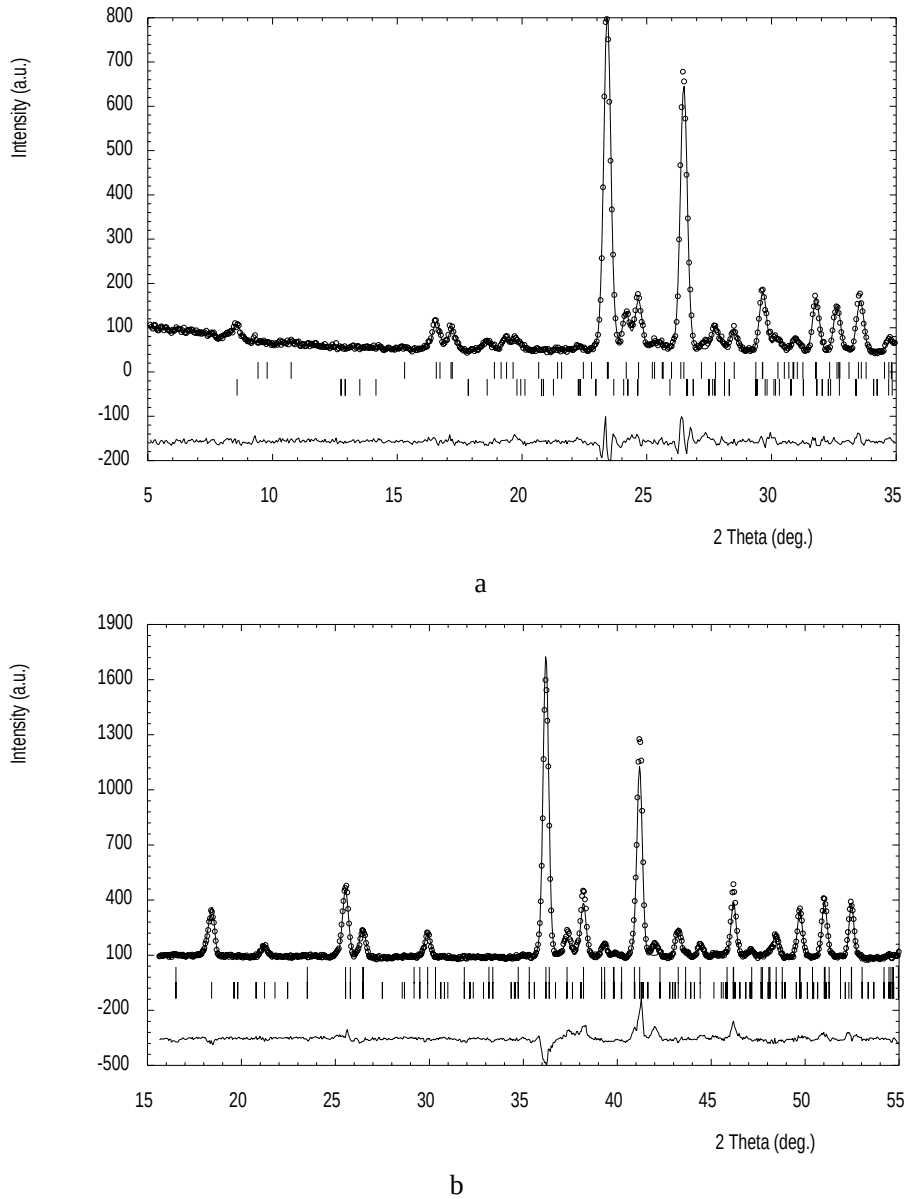

Figure 27. Refinement of D2B neutron diffraction profiles at 2 K of (a) $Mo(PO_3)_3$ (λ= 1.594 Å) and (b) $Fe(PO_3)_3$ (λ = 2.41 Å), The positions of the Bragg reflections for the nuclear (first row) and magnetic (second row) structures are presented. The differences curves are plotted at the botton of the figures.

In order to understand the nature of the magnetic anomalies in the $Fe(PO_3)_3$ metaphosphate, observed in both the magnetization and the specific heat data, a deeper study using neutron diffraction measurements in the 1.5-2.0 K temperature range every 0.5 K was carried out. The thermal evolution of the D1B diffraction patterns is shown in Figure 29(a). The three-dimensional magnetic ordering begins at 9 K, being similar to that obtained from the specific-heat measurements (T_N= 7.8 K).

The intensity of the magnetic reflections continuously increases without reaching saturation probably due to the low temperature at which the magnetic order is established.

The thermal dependence of the ordered magnetic moments is represented in Figure 29(b). The M_x refined magnetic component is always higher than that of the M_z one. At 7.5 K, near the ordering temperature, the ratio M_x/M_z is 2.0. Below 6 K the M_z component undergoes a slight change reaching saturation at 3.5 K. However, the M_x moment continuously increases up to 1.5 K (M_x/M_z = 2.5). This feature does not cause any change in the magnetic structure, but only a slight spin reorientation at low temperature.

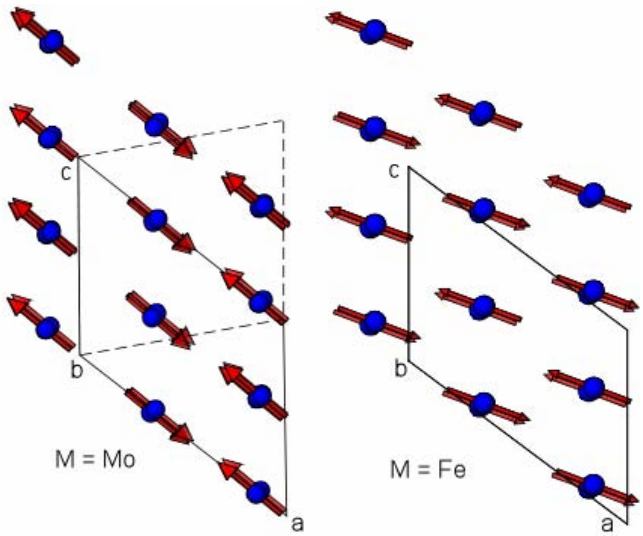

Figure 28. Projection of the magnetic structures in the (010) plane of (a) $Mo(PO_3)_3$ (where dashed lined represents the Ia unit cell) and (b) $Fe(PO_3)_3$. The directions of the electronic spins and the fundamental unit cells in the Cc space group are shown for comparison.

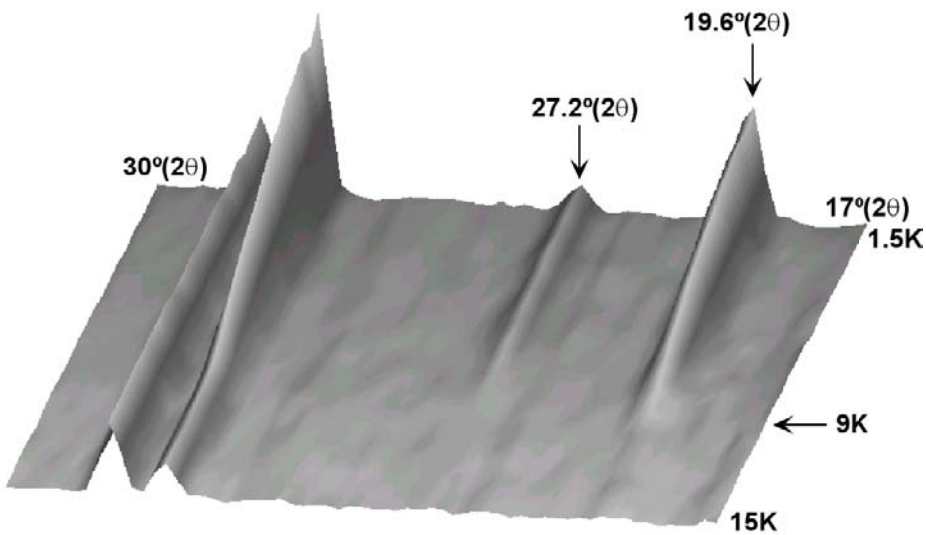

(a)

Figure 29 (Continued).

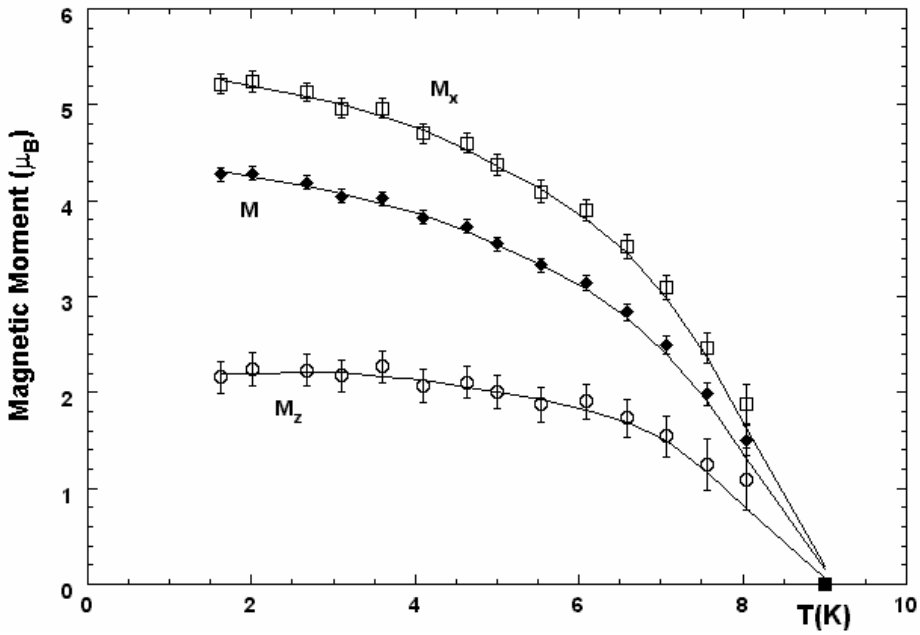

(b)

Figure 29. Thermal evolution of (a) neutron diffraction patterns, and (b) the ordered magnetic moments [M, Mx and Mz] for the $Fe(PO_3)_3$compound.

On the other hand, the neutron diffraction patterns do not show any atypical thermal evolution at temperatures less than T_N = 8 K. Consequently, the magnetic anomalies observed in the specific heat study can not be attributed to the presence of magnetic transitions.

8. MAGNETO-STRUCTURAL CORRELATIONS

The magnetic interactions in the B and C chromium metaphosphates and iron and molybdenum ones are only propagated *via* (PO_4) tetrahedra (Cr-O-P-O-Cr) and can be described as super-superexchange [58] interactions owing to the exchange M-O-M interactions are absent in all the compounds. The super-superexchange magnetic couplings are always antiferromagnetic and are characterized by both the O-P-O angles and the M-O bond lengths. The shorter metal-metal distances range between 5.0 and 6.2 Å (see Table 4) and consequently direct interactions are negligible. The magnetic exchanges are more effective for the shorter M-O distances and for an angle near 109° (tetrahedral angle) [51]. For these compounds, the metal-oxygen distances are approximately 2.0 Å and the O-P-O angles are quite different (110-120°) from those of tetrahedral geometry. In this sense, the weak antiferromagnetic interactions observed in both chromium compounds are a consequence of the large distances between the M(III) ions and the open angles in the M-O-P-O-M pathways.

Schematic views of the most important exchange pathways in the B and C chromium types metaphosphates are given in Figure 30. For $Cr(PO_3)_3$, [see Figure 30(a)] the chromium-chromium interactions principally occur through one and two (PO_4) groups. Nine exchange

pathways involve one phosphate group with the following O-P-O angles: i) Cr(1)-O-P-O-Cr(2) with values of 113 and 120°, respectively; ii) Cr(1)-O-P-O-Cr(3) with 111 and 118° and Cr(2)-O-P-O-Cr(3) with 113 and 114°; iii) finally, the Cr(1)-O-P-O-Cr(1); Cr(2)-O-P-O-Cr(2) and Cr(3)-O-P-O-Cr(3) pathways exhibit angles of 108, 122 and 101°, respectively.

Table 4. Selected geometrical parameters, bond lengths (Å) and angles (°) related to the possible magnetic superexchange pathways for $M(PO_3)_3$ (M^{III}= Mo and Fe) and $Cr_2(P_6O_{18})$

$M(PO_3)_3$	*Direct distance M-M (Å)*	*Length of exchange pathway (Å)*	*Angles (°) M-O-P*	*O-P-O*	*P-O-M*
M(1)-O-P -O-M(3) Mo (AF)	5.58	7.08	149.2(6)	116.0(6)	139.3(6)
(Solid line in Fig. 31) Fe (AF)	5.28	6.94	147.4(4)	116.9(3)	136.7(3)
M(1)-O-P -O-M(3) Mo (AF)	5.94	7.22	138.4(6)	121.1(6)	158.0(7)
(Solid Line) Fe (AF)	5.36	6.95	141.4(3)	117.8(4)	155.7(4)
M(2)-O-P -O-M'(2) Mo (AF)	5.40	7.14	144.4(6)	119.7(6)	154.4(6)
(Solid line) Fe (AF)	5.32	6.89	147.2(4)	120.7(4)	149.5(4)
M(1)-O-P -O-M'(1) Mo (F)	5.75	7.15	139.5(7)	118.1(6)	133.3(5)
(Point line) Fe(AF)	5.57	6.87	147.4(4)	111.4(3)	135.7(3)
M(1)-O-P -O-M(2) Mo (AF)	5.37	7.10	135.4(5)	111.1(5)	140.5(7)
(Point line) Fe (AF)	5.33	6.98	131.6(5)	115.2(2)	140.2(3)
M(1)-O-P -O-M(2) Mo (F)	5.44	7.15	140.5(7)	116.1(5)	142.6(5)
(Point line) Fe (AF)	5.82	7.02	144.5(3)	119.1(2)	142.4(3)
M(2)-O-P -O-M(3) Mo (F)	5.66	7.05	140.2(5)	116.1(5)	139.2(7)
(Dashed line) Fe (AF)	5.55	6.91	138.0(3)	118.1(2)	138.8(3)
M(2)-O-P -O-M(3) Mo (F)	5.89	7.03	144.8(7)	118.9(5)	144.4(5)
(Dashed line) Fe (AF)	5.82	6.92	140.5(3)	115.5(2)	150.1(3)
M(3)-O-P -O-M'(3) Mo (F)	5.97	7.25	140.6(6)	112.1(5)	147.2(5)
(Dashed line) Fe (AF)	5.80	6.93	144.9(3)	119.6(3)	146.9(3)
$Cr_2(P_6O_{18})$					
Cr-O(4)-P(1)-O(5)-Cr	5.36	6.86	147.9(9)	117.9(5)	137.1(8)
Cr-O(6)-P(2)-O(7)-Cr	6.19	6.86	137(1)	117.1(8)	139.2(9)
Cr-O(8)-P(3)-O(9)-Cr	5.01	6.87	135.3(8)	117.3(6)	132.3(7)

As can be deduced all contributions favor weak antiferromagnetic interactions. The Cr-O-P-O-Cr angles being the origin of the overall magnetic behavior, do not show any trend in $Cr(PO_3)_3$. These values are similar to those observed for $Mo(PO_3)_3$. A view of the most important exchange pathways in both iron and molybdenum metaphosphates is given in Figure 31. Solid lines represent connection between (100) layers in the [101] direction (*Cc* setting) with always antiferromagnetic interactions (M= Mo, Fe). The values of the bond distances and angles in the exchange pathways of the chromium and molybdenum phases are clearly different from those of the $Fe(PO_3)_3$ where small magnetic frustration in the (100) layers were observed [15]. This frustration in the layers of $Fe(PO_3)_3$ resulting from the competition between super-superexchange interactions due to the connectivity in the (100) layers are also present (see Figure 31). This fact could explain the presence of a weak ferromagnetic component as was observed from magnetic measurements. These results confirm than the different (MO_6) octahedral geometry together with the electronic configuration of the metal ions are responsible for the magnetic behavior observed in the $M(PO_3)_3$ (M= Cr, Mo, Fe) metaphosphates.

In the case of B-type $Cr_2(P_6O_{18})$ [see Figure 30(b)], the presence of one and two exchange magnetic pathways is also observed. However, the Cr(III) ions are equivalent with a centrosymmetric element simplifying the magnetic pathways in this phase. The Cr-O-P-O-Cr

interactions between only one phosphate group exhibit an O-P-O angle of approximately 117° favoring antiferromagnetic interactions [58] (see Table 4). The Cr-O-P angles show values between 132-148° which are practically similar to those obtained in the $M(PO_3)_3$ (M= Cr, Mo, Fe) metaphosphates.

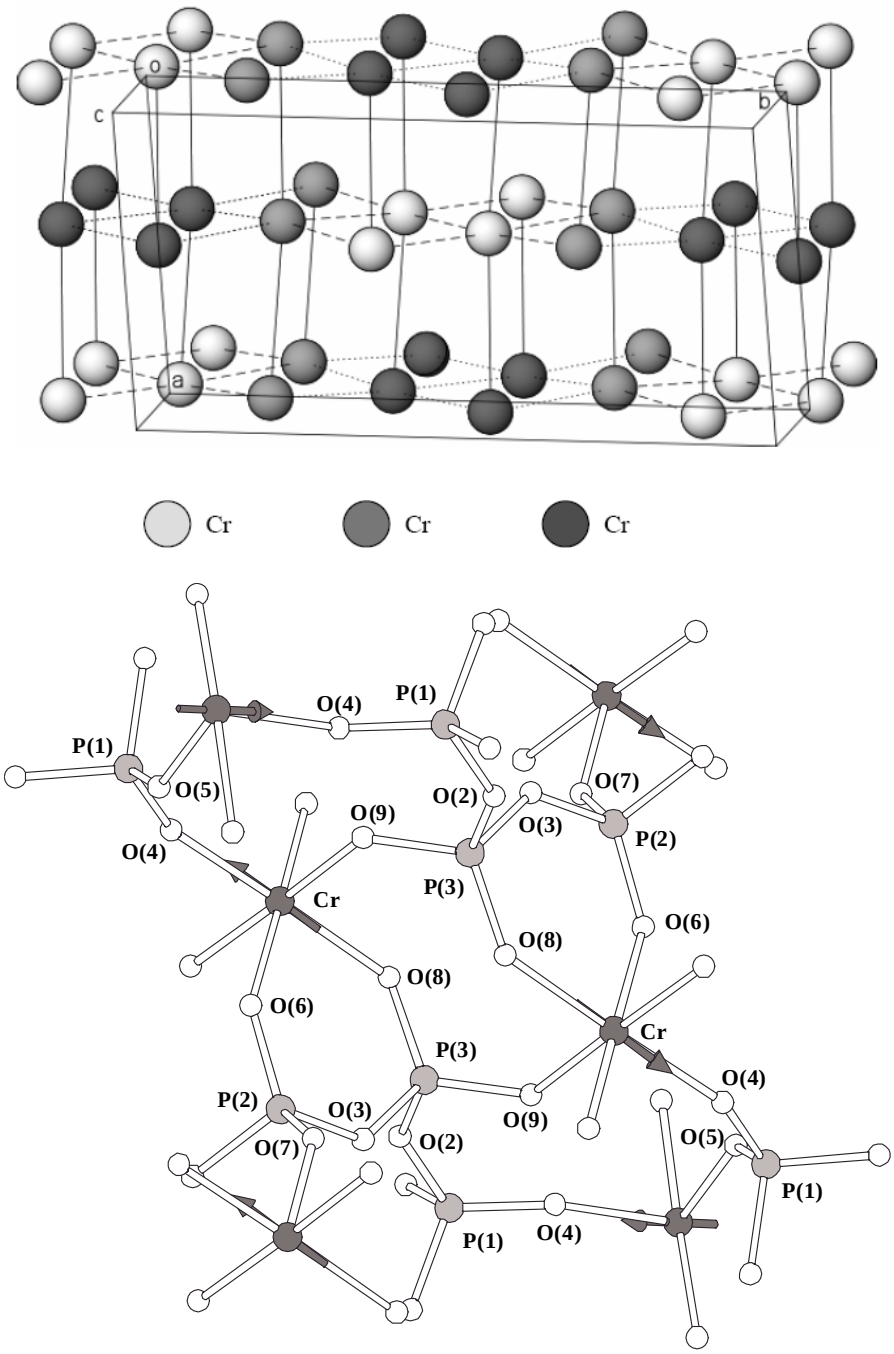

Figure 30. Schematic views of the exchange pathways for (a) $Cr(PO_3)_3$ and (b) $Cr_2(P_6O_{18})$.

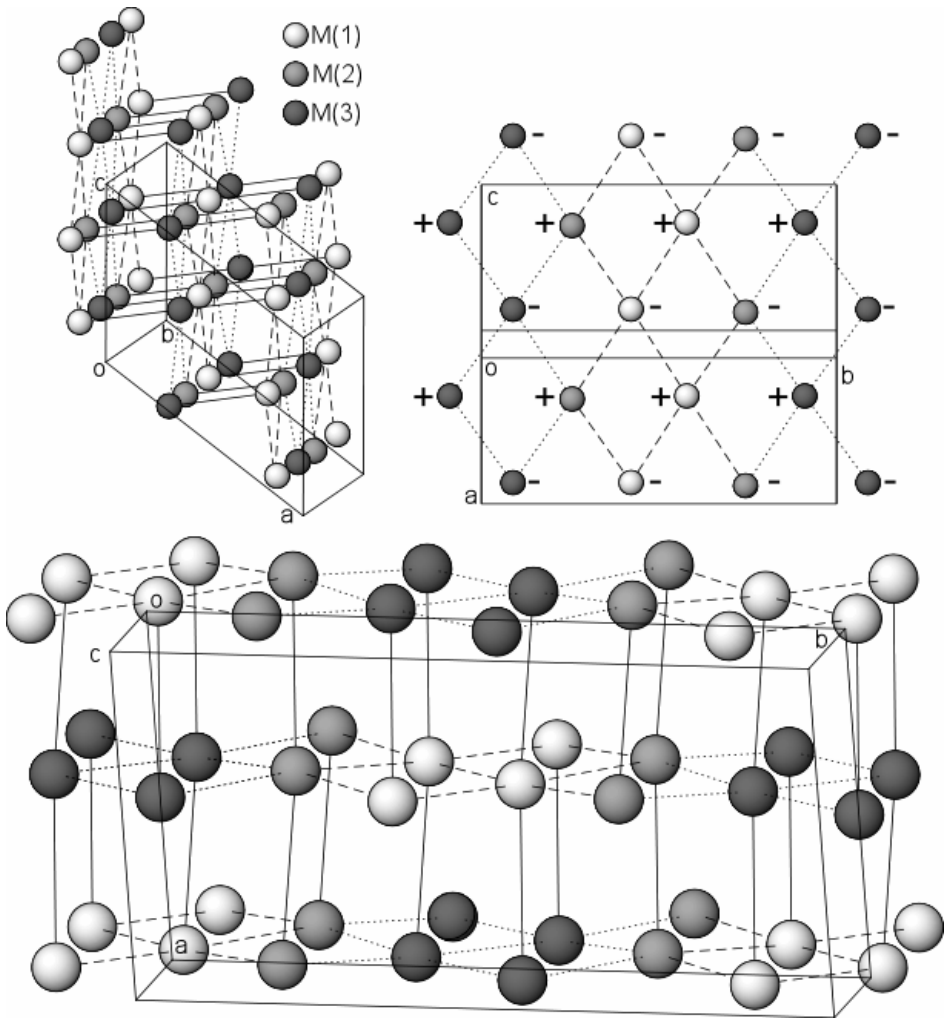

Figure 31. Schematic views of the exchange pathways for $M(PO_3)_3$ (M= Mo and Fe). Exchange through one (PO_4) group only are represented for clarity. Projection of the spin orientation up (+) and down (-) in a layer for $Fe(PO_3)_3$ is shown. In the case of the Mo phase the orientations are equal in each layer exhibiting ferromagnetic arrangements.

These angles are characteristic of antiferromagnetic couplings, being in good agreement with those observed in other phosphates and oxo acids (sulphuric, molydic…) exhibiting these kinds of magnetic interactions [51,54,57]. These types of interactions are observed in other chromium salts such as α-and β-$Cr(XO_4)$ (X= P, As) in which Cr-O-Cr exchange pathways are also present increasing the force of the magnetic interactions [59].

Finally, considering the similar exchange magnetic angles in both B and C type $Cr(PO_3)_3$ metaphosphates, the differences observed in the magnetic behavior of these phases can be explained considering the different packing of both (CrO_6) octahedra and (PO_4) tetrahedra. In this way, the stronger packing (ρ_{exp}= 3.11 gcm^{-3}) of $Cr(PO_3)_3$ [(PO_4) groups disposed in chains] than that of $Cr_2(P_6O_{18})$ in which the (PO_4) tetrahedra are ordered in cycles of six (ρ_{exp}= 2.51 gcm^{-3}) could be responsible for the weaker antiferromagnetic interactions observed in the latter compound as described from the magnetic measurements. On the other

hand, for iron and molybdenum metaphosphates, the higher spin number in Fe(III) (S= 5/2) than in Mo(III) (S= 3/2) and its magnetically isotropic behavior [41] can gives rise to new competing interactions. So, the differences observed in the magnetic behavior of the molybdenum and iron metaphosphates can be attributed to both the slight geometrical differences and the small magnetic frustration in the (MO_6) octahedra together with the electronic configurations in M(III) (d^3) ions with respect to the Fe(III) (d^5) ones. The complexity of the three-dimensional arrangements, the presence of distinct exchange pathways and the existence of nine distinct phosphorous ions make it impossible to find a simple magnetic model to explain the differences in the magnetic behavior observed in these systems.

9. MAGNETOCALORIC EFFECT IN $M(PO_3)_3$ (M= FE, CR AND MO) METAPHOSPHATES

The magnetocaloric effect (MCE) is the heating or the cooling of magnetic materials due to the varying magnetic field. Actually there is a renewed interest in MCE due to its possibilities of application in magnetic refrigeration [60]. In this way, the research in the area of magnetic refrigeration has been concentred in found materials with large magnetocaloric response capable of operating at different temperatures range, depending on the intended application. Hear, we presented the magnetocaloric properties of the $M(PO_3)_3$ metaphosphates (M= Fe, Cr and Mo) studied by means of heat capacity under fields up to 90 KOe. Previous studies of the magnetic properties show that this family orders antiferromagnetically at temperatures closer to the liquefaction of helium one. At zero field, the heat capacity shows a well-defined λ-type anomaly centered at 7.8, 4.2 and 4.1 K for M= Fe, Cr and Mo respectively, which is associated to the presence of long-range magnetic order. With increasing magnetic fields, initially the peak becomes broader and shifts to lower temperatures; confirming the antiferromagnetic character of the transition. However, in the Cr and Mo compounds, at higher field a broad maximum emerges above the Néel temperature indicating a transformation to ferromagnetic behavior. We have found than both the isothermal magnetic entropy (ΔS) and the adiabatic temperature change (ΔT), display a peak around the Néel temperature in the three studied materials. At low fields the MCE is negative ($\Delta S>0$ and $\Delta T< 0$) proving the antiferromagnetic order, however by increasing the field the MCE become positive. In particular, the stronger MCE has been found in $Cr(PO_3)_3$ which exhibits a maximum value of ΔS= -5.4 J/Kmol and ΔT= 11.5 K at $\mu_0 H$= 90 KOe. These values are larger considering the small magnetic moment of the Cr(III) (S= 3/2) and show that $Cr(PO_3)_3$ is a good candidate to be used in magnetic refrigeration at low temperatures.

10. CONLUDING REMARKS

The $M(PO_3)_3$ (M= Ti, V, Cr, Mo and Fe) metaphosphates have been synthesized by the ceramic method at 800 °C in air, except the titanium phase which synthesis required a inert nitrogen atmosphere. The IR spectra show bands characteristic of metaphosphates groups with chain or ring structure, this later observed for the chromium(III) hexametaphosphate.

The diffuse reflectance espectra allowed the assignation of the all electronic bands for every metallic cation. The Dq , B and C parameters were calculated. The ESR spectra were collected at room temperature and at 4.2 K. For the $M(PO_3)_3$ (M= Cr and Mo) the results have been explained on the basis of the existence of more than one different environment for the metallic cations, in accordance with the nuclear crystal structure of this phase. The doped aluminium metaphosphates with Cr(III) and Mo(III) ions indicate the presence of one center with $|D| > h\nu$ and two centers with $|D| < h\nu$. The ESR spectrum of titanium compound has been discussed on the basis of a effective trigonal symmetry, being the g-value 1.97. This one of the vanadium compound exhibits a weak signal attributed to V(IIII) ions, with a zero-field splitting parameter D estimated between 2 and 8 cm^{-1}. For the iron(III) metaphosphate the ESR spectra remains isotropic form RT to 4.2 K, with g= 2.0. Magnetic measurements of the chromium, molybdenum and iron compounds show antiferromagnetic interactions. The J/k exchange parameter has been evaluated for the Cr(III) and Fe(III) metaphosphates using a 3D antiferromagnetic isotropic Heisenberg model. The values obtained are, approximately, 0.3 K. For the $Fe(PO_3)_3$ and $Cr_2(P_6O_{18})$ besides has been found a weak ferromagnetic contribution intrinsic to the sample at low temperature. The Ti(III) is the only metaphosphate for which has been found a ferromagnetic behavior. The magnetic structures of the of the B and C type-$Cr(PO_3)_3$ and $M(PO_3)_3$ (M= Fe, Mo) have been resolved, indicating the existence of predominant antiferromagnetic superexchange couplings propagated *via* (PO_4) tetrahedra. A phenomenon of magnetocaloric effect has been found in the iron, chromium and molybdenum metaphosphates, being the stronger one this observed for the chromium phase, which allows us to consider this phase a good candidate to be used in magnetic refrigeration at low temperatures.

ACKNOWLEDGEMENTS

This work has been financially supported by the “Universidad del País Vasco” (UPV/EHU) (9/UPV00169.310-13494/2001).

REFERENCES

[1] Haushalter, R.C.and Mundi, L.A. *Chem. Mater.* 1992, 4, 31.
[2] Clearfield, A. *Chem. Rev.* 1998, 88, 125.
[3] Weckhuysen, B.M., Schoonheydt, Mabbs, F.E. and Collinson, J. *Chem. Soc, Faraday Trans.* 1996, 92, 24312.
[4] Chen, J.D., Dakka, J., Neeleman, E. and Sheldon, R.A. *J. Chem. Soc. Chem. Commun.* 1993, 1379.
[5] Van de Meer, H. *Acta Crystallogr*., Section B, 1976, 32, 2423.
[6] Domanskii, A.I., Yu. F.,Shepelev, F., Smolin, I. and Litvin, B.N. *Sov. Phys. Crystallogr.* 1982, *27*, 140.
[7] Harrison, W.T.A., Gier, T.E. and Stcky, G. *Acta Crystallogr*. Sect., C, 1994, 50, 1643.
[8] Rittner, P. and Glaum, R., *Z. Kristallogr.* 1994, 209, 162.
[9] Middlemis, N. Hawthorner and Calvo, *Can. J. Chem.* 1877, 55, 1673.

[10] Watson, I.M., Borel, M.M., Charbon, J. and Leclaire, A. *J. Solid State Chem.* 1994, 111, 253.
[11] Remy, P. and Boullé, A. *C. R. Acad. Sci. Paris* 1964, 258, 927.
[12] Remy, P. and Boullé, *Bull. Soc. Chim. Fr.* 1972, 6, 2213.
[13] Gruss, M. and Glaum, R. *Acta Crystallogr*., Sect. C, 1996, 52, 2647.
[14] Bagieu-Beucher, M. and Guitel, J.C. *Acta Crystallogr.*, Sect. B, 1997, 33, 2529.
[15] Elbouaanani, L.K., Malaman, B. and Gerardin, R. *J. Solid State Chem.* 1999, 148, 455.
[16] Rojo, J.M., Mesa, J.L., Lezama, L., Rojo, T., Olazcuaga, R., Guillen, F. *Ann. Chim. Sci. Mat.* 1998, 23, 107.
[17] Rojo, J.M., Mesa, J.L., Lezama, L., Rojo, T. *J. Mater. Chem.* 1997, 7(11), 2243.
[18] Rojo, J.M., Mesa, J.L., Lezama, L., Rojo, T. *J. Solid State Chem.* 1999, 145, 629.
[19] Rojo, J.M., Mesa, J.L., Calvo, R., Lezama, L., Olazcuaga, R., Rojo, T. *J. Mater. Chem.* 1998, 8(6), 423.
[20] Farmer, V. C., *The Infrared Spectra of Minerals*, Mineralogical Society, London, 1974.
[21] Rulmon, A., Cahay, R, Liegois-Duychaersts, M and Tarte, M. *Eur. J. Solid State Inorg. Chem.* 1991, 28, 207.
[22] Bauer, W.H. *Acta Crystallogr.*, Sect. B, 1974, 30, 1195.
[23] Lever, A.B.P., *Inorganic Electronic Spectroscopy*, Elsevier Science Publishers B.V., Amsterdam, Netherlands (1984).
[24] D. Sutton, *Espectros Electrónicos de los Complejos de los Metales de Transición*, Reverté, (1975).
[25] Tofield, B.C., Crane, G.R., Pasteur, G.A and Sherwood, R.C. *J. Chem. Soc. Dalton*, 1975, 1806.
[26] Dallinger, R.F. and Woodruff, W.H. *J. Am. Chem. Soc.* 1997, 99, 1581.
[27] Sugiura, Y. and Hiriyama Y. *J. Am. Chem. Soc.* 1997, 99, 1581.
[28] Weber, M.J., Brawer, S.A. and Degroot, A.J. *Phys. Rev. B*, 1981, 23, 11.
[29] Hipps, K.W. Inorg. Chem. 11989, 19, 1930.
[30] Menil, F., J. *Phys Chem. Solids*, 1985, 46, 763.
[31] Brand, R. A., Lauer, J., Herlach, D. M. *J. Phys. F: Met. Phys*. 1983, 13, 675.
[32] Terminiello, L. and Mercader, R.C. *Hyper Interactions* 1989, 50, 651.
[33] Beltrán-Porter, D., Olazcuaga, R., Fournes, L., Menil, F. and Le Flem, G, *Rev. Phys. Appl.* 1980, 15, 115.
[34] Long, G.J., Cheetham, A.K. and Battle, P.D. *Inorg. Chem.* 1983, 22, 3012.
[35] Abragam, A and Bleany B Electron Paramagnetic Resonance of Transtions Ions, Dover Publications, New York, 1970.
[36] Chiba, Y., Yamagishi, K. and Ohkura H. *Jnp. J. Appl. Phys.* 1988, 27, L1929.
[37] Gourier, D., Colle, L., Lejus. A.M., Vivien, D. and Moncorge, R. *J. Appl. Phys.* 1988, 63, 1144.
[38] Carlin, R., O'Connor, C.J. and Bathia, S.N. *Inorg. Chem.* 1976, 15, 985.
[39] Carlin, R. *Magnetochemistry*, Springer, Berlin, 1986.
[40] Averill, B.A. and Orme-Johnson, W.H. *Inorg. Chem.* 1980, 19, 1702.
[41] Pedersen, E. and Toftlund, H. *Inorg. Chem.* 1974, 13, 1603.
[42] Mabbs, F.E. and Collinson, D. *Electron Paramagnetic Resonance of d Transition Metal Compounds*, Elsevier, Amsterdam, 1992.
[43] Bencini A. and Gatteschi, D. *EPR of Exchange Coupled Systems*, Springer-Verlag, Berlin-Heidelberg, 1990.

[44] Cheung, T.T.P., Soos, Z.G., Dietz, R.E. and Merrit, F.R. *Phys. Pev.* 1978, B17, 1266.
[45] van Vleck, J.H. *The Theory of Electrical and Magnetic Susceptibilities*, Oxford University Press, Oxford 1932.
[46] Rushbrooke, G.S. and Wood, P.J. *Mol. Phys.* 1963, 6, 409.
[47] Hitzfeld, M., Zieman, P., Buckel, W. and Claus, H. *Phys. Rev.* 1984, B29, 5023.
[48] Rojo, J.M.; Pizarro, J.L., Rodríguez-Martínez, L.M., Fernández-Díaz, M.T., Rodríguez-Fernández, J., Arriortua, M.I., Rojo, T. *J. Mater. Chem.* 2004, 14, 992.
[49] Rojo, J.M.; Pizarro, J.L., Rodríguez-Fernández, J., Greneche, J.M., Arriortua, M.I., Fernández- Díaz, M.T., Rojo, T. *J. Mater. Chem.* 2003, 13, 1723.
[50] Kopinga, K., Borm, P.W.M. and De Jonge, W.J.M. *Phys. Rev B* 1974, 10(1), 4690.
[51] Anderson, P.W., *Magnetism*, ed. Rado, G. and Suhl, H. vol. 1, Academia Press, San Diego, 1963.
[52] Forsyth, J.B., Jonson, C.E. and Wilkinson, C *J. Phys. C: Solid State Phys* 1970, 3, 1127.
[53] Bertaut, E.F. *Acta Crystallogr.*, Sect A, 1968, 24, 217.
[54] Battle, P.D., Gibb, T.C., Nixon, S. and Harrinson, W.T.A. *J. Solid State Chem.* 1988, 75, 21.
[55] Attfield, J.P., Battle, P.D., Cheetham, A.K. and Johnson, D.C. *Inorg. Chem.* 1989, 28, 1207.
[56] Battle, P.D., Giba, T.C. and Lightfoot, J. Soli State Chem. 1980, 84, 271.
[57] Riou-Cavellec, M., Riou, D. and Ferey, G. *Inorg. Chim. Acta* 1999, 291, 317.
[58] Mays, J.M. *Phys. Rev.* 1963, 131, 38.
[59] Battle, J.P.D., Cheetham, A.K., Harrison, W.T.A., Pollard, N.J. and Faber *J. Solid State Chem.* 1985, 55, 221; Fanjat, N., Barj, M., Schaerpf, O and Lucazeu, G., *J. Phys. Chem. Solids* 1993, 54, 1515; Yamauchi, T. and Ueda, J. *J. Magn. Magn. Mater.* 1998, 177-181, 705.
[60] Tishin, A.M. and Spichkin, Y.I. *The Magnetocaloric Effects and its Applications*, IOP Publishing Ltd. 2003.

In: Developments in Ceramic Materials Research
Editor: Dena Rosslere, pp. 141-172
ISBN 978-1-60021-770-8

Chapter 5

THE USE OF CERAMIC POTS IN OLD WORSHIP PLACES

Dimitris Skarlatos[1], Tilemachos Zakinthinos[2] and Ioanis Koumanoudis[3]

[1]University of Patras, Greece
[2]University of Patras, Greece
[3]Fellow of N.T.U.A., Greece

ABSTRACT

During the Romanesque and Gothic time, certain churches and mosques were fitted with ceramic pots embedded in the walls or in the ceiling vaults. The purpose of this action was probably related to acoustic problems, since ceramic pots were the only available way to control and adjust the acoustic response of large rooms. Their effectiveness though is still unknown. Research in old orthodox churches in Greece was performed to investigate the kind of ceramic pots used, the way of embedding on the wall and finally their effect based on most of the acoustic indexes used today for the determination of the acoustic quality in a room. The results were compared with other research performed in Churches and Mosques in other countries.

An analysis of the impulse response of closed spaces with and without ceramic pots, which actually are Helmholtz resonators, showed that their effect on the acoustic quality of a room is rather poor. Their effectiveness is restricted mainly to the low frequency region. A selective amplification of sound in the near field of resonators was observed as well as a small attenuation in the reverberant part of the field in the resonant frequency and near a higher overtone. A remarkable increase of Clarity and Definition at resonant frequency was also observed. A computer simulation program, based on energy coupling method between the pots and the room, showed that the number of pots per unit volume is the most important parameter that affects the sound quality.

1. INTRODUCTION

During the Romanesque and Gothic period certain churches and mosques were fitted with ceramic vases [1-10]. The purpose of this action was probably related to acoustic problems in

large rooms, since vases were the only available way to control and adjust the acoustic response of rooms, but their effectiveness is still unknown. If vases were effective, why did their use during the last centuries stop? On the side, why were they found in almost all Europe and western Asia? No text on their function has ever been discovered [3, 4, 5, 8].

An aspect on the use of pots is that some Greek amphitheatres were provided with such resonators in order to produce a sensation of artificial reverberation [11]. Some acousticians, for example Knudsen [12], believed that the vases used, which actually are Helmholtz resonators, acted as sound absorbers. Some others believed that they were used for voice reinforcement [13, 14]. On the other hand, there were others who did not accept the possibility that sound vases can improve the acoustics of a room, and believed in the randomness of the result. This opinion was based on experience and not on scientific conclusions, and therefore was unconvincing.

Bruel wonders why 1000 years later Danes placed vases in their churches [15]. Desarnaulds et al. note that the principal function of the vases was to amplify and make the voice resound, but their utility was always controversial [3, 4].

According to Mijic and Koumanoudis, the resonators in churches were ineffective for three reasons: They were installed in very small churches where the additional absorption is not significant, their resonant frequencies were too low in relation to the frequency content of worship service, and lastly, in most cases there were too few resonators to achieve audible changes in the acoustic response of the church [1, 5]. According to Junger, Helmholtz resonators were used to increase or provide reverberation time of open air theaters in ancient Greece and to shorten low frequency reverberation times in Swedish and Danish churches from the thirteenth century onward [16].

2. HISTORICAL

First reference to the theory of resonators was by Aristotle (384-322 BC). In his book "Problems" Aristotle wonders: "Why is it that if ones buries a large jar or empty pots with a lid on, the building echoes more and also if there is a well or cistern in the house?" (Problems XI, 7-10) [17]. Aristotle answered his own question by adopting the theory that the contribution of the vases to the acoustics of the rooms was mainly due to the restricted volume of air in them and the compact texture of walls of the jars or vases, since concave shapes resound more.

Vitruvius (80-25 B.C.), in his well-known work "De Architectura," proposed putting bronze vases in special places of the Roman theaters. In book V Vitruvius wrote: "…*On this principle of arrangement, the voice, uttered from the stage as from a centre, and spreading and striking against the cavities of the different vessels, as it comes in contact with them, will be increased in clearness of sound, and will wake an harmonious note in unison with itself…" Vitruvius book V Ch V.3* [18]. This means that although Vitruvius, in order to name metallic or clay vases used the Greek word "echea" which simply means sounders, the purpose of Vitruvius' vases was probably not the amplification of sound but the improvement of sound quality. The vases according to his descriptions were placed in such a way in specially shaped cavities of the landing or landings of ancient theatres (see Figure 1).

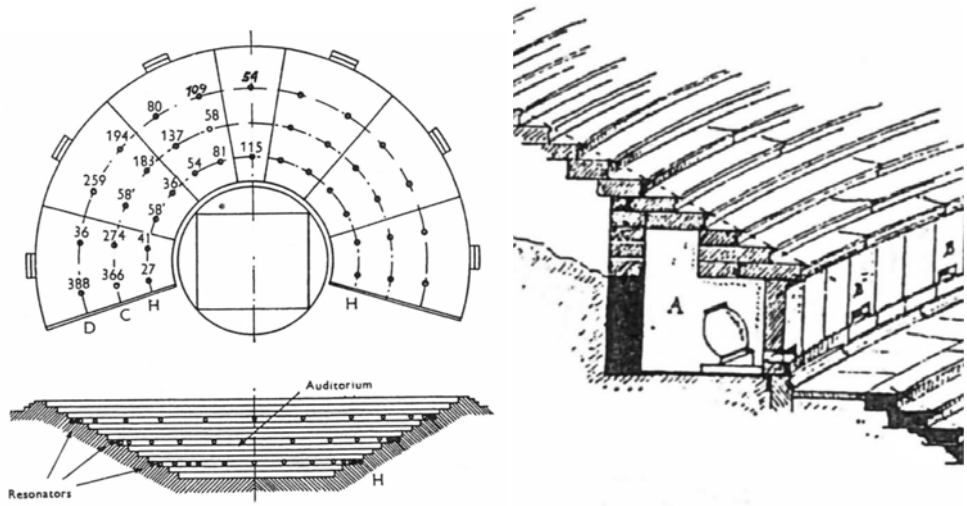

Figure 1. The arrangement of resonators in a Greek open theatre according to Vitruvius After Drum [19].

This credible theory of Vitruvius was never corroborated by archaeologists as no sound vessels or cavities were ever discovered in ancient theatres. The information that some of ancient Greek theatres were supplied with vases come from Vitruvius:"*If, however, it is asked in what theatre these vessels have been employed, we cannot point to any in Rome itself, but only to those in the districts of Italy and in a good many Greek states. We have also the evidence of Lucius Mummius, who, after destroying the theatre in Corinth, brought its bronze vessels to Rome, and made a dedicatory offering at the temple of Luna with the money obtained from the sale of them. Besides, many skilful architects, in constructing theatres in small towns, have, for lack of means, taken large jars made of clay, but similarly resonant, and have produced very advantageous results by arranging them on the principles described.*" *Book V Ch V.8* [18].

It is well-known that Vitruvius' work had a great influence on Europe for centuries and especially on the issue of sound vases. Many West European researchers of the past centuries who studied old monuments of their countries and found walled-in vases belonging to the category of sound vases, interpreted their presence and purpose based mainly on Vitruvius.

The existence of concave ceramic vases, of various shapes and sizes, has been established inside the mass of the walls and domes of many Christian temples in the Greek territory, dating from the Early Christian, Byzantine and Post-Byzantine eras. They can be divided into two categories.

In the first category belong the so called structural vases. Some of the vases of this category are not visible and can only be identified, after careful inspection of the interior surfaces of the walls and domes of the temples.

This group of walled-in vases, can be urn-shaped, spherical or tubular, and can usually be discovered in cases of restoration work, or when we look into some destroyed churches. These vases are generally located in cylindrical or spherical domes and in areas with large concentrations of inert building material, such as dome crests, in heat-insulating chambers, or when low protruding domes are turned to a horizontal chamber (through weight reduction or

collection of rain water), or for other purposes, such as the drawing out of smoke and the ventilation of fires, water pipes, under-burners, in fireplaces, etc [20].

The appearance of walled-in "structural vases" draws its origin from the Lombards or Campanians and then from the Romans [21]. It was later adopted by the Byzantines and went on to be applied during and after the Middle Ages (figure 2b) [22]. It is not an exaggeration to mention that the use of concave structural elements continued much later during the age of concrete. In France, for instance, the concrete dome of the market of Vallées á la Carenne-Colombes includes concave structural pipes, as in other modern structures (figure 2c) [23].

The second group of walled-in vases, the acoustic vases or sound vases, are coupled acoustically with the interior of the church through an opening. Sometimes this opening is not easily observed since it was covered with mortar during restoration work [1, 5, 10].

Architectural history tells us of the spreading of ceramic vases from the early Byzantine techniques (only on the niche domes of the sanctuary of Early Christian Basilicas with wooden roofs) and then in a multitude of dispersed temple dome roofs of this period, as in Ravenna of Italy (e.g. Ursiana Basilica, St. Vitali church, Neognano Baptismal, [24 - 26] with spherical domes built with tube-like vases), in Constantinople (e.g. the church of Saint Sofia and Saints Sergio and Bacchus, the Magganians' Palace, 8th century A.D., etc.[27], domes with tube-like and pot-like vases) and also in Greece (e.g. Scripou, 9th century, Saint Lucas in Steiri, 11th century, Agioi Asomatoi Theseion, 11th century [28], Parigoritissa Artas, 13th century [29], Afentiko Mystra, 14th century [29], and Porta Panagia Artas, with inert material masses along with pot-like vases). At this point, it is necessary to mention that ceramic vases have also been found in Syria, Algeria, Tunisia, Chaldea, and even in India [21, 30]. After the Renaissance, walled-in vases were found in walls and domes in many European countries such as: France (e.g. in Palais de Justice, Palais Royal, Bource, Madlein and a multitude of other buildings of the 18th century), in England (e.g. in the Dover House, the London Stock Market, 18th century, and in St. George's Hall of Liverpool, 19th century), in Russia (e.g. Saint Sophia of Kiev, Moscow's Kremlin, etc.) and finally in Spain and Cyprus [31, 32].

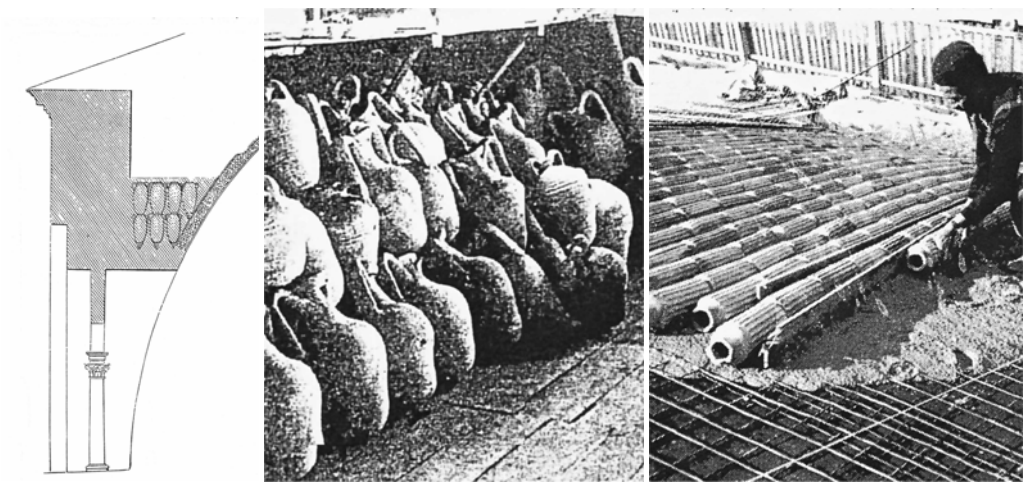

a b c

Figure 2. Structural vases found in Ravena St Vistule (a) in Constantinople (b) and in the market of Vallées á la Carenne-Colombes (c).

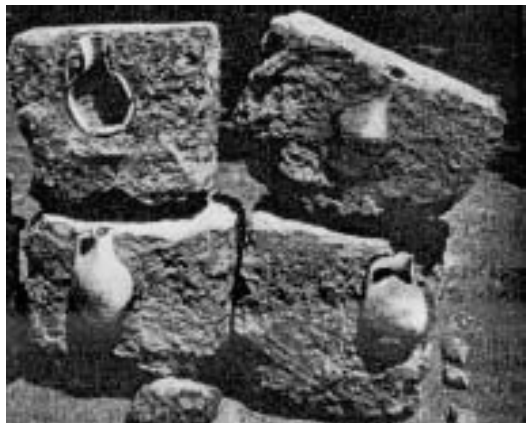

Figure 3. Acoustic walled in vases (after Desarnaults) [3].

Byzantine or Medieval texts made no mention of the system of walling-in sound vases for acoustic purposes, despite the contemporary spreading out of them in churches, not only in Greece, but also in the whole of Europe and elsewhere.

The names usually used for sound vases found in churches are vases, pots, and jars. In Greek tradition there are many names for walled-in acoustic vases, like Vaza, Vikia, Kanatakia, Clinikia, Stamnes and finally Antiphonites. Only the last name, Antiphonites (resounders), characterizes the purpose of the vases, whereas the others merely describe, with local terminology, the shape of the vessel. Besides, priests, monks and caretakers of the churches had no knowledge of the purpose of the sound vessels, while most of them knew of the walling-in of sound vessels for acoustic purposes. They believed then, without doubt, that the sound vases were the means of strengthening the voice of priests or cantors, because the sound vases "made the church resound", hence the name of the resounders. Obviously, they had no understanding of the acoustic requirements of the area of a church, which was not supposed to resound. Furthermore, a few of them accepted certain cabalistic interpretations, completely unfounded, but quite interesting for being so imaginative. In the end, there are many points in common between Greek tradition and the tradition of other European peoples, with a prevalent aspect being the acoustic purpose.

The influence of Vitruvius in Europe on architectural studies and knowledge was catalytic at least until 1829 when H. Bulle questioned the sound vases of ancient theatres and the theory of Vitruvius, for having based it on the groundless theory of music harmony of Aristoxenos of Tarantos [33]. Nevertheless there are some differences between the description of Vitruvius vases and those found in worship places. These differences are: the vases were located in the interior of closed spaces, they were not bronze, but ceramic, they were placed far from the auditor's ear and finally they were almost always surrounded by masonry. The fact that vases were encountered only in churches and not in palaces or castles is an indication that they were used for acoustic purposes. Crunelle [8] points out an historic curiosity: Almost everything is known about the resonators of the Roman era thanks to the text of Vitruvius, although not a single vase has been found; on the other hand, we possess many examples of medieval acoustic pottery, yet no text on their function has ever been discovered. Rene Floriot has shown that they are above all correctors of acoustics [8].

Some acousticians, based on the theory of Vitruvius and of Helmholtz, dealt properly with the issue of the effectiveness of the sound vases, e.g. H.Bagenal, V.Knudsen,

G.M.Harris, P.Bruel and others. The studies of R. Floriot, J.M. Fontaine, Y. Loerinck, V. Papathanasopoulos and other researchers on the sound vases of European churches are very significant [34].

Greek researchers have based their opinions on tradition and have interpreted the presence of the sound vases "for the improvement of acoustics, or for acoustic reasons, or for sound amplification, or as an acoustic tradition, and at the same time for lightening purposes, etc." Unfortunately, none of them has dealt extensively with it, because they referred to the matter only after the discovery of some new findings (sound vases), and never made any retrospective research of them with other countries in order to compare.

The matter was never examined spherically, because the known examples were sporadic and random.

A limited number of them believe that the sound vases are a continuation of the (non-existent) sound vases of Vitruvius, others believe that they come vaguely from the East or Byzantium or both – two or three of them believe that the sound vases originated from Denmark or Scandinavia, i.e. their home countries, perhaps due to lack of information.

3. SOUND VESSELS IN WORSHIP PLACES

3.1. Shapes of Sound Vessels

In Europe the vases used were either specially manufactured or else vases of ordinary domestic type, greatly varying in shape. Most of them were between 20 cm and 30 cm in length and 13 -15 cm wide at the mouth [27] In Anatolia the vases found in Mosques designed by Sinan (Ottoman architecture) had smaller openings. In the dome of Blue Mosque, for example, two groups of terracotta vases were found. The first group had small openings with a radius of 1.5 cm and the second group wider openings with a radius of 6 cm. Their length, including the neck, was about 50 cm [9].

The vases found in Greek churches can be listed into 3 different categories: a) Spherical (approximately), the number of which is 909, making up 93.9%, b) tube-like, with or without bottom, which are 22 and making up 23% and c) the various shapes of cavities, numbering 38 and making up 3.8% of the total of sound vases [5, 6].

All vases found in Greece, regardless of shape are made entirely of clay, usually of a red mass with a visible mixture of a sandy material. Sometimes the clay has the colour of ash. On the inner surface of the walls of the vessels, the fingerprints of the potter are evident. We can also discern evidence of the successive circles imprinted on the walls of the vases, vertical to the main axis of them, proving that these had been manufactured with the traditional method of the potter's wheel. The firing and tempering of the clay varies from vase to vase, since the glazing of the interior is generally absent. A coloured glazing decoration was observed on the outside wall of certain vases, e.g. Aegina (figure 4a) or Arta along with an engraving on the perimeter with decorative patterns. This observation proves that the engraving of the patterns was made on damp clay followed by the colouring. Figure 4 shows the shapes of vases found in Greek churches in island of Aegina (a, b) in Viotia (c) in Attica (d) and on the island of Salamis. Figure 5 shows some of the vases found in European countries: in France (a) [35], in England (b) [36], in Denmark (c) [37] and in Switzerland (d) [38].

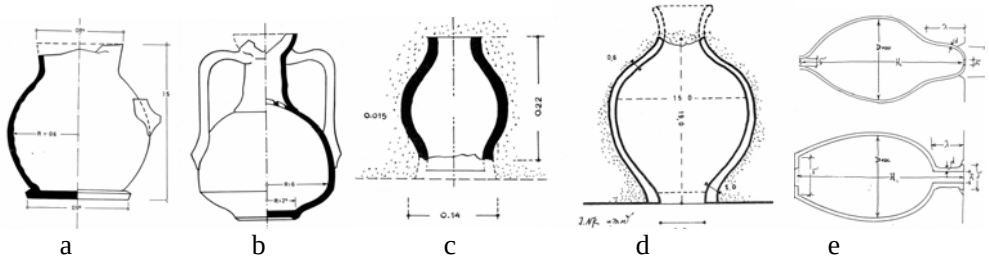

Figure 4. Shapes of sound vases found in Greece.

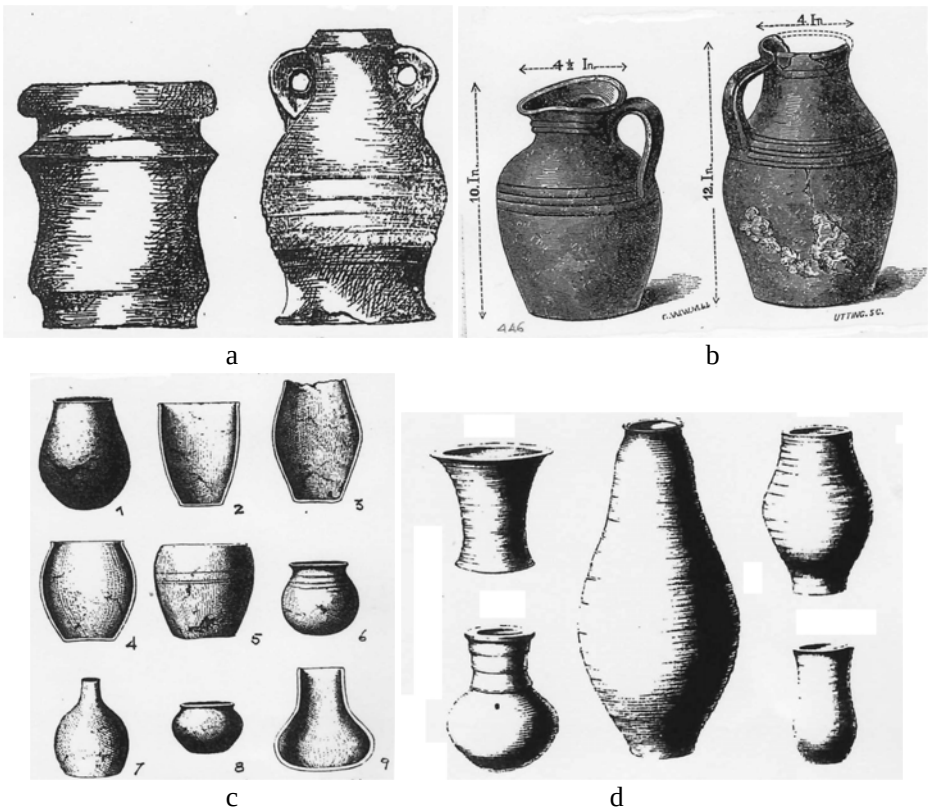

Figure 5. Shapes of vases found in Churches in Europe.

In some Greek churches the sound vases were not of the same size or shape, a fact which proves that there was no particular size of clay vase that was being systematically used as a "sound vase". Acoustically, these differences lead to various results, if we were to accept the positive contribution of the sound vases. This leads to the conclusion that the sound vases of the churches were ordinary household vases and were not manufactured especially for this purpose. It is not known how they were collected. Probably they came from a collection of donations, or from offerings of believers, because they were costly. The limits within which the various basic dimensions of the spherical or tubular sound vessels found in Greece, is shown in table 1 [4] (the letters correspond to figure 6b).

Table 1. Dimensions of spherical or tubular Vessels (cm)

δ1	1-24	D_{max}	30-90	H	10-55
δ′	1-20	Δ	6-14	H1	14.5-50
δ	2-11	d	0.4-2	λ	1-10
Δ1	3-16	d’	0.8-1.5		

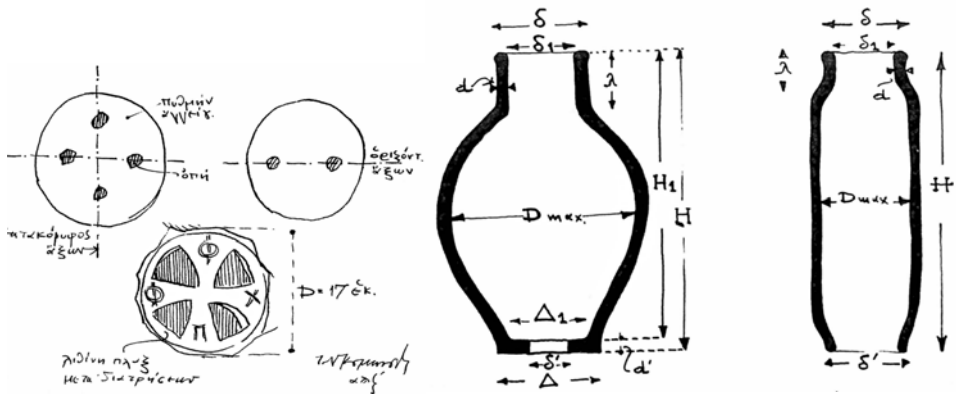

Figure 6. Vases with rare hole arrangement on its base (a) up, Stone with decorative opening placed on the vase opening (a) down, Cross sectionsof typical spherical & tubular Greek vases (b) [4].

Spherical vases are either with or without a neck, or they are shaped as a jar, a jug, a pot or an urn, i.e. they are the ordinary clay vessels of the era. The tubular vases are sometimes clay pipes (known also as quarter wavelength resonators) and sometimes cylindrical vessels. It must be noted that in contrast with the Helmholtz resonator whose feature is its resonant frequency for which the wavelength is considerably greater than its dimensions, the length of quarter- wavelength resonator assembly has a size that is comparable to the wavelengths on its resonance [2]. In some churches instead of vases, cavities in the wall were found (see figure 7b). The cavities in the buildings were either formed during construction, or came from the combination of a structural cavity and a vase, or a cavity formed and then blanked off using a perforated slab, for the reduction of the cross section and for decoration.

a b

Figure 7. Resonators in Agios Stefanos, Meteora Greece (a) and Uncovered cavities in the church of St Nicolas of Platani, Patras, Greece (11th Century Church). The cavities were partially filled afterwards (b).

3.2. Wall-in Positions

The method of use of medieval acoustic vases in Western Europe may be summarized as follows: a) Areas of spaced vases in two or three rows inserted in stone walls of the interior above ground level usually 2.5 m from the floor with their mouths opening inwards to the nave or choir (e.g. St Clement's, Kent). b) A single or double row of vases inserted in the stone walls just bellow the ceiling, trusses or vault, often extending down the full length of both side walls (e.g. St Nicolas, Leeds). c) At regular intervals across the stone barrel vaulting of the choir (St Martin, Angers) d) In the sleeper walls bellow the choir stalls or in pits or cavities (e.g. St Peter Mancroft, Norwich) [27].

The most common positions where the vases were found in Greek orthodox Churches are: a) Dome crests. b) Niche crests. c) Bases of cylindrical domes and occasionally in the inside part of the dome, d) Occasionally on the panel of the dome, e) Panels of antennas of cross-shaped buildings, f) Cylindrical walls of triple-aisle churches, g) Irregularly positioned in walls and occasionally in other kinds of domes [6]. A general observation is that, depending on the architectural type of the church, a similar walling-in technique is maintained, but the number of sound vases varies.

3.3. Ways of Walling-in

In Greece the following walling-in rules were followed systematically – regardless of the period – with a very few, rare deviations [5].

Case a. With the spout-top of the vases facing the area of the temple: 65.8%.

Case b. With a perforated bottom facing the area of the church: 32.7%.

A percentage of 1.5%, cannot be determined due to their position.

The main axis of the vases is arranged vertically towards the wall surface and the opening of the vase is on the same level with the plaster or directly below its thickness, usually visible. When we have perforation of the bottom, the hole can have various shapes.

Mijic et al. discovered that only in a wooden church in Serbia, where vases have been found, were they not build into the wall but instead were hanging freely in the attic space [1].

According to Kayili the resonators in Mosques were installed at the corners of joining walls and ceiling, where critical points for normal modes of rooms are, especially for oblique modes. [9, 10].

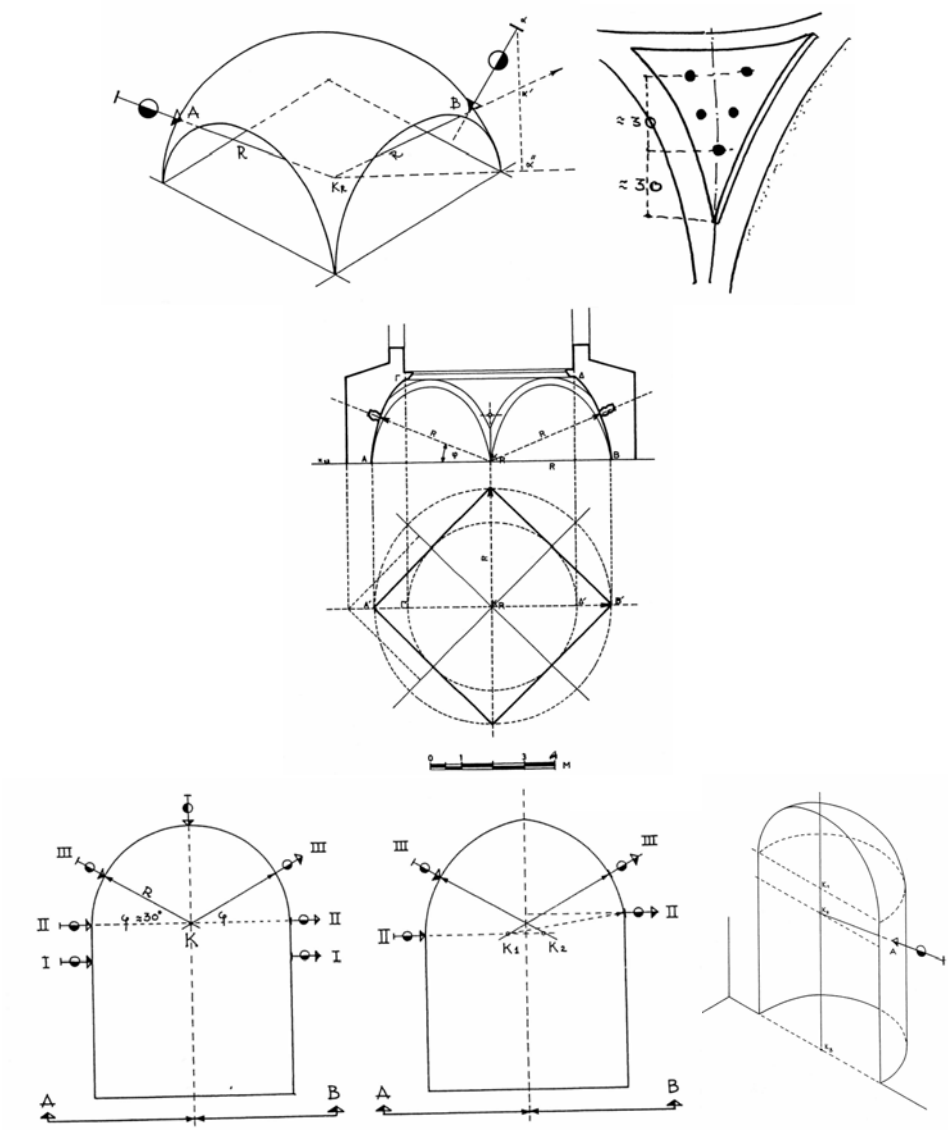

Figure 8. Wall in positions of sound vessels.

The perforating seems to have been made before the walling-in. In cylindrical or spherical surfaces, the axis of the vase is arranged in the same direction of the radius of the cylinder or of the sphere of the wall surface. An exception is observed when the vase is placed with its main axis facing upwards, in which case a hole is opened at the side of its volume. One might ask why this arrangement. At this point it is important to stress that the shape of the aperture of the sound vessel affects its acoustical performance.

In Europe some of the vases with large mouths were often reduced in aperture by being placed behind perforated stone or wooden screens or partly plugged with a wooden block (e.g. Denford Northamptonshire, St Mary-le-Tower Ipswich) [27, 16]. According to Bruel in some cases in Scandinavian churches, additional frictional resistance was provided by

inserting peat soil or ashes in the resonator's cavity. Bagenal mentions that such resonators were also found in medieval English Churches (see figure 9) [16].

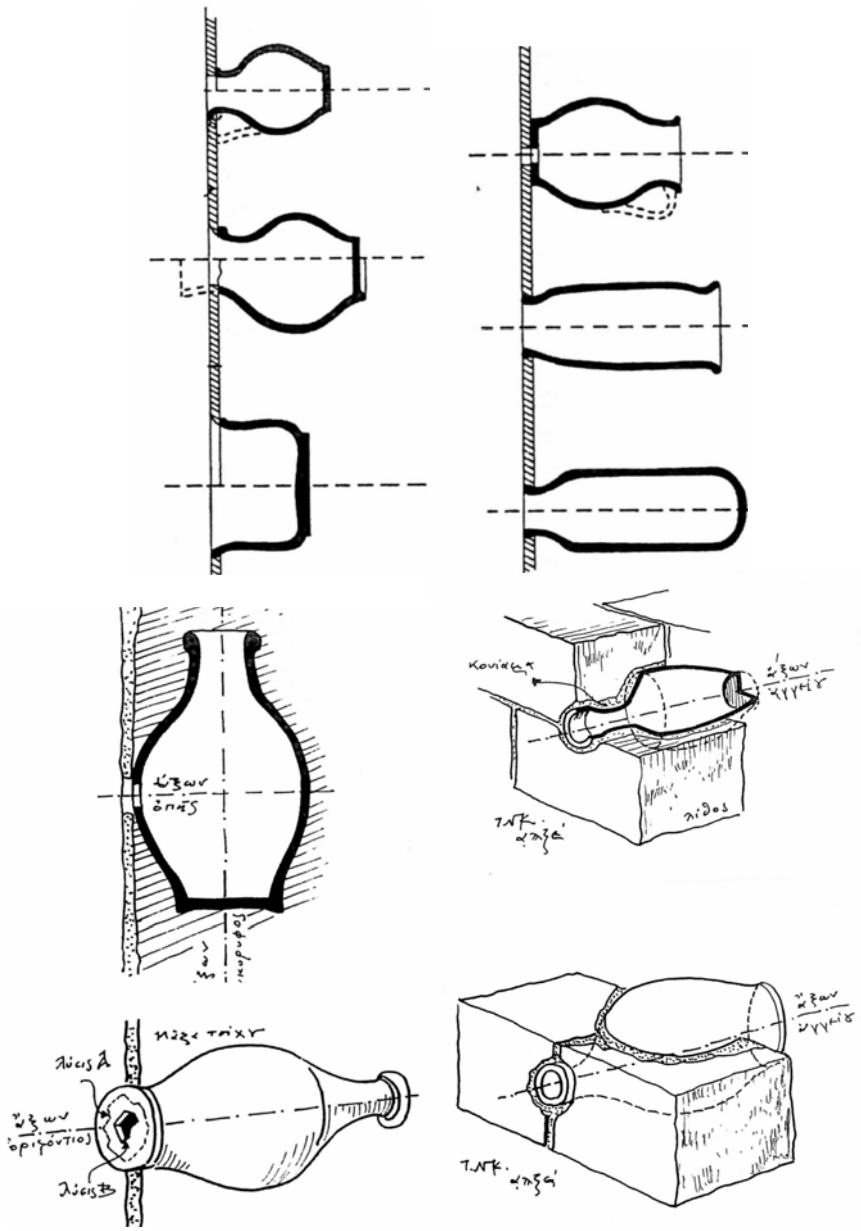

Figure 9. Arrangement of wall in vases.

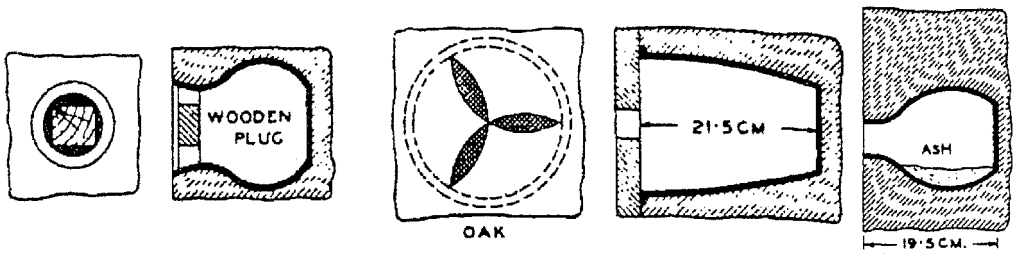

Figure 10. Pots in medieval Scandinavian churches: Plugged vases (a, b) and vase partially filled with ash.

3.4. Resonant Frequencies of Vases

The resonant frequencies of vases depend on their geometry. Measurements of Mijic et al. showed that the resonant frequencies of resonators, found in Serbian Orthodox churches, are within the range of 55.5 – 131 Hz. [2]. Measurements of Carvalho et al. in vases found in Middle Age Churches in Switzerland and other countries, showed that their resonant frequencies are within the range of 237- 444 Hz [7]. The resonant frequency of pots found in the church of St. Andrews in UK is between 350-470 Hz [39]. Kayili estimated the resonant frequencies of pots found in Blue Mosque as follows: pots with small opening, between 100 and 120 Hz and of pots with large opening between 180-200 Hz. [9]. The resonant frequency of vases found in Greece was estimated to be between 131 and 447 Hz.

3.5. Number of Resonators Found in Places of Worship

In some places of worship it is impossible to determine the number of built-in resonators. Some of them were covered by mortar during restoration work and in others parts of the walls were missing. Generally, with some exceptions, the number of resonators found in places of worship is usually small, inadequate to affect the acoustics of large spaces. The Villete church located in Switzerland contains only 4 resonators and the Syens Church has 5 [4]. According to Mijic [1] the greatest number of resonators found in a single church, is 24. Kayili [10] found 144 resonators in Shehzade Mehmet Mosque, and 75 at the dome of the Blue mosque. According to the same researcher, it is written in the building records of Suleymaniye Mosque that 255 small jars have been bought and installed. Also the same researcher found at Sokuullu Pasha Mosque, traces of holes believed to be the openings of resonators. There were thirty six holes in the main dome and 42 to 45 in each of the quarter domes. In Bolognia the cathedral of St. Pedronio, according to Crunell, contains more than four hundred resonators and St. Ietro only twenty five [8]. St Andrews church in UK has a total of 23 vases placed in the Chancel and the walls [Murphy]. Koumanoudis in 10 years of research has visited and studied about 2,500 buildings (churches and monasteries) and found, in 168 of these buildings, 1,057 walled-in vases. Out of these 147 were churches with 969 walled-in sound vases, which correspond to an average number of 7 vases per church [5].

3.6. Architectural types of Greek orthodox churches with pots

In Greek Ecclesiastical architecture, the existence of a great number of architectural types of churches with vases has been confirmed. The different architectural types found, depend on the geographical region (e.g. Islands – Peloponnesus – Mainland Greece). The location of the pots according to the architectural type of church is listed below:

a.1. *Cross-shaped churches (inscribed in general).* Vases are found as a rule on the crests or the bucklers of crests of corner spaces. They are also found on sidewalls and occasionally on the panel of domes.

a.2. *Single aisled Basilicas.* As a rule, the vases are situated on the long sides close or above the bases of the covering dome and occasionally in the dome. On wooden-roofed or flat-roofed basilicas, the vases are situated high on various linear locations.

a.3. *Triple Dome Basilicas*- Vases found in various positions, in perimeter walls, or in the partitions of the sanctuary, and on the crests of the dome.

a.4. *Cross-shaped churches inscribed after the folded transverse antennas of the cross.* The vases are mainly found on the crests of the central dome and close to or along the base of the antennas facing the east or the west. They are also situated on the panels of the North and South parts.

a.5. *Triple- aisle alcove churches in general*- The vases are mainly situated on the crests of the central dome, or even on the secondary walls – if any exist – and occasionally on the lateral walls, or on the cylindrical surfaces of the cylindrical niches, or near the bases of the cylindrical domes.

a.6. *Cross-shaped dome churches*- The vases that were observed were on the long sides and on the walls, on which the transverse chamber is based. Occasionally there are vases on the wall or on the dome of the sanctuary.

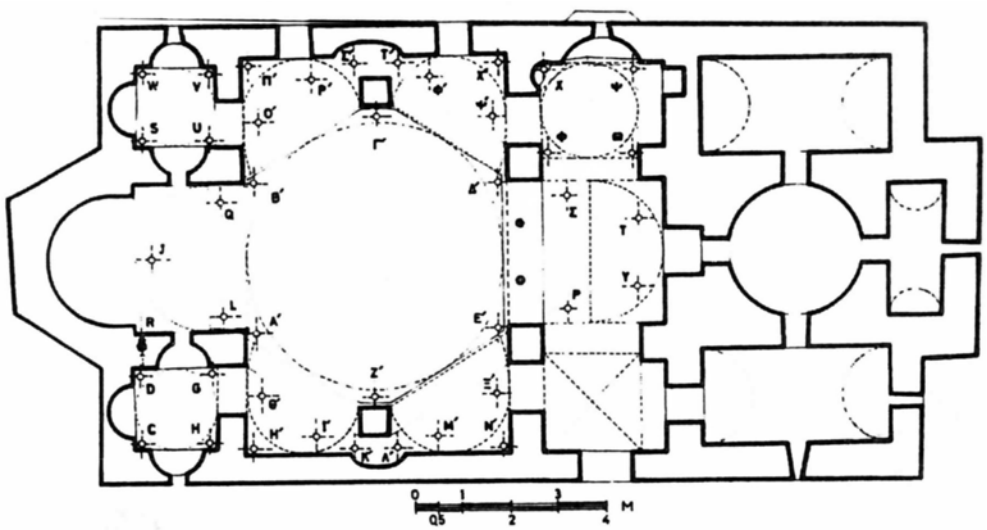

Figure 11. Vases in church of Penteli Attica. The letters denote the position of pots.

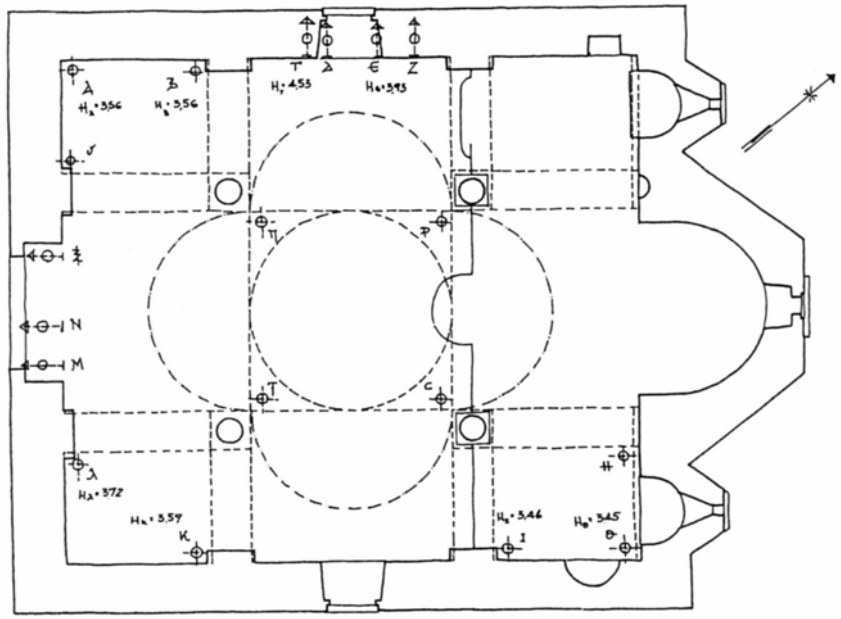

Figure 12. Church of Kareas Attica. The letters denote the position of pots.

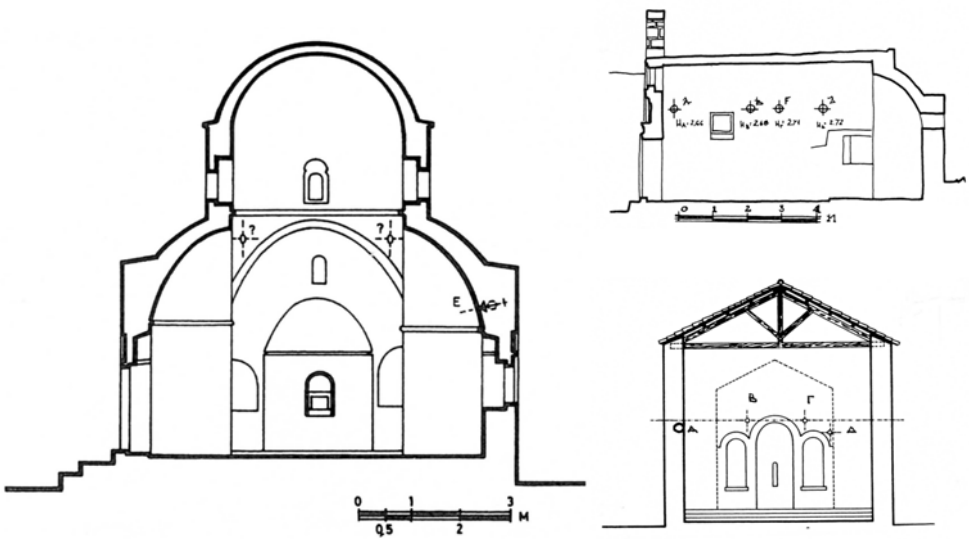

Figure 13. Pots in a church located on Greek islands: Sifnos (left), Patmos (right, up), Lefkas (right, down).

a.7. *Single-aisle Dome Basilicas*- The vases are walled-in on the lateral walls and on the crests of the dome.

a.8. *Square dome churches*- The vases are walled-in mainly on the crests of the dome and occasionally on the panels of the North and South parts.

a.9. *Octagonal churches*- The sound vases are occasionally found in various points of the domes and walls.

a.10. *Cavernous churches*- The sound vases are situated on every part of the church, without determinism or acoustic purpose.

a.11. *Hexagonal churches*- The vases are walled-in in every dome structure and are of any shape, mainly on the crests of domes and of bucklers in general. The number of walled-in vases does not depend on the size of the churches, or their position.

The difference between Greece and other countries – not neighbouring - that the vases are walled-in at different positions, in the walls and domes. Perhaps this arises from the fact that there are different architectural types of the churches.

4. QUALITY OF SOUND IN ROOMS

The propriety of the sound field that is related to certain hearing impressions is an object of psychoacoustics. The physical parameters that describe the so-called "sound quality" in a room can be described by a set of objective parameters called indexes. These indexes according to the procedure from which they can be derived, are divided into categories. All of them can be evaluated from the impulse response of the room.

In the acoustical assessment of concert halls, and other public spaces, reverberation time has long been known to be the most important parameter to judge the acoustic quality of a room. The reverberation time T_{60} is derived from the decay curve and is defined as the time for the sound to die away to a level 60 dB below its original level. This quantity can be measured using the Schroeder integrated impulse response technique [40].

Instead of reverberation time T_{10}, T_{20} and T_{30} are measured. The three reverberation times are used when the impulse is of low level and T_{60} cannot be measured. These parameters show the reverberation time in a part of the response curve, which is usually more useful. T_{10} is derived from the decay curve section between –5 dB and –15 dB below the initial level. From the corresponding slope, T_{10} is calculated as the time to reach –60dB. T_{10} can be used to measure for instance vibrations or *loss factors* in building structures. Most practical T_{10} values range from 0.005 to 10 s.

Proportionally, T_{20} is derived from the decay curve section between –5 dB and –25 dB below the initial level. For T_{30} the same holds, but with –35 instead of –25 dB. From the corresponding slope, T_{20} and T_{30} are calculated as the time to reach –60 dB. Most practical T_{20} and T_{30} values range from 0.1 to 10 s. Most of the time, these three parameters don't have the same value for the same room and that is because of the field which is not diffuse. Besides, for the same time, for different points in a room, according to the spot of the microphone, the three parameters have different values due to the different types of the fields in the room. Thus, in order to measure an unreliable reverberation time, we measure it at many points and we calculate the mean value.

Another useful index is the EDT. The EDT is a magnitude that takes into account the early reflections, which are the most important, and affect a lot the acoustics of a room. We use it when the slope of the reduction rate is not smooth enough. The EDT is derived from the decay curve section between 0 dB and –10 dB below the initial level. From the corresponding slope, the EDT is calculated as the time to reach –60dB. It is closely related to the initial and

the highest grade of the attenuation energy and its configuration. Owing to this, EDT is attached to speech intelligibility. Most practical EDT values range from 0.05 to 10 s.

Although room acoustic characteristics have long been described in terms of reverberation times, other measures are now thought to better indicate the effects of a room on speech or music.

The index that is attached to EDT is the speech intelligibility which reflects on the "quality" of speech. Thus, speech intelligibility is defined as the percentage of the numbers of syllables that can be perceivable from a common listener to the total amount that are delivered during a standard conversation. The less satisfactory percentage is 95%.

In order to evaluate the pattern of time fluctuation of energy density, Thiele introduced an index named "Deutlichkeit" This index is also known as Definition (D_{50}) and is defined by the early-to-total arriving sound energy ratio:

$$D_{50} = \frac{\mathrm{E}_{50}}{\mathrm{E}_{0\to\infty}} 100\%$$

where E_{50} $E_{0\to\infty}$ the energy that arrives during the first 50 ms and the total energy, respectively.

The definition D_{50} is strongly related to speech intelligibility and describes the quality of speech in a room.. D_{50} values range from 0 to 1. The larger value of D_{50} the more distinctness of the speech.

The clarity $\boldsymbol{C_{80}}$ is the logarithmic early-to-late arriving sound energy ratio, where "early" here means "during the first 80 ms" and "late" means "after the first 80 ms" and it is defined as:

$$C_{80} = 10\log\frac{E_{80}}{E_{80-\infty}}$$

where $E_{80}, E_{80-\infty}$ the energy that arrives during the first 80 ms and after the first 80 ms, respectively.

The clarity C_{80} is used to describe the transparency of music. Most practical C_{80} values range from –10 to 50 dB.

The way that the human ear functions and comprehends the sounds is very important in order to evaluate the room acoustics. In particular, the distance between the sound source and each ear is not the same and this is the reason why someone understands where the sounds come from. Besides, one ear may be in the "shadow" of the head in relation to the sound source and the sound level of each ear is different. Even the angle the sound waves arrive at the human ear is important.

For all the reasons above, there is an index named IAAC that measures the difference of the sounds that arrive at each ear. The Inter-aural Cross Correlation Coefficient is defined as the maximum absolute of the normalized inter-aural cross correlation function, over an inter-channel time shift from -1 ms to +1 ms and is given by:

$$IACC(\tau)=\frac{\int_{t_1}^{t_2} p_L(t)\,p_R(t+\tau)\,dt}{\left(\int_{t_1}^{t_2} p_L^2(t)\,p_R^2(t+\tau)\,dt\right)^{\frac{1}{2}}}$$

where $p_R(t)$ and $p_L(t)$ are the sound waves that arrive at the right and left ear respectively.

IAAC is used in architectural acoustics to determine the sense of the spatial distribution quantitatively and the acoustic quality of the sound. Its values range from 0 to1 and if this value is lower than 0.4, the acoustics are considered to be good.

5. Operation of Ceramic Pots

As mentioned before, the Helmholtz resonator is a simple form of sound vessel or any cavity confined by solid walls containing a certain volume of air and bearing a narrow tube-like – not long – neck with an aperture that communicates with the air outside. In practice Helmholtz resonators are lumped, not distributed acoustic elements consisting of a rigid wall cavity of volume V_{res} with a neck of area s and length d . It is assumed that the characteristic dimension of resonators is much smaller than the acoustic wavelength for the frequency of interest. However, theoretically there are other shapes of sound vases, such as: without a neck, or having more than one aperture, or formed by continuous cavities that communicate with each other. An interesting form of Helmholtz resonators is the quarter wavelength resonators which simply are pipes or tubes closed at one end and opened at the other.

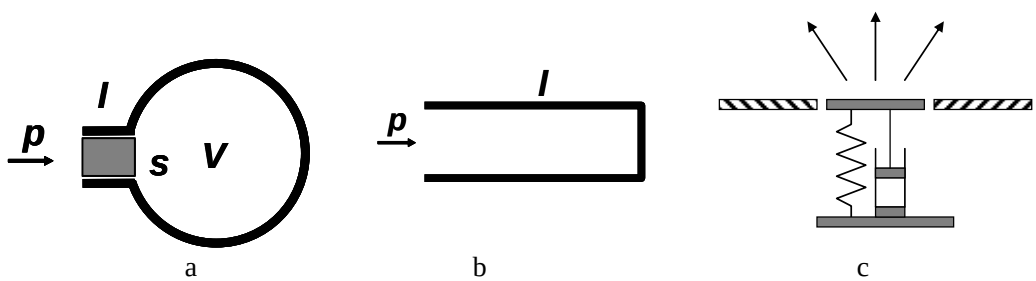

a b c

Figure 14. Simple (a) and quarter wavelength resonators (b) Mechanical analogy (c).

The ceramic pots found in worship places are actually Helmholtz resonators. The resonators behave as a single degree of freedom mass, attached to a spring. The mass of air in the neck of the resonator is excited by acoustic pressure at its aperture. The resonator resonates as a mass-stiffness system resulting in a large response at its resonant frequency.

The resonant frequency of a resonator is given by [41]:

$$\omega_0 = c\sqrt{\frac{s}{(d + d_{cor})V_{res}}} \tag{1}$$

d_{cor} is the "end correction" of the aperture neck. For a resonator with aperture radius r the end correction can be approximated by:

$$d_{cor} = \frac{16r}{3\pi} \approx 1.7r \tag{2}$$

Resonance in quarter wavelength resonators is set up when the cavity length corresponds to a quarter wavelength (or odd multiple) of the frequency of interest. The fundamental frequency of a quarter wavelength resonators is [42].

$$\omega_0 = \frac{2\pi c}{4l} \tag{3}$$

More accurate formulas for resonators with specific geometries have been proposed by Alster, Mohring, Tang and other researchers [43, 44, 45].

Helmholtz resonators have additional resonant frequencies higher than that given by equation (1). The origin of these higher frequencies is quite different from that of the fundamental, for they result from standing waves in the cavity, rather from the oscillatory motion of the mass of the fluid in the neck. The overtone frequencies therefore, depend on the shape of the cavity and are not harmonically related to the fundamental. In general, the frequency of the first overtone is several times as great as that of the fundamental [46].

The sharpness of resonance of a driven Helmholtz resonator, measured by its quality factor is given by:

$$Q_{res} = 2\pi\sqrt{\frac{V_{res}(d + d_{cor})^3}{s^3}} \tag{4}$$

when a resonator is a member of a group of resonators in a wall its function will be affected by the interaction from the other resonators. If the resonators are placed in the wall sufficiently far apart, they should act independently of each other. The limiting distance is [41]:

$$d_0 = \frac{\lambda_0}{\sqrt{2\pi}} \tag{5}$$

The principal function of resonators is sound absorption. The absorbing power of a resonator is characterized by the absorption cross section σ_{abs} which is defined as the ratio of sound energy being absorbed per second by it and the intensity which the incident sound

wave would have at the place of the absorbent object if it were not present and is given by: [41].

$$\sigma_{abs} = \frac{P_{abs}}{I} = \frac{\theta_i}{|\zeta|^2} s \tag{6}$$

where ζ is the total normalized specific impedance of the aperture. A good approximation for ζ is [41]:

$$\zeta = (\theta_i + \theta_r)\left[1 + iQ\left(g + \frac{1}{g}\right)\right] \tag{7}$$

θ_i is the normalized aperture resistance due to internal friction,

θ_r is the normalized specific radiation resistance of the resonator aperture and

$g = \frac{\omega}{\omega_0}$.

For a single resonator mounded in a wall the absorption cross section for any frequency equations (5) and (6) gives [41, 47]:

$$\sigma_{abs} = \frac{\lambda_0^2}{2\pi} \frac{1}{1 + Q_{res}^2\left[g - \frac{1}{g}\right]^2} \frac{4\mu}{(1+\mu)^2} \tag{8}$$

where $\mu = \frac{\theta_i}{\theta_r}$

The acoustic dissipation is mainly due to viscosity and heat conduction losses on the surface of the resonator. Heat conduction losses are negligible compared to viscous losses [41]. The viscous dissipation can be considered made up of two parts, namely the losses on the side wall in the aperture neck and the losses on the parallel wall surfaces. The corresponding acoustic specific resistance is given by [41]:

$$\theta_i = \frac{4R_s}{\rho c}\left(1 + 0.5\frac{d}{r}\right) \tag{9}$$

where R_s is the surface resistance given by:

$$R_s = \frac{1}{2}\sqrt{2\eta\rho\omega} \tag{10}$$

In this equation η is the viscosity and ρ the density of air.

The normalized radiation resistance for a resonator in an infinite wall is [41, 47, 48].

$$\theta_r = \frac{2\pi s}{\lambda^2} \tag{11}$$

A combination of equations (8), (9) and (10) gives for μ

$$\mu = \frac{d\lambda^2}{2\pi\rho crs}\sqrt{2\rho\eta\omega} \tag{12}$$

At resonance the absorption cross section reaches its maximum value. The maximum value under optimum conditions is

$$\sigma_{abs,\max} = \frac{\lambda_0^2}{2\pi}$$

The energy storage in the resonator affects the acoustics of the room. We can assume instantaneous energy exchange between the room and the resonator, a condition which Rschevkin showed to be satisfied in all practical cases [47]. The moving air in the neck radiates sound into the surrounding medium in the same manner as an open ended pipe. Thus the resonator behaves like a circular piston sitting on a very large baffle. The radiation pattern of such a source is omni directional. However it must be noted that when the resonator is embedded in a wall the radiation of sound from the aperture is restricted to the half space only and the corresponding energy density is greater by a factor 2. When the resonator is embedded in a corner the value of this factor is 4.

The intensity of the radiated power from a resonator in a wall at a distance x in the matched case ($\mu = 1$) at resonance is given by the equation [48]:

$$I_s = \left(\frac{\lambda}{2\pi x}\right)^2 I_0 \tag{13}$$

where λ is the wavelength and I_0 the intensity of the incident sound.

The scattering of sound by a resonator is probably more important than its absorption. The power scattered by a resonator and the corresponding cross section is given by [47]:

$$w_r = \frac{\lambda^2}{2\pi}\frac{g^2}{1+Q_{res}^2\left[g-\frac{1}{g}\right]^2}\frac{4}{(1+\mu)^2}Dc = \sigma_{res}\frac{Dc}{4} \tag{14}$$

where σ_{res} is the scattering cross-section

$$\sigma_{res} = \frac{\lambda^2}{2\pi} \frac{g^2}{1+Q_{res}^2\left[g-\frac{1}{g}\right]^2} \frac{4}{(1+\mu)^2} \tag{15}$$

6. The Effect of Vases on the Acoustic Quality of the Churches

6.1. The Effect of Distance from the Pots

As it has been mentioned before, the two major problems all researchers had faced in churches were the small number of resonators in the interior and the low resonant frequency. In order to probably overcome these problems and to explore the effectiveness of resonators more sufficiently, an experiment was carried out in a church. Proper resonators were chosen, checking their resonant frequency and ensuring the relative great number of them. The experiment was carried out in a new Byzantine church (Agia Paraskeyi of Platani) located in Patras, Greece. For the experiment 31 ceramic pots were used (see figure 15). The resonators were placed mainly on the floor at a distance between them of 0.7m (greater than that predicted by equation 4) and some of them at the corners where it had been noticed that there may be greater sound absorption. Each time, the impulse response was measured and analyzed. For the measurement and analysis of impulse responses, the BandK Dirac v 3.1 software installed on a laptop was used.

Using the formula of Alster [43], the resonant frequency of the resonator was calculated to be 325 Hz. To confirm this frequency the following experiment was done. Two ½ inch similar microphones were used. One was placed inside the resonant volume through a small hole on the bottom of the vase and one outside of it. The microphones were connected to a dual channel RTA (Norsonic 840 RTA). The measurements were made in the field that is in the church being tested.

Figure 15. Vases under test.

Figure 16 shows the output of the two microphones using FFT analysis. The gray line (Ch1) corresponds to the microphone outside the pot and the black line (Ch2) to the microphone inside the pot. As one can see from this figure, in the frequency response of the pot, there are three dominant peaks: one at a frequency of 336 Hz which corresponds to the resonant frequency, and two higher overtones at 2617 Hz and 3367 Hz. The observed overtones, as stated above, are not harmonically related to the fundamental since they have a different source of origin [46].

Figure 17 shows the output of the two microphones using narrow band (1/3 octave) analysis, for the same measuring setup. The light gray bars (Ch1) correspond to the microphone outside the pot and the dark gray bars (Ch2) to the microphone inside. The black bar corresponds to the 1/3 octave band that contains the resonant frequency. The corresponding band level for the microphone inside the pot is 18.1 dB higher than the corresponding outside. It is clear in figure 17 that the resonance is quite wide and affects four 1/3 octave bands with center frequencies 200, 250, 315 and 400 Hz. The overtone of 2617 Hz affects slightly the 1/3 octave band of 2500 Hz. These 1/3 octave bands are the bands of interest.

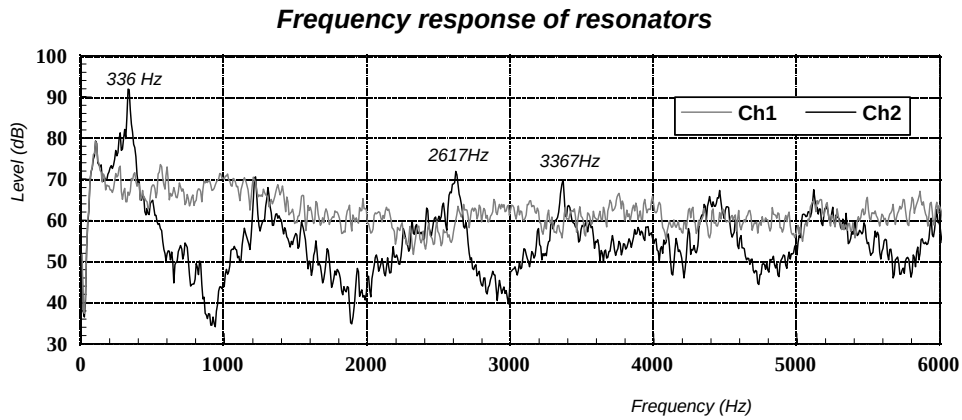

Figure 16. Frequency response of resonators using FFT analysis.

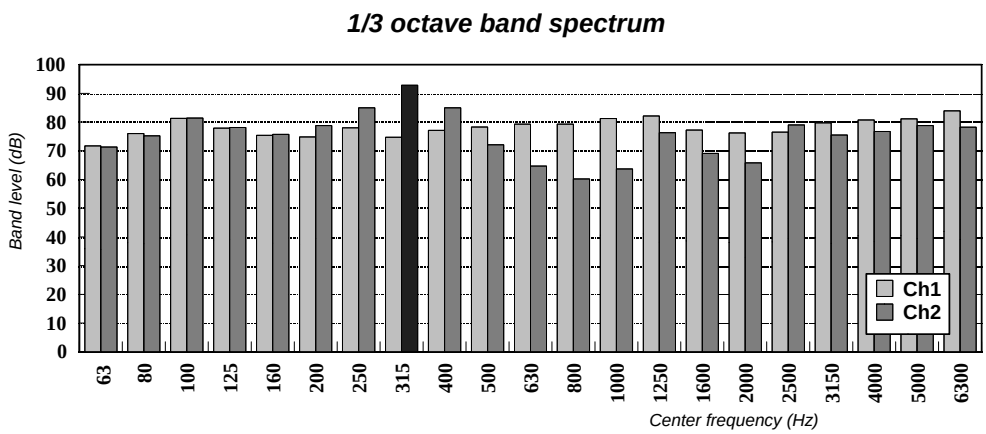

Figure 17. Third octave band spectrum of pots.

In order to find the effect of distance from the resonators to sound quality, the impulse response of the church was measured at various distances from the vases.

To conclude whether the pots have a significant effect on sound amplification, from the impulse response the noise level was calculated. For this measurement one omni-directional microphone at a varying distance (height) from one of them was used. Figure 18 shows the effect of distance from one of the 31 vases inside the church, on the level. As is shown in figure 18 there is a remarkable selective amplification up to 8 dB of sound for the third octave band that contains the resonant frequency only. This amplification is restricted to a small area near the vase. At greater distances, there is an attenuation of sound and this is an indication that the absorption is dominant. It is reasonable, since the resonators according to equation (12) have only a near field component. The effect of distance to the other bands of interest is within the statistical error.

Measurements of Desarnaulds et al [3] showed that in a church with pots in its walls, no significant difference in sound intensity can be found at any distance. An increase of sound intensity was highlighted locally for the resonant frequency of the pot.

Carvalho et al [6] to analyze the sound radiation of a pot, used a short duration noise and measured its response at the opening of the pot after the disappearance of the excitation signal. They found out that when the excitation signal is a pure tone, equal to the pot's resonant frequency, the re-emitted signal by the pot, contains a strong component at the resonant frequency, as well as a weaker contribution at the frequency that corresponds to the second mode of the pot. When the frequency of excitation signal is different from the resonance of the pot, the temporal signal, after cutting off, shows a spectral change of it, in addition to phase shift.

With a pink noise excitation one can also find the presence of the resonant frequency and its odd harmonics.

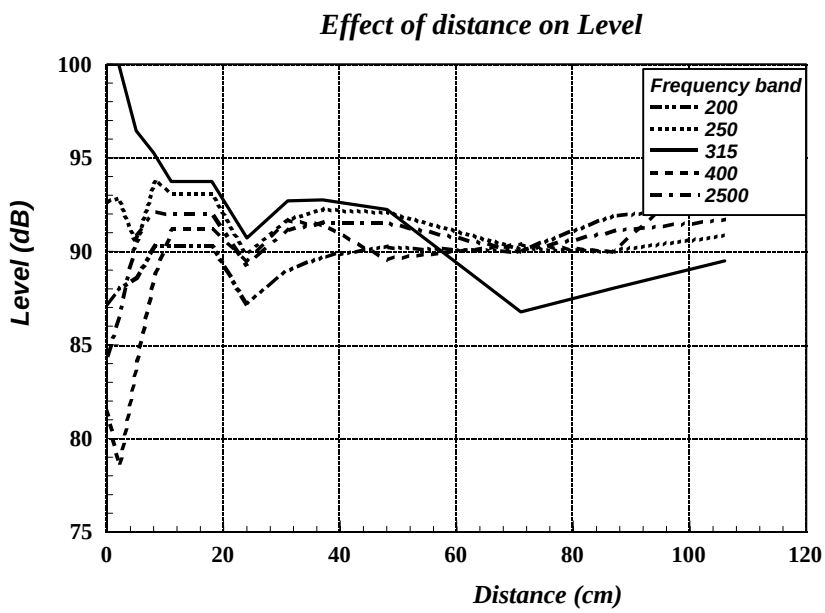

Figure 18. Effect of distance on measured noise level.

The same setup was used for the measurement of T_{30}. Figure 19 shows the effect of distance from one of the 31 vases inside the church on the reverberation time T_{30}. A significant decrease of reverberation time is observed at the frequency band of 200 Hz. The effect of distance to reverberation time of the other bands of interest is negligible.

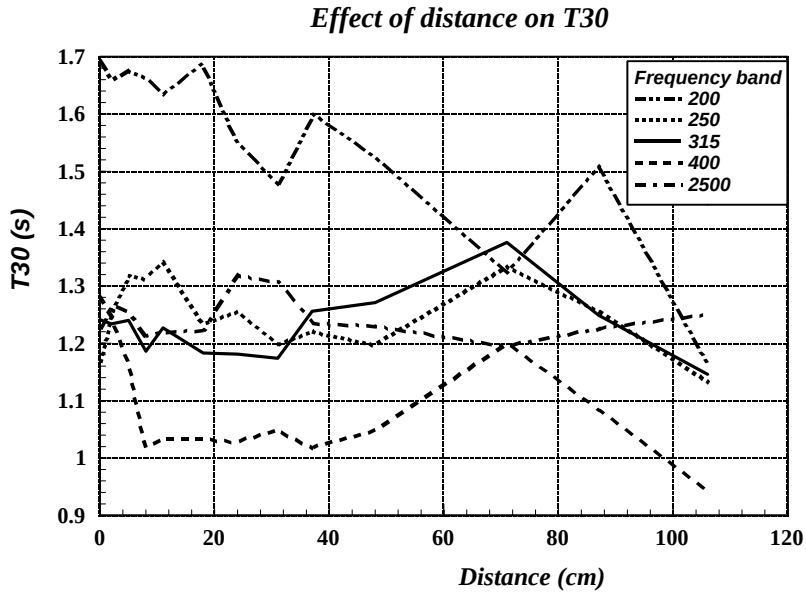

Figure 19. Effect of distance on reverberation time (T_{30}).

The strongest effect of resonators was on energy ratios. Figure 20 shows the effect of distance from one of the 31 vases inside the church on Clarity (C_{80}) and Definition (D_{50}) for all frequency bands of interest.

There is a decrease of Clarity and Definition as regards the distance in all frequency bands of interest. The reduction of D_{50} does not improve the speech intelligibility.

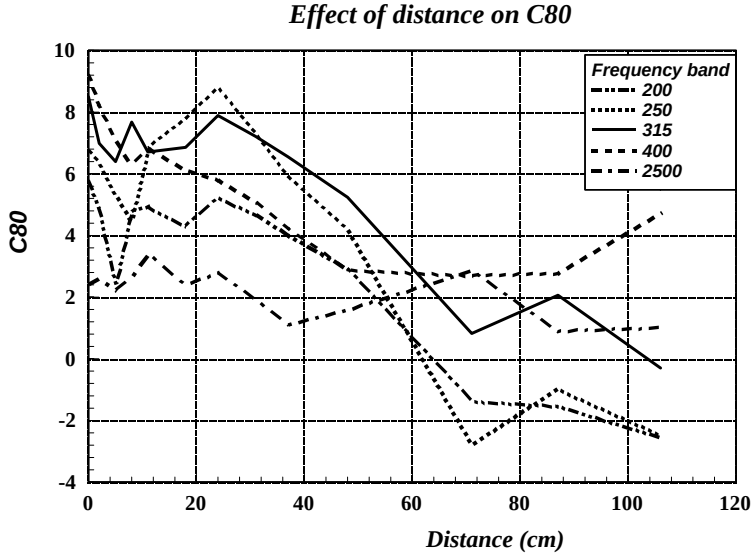

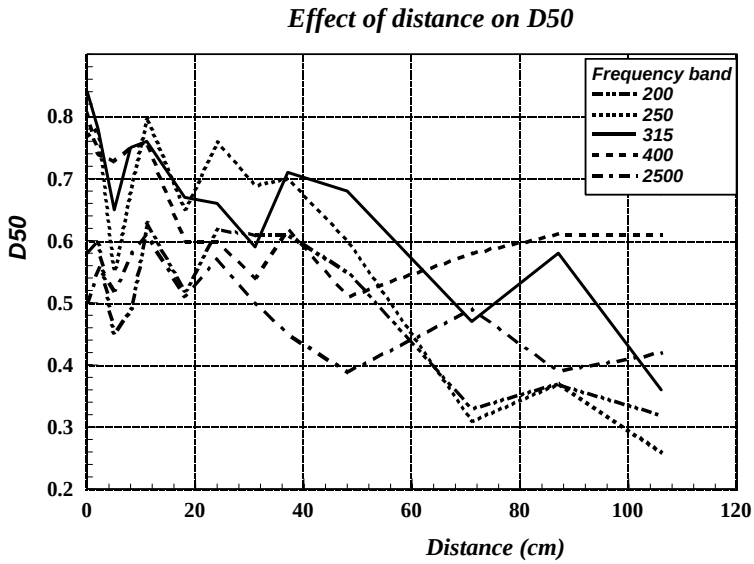

Figure 20. Effect of distance on Clarity and Definition.

No significant change in Rapid Speech Transmission Index (RASTI) and Speech Transmission Index (STI) was observed with the presence of pots. In both cases the mean value of RASTI over eight positions of measuring was 0.58 and the STI was also 0.58.

6.2. The Effect of Number of Pots to Acoustic Quality of the Church

In churches, mosques and other places of worship the main space is divided into several subspaces where strong coupling phenomena exist. For a system of N coupled spaces the energy balance equation can be written [48]:

$$\frac{dD_i(t)}{dt} - \left(2\delta_i + \frac{c\sum_{j=1,j\neq i}^{N} S_{ij}}{4V_i'} \right) D_i(t) + \sum_{j=1,j\neq i}^{N} \frac{cS_{ij}}{4V_i'} D_j(t) = \frac{w_i}{V_i} \tag{16}$$

Using equations (7) and (14), the energy coupling equation can be modified to include the function of resonators [49]:

$$\frac{dD_i(t)}{dt} - \left(2\delta_i + \frac{c\sum_{j=1,j\neq i}^{N} S_{ij}}{4V_i'} + \frac{cn_{res,i}\sigma_{abs}}{4V_i} - \frac{n_{res,i}c\sigma_{res}}{4V_i} \right) D_i(t) + \sum_{j=1,j\neq i}^{N} \frac{cS_{ij}}{4V_i'} D_j(t) = \frac{w_i}{V_i} \tag{17}$$

where D_i, δ_i, V_i the energy density, the damping constant and the volume of the i[th] room,

S_{ij} is the wall aperture area between the rooms i and j

n_{res} the number of resonators of the i[th] room.

A computer simulation program for a system of 11 coupled subspaces, showed that in order to achieve remarkable effects on the acoustics of a church a large number of pots is required [49]. This number is relative to the church volume. A reduced reverberation times in each subspace was observed [1], [2].An other effect is a decrease on EDT and an increase on Clarity and Definition. Figure 21 shows the calculated effect of the number of resonators per unit volume at resonance, under optimum conditions to the above mentioned indexes.

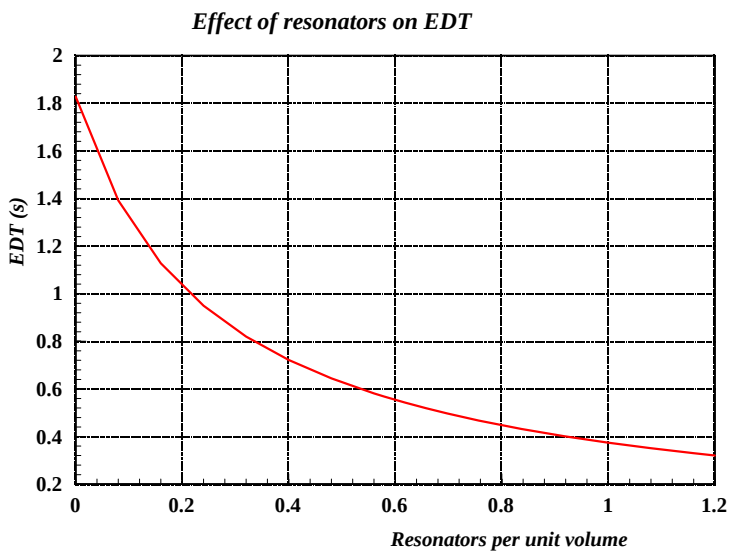

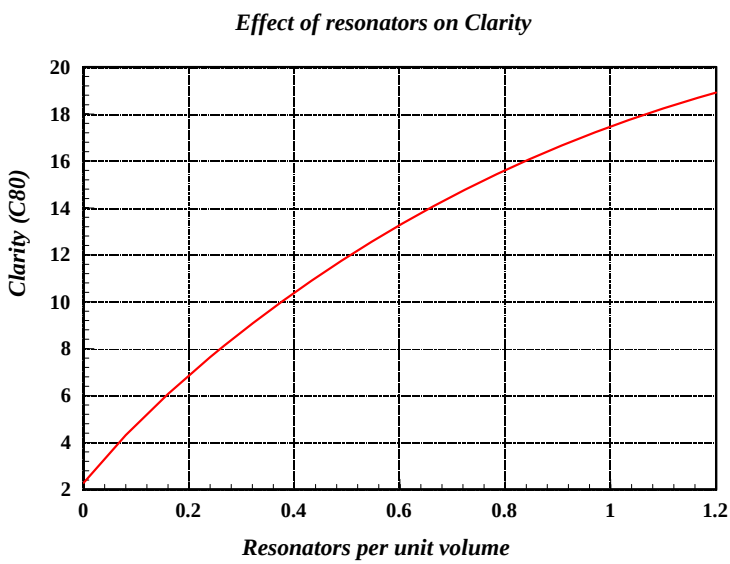

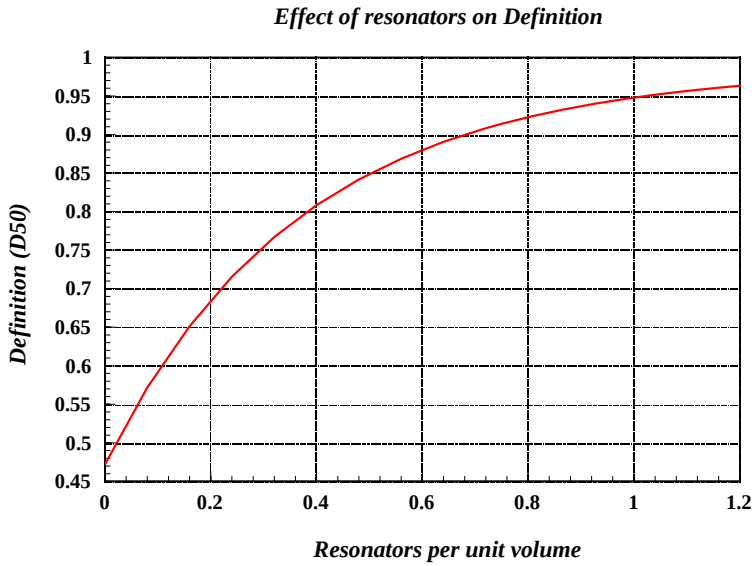

Figure 21. Effect of number of resonators per unit volume on EDT C_{80}, D_{50}.

To find experimentally the effect of resonators on the acoustic quality of a room, an experiment was carried out in an old Byzantine Church (Santa Maritsa) by Zakinthinos et al [50]. For the experiment 480 bottles, instead of pots, were used as resonators, with resonant frequency of 211 Hz. The volume of the church was about 500 m^3, giving a ratio of about 1 resonator per unit volume. The measurements performed at the far field of resonators.

Figure 22 shows the reverberation time in the church with (dotted line) and without the resonators (solid line). It is clear from this figure that there is a decrease of T_{30} mainly in the low frequency region (octave band analysis). This is a consequence of the increased absorption at the corresponding frequencies.

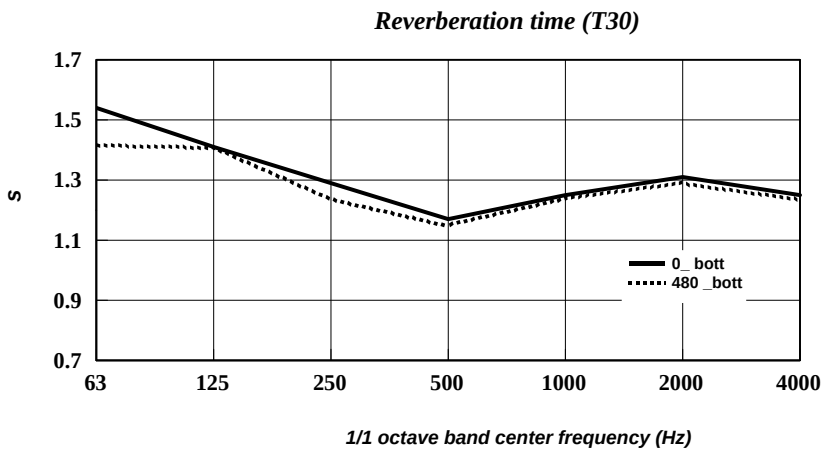

Figure 22. Effect of resonators on reverberation time T30.

Measurements of absorption by Carvalho et al showed that the absorption increases at low frequencies when the pots are located at the corners of the room. Acording to Carvalho this conclusion confirms the relevance of the tradition that often involves the laying out of the acoustic pots in the churches especially near the angles.

Figure 23 shows the change of Clarity and Definition in 1/1 octave band analysis due to resonators. It is clear that there is a decrease of both indexes in the low frequency region with the presence of resonators. The effect of resonators in the mid and high frequency region is mixed.

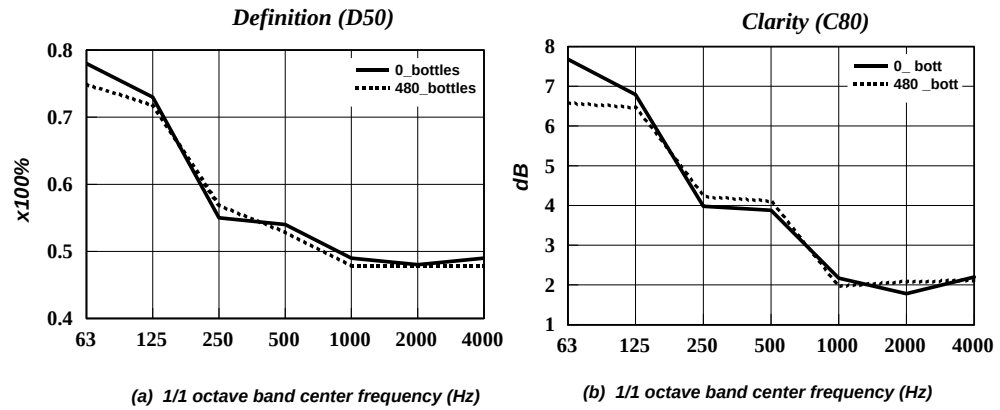

Figure 23. Effects of resonators on Definition and Clarity.

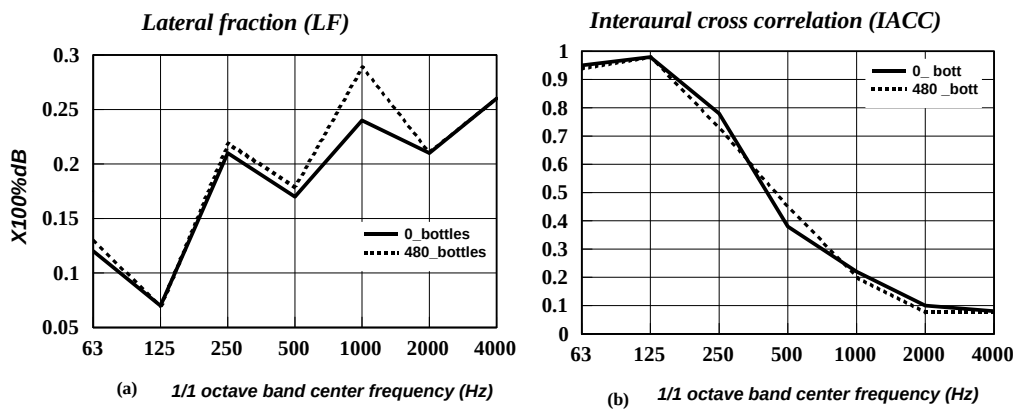

Figure 24. Of resonators on LF and IACC.

For the third octave band that contains the resonant frequency, using a varying number of resonators *D50* can be expressed by the following regression equation (R-squared=0.96) is:

$$D50 = 0.533 + 0.139bv \tag{18}$$

where *bv* is the number of resonators per unit volume.

Similarly *C80* can be written (R-squared=0.9).

$$C80 = 2.07 + 1.88bv \tag{19}$$

Figure 24 shows the effect of resonators in LF and IACC. An increase of LF and IACC was also observed.

7. CONCLUSION

For twelve to thirteen centuries, many official and popular temple builders in Greece, as well as of other European countries, applied the sound vases in the churches. No Byzantine or Medieval texts make any mention of the system of the sound vases. From the architect's viewpoint it can be concluded that: the use of vases was without any scientific knowledge and following a tradition in an uncontrollable fashion.

Most researches of Christian monuments with walled-in sound vases, interpreted these as sound amplifiers in keeping up with tradition. Besides, they lacked the general evidence regarding sound vases and they were not familiar with the relative bibliography.

Probably the clergy, that had access to the libraries of monasteries, must have known of Vitruvius's renowned book, "De Architectura", and perhaps someone who was interested in good acoustics of the chanting and sermons must have imposed the sound vases. This is a hypothesis that is verified by the great influence of Vitruvius on the West for centuries. Thus the sound vases became to the choir masters a strong belief initially, before finally fading away around the $18^{th} - 19^{th}$ centuries, both in Greece and in other European countries.

After Helmholtz and the development of building acoustics, the study of the walled-in sound vases in churches began to be carried out in the proper way.

Generally speaking, the resonators act as a selective amplifier in a short distance from resonators, but reduce the sound level far from them. This amplification is up to 8 dB in the near field of them. This reduction with the distance follows a logarithmic law and in the far field of them an attenuation of sound is observed.

A decrease of reverberation time (T30) was observed. This decrease is restricted to the resonant frequency and in some overtones. The quality factor of pots is quite small and this fact extends the effect of them in a wide frequency band (over one octave) mainly in the low frequency region.

The most significant effect of resonators is on the energy ratios C80 and D50 which seems to be linearly increasing by the number of resonators.

Another effect is that keeping the same number of resonators, a decrease of clarity and definition in the vicinity of resonators was observed. The effect of resonators is not restricted to the resonant frequency. In higher frequencies their effect is also observable but is less important than in the resonant frequency.

The small number of vases found in most of the Christian churches (with some exceptions) has an unobservable effect on the acoustic quality of them and this is an indication that this technique was rather empirical.

Looking at the pots found, there are some points that although seems to be fortuitous, are related to the acoustical properties of resonators. These points are:

1. In Greek theaters, as Vitruvius informed us, resonators were placed under the seats. From the acoustical point of view the volume of resonators is coupled with the volume of the theatre providing this way an artificial reverberation (estimated by Bruel to be 0.2 -0.5 s) which would have not been existed [16].
2. Many sound vases were not especially manufactured. Usually the sound vases found were not of the same size or shape in the same church. From the acoustical point of view each resonator has a resonant frequency at the low frequency region, with a narrow band frequency response. The use of resonators of different shapes and dimensions, each with its own resonant frequency, covers a greater frequency band, since the resonators work as a group of acoustic elements.
3. Many times the sound vases of churches were not absolutely empty. In Scandinavia for example the pots had a pit of ashes inside [16]. Ash and similar materials increase the damping of resonators, broaden the frequency response of them and increases the absorption as well.
4. In some cases the resonators were placed in rows in parallel opposite walls. Parallel surfaces introduce standing waves (axial modes) whose nodes are on the walls. The absorption and scattering of resonators eliminates these phenomena.
5. One of the common places of enwalling was the corners of joining walls. When a resonator is at a corner the radiated power is restricted to a quarter of the space so the efficiency is increased four times. Moreover, corners are critical points for normal modes of rooms especially for oblique modes, which are strong in the low frequency region.
6. Another familiar place was the domes. Most of the domes have a spherical shape and sometimes have a strong influence on the acoustics of the whole room. Firstly they may introduce strong focusing phenomena, and secondly the sound after successive reflections in the dome may produce unflavored echoes. The large scattering cross section of resonators enriches the diffuse sound field minimizing these phenomena.
7. Generally the number of pots per unit volume found in worship places are small completely inadequate to improve the acoustics of large spaces. In some cases for example the mosques designed by Sinnan, this number is large enough and this is not a fortuitous coincidence.

Resonators in the form of perforated panels are used today for controlling the low frequency noise. From the physical point of view the effect of resonators on the acoustical performance of a church is very weak and is restricted to a narrow frequency region. The effectiveness of them depends upon the number of resonators per unit volume, their position in the church and the distance of the audience from them.

REFERENCES

[1] Mijic M., Sumarac- Pavlovic D. “Analysis of contribution of Acoustic resonators found in Serbian orthodox churches” *Building Acoustics 2004*, vol. 11, no3, 197-212 (16).

[2] M.Mijic, D.Sumarac-Pavlovic “Acoustic resonators in Serbian orthodox churches”, *Forum Acusticum*, Sevilla 2002, RBA-05-001-IP.

[3] Desarnaulds V., Loerincic Y., Carvalho P. "Efficiency of the 13th century acoustics ceramic pots in two Swiss churches" *Noise-con 2001*, October 29-31.
[4] Desarnaulds V. "De L'Acoustique des églises en Suisse-Une approche pluridisciplinaire" These No2597, 2002, Ecole Polytechnique Fédérale de Lausanne.
[5] Koumanoudis I. "On the theory of acoustic pots in Greek Churches" *Proceedings of National conference "Acoustics 2002", Patras 2003*, 219- 228 (In Greek).
[6] Koumanoudis I. "On the theory of Christian Church vases" Lectureship Thesis, 1968, National University of Athens (In Greek).
[7] Carvalho P. A., Desarnaulds V., Loerincic Y. "Acoustic behavior of acoustic pots used in middle age worship spaces – A laboratory analysis" *9th international Congress on sound and vibration*, ICSV9.
[8] Crunelle Marc, "Acoustic History revisited" *The Tuning of the World Conference Banff*, August 1993, Canada.
[9] Kayili M. "Evolution of acoustics and effects of worship buildings on it" Forum acousticum, Sevilla 2002.
[10] Kayili M. "Acoustic solutions in classic ottoman architecture" *Foundation for science Technology and Civilisation*, May 2005, Publication ID 4087.
[11] Maekawa Z., Lord P "Environmental and Architectural Acoustics" EandFN Spon, London, 1994.
[12] Knudsen V. 1963 "*Architectural Acoustic*s" http://www.zainea.com/knudsen.htm.
[13] Junger M. "Comments on Review of Acoustics- Historical and Philosophical Development" R. B. Lindsay Ed. [V. O. Knudsen, *J. Acoust Soc Am 55*, 685(1974)]"*J. Acoust. Soc. Am* 1974, vol 56 No2.
[14] Driesch P. "*Acoustic control in enclosures using optimally designed Helmholtz resonators"* PhD Thesis, 2002, The Pennsylvania state University.
[15] Bruel V. "Models of ancient sound vases" *J. Acoust. Soc. Am, 2002*, vol 112, 2333.
[16] Junger M.C. "Helmholtz resonators in load bearing walls" *Noise control Engineering* 1975, vol 4(1), 17-25.
[17] Aristotle "*Problems books I-XXI*" Edited by Goold G., translated by W.S Hett, Harvard University Press London 1993.
[18] Marcus Vitruvius Pollio "*The Ten Books on Architecture De Architectura*". Translated by M. H. Morgan, Harvard University Press 1914.
[19] Durm J. "Handbuch der Architektur. Di Baukunst der Griechen", Leipzig. 1910.
[20] Orlandos A. K. "*Monastiriaki Architectoniki*" 1958 (In Greek).
[21] Davey N. "*A history of building materials*" 1961.
[22] Demangel R. – Mamboury E. "Le cartier de Manganes et la premiere region de Constantinople Paris" vol. II, 1939.
[23] "L *Architecture Francaise*" 1960, 279-80.
[24] Breymann Baukonstruktions Leipzig, Lehre 1903, vol 1.
[25] Fletcer B. "*A history of Architecture*" 1950.
[26] Bovini G. "*Impiego des tubi fittili nelle velte dogli antichiedifici di cultro ravenati*", 1957.
[27] The new Grove dictionary of music and musicians (http// phonoarchive. org/ lib/ Entries/ S00134.htm)
[28] Stikas E. "*The church Ag. Asomati Thesion*" 1950 (In Greek)
[29] Orlandos A. K. "*Parigoritissa Artis*" Athens 1965 (In Greek)

[30] Saladin H. "Manual d' *art Musulman*" vol. 1, 1907.
[31] Donnet F. "*Les poteries acoustique du Couven des Recollets a Anvers*", Anvers, 1897.
[32] Stassov V.V. Izvestija , "*Imperatorskago Archeologhi*", Petersburg. 1863.
[33] Bulle H "*I akoustiki tis Ellinikis Orthodoxis Eklisias*" 1956 (In Greek, Translated from German. Original Title: Undersuchugen an Griechischen teater Munchen)
[34] Papathanassopoulos B. "*The acoustics of the Greek Orthodox Church*" Athens, 1956 (In Greek)
[35] Guyencourt V. "*Memoire sur l' ancienne eglise des Cordeliers d'Amiens*" Amienes, 1891.
[36] Minns G. W.W. "*Acoustic Pottery. Norfolk Archaeology*". Vol. VII., Norwich, 1872.
[37] Salomon E. "*Notices sur l' ancien Temple – Neuf et l'ancien gymnase de Strasbourg*", Strasbourg, 1876.
[38] Makerprang M. "*Lydpotter I danske kirke*" Köpenhamn, 1905.
[39] Murphy D. "Archaeological acoustic space measurement for convolution reverberation and auralization applications" *Proc. of the 9th Int. conference on Digital audio effects*, September 2006, Montreal Canada.
[40] Shroeder M. R. "New method of measuring reverberation time" *J. Acoust. Soc. Am*, 1965, vol 37, 1187.
[41] Ingard Uno "On the theory and design of Acoustic resonators" *J. Acoust. Soc. Am*, November 1953, Vol 25, No 6.
[42] Field C. D., Fricke F. R., "Theory and application of quarter –wave resonators. A prelude to their use for attenuating noise entering buildings through ventilation openings" *Applied Acoustics*, 1998, vol 53 No 1-3.
[43] Alster M. "Improved calculation of resonant frequencies of Helmholtz resonators" *Journal of sound and vibration*, 1972, vol 24(1), 63-85.
[44] Mohring J. "Helmholtz resonators with large aperture" *Acustica*, November 1999, Volume 85, Issue 6, Pages 751-763.
[45] Tang S.K "On Helmholtz resonators with tapered necks" Journal of Sound and vibration, 2005, vol 279, 1085-1096.
[46] Kinsler L., Frey A., Coppens A., Sanders J. "*Fundamentals of Acoustics*" 1982, Willey.
[47] Gilford C. L. "Helmholtz resonators in the acoustic treatment of broadcasting studios" *British Journal of Applied Physics*, March 1952, vol. 3, 86-92.
[48] Kuttruft H. "Room Acoustics" *Elsevier Applied Science third Edition*, 1991.
[49] Skarlatos D., Zakinthinos T. "The effect of resonators on the acoustics of coupled spaces" *Euronoise 2006*, Tampere, Finland.
[50] Zakinthinos T Skarlatos D. "The effect of ceramic pots on the acoustics of old orthodox churches" *Applied acoustics 2007* (In press).

In: Developments in Ceramic Materials Research
Editor: Dena Rosslere, pp. 173-209
ISBN 978-1-60021-770-8

Chapter 6

MODELING OF THERMAL TRANSPORT IN CERAMICS MATRIX COMPOSITES

M. A. Sheik*
School of Mechanical, Aerospace and Civil Engineering
The University of Manchester
P O Box 88, Sackville Street Building
Manchester M60 1QD, United Kingdom

ABSTRACT

Modelling and analysis of a unique geometrically representative Unit Cell has been shown here as the key to predicting the macro thermal transport behaviour of composites, which otherwise requires the employment of a vast experimental infrastructure. Sophisticated materials, such as woven Ceramic Matrix Composites (CMCs), have very complex and expensive manufacturing routes, used by just a few research organizations. This broadens the scope of a modelling strategy to be adopted for the characterization of all possible material designs with various possible constituent volume fractions by using a commercial FE code such as ABAQUS. The variation of material constituents can be incorporated in the Unit Cell model geometry with subtle manipulation of key parameters dictated by quantitative SEM morphological data. Two CMC material systems have been modeled in the present study. The first material has been analysed with a focus on the homogenization of microscopic constituent material properties into the macroscopic thermal transport character. The actual set of property data used for the Unit Cell of this material is obtained from the cumulative property degradation results extracted from the analyses of three sub-models based on the material's unique porosity data. After validating the modeling methodology through a comparison with the experimental data, a geometrically more challenging CMC is modelled with a detailed incorporation of its morphological complexity in order to predict its macroscopic thermal transport behavior. Finally, it is shown how these models can be more efficiently analysed in a multi-processing parallel environment.

* Tel: +44 (0) 161 306 3802; Fax: +44 (0) 161 306 3803; E-mail: m.sheikh@manchester.ac.uk

1. INTRODUCTION

Ceramic Matrix Composites (CMCs) are considered to be possible replacement for metallic super-alloys in high-temperature parts of aero-engines and heavy-duty gas turbines, and for applications such as nozzles in rocket engines. Increased operating temperatures from 900-1200°C for coated super-alloys to above 1300°C for CMCs have the potential to achieve higher thermal efficiencies and lower emissions [1]. Such applications require good thermal properties for heat transfer in CMC engine components. Compared to metallic alloys, a deficiency of CMCs is the degradation of thermal transport properties due to internal damage. An ability to predict thermal transport in CMCs is a primary requirement at the design stage. The presence of damage and cracks can be introduced in either manufacturing or in service. Firstly, damage during manufacturing is introduced as a result of the different thermo-mechanical properties of the constituent materials, which during cooling introduce thermal gradients, thermal stresses, localized failure and hence damage. This manifests itself after cooling as micro-porosity. Secondly, damage is created in service [2], [3] by mechanical overloads, fatigue, time-dependent and environmental effects. As damage evolves a limiting condition is reached when an engineering component becomes mechanically unserviceable. It then requires either repair or replacement. The dominant effect on material serviceability is that the thermal transport properties are dramatically reduced due to the evolution of damage, which can be highly directional. The overall impact is to render the component thermally unserviceable due to impaired thermal efficiency. There is a very strong coupling between mechanical behavior and thermal properties which is not currently well understood; and is not capable of being accurately predicted at the present time. Hence one of the drivers for current research on CMCs is the need to describe and predict these effects at the design stage. This is to be achieved through the establishment of effective modeling procedures.

The modelling of CMCs requires a number of factors to be taken into account, which influences their thermal transport, such as the architecture of the composite, the properties of constituent material, and the influence of defects [4]. Early approaches to the thermal finite element modelling were two dimensional; for example unidirectional long fibre composites have been studied by Lu and Hutchinson [5] for longitudinal thermal transport, and by Klett et al.[6] for longitudinal and transverse thermal transport. The main limitation of such models is their simplicity, which does not reflect the complexities of real composites. A complex weave model of a plain weave CMC was presented by Sheikh et al. [7]. This model was 3-dimensional, and represented a relevant development towards the modelling of complex composites architectures. They introduced the effect of directionality in thermal transport by introducing the individual properties of fibre and matrix. However, the model was deficient since the influence of initial porosity was not taken into account.

A developmental modelling strategy is set, which took account of the following factors:

(i) categorise manufacturing or initial porosity;
(ii) create an ability to numerically model it; and
(iii) subsequently, further develop this to a point where growth and coalescence of initial porosity due to applied loadings and thermal strains can be accurately predicted; and, in addition, couple this with the degradation of mechanical and thermal properties.

But first, for each porosity classification, finite element analysis techniques are used to quantify the effect of each class of porosity on the spatial heat transport properties assessed at the level of a micro Unit Cell. In the analysis care is taken to accurately model porosity volume fractions and characteristic defect lengths. However, thermal properties determined using one model is included in subsequent models. It is in this way that the synergy between different classes of porosity is assessed.

The two CMC materials used for modeling here are: (1) DLR-XT, a [0/90] plain weave laminate, and (2) HITCO, a complex 8-Satin Weave CMC. Geometric models for both are built from SEM Micrographs. For DLR-XT a Unit Cell model is built using 4 quarter parts which assemble together to form the Unit Cell with fibre tows and matrix together. In contrast, the Hitco Unit Cell is created as a single part since this Representative Volume Element (RVE) is the smallest and unique geometric entity that cannot be further simplified.

For the thermal characterization of the two chosen materials through extensive finite element modelling, two thermal properties are evaluated using steady-state and transient analysis respectively. First is Thermal conductivity which is one of the driving forces in designing materials for thermal applications. The other is thermal diffusivity, which is an important parameter for controlling thermal transport, defined as the ratio of a material's capacity to conduct heat versus its capacity to store it. Experimental work is conducted for validation purposes by making thermal diffusivity measurement by the laser flash method [8]. The materials are thermally analysed with and without the external mechanical load in order to establish a correlation between the mechanical damage on a CMC causing degradation of its thermal diffusivity.

With the increase in the geometric complexity of the CMCs, the requirement of the computing resources rises considerably. This is reiterated by the current modeling effort with HITCO 8-harness satin weave geometry. It is shown that with the multiplication of the Unit Cell (each containing around a million elements) across the lamina and then the laminate, demand for computational power increases drastically. Special arrangement is therefore required for conducting analysis of such large FE models. The solution is shown here to be the use parallel processors in a High Performance Computing (HPC) environment.

2. CERAMIC MATRIX COMPOSITES (CMCS)

Generally, ceramics cover a wide variety of non-metallic, inorganic compounds that are frequently processed at high temperatures. Starting compounds of ceramics can be borides, carbides, nitrides, oxides, silicides, phosphides, chalcogenides and their complex compounds, both natural and synthetic [9]. Compared to metals these compounds have higher melting temperatures, elastic moduli and hardness, and lower densities, and electrical and thermal conductivities.

Ceramics can be broadly grouped into two classes, namely, conventional ceramics and high performance ceramics. Technical ceramics, which are employed for the fabrication of CMCs, exhibit extraordinary resistance to heat, chemicals and wear [10].

Fibres used in ceramic matrix composites fall into three general categories based on their diameter: monofilaments, textile fibres and whiskers. In addition, reinforcements in the form of particulates and platelets are also being utilised in ceramic composite designs. In ceramic

composites the reinforcements usually increase the strength indirectly by increasing the toughness of the matrix.

The selection of matrix materials for ceramic composites is strongly influenced by thermal stability and processing considerations. Common matrix materials include oxides, carbides, nitrides, borides and silicides.

Engineered ceramics are used in thermal and structural applications requiring high temperature resistance, high hardness and chemical inertness. Applications that exploit the thermal structural properties of ceramics commonly include cutting tool inserts, wear resistant components, ballistic armour, heat exchangers, burner tubes, prosthetics, dental implants, heat engine components and thermal barrier coatings [11].

2.1. Manufacturing of CMCs

CMCs can be processed either by conventional powder processing techniques used for making polycrystalline ceramics or through novel techniques specifically developed for such purposes [11]. Since this chapter includes the modelling of a composite manufacturing porosity, it is instructive to outline some of the important processing techniques [2], [12], utilised in the fabrication of CMCs. Technical details of the manufacturing processes as well as the relative merits and disadvantages of the different fabrication methods are also discussed.

2.1.1. Infiltration

Infiltration of a preform constructed of reinforcement can be executed with a matrix material in solid, liquid or gaseous form. Liquid infiltration demands proper control of the fluidity of liquid matrix. The process results in a high density matrix without pores in the matrix. Besides, only a single processing step is required to attain a homogeneous matrix. However, high processing temperatures can cause unfavourable chemical reactions between the reinforcement and the matrix. Ceramics have relatively high melt viscosities, which render the infiltration of the preform a difficult operation. In addition, thermal expansion mismatch between the reinforcement and the matrix, a large temperature interval between the processing and room temperature as well as the low strain to failure of ceramics are factors that impede the production of a CMC devoid of cracks. Similarly, the matrix is prone to cracks due to the differential shrinkage between the matrix and the reinforcement on solidification. Figure 1 schematically represents the liquid infiltration process.

2.1.2. Polymer Infiltration and Pyrolysis

Ceramic matrix in a composite can be accomplished from the usage of polymeric precursors. Polymer infiltration and pyrolysis (PIP) constitutes an attractive processing route because of the relatively low cost as compared to the generally high costs of CMC fabrication. Apart from the cost factor, the process is able to maintain small amounts of residual porosity and minimal degradation of fibres. Furthermore, this approach allows near net-shape moulding and fabrication of composites near their full densities. In PIP, fibres are infiltrated with an organic polymer, which is heated with raised temperatures and pyrolysed to form a ceramic matrix. Due to the relatively low yield during the conversion from polymer to

ceramic, multiple infiltrations are necessary to obtain an acceptable density of the composite. Polymeric precursors for ceramic matrices permits the usage of conventional polymer composite fabrication technology that is readily available and capitalise on processes used to make polymer matrix composites. Complex shape forming and fabrication are possible and the fairly low processing and pyrolysing temperatures prevent fibre degradation and the formation of unsolicited reaction products at the fibre/matrix interface.

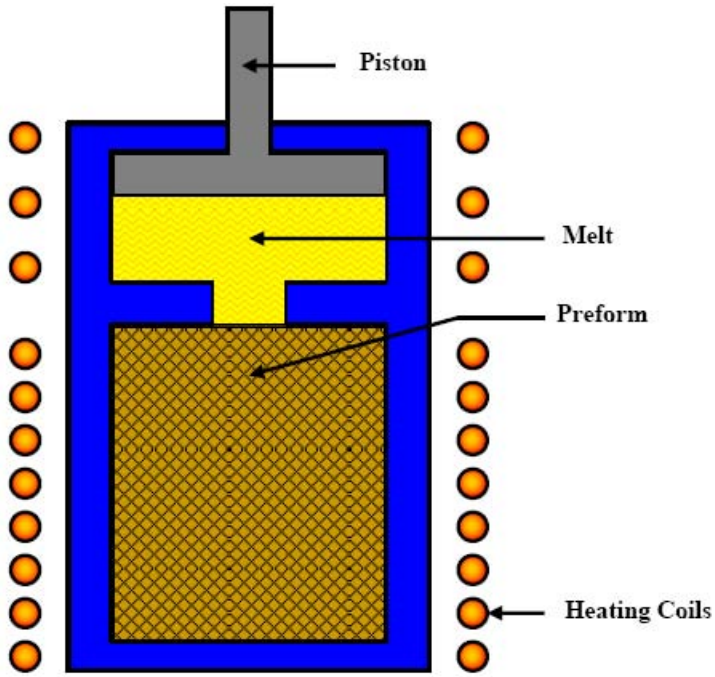

Figure 1. Schematic diagram of the infiltration technique.

2.2. Thermal Behaviour of CMCs

The behaviour of composite materials is often sensitive to changes in temperature. Such trends are displayed due to the temperature-dependent response of the matrix to an applied load. Also, alterations in temperature can induce internal stresses because of a differential thermal contraction and expansion. These stresses ultimately affect the thermal expansion of the composite. Furthermore, thermal gradients are especially deleterious to CMCs as they possess relatively lower thermal diffusivities and are inherently heterogeneous. A thermal gradient is inversely related to thermal diffusivity (α) of a material, which is in turn related to thermal conductivity (k), specific heat (C_p) and density (ρ) of the material [2] as:

$$\Delta T = F\left(\frac{1}{\alpha}\right) = \left(\frac{C_p \rho}{k}\right) \tag{1}$$

During the cooling from a typically high processing temperature of CMCs, very high thermal stresses ensue as a result of the thermal mismatch between the reinforcement and the matrix. In the instance of a fibrous composite, an interfacial pressure develops during the cooling phase. Thermal stresses generated are dependent on the reinforcement volume fraction 'V', reinforcement geometry, thermal mismatch ($\alpha_F < \alpha_M$) temperature interval 'ΔT' and also the modulus ratio (E_F/E_M).

Generally, during cooling, the matrix tends to contract more than the reinforcement putting the reinforcement in compression ($\alpha_F < \alpha_M$). This mismatch is difficult to eliminate, but it can be manipulated to extract desirable characteristics of the composite. Through a prudent choice of components, it is feasible to acquire a favourable residual stress pattern rather than adverse final attributes at the end of the processing. In CMCs, crack deflection at the fibre/matrix interface is beneficial for the augmentation of toughness in the composite. Frequently, interfacial coatings, that are primarily mechanical in nature, are introduced in CMCs to optimise stress distribution and bonding at the fibre/matrix interface.

The longitudinal expansion coefficient of a composite is given by:

$$\alpha_{C-Longitudinal} = \frac{\alpha_M E_M \nu_M + \alpha_F E_F \nu_F}{E_M \nu_M + E_F \nu_F} \tag{2}$$

Similarly, the transverse expansion coefficient of a composite is expressed by:

$$\alpha_{C-Transverse} = (1+\nu_M)\alpha_M V_M + (1+\nu_F)\alpha_F V_F - \alpha_{C-Longitudinal}\,\bar{\nu} \tag{3}$$

where:

$$\bar{\nu} = \nu_F V_F + \nu_M V_M \tag{4}$$

and '*V* ' is the volume fraction, '*E* ' is the Young's Modulus, 'ν ' is the Poisson's ratio and the subscripts '*C* ', '*F* ' and '*M* ' refer to composite, fibre and matrix, respectively [13].

For a unidirectional fibre reinforced composite, a prediction of thermal conductivity in the longitudinal (*l*) and the transverse (*t*) directions is proposed by Behrens [14] as:

$$k_1 = k_{cl} = k_{Fl} V_F + k_M V_M \tag{5}$$

$$k_2 = k_{ct} = \frac{k_{Ft} k_M}{k_{Ft} V_f + k_M V_M} \tag{6}$$

where, subscripts '1' and '2' denote the principal directions of the unidirectional composite. In case of woven fabric-reinforced composites, such formulation is not applicable since non-homogenous material phases are intermixed and intertwined in one volume. One direct

solution to this problem is finite element simulations which entail the geometric details, property data and detailed boundary conditions to set up the model.

Because of the inherent heterogeneity of a composite and thermal property mismatch in constituents, even a uniform temperature change will result in thermal stresses. In absence of any variable temperature gradient the thermal strain is [2]:

$$\varepsilon_T = \Delta\alpha \cdot \Delta T \tag{7}$$

2.3. Experimental Measurements of Thermal Diffusivity

The theory and experimental procedure for the thermal diffusivity measurement by the flash method requires the surface of a small sample being irradiated with a laser pulse, and the temperature response at the opposite surface recorded. The recorded data would be the temperature- time profile of the rear face. The plot for temperature rise $\Delta T/\Delta T_{\max}$ measurement against time would highlight the peak value of 1 at a certain time. Considering the initial temperature condition of 20^{o}C, the time for half temperature rise value 0.5 would be noted as half-rise time $t_{1/2}$. For each test these are obtained to calculate the thermal diffusivity α using Equation 8 for a thin disc specimen, which has one face uniformly irradiated in one-dimensional (1D) heat flow:

$$\alpha = 0.139\left(\mathrm{L}^2 \Big/ t_{1/2}\right) \tag{8}$$

where L is the sample thickness and $t_{1/2}$ is the experimentally obtained half-rise time.

Two experimental test rigs have been used in the current analysis for the measurement of thermal diffusivity. These will be referred to as Test Rig 1 and Test Rig 2. A schematic diagram of apparatus in Test Rig 1 is shown in Figure 2, and is fully described in [8]. This rig has been used to test materials for their thermal diffusivity over a wide temperature range (300 - 3000 K). It requires thin specimens, which are normally subjected to one-dimensional heat flow - but also allows both radial and axial heat flow by irradiating only the central region of larger specimens – Figure 2.

Test Rig# 2 which is shown in Figure 3, is similar to Test Rig 1 in terms of pulse source, detection and amplification system, and recording and analysis facility. It is designed, however, to measure thermal diffusivity whilst the specimen is mechanically loaded. The rectangular plate specimens are held in the grips of a mechanical testing machine which allows continuous monitoring of the externally applied mechanical load and induced strains. Information about any possible bending of the specimen is also obtained to ensure that the measurements of thermal transport properties correspond to a case of purely tensile loading only.

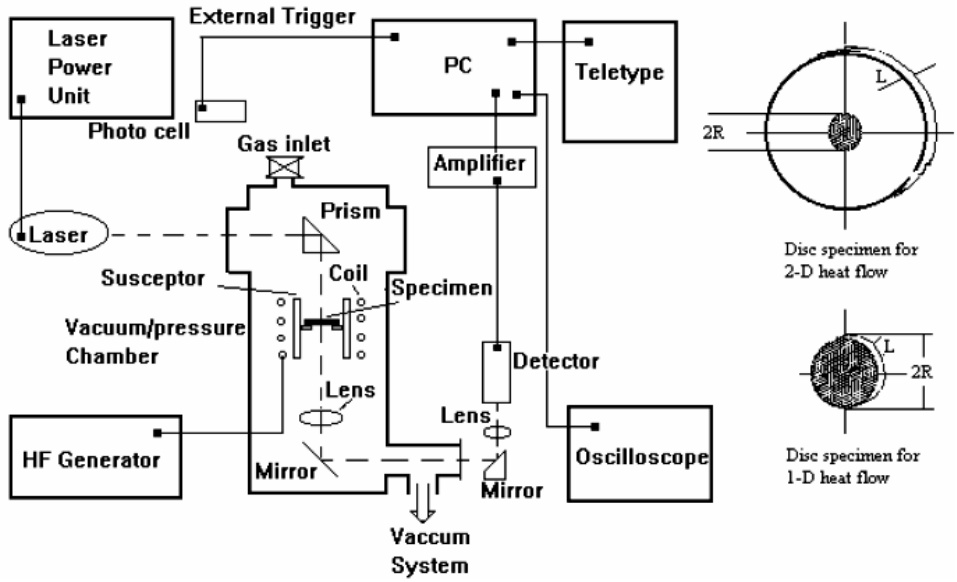

Figure 2. Schematic diagram of apparatus in test rig 1.

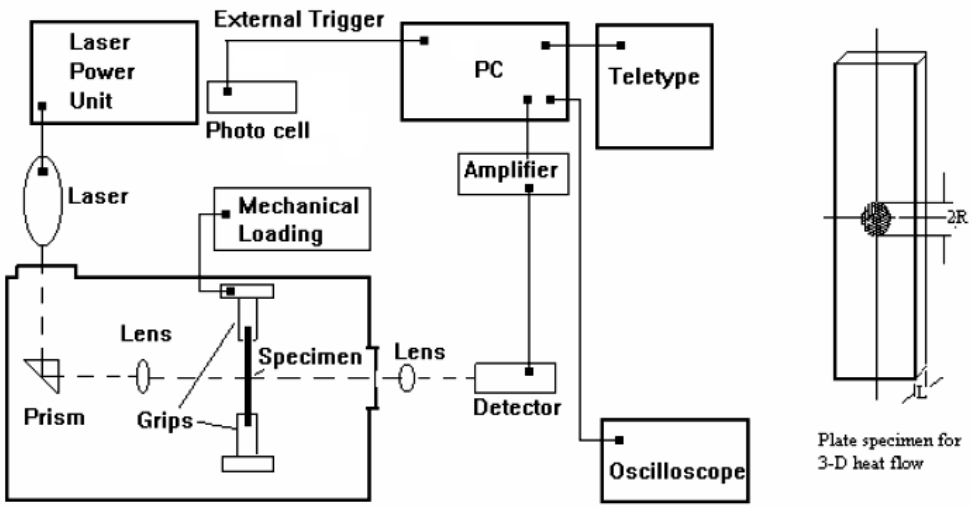

Figure 3. Schematic of apparatus in test rig 2.

3. MODELLING OF A PLAIN WEAVE CMC

3.1. Manufacturing Process

One of the materials under consideration [15] is DLR-XT, a 10 laminate CMC material developed by the German Aerospace research Establishment, Stuttgart, Germany for aerospace applications involving high-temperature gas turbine components.

T300 carbon fibres manufactured from carbon are arranged in tows, which have been used to form a plain weave (Figures 4 and 5) to generate a single laminate. Ten such laminates are assembled to form a sheet of the DLR-XT composite. The laminate bundle is infiltrated with a polymer, which is thermally decomposed to leave a carbon char. This in turn is infiltrated with liquid silicon, which reacts with the carbon char to give silicon carbide, which forms the matrix around the carbon fibre bundles.

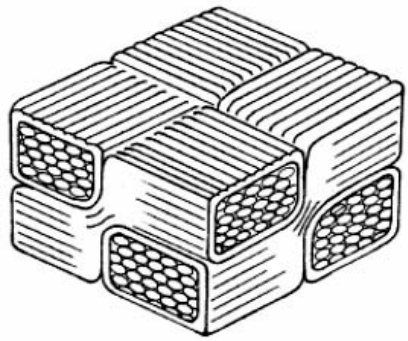

Figure 4. DLR-XT - schematic view of a composite macro unit cell of a single laminate.

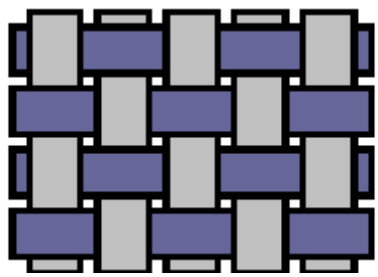

Figure 5. Diagrammatic plan view of a plane weave configuration.

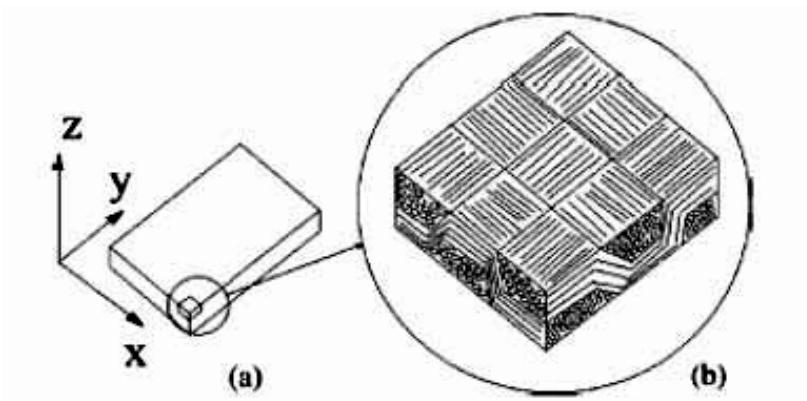

Figure 6. Schematic drawing of (a) a material laminate; (b) a lamina element and global coordinate system.

Ten sheets of the woven carbon fibre fabric are assembled between forming platens; which are then housed within a chemical vapour infiltration (CVI) chamber. The assemblage is then CVI processed, and the effect of temperature and pressure results in the fibres within each tow being embedded within a carbon matrix, created by diffusion of carbon from the fibres. The tows are, in turn, embedded within the infiltrated silicon carbide matrix. The process involves time-dependent temperature and pressure distributions within the structure of the laminate. Figure 5 schematically represents a plain weave arrangement and Figures 4 and 6 illustrate the geometric configuration and coordinate global system of this material.

3.2. Classes of Porosities

Internal damage in the form of cracks and voids can be introduced either during manufacturing or in service. During manufacturing, damage is caused by a mismatch of thermo-mechanical properties of the constituent materials, thus inducing thermal gradients, thermal stresses, localised failure and hence damage when cooled. This manifests itself after cooling as micro-porosity. Additionally, damage is created in service by mechanical overloads, fatigue, time-dependent and environmental effects. As damage evolves, a limiting condition is reached when an engineering component becomes mechanically unserviceable. It then requires either repair or replacement. The dominant effect on material serviceability is that the thermal transport properties are dramatically reduced due to the evolution of damage, which can be highly directional, ultimately rendering the component thermally unserviceable due to impaired thermal efficiency. Despite the existence of a very strong coupling between mechanical behaviour and thermal properties, these relations are currently ill comprehended and are not capable of being accurately predicted at the present time.

Paolo et al [16] have achieved the quantification as well as classification of initial porosity through the usage of optical electron microscopy and SEM. These techniques have been selected for their ease of use and availability; and, for their potential to cross check observations and measurements. 4 classes of porosities have been identified and schematically shown in Figure 7.

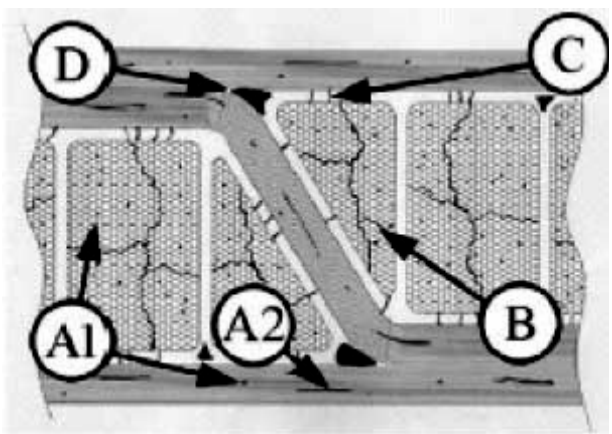

Figure 7. Schematic drawing of a general plane orthogonal to either the X or the Y-direction illustrating the four classes of porosity. [Circled letters denote the porosity type].

3.2.1. Inter-Fibre Micro-Porosity (Class A)

This type of porosity occurs between adjacent fibres contained within a tow. It comprises either of a series of voids or large cracks between the fibres. These can be seen within as black dots A1 or cracks parallel to fibre tows A2 in Figures 8(a)-(c) and schematically represented in Figure 7.

These two kinds of porosity are mainly generated by the manufacturing process. The spheroidal pores, shown in Figure 8(b), are the result of incomplete infiltration due to shrinkage from the processing temperature which is around 1550°C for molten silicon impregnation. The shrinkage de-bonding is due to different thermal contractions of the fibre and the matrix during cooling. This generates thermal stresses across the interface, which in turn causes interface de-bonding.

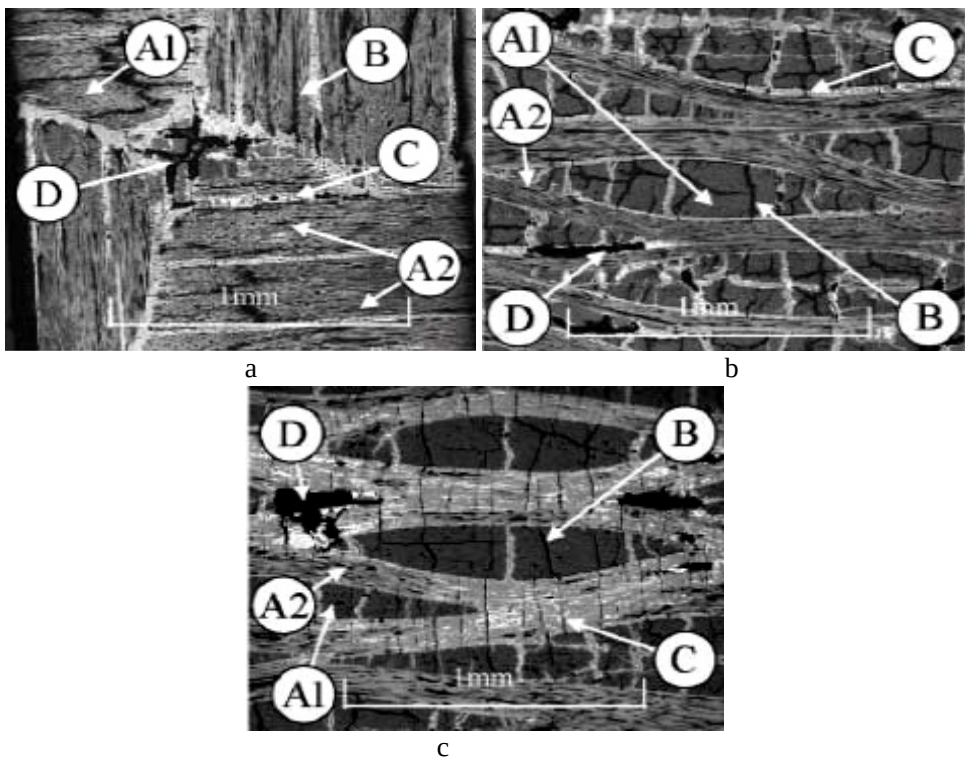

Figure 8(a)-(c). Three different images of orthogonal planes obtained using optical microscopy. (a) Plane normal to laminate and the Z axis, (b) plane normal to X axis, and (c) plane normal to Y axis. The locations of four different classes of porosity (A, B, C, D) are indicated.

3.2.2. Trans-Tow Cracks (Class B Porosity)

This class of porosity may be observed as cracks B in Figure 8(a)-(c). The porosity is comprised of cracks, which run through the tows in planes parallel to the fibres. They occur in planes which are orthogonal to X, Y and Z directions. Porosity classes A and B are also shown schematically in Figure 7. Cracks of this type are formed during manufacture as a consequence of differential cooling, coupled with the different mechanical/thermal properties in adjacent orthogonal tows.

3.2.3. Matrix Cracks (Class C Porosity)

This class of porosity is composed of cracks, embedded in the matrix, which surround the tow in planes perpendicular to the tow axes. C matrix cracks run circumferentially around the tows. The generation of the matrix cracks occurs during cooling of the composite due to tensile stresses generated in the matrix arising from the difference in the values of the linear coefficients of thermal expansion for the matrix and the fibre parallel to its axis. Class C porosity is schematically given in Figure 7. Figure 8(b) is a section taken in the Y-Z plane which cuts through the tow centres running in the Y direction. This is shown in Figure 10(a). Likewise, Figure 8(c) is a section taken in the X-Z plane which cuts through the silicon carbide matrix encapsulating the tows running in the X-direction. Hence it can be seen that the Class C matrix cracks run circumferentially around the tows as shown schematically in Figure 10(b). In addition, Figure 9 shows a SEM primary electron image of Class C defects in a plane normal to the X direction.

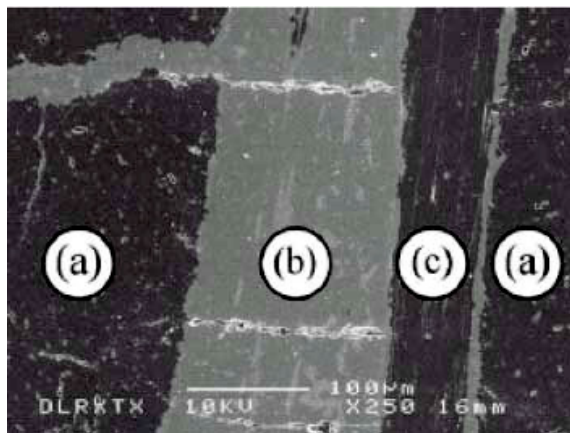

Figure 9. Class C porosity (matrix cracks): SEM primary electron image of a plane normal to the X direction. Region (a) has fibres running normal to the plane; region (b) is silicon carbide matrix; and region (c) has fibres running parallel to the plane. The matrix region (b) surrounds the fibre tow (c). Two Class C periodic matrix cracks are shown in region (b) which are circumferential to the in-plane tow (c).

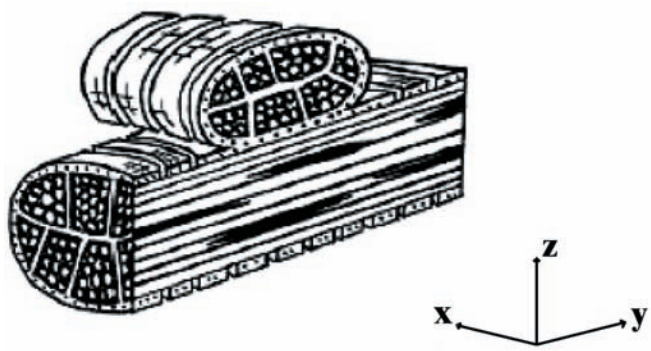

Figure 10(a). Two orthogonal tows sectioned normal to the X-axis in a Y-Z plane cutting through the centre of the lower tow.

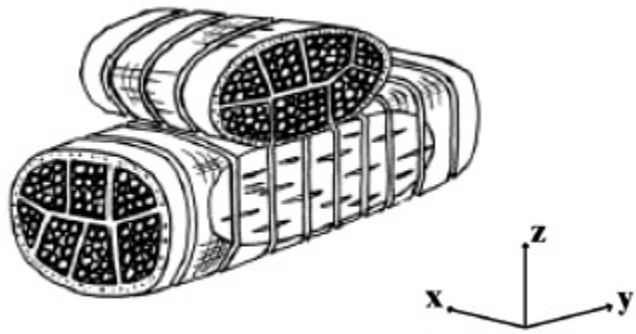

Figure 10(b). Two orthogonal tows sectioned normal to the Y axis in a X-Z plane cutting through the silicon carbide matrix encapsulating the lower tow.

3.2.4. Denuded Matrix Regions (Class D Porosity)

This type of porosity is due to the large voids, which occur at the intersection of four orthogonal tows. This class of porosity occurs during manufacture due to difficulties in the CVI process, these are largely due to the difficulty and time required to fill the large void which occurs at the intersection of four tows. Porosity of such type is illustrated in Figure 8(a)-(c), Figures 7 and 11.

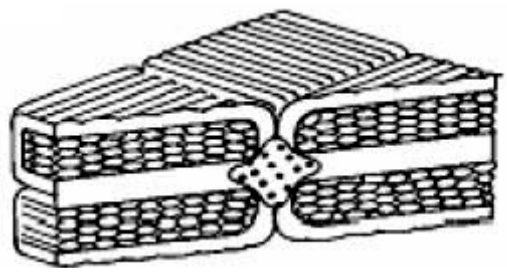

Figure 11. A schematic view of a section through a unit cell showing one unit of Class D porosity (spotted region).

3.3. Quantification of Porosity

Various classes of porosities for DLR-XT are quantified by utilising a porosimeter as well as detailed observations of optical micrographs. The porosimeter received its input data in the format of a digital two dimensional surface image. A software was then used to edit black and white images by the selection of a group of varying levels of greyness. Discernment between levels of greyness and porosity area fractions was calibrated with standard reference test pieces. Eventually, the result generated was an area fraction expressed as a percentage. Pertinent area fractions in connection with porosity classes A and D are quantitatively determined with the porosimeter. Optical micrographs were used in the case of porosity classes B and C. For these two classes of porosities, the length scale is that associated with the height of the tow measured in the Z-direction. This is equal to the diameter of the circle

inscribed in the tow, which corresponds to the tow diameter. In Class B porosity, cracks are characterised by their frequency (number of cracks per tow), their length in the tows' cross-sectional plane and their depth parallel to the tow axis. A Class C porosity crack is characterised by its length, depth and periodicity. As these cracks surround the entire tow, the length is equivalent to the tow circumference, hence related to the average tow diameter. All these measurements are summarised in Tables 1 and 2 below.

Table 1. Area fraction for Class A and D porosity

Area fraction for Class A and D porosity

Class	Type	Area fraction (%)	Sample size	Variance
A1	Area fraction of the spheres	0.0200	8	0.05
A2	Area fraction of the shrinkage debonding	0.0059	8	0.05
A2	Length of major-axis of debonding surface = 0.06 mm	–	–	–
A	Total area fraction of porosity of class A	0.0259	8	0.05
D	Total area fraction of porosity of class D [obtained from a montage of 12 optical images representing a complete cross-section of the laminate]	0.0256	1	–

Table 2. Crack geometry and periodicity for Class B and C porosities

Cracks geometry and periodicity for classes B and C porosity

Class	Cracks main characteristics	Sample size	Variance
B	Crack depth = 1.28 × tow diameter	13	0.23
B	Equivalent number of cracks in planes parallel to tow axes = 2		
	No. of cracks normal to Z-axis: average = 0.71 (11 tows have no crack, 23 tows have 1 crack, 1 tow has 2 cracks)	35	0.267
	No. of cracks parallel to Z-axis: average = 1.57 (17 tows have 1 crack, 16 tows have 2 cracks, 2 tows have 3 cracks)	35	0.12
B	Crack length = 1.1 × tow diameter	25	0.0048
C	Crack separation or periodicity = 0.308 × tow diameter	57	0.008
C	Crack length = tow circumference, average tow diameter = 0.18 mm	20	0.0012
C	Crack depth = thickness of the SiC matrix = 0.0225 mm	25	0.0002

3.4. Thermal Transport Modelling of DLR-XT

This first 3-dimensional model for DLR-XT (C/C – SiC CMC) is developed from the SEM micrographs (Figure 12) and represents a relevant development towards the modelling of complex composites architectures. In this model the effect of directionality in thermal transport is taken into account by introducing the individual properties of fibre and matrix. However, the model, as shown in Figure 13, is deficient since the influence of initial porosity is not taken into account.

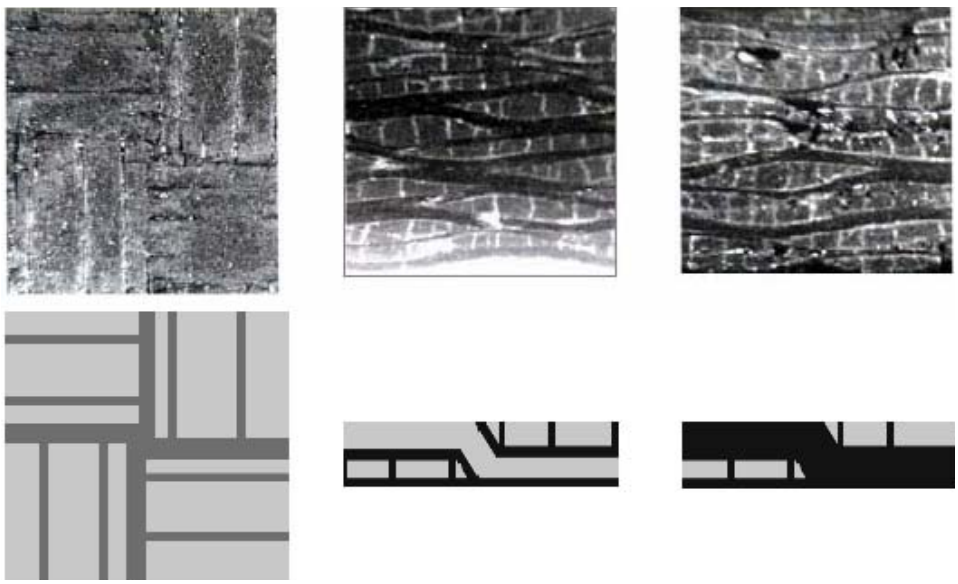

Figure 12. Generation of a Geometric Model using SEM Micrographs.

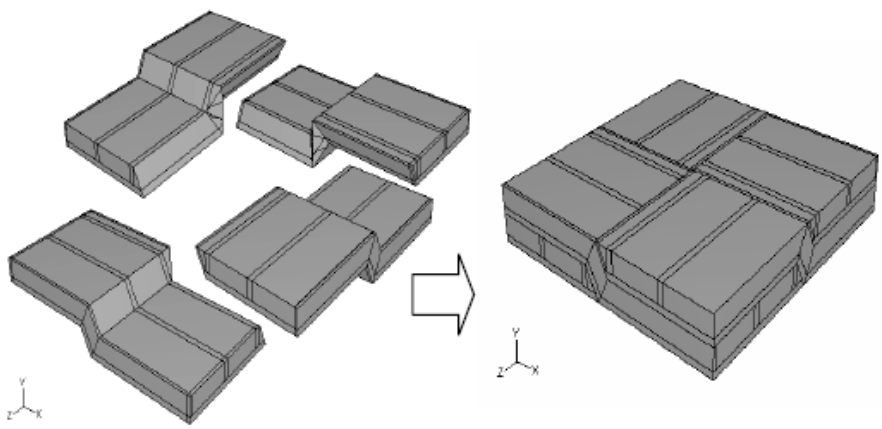

Figure 13. Unit cell geometry assembled from 4 quarter parts having a fibre volume fraction of 65%.

Hence, for each porosity classification, finite element analysis techniques is used to quantify the effect of each class of porosity, discussed in section 3.2, on the spatial heat transport properties assessed at the level of a micro Unit Cell. In the analysis care is taken to

accurately model porosity volume fractions and characteristic defect lengths, discussed in section 3.3 and given in Tables 1 and 2.

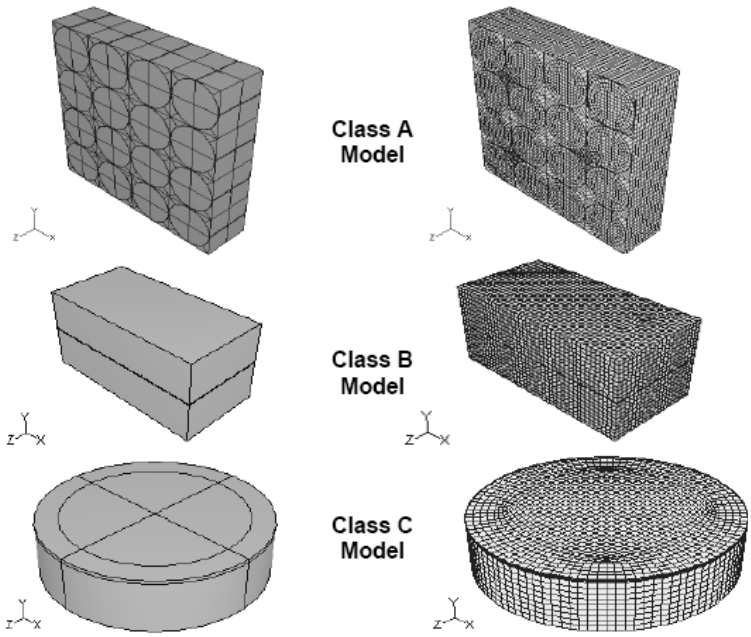

Figure 14. Porosity sub-models along with their respective FE meshes.

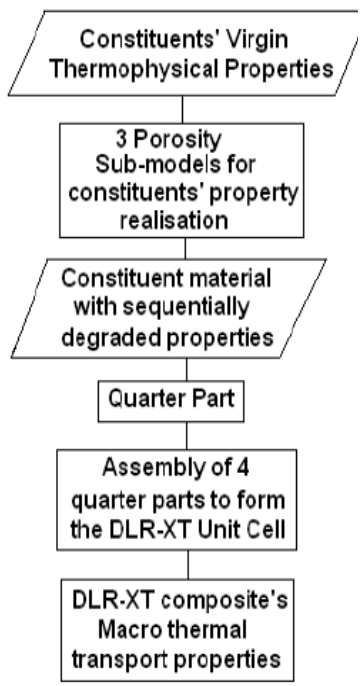

Figure 15. Flow chart for thermal transport modelling of DLR-XT CMC Material.

The thermal properties determined using one model is included in subsequent models. It is in this way that the synergy between different classes of porosity is assessed. Figure 15 shows the flow chart for thermal transport modelling of this DLR-XT CMC material using sub-models shown in Figure 14 and incorporating porosity type D, shown in Figure 9.

3.4.1. Thermal Properties

Thermal conductivity is one of the driving forces in designing materials for thermal applications. In a material, heat flow is proportional to the temperature gradient with the constant of proportionality being the thermal conductivity. Its general form is

$$q_i = -k_{ij} \frac{d\,T}{d\,x_j} \tag{9}$$

where q_i is the heat flux and k_{ij} is the thermal conductivity. This is a second-order tensor and in most cases a symmetric one. Another important parameter for controlling thermal transport is thermal diffusivity α. It is defined as the ratio of a material's capacity to conduct heat versus its capacity to store it. It is related to thermal conductivity k, specific heat C_p and density ρ as:

$$k = \alpha \rho C_p \tag{10}$$

Relevant thermal properties of CMC constituents, shown in Table 3, along with air for the pores or cracks are employed for the thermal transport models.

Table 3. Standard thermal property values of constituent materials

Material	k (W m^{-1} K^{-1})	ρ (kg m^{-3})	C_p (x10^{-6})(J kg^{-1} K^{-1})
Carbon Fibre Transverse	4	1928	921
Carbon Fibre Longitudinal	40	1928	921
Carbon Matrix	10	1800	717
SiC Matrix	70	3200	1422
Air	0.001	1	1

Finite-element methods for determining the thermal transport properties of solids are based on the two thermal analyses; Steady State and Transient. The steady state thermal

analysis using FEM involves applying a temperature gradient $\Delta T/\Delta x$ across the composite section in a 1D heat flow simulation. Using Fourier Law, k_x, is given as:

$$k_x = q_x \frac{\Delta x}{\Delta T} \tag{11}$$

where q_x is the overall heat flux in the x-direction calculated by integrating the nodal flux values across rear face. In the current analysis, q_x is obtained using the nodal flux values (in x-direction) given by the FE solution on one of the faces where the temperature boundary condition is applied as in Figure 16. However, due to a high degree of mesh non- uniformity and a significant difference in the thermal properties of the matrix and fibre, the nodal flux values vary quite considerably across that surface, and the summation employed to calculate the overall flux as:

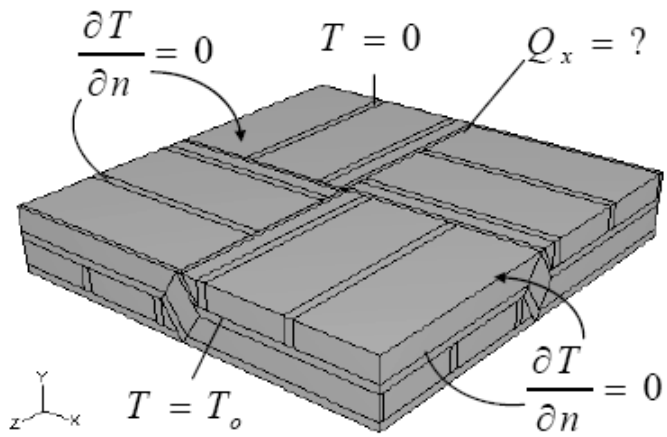

Figure 16. Boundary conditions for steady-state FE analysis.

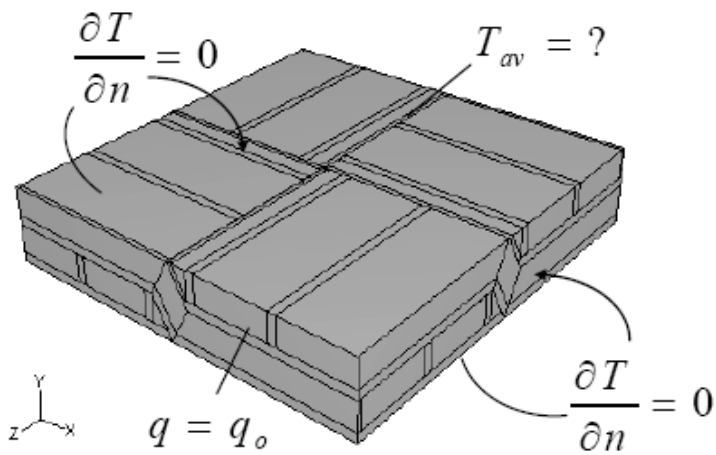

Figure 17. Boundary conditions for transient analysis.

$$q_x = \sum_{i=1}^{N} q_i A_i \Big/ \sum_{i=1}^{N} A_i \tag{12}$$

In the case of transient thermal analysis, a heat flux is applied to one face (Figure 17) of the composite section for a short time and the temperature history is recorded on the opposite face to simulate the experimental conditions. The temperature profile is obtained by averaging temperature across the complete rear face. This is obtained from an expression similar to Equation 12, as here q_i is replaced by the nodal temperatures T_i as:

$$T_{av} = \sum_{i=1}^{N} T_i A_i \Big/ \sum_{i=1}^{N} A_i \tag{13}$$

T_{av}, the average temperature, is calculated for each time step through the transient analysis and a temperature history is recorded. Assuming 1D uniaxial heat flow, the half rise time related to this average temperature value is then used in Equation 8 to calculate thermal diffusivity α and thermal conductivity k is found from Equation 10. The remaining scalar properties, density ρ and specific heat C_p for the composite are determined using the rule of mixtures in Equation 14 shown in Table 4. It is important to emphasize that two different volume fractions are involved here. One is 75% Carbon fibre with in the Carbon matrix, forming the fibre tow. The other is the 65% fibre tow in the composite with remaining being SiC matrix surrounding it. Using rule of mixtures, specific heat C_p and density ρ as calculated as:

$$\left.\begin{aligned} \rho_C &= \rho_f V_f + \left(1 - V_f\right)\rho_m \\ Cp_C &= Cp_f V_f + \left(1 - V_f\right) Cp_m \end{aligned}\right\} \tag{14}$$

Table 4. C_p and ρ for CMC from constituent materials' property values

Material Property	Carbon Fibre	Carbon Matrix	SiC Matrix	Composite
Density ρ (kg m^{-3})	1928	1800		
	1832 (fibre tow)		3200	
	2310.000			
Specific Heat C_p (x 10^{-6} J kg^{-1} K^{-1})	921	717.48		
	870.12 (fibre tow)		1422	
	1063.278			

3.4.2. Thermal Analysis of DLR-XT – Strategy and Results

The morphology and the geometric structure of the material has been translated into a three-dimensional macro unit cell model, as shown in Figure 13. Following that, microscopic sub-models of porosity types A, B, C, as shown in Figure 14, have been created for steady-state finite element analyses similar to that performed for the macro unit cell model. Class D porosity is then introduced in the main unit cell model, where a denuded portion of the central section, as shown in Figure 11, is created. The results of these analyses in the form of the degraded fibre tow and matrix thermal properties are listed in Table 5.

Material properties for the fibre tow and the matrix in the macro unit cell are the prescribed values tabulated in Table 5. Assignment of degraded thermal properties hence addresses the influence of initial porosities on the thermal behaviour of the material.

From Table 6 an obvious degradation of the overall composite thermal conductivity is noted during the sequential introduction of each type of porosity. In addition, it is also evident that Class B porosity (trans-tow cracks) has a dominant effect on the transverse thermal conductivity, 'k' value for the composite whereas Class C porosity (matrix cracks) mainly affects the longitudinal 'k' value. To a certain extent, the latter value is also influenced by shrinkage de-bonding or Class A2 porosity. These results conclude that Class C porosity is the primary form of defect that causes the most appreciable reduction of overall spatial thermal conductivity profile of the CMC when these values are used at the macro unit cell level.

Finally, the analysis of 3D thermal transport carried at the composite macro Unit Cell level, in combination with the fourth class of porosity, the Denuded Matrix Regions, produced the final k values are presented in Table 7.

Table 5. Degradation of thermal conductivity with sequential introduction of each class of porosity

		C tow	SiC matrix
For Virgin Material ($W\ m^{-1}\ K^{-1}$)	Longitudinal (∥)	32.4075	70
	Transverse (⊥)	5.086	70
For Material with Class A Porosity ($W\ m^{-1}\ K^{-1}$)	Longitudinal (∥)	32.3444	70
	Transverse (⊥)	5.0368	70
For Material with Class A and B Porosity ($W\ m^{-1}\ K^{-1}$)	Longitudinal (∥)	32.24	70
	Transverse (⊥)	4.44125	70
For Material with Class A, B and C Porosity ($W\ m^{-1}\ K^{-1}$)	Longitudinal (∥)	29.683	29.683
	Transverse (⊥)	4.44125	70

Table 6. Tabulation of degraded thermal conductivity values of through-thickness and in-plane flow direction along with its overall sequential degradation in the unit cell. Values in parenthesis show the percentage reduction with respect to virgin material

	C Tow		SiC Matrix		Macro Unit Cell	
Thermal Conductivity ($W\ m^{-1}\ K^{-1}$)	$\parallel$	$\perp$	$\parallel$	$\perp$	In Plane	Through Thickness
Values for Virgin Material	32.407	5.086	70	70	34.89	16.29
Values for Material with Class A Porosity	32.344	5.036	70	70	34.85	16.23
Values for Material with Class A and B Porosity	32.24	4.441	70	70	34.55	15.52
Values for Material with Class A, B and C Porosity	29.68	4.441	29.683	70	26.94	15.09
Values for Material with Class A, B, and C Porosity used in Class D Porosity affected unit cell	29.683	4.441	29.683	70	25.06	13.64

Table 7. Comparison of 1D experimental results vs. FE analyses results for thermal conductivity, k ($W\ m^{-1}\ K^{-1}$)

Direction	Experimental	FE Modelling	
		Steady-State	Transient
Through Thickness	14.39	13.639	11.55
In-Plane	22.45	25.06	25.16

A further correlation can be established between the mechanical damage on a CMC causing degradation of its thermal diffusivity through the same modelling strategy. A range of property values are given to the class-C sub-model and the eventual overall effects plotted in Figure 18. It represents the resulting degradation in thermal diffusivity from a successive increase in matrix crack density. Although this does not account for the total reduction of the

thermal property derived from the experimental data, given in Figure 19, a 50% reduction is shown to have occurred due to matrix cracking.

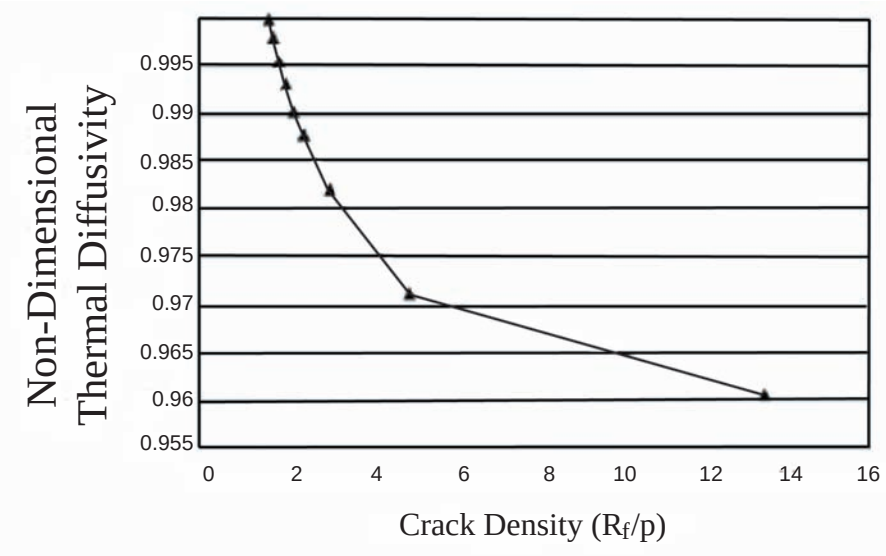

Figure 18. Degradation of through-thickness thermal diffusivity with increasing crack density due to external mechanical loading. 'R_f' represents the tow diameter and 'p' denotes the periodicity of matrix cracks.

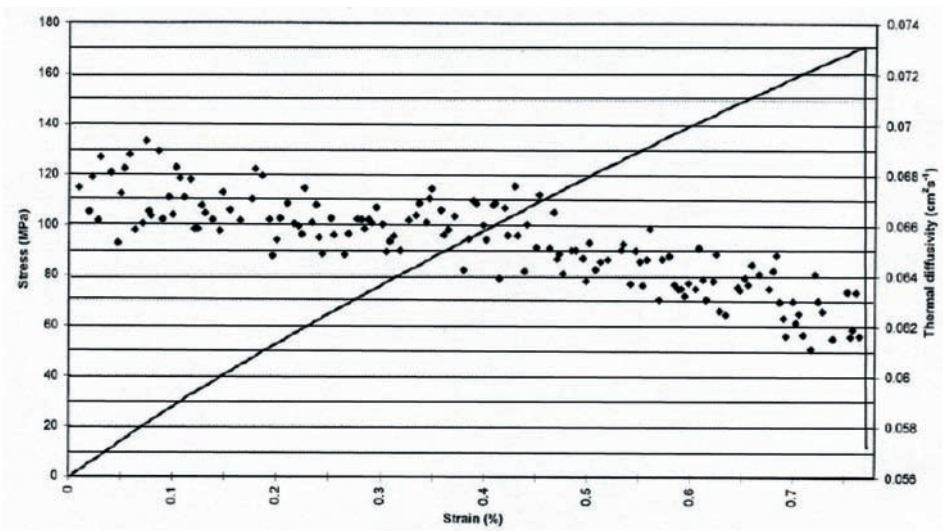

Figure 19. Experimental results for the degradation of thermal diffusivity of the DLR-XT CMC material with external mechanical loading.

4. MODELLING OF A COMPLEX 8-SATIN WEAVE CMC

A recognition of the generic architecture of 8 Harness Satin weave is required that bears close resemblance with the actual morphology of the material such as shown in Figure 20.

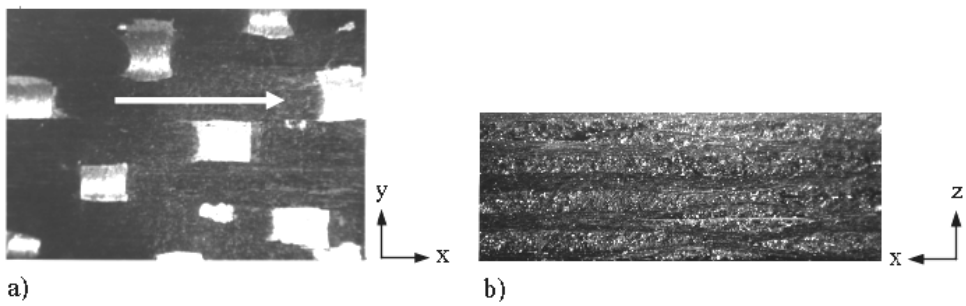

Figure 20. (a) Top view (b) Side view of a 8-Satin Weave Composite laminate with arrow showing fill fibre direction.

The architecture shown in Figure 21(a) has been used here for modelling as it follows the sequence seen in the micrograph in Figure 20(a) which shows the top side of the sample used for the thermal diffusivity measurement in the experimental rig described earlier.

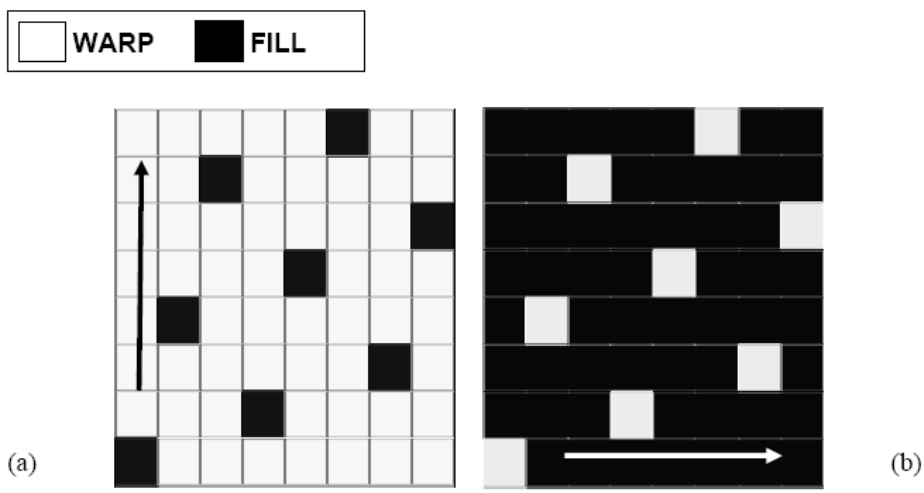

Figure 21. Generic architecture of the 8-harness satin weave (a) Warp side (b) Fill side, arrows showing fibre tows direction.

It is also important to specify the stacking sequence and orientation of each lamina in the composite laminate tested since the effects of the off-set lay up of multiple laminae in a composite laminate does have effects on the analyses. Woo and Goo [17] have effectively proven this parameter as quite dominating for, at least, through-thickness measurement. But in order to establish the basic sequence of modelling and analysis methodology, a single lamina is used in this simulation. A RVE Unit Cell is chosen from this single lamina and not of the stack in a laminate which will form the next phase of this study in regards to computational challenges involved.

HITCO composite architecture comprises of a laminate with 10-12 laminae of 8-harness satin weave of Carbon-Carbon fabric stacked up to form the final composite laminate with Graphite matrix. The schematic with a single lamina considered as the Unit Cell in Figure 22 has been the starting point for modelling, with various other feature details that have been closely examined being mentioned during the course of RVE Unit Cell modelling.

This RVE Unit Cell model has been formed with due correlation with the two micrographs showing the weave formation from the top and the side edges captured, as shown sketched in Figure 22.

The sketch also shows schematically how simultaneously these features are to be captured in modelling. It is evident from the edge micrograph in Figure 20(b) that a single lamina can not be isolated from the laminate stack due to the present nesting of the weave, overlapping and encroachment of the top and bottom laminae on to the middle laminae, resulting in a very compact intertwined fibre tow structure. As a start the nesting factor, more geometrically random than repeated, has been ignored in modelling in order to avoid double complexity with the weave.

Figure 22 shows the schematic view of the Unit Cell that is created with the help of micrographs of the HITCO CMC composite sections through the XY and XZ planes shown in Figure 20(a) and 20(b) respectively, coupled with the generic architecture details of the 8 harness satin weave. Bright areas in Figure 20(a) denote Carbon fibre tow of the warp and dark areas denote segments of the Carbon fill fibre bundles in the composite. From within these features a 3D Unit Cell is identified, which on replicating itself across in three spatial directions produces the macro-structure of the CMC. A brief but specific outline of the modelling undertaken with ABAQUS/CAE is given here.

Standard modelling procedure in ABAQUS/CAE has been sequentially detailed earlier for the DLR-XT Unit Cell. It was built using 4 quarter parts that assemble together to form the Unit Cell with fibre tows and matrix together. In contrast, the HITCO Unit Cell has been created as a single part since this RVE is the smallest unique geometric entity that cannot be further simplified or divided. For HITCO, first the fibre tows, warp and fill, are separately created and then the matrix region is ‘filled’ around it in the cuboidal envelope of the 3D Unit Cell outline.

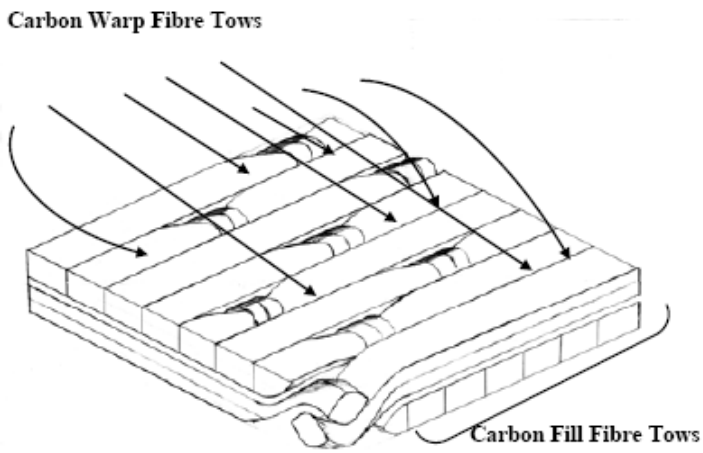

Figure 22. Schematic drawing of the 8 harness satin weave material single lamina.

The key to capturing the crimp form in the 8 harness satin weave has been the ‘loft’ part modelling tool in ABAQUS/CAE which allows the accurate generation of the changing cross-section, especially at the interlacement points where the warp tows pinch the fill carbon tows and vice versa. A minimal gap is left between these two crossing tows to model the Carbon matrix by ‘inserting cell’ as seen present there in Figure 20(b).

Ideally the fibre bundles are considering having a lenticular cross-section shape shown in Figure 23(a). On one hand these bundles are seen compressed at the tow crossover locations and then these same tows join their neighboring tows in the same lamina and take up a clearly rectangular shape after compaction. This transformation from a rectangular area to a lenticular one and back can only be modeled with ‘lofting’ as explained in Figure 24. ‘Loft’ function in ABAQUS/CAE allows the creation of a 3D object from a pair of 2D sketches and also with the help of the tracer path, where needed. As an example a lenticular and a rectangular area are shown in Figure 24(a) and then ‘lofted’ together in Figure 24(b). ‘Extrusion’ function used earlier in the DLR-XT Unit Cell geometry is similarly used here for generating constant cross-section volumes as seen in Figure 25 model forming straight sections between the curved sections. The ‘sweep’ function has been used to create the crossover sections shown as an example in Figure 23. The Unit Cell is shown in Figure 25 without the Carbon matrix enveloping the 8-Harness Satin cloth.

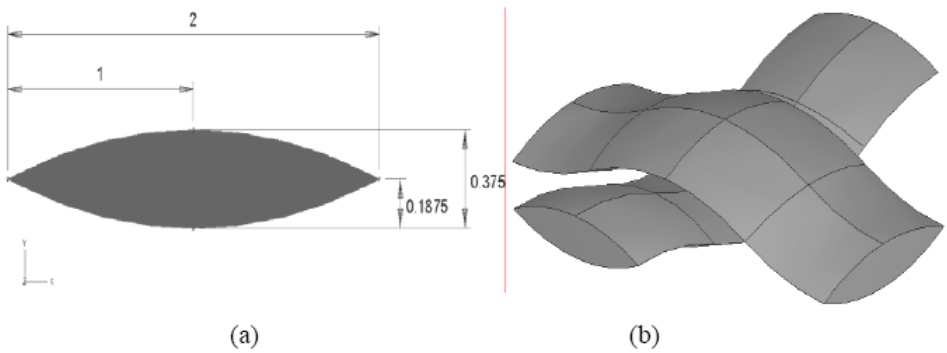

Figure 23. (a) The lenticular area, used for the ‘sweep’ and ‘loft’ function for creating volumes, (b) same sketch used to form the crossover in the weave between warp and fill tows.

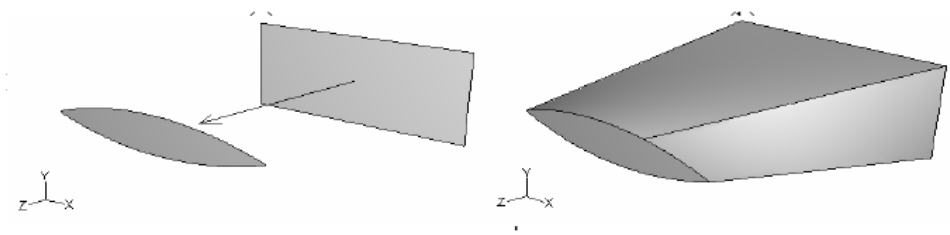

Figure 24. Using Loft function (a) between two surfaces, creating (b) final volume.

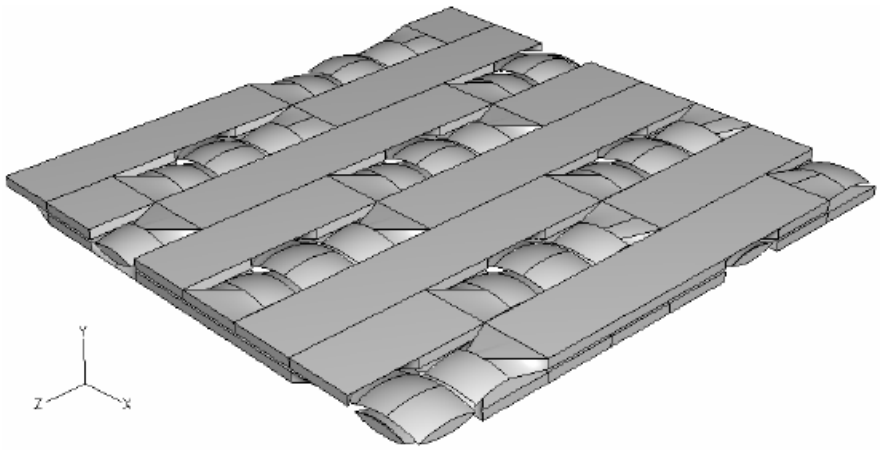

Figure 25. Warp and Fill Fibre Tow geometry with the HITCO composite Unit Cell developed from the optical micrograph with fibre-volume fraction V_f =50 %.

In designating an RVE Unit Cell with fibre tows that exhibit orthotropic thermal properties, the regions created with 'Loft' and 'Sweep' function have been assigned special polar coordinate systems. These have been necessary in order to dictate the fibre orientation and their directional property bias as shown superimposed upon a single fill fibre tow in Figure 26. The assignment of the local polar coordinate system requires selection of a discrete volume or region. This region is then assigned a unique local coordinate system, rectangular or polar, which ever is applicable. To obtain distinct regions, it was imperative to divide bigger regions of the fibre tow into smaller ones from places where the curvature sign was changing.

This can be seen in Figure 25 where partitioning sections with lines are visible in both warp and fill fibre tows that run parallel to the lenticular area outline, used for the fibre tow generation with the 'sweep' function. After separating these unique regions, different local coordinate systems are created with relevant selection of coordinates for centers of curvature and assigned to each curved section. The concern of the various regions thermally interacting with each other that had arisen in the DLR-XT Unit Cell does not arise here as in the present case of HITCO material, the RVE Unit Cell has been generated as a continuous volume. Therefore, there is no need for any interaction property definition within itself. The need for these interactions may arise when multiple RVE Unit Cells are brought together to form a larger section of the composite lamina or during the stacking to form the prototype laminate. Moreover, the HITCO composite laminate has around 8 to 12 laminae stacked upon each other in various positions with respect to specific features of the weave pattern such as the location of fibre tow crossover points. For through-thickness interaction between the laminae, again, care is needed while assigning thermal properties at the common 'tied' surfaces i.e., between master and slave surfaces defined with proper thermal interaction properties.

An important aspect of an FE analysis has always been the selection and discretisation density of elements for bringing in the governing equation within the mesh for solution. Having the luxury to selectively 'mesh' individual regions, with various element types available, makes the meshing process very thorough and interesting, but at the same time, certain constraints always restrict selection from all available options. The 3D tetrahedral,

linear diffusion, 4-noded DC3D4 element has been used in the complete RVE Unit Cell model.

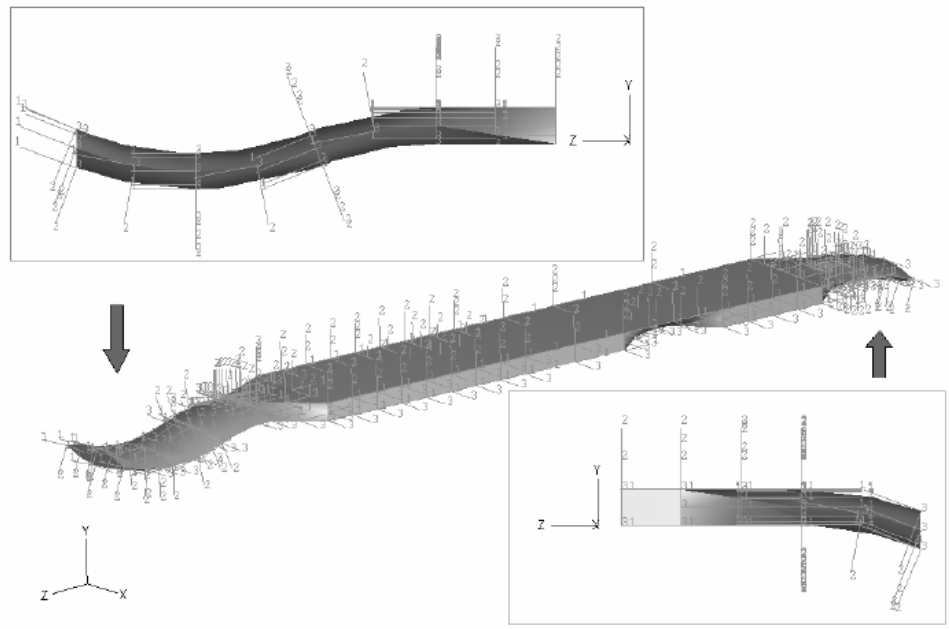

Figure 26. Material Orientation setup with local polar coordinate system, insets showing curved ends in close-up.

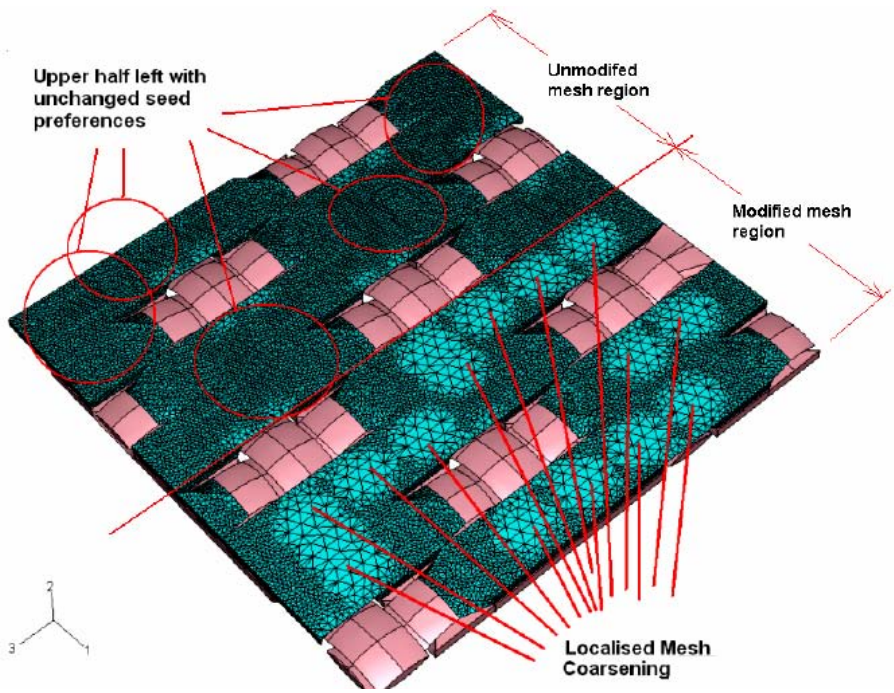

Figure 27. Suggested local coarsening in the mesh of HITCO RVE Unit Cell.

In spite of the big advantage of computational economy of the structured ‘brick’ elements in ABAQUS/CAE over the tetrahedral ones, the complexity of the weave and presence of sharp intricate curves and edge slivers between the fibre tow and matrix regions forced the only option as the tetrahedral elements. In order to reduce the problem size, some local mesh coarsening has been suggested at places where possible. An example shown in Figure 27 does highlight this possibility but the reduction in the computational load on the hardware platform has been minimal and therefore it is not considered worth the effort. A properly meshed Unit Cell is shown with the matrix region in Figure 28 and completely without them in Figure 29 where it shows 1,300,955 elements and 240,066 nodes.

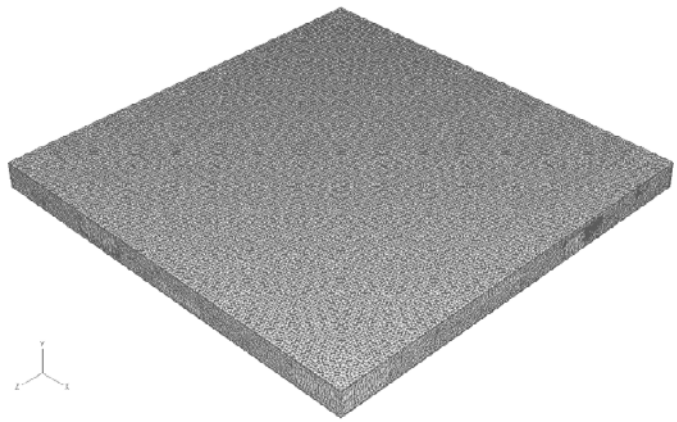

Figure 28. Meshed Unit Cell using a total of 1,300,955 DC3D4 elements.

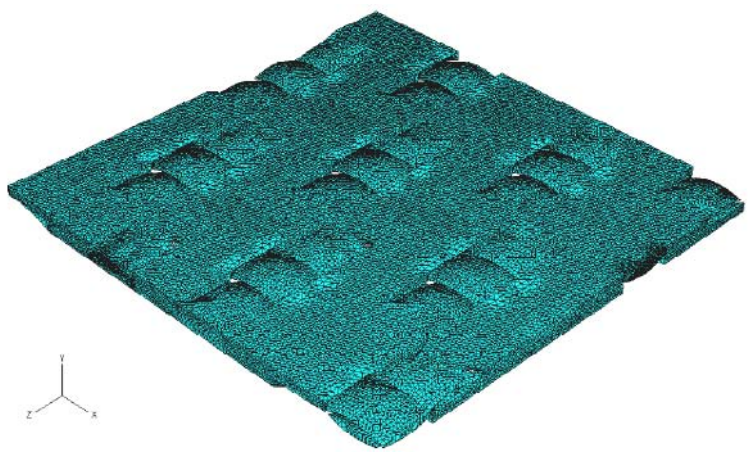

Figure 29. Meshed Unit Cell shown fibre tows but without matrix region.

An inherent complexity faced during the meshing process was the internal mesh generation around the sharp edge slivers shown in Figure 30. A local seeding bias of further refined element edge size had been determined after many trials for an optimum value in order to manage a complete element formation at these odd geometric regions.

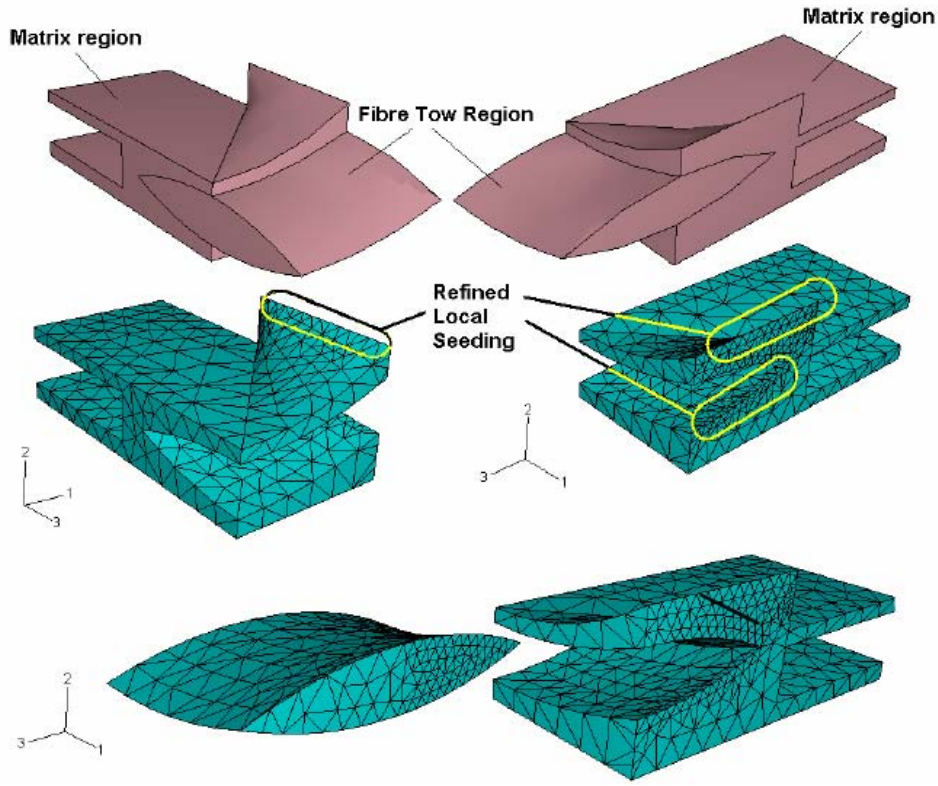

Figure 30. Edge slivers meshed with refined local seed adjustment.

4.1. Thermal Analysis

The boundary conditions set have been shown in Figure 31 for 1D Steady State heat flow in x-direction. A temperature gradient is applied across the section of the Unit Cell to allow heat flow in the direction for which the average thermal transport property is required. For the determination of k_x, as in this case, a temperature gradient '$\Delta T/\Delta x$' is applied in the x-direction and the average heat flux, q_x, is calculated for use in Eq. (12). All intermediate outer surfaces are assumed perfectly insulated ($\delta T/\delta n = 0$). The adiabatic condition is set by default on all surfaces by ABAQUS/CAE when the temperatures on two faces are set in the initial step. The temperature is given a value of T_o = 100 degrees on front face, where as for the rear face, no change is made and it remains at the default zero temperature state, creating a difference of ΔT = 100 across.

In spite of the minimal availability of precise constituent material data, a selection has been made from within reasonable bounds for material thermal property values. This exercise has also established a preliminary benchmark for assessing various computational aspects in the analyses. For true comparisons, first the basic execution of a single RVE Unit Cell analysis had to be perfected. More importantly, the choice of this RVE geometry had also been geared towards the fact that the complete CMC laminate could be modeled by simple replication of its Unit Cell. This has been achieved by sequentially joining multiple Unit Cells

together, as shown in Figure 27, through X- and Z-directions to form a single lamina and then stacking these in Y-direction to form the full laminate prototype.

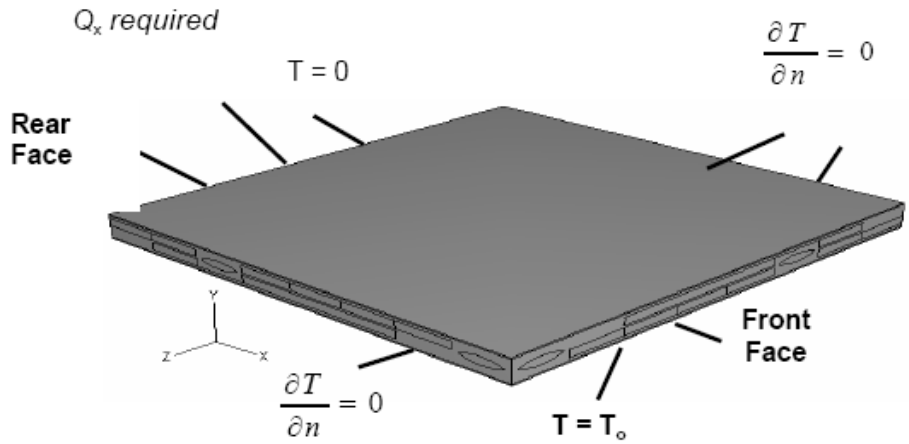

Figure 31. Boundary Conditions for steady-state FE thermal analysis for HITCO RVE Unit Cell.

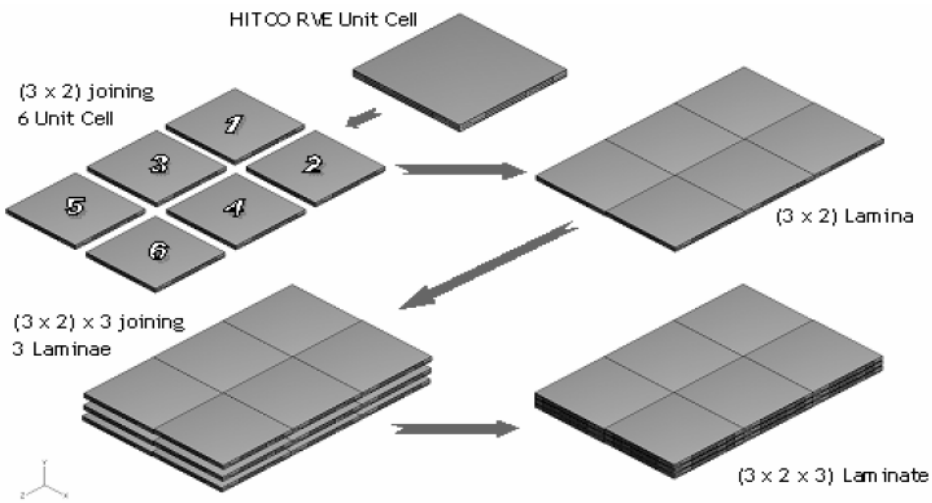

Figure 32. Formation of the Composite test specimen sample using multiple HITCO RVE Unit Cells.

Using the chosen set of constituent material properties, a steady-state analysis has been conducted. The local coordinate system assignment has insured that the heat flux must conform to the vectors dictated by fibre tow's orthotropic orientation system, as seen in a vector plot in Figure 30. Arrows in the enlarged section of Figure 31 clearly show the desired heat flow direction following the curves of the fibre tows. The flow has been enforced by the material property orientation enforced during assignment of local coordinate system for fibre tow sections bending along the tow interlacement points. A profile of in-plane heat flux for the HITCO RVE Unit Cell has been shown in Figure 32 'without the matrix region' so that heat flux in the warp fibre tows is clearly visible. Amongst the expected flux contours, there are certain flux hot spots present in the plot that can also be explained. These are typically

present at the edges of the rectangular tow structure that changes its cross-sectional shape from rectangular to lenticular and back i.e. places where fibre tows have been pinched due to the interlacement and so these are bent abruptly, hence the heat flow is subsequently diverted. This results in the observed flux concentration.

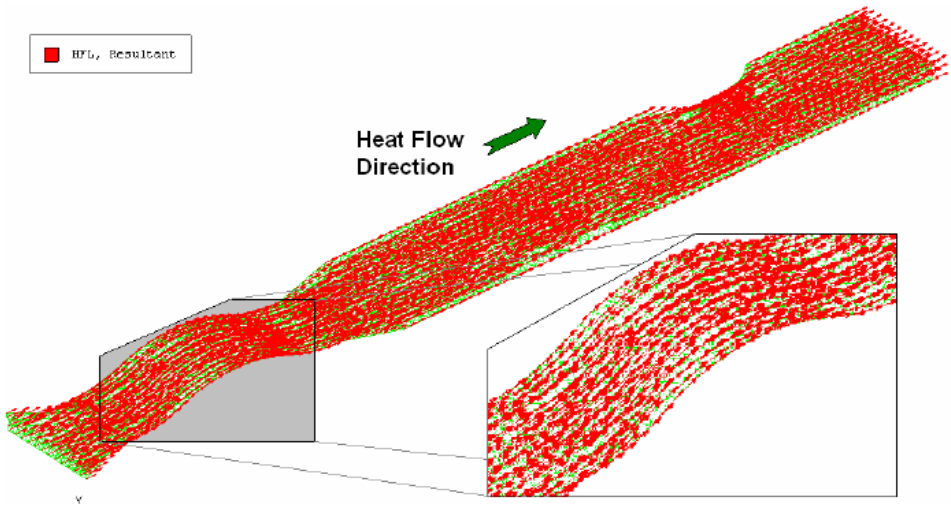

Figure 33. Vector Plot of a single warp tow for an in-plane steady-state heat flow, the inset showing a close-up view of the interlacement point showing flow vector conforming to the curvature.

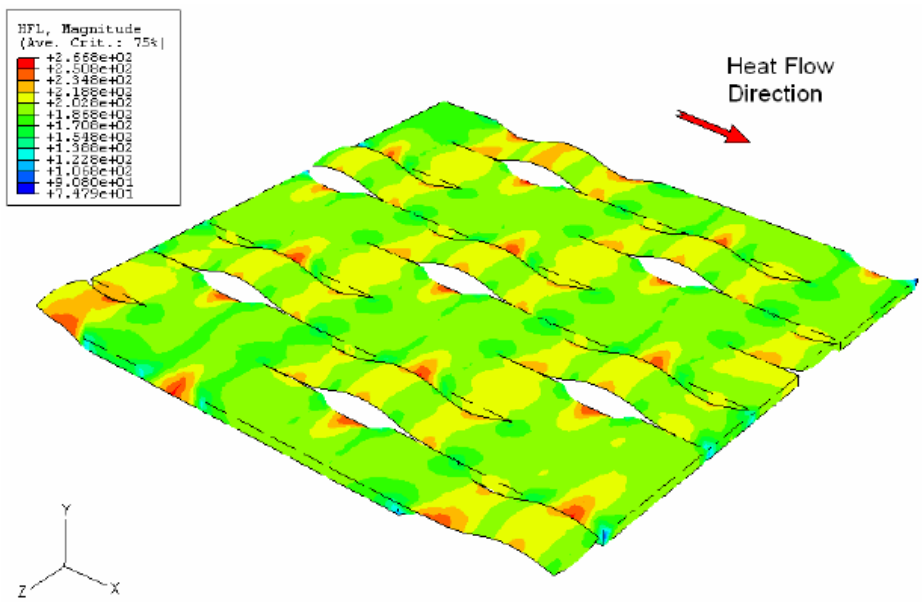

Figure 34. 'In-plane' steady-state heat flux in X-direction (arrow) for the HITCO RVE Unit Cell showing only the 'Warp' fibre tows.

These are also signs of less sudden changes in flow direction at the crossover locations which forces flux concentration there as well although to a less degree than the shape change phenomenon mentioned above. This behavior has been expected within such a crimp weave composite cloth and shows a thermal behavior that could be expected of a woven composite. Although this behavior may be slightly reduced with the help of certain effort in smoothing the remaining sharp cuts on the lofted regions during the modelling process but its positive impact is expected to be minimal and therefore not a worthwhile exercise.

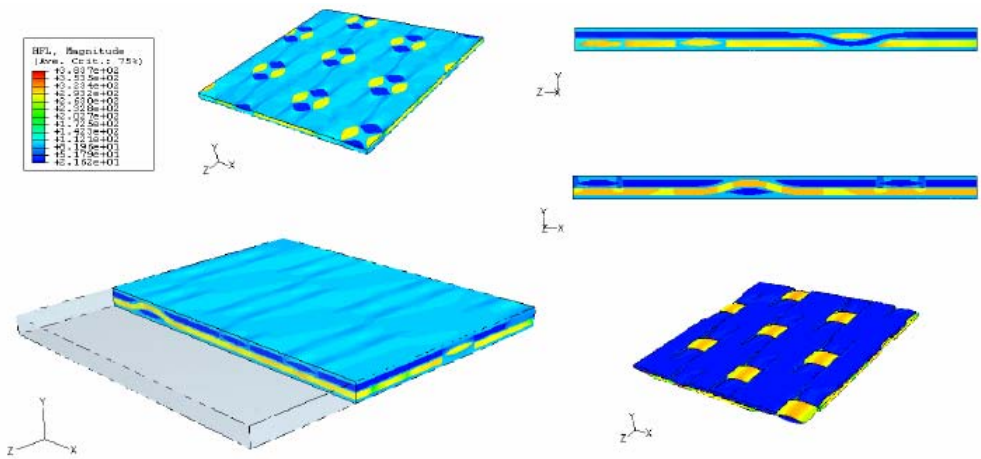

Figure 35 'In-plane' Steady-State heat flux in X-direction (arrow) for the complete HITCO RVE Unit Cell with flow contours seen (a) in an in-plane slice across XZ-plane, (b) across thickness in YZ-plane, heat flowing normal to the page, (c and d) across thickness in XY-plane, (e) in fibre tows only (without matrix).

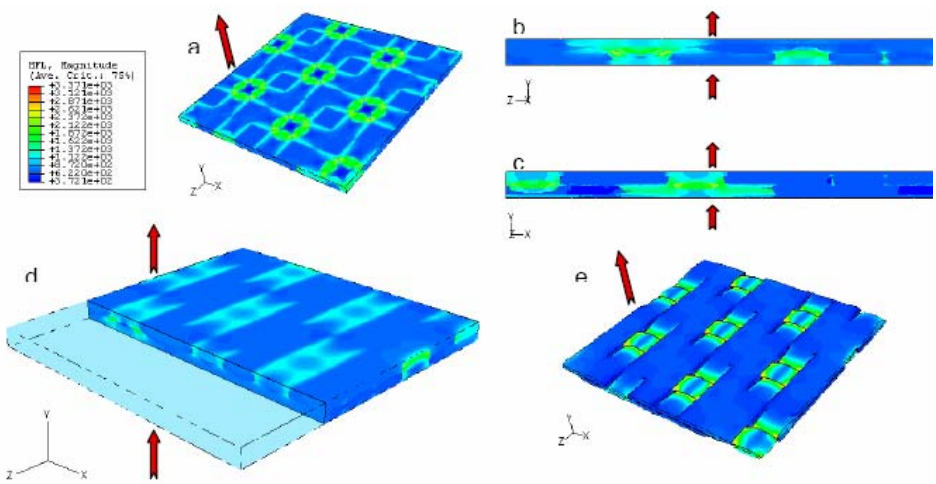

Figure 36. 'Through-thickness' Steady-State heat flux in Y-direction (arrow) for the complete HITCO RVE Unit Cell with flow contours seen (a) with in-plane slice across XZ-plane, (b) across thickness in YZ-plane, heat flowing normal to the page, (c and d) across thickness in XY-plane, (e) in fibre tows only (without matrix).

The heat flux concentration is 25% greater than the in-plane heat flux (light green) indicating that sudden change in flow direction has been dictated by fibre tow undulations and this is how the heat is expected to flow through the composite fabric across the dominant heat flow x-direction. An overall flow contour summary is given in Figure 32 and Figure 33 for in-plane and through-thickness heat flow scenarios respectively for the full composite RVE Unit Cell (except in Figures 32(e) and 33(e) where matrix is removed). The arrows depict the prevailing heat flux direction in each case.

It is imperative that the final results obtained bare similarity to the experimental data and this has been shown in Table 8 with limited input information for the FE analysis as far as constituent material properties are concerned. The input values taken for the modified matrix region was calculated from Equation 14 using rule of mixtures as the matrix and air in voids and cracks, comprising the bulk porosity, do have isotropic thermal conductivity. Hence an input value of k_{mp} = 18.72 has been used based on the values of k_m and k_p given in Table 9.

Table 8. Values of Thermal Conductivity of the Constituent Materials

Material	k (W m^{-1} K^{-1})	Volume Fraction (%)
Carbon Fibre Transverse	7	50
Carbon Fibre Longitudinal	70	
Carbon Matrix	28	39
Air (porosity)	0.001	11

Table 9. FE analyses compared with Manufacturer's Thermal Conductivity Data (W.m^{-1}K^{-1})

	Experimental Data	Numerical Analysis (Steady-State)
In-plane	28	25.656 (+ 8%)
Through-Thickness	8	9.79 (- 22%)

5. COMPUTATIONAL ASPECTS

It has been highlighted earlier that with the increase in the geometric complexity of the CMCs, the requirement of the computing resources has risen. This has been reiterated by the current modelling effort with 8-harness satin weave geometry, apart from the modelling challenge of the HITCO materials' fibre tow weave pattern which alone has been massive enough. It can be reckoned that with the multiplication of the Unit Cell (each containing around a Million elements) across the lamina and then the laminate, demand for computational power increases drastically. Special arrangement is therefore required for conducting analysis of such large FE models.

Earlier DLR-XT Unit Cell had been managed within a single-CPU desktop machine operating on Windows XP with 80 Gigabytes storage space and 512 Megabytes physical memory. It has also been observed how the machine had been swapping its hard disk for need of fast storage; as much as 1.8 Gigabytes at times, almost 4 times the physical memory. In that case, the element count had not exceeded 200,000 whereas in the present case this figure

exceeds 1 Million in the HITCO Unit Cell model. Moreover, the real simulation for HITCO samples may definitely involve the analysis of a full laminate such as the one formed at the end in Figure 27. This would mean the multiplication of element count for a single RVE Unit Cell with the total number of Unit Cells used to form the laminate, e.g., 18 from the example shown in Figure 27. It is emphasized here that even in the presence of a much more powerful PC - 3 GHz, single processor, 1GB physical memory - a thermal analysis with just two Unit Cells joined together has not been successful, clearly exhibiting the limitation of a single processor PC when ABAQUS/CAE [18] is conducting a simple steady-state analysis on such a model.

The next option used is an SGI Onyx 300 machine with 32 SGI R14000 MIPS processors running at 600 Megahertz. Each such processor having a peak speed of 1.2 Gigaflops makes the total peak speed of the machine of approx. 38 Gigaflops. But the system is a shared memory machine with 16 Gigabytes of physical memory, permitting both shared memory and distributed memory programming models to all users simultaneously. Although the analyses conducted on this machine have already yielded better memory management scenarios compared to single processor Windows PC, but still certain ABAQUS code limitations regarding thermal analysis mentioned in the software reference documentation has made the scope for speedup gain rather narrow. Proof of this behavior has been seen through initial runs conducted using increasing number of parallel processors. Some trends for ABAQUS and its solver performance are clearly seen in Table 10. Here the comparison is made with tests that were run on the same Unit Cell with a monotonic tensile loading. Increased speed up hints at the advantage gained by the use of multiprocessor platform for the mechanical analysis of HITCO Unit Cell model and larger models are considered to be solved faster here but only in the regime of mechanical loadings. For thermal application simulation, this study suggests that in order to benefit from parallelization which is inevitable therefore crucial for larger models, further investigation are necessary in improving solver performance. This has also led the present study towards another domain of parallelization specially coded for finite element modelling and it is being pursued simultaneously now.

Table 10. Speed-up observed for, a comparison (percentage) between 1-D steady-state heat transfer analyses for thermal conductivity measurement and 1-D monotonic tensile loading for determining composite stiffness employing parallel processing

Processors	Thermal Analysis (%)	Mechanical Analysis (%)
2	7	12
4	9	20
8	10	24

5.1. Parallel Processing

Results are now presented of thermal analysis of a benchmark heat flow problem, as defined in Figure 34, in a multi-processor environment. Figure 35 shows the analysis speed-up against the number of processors with an increasing mesh size.

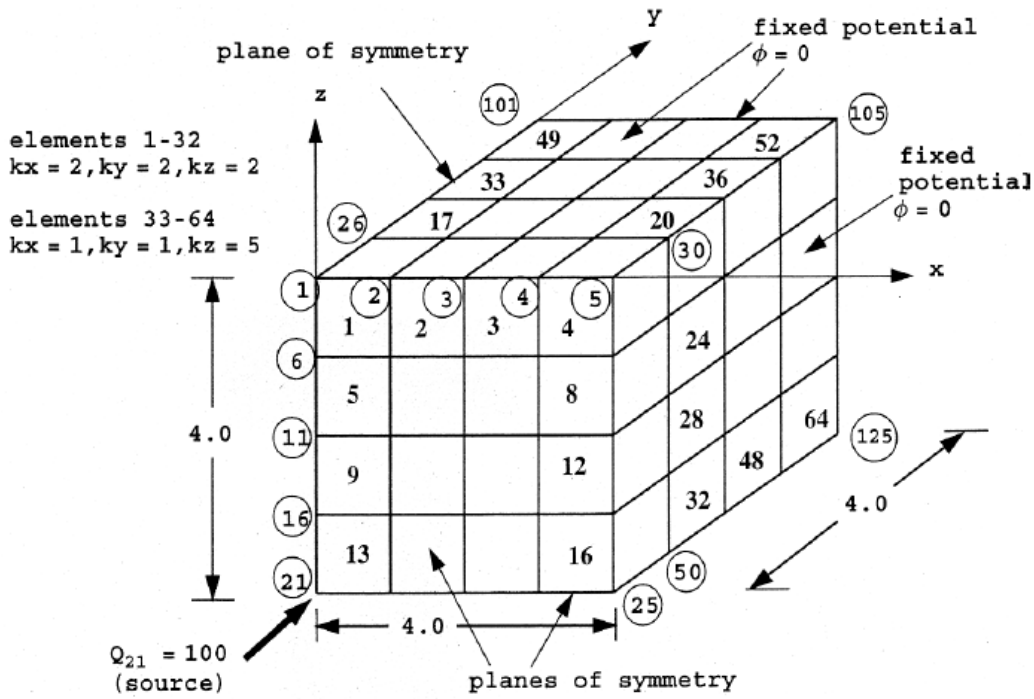

Figure 37. A benchmark steady-state thermal problem for parallel processing.

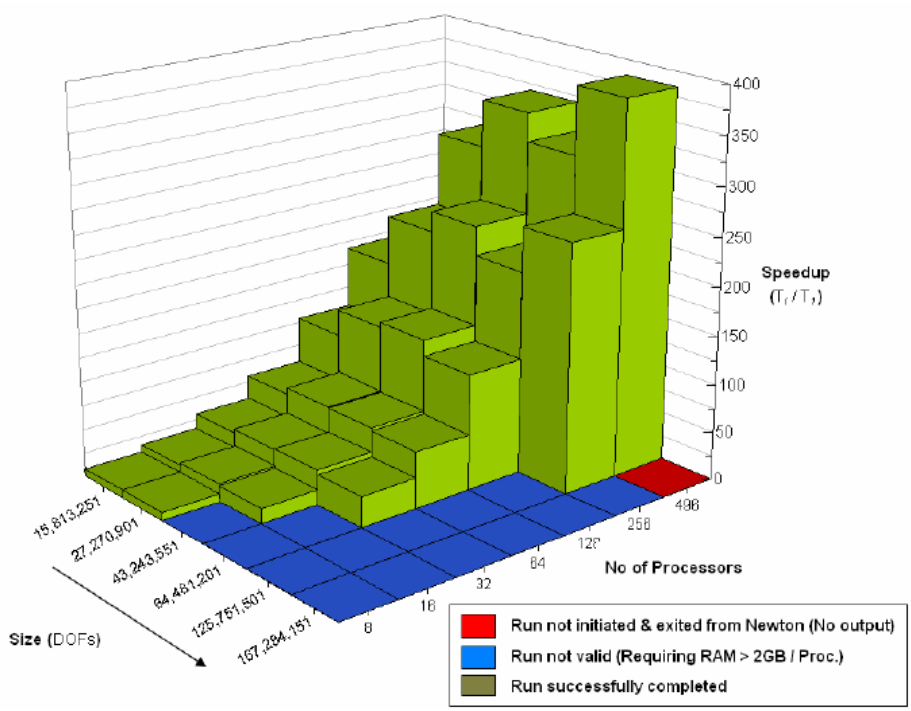

Figure 38. Results of scalability studies.

CONCLUSIONS

Unit Cell Modelling technique is useful for thermal transport analysis of composites. Based on the DLR-XT Unit Cell modelling with sub-modelling of manufacturing porosities for capturing sequential material degradation and also on just bulk porosity introduction in HITCO, this approach has been shown successfully for even complex weaves like 8-harness satin. A bulk porosity of 11% has been accommodated within the matrix with reduction in the matrix thermal conductivity, managed by using the 'rule of mixtures'.

Comparison of FE analyses results from ABAQUS with the experimental results have shown good agreement, with emphasis to the extent of individual role of different porosities in DLR-XT. In material by HITCO, the variability has been seen due to the variety of stacking orientation and phase shift between the laminas. The increased degrees-of-freedom per RVE Unit Cell has also challenged the computational prowess of the present facilities, prompting the use of parallel computing wisely.

REFERENCES

[1] A.G. Evans and R. Naslain. High-temperautre Ceramic-Matrix Composites, Vol. I and II, *Ceramic Transaction*, 57, 1995.

[2] K. K. Chawla, Ceramic Matrix Composites, Second Edition, Chapman and Hall, 2003.

[3] D. A. G. Bruggemann. *Ann. Phy*., 24, 1935, p. 636.

[4] P. Del Puglia, M. A. Sheikh, An overview of thermal transport models for composites, *Proceedings of XXX AIAS* (Associazione Italiana per l'Analisi delle Sollecitazioni) Conf., Alghero (Italy), University of Cagliari, Dep. of Ingegneria Meccanica, 2001, pp.687-696.

[5] T.J. Lu and J. W. Hutchinson, Effect of matrix cracking on the overall thermal conductivity of fibre-reinforced composites, High-temperature Structural Materials, Editors: R. W. Cahn, A. G. Evans and M. McLean London: Chapman and Hall, London, 1996, pp.177-192.

[6] J. W. Klett, V. J. Ervin, D. D. Edie, Finite-element modelling of heat transfer in carbon/carbon composites, *Composit. Sci. Technol*., 59, 1999, pp. 593-607.

[7] M. A. Sheikh, S. Taylor, D. R. Hayhurst, R. Taylor, Microstructural Finite Element Modelling of a Ceramic Matrix Composite to predict Experimental Measurements of its Macro Thermal Properties, *Modelling Sim Mater Sci Eng*, 9, 2001, pp. 7-23.

[8] M. A. Sheikh, S. Taylor, D. R. Hayhurst and R. Taylor, Measurement of Thermal Diffusivity of Isotropic Materials using the Laser Flash Method and its validation by Finite Element Analysis, *J. Phys. D: App. Phys.* 33, 2000, pp. 1536-1550.

[9] V. I. Trefilov. 1995. *Ceramic And Carbon Matrix Composites*. London: Chapman and Hall.

[10] K. K Chawla. 1998. *Composite Materials: Science and Engineering* (2nd Edition). Springer-Verlag, New York.

[11] S. T. Peters. 1998. *Handbook of Composites* (2nd Edition).Springer - Verlag.

[12] F. L. Matthews, R. D. Rawlings. 1994. *Composite Materials: Engineering and Science*. London: Chapman and Hall.

[13] D. Hull, T. W. Clyne. 1996. *An Introduction to Composite Materials* (2nd Edition), Cambridge University Press.

[14] E. Behrens, Thermal Conductivities of Composite Materials, *Journal of Composite Materials 2* (1968) 2-17.

[15] J. K. Farooqi and M. A. Sheikh, Finite Element Modelling of Thermal Transport In Ceramic Matrix Composites, *Computational Materials Science*, 37, pp. 361-373, 2006.

[16] P. Del Puglia, M.A. Sheikh, D.R. Hayhurst, Classification And Quantification Of Initial Porosity In A CMC Laminate, Composites Part A: *Applied Science and Manufacturing* 35 (2004) 223-230.

[17] K. Woo and N. S. Goo, Thermal conductivity of carbon-phenolic 8-harness satin weave composites, *Composite Structures*, vol. 66, no. 1-4, pp. 521-526, 2004.

[18] ABAQUS Version 6.5 Documentation, Hibbit, Carlsson and Sorenson Inc, Providence, RI, 2005.

In: Developments in Ceramic Materials Research
Editor: Dena Rosslere, pp. 211-240
ISBN 978-1-60021-770-8

Chapter 7

PROGRESS IN POROUS PIEZOCERAMICS

R. Ramesh*[*], *H. Kara*[#], *Ron Stevens and C. R. Bowen
Department of Engineering and Applied Sciences,
University of Bath, Bath BA27AY, UK
[*]Naval Physical and Oceanographic Laboratory, Cochin-682 021, India
[#] Johnson Mathey Ltd., UK

ABSTRACT

Synthesis, characterization, device fabrication, modeling and underwater evaluation of porous piezoceramics used in the form of 3-3 piezocomposites are discussed in detail. Piezocomposites have drawn considerable attention in recent years due to their potential application in medical ultrasonic and underwater transducers. Piezocomposites with 3-3 connectivity are produced from porous piezoceramics by filling the pores with suitable polymer materials. In this two-phase material, the PZT and the polymer are self-connected in three dimensions. Synthesis of porous PZT structure by two techniques, namely, BURnout Plastic Spheres (BURPS) and foam reticulation techniques used to obtain wide range of porosity are described. Samples with ceramic volume fraction ranging from 10% to 100% are synthesised and are characterized in terms of their microstructure, piezoelectric charge (d_{33}, d_{31}) and voltage (g_{33},g_{31}) coefficients, the hydrostatic coefficients (d_H and g_H) and hydrostatic Figure-of-Merit. Variations in dielectric, mechanical and piezoelectric properties as a function of ceramic volume fraction/ porosity are discussed. The experimental results are compared with that of a simple analytical model. Finite element modeling (FEM) studies are carried out on hydrophones constructed from porous and dense PZT discs. An axisymmetric model is proposed for dense PZT hydrophone and is validated by an analytical model. A 3-dimensional model is proposed for porous PZT hydrophones. The FEM results agree well with that of the experiments. Details of the hydrophones fabricated with PZT-air and PZT-polymer composites with different configurations are presented. The acoustic performance of the transducers is evaluated underwater. The receiving sensitivity, the electrical impedance spectra and the directional response of the hydrophones are measured in the frequency range (10-100) kHz. These studies show that the 3-3 piezocomposite transducers have better properties than the transducers made out of dense PZT. The improved properties are the higher hydrostatic coefficients, higher receiving sensitivity and flat response over a wide frequency range. This suggests that the 3-3

piezocomposites made up of porous piezoceramics are very useful for wide-band hydrophone applications. A detailed picture of these studies and the salient features of these materials will be discussed.

Keywords: *Piezoelectric, piezoceramic, porous, piezocomposite, hydrophone, Finite Element Modelling.*

1. INTRODUCTION

Piezoelectric ceramic materials, such as Lead Zirconate Titanate (PZT), are widely used as active components in transducers used for sonar, under-water communication, under-water imaging, medical imaging and non-destructive evaluation, because of their high electromechanical coupling coefficient and low electrical and mechanical losses [1]. However, their higher specific acoustic impedance, higher weight factor and poor mechanical properties are undesirable in certain applications. On the other hand, the piezoelectric polymers like polyvinylidene difluoride (PVDF) have very low specific acoustic impedance offering excellent impedance matching with water or human tissues [2] The serious drawbacks of these materials are very low values of electromechanical coupling coefficient and dielectric constant. Recently, piezocomposite materials have been developed by combining active piezoelectric materials with passive polymers, thereby taking advantages of the desirable features of both the constituent materials [3]. They exhibit superior electromechanical properties compared to the piezoceramic materials.

Some of the advantages of the piezocomposites are, higher electromechanical coupling coefficients, low specific acoustic impedance, a wide range of dielectric constant, low dielectric and mechanical losses, variable sound velocity, low mode- coupling, ease of subdividing into acoustically isolated array elements and formability into complex curved shapes, etc [4] However, all the benefits are not been achieved simultaneously and composites with the best characteristics are generally achieved through optimization of various parameters [5] Piezocomposite transducers with predetermined properties can be tailor-made for a specific application by optimizing the type and proportion of ceramic and polymer components and their relative arrangements in the composite structure [6].

In piezocomposites, the piezoceramic and polymer phases are physically connected in three dimensions in a systematic arrangement called *connectivity* [7]. Although piezocomposite of various connectivities do exist theoretically, only certain categories, such as, 1-3, 2-2 and 3-3 connectivities are technically feasible to fabricate and are found useful for practical applications [8, 9, 10].

1-3 piezocomposites have been studied extensively and various modelling and experimental studies have been reported in literature [11, 12]. Although, 1-3 composites are highly useful for transducer applications, their production is tedious and expensive [8]. 3-3 piezocomposites prove to be an alternative, with comparable material properties and relatively simpler method of synthesis [8]. 3-3 piezocomposites in the form of porous PZT materials show considerably improved transducer characteristics. Experimental studies on porous piezoelectric structures indicate that they have high hydrostatic figure-of-merit [13] and high receiving sensitivity [14, 15]. However, their depth-handling capability and the

stability to hydrostatic pressure have yet to be proved. The mechanical strength of the transducer can be improved by filling with a polymer as second phase.

In certain cases, depending on the method of synthesis, the 3-3 piezocomposites are found to coexist with 0-3 composites for intermediate ceramic volume fractions. The material properties of these composites with mixed connectivities can be evaluated using theoretical models [16, 17]. Some theoretical models have been proposed to study the material properties of ideal 3-3 piezocomposites [18, 19]. Bowen *et al*. [20] proposed a model, in which the '*unit cell*' is split into four volumes with series/ parallel combinations of piezoceramic and polymer components. This model assumes that only certain volumes contribute effectively to the piezoelectric charge coefficients and dielectric constant, depending on the alignment of piezoceramic component with respect to the stresses applied in the longitudinal and lateral directions. Effective material parameters of the composites can be determined from the material properties of the constituent material phases, in an average sense [21]. These models are useful to determine the material properties of the porous piezoceramics.

However, the transducer characteristics of these materials have not been studied extensively, for which Finite Element Modelling (FEM) would be a simple and effective tool. FEM studies on 1-3 piezocomposite transducers have been reported [22, 23]. In these studies, only one *unit cell* of the composite block has been modelled, assuming that it represents the entire piezocomposite structure. Although these models can give material parameters like piezoelectric coefficients, to considerable accuracy, they are inadequate to predict the lateral-mode resonance of a transducer of finite dimensions [24]. Hence, real-size 3-dimensional FEM studies are necessary to evaluate the device characteristics of piezocomposite hydrophones.

The transducer characteristics of the porous piezoceramics and polymer filled piezocomposites are evaluated to demonstrate their suitability to underwater applications [14, 15, 25]. The receiving voltage sensitivity of the 3-3 Piezocomposites hydrophones is found to be higher than that of the hydrophones constructed from dense PZT materials.

This chapter presents a detailed picture of synthesis and characterisation of porous piezoceramics, variation of material parameters with the ceramic volume fraction, a method to estimate the effective material parameters of 3-3 piezocomposites, finite element modelling of the transducer devices fabricated using porous piezoceramics to estimate the acoustic performance, construction of piezocomposite hydrophones and evaluation of various underwater transducer characteristics.

2. SYNTHESIS AND CHARACTERISATION OF POROUS PIEZOCERAMICS

There are a number of techniques to synthesise porous structures, for example, newly developed rapid prototyping [26] and free form fabrication [27] processes where a desired porous structure is built up layer by layer, mixing ceramic powder with a fugitive binder [28] (BURPS technique, an acronym for 'BURned-out Plastic Spheres'), replicating a porous structure by coating it with a ceramic slurry and burning it out during sintering (lost wax replication of a coral skeleton [29] and polymeric sponge [30] techniques). Of these, the BURPS and polymeric sponge techniques are relatively easier to implement for large-scale

production. The polymeric sponge technique is being used successfully to commercially produce high temperature ceramic filters [31].. The processing technique involves impregnation of polyethylene foams with a ceramic slip and controlled sintering with an intermediate temperature hold for removal of the foam.

The BURPS technique produces a porous structure by mixing ceramic powders with polymer spheres followed by compaction and controlled sintering. A 3-3 BURPS piezocomposite showed that the hydrostatic figure of merit increases with increasing polymer fraction [28]. However, the polymer fraction is only varied between 30 and 70% volume, since it is not feasible to produce a higher pore content ceramics using the BURPS technique. Creedon *et al*. [30] produced PZT/polymer composites having 85-90 vol. % porosity by a polymeric sponge technique and they also found an increase in hydrostatic sensitivity with increasing polymer fraction. 3-3 piezocomposites are usually produced by manufacturing a porous ceramic structure and subsequently impregnating the porosity with a polymer. The porosity can also be left as air.

This section describes the production of a range of porous ceramics of PZT-5H ranging from 9 to 92 vol. % porosity using both the BURPS and polymeric sponge techniques, characterisation in terms of d_{33}, d_{31}, ε, d_H, g_H and *Figure-of-Merit* before and after polymer impregnation and the effect of ceramic/ polymer volume fraction on the properties.

2.1. Material Synthesis

Porous piezoceramics are synthesised using two techniques, namely, BURPS and foam-reticulation techniques. Commercially available PZT-5H spray dried powder (Morgan Electroceramics, Vauxhall Industrial Estate, Wrexham, UK) is compacted and sintered at 1200°C for 2 hours to form monolithic PZT ceramics of 4 mm thickness and 40 mm diameter. For the BURPS technique, the PZT powder is mixed with acrylic thermoplastic resin (ATR) and polyethylene oxide (PEO) at various weight ratios to produce a range of pore volume fractions. The mixed powder is then uniaxially compacted at 50 MPa. The compacts are then subjected to a burnout cycle, heating with a ramp rate of 1°C/min (to 600°C for an hour) to remove the organic phase, before final sintering at 1200°C for 2 hours. For the polymer sponge technique, a ceramic slip of 80 wt. % PZT, 3 wt. % PVA, 0.75 wt. % dispersing agent and distilled water is prepared by ball milling for at least 6 hours. A number of polyethylene sponges of different cell sizes are cut and impregnated with the PZT slip. The excess ceramic slip is removed by compressed air. The green ceramic foams are then introduced to the same burnout cycle as above, before final sintering at 1200°C for 2 hours.

Self-adhesive aluminium electrodes (150μm) are used for the porous samples (PZT-air composites) while dense PZT and PZT-polymer composites are electroded with a silver paste. All the samples are individually poled at 110°C and 12.5 kV for 10 minutes using corona poling. The corona tip height is set to 30 mm. Some of the poled samples are filled with suitable low viscosity polymer under vacuum in order to obtain PZT-Polymer composites.

2.2. Characterisation

The porous piezoceramics are characterized first, using Scanning Electron Microscopy (SEM) studies to verify the structural connectivity and then, by measuring different material coefficients. Piezoelectric charge coefficients (d_{33} and d_{31}) and permittivity are measured using Berlincourt d_{33} Piezo Meter (Take Control, University of Birmingham Research Park, Vincent Drive, Birmingham, UK) and LCR meter (HP 4263B, Hewlett Packard Japan Ltd., Hyogo, Japan) respectively. These values are used to derive the hydrostatic charge (d_H) and voltage (g_H) coefficients and hydrostatic figure of merit (*FoM*).

2.3. Microstructures

The microstructure of the various PZT-air/ polymer composites synthesised are characterised to verify the connectivity pattern of the composite structure. Microstructures of the various PZT-Air and PZT-Polymer composites are shown in Figures 1 and 2, respectively. Depending on the PZT ceramic volume fraction, there are two distinct connectivity patterns observable in the composites. The composites with high PZT volume content (>60%) shows 3-0 connectivity (i.e. discrete polymer or pore phases within PZT matrix), while composites with low PZT volume content (<40%) shows clear 3-3 connectivity. The composites falling in between these limits (40-60 vol. % PZT) showed a mixture of 3-0 and 3-3 connectivity.

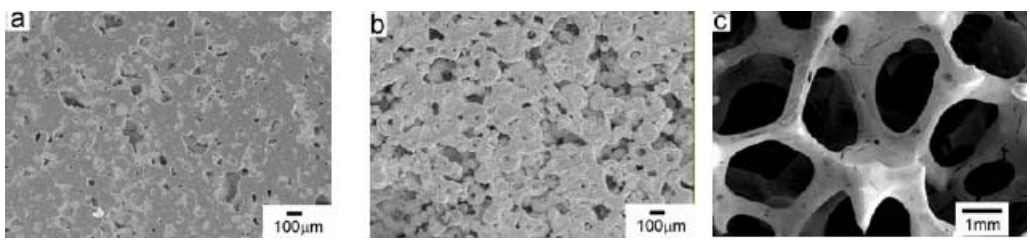

Figure 1. SEM micrographs of PZT-Air composites with different PZT volume fractions: (a) 80 %, (b) 44 % and (c) 17 %.

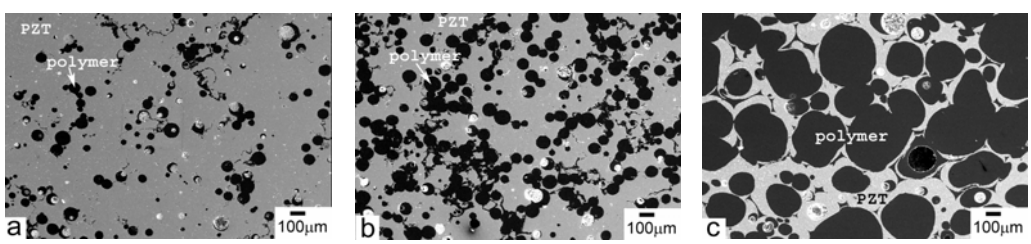

Figure 2. SEM micrographs of PZT-Polymer composites with different PZT volume fractions: (a) 85 %, (b) 59 % and (c) 21 %.

It can be seen from these figures that the composites synthesised using foam-reticulation technique shows perfect 3-3 connectivity (i.e. both the polymer and PZT are fully interconnected). The composites synthesised using the BURPS technique shows different pore morphology due to the different morphologies of the fugitive polymer phases used to

create the pores. The spherical ATR results in rounded pores (Figure 1) whereas irregular PEO results in more irregular pore morphology (Figure 2).

2.3.1. Dielectric constant

Figure 3 shows the variation in dielectric constant of 3-3 piezocomposites prepared using different techniques. Dielectric constant decreases with decreasing ceramic content. There is no significant difference in properties between PZT-Air and PZT-Polymer composites. This is due to the comparable permittivity values of air and polymer phases. It is also interesting to note that at ~ 60% PZT ceramic volume, where the 3-0 connectivity starts appearing, the permittivity deviates into two separate lines. This is due to the extensive cracks, revealed by cross-sectional SEM examinations, lying parallel to the surface. These cracks, which occur after green compaction due to relaxation of the elastic ATR spheres, prevent connectivity of the ceramic between the electroded surfaces, hence reducing the permittivity considerably. However, it should also be noted that pore anisotropy can also be a reason for this deviation between ATR and PEO samples since higher permittivity is obtained when specimen with pores align along the thickness direction compared to those normal to the thickness direction [32].

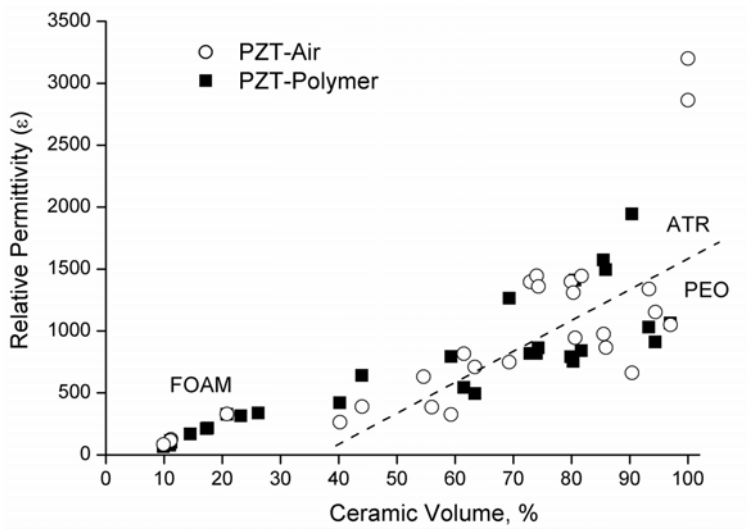

Figure 3. Variation of dielectric constant of 3-3 composites with ceramic volume fractions.

2.3.2. Piezoelectric Coefficients

Piezoelectric coefficients depend strongly on the amount of piezoceramic component present in a piezocomposite, since this is the dominant contributor to the net piezoelectric property of the composite. The polymer component, being a passive material, contributes mainly to the mechanical properties and indirectly influences the piezoelectric properties of the composites as well.

2.3.3. Hydrostatic Charge Coefficient

Figure 4a shows the variation in piezoelectric charge coefficient with change in ceramic volume fraction. The hydrostatic charge coefficient (d_H) increases with increasing piezoceramic volume fraction, reaching a broad maximum around 50-60 vol. % PZT, for PZT-Air composites. This is in good agreement with analytical models which indicate a broad maximum around 40-50 % PZT for d_H [33]. It is difficult to draw similar conclusion from PZT-polymer composites due to the large scatter of the results. Decoupling of d_{33} and d_{31} coefficients by the polymer and ceramic struts along the direction transverse to the poling direction resulted a large reduction in d_{31} compared to d_{33}, which in turn increases d_H. For PZT-5H, the d_{33}, charge per unit force produced in the direction of polarisation is almost the same in magnitude (513 pCN^{-1}) as the combination of d_{31} and the d_{32}, the charge on the transverse directions, but opposite in sign (-220 pCN^{-1}). Therefore, if a hydrostatic force is applied to monolithic PZT-5H the charges cancel each other out. As seen in Figure 4b, an increase in the d_{33}/d_{31} ratio with decreasing ceramic volume fraction indicates strong decoupling. Air provides better decoupling than the polymer. The d_{33}/d_{31} ratio does not tail down as in d_h which is due to the low values of the d_{33} and d_{31} charge coefficients at low ceramic fraction.

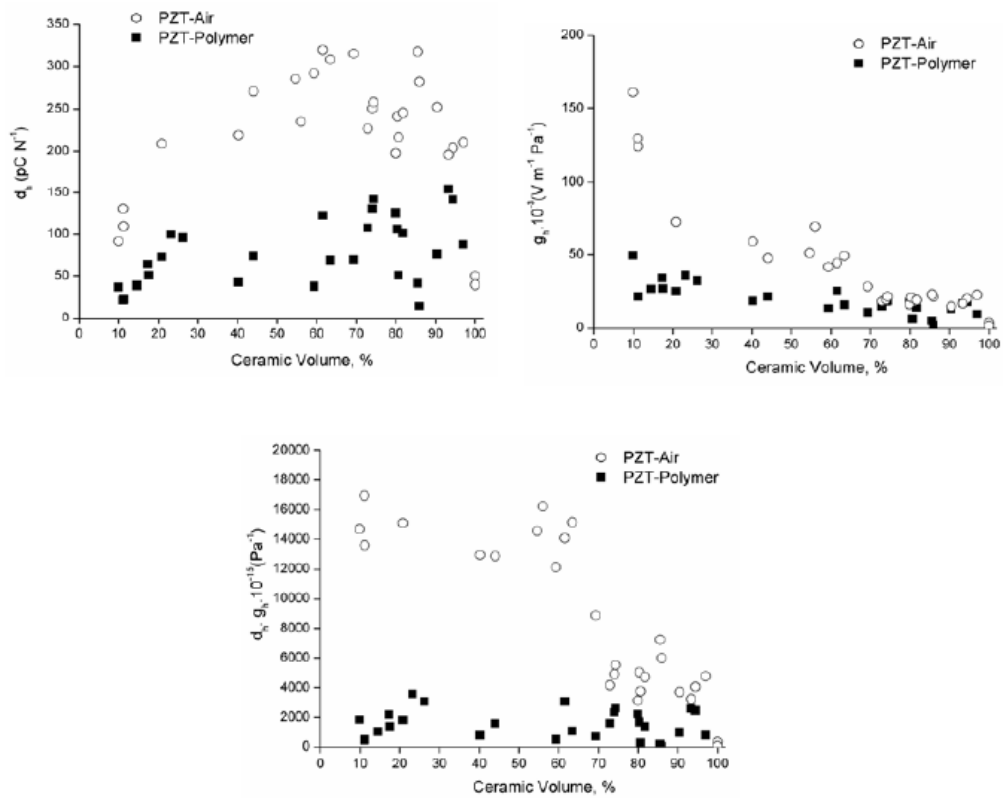

Figure 4. Variation of piezoelectric hydrostatic coefficients of 3-3 composites with ceramic volume fractions; (a) charge coefficient (d_H), (b) voltage coefficient (g_H) and (c) Figure-of-Merit (d_H g_H).

Polymer infiltration of the poled porous ceramics reduced the hydrostatic response of the composites considerably when compared to the PZT-air composites although there is still

improvement over dense PZT ceramic for most of the PZT-polymer composites. The reduction in d_h by polymer infiltration is due to reduction in stress born by the ceramic phase, which is not the case for PZT-air composites where stress is born by the ceramic phase only. As explained earlier extensive cracking in BURPS (ATR) samples hinder the stress or charge transfer between the electroded faces, resulting in a dramatic reduction in d_H compared to BURPS (PEO) samples.

The hydrostatic charge coefficient is shown to be a function of the Young's modulus of the polymer [33] increasing with decreasing stiffness due to an increase in stress transfer into the PZT ceramic phase. The epoxy resin used in this work had the Young's modulus of 2.8 GPa determined by tensile testing. It has been reported that the softer epoxy yields lower acoustic impedance and higher electromechanical coupling [34]. Therefore the type of epoxy utilised will also be influential on the electromechanical properties. Weak bonding of the polymer to the ceramic might also contribute to a reduction in d_H due to reduction in stress transfer efficiency.

2.3.4. Hydrostatic Voltage Coefficient

As shown in Figure 4b, the hydrostatic voltage coefficient, g_H, increases with decreasing piezoceramic volume fraction. The increase in g_H is more pronounced for PZT-air composites due to the higher d_h values. As low permittivity air or polymer replaces the high value dielectric PZT phase, an increase in g_H is expected since g_H is inversely related to the permittivity (ε). In a 3-3 composite, the improved d_h and the reduction in permittivity will increase g_H. Furthermore, a decrease in the PZT ceramic volume fraction will lead to the PZT ceramic component bearing more stress, resulting an increase in electric field per unit hydrostatic stress. The highest hydrostatic voltage coefficient measured for the PZT-air and PZT-polymer composites are 49.4×10^{-3} and 161×10^{-3} $Vm^{-1}Pa^{-1}$, respectively. These values are considerably higher than that of dense piezoceramic (3.7×10^{-3} $Vm^{-1}Pa^{-1}$). The Young's modulus of the polymer is also thought to influence g_H [33]. As the compliance of the polymer increases, stress transfer from the polymer to the PZT ceramic phase will also increase, thus increasing g_H.

As the permittivity decreases with decrease in ceramic content, the capacitance of the piezocomposite will reduce to an unacceptable level for hydrophone applications. In addition, there will be a breakdown limit where the piezoceramic phase cannot bear the hydrostatic stress (mechanical breakdown) or such a high level of stress in the active ceramic phase will result in de-poling.

2.3.5. Hydrostatic Figure of Merit

The hydrostatic Figure-of-Merit (*FoM*) defines the hydrophones' sensing and actuating capability. The figure of merit is a product of d_h and g_H, and expresses the optimum value of an active element for hydrophone applications and is also a figure of merit for the noise level [10]. Optimum values are shown around 20% piezoceramic volume fraction, as shown in Figure 4c. Although both PZT-air and PZT-polymer composites follow a similar trend, the PZT-Polymer composites have smaller values than that of PZT-Air composites due to their low d_h values, the reasons having been explained in the earlier section. Nevertheless, there is a significant improvement from a dense PZT (368×10^{-15} Pa^{-1}) compared to a 20% PZT-

polymer composite (1821×10^{-15} Pa^{-1}). This improvement is more pronounced in the case of the 20% PZT-air composite, which has a value of 15095×10^{-15} Pa^{-1}.

3. EFFECTIVE MATERIAL PARAMETERS

Consider a 3-3 piezocomposite made up of porous piezoceramic and polymer components. The material coefficients of the piezoelectric resonators can be accurately determined from the measured electrical impedance spectrum [35]. Different sets of coefficients are determined from different shapes of the piezoelectric resonators and exciting them in specific modes, viz., thickness-mode of thin plates, radial-mode of discs, axial-mode of thin rods, lateral-mode of bars and so on. However, it is sometimes difficult to prepare piezocomposite specimens in all shapes. Approximate material properties of composites can be easily determined using rule of mixtures. Effective material parameters of piezocomposites can be determined from the material parameters of the constituent phases, viz. piezoceramic and polymer [6, 11].

3.1. Constitutive Relations

The effective material parameters of a composite are strong functions of the amount of ceramic and polymer components present in it. Some parameters obey simple linear relations and others do not. Several material parameters can be determined from the constitutive relations described in this section.

The density of the composite is given by,

$$\overline{\rho} = \rho^c v^c + \rho^p v^p \tag{1}$$

where ρ and *v* are the density and volume fraction of the ceramic and polymer phases marked by the superscripts *c* and *p*, respectively. The bar over the character represents the effective materials parameters of the composite.

The acoustic impedance is given by,

$$\overline{Z}_{aco} = \sqrt{\overline{c}_{33}^{-D}\,\overline{\rho}} \tag{2}$$

The stiffness coefficient at constant electric field is given by,

$$\overline{c}_{33}^{-E} = v^c \left[c_{33}^E - \frac{2v^p \left(c_{13}^E - c_{12}\right)^2}{v^c \left(c_{11} + c_{12}\right) + v^p \left(c_{11}^E + c_{12}^E\right)} \right] + v^p c \tag{3}$$

The dielectric permittivity at constant strain is given by,

$$\bar{\varepsilon}_{33}^{S} = v^{c}\left[\varepsilon_{33}^{S} + \frac{2v^{p}e_{31}{}^{2}}{v^{c}\left(c_{11}+c_{12}\right)+v^{p}\left(c_{11}^{E}+c_{12}^{E}\right)}\right] + v^{p}\varepsilon \tag{4}$$

The piezoelectric coefficients are given by,

$$\bar{e}_{33} = v^{c}\left[e_{33} - \frac{2v^{p}e_{31}\left(c_{13}^{E}-c_{12}\right)}{v^{c}\left(c_{11}+c_{12}\right)+v^{p}\left(c_{11}^{E}+c_{12}^{E}\right)}\right] \tag{5}$$

$$\bar{d}_{31} = v^{C}\left[d_{31} + d_{33}\frac{v^{P}\left(s_{12}-s_{13}^{E}\right)}{v^{C}s_{11}+v^{P}s_{33}^{E}}\right] \tag{6}$$

$$\bar{d}_{33} = \frac{d_{33}v^{C}s_{11}}{v^{C}s_{11}+v^{P}s_{33}^{E}} \tag{7}$$

The hydrostatic coefficients are given by,

$$\bar{d}_{h} = \bar{d}_{33} + 2\bar{d}_{31} \tag{8}$$

$$\bar{g}_{h} = \frac{\bar{d}_{h}}{\bar{\varepsilon}_{33}^{T}} \tag{9}$$

The thickness-mode electromechanical coupling coefficient is given by,

$$\bar{k}_{t}^{2} = \frac{\bar{e}_{33}^{2}}{\bar{\varepsilon}_{33}^{S}\bar{c}_{33}^{D}} \tag{10}$$

The electrical impedance of the composite plate vibrating in thickness-mode is given by,

$$\bar{Z} = \frac{1}{j\omega\bar{C}_{0}}\left[1-\bar{k}_{t}^{2}\frac{\tan(\alpha t)}{\alpha t}\right] \tag{11}$$

where, t is half thickness of the composite plate

$$\alpha = \omega\sqrt{\frac{\bar{\rho}}{\bar{c}_{33}^{D}}} \tag{12}$$

$$\omega = 2\pi f \tag{13}$$

and $\bar{C}_{0}$ is the clamped capacitance as given by,

$$\overline{C}_0 = \frac{\overline{\varepsilon}_{33}^{S} A}{2t} \tag{14}$$

where *A* is the surface area of the electrodes.

3.2. Variation of material parameters with ceramic volume fraction

The material parameters of the 3-3 piezocomposites are estimated using the present model. Figures 1-3 show the variation of material parameters of a piezocomposite as a function of ceramic volume fraction. In all the figures, the solid lines represent the analytical data and markers represent the experimental data.

Figure 1 shows the variations in the dielectric constant K_{33}^{T}, piezoelectric charge coefficients $\overline{d}_{33}$, $\overline{d}_{31}$ and $\overline{d}_{H}$, voltage coefficient $\overline{g}_{H}$ and Figure-of Merit ($\overline{d}_{H}\overline{g}_{H}$) as a function of ceramic volume fraction. Figure 5a shows the variation of dielectric constant with ceramic volume ratio. For low ceramic volume fractions, the experimentally measured values are very close to the predicted values.

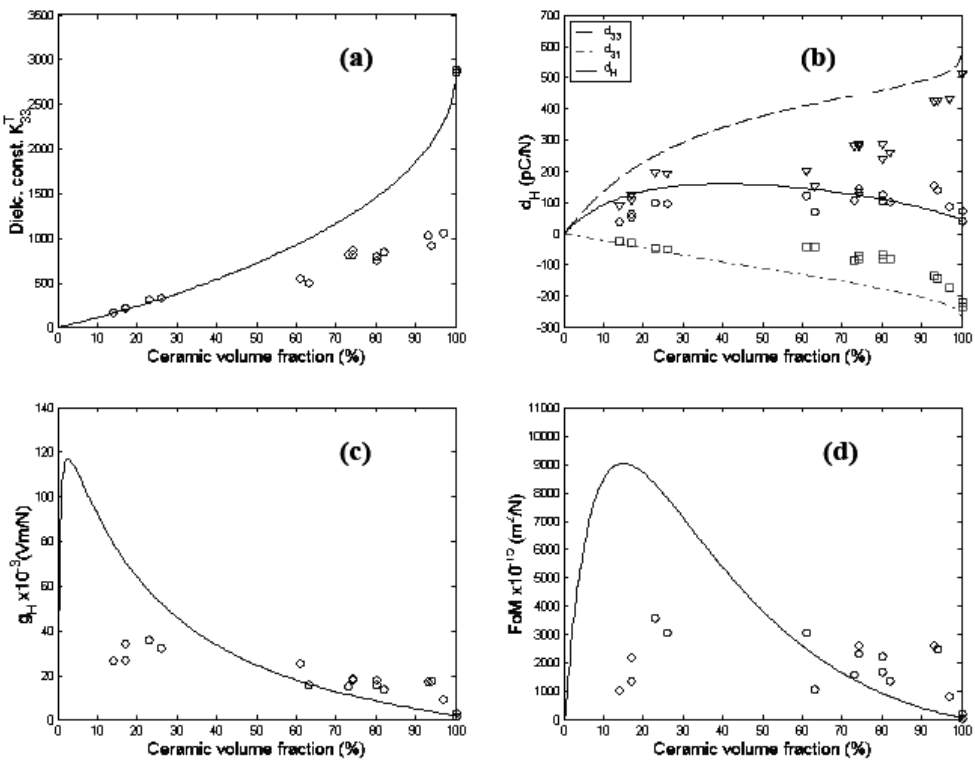

Figure 5. Variation of (a) dielectric constant, (b) hydrostatic *d* coefficient, (c) hydrostatic *g* coefficient and (d) hydrostatic Figure-of-Merit, with ceramic volume fraction. Markers are the experimental data and solid lines are the analytical curves.

The lower value of the experimental values for higher ceramic content may be due to the presence of isolated pores. This lowers the capacitance of the composites even for a small addition of polymer, because of serial connection with PZT. Similar effect of 0-3 connectivity on permittivity has also been reported in the literature [17]. As seen in Figure 5b the hydrostatic charge coefficient increases with the ceramic volume ratio and reaches a maximum at around 30-40 %. It can be seen from the figure that the experimental data agree with the analytical result. In Figs.1c and 1d, the analytical curves show a maximum in the region of low ceramic volume fractions and the value of FoM is about three orders of magnitude higher than that of the dense piezoceramics. The experimentally measured values lie around the analytical curve for high ceramic volume ratios.

Figure 6a shows that the density of the piezocomposite is a linear function of the ceramic volume fraction and follows the simple 'rule of mixtures'. Figure 6b shows the variations in the thickness-mode electromechanical coupling coefficients ($\overline{k}_t$) of the composites. The analytical values are estimated using Eq.10 and the experimental values are obtained from the resonance (f_r) and anti resonance (f_a) frequencies of the electrical impedance spectra. $\overline{k}_t$ increases with the ceramic volume fraction, unlike the case of a 1-3 piezocomposite, for which the $\overline{k}_t$ curve shows a broad maximum for intermediate volume fractions [11].

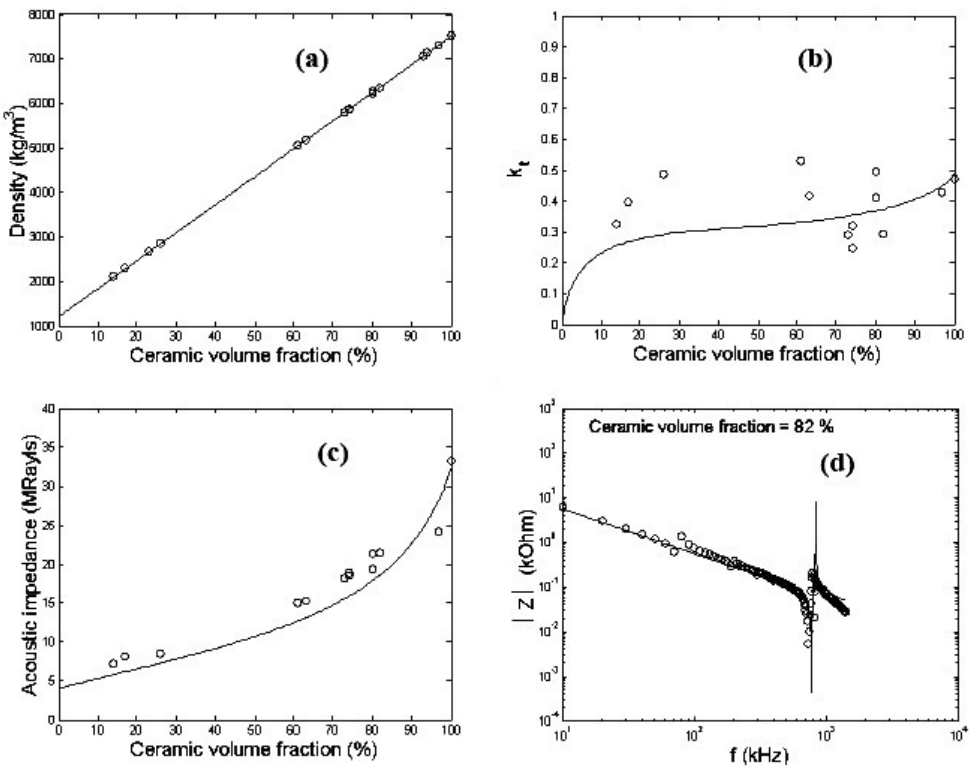

Figure 6. Variation of (a) density, (b) thickness-mode coupling coefficient and (c) acoustic impedance, with ceramic volume fraction. (d) electrical impedance spectrum. Markers are the experimental data and solid lines are the analytical curves.

The acoustic impedance ($\overline{Z}_{aco}$) data estimated using Eq.2 and obtained from the values of f_r and f_a [35] are shown in Figure 6c. The deviations in the experimental values of $\overline{k}_t$ and $\overline{Z}_{aco}$ from the analytical results may be due to the broadening of resonance for lower ceramic volume ratios and difficulties involved in precisely determining the resonance and anti resonance frequencies. The electrical impedance spectra of the composite discs are estimated using Eq.11 and a representative plot for the case of 82 % ceramic volume fraction is shown in Figure 6d. The resonance peak corresponds to the thickness-mode vibrations. It can be seen from the figures that the experimental results are in good agreement with the analytical results. This indicates that this analytical model gives rise to reasonably acceptable results.

Electrical impedance spectra of a 3-3 piezocomposite are plotted for different volume fractions and are shown in Figure 7. The thickness-mode resonance behaviour does not vary linearly with piezoceramic content. The resonance and antiresonance frequencies show a minimum for a ceramic volume fraction of about 45%. Lower value of electrical impedance at resonance is desirable for ultrasonic transmitting application, because this leads to enhanced transmitting response. For such an application, a 3-3 piezocomposite transducer with about 45% piezoceramic volume fraction is preferable.

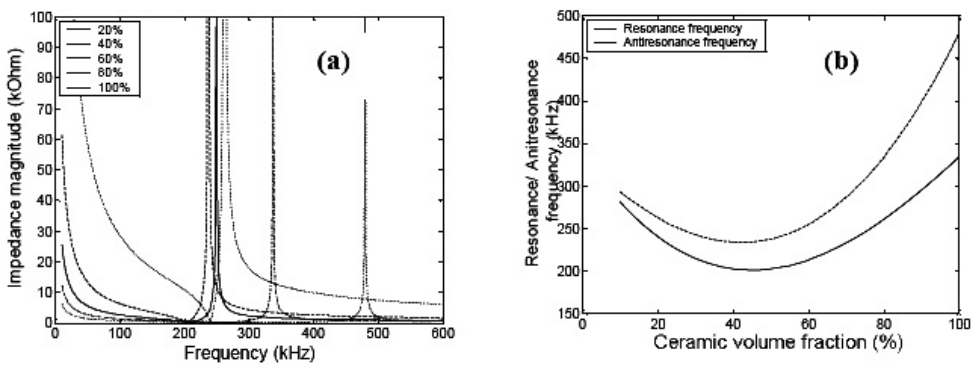

Figure 7. Variations in (a) electrical impedance spectrum and (b) resonance and anti-resonance frequencies, with ceramic volume fraction.

4. FINITE ELEMENT MODELLING OF POROUS PIEZOCERAMICS

Several analytical models have been proposed to study the characteristics of ideal 3-3 piezocomposites [36, 37, 20]. All these models deal only with materials aspects of the composites. However, the transducer characteristics of these materials have not been studied extensively, for which Finite Element Modelling (FEM) would be a simple and effective tool. FEM studies on 1-3 piezocomposite transducers have been reported by several authors, for example [Ref. [38]. In these studies, only one *unit cell* of the composite block has been modelled, assuming that it represents the entire piezocomposite structure. Although these models can give material parameters like piezoelectric coefficients, to considerable accuracy, they are inadequate to predict the lateral-mode resonance of a transducer of finite dimensions. Hence, real-size 3-dimensional FEM studies are necessary to evaluate the device

characteristics of piezocomposite hydrophones. 3-dimensional FEM studies on 1-3 piezocomposites [23] and 3-3 piezocomposites [39] have demonstrated the importance of real-sized models.

Before attempting to model the complicated structures of porous piezoceramics, it is worthwhile to model a dense piezoceramic element of simple geometry and validate the results with analytical or experimental data. Then, it can be extended to more complicated geometrical shapes of 3-3 piezocomposites.

Several specialised finite element packages are available to model piezoelectric systems. Some of the popular and commonly used packages are, ATILA, ANSYS, PAFEC, and PZFLEX. Each one has its advantages and disadvantages. The multi physics module of ANSYS offers a convenient way of generating complicated structures and is well suited for porous piezoceramic systems.

4.1. Model of Dense PZT Discs

Due to the simplicity in geometry, the dense PZT disc hydrophones are modelled by using 2-dimensional axisymmetric harmonic analysis. Consider a PZT disc of length *L* and radius *a* as shown in Figure 8. Uniform electrodes are coated on the top and bottom flat surfaces and it is poled in the axial direction. The hydrophone is encapsulated by an acoustically transparent rubber and is surrounded by water medium. The details of the axisymmetric model and the finite element mesh are shown in Figure 9. Axisymmetric coupled-field elements are used for the active material. The model includes the PZT hydrophone and the surrounding fluid (water) medium.

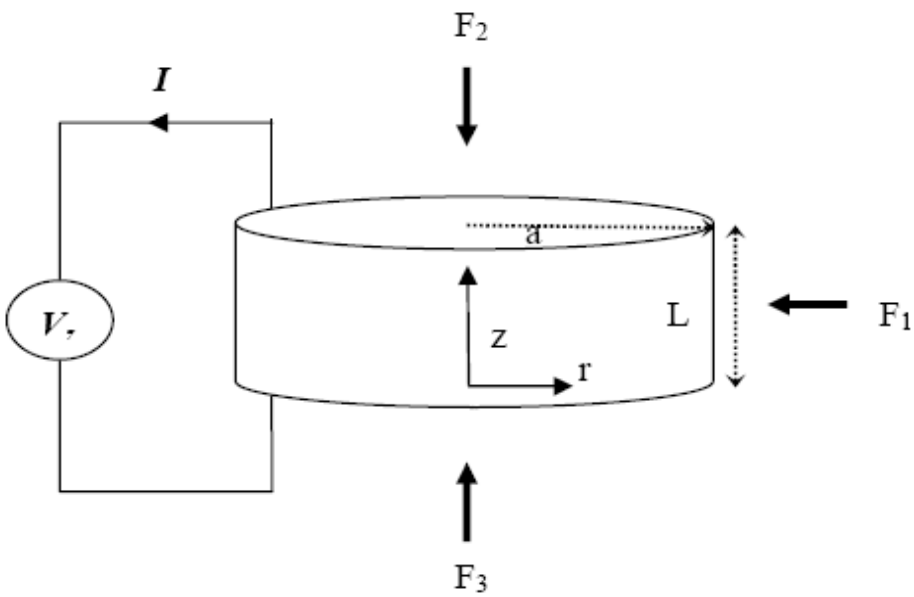

Figure 8. Geometry of piezoceramic disc modeled. *V* is the voltage across the electrodes and F_1, F_2 and F_3 are the forces acting on the surfaces.

A small section of the fluid medium, which is in contact with the solid elements is assigned with acoustic elements capable of handling fluid-structure interactions. In all other fluid elements, the displacement degree of freedom (d.o.f) has been suppressed. This significantly reduces the memory requirement and the computing time. The outer boundary of the fluid mesh contains infinite acoustic damping elements. This ensures that the acoustic waves are not reflected at the boundary, simulating the infinite extent of the fluid medium. In order to obtain better numerical accuracy, the size of the mesh has been kept small compared to the dominant wavelength of the sound waves in PZT as well as in water in the vicinity of the hydrophone. That means, the mesh size has been maintained to be less than or equal to $\lambda/5$ of the highest frequency (100 kHz) studied.

The nodes lying on the top and bottom electrode surfaces of the PZT disc are coupled individually and voltage d.o.f is activated. Nodes on all outer surfaces are coupled and pressure d.o.f is activated. Two different boundary conditions are applied for the present studies. In the case of the receiving sensitivity measurement, an acoustic wave of known pressure P excites the transducer from the fluid medium and the voltage generated at the electrodes is determined. For electrical impedance measurement, the outer surfaces of the transducer are stress-free and a known voltage is applied between the electrodes. Impedance is calculated from the charge collected at the electrodes. Harmonic analysis with no damping is performed in the frequency range 10 kHz-100 kHz.

The electrical impedance spectrum for the dense piezoceramic hydrophone in the frequency range 10-100 kHz obtained by analytical [40], FEM and experimental studies are shown in Figure 10a. The specimen used in the experimental study is made up of PZT5H with the geometry described in Figure 8. It is seen from Figure 10a that the FEM results agree well with the analytical and experimental results. The resonance peaks observed at around 50 kHz correspond to the fundamental radial-mode of vibrations.

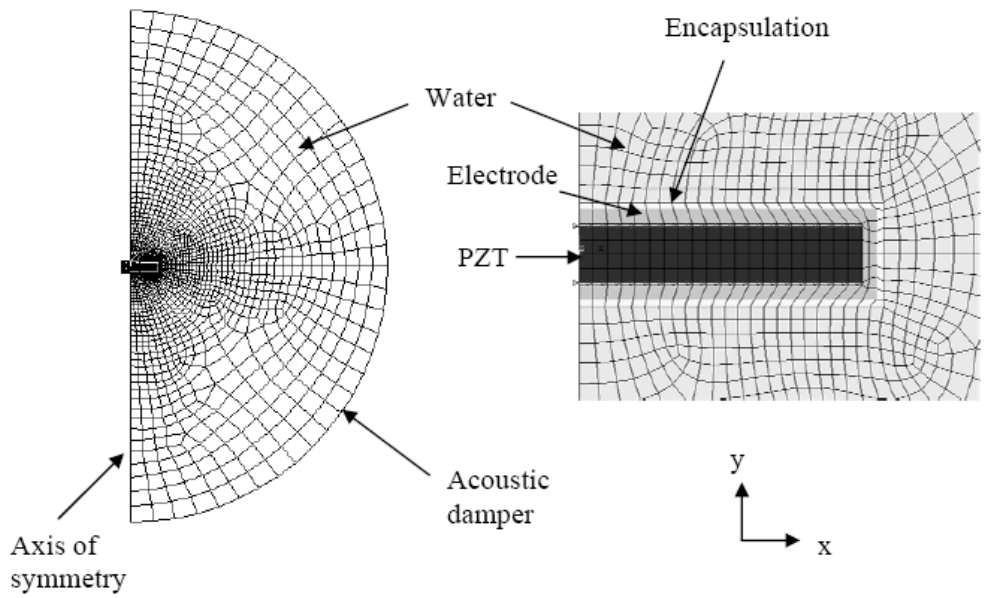

Figure 9. The axisymmetric (2D) Finite Element Model of a dense piezoceramic disc.

Figure 10b shows the free-field voltage sensitivity in water for the dense PZT hydrophone obtained by analytical model, finite element model and experimental studies.

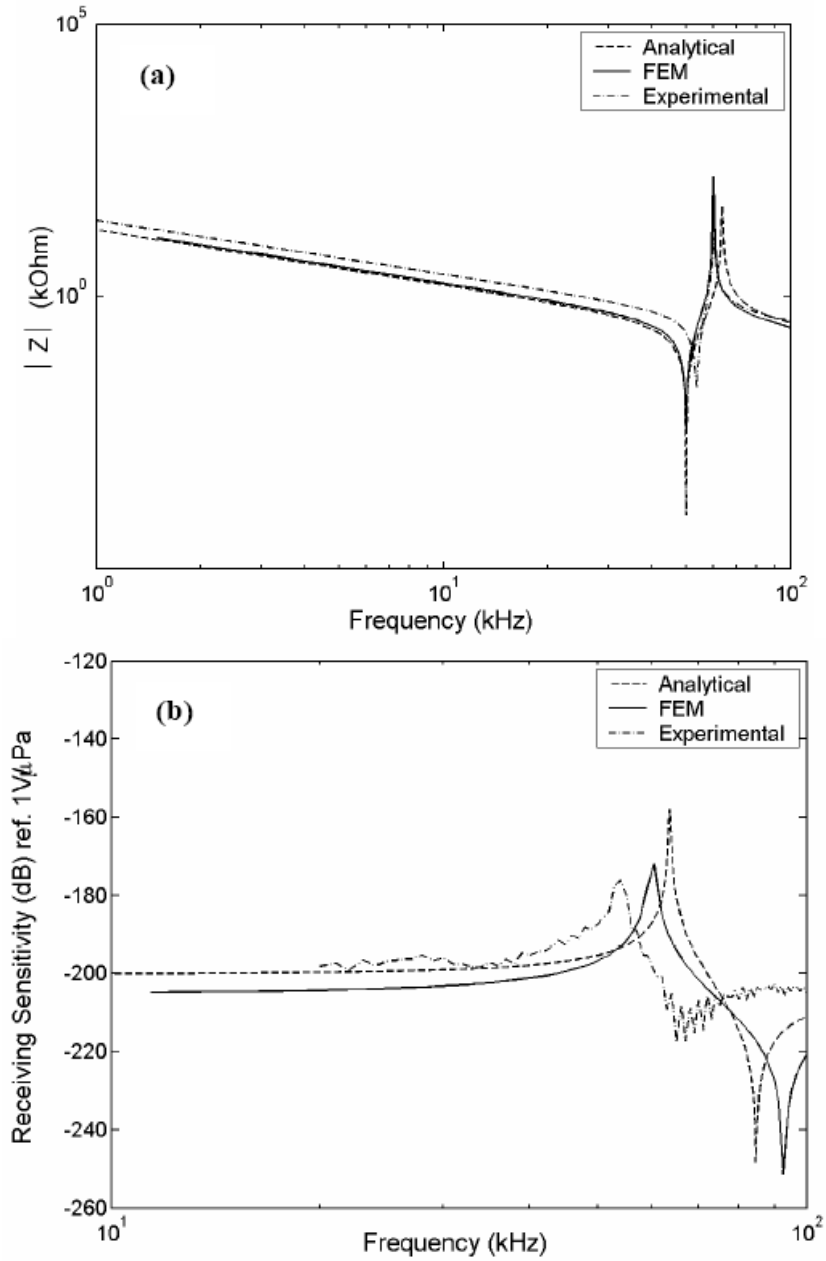

Figure 10. Comparison of FEM results with analytical and experimental data (a) electrical impedance spectrum and (b) receiving voltage sensitivity of a dense piezoceramic disc hydrophone.

In the analytical model, the effect of encapsulation and water loading are not considered. This could lead to a shift in the resonance frequencies as seen in the figure. The polyurethane rubber used for encapsulating the hydrophone has acoustic impedance close to that of water and hence is assumed to be acoustically transparent. It can be seen from the figure that the

sensitivity curve is flat for frequencies below 50 kHz. The radial mode resonance appearing at around 50 kHz is not generally desirable for hydrophone applications, since it limits the operating frequency band. An ideal hydrophone has a constant receiving sensitivity over a wide frequency range [41]. The resonance peaks can be shifted beyond the operating range by carefully selecting the dimensions of the active elements.

4.2. Model of Porous PZT Discs

The porous PZT has an intricate structure that can not be generated by rotating the structure about the symmetric axis and hence a 2-dimensional axisymmetric model is not useful. Therefore, a 3-dimensional model is required to characterise hydrophones made up of porous piezoceramics with finite dimensions.

In modelling piezocomposites, it has been a general practice to model only an *unit cell* of the structure, assuming that it is representative of the entire piezocomposite structure [iv]. However in certain cases, the results of the *unit cell* model deviate from the actual values, especially in the determination of resonance frequencies [24]. The *unit cell* model can correctly predict the resonance frequencies corresponding to the thickness-mode vibrations, whereas it cannot predict the lateral-mode (radial-mode) resonance frequencies if the lateral dimensions of the transducers are finite and comparable to the thickness. Even, the application of periodic boundary conditions can only simulate the infinite extent of the lateral dimensions (x-y plane). Further, in the case of transducers with finite dimensions, the resonance frequency corresponding to the dimension in the z-direction depends also on the dimensions in the x- and y- directions [24]. It is therefore necessary to use a real- dimensional model. However, this involves large computer memory size and prolonged computational time.

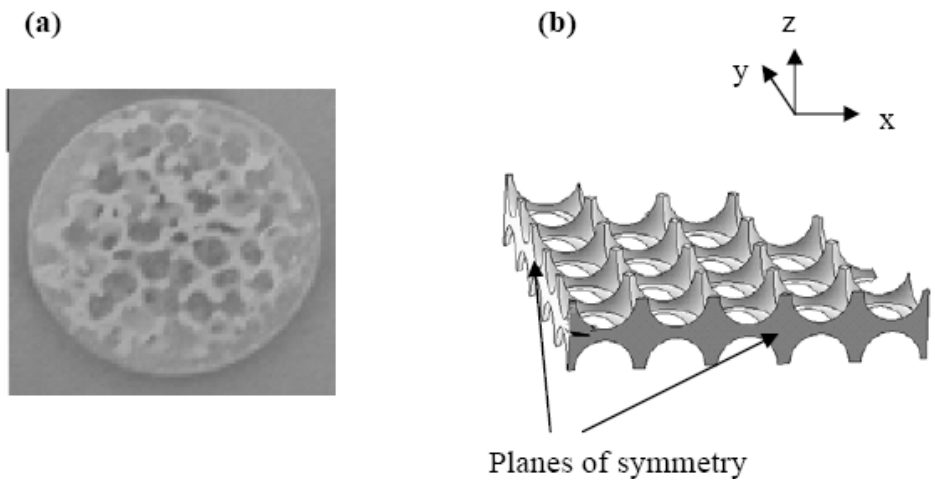

Figure 11. (a) Photograph of the porous PZT disc filled with polymer and (b) 1/4th of the model used for FEM.

The porous piezoceramic structure used in the finite element model of a 3-3 piezocomposite is shown in Figure 11. This is chosen to be as close to the practical structure

of a foam- reticulated piezocomposite sample shown in the figure. The complete 3-D model along with the surrounding fluid medium is shown in Figure 5. One fourth of the geometry is modelled due to symmetry and the plane of symmetry boundary conditions are applied on the xz and yz planes. Although $1/8^{th}$ model could save considerable computing time, the non-symmetry of the electric potential along the z-axis does not allow such a possibility in the present model. The ceramic volume fraction of the piezocomposite disc is taken as 22%. The receiving sensitivity and electrical impedance are evaluated in two successive analyses imposing appropriate boundary conditions. The boundary conditions are same as those of the dense PZT hydrophone explained in the previous section. The material parameters used in the model analysis are given in Table 1.

Table 1. Material parameters used in the model calculations. Data for PZT5H are taken from Ref. [42] and typical values are taken for other materials

Parameter	Value
I. PZT5H	
Elastic coefficients (10^{10} Nm^{-2})	
c_{11}^D	13.03
c_{12}^D	8.33
c_{13}^D	7.33
c_{33}^D	15.89
c_{44}^D	4.22
c_{66}^D	2.4
Piezoelectric coefficients (10^9 Vm^{-1})	
h_{31}	-0.5
h_{33}	1.8
h_{15}	1.13
Density (kgm^{-3})	7500
Dielectric constant	1470
II. Electrode	
Density (kgm^{-3})	8250
Young's modulus (GPa)	110
Poisson's ratio	3.4
III. Encapsulation	
Density (kgm^{-3})	940
Young's modulus (MPa)	2.0
Poisson's ratio	0.45
IV. Water	
Density (kgm^{-3})	1000
Velocity of sound (ms^{-1})	1460

The impedance data for the porous piezoceramic hydrophone obtained by FEM and experimental studies are shown in Figure 6a. In this case, the resonance peaks have almost disappeared, indicating the weak coupling.

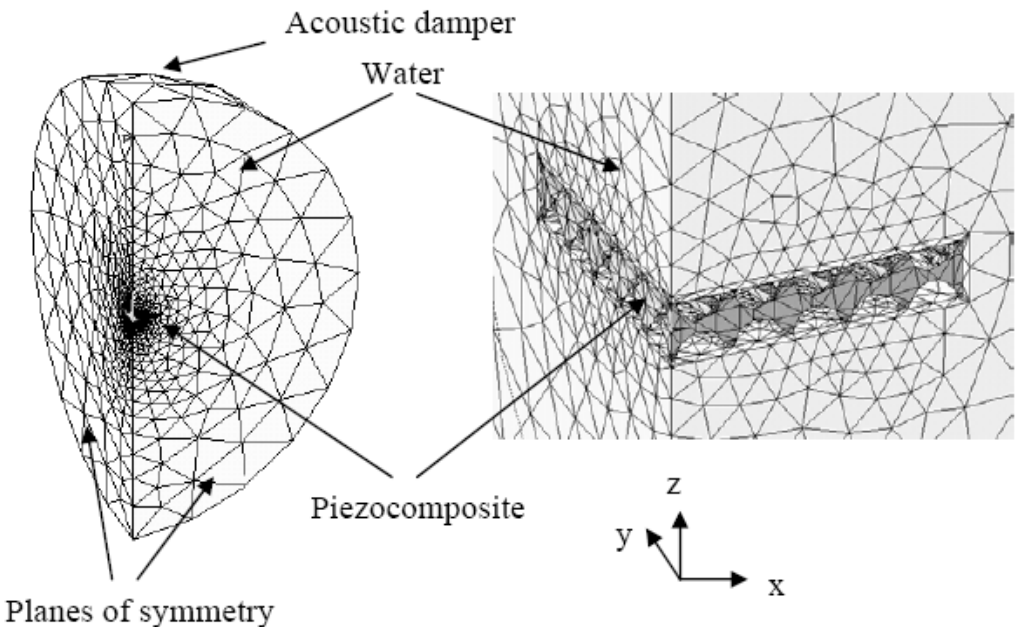

Figure 12. 3D Finite Element Model of a porous piezoceramic disc in water.

Figure 13b shows the receiving sensitivity of the piezocomposite hydrophones obtained by FEM and experimental studies. The sensitivity value is found to be around -210 dB (re. 1V/μPa) and is fairly constant in the frequency range studied. These values are comparable to the experimental values of –(200-205) dB reported for single-element hydrophones with 75% porosity at 100 kHz [15]. A 3x3 array of porous piezoceramic hydrophone, however, shows a higher sensitivity of –193 dB below resonance [10].

FEM studies are limited to 10 kHz in the low frequency side in order to compare with the experimental results, which could not be collected for frequencies below 10 kHz due to limitations in the experimental set up. Ideal porous structures are considered for the finite element model. However, the scanning electron micrographs show the presence of some amount of micro-cracks in the experimentally synthesised foam-reticulated samples [13]. This could lead a small difference between the experimental and model results as seen in Figure 13.

It can be seen from the figures that the resonance peaks corresponding to the radial-mode vibrations are very prominent for dense PZT hydrophone and have weakened to a large extent for piezocomposites. This may be due to higher dielectric and mechanical losses of the composites compared to those of dense piezoceramic materials. The sensitivity response is found to be reasonably flat over a wide frequency range. This type of behaviour is desirable for wide-band hydrophone applications.

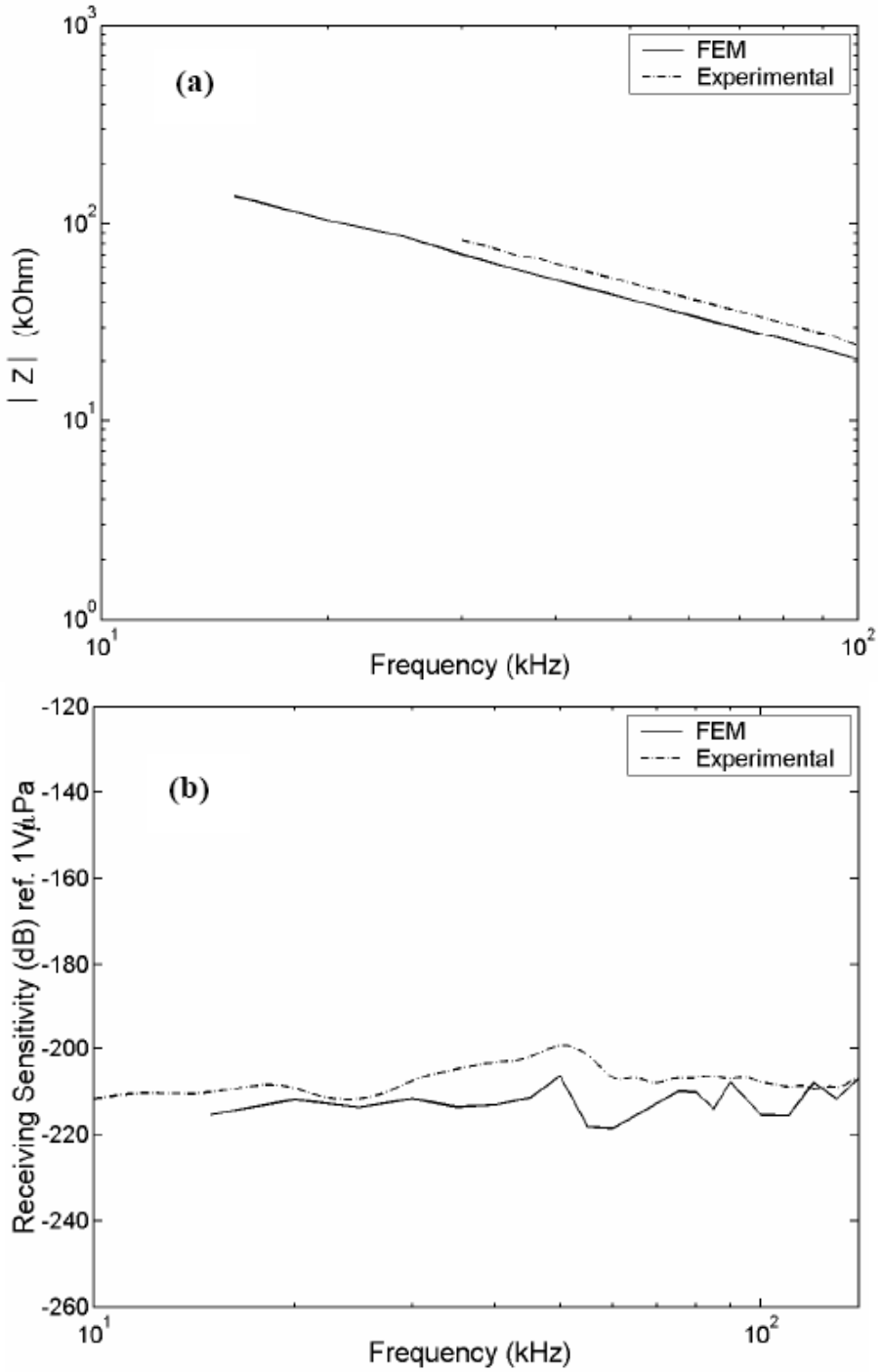

Figure 13. Comparison of FEM results with experimental data (a) electrical impedance spectrum and (b) receiving voltage sensitivity of a porous piezoceramic disc hydrophone.

5. EVALUATION OF POROUS PIEZOCERAMIC HYDROPHONES

As seen in the previous sections, the 3-3 piezocomposites made up of porous piezoceramics are useful materials for transducer applications, especially as hydrophones. The lossy nature of the composite materials leads to wide-band response, which is an important property of a hydrophone. Several commercially available hydrophones have flat frequency response over a large band below the first resonance [41]. However, such a hydrophone made up of dense piezoceramic material requires very careful selection of dimensions of various components used in the device and meets conflicting design challenges. Such a design gets greatly simplified if the piezoelectric component is wideband in nature, like the piezocomposites. This section presents the construction and underwater evaluation of hydrophones made up of 3-3 piezocomoposites and a comparison with hydrophones made up of dense piezoceramic material of the same size [10].

5.1. Construction of Hydrophones

5.1.1. Sample Preparation

Samples required for constructing the hydrophones are prepared using Foam-replication technique described in detail in Section 2. The foam replication method is well known for making reticulated ceramics [43, 44, 45] and involves dipping a polyethylene foam (Foam Engineers Ltd, UK, 10 ppi and 20 ppi) into a ceramic slurry. Since the hydrophones are for passive mode only, the ceramic chosen for this study is PZT-5H (Morgan Electroceramics, UK), a soft piezoelectric for sensor applications due to its high d_{33} piezoelectric coefficient. The ceramic-coated foam is then heat treated to remove the polyethylene foam structure at 600 °C for 1 hour. The remaining ceramic skeleton is then sintered at 1200 °C for 2 hours. Variation of the ceramic volume fraction, by changing the foam pore size or degree of coating, can be used to tailor the piezoelectric charge coefficients (d_{33}, d_{31}), permittivity (ε_{33}^{T}) and acoustic impedance. The d_H of the material reaches a maximum at approximately 50% ceramic volume fraction, while the g_H is a maximum at approximately 10-20% ceramic volume fraction [46]. Since g_H is related to the electric field per unit hydrostatic stress, hydrophone materials with high g_H are produced for this work with 11% and 22% PZT ceramic volume fractions by using 10 ppi and 20 ppi polyethylene foams, respectively.

After heat treating and sintering, the discs (11% PZT and 22% PZT) are ground by SiC abrasive paper to dimensions of 40 mm diameter and 4±0.1 mm thickness. The 4 mm thickness is larger than the pore size of the material and ensures sufficient ceramic material is connected through the ceramic thickness. A dense PZT ceramic with same dimensions and tolerance is also prepared from the same ceramic powder for direct comparison. Due to the low strength of the 11% PZT disk, it is impregnated with epoxy (Specifix 40, Struers, Germany) to improve its mechanical strength. It acts as a 3-3 piezocomposite.

Silver electrodes (~100 mm thick) are applied by brushing on silver conductive paint (RS Products, UK, Product 186-3593) to the two faces. The discs are subsequently poled in the thickness direction using a custom made corona poling using a 30 kV DC power supply (Glassman Europe Ltd., Product FC30P4) at an electric field equivalent to 2 $kVmm^{-1}$.

Piezoelectric charge coefficients, permittivity and impedance data are collected using the method described in Section.2.1.

The measured piezoelectric and dielectric properties of the dense PZT ceramic and piezocomposites are given in Table 2. This table shows that the reduction in d_{31} is significantly greater than that for d_{33}. Consequently, g_H and figure of merit ($d_H.g_H$) are improved for the piezocomposites compared with dense PZT. However, the dielectric constant and hence, the capacitance of the piezocomposites is much lower than that of the dense piezoceramic material.

Table 2. Properties of dense piezoceramic, 22% PZT-Air composite and 11% PZT-Polymer composite. The parameters d_{33}, d_{31}, ε_{33}^{T}, device capacitance and receiving sensitivity have been measured and the parameters d_H, g_H are $d_H.g_H$ are calculated

Material	d_{33} pCN^{-1}	d_{31} pCN^{-1}	ε_{33}^{T} $x10^{-9}$ Fm^{-1}	d_H pCN^{-1}	g_H $x10^{-3}$ VmN^{-1}	$d_H.g_H$ $x10^{-15}$ Pa^{-1}	MdB re. $1V\mu Pa^{-1}$	Device Cap.pF
PZT-5H	513	220	25.3	72.8	2.87	209	-205	5050
22% PZT-Air	210	29	2.8	152	54.2	8238	-198	800
11% PZT-Polymer	35.7	7	0.67	21.7	28.3	614	-215	210

5.1.2. Hydrophone Assemby

The porous piezocomposites show a low permittivity, which results in a low measured device capacitance values compared to the dense PZT hydrophone (Table 2). Since the capacitance of the cable used (RS Products**)** is 42 pF m^{-1} and a 1.5m cable used for each hydrophone, the capacitance of the devices is increased in order to reduce the cable loading effect which can lead to a decrease in the hydrophone sensitivity. To achieve this, two discs of piezocomposite are attached back-to-back using an electrically parallel connection. The configuration is shown in Figure 14. The pieces are attached to a 0.15 mm thick copper plate electrode with conductive epoxy (RS Products, UK, Product 186-3616) in opposite poling directions. The remaining two faces are then attached with copper electrodes and soldered to a cable. The middle electrode is used as the positive lead and the two outer electrodes are connected to the cable shield. Finally, the whole assembly is molded in 1mm thick polyurethane for water isolation (Figure 14). The dense PZT ceramic hydrophone is also assembled in the same way with the same thickness for a direct comparison. In order to ensure the structural integrity of the device assembly, an impedance spectrum is measured, in air, at every stage of the construction using Solartron Impedance Analyser (Model 1260, USA). The impedance spectra so recorded do not show any spurious peaks, indicating proper structural integrity of the hydrophones.

For any underwater application, hydrophones are normally used in the form of an array. Hydrophone arrays covering large surface area are desirable for certain applications because, it enhances the signal-to-noise ratio of the receiver system. Further, acoustic imaging systems require arrays of hydrophones to collect information arriving from different angles with respect to the position of the array itself. Characteristics of hydrophone arrays are found to be

deviate from that of the single-element hydrophone. Therefore, it is important to evaluate the arrays in order to assess their underwater performance.

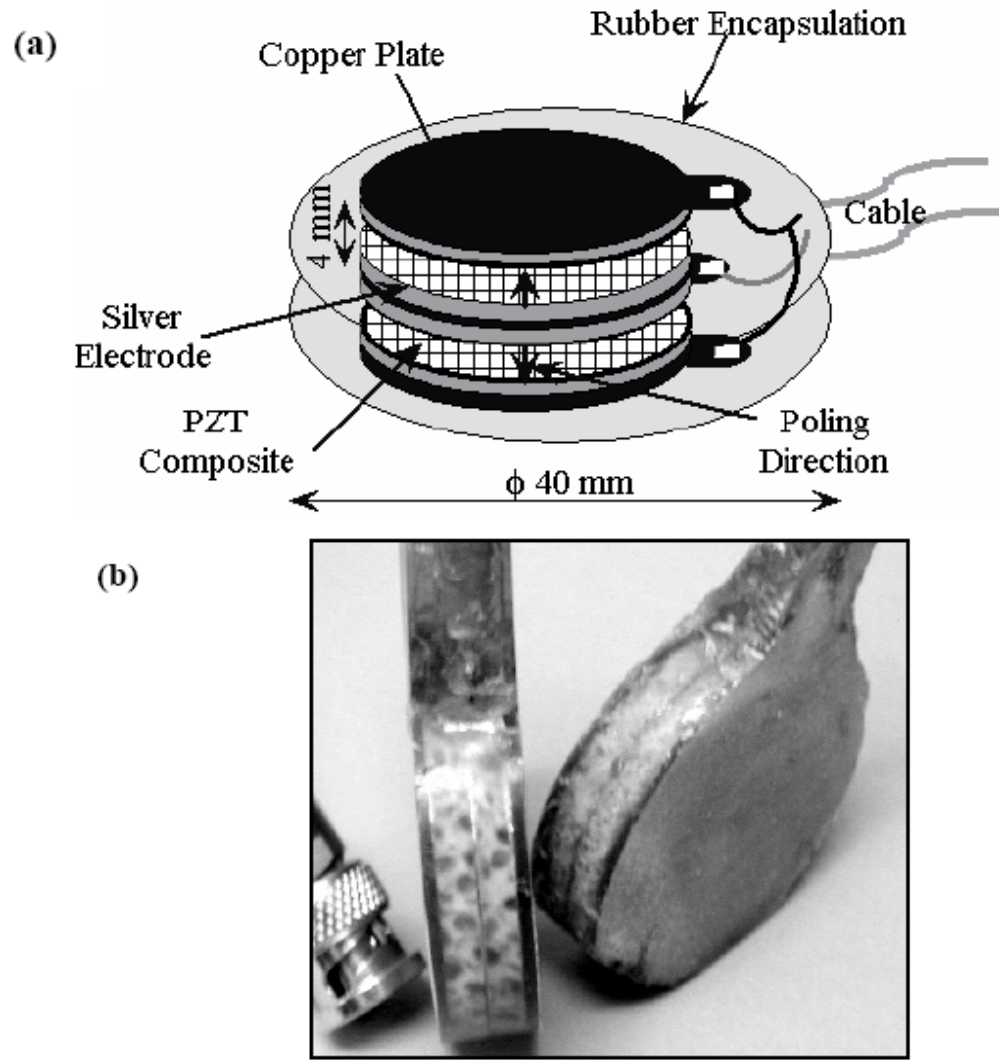

Figure 14. (a) Schematic design and (b) assembled piezocomposite hydrophones.

Figure 15a shows the photograph of a 3x3 hydrophone array assembled using square pieces of porous piezoceramics and Figure 14b shows the array after encapsulation.

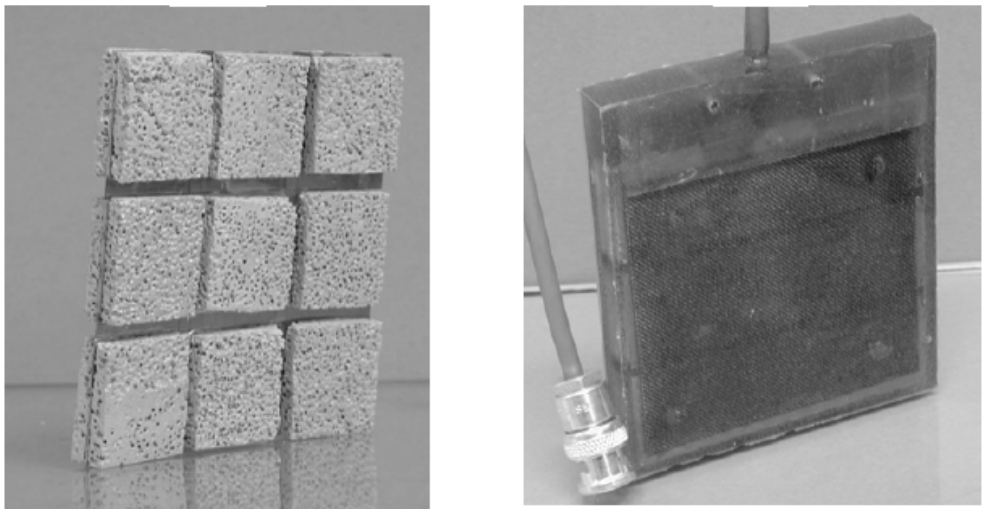

a b

Figure 15. Porous piezoceramic hydrophone array (a) before and (b) after encapsulation.

5.2. Evaluation of Hydrophones

The assembled piezocomposite hydrophones are tested in a 1.5 x 1.5 x 2.8 m^3 water tank in the frequency range 20-100 kHz. The experimental setup is shown in Figure 16.

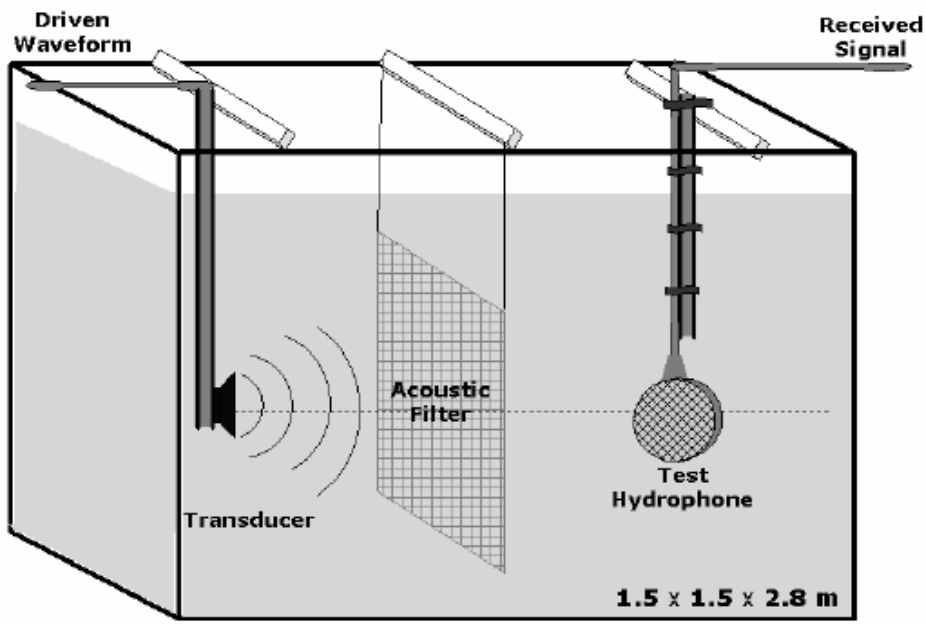

Figure 16. Schematic view of the tank used for acoustic measurements.

A custom made parametric array is used as the acoustic source. The hydrophone sensitivities are measured by comparing the hydrophone outputs with those of a calibrated Brüel and Kjær 8103 hydrophone (B and K 8103, Denmark). The outputs of the hydrophones are amplified by 60 dB with a Brookdeal 9452 precision a.c. amplifier and displayed on a Lecroy 9304C digital oscilloscope remotely controlled by a computer for data acquisition. The input impedance of the pre-amplifier is very high (~5 GΩ), so that it does not affect the voltage developed by the standard hydrophone. Further, the same amplifier is used for the piezocomposite and standard hydrophones, so that the common errors are cancelled out when we take the frequency response, which is a ratio of two outputs. The hydrophone is evaluated in a far-field condition. For each acquisition, the waveforms are averaged over 100 sweeps and uniformly sampled over 1000 points. The angular response of the hydrophones is measured by mounting the hydrophones on a rotating table that is remotely controlled by the computer.

Figure 17 shows the results of acoustic measurements of the dense PZT hydrophone, the piezocomposite hydrophones (11%PZT-polymer and 22%PZT-air) and the BandK 8103 hydrophone in the form of time-domain signals. The dense PZT and piezocomposite hydrophones have significantly different responses to the acoustic pulse. The dense PZT hydrophone showed a 'ringing' behaviour with a long tail (Figure 17a) and is not useful for high-resolution applications, whereas the piezocomposite hydrophones, as well as the BandK hydrophone produced short clean output pulses (Figure 17b) characteristic of a broadband transducer. The voltage output from 22% PZT-air composite is higher, while at the same time, retaining a relatively clean short pulse. The high output from the piezocomposite hydrophones for a given acoustic input signal is also reflected on the measured sensitivity graph, shown in Figure 18, which illustrates that radial resonances are suppressed in the composites when compared with the sharp resonance peak obtained for dense PZT. Suppression of the radial resonances gives a flatter response to the hydrophone.

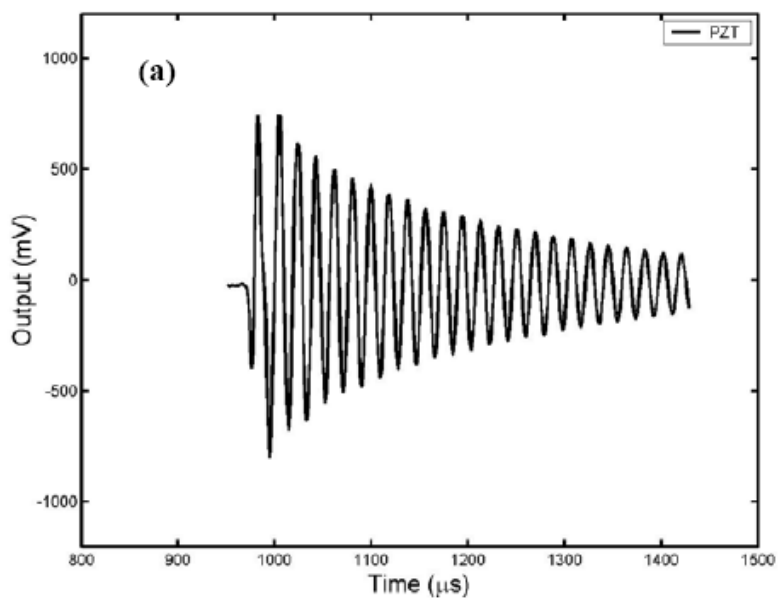

Figure 17. (Continued).

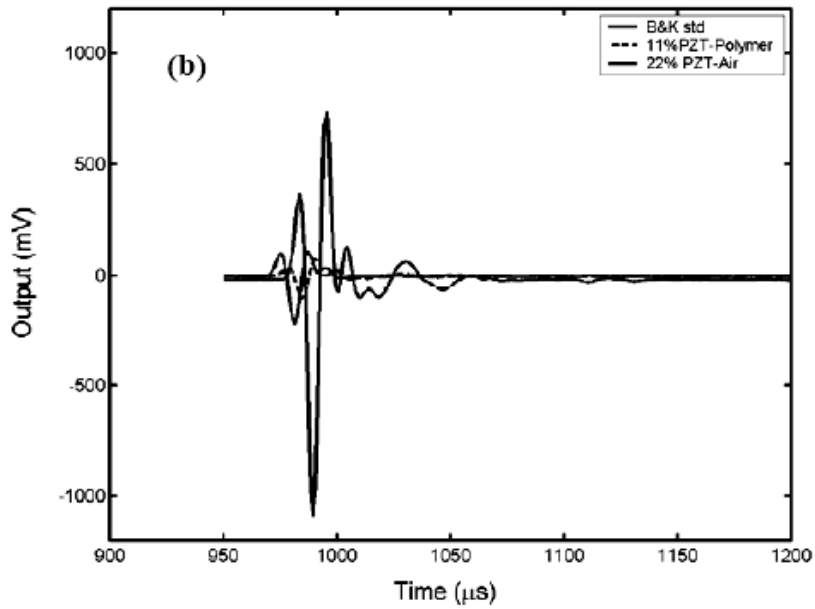

Figure 17. Time-domain output of (a) dense PZT hydrophone and (b) 11% PZT-polymer and 22% PZT-air piezocomposite hydrophones in comparison with standard hydrophone (B and K 8103).

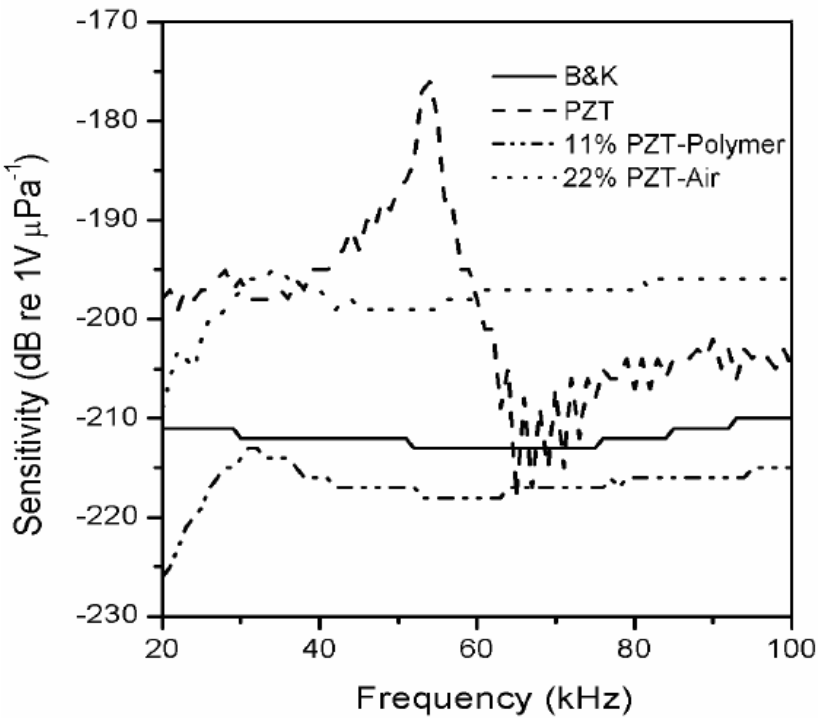

Figure 18. Measured receiving voltage sensitivity of different types of hydrophones.

In this case the piezocomposite hydrophones showed a flat response up to 100 kHz. This clearly demonstrates that reticulated piezocomposites can be beneficial for broadband receiving applications. The 22% PZT-air hydrophone is more sensitive than the 11% PZT-polymer hydrophone reaching a value of -198 dB re 1V μPa^{-1} compared to the value of -218 dB re 1V μPa^{-1}. Although the depth sensitivity of PZT-air materials may be limited due to their low mechanical strength and possible damage by crushing, the composites may be of use in shallow waters (<100m). For deeper waters PZT-polymer composite hydrophones would provide high mechanical strength and stability with a small reduction in receiving sensitivity. The sensitivity of both hydrophones might further be improved by optimising the composite structure in terms of choice of polymer phase (Young's modulus, Poisson's ratio), piezoceramic phase (g_{33}, g_{31}), ceramic volume fraction and pore architecture (pore size and shape).

Figure 19 shows the receiving sensitivity of the single-element and multi-element hydrophone array made up of PZT-air piezocomposite (porous PZT). It can be seen from the figure that the sensitivity is fairly constant over the frequency band 20-100 kHz.

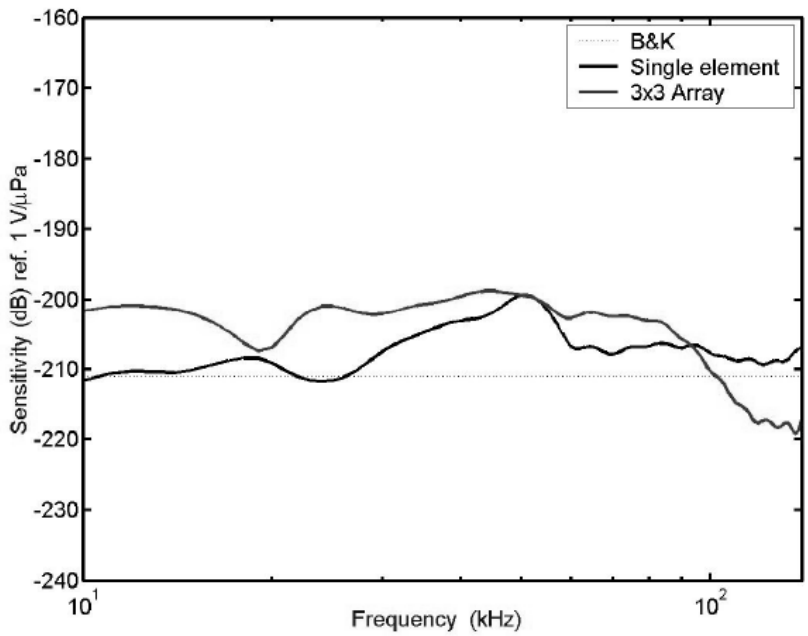

Figure 19. Receiving sensitivity of single-element hydrophone and 3x3 hydrophone array fabricated from porous PZT.

Figure 20 shows the directivity pattern of PZT-polymer composite hydrophone at various frequencies. As expected, the hydrophone displayed a dipole response with maximum sensitivity in the axial direction. The beam widths are about 60°, 45° and 30° at 50 kHz, 75 kHz and 100 kHz, respectively. The variation in the beam width is consistent with that expected for a disc with uniform sensitivity over its surface. An omni-directional response is expected at very low frequencies, at which measurements could not be carried out due to experimental limitations.

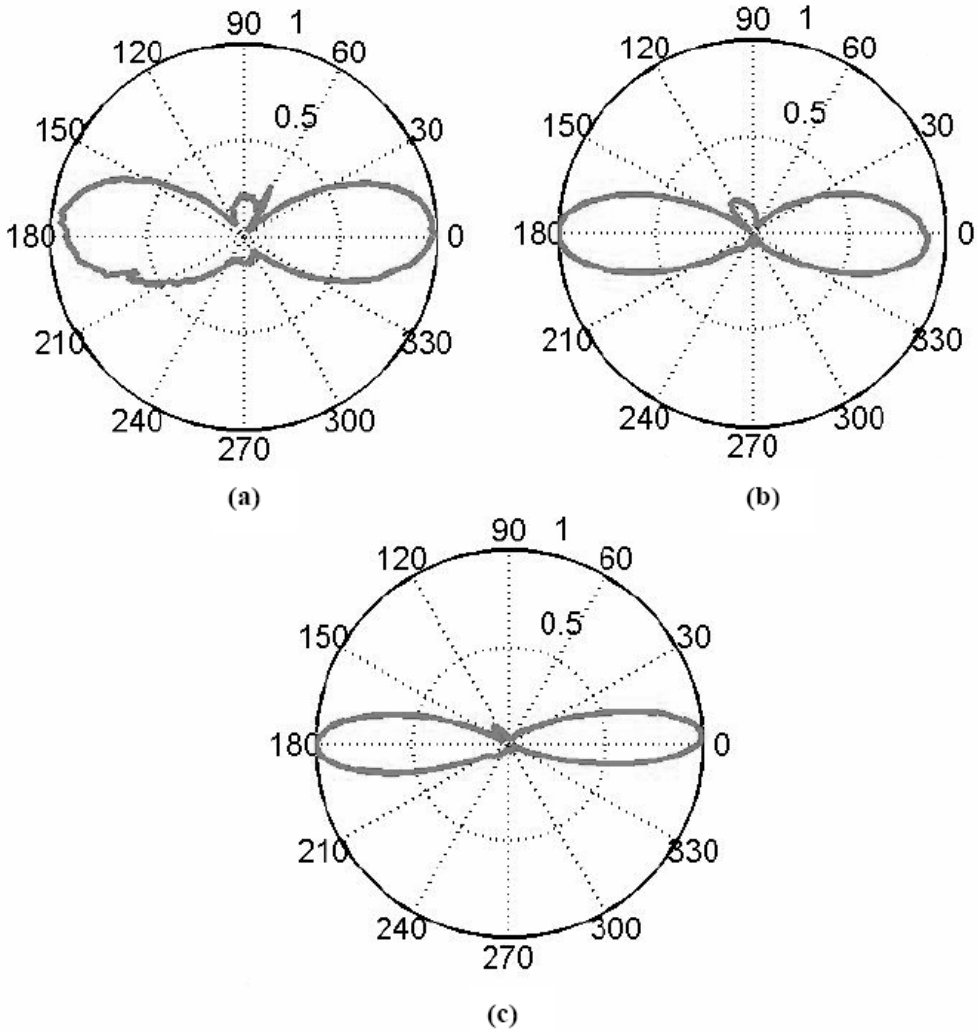

Figure 20. Measured directivity patterns of piezocomposite hydrophones at (a) 50 kHz, (b) 75 kHz and (c) 100 kHz.

6. CONCLUSIONS

Porous piezoceramics samples with ceramic volume fraction ranging from 10% to 100% are synthesised by BURPS and foam-reticulation methods and are characterized in terms of their microstructure, piezoelectric charge (d_{33}, d_{31}) and voltage (g_{33},g_{31}) coefficients, the hydrostatic coefficients (d_H and g_H) and hydrostatic Figure-of-Merit. The composites with PZT volume content >60% show the presence of 3-0 connectivity while composites with ceramic volume content <40% show clear 3-3 connectivity. The composites falling in between these limits (40-60 vol. % PZT) show a mixture of 3-0 and 3-3 connectivities. Effective material properties determined using a simple analytical model are comparable with that of the experiments. Dielectric, mechanical and piezoelectric properties are found to vary

strongly on ceramic volume fraction/ porosity. Hydrostatic figure of merit is found to be maximum for about 20% piezoceramic volume fraction. Although both PZT-air and PZT-polymer composites follow a similar trend, the PZT-Polymer composites have smaller values of hydrostatic coefficients than that of PZT-Air composites. The transducer characteristics of dense and porous piezoceramics are estimated using 2D and 3D Finite Element Modelling (FEM), respectively and the results are validated by experiments. Hydrophones are fabricated with PZT-air and PZT-polymer composites and their acoustic performance is evaluated underwater. The receiving sensitivity, the electrical impedance spectra and the directional response of the hydrophones are measured in the frequency range (10-100) kHz. The 3-3 piezocomposite transducers have higher receiving sensitivity and broader frequency response than the transducers made out of dense PZT. This suggests that the 3-3 piezocomposites made up of porous piezoceramics are very useful for wide-band hydrophone applications.

REFERENCES

[1] Wilson, A.B, *Introduction to the theory and design of sonar transducers*, Peninsula Publishing: CA, 1988.

[2] Bowen, L.F, *Proc. Ultrason. Symp*. 1992, 539-547.

[3] Skinner, D.P, Newnham, R.E, and Cross, L.E, *Mater. Res. Bull*. 1978, 13, 599-607.

[4] Smith, W.A, *Ferroelectrics* 1989, 91, 155-162.

[5] Sigmund, O and Torquato, S, *Smart Mater. Struct*. 1999,8, 365-379.

[6] Smith, W.A, *Proc. IEEE Ultrason. Symp*. 1985, 642-647.

[7] Newnham, R.E, Skinner, D.P and Cross, L.E, 1978,13, 525-536.

[8] Bowen, L, Gentilman, R, Fiore:D, Pham, H, Serwatka, W, Near, C and Pazol, B, *Ferroelectrics* 1996, 187, 109-120.

[9] Zhang, Q.M, Chen, J, Wang, H, Zhao, J, Cross, L.E and Trottier, M.C, IEEE Trans. Ultrason. *Ferroelec. Freq. Control*. 1995, 42, 774-781.

[10] Marselli, S, Pavia, V, Galassi, C, Roncari, E, Cracium, F and Guidarelli, G, *J. Acous. Soc. Am*. 1999, 106, 733-738.

[11] Smith, W.A and Auld, B.A, IEEE Trans. *Ultrason. Ferroelec. Freq. Control*. 1991, 38, 40-47.

[12] Ramesh, R and Vishnubhatla, R.M.R, *J. Sound. Vib*. 1999, 226, 573-584.

[13] Kara, H, Ramesh, R, Stevens, R and Bowen, C.R, IEEE Trans on Ultrason. *Ferroelec. Freq. Control*, 2003, 50, 289.

[14] Arai, T, Ayusawa, K, Sato, H, Miyata, T, Kawamura, K and Kobayashi, K, *Jpn. J. Appl. Phys*. 1991, 30, 2253-2255.

[15] Ina, K, Mano, T. Imura, S and Nagata, K, *Jpn. J. Appl. Phys. Part I*, 1994, 33, 5381-5384.

[16] Gomez'T.E, Montero de Espinosa, F, Levassort, F, Lethiecq'M, James, A, Ringgard'E, Millar, C.E and Hawkins, P, *Ultrasonics* 1998, 38, 907-923.

[17] Levassort, F, Lethiecq, M, Sesmare, R and Tran_huu_Hue, L.P, IEEE Trans. Ultason. *Ferroelec. Freq. Control*, 1999, 46, 1028-1033.

[18] Banno, H, *Jpn. J. Appl. Phys. Part I*, 1993, 32, 4214-4217.

[19] Dunn, M.L and Taya, M, *J. Am. Ceram. Soc*. 1993, 76, 1697-1706.

[20] Bowen, C.R, Parry, A, Kara, H and Mahon, S.W, *J. European Ceram. Soc*. 2001, 21, 1463-1467.
[21] Ramesh, R, Kara, H and Bowen, C.R, *Ferroelectrics* 2002, 273, 383-388.
[22] Hayward, G and Hossack, J.A, IEEE Trans. *Ultason. Ferroelec. Freq. Control*, 1991, 38, 618-629.
[23] Ramesh, R, Durga Prasad, C, Vinod Kumar, T.K, Gavane, L.A and Vishnubhatla, R.M.R, *Ultrasonics* 2006, 44, 341-349.
[24] Qi, W and Cao, W, *Ultrasonic imaging*, 1996, 18, 1-9.
[25] Ramesh, R, Kara, H, Stevens, R, Jayasundare, N, Humphrey'V and Bowen, C.R, *Integrated Ferroelectrics* 2004, 64, 201-206.
[26] Tuttle, B.A, Smay, J.E, Cesarano, J.D, Voigt, J.A and Olson, W.R, *25th Ann. Int. Conf. on Advanced Ceramics and Composites*, January 21-26, 2001, Cocoa Beach, Florida.
[27] Safari, A, Danforth, S.C, Jafari, M and Allahverdi, M, *25th Ann. Int. Conf. on Advanced Ceramics and Composites*, January 21-26, 2001, Cocoa Beach, Florida.
[28] Rittenmyer, K, Shrout, T, Schulze, W.A and Newnham, R.E, *Ferroelectrics* 41, 1982, 189-195.
[29] Skinner, D.P, Newnham, R.E, Cross, L.E, *Mat. Res. Bull.*, 13, 1978, 599-607.
[30] Creedon, M.J, Gopalakrishnan, S and Schulze, W.A, *Ferroelectrics* 1995, 299-302.
[31] J. Saggio-Woyansky, Scott, C.E and Minnear, W.P, *American Ceramic Society Bulletin*, 71, 1992, 1674-1682.
[32] Bowen, C.R and Kara, H, *Materials Chemistry and Physics*, 75, 2002,.45-49.
[33] Bowen, C.R, Perry, A, Kara, H and Mahon, S.W, *J. Eur. Ceram. Soc*. 21, 2001,1463-1467.
[34] Smith, W.A, Shaulov, A.A and Auld, B.A, *Ferroelectrics* 91, 1989, 155.
[35] *IEEE Standard on piezoelectricity* ANSI/ IEEE Std – 176, 1978, The Institute of Electrical and Electronics Engineers Inc, New York.
[36] Banno, H, *Jpn. J. Appl. Phys. Part I*, 32, 1993, 4214-4217.
[37] Dunn, M.L and Taya, M, *J. Am. Ceram. Soc*. 76, 1993, 1697-1706.
[38] Hayward, G and Hossack, J.A, IEEE Trans. Ultason. *Ferroelec. Freq. Control*, 38, 1991, 618-629.
[39] Ramesh, R, Kara, H and Bowen, C.R, *Computational Materials Science*, 30, 2004, 397-403.
[40] Ramesh, R, Kara, H and Bowen, C.R, *Ultrasonics* 43**,** 2005, 173-181.
[41] Hydrophones – their characteristics and applications, in *Introduction to underwater acoustics*, Band K Application note, Bruel and Kjaer, Denmark.
[42] Berlincourt, D and Krueger, H.H.A, *Important properties of Morgan Matroc piezoelectric ceramics*, TP-226, Morgan Matroc Ltd. U.K
[43] Creedon, M.J and Schulze, W.A, *Proceedings of the 10th IEEE International Symposium on Applications of Ferroelectrics* 1996, 527-530.
[44] Creedon, M.J, Gopalakrishnan, S and Schulze, W.A, *Proceedings of the 9th IEEE International Symposium on Applications of Ferroelectrics* 1995, 299-302.
[45] Lange, F.F and Miller, K.T, *Adv. Ceram. Mater.* 2, 1987, 827–31.
[46] Kara, H, Perry, A, Stevens, R and Bowen, C.R, *Ferroelectrics* 265, 2002, 317-332.

In: Developments in Ceramic Materials Research
Editor: Dena Rosslere, pp. 241-260
ISBN 978-1-60021-770-8

Chapter 8

FIELD EMISSION DISPLAY ON CERAMIC

Li Chen
The University of York, Heslington, York, YO10 5DD, UK

ABSTRACT

Scientific advances concerning many ceramic materials have enabled technological breakthroughs globally. The superior combinations of thermal, insulating, electrical and mechanical properties have become the basis of huge applications in the packaging of microelectronics and power semiconductors. Miniaturization and integration of metal via into ceramic substrate make it feasible to construct multilayer circuit inter connections. This advantage provides the possibility to mount electronics component and circuitry directly onto both side of ceramic substrate. This packaging advance makes ceramic very attractive to field emission display application. Field emission display is able to combine the high quality images and large viewing angles of cathode ray tube, while delivering it in the flatness attributed to liquid crystal display, and utilizing just a fraction of the electrical power required by plasma display panel. Field emission display is predicted to be one of the most promising flat panel displays that will take off in the future. Currently relying on the semiconductor thin film micro-fabrication technology, field emission displays are fabricated mostly on soda-lime glass substrate. Although this is compatible to the liquid crystal display technology, the row and column electrodes of a field emission display have to be allocated to the sides of glass substrate. Furthermore, the existing technology still has difficulties to deliver large area micro field emitters with acceptable uniformity. If the key components of micro field emitter matrix pixels can be produced entirely on the front side of ceramic substrate, and are electrically connected to the backside drive and control circuit through the micro via, this allows construction of micro field emitters right up to the edge of ceramic substrate. In addition, a large size display can be constructed by tiling ceramic substrates precisely. In this chapter, the micro-fabrication of field emitters on ceramic substrate is presented. Electron emission characteristics of these micro field emitters were studied, and results from the microstructures are analysed.

INTRODUCTION

Development of Display Technology

The display is such a critical human interface of electronic entertainment system that experts from academia as well as industry have been working for decades to create them larger, lighter, brighter, and thinner - particularly for television receivers and computer monitors. There have been different technologies such as Cathode Ray Tube (CRT), Thin Film Transistor Liquid Crystal Display (TFT-LCD), Plasma Display Panel (PDP), Organic Light Emitting Diode (OLED) display emerged since the last century, and promised to take the display industry where it has never gone before. They all were expected to gain wide acceptance for use as television receivers. Today's display market offers an abundance of choices of these technologies, each with their own advantages and disadvantages. CRT displays are heavy, bulky, and limited in size for direct view applications. PDPs are very electrical power hungry, suffer from lower brightness, and have the potential for screen burn-in. TFT-LCDs are limited in size due to manufacturing constraints, are costly, and suffer from narrow viewing angle and slow refresh rates. OLEDs suffer from stability and lifecycle issues.

The introduction of High Definition Television (HDTV) spurs display industry even further. HDTV provides means for transforming entertainment experiences by delivering crystal clear video in high resolution, high-fidelity surround sound, and the ability to drive interactive applications. Take-up of high definition services is accelerating in the USA and in other countries. With Sky's announcement that it has been examining the technical details for a launch of high definition services, and BBC increasing its amount of ongoing and archive programming broadcast as part of its HDTV trial, it now appears that HDTV will become a reality in the UK over the next few years.

Because of the inherent flaws in current display technology for HDTV, researchers have turned to micro tip based Field Emission Display (FED) and carbon nanotubes based FED to create a new class of large area, high resolution and low cost flat panel displays. Researchers believe that FED is the technology of choice for ultra high definition, wide screen televisions. It is this technology that will be able to support the HDTV revolution at adequate cost. The FED technology shares many similarities with traditional CRT technology. As for FED and CRT, electrons are extracted out of electron gun(s), and are accelerated in vacuum towards phosphor coated faceplate anode, collide with phosphor to create illumination through conventional process of electroluminescence [1]. The main difference is that, for FEDs, electrons are generated from cold micro field emitters rather than thermal emitters. Therefore the device consumes much less electrical power, and displays can be turned on instantly. Instead of one single point electron gun in a monochrome CRT or three point electron guns in a colour CRT, in a FED, each pixel comprises arrays of micro field emitters from which electrons are emitted [2]. In a CRT, electrons emitted from its electron source are deflected and scanned across the phosphor screen under the action of electromagnetic deflection coils to produce an image, while in a FED, hundreds if not thousands electron micro cathodes in high density are used for lighting each pixel. Thus there is no need of the bulky electromagnetic deflection coils for scanning the electron beam, and no need for refocusing individual electron beam [3]. Electrons emitted from the micro cathodes site directly below

the phosphors of a pixel to create an image, as a result the panel thickness can be reduced down to several millimetres [4]. Another advantage of a FED structure over a CRT is the reduction in the number of drivers by a factor of three (one single emitter sends electrons towards a sub-pixel which is successively red, green and blue).

Field Emission Display Technology and Advanced Ceramics Technology

For an electron to leave a material, the electron must gain energy to exceed the work function, which is a potential barrier at the surface of a metallic conductor that binds electrons to the material. This can be accomplished in a variety of ways, including thermal excitation in the case of thermionic emission, electron and ionic bombardment in the case of secondary electron emission, and the absorption of photons in the case of photoelectric emission. Field emission differs from all these forms of electron emission in that the emitted electrons do not gain an energy which exceeds the material's work function.

Field emission phenomenon results from the tunnelling of electrons from a metal or a semiconductor into the vacuum under an application of a strong electric field. The high electric field applied to the vicinity of the surface of a substance to low and thin the potential barrier on the surface, so that free electrons with high potential energy inside the substance can have possibility to tunnel through the thinned potential barrier and leave the surface. Since there is no heat transfer involved in the electron emission, field emitters are called cold cathode electron source [5]. To achieve a low operating voltage of a cold field emitter, in the case of a micro tips based FED, the tips are manufactured into very sharp form so that the local electric field strengths become high enough for even a moderately low voltage applied to the adjacent gate electrode [6]. Using a low work function material could also significantly reduce the turn on gate voltage for a field emitter. The most popular low work function material for forming a micro tip is molybdenum [7]. The micro tip field emitter fabrication technique was initially invented by Dr. Charles A. "Capp" Spindt at the Stanford Research Institute (now called SRI International) in 1968 [8]. The principal component of a Spindt cathode comprise a basic triode structure: a bottom cathode conducting layer, on which molybdenum micro tips in conical shape reside; a top gate conducting electrode layer, and an insulating oxide layer in between [9]. In the fabrication process, molybdenum cones with tip radii less than 30 nm are deposited by electron beam evaporation into the emitter wells. The cone forming process is self aligned. The advantages of such a structure include the high electron drawing efficiency since the electron emission portion is arranged in the vicinity of the centre of gate electrode where the electric field is most concentrated, the in-plane uniformity of drawn current is high, and the directivity of electron emission is regular, compared to the other field emission device.

Spindt's development stimulated the technology further into a concept to use field emitter arrays in a matrix addressed display (FED) conceived by the SRI team of which Spindt was a member, and patented by M. E. Crost, K. R. Shoulders and M. H. Zinn in 1970 [10]. By 1972, the SRI group had overcome more engineering problems to demonstrate to their satisfaction that it was feasible to manufacture FEDs [11]. Their new fabrication methods were patented by C. A. Spindt, K. R. Shoulders, and L. N. Heynick in 1973 and 1974 [12, 13, 14]. However SRI was unable to obtain funding to develop the FED concept in the decades of the seventies and early eighties. The idea was picked up and the initiative to develop the

technology moved to the *Laboratoire d'Electronique de Technologie et de l'Informatique* (LETI), a research arm of the French Atomic Energy Commission, in Grenoble. Earlier field emission studies showed that electron emission current from the Spindt micro tip field emitter was unstable, and might trigger irreversible catastrophic break down of the device [6, 9]. This was a key technological hurdle that slowed down the FED development. To tackle this problem, Robert Meyer of LETI patented a method for fabricating an array of molybdenum micro tips with a lateral ballast resistive layer [15]. The ballast resistive layer can effectively reduce the potential difference between the cathode tip and the gate electrode as more electron current flows out of the emitter [16]. Therefore, it evens out the electron emissions from the individual arrays across the display. The ballast resistive layer also helps to reduce the undesirable electric arcing between the field emitter cathode and phosphor anode, and thus improve the performance and prolong the life of FED [17, 18]. The LETI group was able to demonstrate publicly that FEDs constructed with lateral resistive layers could be manufactured with desired uniformities and had expected lifespans needed for commercial displays [19]. This stimulated the development of FEDs by many researchers in America, Europe and Asia in the 1990's.

However, the difficulty associated with scale-up of the Spindt type micro field emitters is the large size of electron beam evaporator required to deposit molybdenum micro tips. To ensure the evaporant reaches the cathode faceplate to form sharp cone tips, the distance required between the molybdenum source and the sample panel holder must be large. A study performed at Samsung showed that for an evaporator with throw of 72 cm, an angle variation of 0.8° resulted in a tip radius of curvature change of 2 nm over a 6 cm distance along the substrate [20]. This tip radius variation resulted in a 75% decrease in emission current for tips at the edge of the substrate versus those tips in the centre. The Spindt type micro tips based FED belongs to the first generation FEDs, which relay on thin film technology and semiconductor processing methods. Despite its success in achieving performance, it is still a high cost technology. In addition, it suffers from scalability problem.

In the development of second generation FEDs, researchers have directed efforts towards reducing the overall display cost by replacing the refractory metal emitter material with alternative cold field emitters. If the switching voltage for the alternative field emitters is reduced below the Spindt type micro tip cathode required gate voltage value, which is typically between 20~60 V, this allows the use of smaller and cheaper driving circuits. Research has been investing materials which possess either a lower work function or material structures with larger intrinsic electric field enhancement.

Among the investigated material candidates of field emission cathode for FED application, carbon based materials have experimentally demonstrated the most encouraging field emission properties [21, 22]. Early investigation into diamond showed excellent field emission property, which is believed benefit from the property called negative electron affinity [23], which is related to the material's work function. However, the challenge here is how to pump electrons into the conduction band for these materials. Diamond like carbon materials also have negative electron affinity, and electrons can be emitted into the vacuum at a very low electric field from the materials [24]. Subsequent investigation into pure graphitic materials including nanostructure graphite was also proofed to be good field emission materials [25].

Since the multi-walled carbon nanotubes was discovered by Sumio Iijima in 1991 [26] and the single walled nanotubes was synthesized giving carbon structures of 1.4 nm in

diameter and several microns in length in 1993 [27], extensive studies of carbon nanotubes' material and physical properties began. Today, carbon nanotubes are driving scientific research. The basic research field has several important directions including chemistry, electronic transport, mechanical and field emission properties.

A carbon nanotube is a very small piece of graphite, a derivative of carbon, rolled up into a very small tube. It is not a metal, but a very strong structure built entirely out of covalent bonds with field emission properties. Carbon nanotubes are high in aspect ratio and whisker-like in shape, which is favourable for field emission. Even for moderate voltages, a strong electric field develops at the free end of supported carbon nanotubes because of their sharpness. This was observed by de Heer and co-workers at EPFL in 1995 [28]. Carbon nanotubes are chemically stable, therefore they only react under extreme conditions such as extremely high temperatures (2500°C) with oxygen or hydrogen; consequently, the problems of reacting with resident gases, overheating, or tip deformation are not serious with carbon nanotubes as compared with micro tip field emitters. It was realized immediately that these nanotube field emitters must be superior to conventional electron sources and might find their way into all kind of applications, most importantly flat panel displays [29, 30]. It is remarkable that after only five years Samsung actually realized a very bright colour field emission display, which will be shortly commercialised using this technology. Carbon nanotube based FED research is very active in the USA, Europe and Asia. Big companies such as Motorola Inc [31], Samsung Group [32], and Sony Group are aggressively pursuing FED technology using carbon nanotubes.

Apart from the well known electrical power saving advantage, another major advantage of the FED technology is that the display is thin and light. Although it has the optical quality of a CRT, it does not produce X-rays since the voltage applied to phosphor screen is no more than 6 to 8 kV as compared to the voltage of 15 to 30 kV required to apply to phosphor screen in the case of CRT. FEDs are not sensitive to magnetic fields or large temperature variations. For all of these reasons it can find wide range of applications in industrial and automobile applications, or as a monitor for scientific and medical instruments such as mass spectrometers or oscilloscopes. Versions have also been developed for avionics and this technology could possibly be considered for manned space systems. FED is emerging as a potential threat to the big TFT-LCD dominant display market. In general, FEDs offer the prospect of flat panel displays which are superior to TFT-LCD screens in brightness, colour rendition, response time and operating temperature range. FED has demonstrated its advantages: high contrast ratio, great brightness, consuming low power, wide viewing angle, excellent colour gamut, can be used in harsh environment such as in wider range of operating temperature, and in radiation condition.

Nowadays, the most popular substrate material on which FEDs are fabricated is the soda-lime glass, which is compatible to the TFT-LCD technology. There are many advantages of using the soda-lime glass over other materials for display application. For example, soda-lime glass is vacuum compatible, the material cost is inexpensive, the mature technique enable the soda-lime glass to be made very flat over a relatively large area, and it can be coated with a variety of materials using Very Large Scale Integration (VLSI) thin film technology [33]. However, the fabrication of the Spindt type micro tips, using micro fabrication technique, has difficulties to produce large area field emitters with acceptable uniformity [34]. So far, FEDs constructed with the Spindt type micro field emitters, as well as the carbon nanotubes have only been produced on small and medium size substrates.

The continuing evolution of the ceramics and the associated technologies is accelerating rapidly. With the advances of understanding in ceramic chemistry, crystallography and the more extensive knowledge gained in regard to the production of advanced and engineered ceramics that the potential for these materials has been realised. One of the most prominent examples of this rapid and accelerating technological development is the electronics industry, in specific the simple transistor. The concept of the simple transistor is believed to be one of the most significant electronic engineering achievements in the last century. The demand for miniaturisation and packing the maximum amount of transistors into the smallest space spurs the development in ceramic application for packing in the electronics industry.

Brittle by nature, ceramics having a complex chemistry and requiring advanced processing technology and equipment to produce, perform best when combined with other materials such as metals and polymers, which can be used as support structures. Ceramic material is mechanically very hard and stable. Oxide ceramics possess properties such as oxidation resistant, chemically inert, electrically insulating, generally low thermal conductivity, slightly complex manufacturing and relatively low cost. Advanced ceramic material provides an advantage that a metal via can be easily buried inside the soft substrate before the material goes through the high temperature hardening treatment. This unique feature makes it feasible to construct multilayer electrical circuit interconnections. It therefore, provides the possibility to mount electronics components and circuitry directly onto both sides of ceramic substrate. This intrigued the birth of a new idea that if micro field emitter matrix pixels can be produced entirely on a mirror flat front side of a ceramic substrate, and are electrically connected to the backside drive and control circuit; this allows the structure of micro field emitters built right up to the edge of ceramic substrate. If this is achievable, it compares favourably with the soda-lime glass substrate, where the column and the row electrode connections of the micro field emitter matrix on the back plane of a FED have to be allocated to the sides of substrate. To make it even more attractive, a large size of display can be constructed by tiling up the ceramic substrates precisely.

In FEDs, small spacers have to be allocated between the anode screen and cathode substrate to create a vacuum space for electron beams to travel. Candidates for spacer have to be mechanically strong to sustain the atmospheric pressure, and to be highly insulating to sustain the high electrical potential without electric break down. Amazingly, ceramic material has already been proposed as a spacer to support the faceplate phosphor screen against the cathode back plane in the FED application [35, 36]. This is because the modern ceramics technology has provided new materials with better performance than other candidate materials such as glass and polymer.

In the following section, an experimental study on a successful fabrication of the Spindt type micro tip field emitters on ceramic substrate is presented. A systematic electrical characterisation of these micro field emitters was carried out. The acquired experimental data were analysed and the field emission electrical performance were evaluated.

EXPERIMENT

Micro-Fabrication of FED on Ceramic Substrate

A special oxide ceramic was chosen for fabrication of micro field emitters because the material demonstrated superior performance in severe service application environments. The FED application will benefit from the following by using this material: excellent corrosion resistance in plasma and chemical etching environments; superior dielectric strength which helps to prevent electrical arcing during operation; ceramic materials prevent static charge build-up during transport; excellent thermal stability provides extremely stable substrate in a wide range of operating temperatures. A surface treatment to the ceramic substrates was initially performed in order to meet the fabrication requirement for micro field emitters. Substrates were mechanically lapped, followed by a fine polishing process, which would generate a mirror flat front surface. It is crucial to acquire a flat surface on which the micro field emitter will reside. The roughness of the front surface was controlled to be less than 100 nm. This specification figure was evaluated utilizing a profiler in a line scanning mode in a measurement over the entire substrate. The substrates were then diced into smaller pieces in square shape with a dimension in 2×2 inches.

A standard wafer cleaning procedure was adopted to clean the ceramic substrate, in order to remove any organic contamination and small particles on the surface. The ceramic samples were immersed into an ultrasonic bath containing acetone solvent. The acetone was pre-heated before pouring into the ultrasonic bath container, so that organic contamination can be dissolved more efficiently. After a 30 minutes agitation in the ultrasonic bath, the substrates were taken out and blown dry using a dry nitrogen gun. This was immediately followed by a 10 minutes Iso Propernol Alcohol rinse.

After the surface cleaning treatment, the ceramic substrates were clamped on three special sample holders. These sample holders were then loaded into an electron beam evaporator E2000 (Scientific Vacuum Systems Ltd.) for metallization. The evaporator was pumped down quickly into a high vacuum condition under a full speed operation of a turbo molecular pump backed by a rotary roughing pump. Halogen lamp heaters inside the vacuum chamber were then turned on to illuminate the ceramic substrates. The radiation energy generated by the illumination would transfer to the ceramic substrates directly, and heat up the ceramic surface. Any moisture and gas molecules absorbed on the ceramic substrates' surface would be gradually vaporized, and pumped out of the vacuum chamber through the pumping system. This dehydration treatment is crucial for the following metal deposition processing. It would enhance the adhesion of the deposited material to the substrate. After a 30 minutes dehydration processing at a temperature of 300°C inside the vacuum chamber, a 0.25 μm thick molybdenum thin layer was evaporated on the ceramic substrates.

When the vacuum chamber was cooling down to room temperature, the ceramic substrates were taken out from the evaporator. A thin layer of photo resist was spin coated on top of the molybdenum film. The photo resist was slightly hardened by taking a soft bake process for 1 minute. A standard photo lithography patterning was carried out using a Karl Suss MA6 mask aligner to define the molybdenum film into conducting tracks, which would be used as a cathode electrode. Followed by a photo resist developing process, a wet chemical etching process was employed to remove molybdenum in the exposed pattern area. Till now,

the back contact cathode electrode was formed, which defines the pixel pitch in a vertical direction.

The photo resist was stripped off in an acetone solution afterward. The ceramic samples were then loaded in a Plasma Enhanced Chemical Vapour Deposition (PECVD) system DP800 (Oxford Plasma Technology). The PECVD vacuum system was pumped down while the ceramic samples were being heated up. When a process base pressure was achieved and the chamber's temperature was stabilised at 300°C, a 1.2 µm thick SiO_2 thin film was deposited on the ceramic samples surface, using a gas mixture of SiH_4 and N_2O. After the vacuum chamber was cooling down to room temperature, the system was vented with dry nitrogen. The ceramic samples were re-assembled back on three sample holders, and were loaded in the electron beam evaporation system. This time, the second layer of molybdenum in a thickness of 0.2 µm was deposited at an elevated temperature. This molybdenum layer would be used as the gate electrode, separated from the first molybdenum layer by the SiO_2 thin layer. This was followed by another photo lithography patterning using the mask aligner to define the molybdenum gate electrode tracks, which are perpendicular to the previously patterned back contact electrode tracks. The top gate electrode specifies the pixel pitch in the horizontal direction. Here, a wet etching solution was used to etch the molybdenum in the exposed pattern area on the top gate layer.

After stripping off the photo resist, a new layer of photo resist was spin coated on the ceramic samples. The photo resist was softly baked, ready for the following critical lithography patterning, which defines the gate hole arrays on the top molybdenum layer. The gate hole arrays should be defined symmetrically within the gate electrode tracks overlapping the back contact cathode electrode. This was achieved through a photo lithography utilizing a GCA 8000 DSW Wafer Stepper. This photo lithography produced 1.5 µm in diameter aperture arrays in the photo resist. Figure 1 shows a high resolution Scanning Electron Microscope (SEM) photograph of a cross section of a patterned hole in the photo resist.

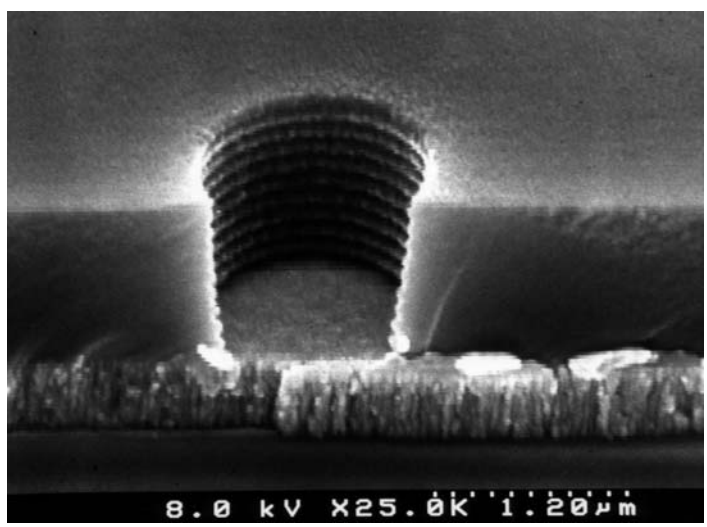

Figure 1. Cross section of a 1.5 µm in diameter hole defined in the photo resist. Standing wave caused ripples developed on the profile of photo resist sidewall.

In order to control the dimension of gate apertures more precisely, instead of using wet etching process, a Reactive Ion Etching (RIE) method was adopted to etch the top molybdenum layer down to the SiO_2 through the pattern holes in photo resist. A SF_6 reaction gas was used for this molybdenum dry etching process using a facility System 90 (Oxford Plasma Technology), along with the patterned photo resist as a mask. Figure 2 shows a top view of four gate aperture arrays in the gate electrode tracks in the vertical direction, overlapping over the back contact electrode in the horizontal position.

To take the advantage of dry etching technique, which produces repeatable high quality thin film through accurate process control, an anisotropic reactive ion etching recipe was developed for etching the SiO_2 dielectric between the two molybdenum layers through the small openings of molybdenum gate holes. This SiO_2 etching process was performed in a system CME 800 (Oxford Plasma Technology), using the combination feeding gases of CHF_3 and C_2F_6 to form cylinder shape cavities. Figure 3 illustrates a SEM image showing a cross section of a cylinder cavity within the SiO_2 after the dry etching process. These small cavities were enlarged by removing more SiO_2 through another wet etching process in a buffered HF solution. This further etching process is aimed to clean any SiO_2 residue left on the back contact cathode molybdenum. It could cause a serious electrical conductive problem for the molybdenum micro tips to be formed on the back contact electrode tracks if there were any SiO_2 residues left. Un-predicted field emission behaviour from the emitters would result when the device is powered up. The photo resist was stripped off afterward. A SEM photograph showing a cross section image of a SiO_2 cavity after the buffered HF etching and photo resist stripping is shown in Figure 4.

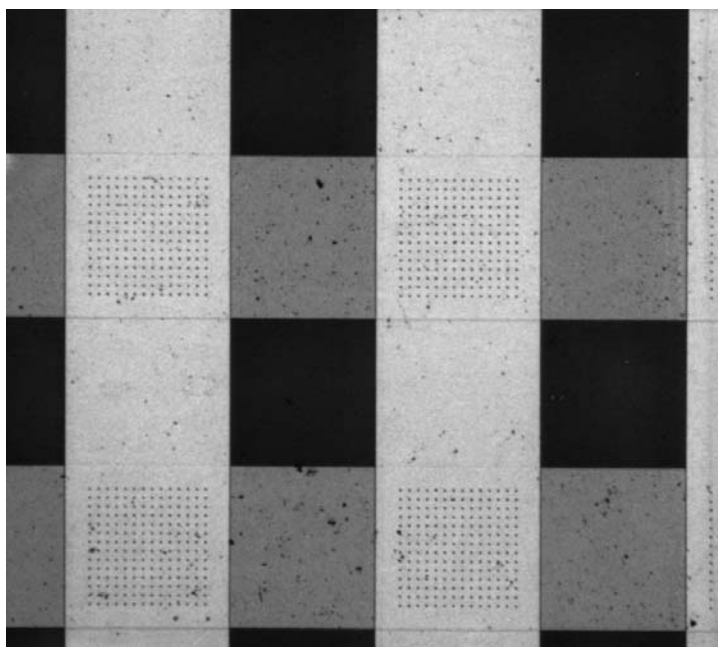

Figure 2. Top view of a gate hole arrays patterned on the intersection of gate electrode tracks and cathode electrode tracks.

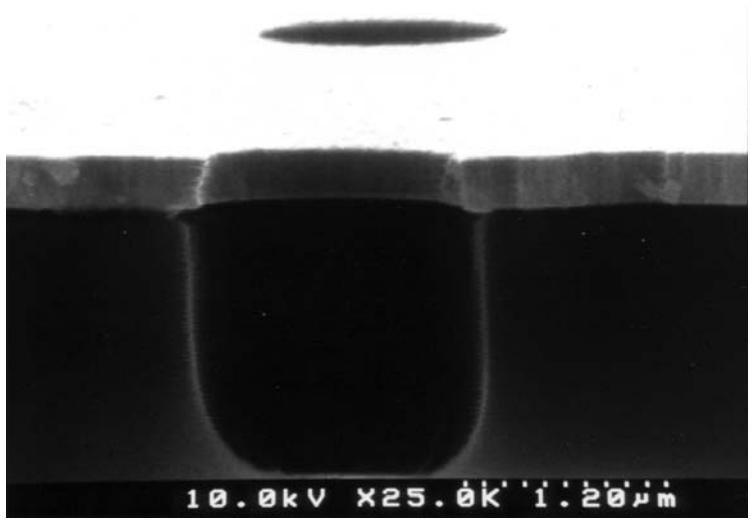

Figure 3. Vertical sidewall formed in SiO_2 cavity after anisotropy dry etching.

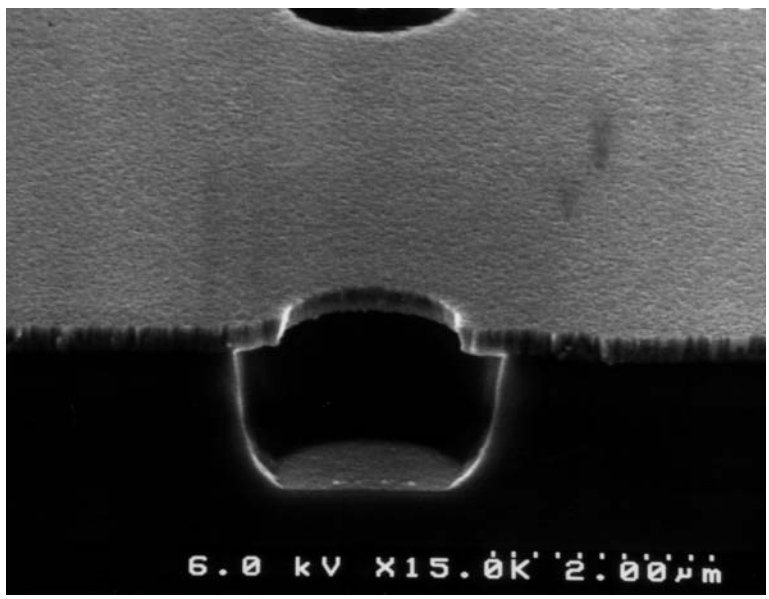

Figure 4. Clean back cathode contact revealed inside the SiO_2 cavity.

The ceramic samples were re-loaded back into the electron beam evaporation system. When a base pressure and a specific elevated temperature of the system were reached, an aluminium parting layer was deposited on the gate molybdenum layer. This was achieved by rotating the sample holders at a slant angle with respect to the evaporation aluminium source, while the aluminium evaporation process was taking place. The reasons for tilting the sample holders and keep them rotating during the process are for the following purposes. First, it prevents the aluminium evaporant from depositing onto the back contact electrode layer through the cavity openings previously formed; second, it will produce smaller aluminium apertures than the gate holes underneath, which is useful for the following metal lift-off

process. The thickness of this buffered aluminium layer was around 0.2 μm. The sample holders were turned back to their normal position after the aluminium deposition process.

The molybdenum micro cone forming process is the key process to produce the micro field emitters. Sample holders were rotating as satellites around their orbit centre, from which the molybdenum evaporation source was located 600 mm below; the sample holders were also spinning on their own axis during the deposition process so as to form cone structures inside the gate cavities. Radiation energy transmitted from the halogen lamp heaters to the ceramic samples during the deposition was in an attempt to release the stress building up upon the deposited film. In order to fully form conical shape, the thickness of molybdenum film was monitored during the process to be just beyond an empirical value. Over dose deposition of molybdenum not only leads to material wasted unnecessarily, but also increases the risk of a thin film peeling, which is due to an extensive stress built in a thick molybdenum film. A SEM photograph shows a cross section of a molybdenum cone tip after deposition process in the Figure 5.

The final photo lithography process to pattern the top molybdenum film into opening windows is designed for the lift-off process. The mask aligner was re-used here for this lithography patterning. Followed the lithography and photo resist developing process, a wet etching method was employed to etch away the molybdenum down to the aluminium layer through the photo resist mask opening windows. The lift off process was performed in a fresh NaOH solution to dissolve the aluminium buffer layer, and thus lifting materials above. The entire fabrication process ended with nitrogen blow-dry of the samples. Figure 6 shows an array of the micro field emitters after the entire fabrication processes. The emitter tips with gate structures are evenly distributed.

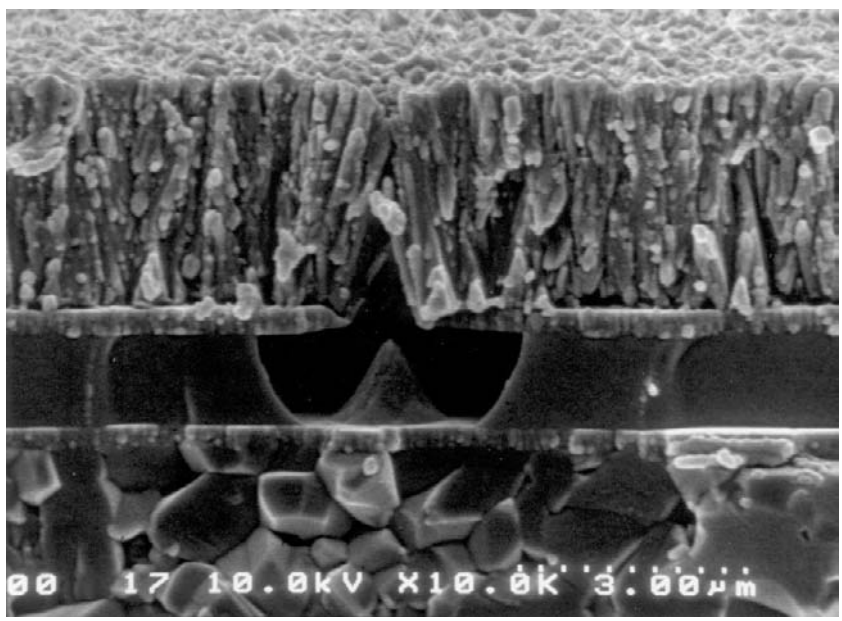

Figure 5. Micro cone tip formed after molybdenum deposition. Vertical crystallized molybdenum film on the top layer and larger grain structure with irregular shape ceramic substrate in the low layer are visible.

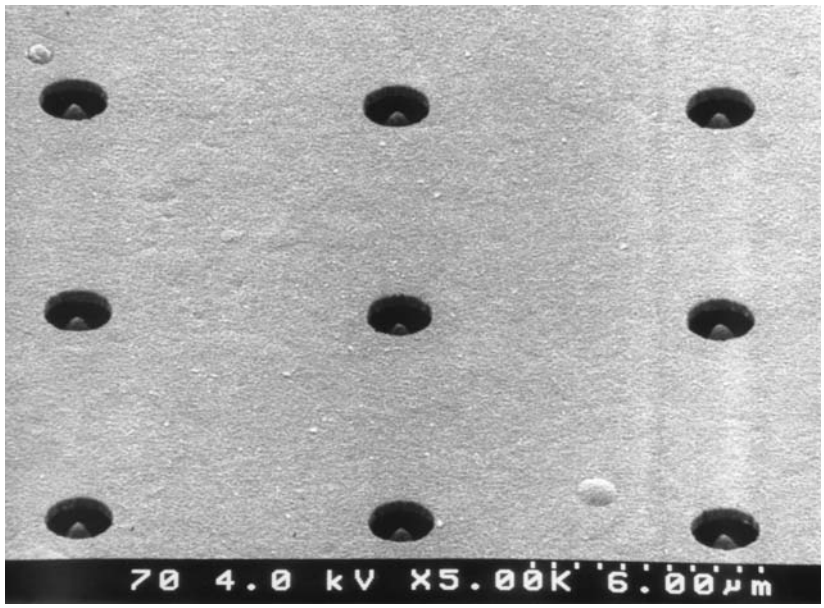

Figure 6. Molybdenum micro tips with gate structure.

Electrical Characteristic Study: Electrical Set up

Molybdenum micro field emitters belong to the vacuum microelectronics devices, therefore it is vital to create a clean ultra high vacuum condition for these devices to work. The electrical characterisation of the micro field emitters on ceramic was performed inside a turbo molecular pump based ultra high vacuum system. A special designed mechanical jig was built to mount the ceramic sample, and make the associated electrical connections to the gate electrode and back contact electrode. A low voltage phosphor screen with a dimension of 2×2 inches was electrically insulated and physically separated from the micro field emitters with a small spatial gap of approximately 2 mm. The phosphor screen is made of a piece of glass, coated with a conducting layer of indium tin oxide, on which a thin layer of phosphor power was coated. When the phosphor screen is powered up with positive high voltage potential, it accelerates the negatively charged electrons towards it if electrons are emitted from the micro field emitters. A schematic diagram showing the experimental set up is illustrated in Figure 7. The back contact cathode electrode of micro field emitters was electrically grounded to a common earth. The gate electrode and the back contact cathode electrode were connected to a Keithley source meter model 2400, which provides a voltage source supply to the device under test, and acts as a micro ampere current meter for the close loop electrical circuit. In this case, any leakage current passing through the gate electrode and the micro field emitter cathode electrode was monitored by the source meter 2400. To prevent the source meter from short circuit in case of an un-predicted discharging event between the gate electrode and cathode electrode, an external resistor was loaded in series between the Keithley source meter 2400 and the gate electrode.

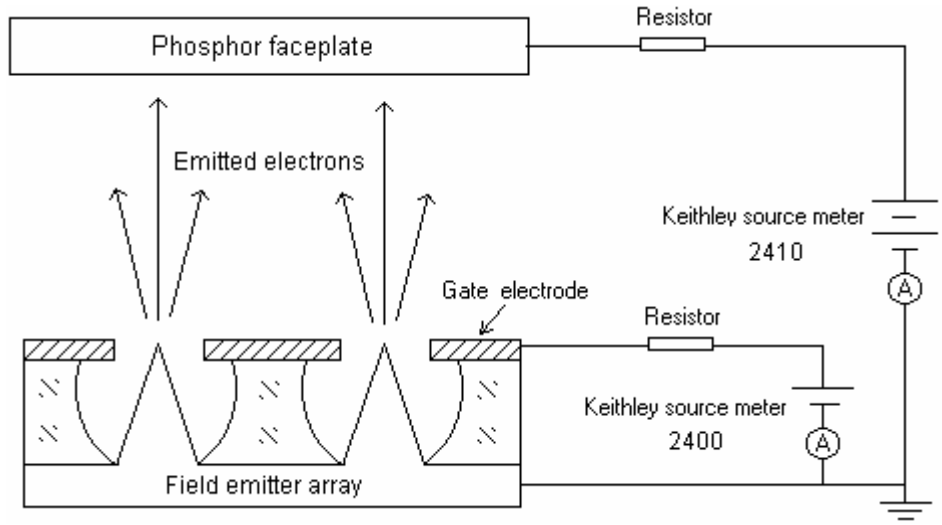

Figure 7. Schematic diagram of the field emission characterisation setup.

Another Keithley source meter model 2410, with an ability to supply a higher voltage up to 1.1 kV, was used to power the phosphor screen anode referenced to the common ground. The source meter 2410 monitors the emission electron current collected by the phosphor screen anode. Both the Keithley source meters are programmable. They communicated automatically to the central control system - a personal computer (PC) via a General Purpose Interface Bus (GPIB). The entire automatic control and data acquisition between the PC and the two source meters were achieved through a specific software control program, designed using the instrument oriented LabVIEW package (National Instruments).

Ultra high vacuum condition can be achieved quicker by baking the vacuum test chamber at an elevated temperature in the range of 150°C~200°C. A base pressure of 5×10^{-10} mbar was acquirable after an overnight bake out, followed by cooling down to room temperature.

Electrical Characteristic Study: Experimental Data Results

One basic electrical characterisation of the micro field emitters is to obtain the emission electron current as a function of the gate voltage curve (I-V curve). This was performed by ramping up the gate electrode potential voltage from 0 up to a certain value, normally less than 200 V, while measuring the emission electron current from the field emitter cathode. To enhance the efficiency of emitted electrons to impinge the phosphor screen anode, the emitted electrons are attracted toward the anode electrode under an action of a strong static electric field. Electrons collided into the anode, where a current flow was detected through the electrical circuit. Another important I-V curve to characterise the micro field emitters is to obtain a curve of the leakage current versus the gate voltage. This I-V curve reveals the quality of the SiO_2 dielectric layer, which separates the gate electrode and the cathode. Here, the leakage current was acquired by the Keithley source meter 2400 in the experiments. A specific emission current and leakage current via gate voltage characteristics obtained from a micro field emitter array is illustrated in Figure 8 (a).

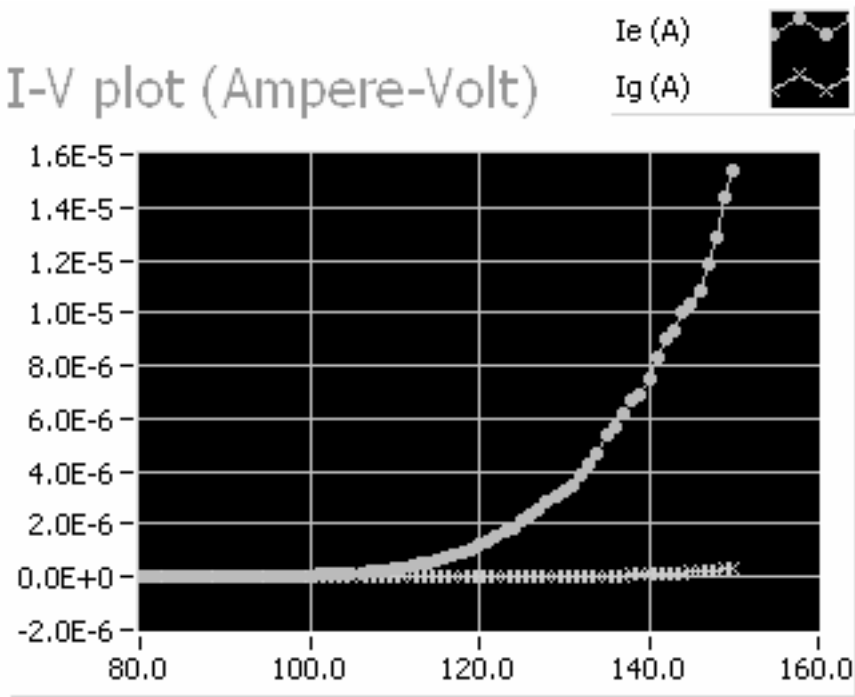

Figure 8(a). I-V curve from a micro field emitter array. Emission current Ie (unit: ampere) and leakage current Ig (unit: ampere) via gate voltage Vg (unit: volt) up to 150 V.

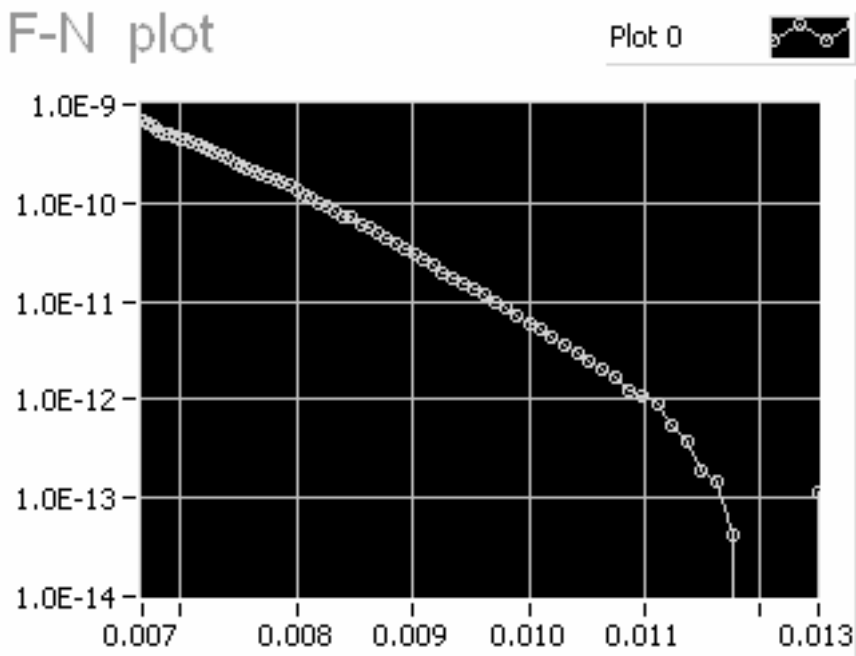

Figure 8(b). Fowler-Nordheim plot indicates the field emission mechanism.

In this figure, the curve shows a gate potential voltage ramped from 80 V up to 150 V, with increment of 1 V in step. The leakage current value was far below 1% of the emission current value for the whole course, indicating a good quality of the dielectric insulating layer.

Field emission can be described in physics by the Fowler-Nordheim equation [37], which can be written in a simple form as:

$$I = aV^2 e^{-\frac{b}{V}} \tag{1.1}$$

where I – emission current

V – applied electric field potential voltage

a and b are treated as constants that are related with the emitting area and geometric factor of the emitter.

Equation (1.1) can be rewritten in another mathematics function as the following:

$$\ln\left(\frac{I}{V^2}\right) = -\frac{b}{V}\ln a \tag{1.2}$$

Ideally plotting $ln(I/V^2)$ versus $1/V$ should yield a straight line. In fact, this linear form of Fowler-Nordheim plot is widely used in practice to distinguish field emission mechanism from other electron emission mechanisms. Converting the I-V curve into the function $ln(I/V^2)$ versus $1/V$ gives Fowler-Nordheim plot. Figure 8 (b) shows the Fowler-Nordheim plot version of the I-V curve in Figure 8 (a). The linear curve proves the nature of field emission mechanism from the micro field emitters.

To use the micro field emitters for display application, it is important to study the emission stability and life time characteristics. In the stability test, individual pixel of the micro field emitters was randomly chosen and was applied to a fixed gate potential voltage while the emission current was monitored over a period of time. A LabView test graph showing an emission current trace for a length of 17.5 hours from a pixel is illustrated in Figure 9. The data were acquired after a preliminary tip cleaning process at a high emission current of ~8×10^{-5} A by keeping the gate voltage at 155 V for 30 seconds, followed by reducing the gate potential down to a lower value of 150 V for this life time test. The emission current and the leakage current data were collected, averaged and stored in memory every minute under the control of the automatic data acquisition system. The leakage current value is well below 1% of the emission current over the entire test period, indicating a high quality SiO_2 insulating layer.

In order to investigate the uniformity of emission current from the micro field emitters on ceramic substrate, a comparison study with micro field emitters on silicon wafer was performed. To do this, an identical fabrication procedure to produce micro field emitters on ceramic substrate was applied to silicon wafers. The wafers were diced into the same dimension as the ceramic substrate. After a surface cleaning treatment, a thin dielectric layer of SiO_2 was deposited using PECVD onto the silicon substrates to insulate the surface. Then the silicon substrates went through the same batch process along with the ceramic substrates for micro field emitters' fabrication.

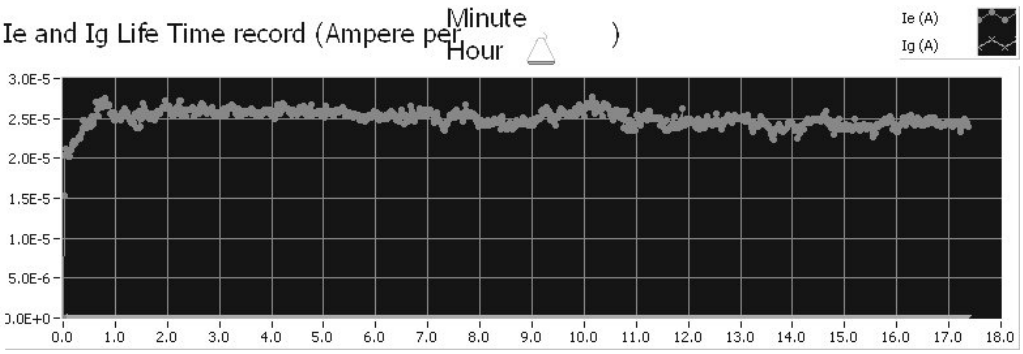

Figure 9. Life time test of a micro field emitter array at a gate voltage of 150 V over a period of 17.5 hours.

In order to statistically identify the emission current uniformity, electron current maps from different samples have to be acquired in the electrical characteristic study. This was achieved by firing the whole micro electron emitter guns on substrate pixel by pixel at a fixed gate potential voltage, while monitoring the emission current collected by the anode screen and read out via the Keithley source meter 2410. For comparison, Figure 10 illustrates two graphs representing electron current distributions from a ceramic sample and a silicon sample. Each tested sample has 20×20 pixels. Pixels are evenly spread over three-quarters of a 2×2 inches area in the centre. The statistic evaluation of emission current uniformity shows equivalent performance for the ceramic sample and silicon sample.

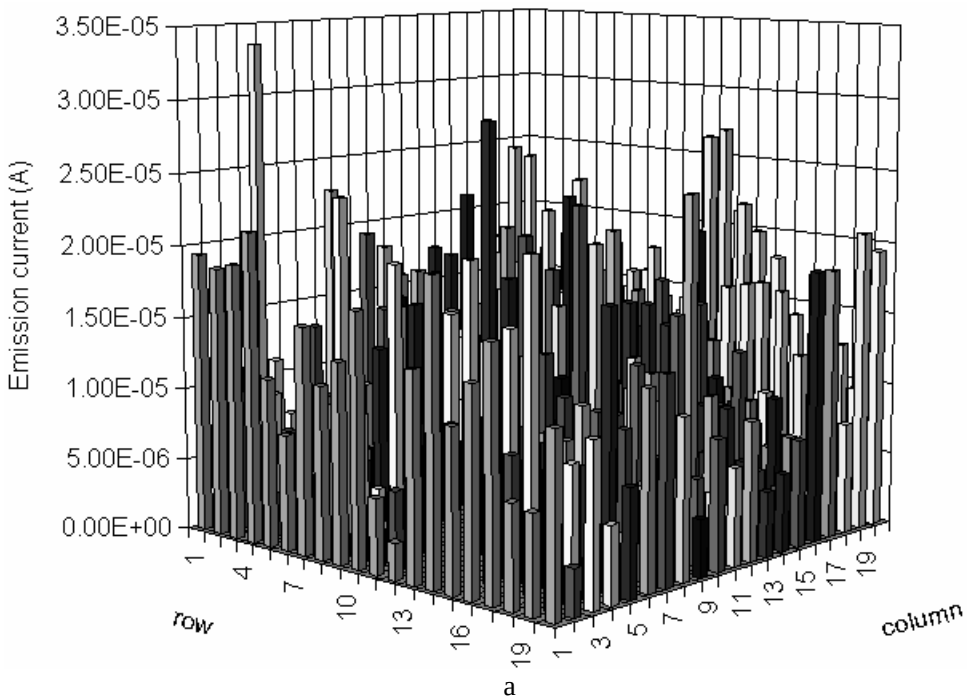

a

Figure 10 (Continued).

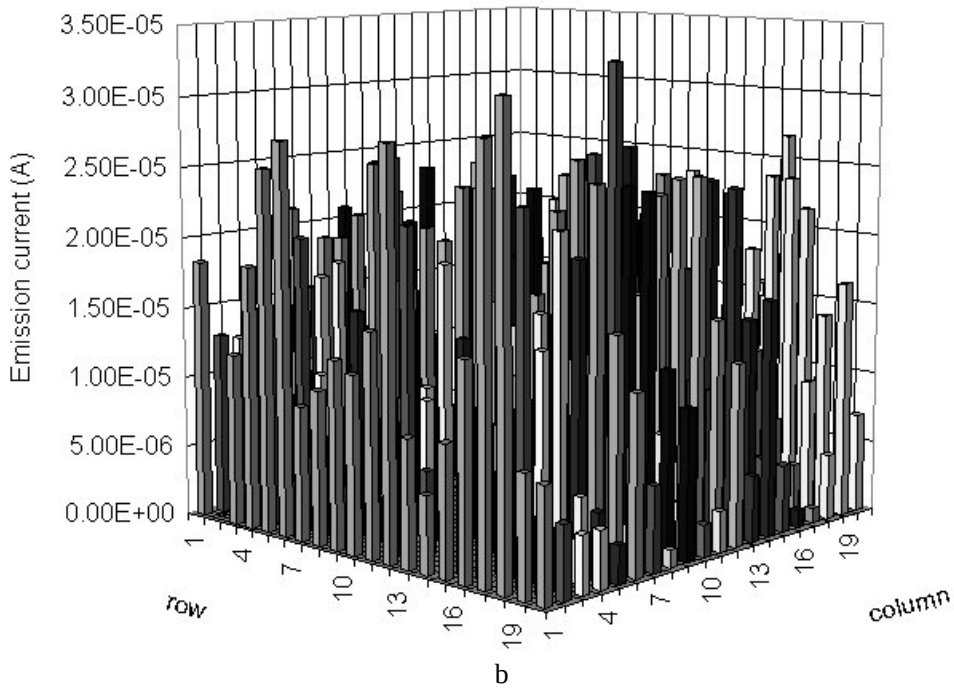

Figure 10. Field emission current maps from 20×20 pixels. (a) Data collected from a ceramic substrate with average current 10.2 μA, and standard deviation 5.57 μA; (b) Data collected from a silicon substrate with average current 10.8 μA, and standard deviation 7.1 μA.

The micro field emitters are vacuum microelectronics devices. Their performances are very sensible to the surrounding environment. Any gases absorption and desorption to the tips surface would influence their field emission behaviour. In particular the tips without surface cleaning treatment could demonstrate very noisy field emission because resistive heating to the tip by the emission current causes temperature rise, therefore contaminants and gas molecules tend to desorb from the surface, causing the work function changes on the field emission sites. In the electrical characteristic study, variation of emission current was associated with image brightness variations on the phosphor screen. It was also revealed on the pressure reading from an ion gauge, which was located further away from the emission site. Pressure bursts from the initial base pressure of 5×10^{-10} mbar without firing the field emitter guns, to 2×10^{-6} mbar when electrons heavily bombard on the phosphor screen were observed. This suggested a far worse vacuum condition in the narrow space between the phosphor screen and the emitter cathode back plane. Plasma can be triggered easily under this condition due to the large quantity of gas molecules released from the phosphor under the intensive electron bombardment. Figure 11 shows an image of plasma struck on the phosphor screen when an emission current impinged the phosphor causing a pressure rise in the local area. Micro field emitter destruction was inevitable under this condition. A SEM image showing a destructive microstructure from a field emitter array on a ceramic sample after a characteristic study is shown in Figure 12. Melted molybdenum surface, deformed gate apertures and evaporated cone tips are visible. Phosphor particles landing on a field emitter is the evidence of a plasma discharge event.

Figure 11(a). Plasma generated on the phosphor screen as high emission current impacts on the screen causing gases release into the surrounding vacuum.

Figure 11(b). Field emission electrons from one pixel of field emitter array hit the phosphor screen and generate bright illumination.

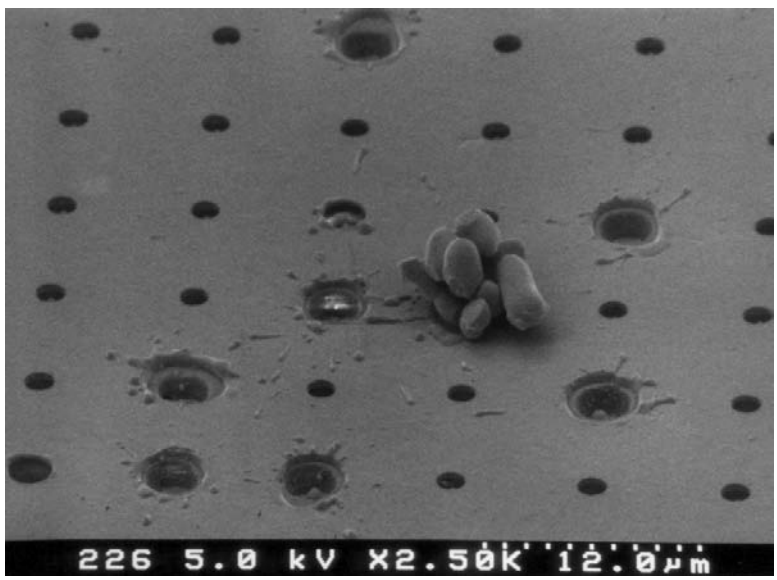

Figure 12. Destructive of micro field emitter structure after field emission test.

CONCLUSION

The global market for flat panel displays is booming. Tremendous growth in flat panel display popularity is due largely to the improvements in quality and affordability the technologies of TFT-LCDs, PDP, OLED etc. provide. It is not surprising that alternative FED technology continue to attract investment because it holds the promise of surpassing other displays in performance, and price. Despite the many advantages of the Spindt type FEA

fabrication technique, scaling this method to large area substrates, especially larger than 400 mm on the side, is still a major technical challenge.

The modern ceramics for engineering applications can be considered to be non-traditional. The new and emerging family of ceramics is referred to as advanced, new or fine, and utilise highly refined materials and new forming techniques. These new advanced ceramics, when used as an engineering material, possess several properties which can be viewed as superior to other materials' properties. The packaging capability for electronics plus other properties such as chemical inertness, dimensional stability and mechanical hardness are attractive to FEDs application. In this chapter, the fabrication of the Spindt type micro field emitters on ceramic substrate is presented. Systematic electrical characteristics studies of the micro field emitters on ceramic are reported. In a comparison study, micro field emitters on ceramic substrate have demonstrated equivalent electrical performance as micro field emitters on silicon substrate. The ceramic unique packaging capability allows building the row and column electrodes and electrical driver to the back of substrate, which makes it feasible to scale up FED by tiling with small FEDs on ceramic.

The on going research efforts focus on the development of next generation of FEDs, such as those based on carbon nanotubes cold cathodes. These new materials offer exciting new possibilities to produce cheaper and more robust displays. However, much of the physics which governs the operation of the Spindt type based FEDs remains unchanged. In other words, technological hurdles such as long term cathode reliability and high voltage break down have to be addressed regardless of the type of field emission cathode used. The mature thin film technique could allow the carbon nanotubes cathodes to be built on ceramic easily. It will not be surprised to see large panel FEDs sale on the market in the future as the techniques are already there.

REFERENCES

[1] A. Talin, K. A. Dean, J. E. Jaskie, *Solid State Electronics* 2001, 45, 96-976.

[2] S. Itoh, M. Tanaka, T. Tonegawa, *J. Vac. Sci. Technol*. B, 2004, 22 (3), 1362-1366.

[3] I. Shah, *Phys. World*, 1997, 45-48.

[4] B. R. Chlamala, Y. Wei, B. E. Gnade, *IEEE Spectr*. 1998, 35 (4), 42-51.

[5] Robert B. Smith, "Electronics Developments for Field Emission Displays," *Information Display* February 1998, v.14, no. 2, p. 12.

[6] I. Brodie and C. A. Spindt, *Advances in Electronics and Electron Ph*ysics 1992, Vol. 83, 1-106.

[7] C. A. Spindt, C. E. Holland, A. Rosenreen and I. Brodie, IEEE Trans. *Electron Devices* 1991, 38(10) 2355-2363.

[8] C. A. Spindt, *J. Appl. Phys.* 1968, 39 (7), 3504-3505.

[9] P.R. Schwoebel, and I. Brodie, *J. Vac. Sci. Technol*. B 1995, 13 (4), 1391-1410.

[10] M. E. Crost, K. R. Shoulders and M. H. Zinn, 1970, *US Patent* 3,500,102.

[11] Jules D. Levine, "Field Emitter Displays," presentation made at the Flat Panel Display *Processing and Research Tutorial and Symposium*, San Jose Convention Center, June 21-22, 1995

[12] C.A. Spindt, K.R. Shoulders, and L.N. Heynick, *U.S. Patents* 3,755,704 (1973).

[13] C.A. Spindt, K.R. Shoulders, and L.N. Heynick, *U.S. Patents* 3,789,471 (1974).
[14] C.A. Spindt, K.R. Shoulders, and L.N. Heynick, *U.S. Patents* 3,812,559 (1974).
[15] C. Py, and R. Baptist, *J. Vac. Sci. Technol. B*, March 1994, vol. 12, issue 2, 685-688.
[16] A. Ghis, R. Mayer, P. Ramboud, F. Levy and T. Leroux, IEEE Trans. *Electron Devices* Oct.1991, vol. 38, no. 10, 2320-2322.
[17] S. Itoh, T. Niiyama, M. Taniguchi and T. Watanabe, *J. Vac. Sci. Technol. B* May 1996, vol. 14, issue 3, 1977-1981.
[18] R. Baptist, F. Bachelet and C. Constancias, *J. Vac. Sci. Technol. B* March 1997, vol. 15, issue 2, 385-390.
[19] R. Meyer, A. Ghis, P. Rambaud, and F. Muller, *Technical Digest of Japan Display'86* 1986, 513.
[20] J. H. Cho, A. R. Zoulkarneev, J. W. Kim, J. P. Hong, J. M. Kim, 'Simulation and fabrication of Spindt type field emitter arrays' *Technical Digest of the 10th International Vacuum Microelectronics Conference*, Kyongju, Korea, 1997, p.401.
[21] M.W. Geis, N.N. Efremow, J.D. Woodhouse, M.D. McAleese, M. Marchywka, D.G. Socker and J.F. Hochedez, *IEEE Electron Dev Lett* 1991, 12, 456–459.
[22] M.W. Geis, J.C. Twichell, N.N. Efremow, K. Krohn and T. Lyszczarz, *Appl. Phys. Lett.* 1996, 68, 2294–2296.
[23] F.J. Himpsel, J.A. Knapp, J.A. van Vechten and D.E. Vechten, *Phys. Rev. B* 1979, 20, 624–627.
[24] G.A.J. Amartunga and S.R.P. Silva, *Appl. Phys. Lett.* 1996, 68, 2529–2531.
[25] B. F. Coll, J. E. Jaskie, J. L. Markham, E. P. Menu, A. A. Talin, P.von Allmen, Mater Res Soc Symp Proc 1998, vol. 498. Warrendale, PA: *Materials Research Society*, 185–196.
[26] S.Iijima, *Nature* 1991, 354, 56-58.
[27] D.S. Bethune, C. H. Klang, M. S. De Vries, G. Gorman, R. Savoy, J. Vazquez, *Nature* 1993, 363, 605-607.
[28] W. A. de Heer, A. Heer and D. Chatelain, *Science* 1995, 270, 1179–1180.
[29] N. Kumar, H. Schmidt and C. Xie *Solid State Technol* 1995, 38 (4), 71–72.
[30] W.B. Choi, D.S. Chung, J.H. Kang, H.Y. Kim, Y.W. Jim, I.T. Han, Y.H. Lee, J.E. Jung, N.S. Lee, G.S. Park and J.M. Kim, *Appl. Phys. Lett* .1999, 75, 3129–3131.
[31] K. A. Dean, et al., "Color Field Emission Display for Large Area HDTV", SID 2005 *International Symposium Digest of Technical Papers*, , May 2005, 1936-1939.
[32] W. B.Choi, D. S. Chung, J. H. Kang, H. Y. Kim, Y. W. Jin, I. T. Han, Y. H. Lee, J. E. Jung, N. S. Lee, G. S. Park, and J. M. Kim, *App Phys Lett* November 1999, 75 (20), 3129-3131.
[33] H. Ohsaki, and Y. Kokubu, *Thin Solid Films* 1999, vol. 351, issue 1-2, 1-7.
[34] I. Shah, *Physics World* June 1997, 45-48.
[35] Do-Hyung Kim, Hoon-Sik Jang, Sung-Youp Lee, Hyeong-Rag Lee, *Nanotechnology* 2004, 15, 1433-1436.
[36] C. Xie, and Y. Wei, IEEE Trans. *Electron Dev*. December 2003, vol. 50, no. 12, 2348-2352.
[37] R. H. Fowler and L. W. Nordheim, *Proceedings of the Royal Society of London* 1928, A119, 173.

In: Developments in Ceramic Materials Research
Editor: Dena Rosslere, pp. 261-279
ISBN 978-1-60021-770-8

Chapter 9

COLOURED $ZrSiO_4$ CERAMIC PIGMENTS

S. Ardizzone[1], C. L. Bianchi[1], G. Cappelletti[1], P. Fermo[2] and F. Scimè[1]

[1]Department of Physical Chemistry and Electrochemistry,
University of Milan, Via Golgi 19, 20133 Milan, Italy
[2]Department of Inorganic, Metallorganic and Analytical Chemistry,
University of Milan, Via Venezian 21, 20133 Milan, Italy

ABSTRACT

A sol-gel reaction starting from Si and Zr alkoxides, in water-ethanol mixtures, was employed to obtain praseodymium, vanadium and iron doped zirconium silicate powders (zircon). The reactions were performed by modulating both: a) the amount of metal salt in the starting mixture (Me/Zr molar ratio in the range 0.05-0.1) and b) the temperature of firing (600-1200°C). In the case of V-doped pigments, samples were synthesized also in the presence of a constant amount (0.26 salt/Zr molar ratio) of mineralizers (LiF, LiCl, NaF, NaCl, KF, KCl).

The samples were characterised by X-ray diffraction, SEM micrographs, specific surface area determinations and UV-Vis diffuse reflectance spectroscopy. XPS analyses were performed on V-doped zircon pigments by studying in particular the Zr 3d, Si 2p and V 2p regions. The colour of the pigments was characterized on the grounds of the CIE (Commission Internationale de l'Eclairage) standard procedure (CIE L*a*b* measurements). Results from the structural, morphological and optical characterisations are examined and cross-compared to produce a consistent picture of the key factors leading to the formation, growth and optical properties of the reaction products.

Keywords: *ceramic materials, metal doped-zircon pigments, mineralizers, sol-gel processes, optical properties, X-ray methods, XPS.*

INTRODUCTION

Zircon, $ZrSiO_4$, assumes a garnet-like structure in which guest metal ions can be incorporated to give coloured materials. Their colour is yellow, blue or pink when, respectively, praseodymium, vanadium or iron ions are introduced into the lattice [1-5]. Pigments based on zircon ($ZrSiO_4$) are widely used in ceramic industries because they offer superior stability at high temperatures and in corrosive environments. $ZrSiO_4$ pigments are important from an industrial point of view not only for their structural and chemical properties but also for the interesting tonalities of colour they may develop.

The principal structural unit of zircon is a chain of alternating edge-sharing SiO_4 tetrahedra and ZrO_8 triangular dodecahedra, characterized by the presence of empty octahedric cavities (Figure 1). The metal dopant can be accommodated into the zircon network in interstitial positions, it can substitute either Zr^{4+} or Si^{4+} in their lattice positions or it can form an encapsulated phase. In several cases controversial conclusions are reached in the literature about the actual location of the metal ion and its valence in the zircon lattice [2-16].

In the case of Pr-doped materials, the cations are generally assumed to form a solid solution with the zircon lattice but the actual valence of the dopant (either +3 or +4) has not been definitely established yet. The position occupied by Pr ions has not been clarified, either. In general Pr ions are considered to be located at the triangular dodecahedral positions [3,6,14,15] of Zr^{4+}, however Shoyama et al. [14] suggest that Pr(IV) may substitute for both Zr^{4+} and Si^{4+} of the zircon lattice. In the case of Pr-zircon pigments prepared by a sol-gel procedure [17] we have observed that Pr ions, besides being distributed into the host matrix, were present also in separate crystalline phases.

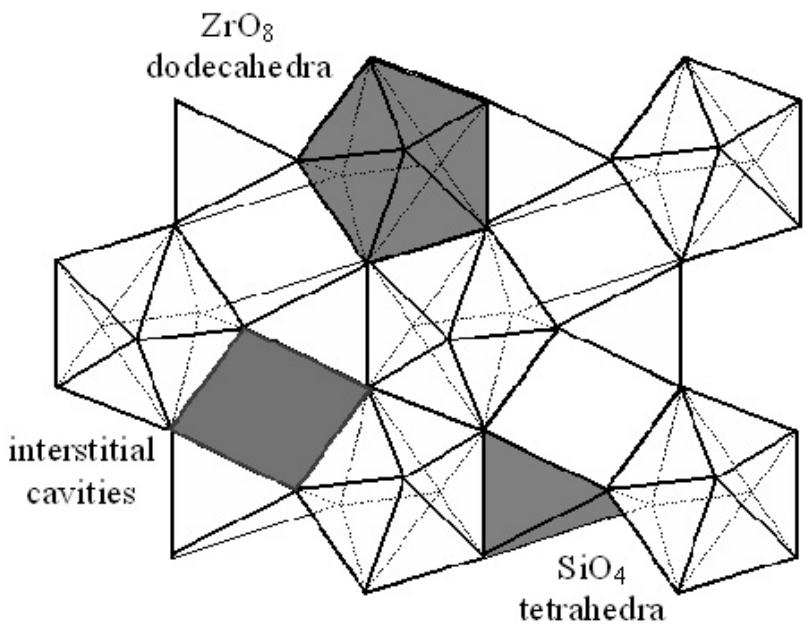

Figure 1. Zircon ($ZrSiO_4$) crystal lattice structure.

In fact separate Pr containing phases (either encapsulated into the host lattice or not) were appreciable in X-ray spectra in the case of the larger Pr amounts and EDX analyses showed, at the same time, a non homogeneous distribution of the metal.

For V-$ZrSiO_4$ pigments the actual location of vanadium in the zircon structure is still unclear and has been the subject of many studies, in some cases leading to controversial interpretations. Several authors suggest that V ions should substitute for Zr in the dodecahedral lattice positions [18,19]. Exactly the opposite conclusion was reached by Di Gregorio and de Waal [20,21] that indicated V^{4+} preferred the tetrahedral silicon site. A further possibility some workers have preferred is that both sites can be occupied to a significant extent [22,23]: Xiayou [22] and Chandley [23] have, in fact, reported very little difference in the energy of the V^{4+} occupying either of the two principal lattice sites. In the case of V-$ZrSiO_4$ prepared in our laboratory by a sol-gel procedure in the absence of mineralizers [24] we have observed, also on the grounds of the elaboration of XANES results, that for vanadium amounts lower than 0.05, the metal is prevailingly substituted to Si in the tetrahedral positions of the lattice, while for loadings larger than 0.05, additional V is only localized in the Zr^{4+} dodecahedral positions of the lattice.

In the case of iron, Tartaj et al. [4] suggest that the formation of a solid solution between the iron cations and the tetragonal zirconia lattice occurs before the formation of zircon. This process generates vacancies which favour the nucleation of zircon. The authors [4] suggest that after the zircon formation iron (III) segregates with the ensuing formation of hematite and that hematite is the only responsible of the red colour of the iron zircon pigment. The same authors have observed by XPS that the surface Fe/$ZrSiO_4$ ratio is comparable to the average iron content of the sample indicating that hematite is homogeneously distributed in the zircon matrix. In the case of Fe-$ZrSiO_4$ samples prepared in our laboratory by a sol-gel procedure [25] we have instead observed, by quantitative elaboration of diffuse reflectance spectra, the concomitant presence of both interstitial iron and hematite, in partial agreement with what reported by Berry et al. [7,8].

The presence in the literature of divergent results concerning various aspects of these systems is, at least in part, due to the manifold features of these materials, and to the close interplay between different parameters introduced by the preparative steps. In fact the adopted preparative route plays, in the present authors opinion, a key role in defining the final features of the pigments. Consistently with these considerations, Monros et al. [5] have recently shown that, in the case of coral-red zircon pigments, the conditions adopted for the sol-gel process and particularly the sequence of the iron addition to the reacting mixture lead to the formation of samples with different phase composition and colour.

In this work Pr-, V-, and Fe-doped $ZrSiO_4$ pigments were obtained by a common sol-gel path. The reaction, starting from Si and Zr alkoxides, in water-ethanol mixtures, was employed to obtain the xerogels which were thermally treated in the temperature range 600-1200°C. The role played by the addition of different mineralizers (LiF, LiCl, NaF, NaCl, KF, KCl) to the reaction mixture was investigated in the case of V-doped pigments which develop the desired blue colour only in the presence of an added salt.

X-ray diffraction data were refined by the Rietveld method and UV-Vis diffuse reflectance spectra were recorded for all samples. XPS analyses were obtained in the case of V-doped pigments to obtain indications on the localization of both mineralizer and metal dopant.

Results from the different characterisations, obtained on the three classes of pigments, are discussed and cross compared, with specific reference to the promoting effect played by the guest metal on the structural features of the material and to the optical and colour characteristics of the powders. In the case of V-doped pigments the role played by different mineralizers in promoting both the structure and the colour is discussed.

EXPERIMENTAL

All the chemicals were of reagent grade purity and were used without further purification; doubly distilled water passed through a Milli-Q apparatus was used to prepare solutions and suspensions.

Sample Preparation

The zircon samples were prepared by a previously reported sol-gel procedure consisting of two different hydrolysis steps [16]. At the beginning $Si(OC_2H_5)_4$ (0.20 mol) was added drop by drop to an aqueous solution containing variable amounts of the metal salt (Fe, Pr or V) previously stirred at 60°C for about 20 minutes in order to achieve the complete dissolution of the dopant ion. Then 0.35 mol of ethanol and 0.10 mol of reaction catalyst (HNO_3 or HCl depending on the counterion of the metal) were added to the mixture which was left under rapid stirring for 30 minutes (i.e. the time of the first hydrolysis step). Subsequently a solution of $Zr(OC_3H_7)_4$ (0.20 mol) and water was added to the mixture. The final suspension was kept under stirring at 60°C for 2 hours (i.e. the time of the second hydrolysis step). The product, cooled at room temperature, was dried in oven at 60°C and then the obtained xerogel was thermally treated at the selected temperature in the range 600–1200°C for 6 hours.

A first series of samples was prepared by using a variable Me/Zr molar ratio in the range 0.005-0.10.

A second series of samples was obtained, only in the case of V-doped pigments, by using a constant V/Zr molar ratio of 0.1 but adding different mineralizers (m) (LiF, LiCl, NaF, NaCl, KF, KCl) before the second hydrolysis step. The m/Zr molar ratio was kept constant at 0.26 for all the syntheses.

Sample Characterisation

Structural characterisation of the powders was performed by X-ray diffraction, using a Siemens D500 diffractometer, using Cu Kα radiation in the 10-80° 2θ angle range. The fitting program of the peaks was a particular Rietveld program [26,27], named QUANTO [28], devoted to the automatic estimation of the weight fraction of each crystalline phase in a mixture.

The peak shape was fitted using a modified Pearson VII function. The background of each profile was modelled using a six-parameters polynomial in $2\theta^m$, where m is a value from 0 to 5 with six refined coefficients.

Specific surface areas were determined by adsorption of N_2 at subcritical temperatures (classical BET procedure) using a Coulter SA 3100 apparatus.

The particle morphology was examined by scanning electron microscopy using a Cambridge 150 Stereoscan. SEM analyses were performed using a Hitachi 2400 scanning electronic microscope. Powder samples were coated with a thin gold layer deposited by means of a sputter coater.

Diffuse reflectance spectra were acquired in the Vis-NIR range from 350 to 1200 nm using a JASCO/UV/Vis/NIR spectrophotometer model V-570 equipped with a barium sulphate integrating sphere. A block of mylar was used as reference sample following a previously reported procedure [29]. The colour of the fired samples was assessed on the grounds of L*, a* and b* parameters, calculated from the diffuse reflectance spectra, through the method recommended by the Commission Internationale de l'Eclairage (CIE) [30]. By this method the parameter L* represents the brightness of a sample; a positive L* value stays for a light colour while a negative one corresponds to a dark colour; a* represents the green (-) $\rightarrow$ red (+) axis and b* the blue (-) $\rightarrow$ yellow (+) axis.

XPS spectra were obtained using an M-probe apparatus (Surface Science Instruments). The source was monochromatic Al Kα radiation (1486.6 eV). A spot size of 200 x 750 μm and a pass energy of 25 eV were used. The energy scale was calibrated with reference to the $4f_{7/2}$ level of freshly evaporated gold sample, at 84.00 ± 0.1 eV, and with reference to $2p_{3/2}$ and 3s levels of copper at 932.47 ± 0.1 eV and 122.39 ± 0.15, respectively; 1s level hydrocarbon-contaminant carbon was taken as the internal reference at 284.6 eV. The accuracy of the reported binding energies (BE) can be estimated to be ± 0.2 eV.

RESULTS

Pr-, V-, Fe-Doped Pigments

Structural and Morphological Aspects

The structural features of the three families of pigments (Pr-, V- and Fe-doped zircon) are first compared by considering samples prepared at an intermediate calcination temperature (1000°C). Figure 2 reports the comparison between the X-ray pattern of four samples obtained in the same experimental conditions with a Me/Zr molar ratio of 0.02. In order to obtain an accurate quantitative estimation of the phases present in the powder, the spectra of all samples have been fitted with the Rietveld program QUANTO; the results are reported as insets to the diffractograms. In the absence of the guest ion (Figure 2a) the sample shows a large quantity of amorphous phase and the only crystalline phases are monoclinic and tetragonal zirconia. No crystalline phases related to silica can be appreciated. Upon addition of praseodymium (Figure 2b), instead, tetragonal zirconia is the major component and the amorphous amount is reduced. No monoclinic ZrO_2 is appreciable. The presence of vanadium (Figure 2c) further promotes the crystal growth of the sample: the desired phase zircon ($ZrSiO_4$) is formed, although to a limited extent (about 10%) and ZrO_2 in the tetragonal form

is the major component. The phase compositionof Fe-$ZrSiO_4$ (Figure 2d) is intermediate between V- and Pr-doped samples, the presence of zircon being around 5%. In this case the presence of hematite, either present as an incapsulated phase or segregated can be appreciated.

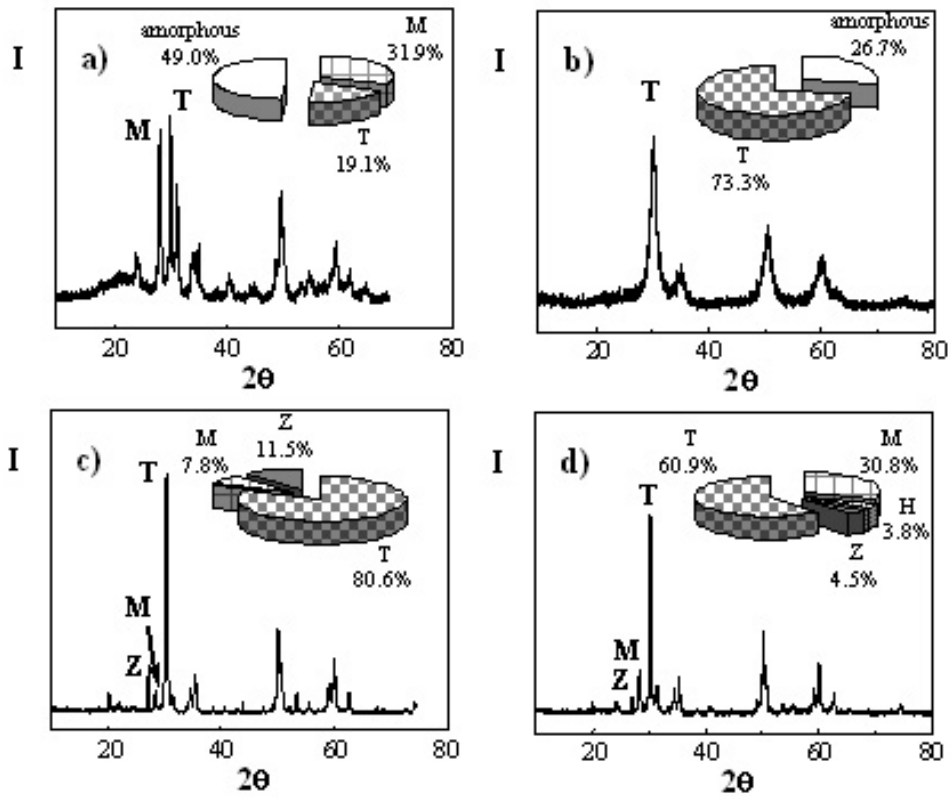

Figure 2. Powder X-ray diffraction lines of a) non doped, b) Pr, c) V, and d) Fe doped pigments at the same metal/Zr content (0.02 molar ratio) calcined at 1000°C. T and M: tetragonal polymorph and monoclinic zirconia (ZrO_2), respectively; Z: zircon ($ZrSiO_4$); H: hematite. Inset: the relative phase enrichment, by Rietveld refinement.

The role played by the metal on the promotion of the crystal growth and formation of the zircon lattice is apparent. This effect has been observed previously in the literature in the case of all the present metal dopants. In the literature the final formation of $ZrSiO_4$ is considered to occur first, by crystallization of a phase having the t-ZrO_2 structure followed by a phase transformation from t-ZrO_2 to m-ZrO_2 and, almost simultaneously, by the reaction between m-ZrO_2 and an amorphous silica rich phase, leading to zircon [31,32].

The direct cross-comparison between the effects produced by the three metals in samples obtained by the same preparative route is, instead, not commonly reported in the literature. From results in Figure 2, vanadium appears to be the best promoter of the structure and the promoting sequence is: V>Fe>Pr. The same sequence is maintained also at a higher calcination temperature (1200°C). Figure 3 reports the amount of zircon phase in the samples, obtained by quantitative elaboration of X-ray diffraction data, as a function of the metal loading. The comparison between the three series of pigments is striking.

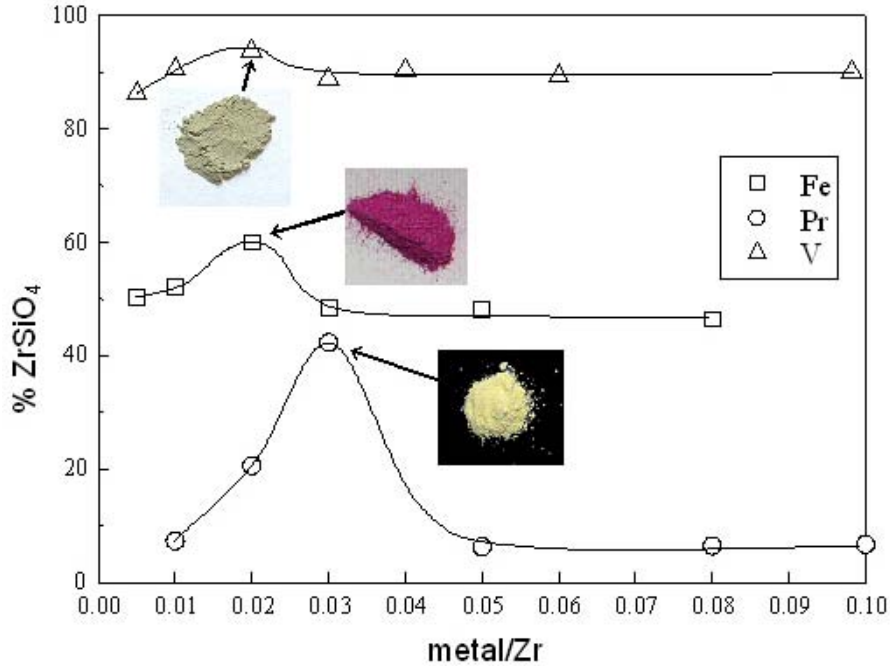

Figure 3. Zircon-phase mass per cent as a function of the metal/Zr content of pigments calcined at 1200°C. Inset: photographs of the pigment colours.

In the case of vanadium the amount of zircon phase ranges in any case around 90% and shows very little dependence on the metal loading. Fe-promoted samples show an average amount of zircon around 50% with a small maximum for Fe/Zr around 0.02. Samples promoted by Pr show, instead, a different trend. The amount of zircon in the samples first rises sharply and goes through a maximum (up to about 40%) for Pr/Zr around 0.03 and subsequently it levels off to low values (around 6%). The trend of the Pr- doped samples might suggest that up to Pr/Zr around 0.03, the guest metal might be present in a solid solution within the t-ZrO_2 lattice favouring nucleation and growth of the zircon structure. The 0.03 molar ratio might represent a solubility limit for the solid solution; larger Pr quantities might support the formation of different crystalline Pr containing phases (*e.g.* the phase $Pr_2Zr_2O_7$ appreciable into the 5, 8, 10% sample diffractograms) thus reducing the nucleating power of the metal.

The largely different effects produced by the three metal ions, on the structural features of $ZrSiO_4$, are not easily interpreted since the function of the guest ion is manifold, complex and not fully clarified. However, since, the metal cations are generally assumed to form a solid solution with the zircon lattice occupying either the tetrahedral silicon sites or the dodecahedral Zr positions, or even both, the matching of the sizes, between the guest metal ion and the ions in the lattice, is not a trivial fact. The size of a tetrahedral Si^{4+} is reported to be 0.40-0.54 Å, that of Zr^{4+} in the dodecahedral site 0.84-0.98 Å. The radius of V with a number of coordination 6 is 0.59 Å. Literature data show that upon doping with V, the unit cell volume of $ZrSiO_4$ expands [24]. This effect is interpreted as the result of substituting a larger ion (V^{4+}) for a smaller one (Si) in the lattice tetrahedral positions. The sizes of Fe and Pr are 0.645 and 1.013 Å respectively. It appears therefore that in the series V-Fe-Pr the size

of the ion increases progressively thus making the reticular substitution more difficult and shifted at higher temperatures. Figure 3 reports also, as inset, the photographs of the pigments, to show their actual colour. Both Fe- and Pr-doped powders show the desired pigment colour, red and yellow, respectively; V-doped zircon, instead, presents a dark green shade of colour which is not the desired blue. This argument will be resumed in the following in the discussing Figure 6 and in the subsequent part.

Figure 4 reports the specific surface areas of the precursors before the calcination step. The surface areas decrease progressively in passing from the un-doped sample to the metal doped with a sequence: Pr>Fe>V. This sequence represents, with an inverse trend, the same effects observed for the structural features. The "structuring" role of the metals, observed in the X-ray patterns, is mirrored by a change in the morphological features of the gel, which apparently becomes more compact and intertwined the more structure promoting the metal is. Consistent informations can be obtained by examining SEM micrographs of the pigments calcined at 1200°C. In the case of Pr-doped samples (Figure 5a) large shapeless aggregates, composed by rounded particles can be appreciated.

The most apparent feature in this micrograph is the presence of a covering layer on top of the particles. It must be recalled that in the case of this sample SiO_2 is still amorphous for about the 80 % of the initial amount. The aspect of the powder changes significantly in the case of Fe-doped samples (Figure 5b). No more "covering" effects are appreciable, possibly because in this sample the fraction of amorphous silica is much lower (about 40%). The particles are well defined (average size in the range of 100-200 nm), with a spheroidal or prismatic shape. In the case of V-doped pigments (Figure 5c) the morphology is remarkably different and shows the advanced growth of the V-doped pigment: the particles are much bigger, possibly aggregates of smaller ones, spheroidal or rounded off twins with a relatively large size distribution.

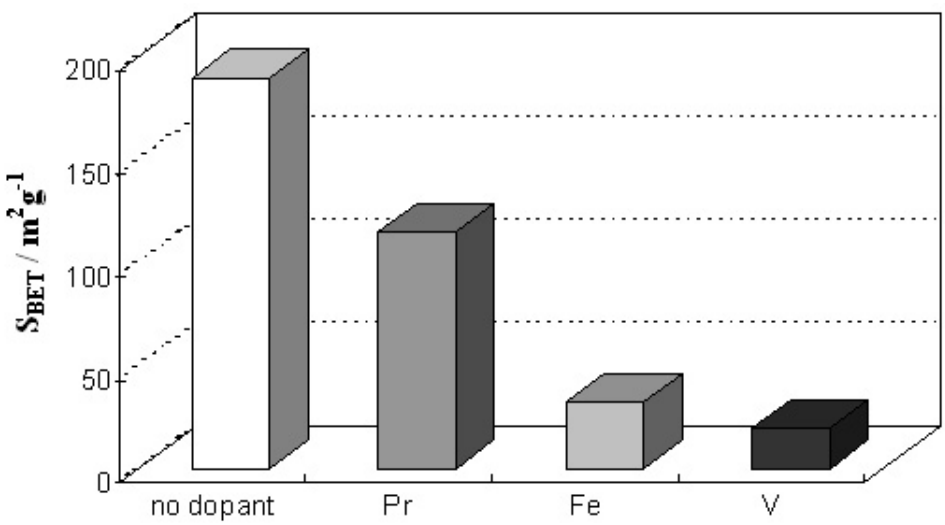

Figure 4. Trend of BET surface areas for undoped and doped (V, Pr, Fe) sol-gel precursors at 0.02 metal/Zr molar ratio.

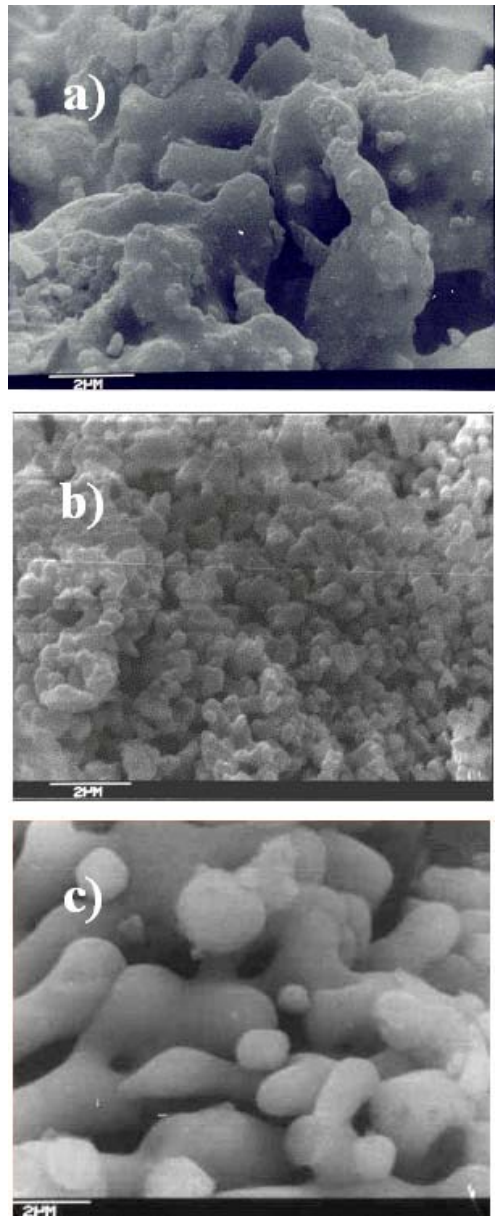

Figure 5. SEM images of 1200°C calcined samples a) $Pr_{0.02}$, b) $Fe_{0.02}$ and c) $V_{0.02}$.

Colour Properties

The diffuse reflectance spectra of the three families of pigments have been elaborated to give the L*, a*and b* parameters (CIE) to assess their colour (Figure 6), as a function of the dopant amount.

Pr- doped compounds are all grouped at the positive side of the b* axis, in correspondence of the large and positive L* values, indicating that all materials show a light yellow colour, not largely affected by the dopant content. In the case of iron as the guest metal, the pigments are red (positive a* axis) and their colour becomes more intense (lower

L* axis)with increasing the dopant content. The V-doped samples are all green (negative a* values) with a shade which becomes darker the larger the dopant amount.

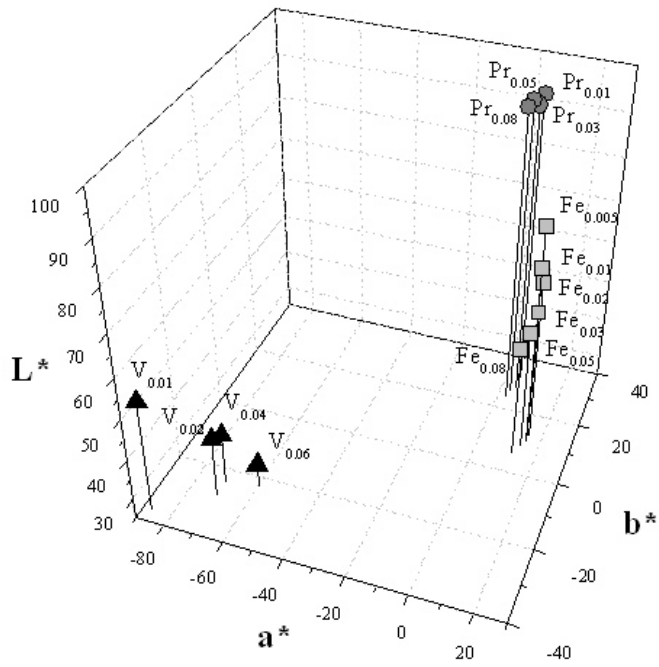

Figure 6. CIE L*a*b* parameters of 1200°C heated samples for the three guest ions, at variable metal/Zr content.

V-Doped Pigments. Role of Mineralizers

Structural Aspects

In the case of vanadium doped pigments several attempts are reported in the literature to stabilize the blue colour in the absence of mineralizers either by using the sol-gel process or adopting high temperatures [33]. Only for very low vanadium loadings and high calcination temperatures a light blue colour can be obtained. Otherwise when no mineralizers are added a greenish, unsatisfying, colour of the pigment is invariably obtained, as shownin Figure 4 and Figure 6.

Although it is generally acknowledged that the presence of a mineralizer, generally NaF, is necessary in order to achieve a satisfying shade of colour, the specific function of the salt has never been fully clarified. Eppler studied the role played by the mineralizer in the structure formation of $ZrSiO_4$ by means of the marker technique. He concluded that the acceleration of the zircon crystallization, produced by NaF, takes place through the formation of SiF_4 which volatilizes thus favouring the transport of Si species into the zirconia phase [1,12,13].

In the case of yellow Pr pigments, however, we have observed [17] that, besides the possible effect provoked by the fluoride anion, the cationic partner of the salt played a

relevant role in promoting the zircon structure, the promotion being more efficient for small monovalent cations and less efficient for large monovalent or divalent cations.

Monros [34] and Lusar [35] report, in the case of V-doped pigments, added with NaF, a promotion of the zircon structure at lower temperatures with respect to the absence of mineralizers and a contraction of the unit cell volume, consistently with results obtained by our group [24]. These authors interpret the contraction of the unit cell volume as due to the partial substitution of O^{2-} in the lattice by smaller F^- ions.

In this work the role played by several mineralizers, directly added to the sol-gel mixture was investigated. The alkaline cations sequence, both as fluorides and also as chlorides, was investigated to highlight the possible role of either (or both) cations and anions. All mineralizers were added at the constant molar ratio of 0.26 which, in the case of NaF, was found to be the amount best promoting the zircon structure (at 800°C) and also yielding the cell volume closer to the one of pure zircon [24]. To the authors best knowledge, no such systematic investigation is present in the literature.

The evolution of the zircon percentage with the temperature of calcination for the present samples obtained at constant vanadium content (V/Zr = 0.1) and in the presence of different mineralizers is shown in Figure 7.

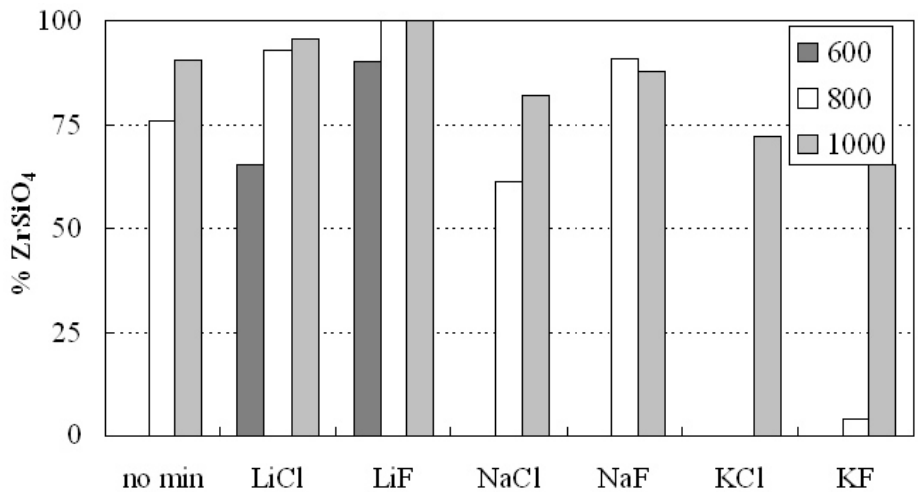

Figure 7. Zircon-phase mass per cent for $V_{0.10}$ doped pigments calcined at 600, 800, 1000°C as for different mineralizers (0.26 min/Zr molar ratio).

As a general trend the promotion of the zircon phase increases with increasing the temperature of calcination, both in the absence and in the presence of mineralizers. In the absence of mineralizers, although the fraction of zircon phase may be relevant, the colour never becomes blue. At 600°C the zircon phase is formed only in the presence of Li salts, to larger extents in the case of LiF which promotes the formation of the zircon phase up to 90%. At any temperature Li salts promote the zircon phase better than any other mineralizer; in the presence of LiF the zircon percentage is 100% both at 800 and 1000°C. The colour of the pigments promoted by Li salts is in any case light blue (see in the following Figures 10 and 11).

In the case of the Na salts, and also in the absence of mineralizers, the zircon phase starts to form only at 800°C, while for K salts the formation of zircon is significant only at 1000°C.

It is interesting to observe that the sample which shows the most intense blue colour (see in the following Figs. 10 and 11) is the sample obtained with NaF and calcined at 800°C, although the amount of zircon phase, for this sample, is lower than for the sample obtained at the same temperature in the presence of LiF. From the trend in Figs.7 and 8 the sequence of promotion of the zircon lattice follows for the cations Li>Na>K; the cation promotion trend follows the reverse trend of their crystallographic radii, Li<Na<K. The high mineralizing power of Li and Na salts could be explained by their possible incorporation in the zircon phase, occurrence which due to the large size of potassium could take place only at 1000°C. The lower intensity of the colour of the pigments prepared in the presence of Li salts with respect to the samples prepared with Na (see in the following Figs. 10 and 11) is possibly to be related to the competition between Li and V for the same positions in the zircon lattice (the two ions show very comparable radii for the same coordination). This argument will be resumed in the following when commenting XPS results.

Li and Na fluorides show better structuring properties with respect to the relative chlorides (Figure 8); in this case a possible improved fluidifying action played by the fluoride anions with respect to SiO_2 can be envisaged. No important differences can be appreciated between KF and KCl in the promotion of the $ZrSiO_4$ lattice. In this case the dominant effect is provoked by the larger size of the K^+ ion which delays the zircon formation with respect to Li^+ and Na^+ ions. For NaF and KCl the cation and the anion have very similar crystallographic radii for the same coordination number and might possibly bring about a better synergetic action between cation and anion.

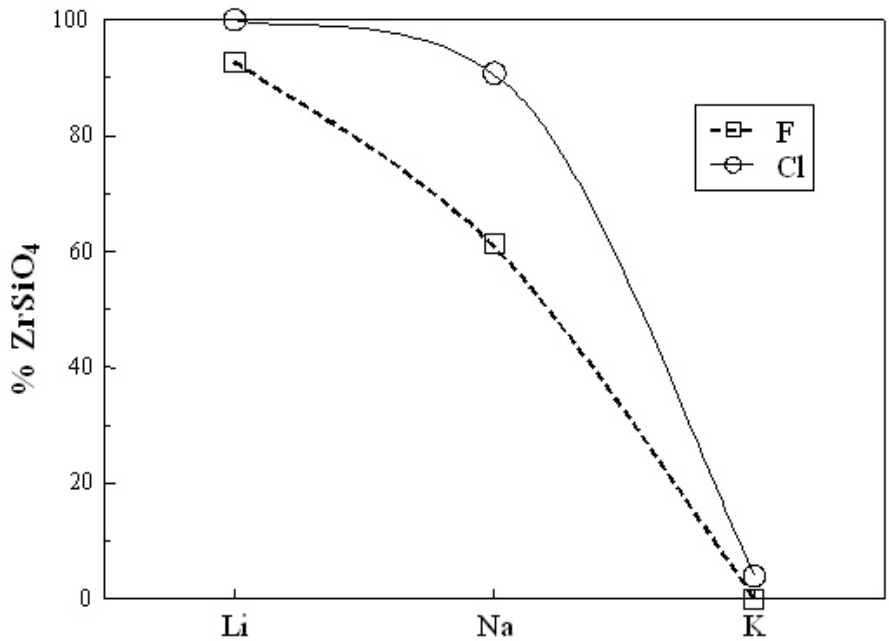

Figure 8. Zircon-phase mass per cent for $V_{0.10}$ doped pigments calcined at 800°C for the three alkali cations in the fluoride and chloride series.

XPS Analyses

The first aspect which can be considered in commenting XPS results is the change in XPS spectra of the V $2p_{3/2}$ region, depending on the final colour of the pigment. The green or yellow powders show the presence of two V components (Figure 9a), while the blue samples show a single component (Figure 9b). The components can be attributed to: i) 517.2 eV V^{5+}, ii) 516.5 eV V^{4+} and iii) 515.6 eV V^{3+}. A further aspect concerns the trend of the V/Zr atomic ratios reported in Table 1. In the case of samples obtained in the absence of mineralizers the observed V/Zr ratio is 0.2 and 0.3 at 800 and 1000°C respectively; these values, when compared with the V/Zr ratio of 0.1 adopted in the synthesis, indicate the occurrence of a certain degree of surface segregation of V with respect to the bulk. Also in the presence of Li salts the V/Zr ratio is around 0.2-0.3 and goes up to 0.6 in the case of LiF at 1000°C. In the case, instead, of the addition of the other mineralizers, the V/Zr ratio drops to values around 0.1 matching the stoichiometric value. These observations suggest that the addition of the mineralizers, all except Li salts, promote the incorporation of the V ion into the zircon lattice. In the case instead of Li salts, Li and V compete for the same positions in the lattice due to the close proximity of their sizes. Li salts therefore, on one side promote the formation of the zircon lattice but, on the other side, "throw out" V from the lattice positions thus making the colour of the pigment less intense.

The Si/Zr atomic ratios range for all the samples around the stoichiometric value of 1.0 except for samples $V_{0.1}$800 and $V_{0.1}$NaCl.800 in which the fraction of zircon is not very high and apparently ZrO_2 is segregated at the surface.

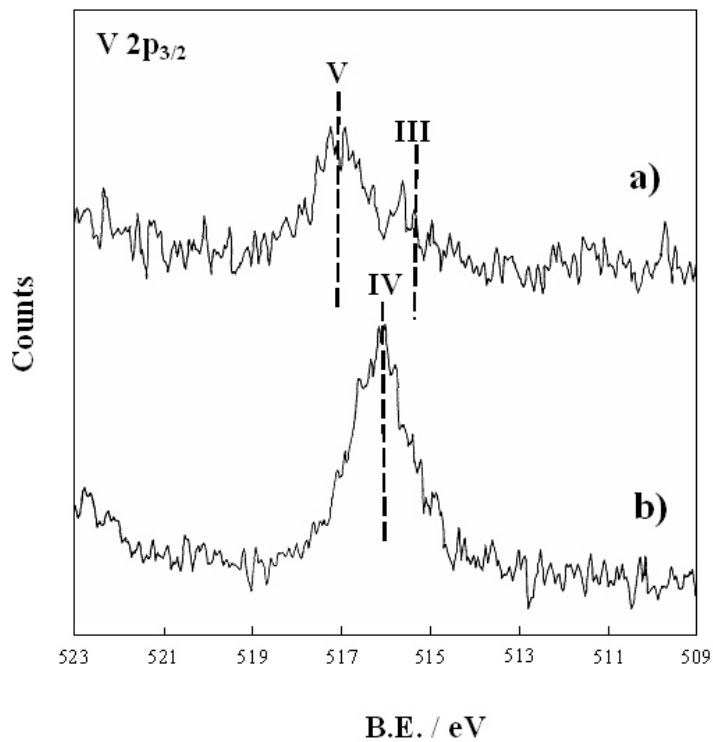

Figure 9. XPS V $2p_{3/2}$ region of a) $V_{0.10}$ and b) $V_{0.10}$NaF calcined at 800°C.

Table 1. XPS atomic ratios of V-doped pigments calcined at 800 and 1000°C with different mineralizers

sample	cation/Zr	V/Zr	Si/Zr
$V_{0.1}$800	-	0.20	0.7
$V_{0.1}$1000	-	0.30	1.0
$V_{0.1}$LiF.800	0.9	0.20	1.2
$V_{0.1}$LiF.1000	0.7	0.60	1.2
$V_{0.1}$NaF.800	0.6	0.08	1.0
$V_{0.1}$NaF.1000	0.7	0.09	1.2
$V_{0.1}$KF.800	0.5	0.09	0.9
$V_{0.1}$KF.1000	0.4	0.10	0.9
$V_{0.1}$LiCl.800	0.9	0.20	1.1
$V_{0.1}$LiCl.1000	1.6	0.30	1.0
$V_{0.1}$NaCl.800	0.6	0.06	0.7
$V_{0.1}$NaCl.1000	0.6	0.08	1.0
$V_{0.1}$KCl.800	0.7	0.20	0.9
$V_{0.1}$KCl.1000	0.5	0.10	1.1

The B.E. of Zr varies between 181.7 and 182.7 eV. These values pertain to Zr(IV) species in zirconium oxides [36]. The BE of the Si 2p peak range between 102.9 and 101.0 eV. Literature data report 103.2 eV for SiO_2 and 101.3 and 102.3 eV are reported for different silicates [36]. In the case of the present samples, not composed by pure zircon, the silicon peak may contain more than one component as the result of both silica and silicate species.

Optical Characterization

Figure 10 reports UV-Vis diffuse reflectance spectra acquired on samples calcined at 800°C containing the same V/Zr molar ratio (0.1) but different mineralizers. All the spectra show a similar shape in the considered region, except for the case of the samples obtained in the presence of KF and KCl. These powders have a zircon content scarce or null, and present a yellow colour, consequently they do not reflect light at low wavelengths. For all the other samples the zircon content is high and the colour vary from green (in the absence of mineralizer) to blue (sample obtained in the presence of NaF) while for the other pigments lighter shades of blue can be appreciated. The spectra are compared to the reference one obtained on the sample without mineralizer which is characterized by a green colour. The sample without mineralizer shows a minimum of reflectance at about 400 nm [35] due to V^{5+} not present in the blue samples. All the samples show: i) a signal at 640 nm [22] attributed to dodecahedral and tetrahedral V^{4+} coordination; ii) a signal at 780 nm [5] due to a shoulder-forbidden transition of V^{4+}. Unfortunately the signal attributed in the literature to dodecahedral V^{4+} (300 nm) [37] is not detectable in our spectra because of the instrumental measurement range.

The presence in the sample without mineralizer of V^{5+} is responsible for its green colour since pentavalent V compounds are yellow.

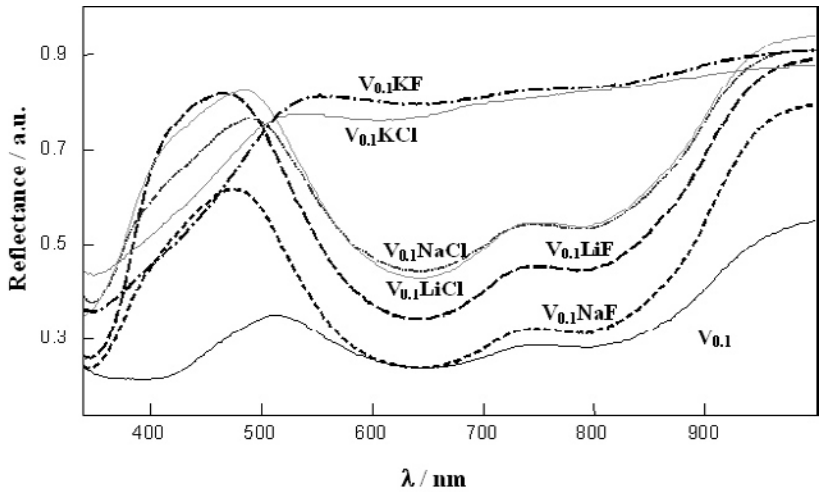

Figure 10. Diffuse reflectance spectra of 800°C samples at 0.10 V/Zr molar ratio, for different mineralizers.

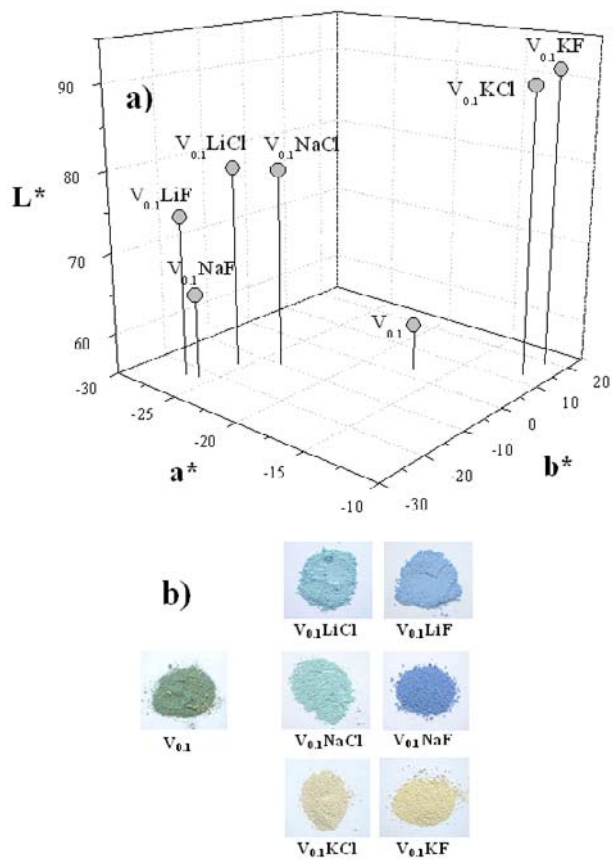

Figure 11. a) CIE L*a*b* parameters of $V_{0.1}$ samples calcined at 800°C with different mineralizers; b) photographs of the pigment colours.

Results in Figure 10 confirm that the blue colour is solely due to V^{4+} species. The role of the mineralizer can be considered to be that of stabilizing the tetravalent state of vanadium, assisting the charge balance in the zircon lattice.

From the diffuse reflectance spectra L*, a* and b* parameters have been calculated. The obtained data are reported in Figure 11. While the sample $V_{0.1}$ without the mineralizer is green (b* small and positive), in the presence of all the mineralizers, except for KF and KCl, the b* parameter is large and negative. The lowest values of b*, corresponding to best development of the blue colour, are obtained with NaF and LiF as the mineralizers. The lower L* value of NaF indicates that the colour is more intense. The large and positive b* values for samples added with potassium salts indicate that the samples show an intense (large L*) yellow colour.

CONCLUSION

Pr-, V-, and Fe-doped zircon pigments were prepared by combining a sol-gel reaction with calcinations steps in the range 600-1200°C. Investigations of the structural features of the calcined products show that all the three metals promote the formation of the zircon lattice at lower temperatures with respect to the un-promoted samples. The three metals show different promoting effects on the formation of the $ZrSiO_4$ structure at all temperatures. The promotion sequence, V>Fe>Pr, follows, inversely, the sequence of the ionic radius of the metal ions. In order to interpret this effect the localization of the metals in the zircon lattice must be discussed. In the case of V-doped pigments the addition of the guest metal was shown to provoke an expansion of the zircon lattice. This expansion is referred to the substitution of a smaller ion with a bigger ion. Considering the present three guest metal ions it can be observed that the size of V^{4+} is the closest one to that of Si in the tetrahedral sites and that the size of the ions increase progressively in passing from V to Pr. The present results allow therefore to draw two different conclusions with respect to this point. First, the sequence is to be related primarily to the matching between the size of the guest metal and that of the species in the lattice; second since the size of Zr in the lattice is much larger than that of Si, the above reported sequence apparently shows that for all the three metals the promoting effect is related to the occupation by the guest ion of the tetrahedral Si^{4+} positions.

The colour properties of the three groups of pigments differ not only intrinsically due to the different colours but also with respect to the colour dependence on the metal content of the samples. The colour of the V-doped samples is invariably green, and in no case assumes the desired blue shade. Apparently there is no direct relation, at least in the case of V-$ZrSiO_4$, between the formation of the zircon structure and the development of the blue colour. To promote the blue colour mineralizers (monovalent salts) must be added to the mixture.

The presence of alkaline metals (Li, Na, K) both as fluorides and as chlorides provokes important variations in the structural and optical features of the pigments. The promotion of the zircon structure follows the order Li>Na>K. In the case of the presence of Li salts zircon forms, to significant extents, even at 600°C. However the most intense blue colour of the pigment is not obtained in the presence of Li salts but by addition of NaF. The low intensity of the blue colour of the Li-promoted pigments is interpreted, on the grounds of XPS

determinations, as due to the competition between Li and V for the reticular positions in the zircon lattice.

ACKNOWLEDGEMENT

Financial support from the Ministry of Education, University and Research (MIUR, FIRST Funds) is gratefully acknowledged.

REFERENCES

[1] Eppler, RA. Resistance of porcelain enamels to attack by aqueous media: II, Equations to predict enamel durability. *Am. Ceram. Soc. Bull*., 1977 56(12), 1068-1070.

[2] Tartaj, P; Serna, CJ; Soria, J; Ocana, M. Origin of color in aerosol-derived vanadium-doped zirconia pigments. *J. Mater. Res*., 1998 13(2), 413-420.

[3] Ocana, M; Caballero, A; Gonzalez-Elipe, AR; Tartaj, P; Serna, CJ; Merino, RI. The effects of the NaF flux on the oxidation state and localization of praseodymium in Pr-doped zircon pigments. *J. Europ. Ceram. Soc*., 1999 19(5), 641-648.

[4] Tartaj, P; Gonzalez-Carrno, T; Serna, CJ; Ocana, M. Iron zircon pigments prepared by pyrolysis of aerosols. *J. Solid State Chem*., 1997 128(1), 102-108.

[5] Llusar, M; Calbo, J; Badenes, JA; Tena, MA; Monros, G. Synthesis of iron zircon coral by coprecipitation routes. *J. Mater. Sci*., 2001 36(1), 153-163.

[6] Badenes, JA; Vicent, JB; Llusar, M; Tena, MA; Monros, G. The nature of Pr-$ZrSiO_4$ yellow ceramic pigment. *J. Mater. Sci.*, 2002 37(7), 1413-1420.

[7] Berry, FJ; Jadon, D; Holloway, J; Smart, LE. Iron-doped zirconium silicate. Part 1. The location of iron. *J. Mater. Sci*., 1996 6(2), 221-225.

[8] Berry, FJ; Eadon, D; Holloway, J; Smart, LE. Iron-doped zircon: the mechanism of formation. *J. Mater.* Sci., 1999 34(15), 3631-3638.

[9] Carreto, E; Pina, C; Arriola, H; Barahona, C; Nava, N; Castano, V. Mossbauer study of the structure of Fe-zircon system. *J. Radioanal. Nucl. Chem*., 2001 250(3), 453-458.

[10] Airey, AC; Roberts, W. Advances in ceramic colors. *Ceram. Eng. Sci. Proc*., 1987 8(11-12), 1168-1175.

[11] Llusar, M; Badenes, JA; Calbo, J; Tena, MA; Monros, G. Environmental and colour optimisation of mineraliser addition in synthesis of iron zircon ceramic pigment. *Brit. Ceram. Trans*., 2000 99(1), 14-22.

[12] Eppler, RA. Kinetics of formation of an iron-zircon pink color. *J. Am. Ceram. Soc*., 1979 62, 47-49.

[13] Li, CH; Eppler, DR; Eppler, RA. Iron zircon pigments. *Ceram. Eng. Sci. Proc*., 1992 13(1-2), 109-118.

[14] Shoyama, M; Nasu, H; Kamiya, K. Preparation of rare earth-zircon pigments by the sol-gel method. *J. Ceram. Soc. Jap., Int. Edition* 1998 106, 279-284.

[15] Ocana, M; Caballero, A; Gonzalez-Elipe, AR; Tartaj, P; Serna, CJ. Valence and localization of praseodymium in Pr-doped zircon. *J. Solid State Chem*., 1998 139(2), 412-415.

[16] Ardizzone, S; Binaghi, L; Cappelletti, G; Fermo, P; Gilardoni, S. Iron doped zirconium silicate prepared by a sol-gel procedure. The effect of the reaction conditions on the structure, morphology and optical properties of the powders. *Phys. Chem. Chem. Phys*., 2002 4, 5683-5689.

[17] Del Nero, G; Cappelletti, G; Ardizzone, S; Fermo, P; Gilardoni, S. Yellow Pr-zircon pigments. The role of praseodymium and of the mineralizer. *J. Europ. Ceram. Soc*., 2004 24(14), 3603-3611.

[18] Demiray, T; Nath, DK; Hummel, FA. Zircon-vanadium blue pigment. *J. Eur. Ceram. Soc*., 1970 53(1), 1-4.

[19] Beltran, A; Bohm, S; Flore-Riveros, A; Igualada, JA; Monros, G; Andres, J; Luana, V; Martin Pendas, A. Ab initio cluster-in-the-lattice description of vanadium-doped zircon: analysis of the impurity centers in vanadium(4+)-doped zircon ($ZrSiO_4$). *J. Phys. Chem.*, 1993 97(11), 2555-2559.

[20] Di Gregorio, S; Greenblatt, M; Pifer, JH; Sturge, MD. An ESR and optical study of vanadium(4+) ion in zircon-type crystals. *J. Chem. Phys*., 1982 76(6), 2931-2937.

[21] de Waal, D; Heyns, AM; Pretorius, G; Clark, RJH. Raman spectroscopic investigations of $ZrSiO_4$:V^{4+}, the blue zircon vanadium pigment. *J. Raman Spectr*., 1996 27(9), 657-662.

[22] Xiayou, H; Gui-Ku, B; Min-Guang, Z. The study of the optical and the EPR spectra of vanadium(4+) in zircon-type crystals. *J. Phys. Chem. Solids*, 1985 46(6), 719-720.

[23] Chandley, P; Clark, RJH; Angle, RJ; Price, GD. Site preference of vanadium doped into zirconium silicate and germanate and of terbium doped into $ZrGeO_4$. *J. Chem. Soc. Dalton Trans.*, 1992 9, 1579-1584.

[24] Ardizzone, S; Cappelletti, G; Fermo, P; Oliva, C; Scavini, M; Scimè, F. Structural and spectroscopic investigations of blue, vanadium-doped $ZrSiO_4$ pigments prepared by a sol-gel route. *J. Phys. Chem. B*., 2005 109(47), 22112-22119.

[25] Cappelletti, G; Ardizzone, S; Fermo, P; Gilardoni, S. The influence of iron content on the promotion of the zircon structure and the optical properties of pink coral pigments. *J. Europ. Ceram. Soc*., 2005 25(6), 911-917.

[26] McCusker, LB; Von Dreele, RB; Cox, DE; Louer, D; Scardi, P. Rietveld refinement guidelines. *J. Appl. Cryst*., 1999 32(1), 36-50.

[27] Hill, RJ; Howard, CJ. Quantitative phase analysis from neutron powder diffraction data using the Rietveld method. *J. Appl. Cryst*., 1987 20(6), 467-474.

[28] Altomare, A; Burla, MC; Giacovazzo, C; Guagliardi, A; Moliterni, AGG; Polidori, G; Rizzi, R. Quanto: a Rietveld program for quantitative phase analysis of polycrystalline mixtures. *J. Appl. Cryst*., 2001 34(3), 392-397.

[29] Borgia, I; Brunetti, B; Mariani, I; Sgamellotti, A, Cariati, F, Fermo, P; Mellini, M; Viti, C; Padeletti, G. Heterogeneous distribution of metal nanocrystals in glazes of historical pottery. *Appl. Surf. Sci*., 2002 185(3-4), 206-216.

[30] CIE, Recommendations on Uniform Colour Spaces, *Colour Difference Equations, Psychometrics Colour Terms*. Supplement n° 2 of CIE Publ. No 15 (EI-1.31) 1971, Bureau Central de la CIE, Paris 1978.

[31] Torres, FJ; Folgado, JV; Alarcon, J. Structural evolution and vanadium distribution in the preparation of V^{4+}-$ZrSiO_4$ solid solutions from gels. *J. Am. Ceram. Soc*., 2002 85(4), 794-799.

[32] Domenech, A; Torres, FJ; Alarcon, J. Electrochemistry of vanadium-doped $ZrSiO_4$: Site-selective electrocatalytic effect on nitrite oxidation. *Electrochim. Acta*, 2004 49(26), 4623-4632.

[33] Tartaj, P; Serna, CJ; Ocana, M. Preparation of blue vanadium-zircon pigments by aerosols hydrolysis. *J. Am. Ceram. Soc*., 1995 78(5), 1147-1152.

[34] Monrós, G; Carda, J; Tena, MA; Escribano, P; Sales, M; Alarcón, J. Different kinds of solid solutions in the vanadium(V) oxide-zirconium orthosilicate-sodium fluoride system by sol-gel processes and their characterization. *J. Europ. Ceramic Soc*., 1993 11(1), 77-86.

[35] Lusar, M; Vicent, JB; Badenes, J; Tena, MA; Monros, G. Environmental optimization of blue vanadium zircon ceramic pigment. *J. Eur. Ceram. Soc*., 1999 19(15), 2647-2657.

[36] Moulder, JF; Stickle, WF; Bomben, KD. *Handbook of X-ray Photoelectron Spectroscopy*, Perkin-Elmer, Eden Praire, 1992.

[37] Valentin, C; Munoz, MC; Alarcon, J. Synthesis and Characterization of Vanadium-Containing $ZrSiO_4$ Solid Solutions from Gels. *J. Sol-Gel Sci. Technol*., 1999 15, 221-230.

INDEX

D

E

F

G

H

I

J

K

L

M

N

O

P

Q

R

S

T

U

V

W

X

Y

Z